De aanhechting van metaaldruppels aan vaste deeltjes in slakken:
een gecombineerde faseveld-experimentele aanpak

Metal Droplet Entrainment by Solid Particles in Slags:
A Combined Phase Field-Experimental Approach

Inge Bellemans

Promotoren: prof. dr. ir. K. Verbeken, prof. dr. ir. N. Moelans
Proefschrift ingediend tot het behalen van de graad van
Doctor in de ingenieurswetenschappen: materiaalkunde

UNIVERSITEIT
GENT

Vakgroep Materialen, Textiel en Chemische Proceskunde
Voorzitter: prof. dr. P. Kiekens
Faculteit Ingenieurswetenschappen en Architectuur
Academiejaar 2016 - 2017

ISBN 978-94-6355-004-8
NUR 971
Wettelijk depot: D/2017/10.500/39

Examination Board

prof. dr. ir. Kim Verbeken, promotor

Ghent University

prof. dr. ir. Nele Moelans, promotor

KU Leuven

prof. dr. ir. Gert De Cooman

Chairman, Ghent University

prof. dr. ir. Dagmar D'hooge

Ghent University

prof. dr. ir. Francisco Antonio Gilabert Villegas

Ghent University

prof. dr. ir. Nele De Belie

Ghent University

prof. dr. ir. Yann Le Bouar

CNRS/ONERA, Paris

dr. ir. Muxing Guo

KU Leuven

dr. ir. Tijl Crivits

Umicore R&D, Olen

Preface

This dissertation is the result of an intense and instructive period. The writing of this thesis was a solo mission and is now finished, but it could never have been accomplished without the valuable help provided by many people, which I try to acknowledge in the following lines, with the risk of forgetting somebody, to whom I herewith apologize.

I wish to express my gratitude to all members of the jury for reading this manuscript and the fruitful discussions. I also wish to acknowledge the Research Foundation - Flanders (FWO) for the support.

Ik zou graag mijn promotoren prof. Kim Verbeken en prof. Nele Moelans willen bedanken voor hun ondersteuning, vertrouwen en interesse, voor de begeleiding en de nuttige discussies. Kim, bedankt voor de altijd-openstaande deur, het vertrouwen dat je mij schonk op vele vlakken en alle ervaringen die je mij liet meemaken. Nele, bedankt om me te willen introduceren in de wereld van het modelleren - waar ik tot voor de start van dit doctoraat niet mee bekend was - bedankt om met veel geduld mijn vragen over datzelfde modelleren te willen beantwoorden en steeds met heel kritische zin mijn werk te lezen.

Gedurende dit doctoraat had ik de kans om zowel in Zwijnaarde (UGent), als MTM (KU Leuven) en Umicore R&D Olen aan de slag te gaan. Omdat ik op al deze werkplekken op heel veel hulp kon rekenen, wil ik graag al deze mensen bedanken.

In KU Leuven bedank ik graag prof. Bart Blanpain omdat ik de CSLM-apparatuur kon gebruiken voor enkele experimenten. Joris Van Dyck, bedankt voor de praktische hulp met diezelfde CSLM-opstelling. Lennart Scheunis, Lieven Pandelaers and Jingjing Liu, thank you for introducing me to Chemapp and its wide range of possibilities. Nico Vervliet en prof. Lieven Delathauwer, bedankt voor het geduld en de interessante discussies bij het uitwerken van een tensorenontbinding eenmaal bleek dat de thermodynamische data van een slak zich niet in een enkele vergelijking laten gieten.

Onder de noemer “vroeger KU Leuven en nu Umicore”: Jeroen Heulens. Jouw model was schitterend om van te kunnen starten. Je angst voor het vinden van fouten was ongegrond. Ik heb een immense bewondering voor jouw werk en die bewondering is enkel gegroeid eenmaal ik zelf zaken begon aan te passen aan de implementatie van het model. Het zit schitterend in elkaar.

In Umicore R&D Olen heb ik enkele smelt experimenten kunnen uitvoeren, waarvoor ik Maurits Van Camp uitdrukkelijk dank. Daarnaast hebben Saskia Bodvin en Danny Leysen me steeds met raad en daad bijgestaan en zorgde de rest van het team voor een ongelooflijk goede sfeer.

Luc Coeck van Umicore R&D wil ik expliciet bedanken, samen met prof. Marc Verhaege om me tijdens mijn opleiding te laten inzien dat het niet erg is als je thermodynamica leuk vindt. Jullie zijn de reden dat ik voor materiaalkunde heb gekozen en ik heb er nog geen moment spijt van gehad (behalve af en toe tijdens de examenperiodes, maar dat sloeg eigenlijk meer op het studeren zelf).

Evelien De Wilde, je was eerst mijn stagebegeleidster, dan mijn thesisbegeleidster, uiteindelijk mijn collega en nu mijn Umicore-contactpersoon. Ik ben heel blij jou een goede vriendin te mogen noemen. Evelien, super bedankt om me zo veel en zo goed te begeleiden, bedankt om me als collega (en nadien ook nog) vertrouwen te geven als ik het nodig had en nu om voor de nodige afleiding te zorgen op momenten dat dat welkom is. Ik hoop dat we nog lang kunnen blijven samenwerken en samen naar huis kunnen rijden.

Preface

Tijl Crivits wil ik bedanken voor de frisse ideeën die hij lijkt te putten uit een bodemloos vat. De investering van die paar taartjes zoveel jaar geleden heeft zichzelf al tienduizend keer terugbetaald. Je gaf me vaak een andere invalshoek als ik ergens vast zat of begon zelfs mee te redeneren (ook al was het bijna bedtijd in Australië) en ook al wist je de details van het probleem niet.

Tijdens mijn doctoraat heb ik de kans gehad om enkele studenten te begeleiden tijdens hun bachelor- of thesiswerk: Jorn Vande Sande, Vincent Cnockaert, Nick Van Bossche en Gerben De Cleene. Alhoewel ik niet bij iedereen thuis was in het onderwerp, wil ik jullie graag bedanken voor de aangename samenwerking. Bij Jorn en Vincent was het onderwerp iets meer aan het mijne gerelateerd en jullie wil ik dan zeker ook bedanken voor de inhoudelijke discussies.

Verder wens ik ook mijn collega's en ex-collega's van de vakgroep te bedanken voor leuke momenten en goede sfeer in Zwijnaarde. Linsey, Babs, Elien, Line, Tom, Emilie, Aurélie, Vincent, Lisa, Tim, Joachim, Frederik, Stefan, Sam, Mathijs, Siebe, Ives, Mathias, Klaas, … bedankt voor de toffe babbels, de soms uitdagende vragen en de hulp bij mijn vragen. A special thanks to my office mates Joanna and Edwin for the great atmosphere and all the cookies.

Daarnaast wil ik zeker mijn familie en vrienden bedanken voor hun onvoorwaardelijke steun en vertrouwen, in het bijzonder Tom & Ingeborg, Bram & Scharon & Febe, Martine & Rudy. Bedankt om voor de nodige afleiding te zorgen en mijn leven kleur te geven ;-).

Tot slot, zou ik graag de drie personen die de fundamenten van mijn leven zijn extra bedanken en eigenlijk wil ik dit werk aan hen opdragen. Mijn ouders hebben mij steeds alle kansen gegeven en zonder hen zou ik niet de persoon zijn die ik nu ben of staan waar ik nu sta. Ik wil jullie zeker zeggen dat ik vind dat jullie mij met de juiste waarden en normen hebben afgezet als mens en hoop oprecht dat ik jullie trots kan maken.

Mama, zonder twijfel de persoon die me de belangrijkste lessen van mijn leven heeft geleerd en die me heeft leren ontstressen (want geloof me vrij, dat was nodig). Het feit dat mensen mij vaak als heel gestructureerd omschrijven, kan ik volledig aan jou toedichten.

Papa, het aantal quotes dat ik aan jou ontleen is eindeloos. Bedankt om me te leren tuinieren, koken, humor te appreciëren en me te introduceren in de wonderen van kaliumpermanganaat.

Ward, ik wil je bedanken voor je onvoorwaardelijk steun en liefde. Jij was steeds een luisterend oor als ik dat nodig had, ook al was 'de oplossing van mijn doctoraat' volgens jou batterijzuur. De 'kick-push'-eend heeft me zonder twijfel door mijn 5 jaar studies en 4 jaar doctoraat geholpen. Daarenboven heeft de zin 'zou je dit niet in een 3 veranderen' vreemd genoeg meermaals voor een doorbraak in mijn doctoraat gezorgd. Ik kan niet in woorden uitdrukken wat je voor mij betekent. Thuis is waar we samen zijn. Ik hou van je.

Bedankt allemaal !

Inge Bellemans

Summary

At present, a higher demand on a lot of metals exists, but the quantity and purity of the ores decreases. The amount of scrap, on the other hand, increases and thus, recycling becomes more important. Besides recycling, there is a continuous drive to improve and optimize existing processes in extractive and recycling metallurgy from a sustainability point of view. One of the main difficulties of the overall-plant yield are metal losses in slags, in both primary and secondary metal production. In general, an increased understanding of the fundamental mechanisms governing these losses could help to further improve production efficiencies.

At this moment, it is generally accepted that two types of metal losses exist: chemical losses and mechanical losses. Chemical losses refer to the dissolution of metal in the slag and are thermodynamically determined. Mechanical losses are entrained metal droplets which do not settle and are not collected in the underlying metal phase. In general, there are four main reasons for mechanical entrainment of metals in slag:

I. entrainment due to furnace charging or slag tapping
II. precipitation of metal from the slag due to temperature fluctuations or chemical reactions
III. gas-producing reactions dispersing the metal into the slag phase when bubbles cross the slag-metal interface
IV. attachment of metal droplets to solid particles in the slag phase which hinders their sedimentation

The first three reasons have been studied extensively in literature. The fourth reason, however, has only been studied recently in a systematic way to obtain knowledge regarding the mechanisms responsible for the interaction. In order to further increase the knowledge on this interaction, this doctoral work investigates the phenomenon further from a fundamental point of view with a combined modelling – experimental approach. At first, a binary model was used to investigate the growth, the wetting behaviour and attachment of the metal droplets. Then, two types of experiments were conducted in limited-component copper-containing systems, illustrating the combined origin of the attachment. Finally, as the experiments showed that the solid spinel particles grew aside metal droplets, the growth of spinel particles in a quaternary oxide system was investigated with a multicomponent phase field model which was coupled to a thermodynamic database. The following paragraphs illustrate the various results and observations from these simulations and experiments.

At first, a model with limited complexity was implemented. The model describes a solid-liquid hypothetical O-M binary system to simulate the metal droplet formation and growth in slags with non-reacting solid particles. This model captures the important features of the droplet formation and growth, but with reasonable simulation and computational requirements. The model was used to investigate the influence of the interfacial energies, the initial supersaturation of the oxidic liquid, the particle morphology, the initialization, the movement of the particle and the speed of this movement of the particle.

The simulations showed that the attached droplets do not have preferred positions, as various places with several configurations and variations in time were encountered. Depending on the interfacial energies, four regimes were observed: no wettability of the metal on the particle, low wettability, high wettability and full wetting. The use of a higher initial supersaturation generally resulted in a

higher metal fraction in the system, but the effect of the initial supersaturation on the fraction of attached metal was not fully conclusive and also varied with time.

As the fraction of solid particles in the system decreased, a lower metal fraction was attached to the solids. In the case of low wettability, the amount of attached metal did not increase with an increasing perimeter per area solid particle, even though the number of available positions for the metal increased. For high wettability, on the contrary, the amount of attached metal increased for an increasing perimeter per area.

The model was also extended to consider realistic microstructures based on actual micrographs of the solid particles. Moreover, the origin of the attachment was investigated by comparing two initialization methods for the metal droplets: by spinodal decomposition of a supersaturated liquid and a method with random positioning of the droplets. Previous work by De Wilde et al. [1–3] resulted in the hypothesis of two possible origins for the attachment: a reactive and a non-reactive origin. The spinodal initialization corresponded to a practical situation where the droplets are formed by a reaction nearby (and possibly together with) the spinel particles, whereas the random initialization corresponded to the situation where the droplets and particles are formed separately and then mixed randomly in the slag. Both initialization methods were considered for two wettability regimes: no and low wettability. In the non-wetting case, the spinodal initialization gave microstructures with the best correspondence with the experiments, but in the low wettability case, the simulation results of both initialization methods corresponded well with the experimental system.

An initial drawback of the model was the absence of any convection or movement of the particles with respect to the fluids in the system, as the latter is clearly present in the real system. Therefore, the existing phase field model was extended to consider rigid body motion of the solid particles in the liquid slag. For this, the Navier-Stokes equation for fluid flow were not solved, but an equation was used to move the phase field profiles in space, resulting in the displacement of the particle with respect to the slag. The influence of this rigid body motion on the wetting regimes as well as on the resulting microstructures was investigated.

Regarding the amount of attached metal, no actual trends could be observed for a relatively slow movement of the solid. At no wettability, the microstructures showed that the rigid body motion could either ‘pick up’ droplets, hereby increasing the amount of attached metal, or it could lose an already attached metal droplet. The low wettability case was similar, but the loss of an already attached droplet was not observed. At higher wetting regimes and full wetting, the influence of the rigid body motion seemed to be smaller, as the attachment was more determined by the interfacial energies and the metallic phase ‘followed’ the solid particle when it moved. The apparent contact angle of the metal was larger when rigid body motion was present, which corresponds to a lower wettability. Thus, due to the motion of one phase with respect to the others, it is possible that actually, i.e. based on only the interface energies, a higher wetting regime is present in the system than based on the observed contact angle.

Afterwards, the speed of movement of the solid particles was varied. This study showed that there was a trade-off between the speed of the movement of the liquid metal, which depends on the attraction of the metal towards the solid particle and is determined by the interfacial energies, and the speed of the movement of the solid particle, which we varied. In the low and high wettability regimes, for slow solid motion, the interfacial energies had the upper hand, but for faster movement,

the metal could not keep up with the solid. Thus, the amount of metal decreased for faster movement. For the non-wetting case, metal droplets coincidentally present on the path of the solid particle got attached, but the solid particle movement could similarly decrease the amount of the attached metal by moving away from the metal droplet. For the full wetting case, on the contrary, the interfacial energy attraction of the metal to the solid was so large that even the largest velocity did not decrease the amount of attached metal.

Moreover, the two abovementioned initialization methods for the liquid metal droplets were considered in microstructures based on real experimental spinel microstructures which also moved with respect to the liquid phases. For the real-micrograph-based simulations, the simulations in the absence or presence of rigid body motion for the spinodal initialization corresponded better to the experimentally observed micrographs than the ones with the random initialization.

To be able to compare the simulations to experimental observations, we also performed two types of experiments, based on the methodology developed by De Wilde et al. [4], to investigate the possible origin of the attachment. Previous experiments with synthetic slags provided insights into this interaction and resulted in two possible mechanisms behind this interaction:

- separately formed droplets and spinel particles get attached to each other due to agitation of the slag and metal phases
- the spinel particles form by a chemical reaction together with a new droplet or alongside a droplet that was already present in the system

One of the experiments inspiring these theories, was an adapted sessile drop experiment investigating the three phases involved (slag and copper on top of a spinel substrate) [3]. During the experiment, the slag phase positioned itself between the metal droplet and the solid spinel substrate. For this to take place, the slag and metal phase seemed to ‘coalesce’. Afterwards, small metal droplets attached to small solid particles within the large slag droplet were observed. However, it is possible that these small metal droplets attached to small solid particles within the slag were formed during the ‘coalescence’ of slag and metal in this experiment.

To verify in more detail whether the small entrained metal droplets were formed due to a reaction or due to this coalescence, an inert tracer element (Ag) was added to the metallic phase in similar experiments during this doctoral study. The small entrained metal droplets within the slag droplet contained Ag, but in very low amounts with respect to the added amount of Ag in the Cu-Ag alloy.

Moreover, a smelting experiment was executed in a system with as few elements as possible, to be comparable to the simulations. The FeO-Fe_2O_3-SiO_2-Al_2O_3-Cu_2O slag was first subjected to an oxidative atmosphere and then to a reductive atmosphere. During the first stage, the metallic copper in the system dissolved into the slag and very few attached metal droplets could be observed. During the reductive stage, however, the concurrent formation of metal droplets and spinel particles, which were attached to one another, was clearly observed. Moreover, as the reductive stage continued, both the spinel particles and the metal droplets grew and remained attached to each other.

The results of both experiments indicate that the entrained metal droplets were formed due to a sequential combination of the two origins: first, very small metal droplets were dispersed in the slag phase, due to the emulsification process or the mixing stage. Then, these metal droplets acted as nucleation sites for the Cu-spinel reactive formation.

The experiments confirmed that a chemical reaction might lay at the origin of the attachment. But the binary model assumed non-reactive solid particles. Therefore, the phase field model used by Heulens [5], considering the isothermal solidification of slags, was extended to consider multicomponent systems to investigate the facetted growth of spinel solids in a quaternary oxide system. It was observed that the growth of the solid spinel phase was influenced to a large extent by the presence of an open boundary in contact with an atmosphere at a specific p_{O2}.

In conclusion, this doctoral work investigated metal droplet entrainment by solid particles in slags with a combination of two experimental set-ups and two phase field models. The binary model with limited complexity already clarified our view of the interaction between metal droplets and non-reacting solid particles to a great extent. For example, the fact that the movement of one phase with respect to the others influenced the apparent wetting regime is very interesting for the interpretation of experimentally obtained results. Moreover, the two different types of experiments confirmed that a chemical reaction might lay at the origin of the attachment, but that it requires nucleation sites in the form of metal droplets before it takes place. However, the first phase field model assumed non-reactive solid particles. Thus, a model concerning the growth of the solid phase in a realistic quaternary oxide system was also considered. Future work needs to consider the interaction of reacting metal droplets with reacting solid particles in a realistic liquid slag.

References

[1] E. De Wilde, I. Bellemans, L. Zheng, M. Campforts, M. Guo, B. Blanpain, N. Moelans, K. Verbeken, Origin and sedimentation of Cu-droplets sticking to spinel solids in pyrometallurgical slags, Materials Science and Technology. 32 (2016) 1911–1924. doi:10.1080/02670836.2016.1151998.

[2] E. De Wilde, I. Bellemans, M. Campforts, M. Guo, B. Blanpain, N. Moelans, K. Verbeken, Sessile drop evaluation of high temperature copper/spinel and slag/spinel interactions, Transactions of Nonferrous Metals Society of China. 26 (2016) 2770–2783. doi:10.1016/S1003-6326(16)64344-3.

[3] E. De Wilde, I. Bellemans, M. Campforts, M. Guo, B. Blanpain, N. Moelans, K. Verbeken, Investigation of High-Temperature Slag/Copper/Spinel Interactions, Metall and Materi Trans B. 47 (2016) 3421–3434. doi:10.1007/s11663-016-0805-8.

[4] E. De Wilde, Methodology Development and Experimental Determination of the Origin of Sticking Copper Droplets in Pyrometallurgical Slags, PhD thesis, Ghent University, 2015.

[5] J. Heulens, Isothermal Crystallization of Metallurgical Slags: Phase Field Simulations Combined with In Situ Experiments (Isotherme kristallisatie van metallurgische slakken: faseveldsimulaties in combinatie met in situ experimenten), PhD thesis, KU Leuven, 2011. https://lirias.kuleuven.be/handle/123456789/318339.

Samenvatting

De vraag naar de meeste metalen blijft toenemen, maar de hoeveelheid en zuiverheid van de beschikbare ertsen verminderen echter. Er blijft ook een grote hoeveelheid schroot beschikbaar en dus wordt recycleren steeds belangrijker. Naast recycleren is er ook een continue drijfveer om bestaande processen in de extractieve en recyclage metallurgie te verbeteren en te optimaliseren vanuit een duurzaamheidsstandpunt. Eén van de grootste problemen in de globale opbrengst van een pyrometallurgische installatie zijn metaalverliezen in slakken, zowel in primaire als secundaire metaalproductie. Over het algemeen kan een beter begrip van de fundamentele mechanismen die deze verliezen bepalen, helpen om de productie-efficiëntie te verbeteren.

Het wordt algemeen aanvaard dat er twee types metaalverliezen bestaan in slakken: chemische verliezen en mechanische verliezen. Met chemische verliezen wordt de oplossing van metaal in de slakfase bedoeld en deze verliezen worden thermodynamisch bepaald. De mechanische verliezen zijn metaaldruppels die worden vastgehouden in de slak, en dus niet zinken en verzamelen in de onderliggende metaalfase. Er worden vier redenen gegeven voor de mechanische obstructie van metaaldruppels in slakken:

I. het laden van de reactor of het tappen van de slak
II. metaalprecipitatie uit de slak door fluctuaties in de temperatuur of door chemische reacties die plaatsvinden
III. gas producerende reacties die metaal verspreiden in de slak wanneer gasbellen het slak/metaal grensvlak passeren
IV. de aanhechting van metaaldruppels aan vaste deeltjes in de slak

De eerste drie opties zijn reeds uitgebreid besproken in de literatuur. De vierde optie werd echter pas recent in een systematische manier bestudeerd om kennis te vergaren over het mechanisme dat verantwoordelijk is voor de interactie. Om de kennis over deze interactie uit te breiden, zal dit doctoraat het fenomeen verder onderzoeken vanuit een fundamenteel standpunt, met behulp van een gecombineerde modelleer – experimentele aanpak.

Eerst werd een binair model gebruikt om de groei, bevochtiging en aanhechting van metaaldruppels te onderzoeken. Nadien werden twee types experimenten uitgevoerd in koperbevattende systemen met zo weinig mogelijk componenten. De resultaten toonden aan dat de oorsprong van de aanhechting van gecombineerde aard was en dat de vaste spineldeeltjes aan de rand van de metaaldruppels groeiden. Daarom werd uiteindelijk de groei van de spineldeeltjes in een quaternair oxidesysteem onderzocht met behulp van een multicomponenten faseveldmodel, dat werd gekoppeld met een thermodynamische database. De volgende paragrafen geven een overzicht van de verschillende resultaten en observaties van deze simulaties en experimenten.

Initieel werd een model met gelimiteerde complexiteit geïmplementeerd. Dit model beschrijft een vast-vloeibaar hypothetisch O-M binair systeem om de vorming en groei van metaaldruppels te simuleren in slakken met niet-reagerende vaste deeltjes. Dit model omvat de belangrijke kenmerken van de druppelvorming en -groei, maar met redelijke simulatie- en berekeningsvereisten. Het model werd gebruikt om de invloed te onderzoeken van de grensvlakenergieën, de initiële oververzadiging van de oxidevloeistof, de deeltjesmorfologie, de initialisatiemethode, de beweging van het deeltje en de snelheid ervan.

De simulaties toonden dat de aangehechte druppels geen voorkeursposities hebben, aangezien ze op diverse plaatsen met verschillende configuraties en variaties in de tijd werden aangetroffen. Afhankelijk van de grensvlakenergieën werden er vier types van bevochtiging van het metaal op het deeltje waargenomen: geen bevochtiging, beperkte bevochtiging, hoge bevochtiging en volledige bevochtiging. Het gebruik van een hogere initiële oververzadiging gaf aanleiding tot een hogere metaalfractie in het systeem, maar het effect van de initiële oververzadiging op de fractie van het aangehechte metaal was niet geheel sluitend en varieerde ook in functie van de tijd.

Wanneer de fractie vaste deeltjes in het systeem verminderde, bleef een lagere metaalfractie vastgehecht aan de vaste deeltjes. Bij lage bevochtiging nam de hoeveelheid aangehecht metaal niet toe naarmate de beschikbare hoeveelheid oppervlakte aan de vaste deeltjes toenam. Bij hoge bevochtiging daarentegen, steeg de hoeveelheid vastgehecht metaal in dit geval duidelijk wel.

Het model werd ook uitgebreid om microstructuren van vaste deeltjes te simuleren die in werkelijke microscopische opnames werden waargenomen. Bovendien werd de oorsprong van de interactie onderzocht door twee initialisatiemethoden voor de metalen druppels te vergelijken: enerzijds door spinodale ontmenging van een oververzadigde vloeistof en anderzijds door een methode met willekeurige plaatsing van de druppels in het systeem. Eerder werk van De Wilde et al. [1–3] leidde tot twee mogelijke hypothesen voor de vasthechting: een reactieve en een niet-reactieve verklaring. De spinodale initialisatie komt overeen met de reële situatie waarin de druppels dicht bij (en eventueel samen met) de spineldeeltjes worden gevormd door een reactie. De willekeurige initialisatie komt overeen met de situatie waarin de druppels en deeltjes afzonderlijk worden gevormd en vervolgens in de slak worden gemengd en zich niet-reactief aan elkaar hechten. Beide initialisatiemethoden werden onderzocht bij twee bevochtigingsregimes: geen en beperkte bevochtiging. Zonder bevochtiging resulteerde de spinodale initialisatie in microstructuren die het beste overeenkwamen met de experimenten, maar in het lage bevochtigingsregime kwamen de simulatieresultaten van beide initialisatiemethoden goed overeen met de experimenten.

Een initieel nadeel van het model was het ontbreken van convectie of beweging van de deeltjes ten opzichte van de vloeistoffen in het systeem. Deze beweging is wel aanwezig in het reële systeem. Daarom werd het bestaande faseveldmodel uitgebreid met starre lichaamsbeweging van de vaste deeltjes ten opzichte van de vloeibare slak. Hiervoor werden niet de Navier-Stokes vergelijkingen voor fluïdumstroming gebruikt, maar werd een vergelijking gebruikt om de faseveld profielen in de ruimte te bewegen, waardoor de deeltjes ten opzichte van de slak werden verplaatst. De invloed van deze starre lichaamsbeweging op de bevochtigingstypes en op de verkregen microstructuren werd onderzocht.

Er kon geen trend worden geobserveerd voor de hoeveelheid aangehecht metaal voor een relatief trage beweging van het vaste deeltje. Bij geen bevochtiging, bleek dat de starre lichaamsbeweging zowel reeds aangehechte druppels kan verliezen als nieuwe druppels kan meenemen, waardoor de hoeveelheid aangehecht metaal toeneemt. Bij beperkte bevochtiging werden vergelijkbare resultaten waargenomen, maar het verlies van een reeds aangehechte druppel werd niet waargenomen. Bij hoge en volledige bevochtiging, leek de invloed van de starre lichaamsbeweging kleiner, aangezien de aanhechting werd bepaald door de grensvlakenergieën waardoor de metallische fase het vaste deeltje ‘volgde’ wanneer het bewoog. De schijnbare contacthoek van het metaal was groter wanneer starre lichaamsbeweging aanwezig was, hetgeen overeenkomt met een lagere bevochtiging. Dus door de beweging van één fase ten opzichte van de anderen, is het mogelijk

dat een hogere bevochtiging, d.w.z. op basis van alleen de grensvlakenergieën, aanwezig is in het systeem dan gebaseerd op de geobserveerde contacthoek.

Vervolgens werd de bewegingssnelheid van het vaste deeltje gevarieerd. Deze studie toonde aan dat er een afweging bestaat tussen de snelheid van de beweging van het vloeibare metaal, die afhangt van de aantrekking van het metaal tot het vaste deeltje en die wordt bepaald door grensvlakenergieën, en de snelheid van de beweging van het vaste deeltje, die we varieerden. In de beperkte en hoge bevochtigingsregimes, bij een trage beweging van het vaste deeltje, hadden de grensvlakenergieën de grootste invloed, maar voor een snellere beweging, bleef de metaalfase niet vastgehecht aan het vaste deeltje. Waardoor de hoeveelheid aangehecht metaal bij een snellere beweging van het vaste deeltje daalde. Bij niet-bevochtiging werden metaaldruppels die toevallig aanwezig waren op het pad van het vaste deeltje aangehecht, maar de beweging van de vaste deeltjes kon eveneens de hoeveelheid van aangehecht metaal verlagen door van een druppel weg te bewegen. In het geval van volledige bevochtiging, daarentegen, was de aantrekking van het metaal tot het vaste deeltje door de grensvlakenergieën zo groot dat zelfs de grootste snelheid de hoeveelheid aangehecht metaal niet verminderde.

Daarnaast werden de twee initialisatiemethoden voor de metaaldruppels beschouwd voor microstructuren van vaste deeltjes gebaseerd op werkelijke experimenteel bepaalde microscopische opnames van de spinelfase. Deze fase bewoog ook ten opzichte van de vloeibare fasen. Voor de simulaties met de aan- of afwezigheid van starre lichaamsbeweging kwamen de simulaties met de spinodale initialisatie beter overeen met de experimenteel waargenomen microstructuren dan de simulaties met de willekeurige initialisatie.

Daarnaast werden er tijdens dit doctoraat twee soorten experimenten verricht, op basis van de methodologie van De Wilde et al. [4], om de mogelijke oorsprong van de aanhechting te onderzoeken en om de simulaties mee te vergelijken. Eerdere experimenten met synthetische slakken verschaften inzicht in deze interactie en resulteerden in twee mogelijke mechanismen achter de metaal-spinel interactie:

- afzonderlijk gevormde druppels en spineldeeltjes hechten aan elkaar als gevolg van beweging van de slak en metaalfasen
- de spineldeeltjes vormen door een chemische reactie naast een druppel die reeds in het systeem aanwezig is of met de slak om een nieuwe aangehechte druppel te vormen

Eén van de experimenten die tot deze hypothese leidde, was een aangepast ‘sessile drop’ experiment (slak en koper op een spinelsubstraat) waarin de drie desbetreffende fasen aanwezig waren [3]. Tijdens het experiment positioneerde de slakfase zich tussen de metalen druppel en het vaste spinelsubstraat. Om dit te laten plaatsvinden, leken de slak en metaalfase tijdelijk samen te vloeien of coalesceren. Daarna werden kleine metalen druppels binnenin de grote slakdruppel waargenomen die gehecht waren aan kleine vaste spineldeeltjes. Het is echter mogelijk dat deze metalen druppeltjes die vasthingen aan kleine vaste deeltjes binnenin de slak, een gevolg zijn van het coalesceren van slak en metaal in dit experiment.

Om te bepalen of de aangehechte kleine metalen druppeltjes werden gevormd door reactie of door deze coalescentie, werd een inert tracerelement (Ag) aan de metallische fase toegevoegd tijdens soortgelijke experimenten in dit doctoraat. De kleine aangehechte metaaldruppels in de slak

bevatten inderdaad Ag; echter in zeer kleine hoeveelheden in vergelijking met de toegevoegde hoeveelheid Ag in de Cu-Ag-legering.

Verder werd een smeltexperiment uitgevoerd in een systeem met zo weinig mogelijk elementen om nadien te kunnen vergelijken met de simulaties. De FeO-Fe_2O_3-SiO_2-Al_2O_3-Cu_2O slak werd eerst onderworpen aan een oxidatieve atmosfeer en nadien aan een reducerende atmosfeer. Tijdens de eerste (oxidatieve) fase, werd het metallisch koper in het systeem opgelost in de slak en werden zeer weinig aangehechte metalen druppels waargenomen. Tijdens de tweede (reductieve) fase werd de gelijktijdige vorming van metaaldruppels en spineldeeltjes, die aan elkaar hingen, waargenomen. Daarenboven bleek dat naarmate de reductieve fase vorderde, zowel de spineldeeltjes als de metalen druppels groeiden en ze aan elkaar bleven vasthangen.

De resultaten van beide experimenten geven aan dat de aangehechte metalen druppels worden gevormd door een sequentiële combinatie van de twee mogelijke methoden: eerst worden zeer kleine druppeltjes metaal gedispergeerd in de slak fase, tijdens de coalescentie of het mengen en vervolgens dienen deze metalen druppels als nucleatieplaatsen voor de reactieve vorming van koper-spinel entiteiten.

De experimenten bevestigden dat een chemische reactie aan de oorsprong zou kunnen liggen van de aanhechting. Maar het binaire model beschouwde niet-reactieve vaste deeltjes. Daarom werd het faseveldmodel van Heulens [5], dat de isotherme stolling van slakken beschouwt, uitgebreid tot systemen met meerdere componenten om de gefacetteerde groei van spineldeeltjes in een quaternaire oxidesysteem te onderzoeken. Er werd waargenomen dat de groei van de vaste spinelfase sterk wordt beïnvloed door de aanwezigheid van een open systeemgrens in contact met een atmosfeer bij een specifieke p_{O2}.

In conclusie, dit doctoraat onderzocht de aanhechting van metaaldruppels aan vaste deeltjes in slakken aan de hand van een combinatie van twee experimentele opstellingen en twee faseveldmodellen. Het binaire model met beperkte complexiteit verduidelijkte reeds het inzicht op de interactie tussen metaaldruppels en een niet-reagerend vast deeltje. Zo is bijvoorbeeld het feit dat de beweging van één fase ten opzichte van een andere de schijnbare bevochtiging beïnvloedt zeer interessant voor de interpretatie van experimenteel verkregen resultaten. Bovendien bevestigden de twee verschillende types experimenten dat een chemische reactie aan de basis van de aanhechting kan liggen, maar dat er nucleatieplaatsen vereist zijn in de vorm van metaaldruppels alvorens de reactie plaatsvindt. Het eerste model beschouwde echter niet-reactieve vaste deeltjes. Daarom werd een model voor de groei van de vaste fase in een realistisch quaternair oxide systeem beschouwd. Toekomstig werk moet de wisselwerking van reagerende metaaldruppels met reagerende vaste deeltjes in een realistische vloeibare slak onderzoeken.

Referenties

[1] E. De Wilde, I. Bellemans, L. Zheng, M. Campforts, M. Guo, B. Blanpain, N. Moelans, K. Verbeken, Origin and sedimentation of Cu-droplets sticking to spinel solids in pyrometallurgical slags, Mater. Sci. Technol. 32 (2016) 1911–1924. doi:10.1080/02670836.2016.1151998.

[2] E. De Wilde, I. Bellemans, M. Campforts, M. Guo, B. Blanpain, N. Moelans, K. Verbeken, Sessile drop evaluation of high temperature copper/spinel and slag/spinel interactions, Trans. Nonferrous Met. Soc. China. 26 (2016) 2770–2783. doi:10.1016/S1003-6326(16)64344-3.

[3] E. De Wilde, I. Bellemans, M. Campforts, M. Guo, B. Blanpain, N. Moelans, K. Verbeken, Investigation of High-Temperature Slag/Copper/Spinel Interactions, Metall. Mater. Trans. B. 47 (2016) 3421–3434. doi:10.1007/s11663-016-0805-8.

[4] E. De Wilde, Methodology Development and Experimental Determination of the Origin of Sticking Copper Droplets in Pyrometallurgical Slags, PhD thesis, Ghent University, 2015.
[5] J. Heulens, Isothermal Crystallization of Metallurgical Slags: Phase Field Simulations Combined with In Situ Experiments (Isotherme kristallisatie van metallurgische slakken: faseveldsimulaties in combinatie met in situ experimenten), PhD thesis, KU Leuven, 2011. https://lirias.kuleuven.be/handle/123456789/318339.

Table of contents

List of symbols and abbreviations

Part A.2

Symbol	Explanation
a	Activity
f	Fraction of solids particles in a melt
g	Gravity constant
p_{O2}	Partial pressure of oxygen
r	Radius of the droplet
R	Gas constant
T	Temperature
u	Sinking velocity / settling rate
γ, σ	Surface tension
Δ	Flotation coefficient
μ, η	Viscosity
ρ	Density
ϕ	Spreading coefficient

Part A.3

Symbol	Explanation
c_k	Concentration
D_k	Diffusion coefficient
F	Free energy of the system
f	Heterogeneous free energy density
f_0	Homogeneous free energy density
f^{α}	Free energy density of phase α
g(ϕ)	Double-well function
J_k	Flux
L_k	Onsager coefficient (in the context of diffusion)
L_k	Kinetic coefficient for evolution equation of non-conserved phase field variable (in the context of microstructural evolution)
M_k	Mobility coefficient
p(ϕ), h(ϕ)	Interpolation function
X_k	Conjugated thermodynamic force
x_k	Molar fraction
ε, κ	Gradient free energy coefficients
η_k	Order parameter
$\widetilde{\mu_k}$	Diffusion potential
μ_k	Chemical potential
σ_s	Entropy production
ϕ	Phase field variable or phase fraction

Part B

Symbol	Explanation
A_S	Curvature of the free energy density of the solid
A_{Sp}	Curvature of the free energy density of the liquid
F	Free energy of the system
$f_{\nabla xM}$	Gradient free energy density for liquid-liquid interfaces
f_{Liquid}	Homogeneous free energy density of the liquid
$f_{S\text{-}L,interf}$	Interfacial energy density for solid-liquid interfaces
f_{Solid}	Homogeneous free energy density of the solid
f_V	Fraction of metal for the random initialization
g(ϕ)	Double-well function
h(ϕ)	Interpolation function
L	Kinetic coefficient for phase field evolution equation
l	Interfacial width
M	Mobility coefficient of metal for diffusion equation
m_x, m_y	Speed of the solid particle in the x- and y-direction
N	System size
W	Depth of the double well
$x_{eq,LM}$	Metallic equilibrium composition of free energy curve of spinodal decomposition
$x_{eq,LO}$	Oxidic equilibrium composition of free energy curve of spinodal decomposition
x_i	Initial supersaturation of the liquid for the spinodal decomposition initialization
x_M	Mole fraction of metal
x_S	Mole fraction of metal in the non-reactive solid particle
γ	Interfacial energy
Δt	Time steps spacing
Δx	Grid spacing
κ_ϕ, κ_{xM}	Gradient free energy coefficients
ϕ	Phase field variable (1 for solid and 0 for liquid)

Part C

Symbol	Explanation
a	Activity
f	Fraction of solid particles in a melt
p_{O2}	Partial pressure of oxygen
η	Viscosity of the slag-solid mixture
η_0	Viscosity of the slag without solids

Part D

Symbol	Explanation
F	Free energy of the system
f_0	Homogeneous free energy density (double-well)
f_b	Bulk free energy density
f_{in}	Interfacial free energy density
L	Kinetic coefficient for phase field evolution equation
l	Interfacial width
L_{crit}	Critical value for kinetic coefficient for diffusion-controlled growth
M	Mobility coefficient of metal for diffusion equation
m	Depth of double-well
x_k	Conserved concentration fields
x_k^i	Phase compositions
Δt	Time steps spacing
Δx	Grid spacing
η_k	Phase field variable
θ	Angle between normal to the interface between two phases and the x-axis
κ	Gradient free energy coefficients
λ, ψ	Anisotropy function
$\widetilde{\mu_k}$	Diffusion potential
μ_k	Chemical potential
σ	Interfacial energy
ϕ	Phase fraction

A. Introduction

“In this house, we obey the laws of thermodynamics!”

- Dan Castellaneta

1. General introduction

The present research concerns the modelling and observation of the attachment of metal droplets to solid particles in liquid slags. The problem statement and the research objectives are introduced in this first chapter. Section 1.1 explains the industrial problem statement, section 1.2 addresses the objectives of the doctoral work and finally section 1.3 gives the outline of this dissertation.

1.1. Industrial problem statement

The domain dealing with extraction or refinement of materials/metals at high temperatures is called pyrometallurgy. Within pyrometallurgical processes, the liquid metal phase is usually present alongside other phases, such as slag (mixture of metal oxides), matte (mixture of metal sulphides), etc. The slag mainly contains the gangue ores, from which the metal is extracted, and is mostly used to remove certain impurities. Moreover, it is also used as an isolation layer and prevents re-oxidation of the molten metal, because, in a typical pyrometallurgical process, the slag floats on top of the molten metal, due to differences in density. Most pyrometallurgical processes consist of several steps, as illustrated in Figure 1.1: first the feed material is charged in the reactor, then this feed material is converted to produce a liquid metal phase and in the end, the separate phases are tapped from the furnace. [1] Before tapping, sedimentation allows for the separation of slag and metal. Unfortunately, this separation is not perfect and industrial Cu smelters [2], Pb reduction smelting furnaces [3,4], ferrochrome smelters [5], etc. suffer from metal rich droplet losses in slags due to insufficient phase separation after sedimentation.

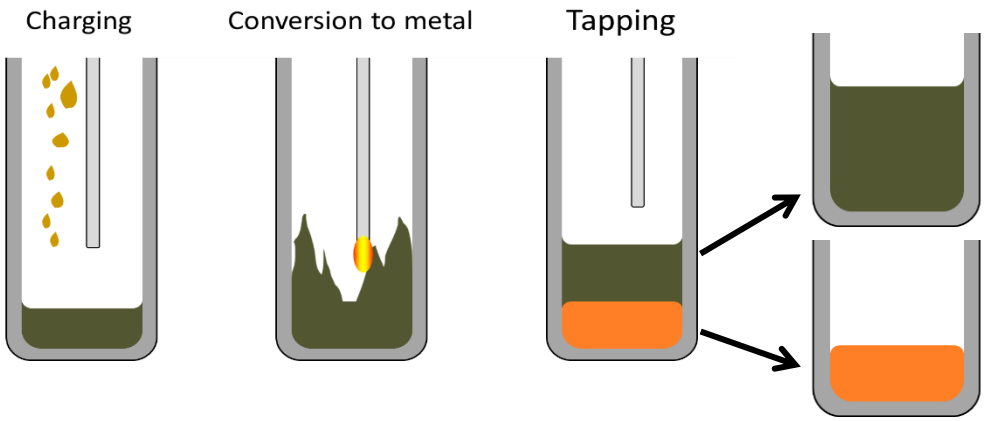

Figure 1.1 Illustration of general steps in a pyrometallurgical process

In terms of sustainability, recycling becomes more important, but, it is also necessary to improve and optimize existing processes in extractive and recycling metallurgy. One of the main difficulties of the overall-plant recovery are the abovementioned metal losses in slags, in both primary and secondary metal production. Generally, these metal losses in slags can be subdivided in two types: chemical losses and physical losses. The amount of chemical losses is thermodynamically determined. The physical losses have several causes, one of them being the attachment of metal droplets to solid particles present in the slag phase which hinder their settling. In general, an increased understanding of the fundamental mechanisms governing these losses could help further improve production efficiencies. In the following paragraphs, the need for a thorough knowledge and modelling expertise of the interaction between solid oxide particles and liquid metal droplets in liquid slags is shown.

1.2. Research objectives

The goal of this doctoral work is to develop a fundamental understanding of the system in which the attachment of metal droplets to solid particles in liquid slags is observed. For this, a combined experimental – phase field modelling approach was chosen, which is illustrated in Figure 1.2.

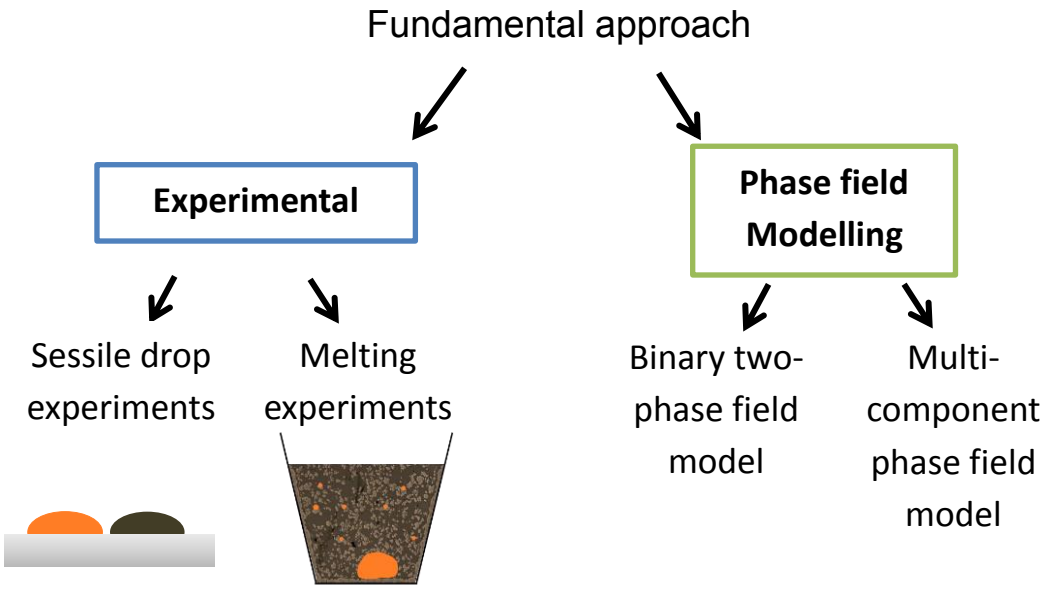

Figure 1.2 Illustration of fundamental combined experimental - phase field modelling approach in this dissertation

The experimental methodology was developed by De Wilde [6] and consists of two complementary experimental set-ups. On the one hand, the interaction between the copper droplets and spinel particles was investigated separately with sessile drop experiments between a spinel substrate and copper and/or slag phases. On the other hand, a method was developed to study the attachment of the droplets in the presence of a surrounding slag system with the use of an industrially relevant synthetic slag system. The latter type of experiments gives the opportunity to obtain a better insight on parameters like sedimentation time or slag height and to verify the observations obtained with the first method.

Experimental investigation of this interaction, however, remains very challenging. Moreover, many experiments are needed to investigate the influence of all parameters and, even though the microstructure and composition can be investigated microscopically, it is very difficult to study the effect of one parameter because it is virtually impossible to keep the others constant. Thus, it can be inconvenient to reveal the underlying chemical and physical phenomena. Modelling can provide a solution for this. [7] Modelling can help to understand the complex phenomena causing changes in the microstructure. However, it should be noted that experiments are still required to validate the model results and thus, modelling cannot replace experiments. Moreover, the experiments can also provide some of the input parameters required for quantitative simulations. Therefore, modelling and experiments can be regarded as complementary methods and can create a synergy that can be very productive. [8]

The phase field method already proved to be a very powerful, flexible and versatile modelling technique for microstructural evolution, e.g. the numerous models for solidification [1,9,10], solid-state phase transformations [11], solid-state sintering [12], grain growth [13], dislocation dynamics

[14], crack propagation [15,16], electromigration [17], etc. The phase field method is also eye-catching because it produces remarkable visual outputs, particularly of morphology, capturing features which are often realistic in appearance. [8,18]

In a first step to investigate the phenomenon, a model with limited complexity was implemented. The model describes a solid-liquid O-M binary system to simulate the metal droplet formation and growth in slags with non-reacting solid particles. This model captures the important features of the droplet formation and growth, but for which the simulation and computational requirements are reasonable. This model with limited complexity already clarified our view on the interaction between metal droplets and solid particles to a great extent, but assumed non-reactive solid particles. The experiments in copper-containing systems, however, confirmed that a chemical reaction might lay at the origin of the attachment. Therefore, the phase field model used by Heulens [1], considering the isothermal solidification of slags, was extended to consider multicomponent systems to investigate the growth of solid spinel particles in a quaternary oxide system.

1.3. Outline of the text

This dissertation is written as a collection of parts of review and research papers. The text is divided in five parts:

A. Part A is an introductory part, containing 3 chapters. The present chapter (Chapter 1) gives a general introduction in the subject of the dissertation and the research objectives. Chapter 2 illustrates the context of the problem, i.e. the metal droplet losses in slags. The experimental methods used in this dissertation are also mentioned in this chapter. Chapter 3 gives an overview of the phase field method in general and some of the developments towards multi-phase field models.
B. Part B describes a first attempt to describe the system with a binary phase field model. In a first chapter, the model is described and in a second chapter, the simulation set-up is discussed. With this simple model, the influences of the interfacial energies, initial supersaturation and particle morphology were investigated. Moreover, realistic microstructures for the solid particles were also considered. These results are shown and discussed in the third chapter. As the real system encounters a lot of movement of the different phases with respect to each other, the movement of the solid particles with respect to the liquid phases was also investigated in a fourth chapter. The conclusions for the binary model are summarized in the fifth chapter.
C. Part C shows the results of the experiments with two set-ups. In the first chapter, the results of a high-temperature sessile drop experiment are shown. The second chapter reports the results of a smelting experiment to induce the reactive origin. Both types of experiments show that redox reactions between the metal, the slag and the solid particles play an important role in the interaction under investigation.
D. Part D starts with an overview of the existing phase field model considering oxide systems. Then, the development of the multicomponent phase field model coupled to a thermodynamic database is reported. A big challenge in modelling realistic systems is the choice of input parameters, to which the third chapter of this part will be dedicated. In a fourth part, the simulation results are shown and discussed. Part D ends with general conclusions of the multicomponent model and possible future work considering this model in particular.

E. Part E summarizes the main conclusions of this doctoral work. Moreover, an outlook for future research directions from both an experimental and modelling point of view is given.

References

[1] J. Heulens, Isothermal Crystallization of Metallurgical Slags: Phase Field Simulations Combined with In Situ Experiments (Isotherme kristallisatie van metallurgische slakken: faseveldsimulaties in combinatie met in situ experimenten), PhD thesis, KU Leuven, 2011. https://lirias.kuleuven.be/handle/123456789/318339.

[2] J. Yannopoulos, Control of copper losses in reverberatory slags - a literature review, Can. Metall. Q. 10 (1970) 291–307.

[3] F.A. Calvo, A. Ballester, Lead losses in the slag of a reduction melting furnace, Erzmetal. 6 (1986) 282–287.

[4] F.A. Calvo, A. Ballester, The settling of metallic lead from lead blast furnace slag, Metall. Trans. B. 17 (1986) 267–270. doi:10.1007/BF02655073.

[5] M.A. Nkohla, Characterization of ferrochrome smelter slag and its implications in metal accounting, Cape Peninsula University of Technology, 2006.

[6] E. De Wilde, Methodology Development and Experimental Determination of the Origin of Sticking Copper Droplets in Pyrometallurgical Slags, PhD thesis, Ghent University, 2015.

[7] N. Moelans, B. Blanpain, P. Wollants, An introduction to phase-field modeling of microstructure evolution, Calphad. 32 (2008) 268–294. doi:10.1016/j.calphad.2007.11.003.

[8] D. Raabe, Introduction, in: Comput. Mater. Sci., Wiley-VCH Verlag GmbH & Co. KGaA, 1998: pp. 111–118. http://onlinelibrary.wiley.com/doi/10.1002/3527601945.ch8/summary (accessed January 22, 2015).

[9] A. Karma, W.-J. Rappel, Quantitative phase-field modeling of dendritic growth in two and three dimensions, Phys. Rev. E. 57 (1998) 4323–4349. doi:10.1103/PhysRevE.57.4323.

[10] W.J. Boettinger, J.A. Warren, C. Beckermann, A. Karma, Phase-Field Simulation of Solidification, Annu. Rev. Mater. Res. 32 (2002) 163–194. doi:10.1146/annurev.matsci.32.101901.155803.

[11] L.-Q. Chen, Phase-Field Models for Microstructure Evolution, Annu. Rev. Mater. Res. 32 (2002) 113–140. doi:10.1146/annurev.matsci.32.112001.132041.

[12] Y.U. Wang, Computer modeling and simulation of solid-state sintering: A phase field approach, Acta Mater. 54 (2006) 953–961. doi:10.1016/j.actamat.2005.10.032.

[13] L.-Q. Chen, W. Yang, Computer simulation of the domain dynamics of a quenched system with a large number of nonconserved order parameters: The grain-growth kinetics, Phys. Rev. B. 50 (1994) 15752–15756. doi:10.1103/PhysRevB.50.15752.

[14] D. Rodney, Y. Le Bouar, Phase field methods and dislocations, Acta Mater. 51 (2003) 17. doi:10.1016/S1359-6454(01)00379-2.

[15] H. Henry, H. Levine, Dynamic instabilities of fracture under biaxial strain using a phase field model, Phys. Rev. Lett. 93 (2004) 105504.

[16] R. Spatschek, E. Brener, A. Karma, Phase field modeling of crack propagation, Philos. Mag. 91 (2011) 75–95. doi:10.1080/14786431003773015.

[17] D.N. Bhate, A. Kumar, A.F. Bower, Diffuse interface model for electromigration and stress voiding, J. Appl. Phys. 87 (2000) 1712–1721. doi:10.1063/1.372082.

[18] R.S. Qin, H.K. Bhadeshia, Phase field method, Mater. Sci. Technol. 26 (2010) 803–811. doi:10.1179/174328409X453190.

2. Metal losses in pyrometallurgical operations - a review [1]

One of the main difficulties of the overall-plant recovery in extractive and recycling metallurgy are metal losses in slags, in both primary and secondary metal production. This review aims to summarize and evaluate the current scientific knowledge concerning metal losses and pinpoints the knowledge gaps. First, the industrial importance and impact of metal losses in slags will be illustrated by several examples from both ferrous and non-ferrous industries. Throughout the remainder of this review, the main focus will be put on the particular issues in copper industry. In a second section, the different types of metal losses in slags will be discussed. Generally, metal losses in slags can be subdivided into two types: chemical losses and physical losses. The fundamental insights concerning the responsible mechanisms will be discussed for each type. Subsequently, an overview of the most frequently used techniques for research investigations of the losses will be given. In a fourth section, a more detailed overview will be given on the post-processing treatment of metal-containing slags, i.e. performing slag cleaning operations. The most frequently applied methods will be discussed.

2.1. Introduction

The domain dealing with extraction or refinement of materials/metals at high temperatures is called pyrometallurgy. The raw materials for metal production (mined ores) contain less and less of the desired metal, thus increasing the ratio of produced slag to produced metal. The slag used to be considered as a waste stream, but is now considered as a secondary resource, e.g. in road building applications or dike fortifications. [1] Due to the recent higher demand on a lot of metals, the decrease in the quantity and purity of the corresponding ores and the increase in the amount of scrap, recycling becomes more important. Besides recycling, it is also necessary to improve and optimize existing processes in extractive and recycling metallurgy to deal with the scarcity of natural resources. [2]

In a pyrometallurgical process, several phases can be present besides the liquid metal: slag (mixture of metal oxides), matte (mixture of metal sulphides), etc. The slag mainly contains the gangue ores, from which the metal is extracted, and is mostly used to remove certain impurities. Moreover, it is also used as an isothermal isolation layer and prevents re-oxidation of the molten metal, because in a typical pyrometallurgical process, the slag floats on top of the molten metal, due to differences in density. In most pyrometallurgical processes, the slag will finally be tapped from the furnace. [1] Sedimentation is frequently one of the last steps (before tapping) in many pyrometallurgical processes, allowing separation of slag and matte/metal. However, industrial Cu smelters [3], Pb reduction melting furnaces [4,5], ferrochrome smelters [6], etc. still suffer from metal rich droplet losses in slags due to insufficient phase separation. These losses remain an important issue in metal extraction and recycling industries and can be reduced by optimizing the phase separation.

[1] This chapter is based on the following publication: I. Bellemans, E. De Wilde, N. Moelans, K. Verbeken, Metal losses in pyrometallurgical operations - a review, Advances in Colloid and Interface Science. Submitted

2.2. Metal production

2.2.1. Lead smelting

The conventional primary lead production process consists of four steps: sintering, smelting, drossing and refining. Feedstock mainly made up of lead concentrate is fed into a sintering machine together with other raw materials like silica, coke and limestone flux. This sinter is in turn fed into a blast furnace for reduction with carbon, which also acts as fuel. Four layers form in the furnace: 'speiss' (the lightest material, basically arsenic and antimony), matte (copper sulphide and other metal sulphides), blast furnace slag (primarily silicates) and lead bullion. Subsequently, all layers are drained off. The speiss and matte are sold for recovery of copper and precious metals to copper smelters. The blast furnace slag, which contains iron, zinc, silica and lime, is stored in piles and is partially recycled. The rough lead bullion from the blast furnace usually requires preliminary treatment before undergoing refining operations. Then, the bullion is agitated in a drossing kettle and cooled just above its solidification point, 370°C - 425°C. A dross composed of lead oxide, along with copper, antimony and other elements floats on the top and solidifies above the molten lead. The dross is removed and is fed into a dross furnace for recovery of non-lead metals. The lead bullion is further refined to remove any remaining non-lead materials in a cast-iron kettle in five stages, leading to lead with a purity of 99.9 – 99.99 %. Secondary production of lead uses old lead-containing scrap as feed. The main source for recycling is old scrap from lead-acid batteries. [7]

2.2.2. Nickel production

Nickel can be extracted from sulphide ores, where pentlandite ($(Ni,Fe)_9S_8$), chalcopyrite ($CuFeS_2$), and pyrrhotite (Fe_7S_8) are the major minerals. Mined sulphide ores contain typically about 1 % Ni, and are concentrated to 7 to 20 wt% Ni by various mineral processing methods. The concentrate is subsequently dried for further handling. Molten matte from the smelting furnace is transferred into a converter for the removal of the final FeS to form a matte with about 0.5 to 2 wt% Fe. This is achieved by blowing air or oxygen enriched air into the matte. It is during this stage with high oxygen pressures that the most valuable metal losses to the slag phase occur, as stated by Toscano and Utigard [8].

2.2.3. Steel production

During the production of pig iron in a blast furnace, oxygen and other impurities are removed from the iron oxide ores by pyrometallurgical processes with reducing reagents and fluxes. Most of the impurities and fluxing agents combine to form a liquid silicate melt called blast furnace slag. This slag is tapped from the blast furnace separately from the iron. The pig iron is then transferred to a steel furnace, where the residual carbon content of about 4 wt% is reduced and other impurities are removed. This process involves the use of lime and silicate fluxes and the formation of steel slag. Steel furnaces, particularly electric arc furnaces (EAF), also may be fed with scrap iron and steel, but again the impurities are removed by fluxing agents which form a slag. Apart from the original furnace feedstock impurities, slags (especially steel slags) also may contain significant amounts of entrained free metals. [9]

- Ferrochrome production

In the production of stainless steel, ferrochrome is the major chromium source. The chromite ores are melted using suitable carbonaceous reductants such as coke, char, etc. During the smelting process, slag is formed and metallic ferrochrome coalesces into droplets, which separate from the slag by settling through the slag to the bottom of the furnace. Ferrochrome slag consists mainly of SiO_2, Al_2O_3 and MgO in different proportions, but also smaller amounts of CaO, chromium and iron oxides, with significant quantities of chromium in the form of partially altered chromite and entrained alloy. [6]

- Ferrovandium production

Ferrovanadium alloys are produced commercially by the reduction of vanadium ore, slag or technical grade vanadium oxide with ferrosilicon, aluminium and to a lesser extent by carbon. A charge consisting of vanadium oxide, reductant, fluxing agents, etc. is fed to an electric arc furnace that is maintained at temperatures of about 1600°C. The nature of the vanadium oxide used as input materials governs the choice of the production route. The use of V_2O_5 as raw material leads to the exothermic reduction, allowing that both iron and the alloy can melt, which results in an effective separation of the alloy and the high alumina slag. Therefore, an aluminothermic reactor can be used. When V_2O_3 and V_2O_4 are used as raw materials, addition of external energy is required to sustain the less exothermic reactions. A high temperature for tapping (1840 °C) is required because of the high melting point of ferrovanadium and this also favours the settling of entrained metal droplets from the slag after tapping. [10,11]

2.2.4. Copper smelting

Copper ores commonly consist of a low concentration (0.5-2 wt% Cu) of copper-iron-sulphide or copper-sulphide minerals (e.g. chalcopyrite $CuFeS_2$ or chalcocite Cu_2S) in combination with a large amount of gangue material (Al_2O_3, SiO_2, …). Pure copper metal is produced from these ores by concentration, smelting and refining. [12] The ores are concentrated by e.g. froth flotation, after which they are smelted in a large hot (± 1250°C) furnace. Under oxidizing conditions, Cu tends to form metallic Cu as well as Cu oxide, as explained extensively by Yazawa [13]: the addition of oxygen to Cu_2S yields Cu instead of Cu_2O. When the latter happens, the Cu_2O dissolves in the slag generated during copper making. The large amount of iron in most copper concentrates creates a large amount of slag, which could allow for more Cu to be lost in it. As a result, it is better to eliminate some of the iron from the concentrate before final copper making. This is why the Cu ores are smelted first to produce a Cu-rich matte (45-75 wt% Cu) and a slag (with the smallest possible amount of Cu), after which this Cu-matte is converted to form impure molten copper (99 wt% Cu) in a separate step. To keep the amount of Cu in the smelting slag as low as possible, it is possible to add a SiO_2 flux to promote slag-matte immiscibility or to keep the furnace hot enough to liquefy the slag. [12]

The converting step of the matte takes place in two sequential stages: the elimination of Fe and other remaining impurities in the ‘slagging blow’ and the ‘copper making blow’, which converts the ‘white metal’ (Cu_2S) to metallic Cu. The copper is then refined in further steps. Because conditions in the converter are strongly oxidizing, converter slag inevitably contains 4-8 wt% Cu. The slag can be treated to recover the remaining Cu and is then sold or discarded. Another possibility is the reuse of the converter slag as a starting bath for the next batch. [12] But this may also affect the final slag loss, because the oxygen potential of the melt is changed and this influences the composition of the

matte and the slag. [14] The secondary production of copper uses scrap as a source of copper. High-purity copper scrap can be found in e.g. electronic wires and electronic waste. [12] It should be noted that the general aspects of primary copper production and scrap recycling are similar. A major difference in the case of scrap recycling is the use of copper as a collector metal[2] for the noble metals, whereas in ore-based production, the primary aim is to produce the pure metal. The yields of the recycling of noble metals could be improved by higher collection rates of e.g. e-scrap and maximizing eco-efficiency.

2.3. Metal losses in slags

Large bubbles are produced during the gas-blowing stages in smelting and converting in several metal production processes. After each stage of gas blowing through the melt, a sedimentation step is necessary before phases can be tapped. The settling time of this step needs to be long enough to allow the different phases to separate, but this time also implies a loss of production time and, consequently, insufficient separations are often encountered in practice. E.g. some metal or matte droplets are often observed as a suspension in the slag. Several industries encounter such losses:

- Lead smelting

One of the factors impeding the total recovery of the lead contained in the sinter is the retention of metal by slag. It is generally accepted that when these losses exceed 2-3 %, the economics of the process are strongly affected. Excessive losses of lead frequently occur in the slag of lead blast furnaces which represents a sizeable economic loss for large scale production furnaces. [4,5]

- Nickel production

According to Solar [16], about two thirds of the total loss occurs in the electric furnace slag, as both dissolved nickel oxide and entrained metal droplets. These chemical and mechanical losses are reported equally. The amount of mechanical losses can vary between different nickel production plants. [16] Furthermore, cobalt, selenium and tellurium are valuable by-products in nickel sulphide smelting and are economically very important. The distribution of these minor elements, however, also affects the quality of the final product and the revenues gained from the by-product. For example, there are cobalt losses to the slag phase during the smelting and converting processes, leading to a conversion of only 30 to 60 % of recovery for the matte phase. [17]

- Steel production

Gudim [18] studied the metal losses during steelmaking in arc furnaces. Metal enters the furnace slag in the form of a film on CO-bubbles, originating from carbon oxidation and in the form of droplets during oxygen blowing. The entrained metal content in the slag can be at least 10 % of the metal mass during oxygen blowing of the bath. Gravity lets the metal droplets settle down from the slag in the metal phase. As the slag goes down in the furnace, its temperature decreases, its viscosity sharply increases, and the conditions for droplet settling deteriorate drastically. Therefore, metal droplets

[2] The copper generated during non-ferrous metal recycling of e-scrap and other precious metal rich materials only has a purity of about 95% because the metallic copper phase acts as the collector of precious metals (Cu, Ag, Au, Pt, Pd, Rh, Ru, Ir) present in the feed mixture. Similarly, lead and nickel are used to collect base metals (Pb, Bi, Sb, Sn, As) and special metals (In, Se, Te). [15]

smaller than 3 mm are usually retained in the slag. The average content of iron in oxidizing steel melting slags is believed to be slightly lower than 20-25%, including 10-15% metallic iron. [18]

- Ferrochrome production

Losses of metal to slag are observed with a significant amount of alloy droplets with a size of 30 µm up to 2000 µm. Some entrained droplets (>1 mm) can be recovered back in the metallic phase, but the remainder stays entrained in the slag. Metal losses to slag can occur throughout the reduction process in the furnace, as well as during the tapping. Both mechanical and chemical losses occur. The slag is further treated to recover some of the entrained metal. The dissolved chrome can be controlled through improved redox-basicity control, while the amount of entrained chrome can be controlled through the control of the slag viscosity. [6]

- Ferrovanadium production

As stated by Vermaak [10], the vanadium recovery in the electro-aluminothermic process is mainly controlled by vanadium losses in the slag, which include metal droplet entrainments and unreduced vanadium oxides in the slag.

- Copper smelting

Last century, the subject of copper losses in slags was already reviewed by Aksoy [19] and Yannopoulos [3]. Yannopoulos [3] depicted the monetary significance of the copper losses by comparing the losses with other important smelting operational costs, as represented in Figure 2.1.

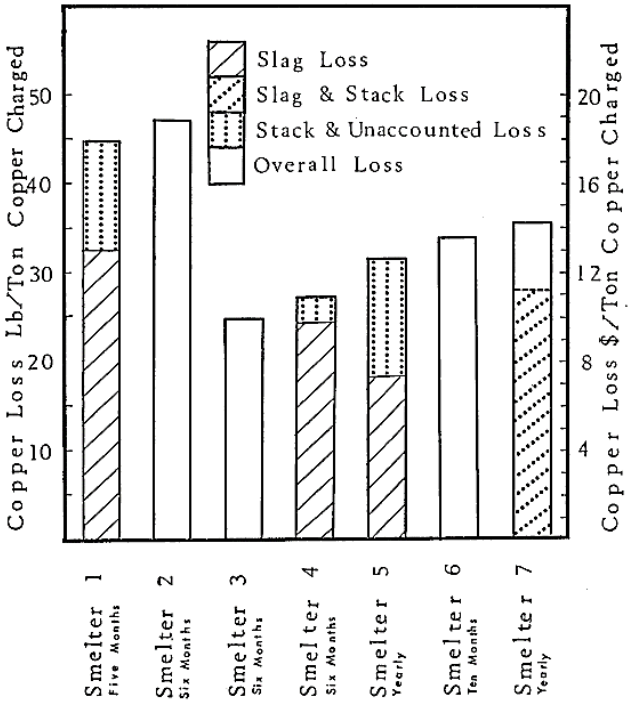

Figure 2.1 Copper losses and their economic impact during smelting in seven plants as summarized by Yannopoulos [3]

The amount of losses depends on the industrial processes used, i.e. which type of furnace. The newer processes produce higher grades of matte, which results in slags with higher copper content. Sridhar et al. [20] estimated that for the annual worldwide primary copper production of 9 billion tons, 181 million tons of copper are discarded via the slag, which represented 400 million dollar at that time.

Smelting furnace slag contains roughly 1-2 % Cu, which rises as the matte grade increases according to Davenport et al. [12] Converter slag contains roughly 4-8 % Cu [12] and smelting slags from the Teniente converter contain up to 8 wt%, according to Warczok et al. [21]. Based on compositions of several industrial slags, Shen [22] noted that the copper content varied between 0.5 and 3.7 wt%. Taking into account the mass of each produced slag, a significant amount of copper is present in this slag. [12,23] Tan [24] described the amount of losses of the Xstrata Copper Smelter process at Mount Isa and concluded that the copper lost to rotary holding furnaces is the single largest loss in the copper smelter. As stated by Degel et al. [25], metal losses in the copper industry are one of the main factors determining the overall plant recovery.

In order to make the pyrometallurgical processes more efficient and minimize metal losses, more knowledge is required on the form and origin of these losses. A small amount of literature can be found on the influencing factors for the decantation of metals in slags. Nevertheless, it is generally accepted [3,14,20,26,27] that the metallic losses in slags have two causes: the chemical dissolution of metals and the mechanical entrainment of metallic droplets. The chemical dissolution of metals is inherent in pyrometallurgical processes and governed by the system's thermodynamic equilibrium. The amount of dissolved metal is correlated with the thermodynamic state of the furnace. [14,27] The difference between the actual amount of copper present and the amount that can be attributed to its dissolution, is usually assigned to the formation of a mechanical dispersion of matte/copper in the slag. [28] Figure 2.2 shows the copper losses in slags as a function of the matte grade in the Tamano flash smelter as indicated by the shaded frame. Maruyama et al. [29] simulated the chemical copper losses within this industrial set-up, using HSC chemistry. The difference between the simulations and the actual industrial data were assumed to be attributed to mechanical losses (indicated by suspension loss).

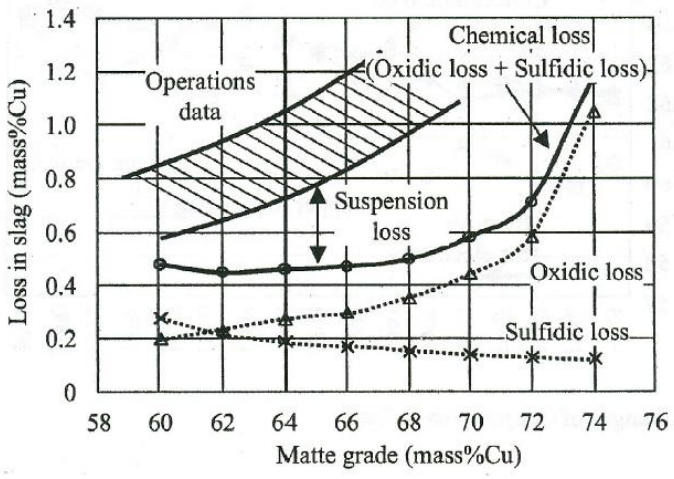

Figure 2.2 Simulation of copper losses in slag at the Flash Smelting Furnace operation at Tamano smelter. The oxide and sulphide losses were calculated using HSC chemistry, the shaded part shows the operation data. The difference between both is attributed to mechanical losses (referred to as suspension loss) [29,30]

Apart from the economic losses associated with these droplets, the process becomes more difficult to handle when Cu droplets are present. The process aspires to an optimal quantity of Cu-oxide in the slag: the amount of copper in the slag is determined by analyses and this sets the oxygen quantity. There is, however, no way to notice the difference between metallic Cu (in the droplets) and the oxidized form (dissolved in the slag) in the short time span available during processing, because the analyses to discover the difference take too long. This indicates that the process control is not

optimal. The copper smelting processes at this moment are usually controlled based on experience, but a better separation can probably be obtained when a more fundamental knowledge of the interactions and phenomena in the formation of droplets and sedimentation is constructed. The different types of losses will be discussed in more detail in the following sections.

2.3.1. Dissolved metal

Chemical dissolution of metals in slags has already been investigated thoroughly in literature [13,31–33]. Initially, copper (and other metals) was assumed to be dissolved in slags as oxides, called the 'oxidic' dissolution. The Cu_2O amount in a slag is related with the thermodynamic state of the furnace and it can be minimized by controlling the furnace according to well-studied metal-matte-slag-gas relationships. [27] The oxidic copper solubility increases with increasing p_{O2} and decreasing temperature. [14,33] The effect of the temperature can be observed in Figure 2.3 and the influence of p_{O2} in Figure 2.4.

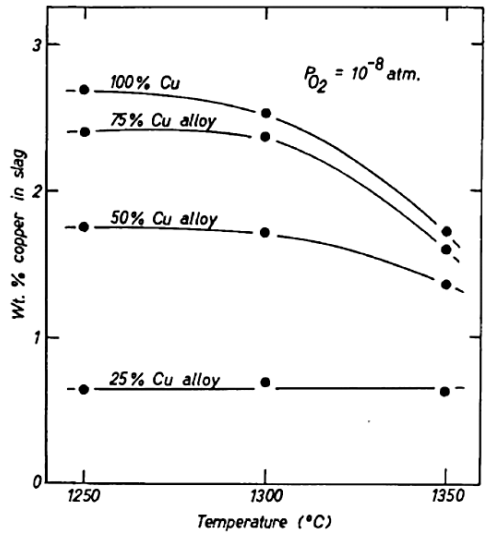

Figure 2.3 Effect of the temperature, at constant p_{O2}, on the solubility of copper in slag [33]

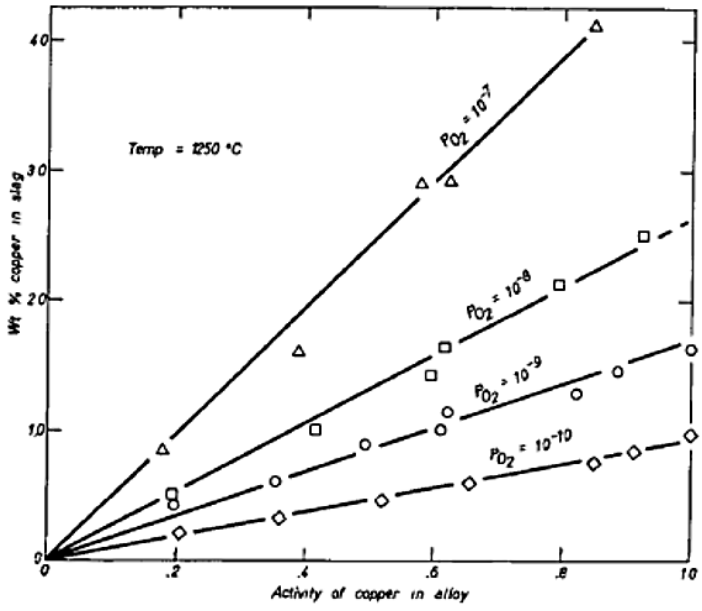

Figure 2.4 Relation between amount of Cu in the slag and the activity of Cu in the alloy as a function of p_{O2}, at constant temperature [33]

Increasing the matte grade also results in a higher copper content in the slag. [3] The silica content can also influence the Cu losses. It was found that the minimum loss of copper due to mechanical entrainment is found at approximately 35% SiO_2. This decrease up to 35% is accounted for by the predominance of the interfacial tension of slag and matte over the viscosity of the melt. SiO_2 addition increases the viscosity and decreases the surface tension. The silica content also has an influence on the magnetite formation (the ratio SiO_2/FeO is important). [3] Other slag constituents also influence the amount of copper lost: increasing FeO decreases the viscosity, increases the density and enhances the reduction of magnetite which in turn enhances the solubility of copper in slag (by forming SO_2 bubbles). The solubility of the matte in the slag is reduced with increasing CaO content, because it reduces the specific gravity and lowers the melting point and the viscosity. CaO also increases the surface and interfacial tension. Al_2O_3 increases the viscosity of the slag, it should, however, be noted that the effect on the copper losses depends on which other slag constituent the alumina replaces. MgO acts in the same way as CaO if it is added in small amounts. [3] CaO is the most effective in decreasing the copper solubility, followed by MgO and Al_2O_3, this order corresponds to that of the basicity of these additives. The results can be explained by the acid-base theory of the slags: the ions of the additives (Ca^{2+}, Mg^{2+} and Al^{3+}) replace some of the copper ions and occupy sites in the silica structure. [34]

Richardson and Billington [35] concluded for sulphur-free slags that copper can only be dissolved after being oxidized and no solubility of atomic copper is present. When the slag coexists with a sulphidic matte phase, the iron silicate slag can dissolve additional copper. Thanks to the ionic theory, the concept of ‘oxidic’ and ‘sulphidic’ dissolutions of copper was developed to explain this phenomenon. [14] Sehnalek and Imris [36] and Nagamori [37] were the first to recognize the sulphidic dissolution of copper. Nagamori found the copper solubility in his experiments to be far greater than that attributed to oxidic loss according to previous work (which was performed on sulphur-free slags). The solubility was related to the presence of sulphur in the slag and the concept of sulphidic dissolution was developed. The molecular or ionic theory of a slag states that a sulphur ion may dissolve in the slag as if it replaces a free oxygen ion, which was originally associated with an iron ion. The sulphur ion may in turn tend to replace some of its coordinating iron ions with copper in accordance with the activity of copper in the matte.

The total dissolved copper in the slag is the sum of the oxidic and sulphidic dissolution. The fractions of both kinds of dissolved copper depend on the composition of the slag. The sulphidic dissolution is in general important for matte grades up to approximately 60% Cu, while oxidic dissolution is the significant mechanism otherwise [14], as illustrated by Figure 2.5 [38]. To decrease the dissolved copper loss in slag, it is effective to raise the Fe/SiO_2 ratio to decrease the oxidic loss. In order to decrease the sulphidic loss, this ratio should be lowered. [29]

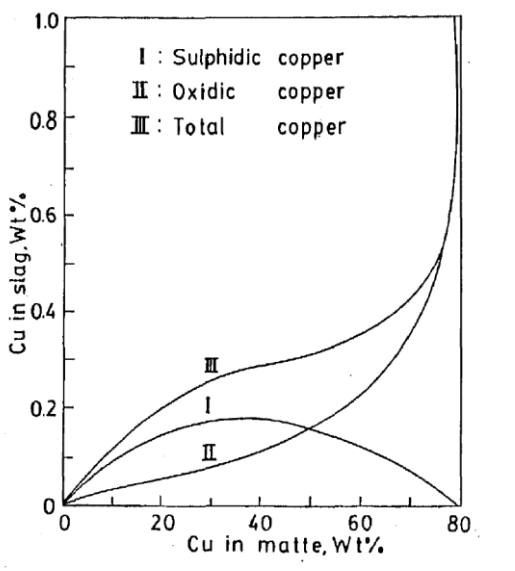

Figure 2.5 Schematic diagram of calculated oxidic, sulphidic and total dissolved copper in commercial reverberatory slag [38]

An increase in Al_2O_3, MgO, CaO or SiO_2 decreases the mutual dissolution between matte and slag, thus the dissolved sulphide content in the slag and the dissolved oxide content in the matte decrease. [13] Apart from the decrease in copper solubility, the Fe^{3+}/Fe^{2+} ratio was also lowered due to the additions of CaO, MgO and Al_2O_3. This effect, however, was smaller at lower oxygen potentials. [34]

Even though it was universally agreed that dissolved copper in slag occurs as both copper sulphide and copper oxide, [26] this idea has been rejected by Gaskell et al. [39] and Sridhar et al. [20]. It was observed that the original data of Nagamori [37] show that the copper content in slags decreases as the sulphur content increases and Sridhar et al. [20] also pointed out that normal investigations use a gas-matte equilibrium to control the oxygen potential (similar as in plant practice). Nagamori used metallic iron in equilibrium with 0-55wt% Cu mattes to control the oxygen potential. With this method, the oxygen potential is lower than in copper smelting and this increases the sulphur solubility. For Cu grades of mattes above 55wt%, Nagamori used copper metal in contact with matte to fix the oxygen potential. This results in an oxygen potential close enough to that in copper smelting. It was observed by Nagamori that in this latter composition range the copper loss is only oxidic. The observations of Sridhar et al. [20] imply that the copper losses in slags can be explained by the oxidation of copper at different oxygen potentials present during the production of different matte grades. No assumption of copper sulphide species in the slag is needed to explain copper losses. Moreover, according to Sridhar et al. [20], it is very unlikely that copper sulphide is present, as the affinity of sulphur for Fe is higher than for Cu. This leads to a higher probability for sulphide ions to be present in the proximity of iron ions. Victorvitch [40] drew a similar conclusion in extensive studies on copper smelting slags.

Although Gaskell et al. [39] and Sridhar et al. [20] made some very good arguments concerning the theory of sulphidic copper, no clear consensus on the dissolution of copper as sulphidic copper has been reached so far. However, usually chemical metal losses in fayalitic slags are assumed to have five different types of dissolution, as described by Mackey. [14] The 'oxidic' dissolution, which occurs when the oxide of an element in the slag is stable under the prevailing gas atmosphere and temperature. 'Sulphidic' dissolution occurs when the dissolved sulphur in the slag forms a stable sulphide with the element. In case both the oxide and the sulphide of the element are unstable under

the process conditions, the element can also dissolve in metallic or gaseous form. This is the 'monoatomic' type of dissolution. An element can occur in the slag in 'molecular' form when the compounds between iron and sulphur are stable under copper smelting conditions. The last type is 'halidic' dissolution, which occurs in the slag at copper smelting conditions provided that some halogens are present in the system.

2.3.2. Mechanically entrained metal droplets

The difference between the actual and thermodynamically predicted metal content in slags can be attributed to the mechanical dispersion of metal and matte in the slag. A significant amount of literature deals with chemically dissolved metal losses to slags, but a large spread on the data is observed. This can be explained by the amount of physically entrained matte or metal, which is usually not measured and which is difficult to calculate accurately. Mechanical losses in the slag can make up to 65-80% of the total copper loss. Mechanical losses depend on the way the furnace is operated, slag viscosity, fluid motion in the slag, residence time, SO_2 generation in the melt, the presence of solid particles which can trap matte droplets, the matte-slag separation, … [14]

The losses due to the droplets are far less controllable than the dissolved metal losses. They are associated with the inadequate decantation of the droplets. The mechanical losses are droplets with varying sizes from several mm to a few µm. [26,41] In general, sedimentation of droplets of a certain phase in another phase can be described by Stokes' equation:

$$u = \frac{2r^2(\rho_{sphere} - \rho_{fluid})g}{9\mu} \quad \textbf{(2.1)}$$

Where u is the settling rate (m/s), ρ_{sphere} and ρ_{fluid} the density of the droplets and the surrounding phase respectively (kg/m³), *r* the radius of the droplet (m), *g* the gravity constant (m/s²) and μ the viscosity of the slag (Pa.s). This equation is valid for laminar flow conditions, which are characterized by a low Reynold number, for rigid spheres or drops/bubbles and approximately valid for liquid droplets rising or settling in an immiscible medium characterized by an immobile surface. [42,43] Larger copper droplets in slags in industrial processes, however, are not necessarily rigid and do not maintain their spherical shape. If the viscosity of the copper droplets is much lower than the viscosity of the slag, internal tensions are created within the droplets and Stokes' equation should be corrected to the Hadamard-Rybczinski equation: [44,45]

$$u = \frac{g \cdot r^2 \cdot \Delta\rho}{3\mu} \quad \textbf{(2.2)}$$

It was found in early experiments that small drops with a diameter less than 0.01 cm behave like rigid spheres as their velocity is described by the Stokes' equation. On the other hand, drops of a sufficiently large size fall within velocities described by the Hadamard-Rybczinski equation. [46] The Stokes and the Hadamard-Rybczynski equation emphasize the importance of the slag viscosity, the size of the sinking droplets and the density difference. To get a fast decantation, the following should be aimed for: [3]

- the difference in density as high as possible. The density of iron silicate slags in copper smelting decreases with the increase in silica content, a decrease in temperature and also with an increase in basic oxide levels. Generally, FeO increases the slag density, while SiO_2 and CaO have the opposite effect.

- the size of the droplets as large as possible. Larger droplets can be achieved by coagulation or growth of smaller droplets. This increases the surface/volume ratio, which is related to the interfacial energy between the droplets and the slag. The droplets can also grow or shrink due to reduction or oxidation reactions.
- the viscosity of the slag should be as low as possible. In the case of high viscosity liquids, small particles can remain entrapped for long periods of time. [47] It should be noted that the viscosity of the slag depends on the fraction solid particles, this is called the "slurry effect" (which is described by the Einstein-Roscoe model equation: $\eta = \eta_0(1-af)^{-n}$ with η the viscosity of the liquid melt with solid particles dispersed in it (Pa.s), η_0 the viscosity of the liquid without solid particles (Pa.s), f the fraction of solid particles in the melt, a the inverse maximum fraction of solid particles and n a constant related to the geometrical particles shape, which is assumed to be 2.5 for spherical particles [48]). The settling rate can be increased by decreasing the viscosity or by using a more reducing environment, as the Fe_3O_4 content of the slag will be decreased. [12]

The settling rate has an important influence on the efficiency of the sedimentation process. Maruyama et al. [29] investigated the influence of the settling time on suspension losses. As expected, it was confirmed that the copper content in the slag layer decreases with increasing sedimentation time. The settling of suspended particles using the Stokes' equation was calculated and is presented in Figure 2.6. [29] For the Tamano Flash smelting furnace, the average settling time of the slag is 4 to 5 hours. Within this time frame, particles with a size larger than 0.13 to 0.15 mm diameter settled. Longer decantation times only have a limited effect on the recovery of the smaller particles. [29]

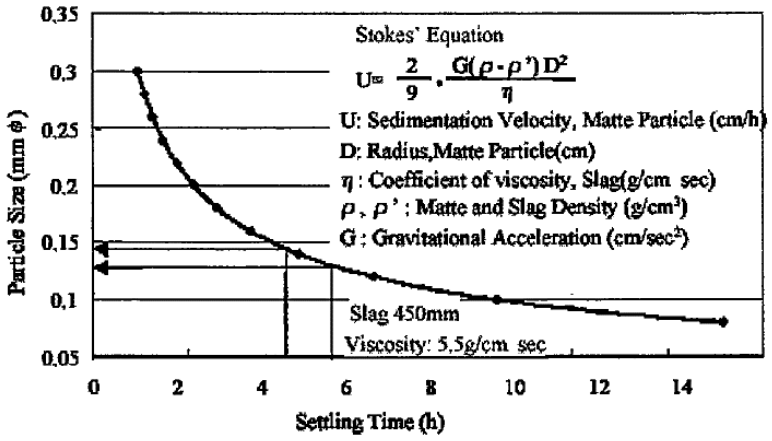

Figure 2.6 Relation between settling time and particle size by Stokes' equation calculated by Maruyama et al. [29]

It was generally believed that phase separations in slag-metal systems occur only due to the buoyancy effect (the large difference in density of the alloy and the slag). Lau et al. [49] checked this hypothesis, by investigating the influence of different gravity conditions on the products synthesized by combustion phenomena. Different systems were investigated in a variety of gravity conditions from 10^{-5}G up to 1.7G (this corresponds to overload gravity and is achieved in a part of the trajectory during parabolic KC-135 flights). The investigation showed that mechanisms driven by surface energy might also play an important role in the sedimentation process. [49] Also note that some copper matte or metal droplets can retain on the surface of the slag due to surface forces, which was experimentally observed by Fagerlund [50]. Poggi et al. [47] defined the critical radius of a droplet

that can rest on the interface by equating the upward force due to surface tension and the weight of the drop:

$$R = \left(\frac{2 \cdot \gamma_{slag}}{4/3 \cdot \rho_{particle} \cdot g} \right)^{1/2} \quad \textbf{(2.3)}$$

With R the critical radius of sphere (m), ρ the density (kg/m³), g the gravity constant (m/s²), γ the surface tension (N/m). It is expected that larger drops sink through the slag/metal or matte surface and that smaller drops float.

Up to this point, the phenomenon of mechanically entrained droplets was described. However, the question remains where and how do these droplets originate? Mechanically entrained matte or metal droplets in slag can originate from a variety of sources: [51,52]

1. Entrainment due to charging of the furnace or tapping of the slag
2. Precipitation of copper from slag due to temperature or oxygen level gradients within the furnace or due to chemical reactions
3. Sulphur dioxide gas, produced in the matte phase, or other gas phases dispersing the matte into the slag as the gas crosses the matte-slag interface
4. Attachment of matte/metal droplets to solid particles present in the slag phase which hinder their settling

The different possibilities will be discussed in more detail in the following sections.

2.3.2.1. Entrainment due to charging of the furnace or tapping of the slag

Liow et al. [53] studied slag tapping operations in the settler region of a copper flash furnace and the influence on the entrainment of a two-layer liquid through a tap hole. Paraffin oil was used in the experiments to resemble the slag, which is more viscous than the heavier metal or matte phase. Water and salt solutions were used to simulate the matte or metal layers. It was observed that a simple ledge can effectively reduce entrainment, due to the formation of a meniscus by the lower liquid layer on that ledge which inhibits the flow.

2.3.2.2. Precipitation of copper from slag due to temperature or oxygen level gradients within the furnace or due to chemical reactions

Regarding the second possibility, it should be noted that the slag phase in industry might not be homogeneous, and local variations in temperature or oxygen levels are possible. The dissolution of copper in the slag is influenced by those parameters, cfr. section 2.3.1. Thus, certain zones in the slag might be characterized by a lower copper solubility, leading to the precipitation of oxidized copper present in the slag as metallic copper droplets. Moreover, a large part of the copper dissolved in the slag can precipitate as metallic copper from iron-silicate slags, even in quenching, according to Jalkanen et al. [28]. In quenched slags, copper is said to be evenly distributed as small size precipitates. The copper particles in a quenched slag are regularly surrounded by a dark sphere. The precipitation of copper during the quenching of the slag is said to be caused by the disproportion reaction of cuprous oxide with Fe^{2+}-ions. This reaction yields metallic copper and Fe^{3+} and explains the rapid disproportion, as supported by the observations of Vehviläinen and Imris et al. [26,28] who suggest that copper is often surrounded by magnetite. [28]

$$Cu_2O + 3FeO \leftrightarrow 2Cu + Fe_3O_4 \quad \textbf{(2.4)}$$

Whenever mass transfer takes place at a certain liquid-liquid interface, various transitory phenomena occur [54]:

- hydrodynamic phenomena originating from interfacial tension gradients,
- lowering of dynamic interfacial tension when mass transfer at the interface is intense,
- spontaneous emulsification by 'diffusion and stranding' mechanisms.

These effects are evidenced by the deformation of a metal drop, immersed in a slag, during intense mass transfer between the two phases. Gaye et al. [54] investigated the influence of mass transfer upon interfacial phenomena with X-ray observations at high temperature. It was shown that, when very high reaction rates are obtained, the tendency towards spontaneous emulsification exists and it was pointed out that part of the reaction takes place in the slag, at some distance from the interface, through a 'diffusion and stranding' mechanism. They also found that for various systems, the interfacial forces seem to disappear when the oxygen flux is larger than 0.1 g.atom/(m².s). Dispersion of one phase into the other may become extremely easy in this case and can occur without external mechanical energy.

Afterwards, Rhamdhani et al. [55] investigated reactions between liquid iron alloy droplets and a liquid slag at high temperature. The observed phenomena, include droplet flattening or spreading (a decrease in apparent interfacial tension of the droplet), interfacial turbulence and spontaneous emulsification (the droplet breaks up into numerous smaller droplets). The first and the last of these possibilities can be observed in Figure 2.7. This figure represents the sequence of steps encountered by Rhamdhani et al. [55,56] during their experiments: in the early stage of the reaction, the recovered droplet has a nearly flat shape, but when the reaction is the most intense in the intermediate stage, numerous droplets, mm and µm in size, were obtained. Apart from this macroscopic emulsification, some microscopic emulsification was also observed in the stage prior to emulsification, some microdroplets can be found near the interface of the single droplet. But although many microdroplets can be observed, they do not change the interfacial area significantly.

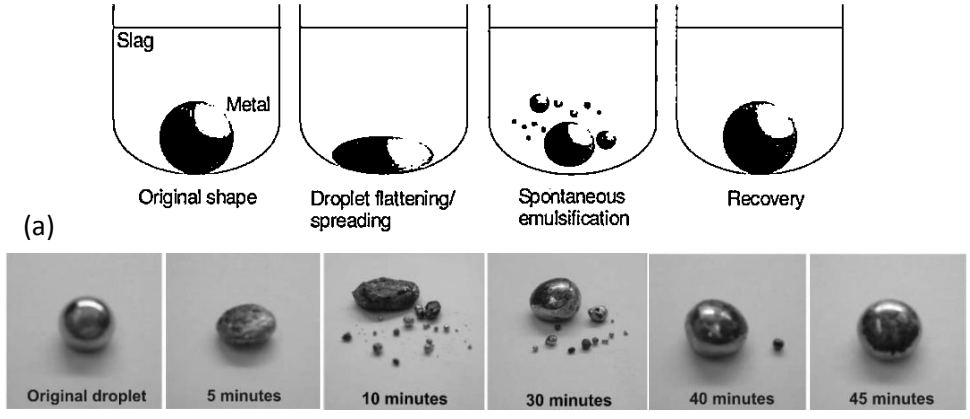

Figure 2.7 Droplet shape changes during high temperature reactions (a) schematic representation[55]; (b) Shape and droplet changes during the reaction between Fe - 4 wt % Al (2.34 g) and CaO-SiO_2-Al_2O_3 at 1650°C [57]

It should be noted that both metal and slag emulsification are observed. Rhamdhani et al. [55] also observed the initiation of emulsification: an interfacial instability causes a protrusion of slag into the metal phase, as the tip goes further into the metal phase it will tend to become spherical to decrease its interfacial area; once necking occurs, detachment of the droplet is favourable in order to decrease its interfacial area; an emulsified slag droplet in the metal phase is then formed. The same mechanism may apply for metal protrusion into the slag leading to metal emulsification in the slag. The first emulsified droplets are in the µm size range, further they may coalesce to form bigger

droplets (in the order of a few tens of μm). A perturbed interface is only observed in the first stages of the reaction.

2.3.2.3. Gas phases dispersing the matte into the slag as the gas crosses the matte-slag interface

The third possibility (SO_2 gas bubbles crossing the interface) has been investigated thoroughly. [47] Any type of gas bubbles can have the same effect of taking matte or metal with it into the slag phase when the interface between the different phases is crossed. [58] Rising SO_2-bubbles can find their origin in the reaction between iron sulphides and magnetite. This reaction is thought to take place near the furnace bottom and the charge banks. [47] Cuprous oxides dissolved in the slag can also react with either Cu_2S (in the matte) or a combination of solid SiO_2 and FeS (in the matte) to produce SO_2 gas bubbles. [59]

This was also illustrated by Holappa et al. [58] for steel production. When gas bubbles pass through the iron/slag interface, small iron droplets burst into the surrounding slag (Figure 2.8 (a)). When the gas bubble exits the interface to the slag phase, a jet is formed to fill the cavity with metal. This jet collapses and produces metal droplets into the slag phase, as illustrated in Figure 2.9 (c and d) and Figure 2.8 (b). It is interesting to note that they observed that with larger bubble sizes the mass of the entrained metal in the slag increases strongly and that smaller bubbles cause practically no entrainment of metal into slag. They also noted that an increase in the interfacial tension of the metal or in the viscosity of the slag reduced the metal entrainment.

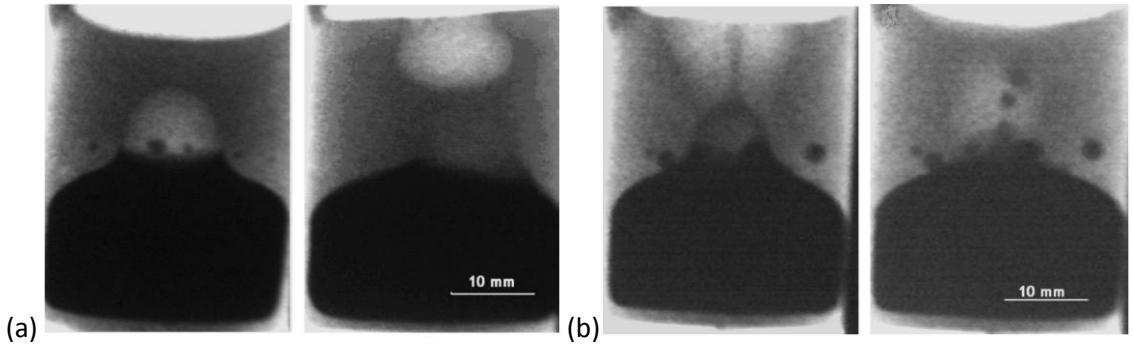

Figure 2.8 (a) X-ray images showing bursting and detaching of a gas bubble from the iron-slag interface (b) X-ray images showing the mechanism of iron droplet entrainment into slag [58]

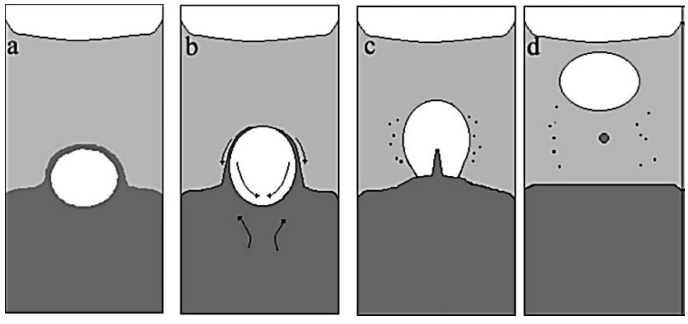

Figure 2.9 Proposed mechanisms for the formation of jet and film droplets in the slag when a gas bubble passes through the iron/slag interface [58]

Thus, the ability of gas bubbles to pick up droplets from the underlying phase into the upper phase is governed by the surface and interfacial tension of the involved liquid phases and gas. Three

situations are possible, as shown in Figure 2.10, where L_2 represents the underlying liquid phase and L_1 the upper phase. [51,52,60]

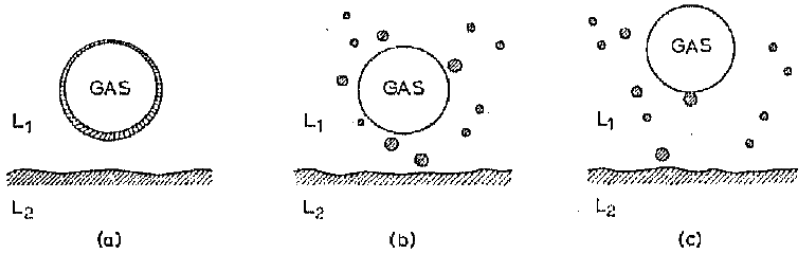

Figure 2.10 Interactions between a gas bubble and liquid droplets in a continuous phase: (a) a film of the underlying phase (L_2) is formed on the gas bubble, (b) droplets of the underlying phase (L_2) are scattered in the upper liquid (L_1), and (c) attachment of the droplets of the underlying phase (L_2) to the bubble through contact [60]

It was suggested that possibility (a) (formation of a film coating on the gas bubble) will occur if the spreading coefficient is positive. The spreading coefficient ϕ is defined as:

$$\phi = \gamma_{L_1/g} - \gamma_{L_2/g} - \gamma_{L_1/L_2} \quad \textbf{(2.5)}$$

Where $\gamma_{L1/g}$ is the surface energy of the lower liquid phase, $\gamma_{L2/g}$ the surface energy of the upper liquid phase and $\gamma_{L1/L2}$ the interfacial energy between both liquids. The metal or matte coating of the bubble can subsequently rupture and scatter smaller droplets into the slag phase. The small droplets are scattered by the rupture of the film, they tend to sink to the lower liquid surface under gravity, but they may become entrapped as rafts of droplets, which float on the top surface of the slag due to surface tension forces or they can be suspended as droplets below small supporting gas bubbles or they may become entrapped in the slag due to the fact that they are extremely fine, hereby settling extremely slowly. [47]

Situation (c) (flotation of the droplet by a gas bubble with contact) will occur if the flotation coefficient (defined in the following equation) is greater than zero.

$$\Delta = \gamma_{L_1/g} - \gamma_{L_2/g} + \gamma_{L_1/L_2} \quad \textbf{(2.6)}$$

Situation (b) (flotation of droplets without contact with the gas bubble) will take place only if this flotation coefficient is less than zero.

The flotation behaviour can alternatively be investigated by the development of a ternary interfacial energy diagram based on the balance between surface and interfacial tension forces acting on a droplet resting on a liquid-liquid interface. [51] The conclusions of this and the abovementioned method are identical. [52] Ip and Toguri [51] made such a ternary interfacial energy diagram for the matte-slag-gas, copper-slag-gas, copper-matte-gas and copper-slag-matte systems at 1473K. They used it to show that matte droplets with more than 32 wt% Cu will not form a film on rising gas bubbles when they collide in the slag phase. The matte droplets will attach themselves to the gas bubbles upon collision and can rise together with the gas bubbles, i.e. are floated, over the whole range of matte composition. Thus, matte flotation in the slag phase cannot be eliminated by altering the matte grade. [51]

Spreading of metallic copper on bubbles is not possible at oxygen pressures between 10^{-12} and 10^{-8} atm. Flotation of copper by gas bubbles is possible at oxygen pressures higher than 10^{-9} atm. Therefore, to avoid the entrainment of metallic copper, the oxygen pressure inside the furnace should be kept below 10^{-9} atm. It should be noted that the possibility exists that copper droplets attach themselves to matte droplets and are floated by rising gas bubbles, irrespective to the matte grade. [51]

2.3.2.4. Attachment of matte/metal droplets to solid particles present in the slag phase which hinder their settling

The rather small amount of literature available on the fourth possibility (attachment to solid particles) mainly focusses on the observation of the phenomenon. Only recently, De Wilde et al. [61–63] investigated the phenomenon in more detail. The phenomenon is observed in industry as the attachment of Cu rich droplets to spinel particles present in the slag. The processes in the Cu smelter take place on temperatures ranging from 1180 to 1250°C. Processing temperatures beneath 1200°C typically produce a subliquidus slag. Due to this subliquidus temperature, the slag contains solid particles, which influence the viscosity of the slag and can even cause entrainment of matte or metal droplets. [12]

Observation of Cu entrainment by solid particles has shown that these solid particles often possess a spinel structure. Investigation of the lead losses in the slag of a reduction melting furnace by Calvo et al. [4] showed a relation between the amount of metal losses and the magnetite (a specific type of spinel mineral) content. Microscopic investigation showed that the magnetite appeared to be associated with the lead particles, as illustrated in Figure 2.11. The amount of magnetite present in the slag is determined by the reduction potential of the furnace, which can be indicated by the sulphur content of the slag (an adequate reduction potential increases the sulphur content).

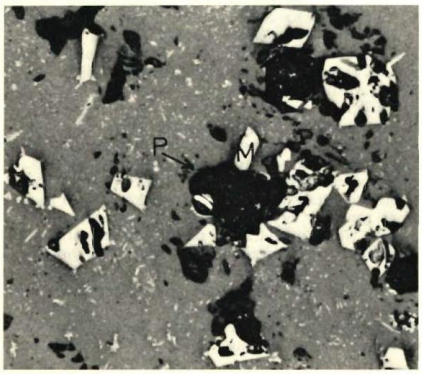

Figure 2.11 Slag with 3.8 wt% lead: (M) Magnetite , (P) metallic lead (magnification x400) [4]

An investigation of the slag of a ferrochrome smelter [6] shows the presence of $(Fe,Mg)(Cr,Al)_2O_4$ spinel and these microstructural elements can be linked to the entrainment of metallic droplets, as shown in the pictures of Appendix B of reference [6]. Two of them are shown in Figure 2.12.

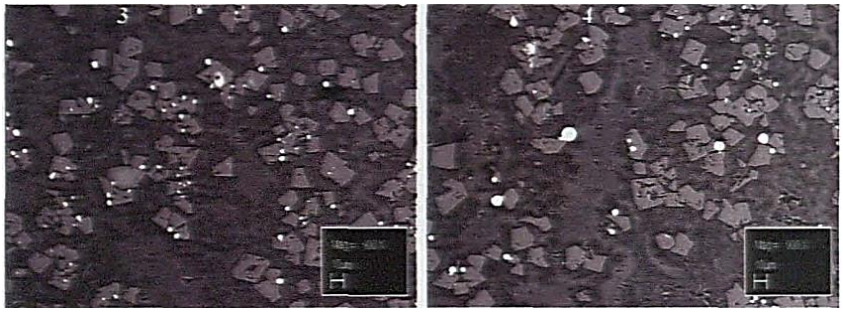

Figure 2.12 SEM backscattered electron images of slag containing metallic droplets [6] (the scale bar in the figure represents 10 μm)

The dependency of the amount of entrained Cu drops on the amount of spinel particles (and on the temperature) can be observed in Figure 2.13.

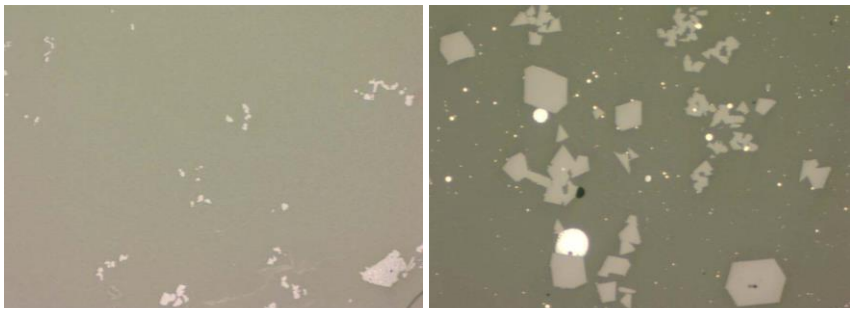

Figure 2.13 Left: slag at 1200°C contains 2% spinels (with Fe and Zn); Right: slag at 1140°C contains 10% spinels which entrain some Cu drops [64]

Magnetite has different effects on the viscosity and settling of Cu droplets: [3]

- Magnetite can be reduced by FeS which produces SO_2 bubbles, which in turn promotes the flotation of matte or copper droplets into the slag, as described above.
- The presence of magnetite promotes the formation of copper ferrites.
- The presence of magnetite increases the viscosity of the slag, which reduces the settling of droplets, cfr. Stokes' equation.
- The disturbance of the phase separation between the slag and matte or alloy through the formation of a magnetite false bottom between the slag and the matte or alloy layers (called a "mushy" zone).

Barker et al. [65] investigated the correlation between magnetite and copper amounts in slags and found a direct connection between the two. Afterwards other investigations delivered the same conclusion: Imris et al. [26] observed the correlation between magnetite content and copper losses in slags, as can be seen in Figure 2.14 (a) and by Barker et al. [65] in an industrial experiment as shown in Figure 2.14 (b).

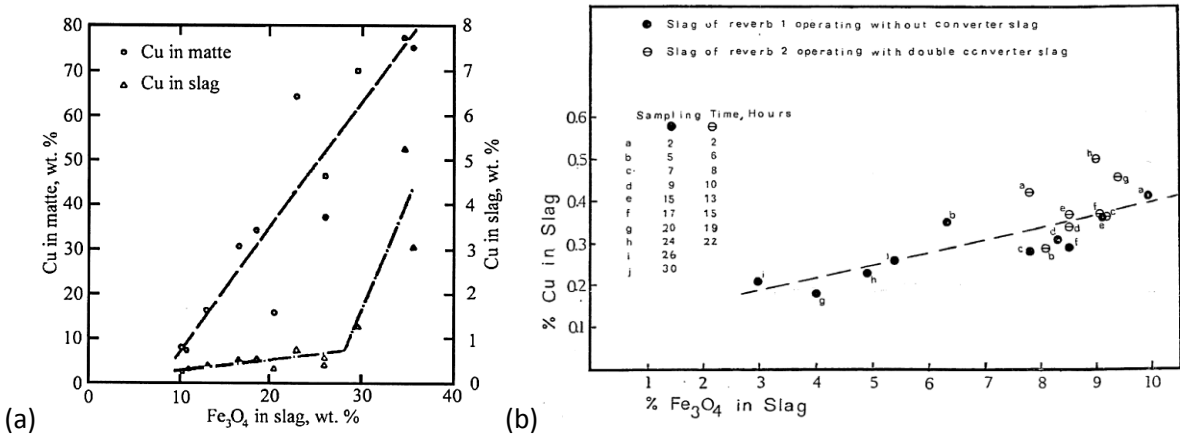

Figure 2.14 (a) Copper content in slag and matte versus magnetite content in slag at 1250°C [26] (b) Special 24 hour industrial test in la Oroya smelter [3,65]

Due to the combination of all interacting influences of magnetite, it is difficult to define a quantitative relationship between magnetite and copper content in the slag. [3,59,65,66] Similar conclusions can be drawn for other (spinel) solids present in slags. An increase in solids in slags will increase the viscosity of slags and lead to slower settling of entrained droplets, which subsequently leads to higher mechanical losses. Furthermore the phase separation can be disturbed due to the presence of solids in different zones in the smelter. [3,26,67] In addition, it is believed that the phenomenon of copper

droplets attached to spinel particles is an important reason for spinel solids hindering the sedimentation process. The presence of spinel solids can be explained by the operation temperature that must be subliquidus.

Nevertheless, it is not clear when or where the attached droplets originate. Are the Cu droplets formed together with the magnetite, according to the disproportion reaction or do the Cu droplets attach themselves to the already present spinel particles or a combination of both? No specific attention had been given to this phenomenon and no knowledge was available concerning the fundamental mechanisms responsible for it, until recently published work of De Wilde et al [62,63,68,69]. They were able to reproduce the attachment in a synthetic slag [62], as illustrated in Figure 2.15.

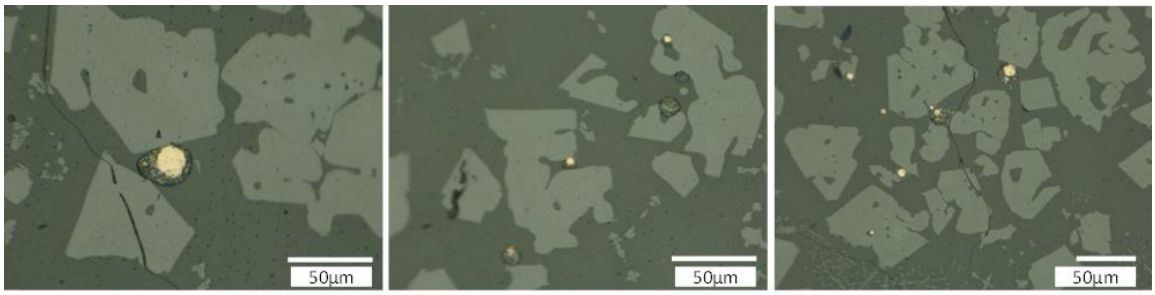

Figure 2.15 Detailed microstructures (LOM) of sticking droplets (Cu-Pb) to (Fe-Zn-Al-O) spinel particles present in slag obtained by melting a mixture of 1.4wt% Al_2O_3-2wt% CaO-17.2wt% FeO-45.6wt% PbO-8.4wt% ZnO-10.1wt% Cu-15.2wt% SiO_2 at 1200°C under a p_{O2} of 10^{-7} atm. [62]

After which they also investigated how this attachment influences the settling time [63] with a model based on the Hadamard-Rybczynski formula and experiments. In the experiments, a clear decrease of the amount of mechanical entrained droplets was noticed in the upper slag layer as a function of time, together with a variation of the amount of mechanically entrained droplets as a function of slag height. Similar observations could be made for the spinel solids present in the slag. The settling rates calculated with the model were of the order of 1 mm/min, which corresponded with the experimentally obtained values. It was observed that the attachment hindered the complete sedimentation towards the underlying copper phase, because the average density of the 'Cu-droplet – spinel' entity is lower than that of the underlying copper. Additionally, the presence of attached spinel particles can obstruct the coagulation of smaller droplets, which also lowers the settling rate.

The origin of the attachment was also investigated by sampling at different moments during melting experiments. Some of the results are shown in Figure 2.17. Moreover, a more fundamental approach was used to investigate the interaction: sessile-drop experiments of slag and/or metal on a spinel substrate at high temperatures [68,69] showed that slag exhibits a better wetting than copper on spinel. This is in contrast with the observation that attached droplets remain attached and settle down. Thus, as slag exhibits a better wetting than copper on spinel, an energy barrier should be overcome by the copper droplets to expel the slag layer.

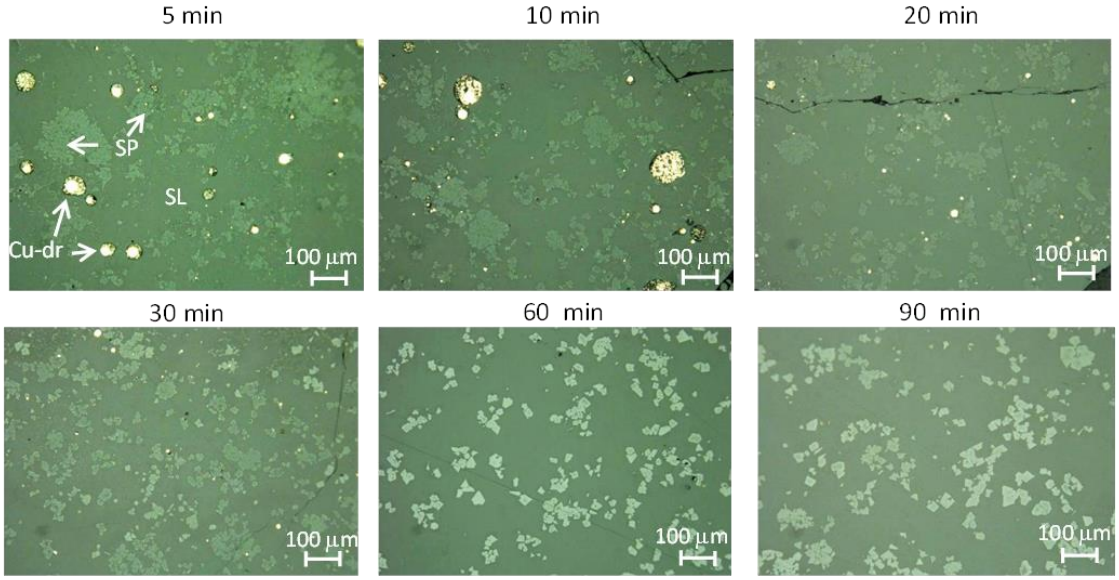

Figure 2.16 Representative LOM pictures of the upper slag layer at 5, 10, 20, 30, 60 and 90 min after bubbling in slag obtained by melting a mixture of 7.3wt% Al_2O_3-9.8wt% CaO-19.4wt% FeO-39.3wt% PbO-6.5wt% ZnO-3.9wt% Cu-13.8wt% SiO_2 at 1200°C under a p_{O2} of 10^{-7} atm. (SL = slag, SP = Al-Fe-Zn-O spinel solids, Cu-dr = copper-lead alloy droplets) [63]

From these observations, De Wilde et al. [63] proposed two different ways to explain the origin of the attachment. Firstly, extensive stirring can be sufficient to induce the attachment. Secondly, a chemical reaction taking place during the evolution towards a thermodynamically more stable state can be responsible for the attachment. While the first assumption seems to be less likely as sticking droplets are also observed in experiments without any stirring, the second option was explored in more detail: a slag that is initially free of any Cu droplets was prepared. After the insertion of a steel bar in the system, the formation of sticking droplets was observed. [70]

A reaction scheme was proposed, including two possible pathways where the spinel solids form together with the copper droplets or form around the copper droplets, depending on the local conditions of the system. In both pathways, redox reactions involving copper (oxides) are essential and within the applied synthetic system, Fe and Fe-oxides play a crucial role. Within the slag system, two different types of spinel phases were present: an Al-rich spinel and an Fe-rich spinel. Throughout all experiments, it was observed that copper droplets were only attached to Fe-rich spinel solids. Furthermore, it was also observed some copper droplets were completely surrounded by spinel solids present in the slag system. Both observations, together with the fact that the attachment occurs even though the slag exhibits a better wetting than copper on spinel, support the explanation of the reactive origin of the attachment [63,69,70].

These observations together with the observations of Durinck et al. [71] suggest a final experiment to confirm the reactive origin of the attachment. The addition of a more noble metal to the copper phase would give the opportunity to reveal whether the droplets present in the slag originate from a redox reaction of the slag (typically not containing the oxide corresponding to the more noble metal) or from the mixing of the slag and metal phase (which results in typically larger droplets containing the more noble metal). Durinck et al. [71] also found that a small amount of iron oxide in the slag has an important effect on its 'reactivity', which might be linked to the fact that iron is a multivalent cation.

2.4. Experimental methodologies

Metal losses in slags can be studied with a variety of methodologies. A first common approach is the use of water-based systems at room temperature. The dispersion of one liquid into another was studied by the use of several liquid combinations, resembling different density ratios (($\rho_{heavier}$ - $\rho_{lighter}$)/$\rho_{lighter}$): oil/water [72,73], oil/mercury [47], kerosene/water [53,74], mercury/ water-glycerine [47] and paraffin-wax/water [53] systems were already investigated in literature. This type of experiments is very useful to gain information regarding temperature independent processes. Poggi et al. [47] made qualitative high speed photographic observations of transport and entrapment mechanisms of argon bubbles carrying a mercury film into the water-glycerine mixture. Liow et al. [53] used this type of experiment to determine the conditions for the entrainment of a second liquid during the withdrawal of the first liquid. The drawback of this type of procedures is that only mechanical types of losses can be studied, and influences of or chemical reactions at high temperatures cannot be included.

A second frequently used approach is to study metal losses in slags by industrial and/or lab scale sampling procedures using industrial and/or synthetic slags. [26,28,59,75,76] This approach allows to monitor the copper losses (both chemical and mechanical) within processes taking place at high temperature by taking samples of the slag, matte or alloy are taken at high temperature. Profound analyses of the samples, combined with mass balances and thermodynamic analyses have provided valuable insights. Note that attention should be paid to the fact that slow cooling of the samples can influence their microstructure, as illustrated by the observations by Jalkanen et al. [28]: even when the slag is quenched properly, a major part of the dissolved copper in the slag precipitates as metallic copper from the slag, present as finely dispersed copper droplets. Imris et al. [26] studied copper losses in slags of the smelting and converting process by comparing thermodynamic calculations with microscopic examination and industrial data. Genevski et al. [76] studied slag melts obtained from flash smelting furnace operations and these industrial slag samples (air and nitrogen cooled) were used to determine copper losses using microstructural analysis combined with material balance calculations. Takeda [75], on the other hand, used synthetic slag and matte, for which the matte grade was varied. Both phases were melted in a silica or magnesia crucible, which was positioned in a reaction quartz tube under a controlled atmosphere. After the required reaction times, the crucibles were cooled and microscopic analyses and chemical analyses were performed. This approach is very widely applicable and accessible and the use of both industrial and synthetic systems has advantages. However, dynamic phenomena will be more difficult to observe and a critical evaluation of the microstructure is an absolute prerequisite.

A third method is the use of models like phase field models [77,78], computational fluid dynamics [24] or other numerical models [79], simulating the process. Tan [24] used computational fluid dynamics to gain understanding on the importance of the slag layer thickness for the entrainment during skimming. These data were compared with physical models. Pirker [79] applied different numerical models (volume of fluid simulations, super imposed Chimera grids, Lagrangian slag droplets) to study the slag entrainment in liquid metal during tapping processes. The use of models and simulations allows to model processes, in which different important parameters are variable to a very large extent. The combination of models with experimental insights can be a powerful tool.

A fourth method is the use of in-situ X-ray imaging, to monitor the behaviour of slag and alloy at higher temperatures. Some examples of such set-ups are shown in Figure 2.17. Holappa et al. [58]

studied the bubble bursting at the iron-slag interface with such a set-up, as explained previously. This technique is very valuable, as the behaviour of the liquid phases can be monitored at high temperatures. It is, however, not applicable for all liquid compositions. The condition to be fulfilled is that one of the liquids present should not absorb the X-rays completely (mostly the slag phase, which will result in light grey colour on the images), while the second liquid should absorb the X-rays (mostly the metal phase), resulting in a black colour on the X-ray images. Therefore, not all slag-compositions can be used. The slag, for example, can only contain limited amounts of Pb. Furthermore, this technique is not widely accessible.

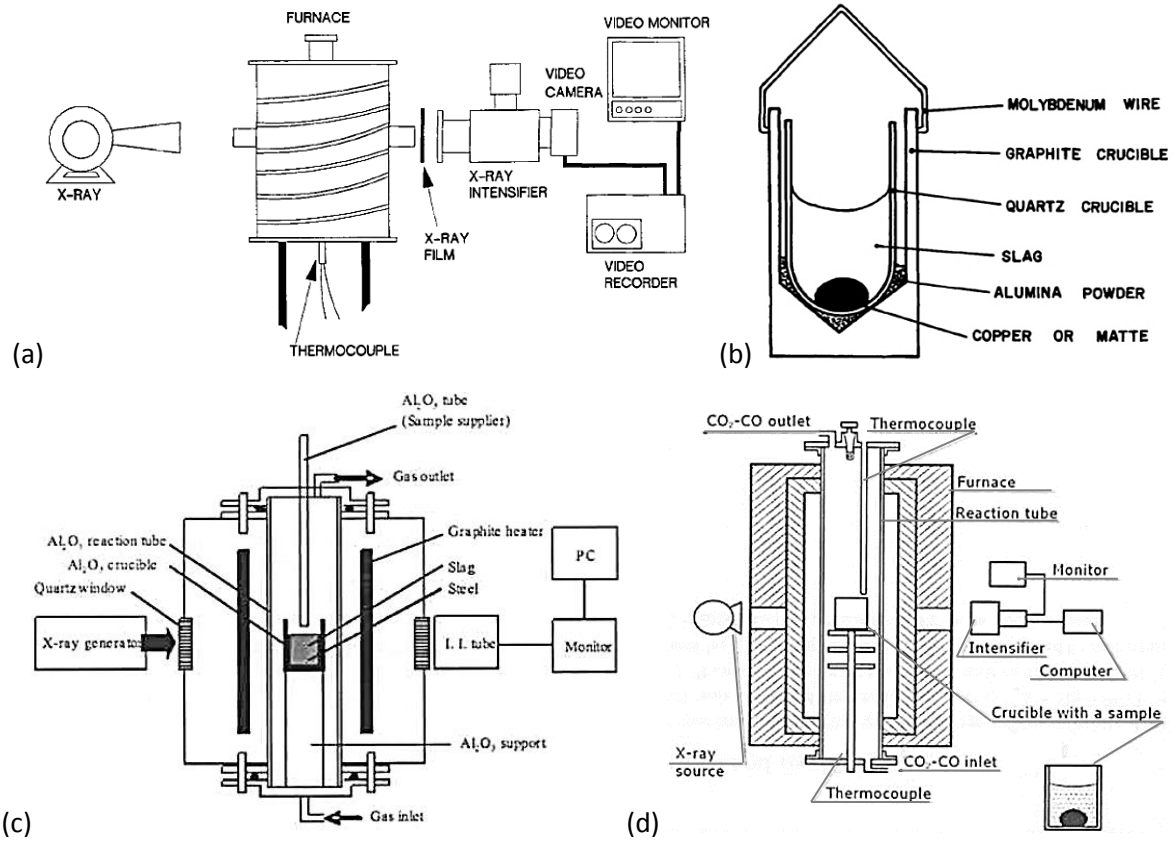

Figure 2.17 (a) X-ray set-up by Ip and Toguri [51] for high-temperature interfacial tension measurements; (b) sample arrangement for interfacial tension measurements in the X-ray set-up of Ip and Toguri [51]; (c) Schematic illustration of X-ray set-up used by Matsushita et al. [80]; (d) Apparatus used by Rogóż et al. [81] for the measurements of the interfacial surface tension in the metal/slag system

Despite the large efforts and the big variety in developed experimental techniques, no specific experimental methodology or set-up has been developed to study the phenomenon of the attachment of copper droplets to spinel solids in slags, until De Wilde et al. [44,61] developed a specific methodology to study this type of metal losses in slags. They approached the industrial problem with two complementary experimental methodologies. On the one hand, the interaction between the copper droplets and spinel particles was investigated separately with sessile drop experiments between a spinel substrate and copper and/or slag phases. On the other hand, a method was developed to study the attachment of the droplets in the presence of a surrounding slag system with the use of an industrially relevant synthetic slag system. The latter type of experiments gives the opportunity to obtain a better insight on factors like sedimentation time or slag height and verify the observations with those obtained with the first method.

2.5. Slag-cleaning operations

In certain cases, metal losses can be inevitable due to furnace operations. [52] Especially if one considers the fact that producing higher-grade mattes in the smelter increases heat generation, reducing fuel costs. It also decreases the amount of S to be removed during subsequent converting, hereby decreasing converting requirements. The only drawback of this way of working is the fact that when the matte grade rises (above 60wt%), the Cu concentration in the slag increases rapidly. [12] Slags are usually used for construction purposes, road construction and dike fortifications. But it is also used as an aggregate in mortar and concrete. However, as leaching of any metals by rain would have serious consequences, it is necessary to use 'clean' slags for these construction purposes. Moreover, the metal value in these slags is too high to justify the common practice of discarding them. The main strategies for minimizing the amount of metal lost in the disposal of the slag are: [12]

- Minimizing the mass of slag generated, which can be achieved in practice by fluxing as little as possible or not at all.
- Minimizing the percentage of metal in the slag, which can be reached by: [12,34]
    - Maximizing slag fluidity (avoiding excessive solid particles and keeping the slag warm enough)
    - Maximizing the surface tension of the slag
    - Minimizing the density of the slag
    - Providing enough SiO_2 (increasing the immiscibility between slag and matte)
    - Providing a settling zone inside the furnace
    - Avoiding tapping of the matte with slag, …
- Processing the slag in a separate step to recover the metal as much as possible (by pyrometallurgical processing and settling or minerals processing of solidified slag). Some of the possible slag-cleaning operations will be summarized in this section. [28]

The metal extraction from slags during slag-cleaning demands time and additional processing costs which should be minimized. [82]

To encourage suspended droplets to settle, conditions such as a low viscosity slag, low turbulence, a long residence time and a thin slag layer are required. These conditions are often difficult to obtain in a smelting vessel; the necessary residence time, in particular, is hard to acquire [12]. This is why slag cleaning is often carried out in a separate operation. [14] The slag cleaning furnaces have two purposes: allowing suspended droplets to finish settling and facilitating the reduction of dissolved Cu oxide. After pyrometallurgical settling, the amount of Cu in the slag is reduced to 0.7-1 wt%. [12]

Several possibilities exist for treating the slag: milling, pyrometallurgical treatment (contact the slag with carbonaceous reductant), electric furnace cleaning (traditional slag cleaning processes based on gravitational settling) [2,14], froth flotation (no recovery of dissolved valuable metals) [28], vibratory sedimentation of metals from the slag, centrifugation of the slags, recovery by addition of molten FeS or CaS, addition of cast iron rich in carbon, fuming (blowing the molten slag with a coal-air mixture, reducing the nonferrous elements by the CO formed and collecting the volatile elements), electrolysis of copper slags, hydrometallurgical treatments of slags, magnetic separation of slags [3], …

The El Teniente slag cleaning furnace process for example, reduces the magnetite and copper content in molten slag (with 7-10 wt% Cu and 12-16 wt% Fe_3O_4 in it) by injection of solid, liquid or gaseous

reductants directly into the molten slag through specially designed tuyeres, followed by a sedimentation stage. The reduction of the magnetite decreases the viscosity of the slag and enhances the settling of the created copper enriched phase. Copper matte inclusions are formed with sizes varying between µm and mm. Bigger inclusions settle down, and collect smaller inclusions due to collisions and coalescence. However, gravitational coalescence only enables partial removal of small inclusions and overall metal recovery is usually not satisfactory. [25] The sedimentation of these inclusions is strongly influenced by the slag motion, which is mainly induced by convection due to temperature gradients in the molten slag. The copper amount in the slag is decreased to less than 1 wt%, thus the slag can be discarded. [26]

The reduction of magnetite can be performed by skimming the converter slag into a ladle containing coal or placing green timber on top of the skimmed slag before returning the converter slag to the smelting stage. [3,29] An even better alternative is the reduction with CaC_2 proposed by Zander et al. [2]: it has a five times higher rate of reduction compared to cokes and the dissolution of CaO decreases the slag viscosity and improves the settling velocity of the copper containing droplets. The influence of additives is not significant, unless the bath is also stirred. Without the bath movement the reduction reactions with the slag take more time compared to adding the reductant under stirring conditions. [2]

Zander et al. [2] investigated the influence of different stirring conditions on the settling behaviour of metallic/matte droplets. It was concluded that heating up the slag to above 1500°C (overheating of the slag) with moderate stirring achieves a maximum decrease of 50% of the copper content. Without stirring a cleaning rate of 18% Cu was obtained. Marginal stirring yields a cleaning rate of 18% Cu compared to the feedstock. Turbulent stirring conditions lead to a cleaning of 23% Cu. Strong turbulence in the melt, by flushing gas injection, hinders the settling of the copper particles. In contrast to that, the gas injection has a positive effect on the lead cleaning, this is due to partial evaporation. By using CaC_2 as a reducing agent under optimal stirring conditions, a maximal cleaning rate can be achieved. Zander et al. [2] also observed that the addition of CaO, MgO and CaF_2 as fluxes decreased the viscosity a lot and decreased the copper content. On a larger scale, the slag stirring can be produced by an electromagnet on the outside of the reactor.

The settling of mechanically entrained droplets in liquid slags can be affected by electric fields. This is due to electrocapillary motion phenomena and it can be used to enhance the recovery of suspended droplets. [45] The speed generated by electrocapillary motion is of the order of cm/s, which yields high processing rates compared to traditional gravitational settling. [52] The drop migration rate due to electrocapillary motion is proportional to the electric field strength and the drop radius. [45]

Warczok and Riveros [45] found that an electric field can increase the settling rate of 5mm-diameter copper drops up to 3 times. It can even cause levitation of the droplets. It should be noted, however, that the enhanced settling due to electric field decreases with increasing drop size or increasing Cu_2O content of the slag (because this affects the surface charge density of the drop). [45] It should also be noted that the migration rate of solid phase inclusions differ from those of liquid phase inclusions. It seems that the droplets of matte or metal follow a migration path that is not obvious. By determining the interfacial tension of the metals or matte droplet-electrolyte as a function of electric potential, it is possible to predict the direction of migration of these droplets. Drop motion is driven by the interaction between the interfacial tension and the electric field. The interfacial tension is a

function of the droplet and slag composition and of the electro-kinetics of the redox reactions on the surface. [52] Choo and Toguri [52] also observed that droplets can migrate to either electrode. Different droplets even migrated past each other across the surface of the slag. Such independent motions suggest the possibility of specific control of the droplet's migration behaviour which can be used in slag cleaning operations.

Another option to extract metals from copper slags is leaching. Frequently applied leachants are ferric chloride with or without prior reduction, sulphuric acid, hydrochloric acid, ammonia, cyanide and so on. At first, cyanide was the most frequently used leachant, but it was replaced by other leachants due to environmental issues. [22] A lot of research has been performed in order to optimize leaching conditions such as temperature, the concentration of sulphuric acid, the leaching time, particle size and so on. [83–86] In general, higher molarities of the leaching acid, higher interaction times and higher temperatures increase the recovery. For the recovery of copper, Basir et al. [83] observed a plateau at 10M (acid molarity) for hydrochloric acid. For sulphuric acid and ammonia, a steep increase in recovery was noted until 4M, a further increase in acidic molarity caused a much smaller improvement in efficiency. For hydrochloric acid and ammonia, a strong increase in the amount of extraction was visible for a temperature up to 90°C. [83] Banza et al. [85] observed a significant improvement in the leaching recovery for copper using H_2SO_4 when a temperature increase from 24°C to 60°C and a 60 minute interaction time was applied. Additional measures such as the addition of hydrogen peroxide (H_2O_2), pressure leaching or leaching in Cl_2/Cl^- system have proved to be able to significantly raise the efficiencies of leaching. [83,87,88] The addition of hydrogen peroxide to leachants increases the rate of copper dissolution. The decomposition reaction of hydrogen peroxide in water and nascent oxygen is catalysed by the metal to be dissolved. Subsequently, metal oxide is formed, which reacts with the acid or ammonia. [83] Herreros et al. [87] proved that chlorine leaching (Cl_2/Cl^- from reaction of NaOCl and HCl) of copper from slags containing metallic copper, copper sulphide minerals and complex sulphides with very small sizes was successful.

Roasting is also applied to clean industrial copper slags. Roasting is used to convert the metals in copper slag into a desired form which can be separated from the slag. A possibility is the reduction of metals in the slags into free metals. This is combined with flotation or leaching for separation of the metals from the slag. Another more effective method is sulphating roasting, in which copper in various forms is converted into soluble sulphates through a series of chemical reactions at 200-600°C by addition of sulphide or sulphate agents. The soluble sulphates are dissolved in water and separated from the slag. Altundogan et al. [89] yielded a high copper recovery of 93% due to roasting of a converter slag with ferric sulphate and subsequently leaching the water.

It is also possible to remove Cu from convertor slags by slowly solidifying, crushing and grinding it and subjecting it to froth flotation. Due to the slow cooling, a lot of the dissolved Cu (oxidic form) reacts with FeO, forming Fe_3O_4 and metallic Cu. This reaction can lower the dissolved Cu content of the converter slag to below 0.5 wt%. [12]

2.6. Summary

It was illustrated that metal losses in slags are a widely occurring problem in different metal industries, both ferrous and non-ferrous. At this moment, it is generally accepted that there are two types of losses: chemical losses and mechanical losses. Chemical losses refer to the dissolution of

metal in the slag. Mechanical losses are entrained metal droplets which do not settle and do not end up in the underlying matte or metal phase.

The amount of chemical losses is thermodynamically determined, but there is no clear consensus on the form of the dissolved metal in the slag. For the mechanical entrainment of metals in slag, on the other hand, three main reasons have been discussed in previous reviews already:

1. Entrainment due to charging of the furnace or tapping of the slag
2. Precipitation of copper from slag due to temperature or oxygen level gradients within the furnace or due to chemical reactions
3. Sulphur dioxide gas, produced in the matte phase, or other gas phases dispersing the matte into the slag as the gas crosses the matte-slag interphase

A fourth reason, however, has only been studied recently in a systematic way to obtain knowledge regarding the mechanisms responsible for the interaction: the attachment of matte/metal droplets to solid particles present in the slag phase which hinder their settling. The results of experiments point towards a reactive origin of the attachment of the metal droplets to the solids spinel particles.

An overview of the several experimental set-ups to investigate metal losses in slags was also presented, as well as an overview of the existing slag-cleaning operations. These slag-cleaning operations remain operational in industry at present, because it is not possible to completely avoid metal losses, either chemical or mechanical.

References

[1] J. Heulens, Isothermal Crystallization of Metallurgical Slags: Phase Field Simulations Combined with In Situ Experiments (Isotherme kristallisatie van metallurgische slakken: faseveldsimulaties in combinatie met in situ experimenten), PhD thesis, KU Leuven, 2011. https://lirias.kuleuven.be/handle/123456789/318339.

[2] M. Zander, B. Friedrich, R. Degel, G. Kleinschmidt, M. Hoppe, J. Schmidl, Improving copper recovery from production slags by advanced stirring methods, in: Düsseldorf, Germany, 2011: pp. 181–195.

[3] J. Yannopoulos, Control of copper losses in reverberatory slags - a literature review, Can. Metall. Q. 10 (1970) 291–307.

[4] F.A. Calvo, A. Ballester, Lead losses in the slag of a reduction melting furnace, Erzmetal. 6 (1986) 282–287.

[5] F.A. Calvo, A. Ballester, The settling of metallic lead from lead blast furnace slag, Metall. Trans. B. 17 (1986) 267–270. doi:10.1007/BF02655073.

[6] M.A. Nkohla, Characterization of ferrochrome smelter slag and its implications in metal accounting, Cape Peninsula University of Technology, 2006.

[7] World Bank Group, Lead and Zinc Smelting, (1998). http://www.ifc.org/wps/wcm/connect/75bb2700488551ffaa34fa6a6515bb18/leadzinc_PPAH.pdf?MOD=AJPERES.

[8] P. Toscano, A. Utigard, Nickel, copper, and cobalt slag losses during converting, Metall. Mater. Trans. B. 34 (2003) 121–125. doi:10.1007/s11663-003-0062-5.

[9] Fundamentals of Steel Product Physical Metallurgy, 1st edition, Assn of Iron & Steel Engineers, United States, 2011.

[10] M.K.G. (Matthys K.G. Vermaak, Vanadium recovery in the electro-aluminothermic production of ferrovanadium, (2007). http://repository.up.ac.za/handle/2263/26591 (accessed February 26, 2016).

[11] M.K.G. Vermaak, P.C. Pistorius, Equilibrium slag losses in ferrovanadium production, Metall. Mater. Trans. B. 31 (2000) 1091–1097. doi:10.1007/s11663-000-0084-1.

[12] W.G. Davenport, Extractive metallurgy of copper, Fourth edition, Oxford: Elsevier Science Ltd, Kidlinghton, 2002.
[13] A. Yazawa, Thermodynamic considerations of copper smelting, Can. Metall. Q. 13 (1974) 443–453.
[14] P.J. Mackey, The Physical Chemistry of Copper Smelting Slags—A Review, Can. Metall. Q. 21 (1982) 221–260. doi:10.1179/cmq.1982.21.3.221.
[15] C. Hageluken, Improving metal returns and eco-efficiency in electronics recycling - a holistic approach for interface optimisation between pre-processing and integrated metals smelting and refining, in: 2006: pp. 218–223. doi:10.1109/isee.2006.1650064.
[16] M.Y. Solar, Slag losses in Laterite smelting - Nicel, in: 2009.
[17] N. Choi, W.D. Cho, Distribution behavior of cobalt, selenium, and tellurium between nickel-copper-iron matte and silica-saturated iron silicate slag, Metall. Mater. Trans. B. 28 (1997) 429–438. doi:10.1007/s11663-997-0109-0.
[18] Y.A. Gudim, S.G. Ovchinnikov, I.Y. Zinurov, Metal losses during steelmaking in arc furnaces and methods for their decreasing, Russ. Metall. Met. 2011 (2011) 495–498. doi:10.1134/S0036029511060103.
[19] Alaetting Mustafa Aksoy, An investigation of copper losses in copper reverberatory slags, PhD dissertation, Department of Metallurgy, Massachusetts institute of technology, 1943.
[20] R. Sridhar, J.M. Toguri, S. Simeonov, Copper losses and thermodynamic considerations in copper smelting, Metall. Mater. Trans. B. 28 (1997) 191–200. doi:10.1007/s11663-997-0084-5.
[21] A. Warczok, G. Riveros, Slag cleaning in crossed electric and magnetic fields, Miner. Eng. 20 (2007) 34–43. doi:10.1016/j.mineng.2006.04.007.
[22] H.T. Shen, E. Forssberg, An overview of recovery of metals from slags, Waste Manag. 23 (2003) 933–949. doi:10.1016/s0956-053x(02)00164-2.
[23] I. Zivkovic, N. Mitevska, I. Mihajlovic, D. Nikolic, The influence of the silicate slag composition on copper losses during smelting of the sulphide concentrates, J. Min. Metall. Sect. B-Metall. 45 (2009) 23–34. doi:10.2298/jmmbb0901023z.
[24] P.F. Tan, Modeling and control of copper loss in smelting slag, Jom. 63 (2011) 51–57. doi:10.1007/s11837-011-0207-y.
[25] R. Degel, H. Oterdoom, J. Kunze, A. Warczok, G. Riveros, Latest results of the slag cleaning reactor for copper recovery and its potential for the PGM industry, in: The Southern African Institue of Mining and Metallurgy, The Southern African Insititute of Mining and Metallurgy, Sun City, South Africa, 2008: p. Paper 7, 197-202.
[26] I. Imris, M. Sánchez, G. Achurra, Copper losses to slags obtained from the El Teniente process, Miner. Process. Extr. Metall. 114 (2005) 135–140. doi:10.1179/037195505X49769.
[27] N. Cardona, P. Coursol, P.J. Mackey, R. Parra, Physical chemistry of copper smelting slags and copper losses at the Paipote smelter Part 1-Thermodynamic modelling, Can. Metall. Q. 50 (2011) 318–329. doi:10.1179/000844311x13112418194761.
[28] H. Jalkanen, J. Vehviläinen, J. Poijärvi, Copper in solidified copper smelter slags, Scand. J. Metall. 32 (2003) 65–70. doi:10.1034/j.1600-0692.2003.00536.x.
[29] T. Maruyama, N. Furui, M. Hamamoto, T. Sunamoto, The copper loss in slag of flash smelting furnace in Tamano smelter, 2003.
[30] L. Andrews, Base metal losses to furnace slag during processing of platinum-bearing concentrates, PhD, University of Pretoria, 2008.
[31] M. Nagamori, Metal loss to slag .2. Oxidic dissolution of nickel in fayalite slag and thermodynamics of continuous converting of nickel-copper matte, Metall. Trans. 5 (1974) 539–548. doi:10.1007/bf02644647.
[32] S.S. Wang, Santander. N. H, J.M. Toguri, Solublity of nickel and cobalt in iron silicate slags, Metall. Trans. 5 (1974) 261–265.
[33] J.M. Toguri, N.H. Santander, Distribution of copper between Cu-Au alloys and silica-saturated fayalite slags, Metall. Trans. 3 (1972) 586–588.

[34] H.G. Kim, H.Y. Sohn, Effects of CaO, Al2O3, and MgO additions on the copper solubility, ferric/ferrous ratio, and minor-element behavior of iron-silicate slags, Metall. Mater. Trans. B. 29 (1998) 583–590. doi:10.1007/s11663-998-0093-z.
[35] F.D. Richardson, J.C. Billington, Copper and silver in silicate slags, Trans Inst Min Met. 65 (1956) 273–297.
[36] F. Sehnàlek, I. Imris, Slags from continuous copper production, Adv. Extr. Metall. Refin. (1972).
[37] M. Nagamori, Metal loss to slag .1. Sulfidic and oxidic dissolution of copper in fayalite slag from low-grade matte, Metall. Trans. 5 (1974) 531–538. doi:10.1007/bf02644646.
[38] I.-K. Suh, Y. Waseda, A. Yazawa, Some interesting aspects of non-ferrous metallurgical slags, High Temp. Mater. Process. 8 (1988) 65–88.
[39] D. Gaskell, J. Palacois, C. Somsiri, The physical chemistry of copper mattes, in: Cambridge, United Kingdom, 1990.
[40] G. Victrovitch, Precipitation of copper on cooling of iron silicate slags, in: Nova Scotia, Canada, 1980.
[41] I. Imris, S. Rebolledo, M. Sanchez, G. Castro, G. Achurra, F. Hernandez, The copper losses in the slags from the El Teniente process, Can. Metall. Q. 39 (2000) 281–289.
[42] A. Scott, J.R. Hudson, Fluid Mechanics: Stokes' law and viscosity, (n.d.). http://isites.harvard.edu/fs/docs/icb.topic1032465.files/Final%20Projects/Fluids%20Drag/stokes%20lab.pdf.
[43] K.O. Fagerlund, H. Jalkanen, Some aspects on matte settling in copper smelting, in: C. Diaz, C. Landolt, T. Utigard (Eds.), Phoenix, Arizona, 1999: pp. 539–551.
[44] I. Bellemans, Towards a methodology to study the interaction between Cu droplets and spinels, Masters thesis, Ghent University, 2013.
[45] A. Warczok, G. Riveros, Electromagnetic buoyancy force of copperinclusions in a liquid slag, in: Santiago, Chile, 2002.
[46] S.S. Dukhin, G. Kretzchmar, B. Miller, Dynamics of adsorption at liquid interfaces, 1st ed., Elsevier, 1995.
[47] D. Poggi, R. Minto, W. Davenport, Mechanisms of metal entrapment in slags, J. Met. 21 (1969) 40-.
[48] S.H. Seok, S.M. Jung, Y.S. Lee, D.J. Min, Viscosity of Highly basic Slags, Isij Int. 47 (2007) 1090–1096. doi:10.2355/isijinternational.47.1090.
[49] C. Lau, A.S. Mukasyan, A. Varma, Materials synthesis by reduction-type combustion reactions: Influence of gravity, in: 2002: pp. 1101–1108. doi:10.1016/s1540-7489(02)80139-0.
[50] K.O. Fagerlund, H. Jalkanen, Microscale simulation of settler processes in copper matte smelting, Metall. Mater. Trans. B-Process Metall. Mater. Process. Sci. 31 (2000) 439–451. doi:10.1007/s11663-000-0150-8.
[51] S.W. Ip, J.M. Toguri, Entrainment behavior of copper and copper matte in copper smelting operations, Metall. Trans. B. 23 (1992) 303–311. doi:10.1007/BF02656285.
[52] R.T.C. Choo, J.M. Toguri, The role of interfacial tension in high temperature nonferrous metallurgy, in: V.I. Lakshmanan, R.G. Bautista, P. Somasundaran (Eds.), Palm Coast, Florida, USA, 1993: pp. 153–167.
[53] J.L. Liow, M. Juusela, N.B. Gray, I.D. Sutalo, Entrainment of a two-layer liquid through a taphole, Metall. Mater. Trans. B - Process Metall. Mater. Process. Sci. 34 (2003) 821–832. doi:10.1007/s11663-003-0088-8.
[54] H. Gaye, L.D. Lucas, M. Olette, P.V. Riboud, Metal-slag interfacial properties : equilibrium values and "dynamic" phenomena, Canedian Metall. Q. 23 (1984) 179–191.
[55] M.A. Rhamdhani, K.S. Coley, G.A. Brooks, Role of oxygen in interfacial phenomena during high temperature reactions, in: G. Irons, S. Sun (Eds.), Hamilton, Ontario, Canada, 2004: pp. 203–217.
[56] M.A. Rhamdhani, G.A. Brooks, K.S. Coley, Kinetics of metal/slag reactions during spontaneous emulsification, Metall. Mater. Trans. B-Process Metall. Mater. Process. Sci. 36 (2005) 219–227. doi:10.1007/s11663-005-0023-2.

[57] M.A. Rhamdhani, K.S. Coley, G.A. Brooks, Analysis of the source of dynamic interfacial phenomena during reaction between metal droplets and slag, Metall. Mater. Trans. B-Process Metall. Mater. Process. Sci. 36 (2005) 591–604. doi:10.1007/s11663-005-0050-z.
[58] L. Holappa, L. Forsbacka, Z.J. Han, Measuring and modeling of viscosity and surface properties in high temperature systems, Isij Int. 46 (2006) 394–399. doi:10.2355/isijinternational.46.394.
[59] I. Imris, Copper losses in copper smelting slags, in: F. Kongoli, K. Itagaki, C. Yamauchi, H.Y. Sohn (Eds.), Sandiego, California, USA, 2003: pp. 359–373.
[60] R. Minto, W.G. Davenport, Entrapment and flotation of matte in molten slags, Can. Min. Metall. Bull. 65 (1972) C36-42.
[61] E. De Wilde, I. Bellemans, S. Vervynckt, M. Campforts, K. Vanmeensel, N. Moelans, K. Verbeken, Towards a methodology to study the interaction between Cu droplets and spinel particles in slags, in: Proc. EMC 2013, 2013: pp. 161–174.
[62] E. De Wilde, I. Bellemans, M. Campforts, A. Khaliq, K. Vanmeensel, D. Seveno, M. Guo, A. Rhamdhani, G. Brooks, B. Blanpain, N. Moelans, K. Verbeken, Wetting behaviour of Cu based alloys on spinel substrates in pyrometallurgical context, Mater. Sci. Technol. 31 (2015) 1925–1933. doi:10.1179/1743284715Y.0000000052.
[63] E. De Wilde, I. Bellemans, L. Zheng, M. Campforts, M. Guo, B. Blanpain, N. Moelans, K. Verbeken, Origin and sedimentation of Cu-droplets sticking to spinel solids in pyrometallurgical slags, Mater. Sci. Technol. 32 (2016) 1911–1924. doi:10.1080/02670836.2016.1151998.
[64] S. Vervynckt, Cu smelting and converting technology, (2012).
[65] I.L. Barker, J.S. Jacobi, B.H. Wadia, Some notes on Oroya copper slags, Trans. Am. Inst. Min. Metall. Eng. 209 (1957) 774–780.
[66] R. Higgins, T.J.B. Jones, Viscosity characteristics of Rhodesian copper smelting slags, Trans Inst Min Met. 82 (1963) 285–298.
[67] N. Cardona, L. Hernandez, E. Araneda, R. Parra, Evaluation of copper losses in the slag cleaning circuits from two Chilean smelters, in: GMDB, Hamburg, Germany, 2010: pp. 2637–2654.
[68] E. De Wilde, I. Bellemans, M. Campforts, M. Guo, B. Blanpain, N. Moelans, K. Verbeken, Sessile drop evaluation of high temperature copper/spinel and slag/spinel interactions, Trans. Nonferrous Met. Soc. China. 26 (2016) 2770–2783. doi:10.1016/S1003-6326(16)64344-3.
[69] E. De Wilde, I. Bellemans, M. Campforts, M. Guo, B. Blanpain, N. Moelans, K. Verbeken, Investigation of High-Temperature Slag/Copper/Spinel Interactions, Metall. Mater. Trans. B. 47 (2016) 3421–3434. doi:10.1007/s11663-016-0805-8.
[70] I. Bellemans, E. De Wilde, L. Claeys, T. De Seranno, M. Campforts, B. Blanpain, N. Moelans, K. Verbeken, Investigation of reactive origin for attachment of Cu-droplets to solid particles, Metall. Mater. Trans. B. (2017).
[71] D. Durinck, P.T. Jones, B. Blanpain, P. Wollants, Air-Cooling of Metallurgical Slags Containing Multivalent Oxides, J. Am. Ceram. Soc. 91 (2008) 3342–3348. doi:10.1111/j.1551-2916.2008.02597.x.
[72] H. Kim, B. Ozturk, R.J. Fruehan, Slag-metal separation in the blast furnace trough, Isij Int. 38 (1998) 430–439. doi:10.2355/isijinternational.38.430.
[73] J. Savolainen, T. Fabritius, O. Mattila, Effect of Fluid Physical Properties on the Emulsification, Isij Int. 49 (2009) 29–36.
[74] G. Akdogan, R.H. Eric, S. Makhoba, Water model of slag-metal dispersion in high-strength bottom blown converter, (n.d.).
[75] Y. Takeda, Thermodynamic evaluation of copper loss in slag equilibrated with matte, in: F. Kongoli, K. Itagaki, C. Yamauchi, H.Y. Sohn (Eds.), Sandiego, California, USA, 2003: pp. 341–357.
[76] K. Genevski, V. Stefanova, Dispersed matte droplets in industrial slag melts from flash smelting furnace, Can. Metall. Q. 47 (2008) 51–58.
[77] I. Bellemans, N. Moelans, K. Verbeken, Phase field modelling of the attachment of metallic droplets to solid particles in liquid slags: Influence of interfacial energies and slag supersaturation, Comput. Mater. Sci. 108, Part B (2015) 348–357. doi:10.1016/j.commatsci.2015.03.019.

[78] I. Bellemans, E. De Wilde, N. Moelans, K. Verbeken, Phase field modelling of the attachment of metallic droplets to solid particles in liquid slags: Influence of particle characteristics, Acta Mater. 101 (2015) 172–180. doi:10.1016/j.actamat.2015.08.074.
[79] S. Pirker, Towards Efficient Modelling of Slag Entrainment during Metallurgical Processes, Steel Res. Int. 81 (2010) 623–629. doi:10.1002/srin.201000084.
[80] T. Matsushita, T. Watanbe, S. Seetharaman, S. Mukai, Interfacial phenomena between molten steel and slag, in: Santiago, Chile, 2009: pp. 703–714.
[81] K. Rogóz, T. Sak, M. Kucharski, Investigations on the interfacial tension between the Ag-Te alloy and the sodium carbonate slag with the use of the X-ray technique, in: Proc. EMC 2011, 2011: pp. 1225–1234.
[82] M.P. Sudbury, D.J. Kemp, The properties and uses of granulated non ferrous slags, in: Minerals and Materials Society, San Antonio, Texas, United States, 2006: pp. 611–620.
[83] S.M.A. Basir, M.A. Rabah, Hydrometallurgical recovery of metal values from brass melting slag, Hydrometallurgy. 53 (1999) 31–44.
[84] C.-Y. Kuo, C.-H. Wu, S.-L. Lo, Removal of copper from industrial sludge by traditional and microwave acid extraction, J. Hazard. Mater. 120 (2005) 249–256. doi:http://dx.doi.org/10.1016/j.jhazmat.2005.01.013.
[85] A.N. Banza, E. Gock, K. Kongolo, Base metals recovery from copper smelter slag by oxidising leaching and solvent extraction, Hydrometallurgy. 67 (2002) 63–69. doi:http://dx.doi.org/10.1016/S0304-386X(02)00138-X.
[86] D.M. Urosevic, M.D. Dimitrijevic, Jankovic; Zoran D, Recovery of copper from copper slag and copper slag flotation tailings by oxidative leaching, Physicochem. Probl. Miner. Process. 51 (2015) 73–82.
[87] O. Herreros, R. Quiroz, E. Manzano, C. Bou, J. Vinals, Copper extraction from reverberatory and flash furnace slags by chlorine leaching, Hydrometallurgy. 49 (1998) 87–101. doi:10.1016/s0304-386x(98)00010-3.
[88] S. Anand, K.S. Rao, P.K. Jena, Pressure leaching of copper converter slag using dilute sulfuric-acid for the extraction of cobalt, nickel and copper values, Hydrometallurgy. 10 (1983) 305–312. doi:10.1016/0304-386x(83)90061-0.
[89] H.S. Altundogan, F. Tumen, Metal recovery from copper converter slag by roasting with ferric sulphate, Hydrometallurgy. 44 (1997) 261–267. doi:10.1016/s0304-386x(96)00038-2.

3. Phase field modelling [3]

To improve the metal-slag phase separation, the fundamental mechanisms governing the attachment of metallic droplets on solid particles in liquid slags need to be identified. For this, an experimental approach can be used, but as stated previously, in such a case, many experiments are needed to investigate the influence of all parameters and it is very difficult to study the effect of one parameter because it is almost impossible to keep the others constant. Thus, it can be inconvenient to reveal the underlying chemical and physical phenomena. Modelling can provide a solution for this. [1] Modelling cannot replace experiments, but can help to understand the complex phenomena causing changes in the microstructure. Thus, modelling and experiments can be regarded as complementary methods. [2]

This chapter introduces the basics of modelling, more specifically phase field modelling. It goes into more detail on the variables, free energy functional, governing equations and interfacial properties in phase field models. Some of the possibilities to solve the equations describing microstructural evolution are also described, followed by options to make the phase field models quantitative. This chapter ends with a historical overview of multi-phase field models and an evaluation of the commercially available phase field software.

3.1. Modelling in general

A microstructure is the sum of all thermodynamic non-equilibrium lattice defects and heterogeneities, arising during materials processing, on a scale from Ångstrom to meter. [2,3] This large spread in length scale is typically subdivided into several categories: atomic, meso and macro scales. The atomic scale refers to the range from nanometre up to submicron level. The meso scale does not deal directly with atoms, but with lattice defect ensembles at the level of a specific grain. The macro scale involves elements usually observable with the naked eye. A schematic breakdown of these length scale regimes and the corresponding level of observations is shown in Figure 3.1. [4]

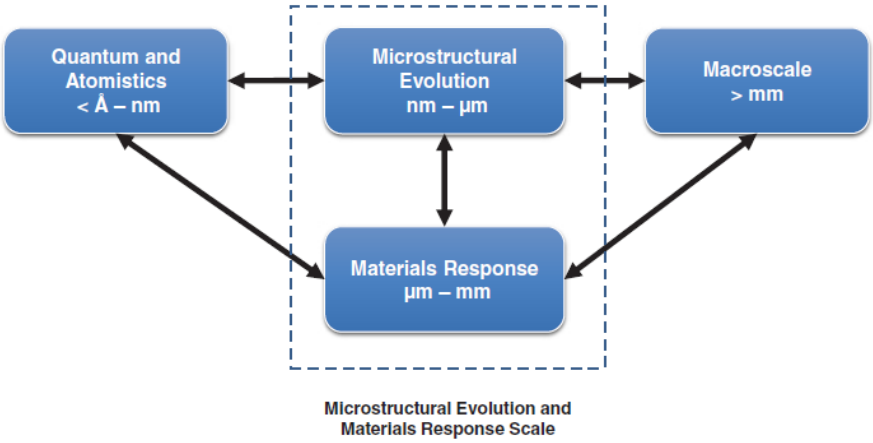

Figure 3.1 Length scale regimes and the corresponding level of observations [4]

In the mesoscale, microstructures are usually complex and consist of several phases and grains, which differ in structure, orientation and/or chemical composition with interfaces in between them. The direction of the evolution of such a microstructure is prescribed by thermodynamics, but the actual

[3] This chapter is based on the following publication: I. Bellemans, N. Moelans, K. Verbeken, Phase field modelling in extractive metallurgy, Critical Reviews in Solid State Materials Sciences. Submitted

evolution path is selected by kinetics. [2] This non-equilibrium character of the evolution leads to a large variety of lattice defect structures and interactions and can affect specific material properties. Optimizing microstructure evolution at the mesoscopic scale is thus of fundamental importance. [2,3] Therefore, microstructures and their evolution are often the centre of attention in materials science and engineering and involve a large diversity of complex processes. [1,3]

The same division of the space into the atomic, meso and macro scales is also encountered in modelling. The word 'modelling' can be used to denote two different terms, namely, mathematical model formulation and numerical modelling. The term 'simulation' on the other hand is used only for numerical simulation. Generally, modelling techniques can be divided into three categories based on the length scales they cover, namely, atomic (nano to submicron), meso and macro scale models. Atomic scale modelling techniques are for example ab-initio or first-principles calculations, molecular dynamics (MD) or Monte Carlo (MC) technique. Meso scale covers techniques dealing not directly with atoms, but to lattice defect ensembles at the grain scale. Meso scale models can be for example: phase field models and cellular automata. The macro scale models include percolation models, cluster models and finite element models. This is summarized Figure 3.2. [2]

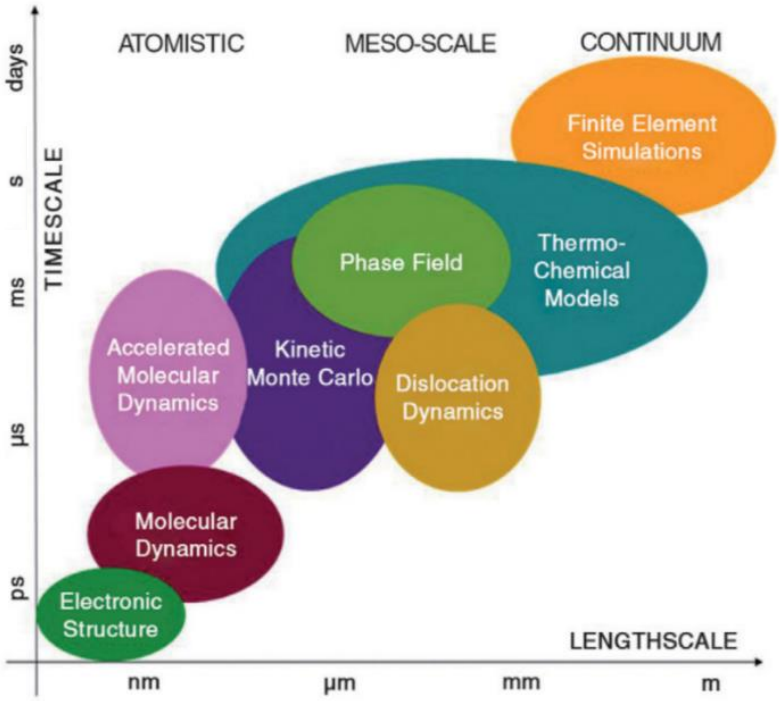

Figure 3.2 Multi-scale theoretical and computational methods used for materials model development and computer simulations [5]

Due to the large amount of atoms involved in mesoscale simulations of microstructures, atomistic models are no longer sufficient, thus mesoscale simulations should span a wider range of scales allowing predictions beyond the atomic scale. This can be done by idealizing the materials as continuum and not explicitly incorporating atomic-scale dynamics. [2] Several types of mesoscale modelling exist and are depicted in the schematic in Figure 3.3. Computational materials science has as goal to apply computational methods to explain and predict material properties and microstructures. [6] Because the properties of the system in a simulation are well-controlled and the effect of each property can be investigated separately, modelling can give a more systematic insight in the role of a specific property or condition. [2]

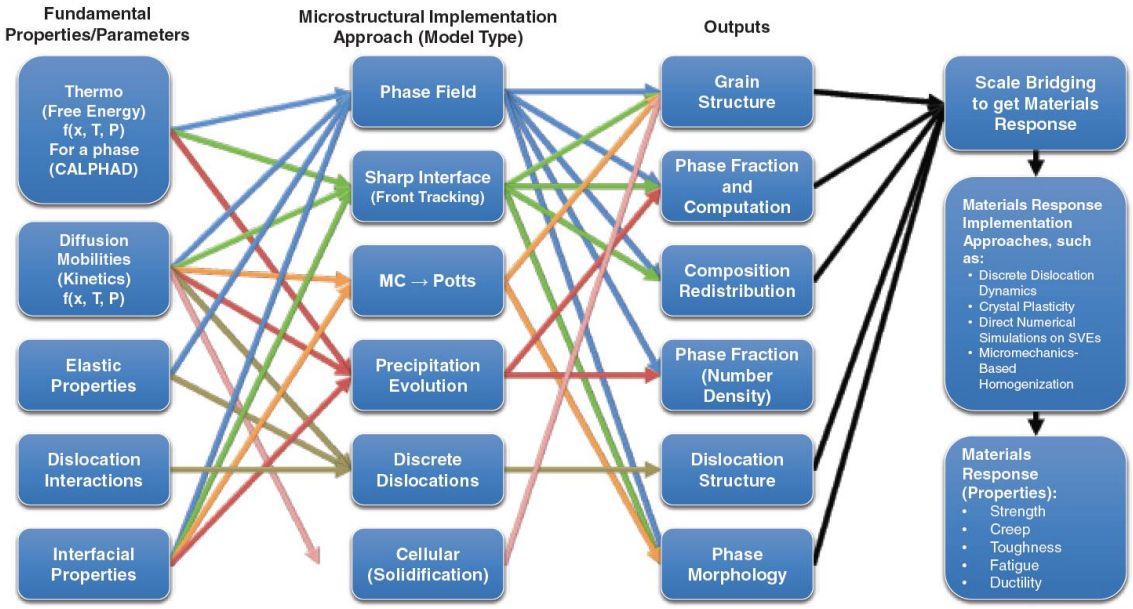

Figure 3.3 Interaction of fundamental properties/parameters, implementation approaches or model types, structural data outputs, and property prediction in mesoscale modelling [4]

One of these types of modelling is phase field modelling (Ginzburg-Landau and Cahn-Hilliard types). Phase field models are generally the best available models to simulate complex microstructures on large scales. Atomic scale models lack the length scale to describe microstructure and also lack the time scale to describe the microstructural evolution. [2] The phase field method can provide the critical link between the atomic level fundamental calculations and the macroscopic constitutive modelling. [3]

Phase field models are mesoscale models based on the diffuse-interface concept, which avoids the explicit interface tracking, in contrast to the more conventional sharp interface counterparts. Phase field models are typically phenomenological, i.e. they are not derived from first-principles but from general observations. They involve parameters which cannot be directly measured from experiments. The phenomenological nature of phase field models can be reduced by using parameters from ab-initio or first-principles calculations. [2]

3.2. The general technique of phase field modelling

The phase field method already proved to be a very powerful, flexible and versatile modelling technique for microstructural evolution (e.g. solidification [7–9], solid-state phase transformations [3], solid-state sintering [10], grain growth [11], dislocation dynamics [12], crack propagation [13,14], electromigration [15], etc.). The phase field method is also eye-catching because it produces remarkable visual outputs, particularly of morphology, capturing features which are often realistic in appearance. [2,16]

Phase field models are phenomenological continuum field approaches with the ability to model and predict mesoscale morphological and microstructural evolution in materials at the nanoscopic and mesoscopic level. [2,3,17] In contrast to macroscopic models, the crystallization kinetics, diffusion profiles and the morphology of individual crystals can be described. [9]

Macroscopic models usually rely on thermodynamic equilibrium calculations, but phase field models are based upon the principles of irreversible thermodynamics to describe evolving microstructures.

[9] Phase field models can be regarded as a set of kinetic equations and because they do not only predict the final thermodynamic equilibrium states but also realistic microstructures, these models should consider several contributions to the thermodynamic functions and kinetics involved. The thermodynamics of phase transformation phenomena determine the general direction of microstructure evolution, ultimately eliminating all non-equilibrium defects, but the kinetics determine the actual microstructural path. This can lead the system through a series of non-equilibrium microstructural states. [2] The total free energy of a system, which is minimized towards equilibrium, is defined as the integral of the local energy density, which traditionally includes interfacial energies and chemical energies of the bulk phases, but also elastic or magnetic energy contributions can be included. The method can in principle deal with a large number of interacting phenomena, because of the inclusion of various energy contributions. [1,16,17] Phase field models describe a microstructure, both the compositional/structural domains and the interfaces, as a whole by using a set of field variables. [3] These field variables are continuous spatial functions changing smoothly and not sharply across internal interfaces, i.e. diffuse interfaces. [1–3,17]

A characteristic feature of the phase field method is that its equations can often be written down following simple rules or intuition, but that detailed properties (which have to be known if quantitative simulations are desired) become apparent only through a mathematical analysis that can be quite intricate. Therefore, it is not always easy to perceive the limits of applicability of the phase field method [18]. Several problems remain [16]: interface width is an adjustable parameter which may be set to physically unrealistic values to bridge the scale gap between the thickness of the physical interfaces and the typical scale of the microstructures, which may result in loss of detail and unphysical interactions between different interfaces. Therefore, to guarantee precise simulations, all these effects have to be controlled and, if possible, eliminated. This is done in the so-called thin-interface limit (cfr. infra): the equations of the phase field model are analysed under the assumption that the interface thickness is much smaller than any other physical length-scale present in the problem, but otherwise arbitrary. The procedure of matched asymptotic expansions then yields the effective boundary conditions valid at the macroscale, which contain all effects of the finite interface thickness up to the order to which the expansions are carried out. [18] Moreover, it is not clear at what point the assumptions of irreversible thermodynamics, on which the equations describing microstructural evolution are based, would fail. The free energy expression originates from a Taylor expansion [19], of which it is not clear to which extent it remains valid. The definition of the free energy density variation in the boundary is sometimes claimed to be somewhat arbitrary and assumes the existence of systematic gradients within the interface. Some say, however, that there is no physical justification for this assumed form in many cases. However, in a liquid-gas system, for example, the density varies continuously over the interface and thus a diffuse interface between stable phases of a material can be seen as more natural than the assumption of a sharp interface with a discontinuity in at least one property of the material.

The next sections will first introduce the background of phase field methods, i.e. non-equilibrium thermodynamics, and a closer look will be taken to the basics of the empirical transport laws (mainly diffusion) and the Onsager equations.

3.3. Background of phase field models: non-equilibrium thermodynamics

The equations for microstructural evolution in the phase field method are derived based on general thermodynamic and kinetic principles, more specifically, it relies on a fundamental approximation of the thermodynamics of irreversible processes, i.e. that the flux describing the rate of the change is proportional to the force responsible for the change. [1,16] Prigogine [20] was the first to develop the thermodynamic treatment of open systems far from equilibrium, hereby generalizing thermodynamics from equilibrium to nonlinear and irreversible thermodynamics. The thermodynamics of irreversible processes deal with steady state processes where free energy is being dissipated making the process thermodynamically irreversible since after the application of an infinitesimal force, the system does not revert to its original state on removal of that force. [16,21] These dissipative systems cannot be described by the classical principles of equilibrium thermodynamics and produce entropy. [20]

A basic assumption of non-equilibrium thermodynamics is that the fundamental equation of state of equilibrium thermodynamics is applicable for non-equilibrium processes not too far from thermodynamic equilibrium. In this way, it is possible to describe the evolution of a system, initially out of equilibrium, towards equilibrium. One should note that several approaches exist within non-equilibrium thermodynamics. The most commonly used type is called 'classical irreversible thermodynamics' or 'local equilibrium thermodynamics', which includes several assumptions that result in new concepts such as internal state variables, local equilibrium, etc. [20]:

- Internal state variables describe the evolution of a homogeneous system out-of-equilibrium towards thermodynamic equilibrium. E.g. the differential of the internal progress variable describes the change taking place in the composition during a chemical reaction. Whenever this differential becomes zero, thermodynamic equilibrium has been reached.
- The concept of local equilibrium divides the system in infinitesimal sub-volumes, which are small compared to the system size and large compared to the atomic distance. Each of these small volume elements is homogeneous and in local equilibrium, i.e. no fluxes are present within and the same function of the local intensive variables as in equilibrium describes the entropy density. The boundaries of the sub-volumes are subject to heat and mass exchange. [20]

For irreversible processes the equations of classical thermodynamics become inequalities. [16,21] For each volume element, mass and energy conservation balances can be established and the entropy density of a volume element can change in time for two reasons: an entropy flow of neighbouring elements and an internal entropy production σ_S due to irreversible processes taking place within. It follows from the second law of thermodynamics that this internal entropy production should be larger than or equal to zero, i.e. allowing the largest energy dissipation rate. A general form of the entropy production is a sum of products of conjugated fluxes and thermodynamic forces:

$$\sigma_S = \sum J_k X_k \tag{3.1}$$

Where each *X* and *J* pair are conjugated quantities. These pairs can be derived from the fundamental equation of state (the combination of the first and second law of thermodynamics) in combination with conservation laws. Note that the choice of reference frame does not change the value of the entropy production, as the entropy production is a physical quantity measuring how the system

approaches equilibrium by irreversible processes. [16,19,22] The next paragraph will go into more detail on one type of conjugated flux-force pairs, i.e. diffusional fluxes and the forces responsible for them.

3.3.1. Empirical transport laws: Fick's linear laws

The simplest description of diffusion is given by Fick's laws, thus laying the basis for the diffusion theory. The first law (3.2) indicates the proportionality between the flux of component B (J_B), expressed as the amount of B passing per unit time through a unit area of a plane perpendicular to the *z* axis, and the concentration gradient. [22]

$$J_B = -D_B \frac{\partial c_B}{\partial z} \tag{3.2}$$

The proportionality coefficient is called the diffusion coefficient, whose variation with temperature typically follows an Arrhenius relation. The diffusion coefficient also varies with concentration (but not its gradient). [22] Several other physical phenomena obey the same type of linear law, e.g. heat conduction can be described by Fourier's law and electrical conduction by Ohm's law. A major difference with Fick's law, however, is the fact that Fick's law does not describe the flux as a function of gradient in a potential, as opposed to the other two. [22] Fick's law for diffusion can be brought into the same form (3.3), i.e. proportionality of the flux to a gradient in potential, which, in this case, is the chemical potential μ_B.

$$J_B = -D_B \frac{\partial c_B}{\partial z} = -L_B \frac{\partial \mu_B}{\partial z} = -L_B \frac{\partial \mu_B}{\partial c_B} \frac{\partial c_B}{\partial z} \tag{3.3}$$

With L_B a phenomenological parameter. Which gives the following:

$$D_B = L_B \frac{\partial \mu_B}{\partial c_B} \tag{3.4}$$

As the negative of a potential gradient is a force, Fourier's, Ohm's and Fick's law can be put in the same form, having a flux proportional to the force. Thus, another way to understand Fick's law is the following: the flux is proportional to the force that acts on the B atoms in the *z* direction and to the number of B atoms feeling this force. The proportionality constant is called the mobility M_B. [22]

$$J_B = -M_B c_B \frac{\partial \mu_B}{\partial z} \tag{3.5}$$

Thus,

$$M_B c_B = L_B \text{ and } D_B = M_B c_B \frac{\partial \mu_B}{\partial c_B} \tag{3.6}$$

The last factor in the equation on the right of (3.6) is called the thermodynamic factor. [22]

3.3.2. Frames of reference

Different frames of reference are possible to define fluxes and this choice will change the form of Fick's law.

- A number-fixed frame of reference requires the number of moles on each side of the reference point to remain constant and thus the sum of the fluxes should be zero. Thus, in a binary system, only one diffusion coefficient would be required and this is called the chemical diffusion coefficient or the interdiffusion coefficient. [22]

- In a volume-fixed frame of reference, no net flow of volume is observed and thus, in a binary system in this frame of reference, one diffusion coefficient would suffice. [22]
- The lattice-fixed frame of reference, however, places inert markers at the crystalline lattice. In this case, it is possible that more A atoms diffuse in one direction than B atoms in the other (i.e. the Kirkendall effect[4] is observed, where the markers appeared to move in a sample as a result of diffusion). In this case, one diffusion coefficient no longer describes the system and intrinsic or individual diffusion coefficients should be used (D_A and D_B). [22]

Notation-wise, the concentration of one component is usually chosen as the dependent concentration, say *n*, giving the following notation: D_{kj}^{n}. This represents the diffusion coefficient coupling the flux of component *k* with respect to the concentration gradient of component *j* when the concentration of component *n* has been chosen as the dependent variable. [22]

Going from one frame of reference to another is possible by a transformation relation, which usually includes the migration rate or Kirkendall shift velocity *v* of one reference frame relative to the other. This transformation between the number-fixed and lattice-fixed reference frames yields Darken's relationship between the interdiffusion coefficient (left-hand side) and the individual diffusion coefficients.

$$D_{BB}^{A\prime} = [(1 - x_B)D_B - x_B D_A] \tag{3.7}$$

3.3.3. Multicomponent systems and cross effects: Onsager relations

The equations above are valid for binary alloys only. Fick's law was first extended to multicomponent systems by Onsager [23]:

$$J_k = -\sum_{j=1}^{n} D_{kj} \frac{\partial c_j}{\partial z} \tag{3.8}$$

Thus the diffusion of a certain component *k* also depends on the concentration gradients of the other components *j* and is, therefore, described by multiple diffusion coefficients. [22] As mentioned above, the fluxes can also be described as linear functions of the driving forces. A Taylor expansion around the equilibrium states where the zeroth-order term vanishes (because here we are only interested in flow caused by chemical potential gradients), gives the following equation: [19]

$$J_k = -\sum_{i=1}^{n} L_{ki} \frac{\partial \mu_i}{\partial z} = -\sum_{i=1}^{n} L_{ki} \sum_{j=1}^{n} \frac{\partial \mu_i}{\partial c_j} \frac{\partial c_j}{\partial z} \tag{3.9}$$

The second equality originates from the fact that the potentials $\nabla\mu_i$ are functions of composition. In principle, these can be expressed as functions of all the concentrations, which was done in (3.9) by means of the chain rule. Thus, due to equations (3.8) and (3.9),

[4] In the Kirkendall effect, the different types of atoms move with different velocities relative to the lattice and thus the individual diffusion coefficients or mobilities differ. This effect was the first observation indicating the presence of the vacancy mechanism for diffusion, as opposed to the previous idea of the place interchange theory, in which diffusion takes place by direct interchange between atoms and not by interchange between an atom and a neighbouring vacancy. [22]

$$D_{kj} = \sum_{i=1}^{n} L_{ki} \frac{\partial \mu_i}{\partial c_j} \quad \textbf{(3.10)}$$

This extension to multicomponent systems makes it possible that the concentration gradient of one component causes another component to diffuse. Onsager continued the generalization to any type of irreversible flux (diffusional, heat, electrical, …):

$$J_k = -\sum L_{ki} X_i \quad \textbf{(3.11)}$$

Where J_k is any type of flux and X_i any type of force (gradient of potential). The pairs of conjugated forces and fluxes can be obtained from the expression for the entropy production. Whenever multiple forces and fluxes are present, each flow J_k is related linearly not only to its conjugate force X_k, but also linearly to all other forces present. [19,22] Thus, the gradient in the chemical potential of one solute still affects the flux of another solute. [16] This description makes it also possible to describe the coupling of several irreversible processes (i.e. the Seebeck, Peltier, Soret effect or others as mentioned in Table 3.1). [2,19,22]

Force \ Flux	Heat	Electric	Diffusion
Temperature gradient	Fourier	Seebeck	Soret thermal migration
Voltage	Peltier	Ohm	Electromigration
Chemical potential gradient	Dufour	Volta	Fick

Table 3.1 Classical examples of cross effects

It follows from the second law of thermodynamics that the matrix with the L_{ik} values should be positive definite, so that $\sigma_S = \sum_i \sum_k L_{ik} X_i X_k \geq 0$. Moreover, Curie's symmetry principle states that phenomena with different tensorial characters (i.e. a scalar versus a tensor) cannot be coupled, as in such a case the crystal symmetry properties could be violated. E.g. heat and mass diffusion couple with both the gradients in temperature and chemical potentials of all components, but the rate of chemical reaction does not couple with the gradients in temperature and chemical potentials of all components. Onsager also showed that the phenomenological parameters L_{ki} should obey symmetry properties if only independent fluxes and thermodynamic driving forces are considered: $L_{ki} = L_{ik}$, which is referred to as the Onsager-Casimir reciprocity relations. [2,19,22] When L_{ki} represents the coefficient in a lattice-fixed reference frame, a transformation to the number-fixed reference frame, would yield the following expression: [19,22]

$$L'_{kj} = \sum_{i=1}^{n} (\delta_{ik} - x_k) L_{ij} \quad \textbf{(3.12)}$$

Due to the conservation of mass in the *n*-component system, the fluxes in a multicomponent case can be rewritten to expressions in terms of the *n-1* independent conjugated forces ($\nabla\mu_i - \nabla\mu_n$). For this, the matrix of the phenomenological parameters *L* is also transformed, using the Gibbs-Duhem equation:

$$L''_{ki} = \sum_{j=1}^{n} (\delta_{ij} - x_i)\, L'_{kj} = \sum_{j=1}^{n}\sum_{r=1}^{n} (\delta_{ri} - x_i)(\delta_{jk} - x_k) L_{jr} \quad \textbf{(3.13)}$$

The phenomenological Onsager coefficients and the empirical diffusion coefficients in any reference frame can be calculated from the atomic mobilities (first defined in (3.5)). Thus, in the equation on the right in (3.13): $L_{jr} = c_j M_j$ for $j=r$ and $L_{jr} = 0$ otherwise. Writing the fluxes as functions of the *n-1* independent concentration gradients (making *n* the dependent one), makes it possible to link all L_{ki} values to the diffusivities:

$$D^n_{kj} = \sum_{i=1}^{n} L_{ki} \left(\frac{\partial \mu_i}{\partial c_j} - \frac{\partial \mu_i}{\partial c_n} \right) \quad \textbf{(3.14)}$$

Moreover, after a transformation of the reference frames from lattice-fixed to number-fixed:

$$D^n_{kj} = \sum_{i=1}^{n} L''_{ki} \frac{\partial [\mu_i - \mu_n]}{\partial c_j} \quad \textbf{(3.15)}$$

In conclusion, in a multicomponent system with *n* components, *n-1* concentration variables may be varied independently. The choice of the dependent variable is arbitrary but often one of the major components is chosen. A full representation of a system with *n* components requires *n(n-1)* individual diffusion coefficients (in the lattice-fixed frame of reference) or *(n-1)(n-1)* interdiffusion coefficients (in the number- or volume-fixed frame of reference), but only *n* independent atomic mobilities. Thus, diffusivities are not independent and it is preferred to store mobilities instead of diffusivities in databases. [22]

3.4. Variables

The microstructures considered in phase field simulations typically consist of a number of grains or phases. The shape and distribution of these grains is represented by functions that are continuous in space and time and are called phase field variables. [1,21] The dependence of the variables on the spatial coordinates enables prescribing composition and phase fields that are heterogeneous within the system and allows simulating both the kinetics and the resulting morphology associated with phase transformations. [2] Characteristic about the phase field method is its diffuse-interface approach. At interfaces, the field variables vary smoothly over a transition/spatial gradient of the phase field variables between the equilibrium values in the neighbouring grains or phases in a narrow region (the right side of Figure 3.4).[2,3]

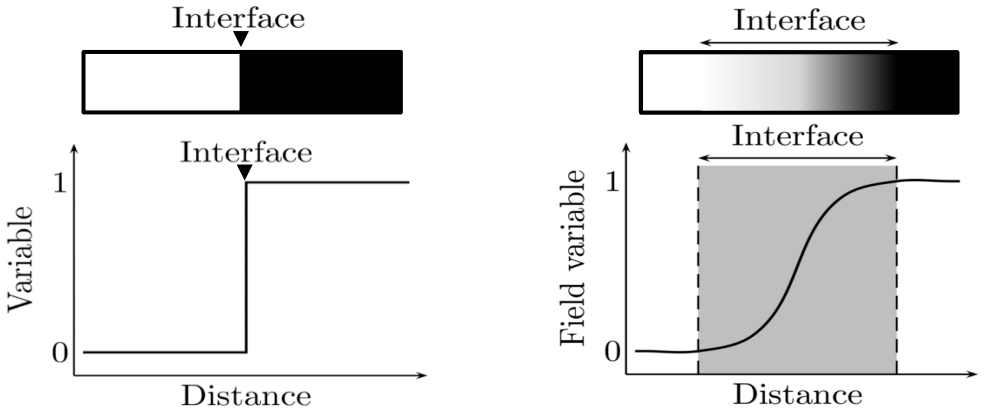

Figure 3.4 Schematic one-dimensional representation of a sharp (left) and of a diffuse (right) interface.

In classical sharp interface models for microstructure evolution, on the other hand, the model equations are defined in a homogeneous part of the microstructure, e.g. a single grain of a certain phase. At the interfaces (with zero-width, as shown on the left of Figure 3.4), the properties change discontinuously from one bulk value to another and certain constraints are applied locally at the interfaces such as local thermodynamic equilibrium and heat or mass balances. The interfaces move as the microstructure evolves, which gives this type of free-boundary problems their name: moving-boundary problems, sometimes also referred to as the Stefan problem. [17,24] Therefore, the interfaces need to be explicitly tracked, which does not facilitate the model formulation and numerical implementation. This is why sharp-interface simulations are mostly restricted to one-dimensional systems or simplified morphologies. [1,3,16,17]

In a phase field model (on the right in Figure 3.4), explicit tracking of individual interfaces or phase boundaries is avoided by assuming diffuse interfaces, where the state variables vary in a steep but continuous way over a narrow interface region. [16] This 'smear out' of the variable can for example be interpreted as a physical decrease of structure in a solid-liquid interface on an atomic scale. [25] The position of the interfaces is implicitly given by the value of the phase field variables. [16] In this way the mathematically difficult problems of applying boundary conditions at an interface whose position is part of the unknown solution, is avoided. Thus the evolution of complex morphologies can be predicted without making any assumption on the shape of the grains. Moreover, in a diffuse interface model, the model equations, for e.g. solute diffusion, are defined over the whole system, thus the number of equations to be solved is far smaller. [9]

The field variables do not correspond to one specific state each, but are characteristic for the distinction between the different states. [25] A division can be made between different types of phase field variables: the first type, are solely introduced to avoid tracking the interfaces and are called phase fields. This type describes which phases are present at a certain position in the system in a phenomenological way and is typically used for modelling solidification. The second type corresponds to well-defined physical order parameters, such as order parameters referring to crystal symmetry relations between coexisting phases, and composition fields. [1,3]

Another very common distinction in the phase field variables can be made between either conserved or non-conserved variables. Conserved or composition variables can be mole fractions or concentrations. In a closed system with n components, $n-1$ mole fractions or concentrations (in combination with the molar volume) completely define the system, due to the conservation of the number of moles in a closed system. Non-conserved phase field parameters can refer to the phases present, the crystal structure and its orientation. Because the variables are non-conserved, no restrictions are present on the evolution of the parameters as is the case for the conserved variables by the conservation of the number of moles. A distinction can be made between order parameters, referring to crystal symmetry relations between coexisting phases, and phase fields, describing which phases are present at a certain position in the system in a phenomenological way. [1,3] In many applications of the phase field model to real materials processes, it is often necessary to introduce more than one field variables or to couple one type of field with another. For example, in the case of modelling solidification, the temperature field T or concentration fields are coupled to the phase field. [3]

3.5. Free energy functional

The possibility to reduce the free energy of the heterogeneous system is the driving force for microstructural evolution. [1,17] The selection of the thermodynamic function of state depends on the definition of the problem. An isolated, non-isothermal system, for example, requires a description based on entropy, whereas the Gibbs free energy is used for an isothermal system at constant pressure and the Helmholtz free energy is appropriate for a system with constant temperature and volume. [16] Because the change in volume during transformations is small, the changes in Helmholtz free energy (defined for a constant volume) will deviate only slightly from the Gibbs free energy (defined for a constant pressure) and the changes in Gibbs and Helmholtz energy between 2 states are almost equal. [1]

In contrast to classical thermodynamics, where properties are assumed to be homogeneous, the phase field method uses a functional of the phase field variables and their gradients as a description for the free energy *F* of the system. The free energy density functional may depend on both conserved and non-conserved field variables, which are, in turn, functions of space and time. [2] Different driving forces for microstructural evolution (reduction in different types of energy) can be considered: [1,17]

$$F = F_{bulk} + F_{int} + F_{el} + F_{fys} \tag{3.16}$$

Where the bulk free energy, the interfacial energy, the elastic strain energy and an energy term due to physical interactions (electrostatic or magnetic) are present, respectively. The bulk free energy determines the compositions and volume fractions of the equilibrium phases. [1,17] The interfacial energy is the excess free energy associated with the compositional and/or structural inhomogeneities occurring at interfaces, of which the existence is inherent to microstructures. [3] The interfacial energy and strain energy affect the equilibrium compositions and volume fractions of the coexisting phases and also determine the shape and mutual arrangement of the domains. [1,17] The different contributions to the local free energy density are typically described by polynomials, of which the form is determined by the thermodynamic or mechanical model chosen to describe the material properties. [1,3,17] The coefficients in the polynomials become parameters of the model, which can be determined theoretically or based on experimental data. [1,17]

When temperature, pressure and molar volume are constant and there are no elastic, magnetic or electric fields, the total free energy of a system defined by a concentration field x_B and a set of order parameters η_k, is for example given by

$$F = \int \left[f\left(x_B, \eta_k, \vec{\nabla} x_B, \vec{\nabla} \eta_k\right) \right] dV = \int \left[f_0(x_B, \eta_k) + \frac{\epsilon}{2} \left(\vec{\nabla} x_B\right)^2 + \sum_k \frac{\kappa_k}{2} \left(\vec{\nabla} \eta_k\right)^2 \right] dV \tag{3.17}$$

$f_0(x_B, \eta_k)$ refers to a homogeneous system where all state variables are constant throughout the system and is called the homogeneous free energy density (J/m³). For the non-conserved variables, it has minima at the values the variables can have in different domains. For the conserved variables, the homogeneous free energy density has a common tangent at the equilibrium compositions of the coexisting phases. $f(x_B, \eta_k, \nabla x_B, \nabla \eta_k)$ is the heterogeneous free energy density (J/m³) and describes the heterogeneous systems, where the diffuse interfaces are present. A completely analogous expression is obtained when phase field variables ϕ are used instead of the order parameters η_k. [1]

The gradient free energy terms $\frac{\epsilon}{2}\left(\vec{\nabla}x_B\right)^2$ and $\frac{\kappa_k}{2}\left(\vec{\nabla}\eta_k\right)^2$ are responsible for the diffuse character of the interfaces: the homogeneous free energy f_0 forces the interfaces to be as thin as possible (due to the increase in energy with an increasing amount of material in the interface having non-equilibrium values), whereas the gradient terms force the interfaces to be as wide as possible (because the wider the interface, the smaller the gradient energy contribution due to the gentle change of the $\eta_k$value over the interface). Therefore, the equilibrium width of the diffuse regions is determined by two opposing effects. [1,8,26] ε and κ_k are called gradient energy coefficients and determine the magnitude of the penalty induced by the presence of the interfaces. [27] They are related to the interface energy and thickness. [1,26] Both terms, the gradient and the potential term, contribute in equal parts to the interface energy [21]

Typical expressions for f_0 are Landau polynomials of the fourth or sixth order in the phase field and composition parameters. These expressions make use of the Landau theory of phase transformations. All the terms in the expansion corresponding to the local free energy density function are invariant with respect to symmetry operations. [26] For one order parameter (e.g. for simulating anti-phase domain structures) this could look like:

$$f_0(\eta) = 4(\Delta f_0)_{max}\left(-\frac{1}{2}\eta^2 + \frac{1}{4}\eta^4\right) \quad \textbf{(3.18)}$$

Where $(\Delta f_0)_{max}$ is the depth of the free energy. $f_0(\eta)$ has double degenerate minima at -1 and +1, which could for example represent the two thermodynamically degenerate antiphase domain states. Note that only even coefficients are present in this polynomial, which finds its origin in the symmetry of the free energy expression around zero because both variants of the ordered structure are energetically equivalent. This expression only depends on one order parameter, but the Landau polynomial can also include compositional variables and order parameters. [1,3,17] For phase field parameters, the homogeneous free energy typically contains an interpolation function f_p and a double-well function $g(\phi)$:

- The interpolation function f_p combines the free energy expressions of the coexisting phases in one expression by weighing them with a function of the phase field parameter.

  $$f_p(x_B, \phi, T) = \big(1 - p(\phi)\big)f^{\alpha}(x_B, T) + p(\phi)f^{\beta}(x_B, T) \quad \textbf{(3.19)}$$

  The free energy expressions of the coexisting phases are usually constructed from thermodynamic data or assumed to have an idealized form. $p(\phi)$ should be a smooth function that equals 1 for $\phi = 1$ and equals 0 for $\phi = 0$ and $p'(\phi) = 0$ for $\phi = 1$ and $\phi = 0$. Mostly the following function is used (with g(ζ) representing the abovementioned double-well function):

  $$p(\phi) = \frac{\int_0^{\phi} g(\zeta)d\zeta}{\int_0^1 g(\zeta)d\zeta} = \phi^3(6\phi^2 - 15\phi + 10) \quad \textbf{(3.20)}$$

  Which satisfies $p(0) = 0$ and $p(1) = 1$ as well as $p'(\phi) = p''(\phi) = 0$ at $\phi = 0$ and 1. Another possibility for $p(\phi)$ could be: [28]

  $$p(\phi) = \phi^2(3 - 2\phi) \quad \textbf{(3.21)}$$

- The double-well potential

  $$g(\phi) = w\phi^2(1 - \phi)^2 \quad \textbf{(3.22)}$$

has minima at 0 and 1 and *w* is the depth of the wells and can either be constant or depend on the composition. The double-well may be regarded as a term describing the activation barrier across the interface. [16] Another free energy function that is sometimes employed in phase field models is the so-called double-obstacle potential,

$$f_0(\phi) = \Delta f(1-\phi^2) + I(\phi) \tag{3.23}$$

where

$$I(\phi) = \begin{cases} \infty, & |\phi| > 1 \\ 0, & |\phi| \leq 1 \end{cases} \tag{3.24}$$

This potential has a computational advantage that the field variable assumes the value of *-1* and *+1* outside the interfacial region, because minimizing the free energy will make ϕ go steeper to its equilibrium value. This is in contrast with the case of the double-well potential (3.22), where the values of the field variable slowly evolve to *-1* and *+1* away from the interface. [3]

3.6. Governing equations

The phase field variables are functions of place and time and evolve towards a system with a minimal free energy functional. The temporal evolution of the variables is given by a set of coupled partial differential equations, one equation for each variable. [1,17] These equations ensure that the free-energy functional *F* decreases monotonically in time and guarantee local conservation of the conserved variables. The equations are derived according to the principles of non-equilibrium thermodynamics. [1,29]

The generalized phase field methods are based on a set of Ginzburg-Landau or Onsager kinetic equations. [2] The temporal and spatial evolution of conserved fields is governed by the Cahn-Hilliard equation, whereas the evolution of non-conserved fields is governed by the Allen-Cahn equation, also called the Ginzburg-Landau equation. [3,16] A thermodynamically consistent derivation of these equations is quite important, because it enables the correlation of the model parameters with each other, as well as the establishment of a sound theoretical background in thermodynamics. [21]

Several transport phenomena, besides diffusion, can have an effect on the microstructure, e.g. heat diffusion, convection and electric current. Using the formalism of linear non-equilibrium thermodynamics, it is straightforward to include these phenomena. However, extra equations will be required: modelling non-isothermal solidification uses the heat equation, whose kinetic parameter can be related to the thermal diffusivity; modelling convection in a liquid requires the combination of the phase field equations with a Navier-Stokes equation, in which the viscosity depends on the phase field variable. [1] Recently, the phase field method was coupled with the lattice Boltzmann equation [30–34], an alternative technique for simulating fluid flow. The next sections describe the two main types of governing equations (Cahn-Hilliard and Allen-Cahn) in more detail.

3.6.1. Ginzburg-Landau equation

The temporal evolution of the non-conserved order parameters and phase fields is described by the Ginzburg-Landau or Allen-Cahn equation. Allen and Cahn [35] postulated that, if the free energy is not at a minimum with respect to a local variation in η, there is an immediate change in η given by

$$\frac{\partial \eta_k(\vec{r},t)}{\partial t} = -L_k \frac{\delta F}{\delta \eta_k(\vec{r},t)} \tag{3.25}$$

This equation expresses that the order parameter evolves proportional with the thermodynamic driving force for the change of that order parameter. The expression for this driving force is obtained with a thermodynamic approach: the dissipation of free energy as a function of time in an irreversible process must satisfy the inequality $\delta F/\delta t \leq 0$ as the system approaches equilibrium. When there are multiple processes occurring simultaneously, only the overall condition should be satisfied rather than the equation for each individual process. E.g. an expansion of the general equation $\delta F/\delta t \leq 0$ gives: [16]

$$\left(\frac{\delta F}{\delta \eta_k}\right)_{c,T}\left(\frac{\partial \eta_k}{\partial t}\right)_{c,T} + \left(\frac{\delta F}{\delta c}\right)_{\phi,T}\left(\frac{\partial c}{\partial t}\right)_{\phi,T} + \left(\frac{\delta F}{\delta T}\right)_{\phi,c}\left(\frac{\partial T}{\partial t}\right)_{\phi,c} \leq 0 \quad \textbf{(3.26)}$$

But to ensure a monotonic decrease in the free energy of the system, it is sufficient that [16]

$$\left(\frac{\delta F}{\delta \eta_k}\right)_{c,T}\left(\frac{\partial \eta_k}{\partial t}\right)_{c,T} \leq 0 \quad \textbf{(3.27)}$$

Assuming that the flux is proportional with the force yields equation (3.25). [16] $\delta F/\delta \eta_k$ represents a variational derivative and applying the Euler-Lagrange equation[5] [36] yields [6]

$$\frac{\partial \eta_k(\vec{r},t)}{\partial t} = -L_k\left[\frac{\partial f}{\partial \eta_k} - \vec{\nabla}\frac{\partial f}{\partial \vec{\nabla}\eta_k}\right] = -L_k\left[\frac{\partial f_0}{\partial \eta_k} - \vec{\nabla}\cdot\kappa_k\vec{\nabla}\eta_k\right] \quad \textbf{(3.28)}$$

In the single-phase field model, an analogous expression is obtained:

$$\frac{\partial \phi(\vec{r},t)}{\partial t} = -L\frac{\delta F(x_B,\phi)}{\delta \phi(\vec{r},t)} = -L\left[\frac{\partial f_0(x_B,\phi)}{\partial \phi} - \vec{\nabla}\cdot\kappa(\phi)\vec{\nabla}\phi\right] \quad \textbf{(3.29)}$$

In phase field models with more than two phases, multiple phase fields ϕ_k are used to describe the phase fractions and therefore λ-multipliers or Lagrange-multipliers are used to ensure that all phase fractions sum up to 1 in every position of the system. L_k and L are positive kinetic parameters, related to the interface mobility (a measure for the speed at which the atoms can reorder from the original structure to the new structure). [1] $L_i = 1/\tau$, is the inverse of the relaxation time associated with how quickly the interface moves. [35]

3.6.2. Diffusion equations

The evolution of the conserved variables obeys a mass diffusion equation, which in turn is based on the continuity equation, stating that any spatial divergence in flux density must involve a temporal concentration change. It is based on linear non-equilibrium kinetics, according to which the atom flux is linearly proportional to the chemical potential gradient (the driving force for change in the composition). This chemical potential is actually the chemical potential difference between two species, i.e. that of the component under consideration and that of the dependent component. [37] If the free energy functional contains a gradient term for the conserved variable(s), this part of the

[5] The functional $A[f] = \int_{x_1}^{x_2} L(x,f,f')dx$ possesses an extremum for a function f that obeys the Euler-Lagrange equation:

$$\frac{\partial L}{\partial f} - \frac{d}{dx}\frac{\partial L}{\partial f'} = 0$$

[6] Note that most of the time, κ_k is assumed to be a constant and independent of the phase fields. In such cases, the divergence of the gradient of the phase field variable ($\vec{\nabla}\cdot\vec{\nabla}\eta_k$) can be rewritten with a Laplace operator: $\Delta\eta_k = \nabla^2\eta_k$

energy functional is called the Cahn-Hilliard energy and the diffusion equation the Cahn-Hilliard equation. This type of kinetic equation can also be interpreted as a diffusional form of the more general Ginzburg–Landau equation. [2] The conserved variables evolve according to an equation of the form

$$\frac{1}{V_m}\frac{\partial x_B(\vec{r},t)}{\partial t} = -\vec{\nabla}\cdot\overrightarrow{J_B} \tag{3.30}$$

The diffusion flux $\overrightarrow{J_B}$ is given by

$$J_B = -M\vec{\nabla}\frac{\delta F}{\delta x_B} = -M\vec{\nabla}\left[\frac{\partial f_0(x_B,\eta_k)}{\partial x_B} - \vec{\nabla}\cdot\epsilon\vec{\nabla}x_B(\vec{r},t)\right] \tag{3.31}$$

Parameter *M* describes the ease by which the atoms can move from one position to another and also determines the change in composition. The diffusion fluxes are defined in a number fixed reference frame, thus 'diffusion potentials' will refer to 'interdiffusion potentials' in the remainder of the text and the parameter *M* is related to the interdiffusion coefficient *D* as

$$M = \frac{V_m D}{\partial^2 G_m/\partial x_B^2} \tag{3.32}$$

The mobility coefficient can also be expressed as a function of the atomic mobilities of the constituting elements M_A and M_B, which in turn are related to tracer diffusion coefficients. [1] Mostly, the mobility coefficient is assumed to be independent of the composition, corresponding to dynamics controlled by bulk diffusion.

3.6.3. Thermal fluctuations

Stochastic Langevin forces are sometimes added to the right-hand side of each phase field equation to account for the effect of thermal fluctuations on microstructure evolution. Moreover, because, except for the initial state of the system, the simulations are deterministic and although they can adequately describe growth and coarsening, they do not cover nucleation[7]. To overcome this limitation, stochastic Langevin forces can be added, transforming the equations into:

[7] As the density and spatial distribution of nuclei are critical in determining the phase-transformation kinetics and the resultant microstructure, which finally dictate the properties of the materials, one of the challenges in phase field modelling is the simulation of the nucleation process. Governing equations in phase field simulations are deterministic with the evolution of the phase field variables toward the direction that decreases the free energy of an entire system. A nucleation event, however, is a stochastic event and may lead to a free energy increase. At the moment, two approaches exist to introduce nuclei within a metastable system: the Langevin noise method and the explicit nucleation method. The former incorporates Langevin random fluctuations into the phase field equations. This reproduces the nucleation process well (with reasonable spatial distribution and time scale) when the metastable parent phase is close to the instability temperature or composition. When a system is highly metastable, on the contrary, it is difficult to generate nuclei with this method, because this yields an unrealistic large amplitude of noise, which can lead to over- or underestimated nuclei densities. [38]
The explicit nucleation method is based on the classical nucleation theory and the Poisson seeding. It incorporates nucleation ad hoc into the simulations. Separate analytical models that describe the nucleation rate and the growth of critical nuclei as a function of composition and temperature are used for this. Once a nucleus reaches the size of a grid spacing, it is included in the phase field representation as a new grain, after which further growth is determined by the phase field equations. Here, the following assumption is made: the

$$\frac{\partial \eta_k(\vec{r},t)}{\partial t} = -L_k \frac{\delta F(x_B,\eta_j)}{\delta \eta_k(\vec{r},t)} + \xi_k(\vec{r},t) \quad \textbf{(3.33)}$$

$$\frac{1}{V_m}\frac{\partial x_B(\vec{r},t)}{\partial t} = \vec{\nabla}\cdot M\vec{\nabla}\frac{\delta F(x_B,\eta_k)}{\delta x_B(\vec{r},t)} + \psi_B(\vec{r},t) \quad \textbf{(3.34)}$$

With $\xi_k(\vec{r},t)$ non-conserved and $\psi_B(\vec{r},t)$ conserved Gaussian noise fields that satisfy the fluctuation-dissipation theorem. Mostly, the Langevin terms are used purely to introduce noise at the start of a simulation and are switched off after a few time steps. [38] The presence of a noise term in the Cahn-Hilliard equation was also derived by Bronchart et al. [39] with a coarse grain method which was shown to lead to a rigorously-derived phase field model for precipitation. These phase field equations are able to describe precipitation kinetics involving a nucleation and growth mechanism.

3.7. Interfacial properties

In multi-phase polycrystalline materials, interfaces are associated with structural and/or compositional inhomogeneities. [26] Interfaces are known as sites with an excess free energy, called the interfacial energy. This can be visualized during chemical etching processes, in which material near and at the interfacial regions is preferentially removed. In the phase field model, the interfacial energy of the system is introduced by the gradient energy terms. [26] The properties of a flat interface between two coexisting phases are determined with the functional of the system energy, such as in (3.17). [40] The interface energy is defined by the difference per unit area of the system and that which it would have been if the properties of the phases were continuous throughout the system. It is given by an integral of the local free energy density across the diffuse interface region. [41] Thus, in the phase field model, the interfacial energy contains two contributions: one from the fact that the phase field variables differ from their equilibrium values at the interfaces and the other from the fact that interfaces are characterized by steep gradients in the phase field variables. For some phase field formulations, there exist analytical relations between the gradient energy coefficients and the interfacial energy and thickness. [3,41] Based on the definition of the interface energy (the difference between the actual Gibbs energy of the system with a diffuse interface and that containing two homogeneous phases each with its equilibrium concentration) and knowing that the equilibrium composition profile will be that which makes the interface energy minimal, yields a proportionality of the interface energy with $\nu(\kappa(\Delta f)_{max})$, where $(\Delta f)_{max}$ is defined as the maximum height of the barrier in the homogeneous free-energy density f between two degenerate minima. [41]

Moreover, the interfacial thickness should be defined, because in theory, a diffuse interface is infinitely wide. [41] One of the drawbacks of the phase field method is that the simulations can be very computationally demanding. In real materials, the interfacial thickness ranges from a few angstroms to a few nanometres. [1,16] To be able to resolve the interface and for numerical stability reasons, there must be at least 5-10 grid points in the interface in the simulations. [8] When using a uniform grid spacing and assuming the real interface width, this results in very large computational

time to nucleate a new phase particle is much shorter than the computational time interval Δt. This method has the disadvantage, however, that a sharp-interfaced nucleus is inserted into the system. This results in a relaxation of the compositional and phase field variables around the newly inserted nucleus. [1,16,38]

times (as the computational time scales with the interface thickness to the $-D^{th}$ power, where D is the dimension of the simulation). It could also result in very small system sizes (of the order of 1 µm for two dimensional systems and 100 nm for three dimensions). These dimensions are too small to study realistic systems and the phenomena therein. [1,16]

All the early models considered the diffuseness of the interface as real and a property of the interface that can be predicted from the thermodynamic functional. A more pragmatic view, however, is that the diffuseness of the phase field exists on a scale that is below the microstructure scale of interest. Thus its thickness can be set to a value that is appropriate for a numerical simulation. [21] Using a broader interface, reduces the computational resources required, but might also lower the amount of detail in the simulation. Adaptive grids might be a solution, as these have a finer grid spacing in the vicinity of the interface. But these are mostly a solution if the main part of the field is uniform and the interfaces only occupy a small part of the volume. It is, however, less useful in systems with multiple grains or domains. [16] This is why most phase field simulations are applied in the 'thin-interface limit': interface widths are used as a numerical parameter and the interfaces are taken artificially wide to increase the system size, without affecting the interface behaviour, diffusion behaviour or bulk thermodynamic properties. [1] This is done by splitting the free energy density functional into an interfacial term and an independent chemical contribution and thus avoiding implicit chemical contributions to the interface energy which scale with the interface thickness. [42] The interface width is thus an adjustable parameter which may be set to physically unrealistic values, as is the case in most simulations. [16]

Here, the interface width is defined based on the steepest gradient (i.e. at the middle of the interface) so that an equal interface width results in equal accuracy and stability criteria in the numerical solution of the phase field equations. [43] It is also important that the model formulation has enough degrees of freedom to vary the interfacial properties while the diffuse interface width is kept constant. In this way the movement of all interfaces is described with equal accuracy in numerical simulations. [41] Mostly, it is assumed that the interface width is proportional to $\sqrt{(\kappa/(\Delta f)_{max})}$, where $(\Delta f)_{max}$ is defined as the maximum height of the barrier in the homogeneous free-energy density f between two degenerate minima. [41] Thus, note that an increase in $(\Delta f)_{max}$ would increase the interfacial energy but decrease the interfacial width, whereas an increase in κ, would yield both a decrease in the interfacial energy and in the interfacial width. [1]

3.8. Numerical solution methods

The microstructural and morphological evolution of the system is represented by the temporal evolution of the phase field variables. [1] This temporal evolution of the phase field variables is described by a set of partial differential equations, which are non-linear and thus should be solved numerically, by discretization in space and time. [1,17,44] Several numerical methods exist, but most of them start with a projection of the continuous system on a lattice of discrete points. Then, the phase field equations are discretized, yielding a set of algebraic equations. Solving these equations yields the values of the phase field variables in all lattice points. The lattice spacing must be small enough to resolve the interfacial profile and the dimensions of the system should be large enough to cover the processes occurring on a larger scale. Note that a smaller lattice spacing will require a smaller time step to maintain numerical stability. The numerical solution methods can be subdivided into several categories: finite difference methods, spectral methods and finite element methods.

The simplest method is the finite difference discretization technique, also called Euler method, in which the derivatives are approximated by finite differences. Several types exist: forward, backward and central differences, depending on the 'direction' of the discretization step in space. A uniform lattice spacing is typically used. The partial differential equations in phase field methods contain both derivatives with space and time, resulting in a discretization in both space and time. The discretization in time can be subdivided in two categories: implicit and explicit methods. The values of the variables at time step *n+1* are directly calculated from the values at the previous time step *n* in the case of explicit time stepping. This is applied to the general evolution equation (3.35).

$$\frac{\partial \eta}{\partial t} = -L\left(\frac{\partial f_0}{\partial \eta} - \kappa \nabla^2 \eta\right) \tag{3.35}$$

Where η is the phase field. In the two-dimensional case, the Laplacian operator can be discretized using a second-order five-point or the biharmonic operator by a fourth-order nine-point finite-difference approximation. The five-point approximation at a given time step *n* for example

$$\nabla^2 \eta_i^n = \frac{1}{(\Delta x)^2} \sum_j \left(\eta_j^n - \eta_i^n\right) \tag{3.36}$$

Where Δx is the spatial grid size and *j* represents the set of first nearest neighbours of *i* in a square grid. The explicit finite-difference scheme can then be written as

$$\eta_i^{n+1} = \eta_i^n + \Delta t \left[\left(\frac{\partial f_0}{\partial \eta}\right)_i^n + \nabla^2 \eta_i^n\right] \tag{3.37}$$

A drawback of this method is the fact that the time step should be small enough for numerical stability, which results in long computation times. The time step constraint is dictated by

$$\Delta t \approx (\Delta x)^2 \tag{3.38}$$

When the Cahn-Hilliard equation, containing the biharmonic operator, is discretized, this square becomes a fourth power. [44] In contrast, implicit methods evaluate the right hand side of the discretized equation in (3.37) on time step *n+1* instead of *n*, resulting in a set of coupled algebraic equations. This requires more intricate solution methods (linearization combined with iterative techniques), but it also allows for larger time steps. [45]

Spectral methods are a class of numerical solution techniques for differential equations. They often involve the Fast Fourier Transform. The solution of the differential equation is written as a sum of certain base functions, e.g. as a Fourier series, being a sum of sinusoids. The coefficients of the sum are chosen in such a way to satisfy the differential equation as well as possible. [45] One of these spectral methods is the Fourier spectral method with semi-implicit time stepping. [44] In this semi-implicit Fourier spectral method, the phase field equations in real space are transformed to the Fourier space with a Fast Fourier Transformation. The convergence of Fourier-spectral methods is exponential in contrast to second order in the case of the usual finite-difference method. Transforming to the Fourier space, yields

$$\frac{\partial \tilde{\eta}(\vec{k}, t)}{\partial t} = -L\left(\widetilde{\frac{\partial f_0}{\partial \eta}}\right)_{\vec{k}} + (ik)^2 L\kappa \tilde{\eta}(\vec{k}, t) \tag{3.39}$$

Where $\vec{k} = (k_1, k_2, k_3)$ is a vector in Fourier space. k_1, k_2 and k_3 assume discrete values according to $\frac{l2\pi}{N\Delta x}$, where $l = -\frac{N}{2} + 1, \ldots, \frac{N}{2}$ with *N* the number of grid points in the system and Δx the grid space.

A tilde (~) above a symbol refers to the corresponding Fourier transform of that symbol. The temporal derivatives are then differentiated semi-implicitly, i.e. the first term in (3.39) is evaluated at time step *n*, i.e. is treated explicitly, to reduce the associated stability constraint. Whereas the second term in the equation is evaluated at time step *n+1*, i.e. is treated implicitly, to avoid the expensive process of solving nonlinear equations at each time step. Solving a constant-coefficient problem of this form with the Fourier-spectral method is efficient and accurate. However, periodic boundary conditions remain inherent to the method.

$$\frac{\tilde{\eta}^{n+1} - \tilde{\eta}^{n}}{\Delta t} = -L\left(\widetilde{\frac{\partial f_0}{\partial \eta}}\right)_{\vec{k}}^{n} - k^2 L\kappa\tilde{\eta}^{n+1} \qquad \textbf{(3.40)}$$

This yields

$$\tilde{\eta}^{n+1} = \frac{\tilde{\eta}^{n} - \Delta t L\left(\widetilde{\frac{\partial f_0}{\partial \eta}}\right)_{\vec{k}}^{n}}{1 + k^2 L\kappa\Delta t} \qquad \textbf{(3.41)}$$

An inverse Fourier transform of the left hand side of (3.41) then gives η^{n+1} in real space. One benefit of this method is the fact that the laplacian is treated implicitly, thus eliminating the need of solving a large system of coupled equations. Moreover, larger time steps can be used as compared to the completely explicit treatment, which would result in spectral accuracy for the spatial discretization, but the accuracy in time would only be of the first order. Thus a better numerical stability is associated with the semi-implicit method. [3,44] Moreover, a smaller number of grid points is required due to the exponential convergence of the Fourier-spectral discretization. Chen and Shen [44] demonstrated that, for a specified accuracy of 0.5%, the speed-up by using the semi-implicit Fourier-spectral method is at least two orders of magnitude in two dimensions, compared to the explicit finite difference-schemes (in the case of three dimensions, the speed-up is close to three orders of magnitude). Note that it is still only first-order accurate in time, but the accuracy in time can be improved by using higher-order semi-implicit schemes, i.e. also taking into account other time-steps than only the n^{th} time step to determine the values in the $n+1^{th}$ time step. These higher-order semi-implicit schemes are, however, slightly less stable than lower-order semi-implicit schemes. [44]

Limitations of the method are the inherent periodic boundary conditions and the fact that the κ and L values are preferably constant to have the most efficient method. The latter may be circumvented by using an iterative procedure [46,47]. Another possibility was presented by Zhu et al. [37], who imposed a compositional dependence on the mobility. They first transformed only the part after the second gradient in the Cahn-Hilliard equation. Then they applied the inverse Fourier transform on it, to multiply it afterwards with the mobility depending on the composition, because a multiplication in real space becomes a convolution in Fourier space. This entity was then transformed again to the Fourier space and then discretized semi-implicitly in time.

Because the spectral method typically uses a uniform grid for the spatial variables, it may be difficult to resolve extremely sharp interfaces with a moderate number of grid points. In this case, an adaptive spectral method may be more appropriate. It has been shown that the number of variables in an adaptive method is significantly reduced compared with those using a uniform mesh. This allows one to solve the field model in much larger systems and for longer simulation times. However, such an adaptive method is in general a lot more complicated to implement than uniform grids. [3]

Finite volume or finite element discretization methods are also used to solve phase field equations. [1] Just like in the spectral methods, the solution of the differential equation is written as a sum of certain base functions, only this time the basis functions are not sinusoids but tent functions; it is also common to use piecewise polynomial basis functions. Thus the main difference between both types of method is that the basis functions are non-zero over the whole domain for spectral methods, while finite element methods use basis functions that are non-zero only on a small subdomain. Thus, spectral methods take a global approach, whereas finite element methods use a more local approach.

3.9. Quantitative phase field simulations

The first phase field simulations were qualitative with the limitation to observation of shape [16,21] and to obtain quantitative results one of the difficulties to overcome is the large amount of phenomenological parameters in the phase field equations. [1] The parameters are related to material properties relevant for the considered process. Ideally, the phenomenological description captures the important physics and is free from non-physical side effects. The choice of the phenomenological expressions and model parameters, on the other hand, is somehow arbitrary and material properties are not always explicit parameters in the phenomenological model. Close to equilibrium, the model parameters can be related to physically measurable quantities [21]: the parameters in the homogeneous free energy density determine the equilibrium composition of the bulk domains; the gradient energy coefficients and the double-well coefficient are related to the interfacial energy and width; the kinetic parameter in the Cahn–Hilliard equation is related to diffusion properties and the kinetic parameter in the Ginzburg–Landau equation relates to the mobility of the interfaces. [1] The parameters may depend on the direction, composition and temperature. The directional dependence, in particular, determines the morphological evolution. [1] Different methodologies can be applied to determine the missing parameters:

- Parameters that are difficult to determine for real materials can be approximated. E.g.: for the chemical energy part of the energy functional, for some materials, the temperature dependent description of Gibbs energies are available and can be directly used in the phase field model. For a system with limited thermodynamic database and when coarsening phenomena are considered, a parabolic function can be a good approximation of a real Gibbs energy function. [26]
- Measuring physical quantities that are linked to the phenomenological parameters. However, not every quantity is easy to determine: experimental information on diffusion properties, interfacial energy and mobilities is scarce. E.g. measuring interfacial free energy of a material by direct experimental techniques is inherently difficult and relates mostly to pure materials [1], but the presence of measurable quantities which are sensitive to the interfacial free energy developed indirect measurement techniques. [41]
- Reducing the dependence on experiments can be done by combining the phase field method with the CALPHAD approach. [1] The CALPHAD (CALculation of PHAse Diagrams) method was developed to calculate phase diagrams of multicomponent alloys using thermodynamic Gibbs energy expressions. [1] Constructing phase diagrams according to the CALPHAD method occurs in two steps.
    - First, free energy expressions are established for all phases present in the phase diagram, describing the free energy as a function of composition and temperature.

These temperature and composition dependences of the free energy can be described by different thermodynamic solution models, e.g.: the substitutional solution model (atoms can freely mix over all lattice sites) and the sublattice model (atoms are only allowed to mix within distinct sublattices). [1] The CALPHAD method starts from the regular solution model and introduces temperature and composition dependence of the interaction parameter with coefficients which must be determined based on experimental (and theoretical) data of thermodynamic properties and phase equilibria through a weighed least-squares fitting procedure. [48] Extrapolation of lower-order / binary subsystems, yields a full thermodynamic description of a multicomponent system using a limited amount of experimental information and thus the simple thermodynamic models make it easy to combine many separate assessments to multicomponent databases. From this description, phase relationships and thermodynamic properties can be calculated for experimentally uninvestigated regions. [1]

- In the second step, the most stable phases are determined for all compositions and temperatures, along with their corresponding compositions and fractions, by minimizing the free energy of the complete system. Moreover, other thermodynamic properties, such as chemical potential, heat of formation, etc. can also be calculated.

Several software-packages can calculate phase diagrams and can optimize the parameters in the Gibbs energy expressions, e.g.: Thermo-Calc [49] and Pandat [50]. DICTRA (DIffusion Controlled TRAnsformations) software [49] on the other hand, contains expressions for the temperature- and composition dependence of the expressions for atomic mobilities, obtained in a similar way as the Gibbs energy expressions in the CALPHAD method. The parameters are determined using experimentally measured tracer, interdiffusion, and intrinsic diffusion coefficients. [1]

Coupling with these thermodynamic databases can retrieve the Gibbs energies of phases and chemical potentials of components. [1] Volume free energy densities are suitable for describing the total free energy functional. However, for evaluation of the chemical contribution in conjunction with thermodynamics databases, molar Gibbs free energy densities are preferred. Therefore, in most phase field models, volume changes are neglected and the molar volumes of all the phases are assumed to be equal and are approximated to be independent of composition. In this way the volume free energy densities can be replaced by the molar Gibbs free energy densities ($f_0 = G_m/V_m$). [51]

- The phase field simulation technique can also be combined with ab initio calculations and other atomistic simulation techniques to obtain parameters that are difficult to obtain otherwise. [1,52] Ab initio calculations are based on quantum mechanics, i.e. solving the Schrödinger equation. For this some simplifying assumptions are required whenever multiple nuclei and electrons are present in the system. This method mainly delivers qualitative results on the relative stabilities of the crystal structure and is very promising as it requires almost no experimental input. Wang and Li [53], for example, give an overview of several studies using the phase field crystal method at microscopic levels to understand and predict fundamental properties of defects such as interfaces and dislocations and the interactions between dislocations and precipitates by using ab initio calculations as model input. These microscopic phase field (MPF) models can predict defect size and energy and thermally activated processes

of defect nucleation, utilizing ab initio information such as generalized stacking fault (GSF) energy and multiplane generalized stacking fault (MGSF) energy as model inputs.
Therefore, in theory, all parameters in the phase field model can be calculated with an atomistic technique. Unfortunately, at this moment, the quantitative results from atomistic simulations themselves are not very reliable. There may be large deviations, up to 200% or 300%, between values for the same properties calculated using different atomistic techniques or different approximations for the interaction potential. [1,52]

Furthermore, once the model is developed and if the role of each model parameter is understood, varying a parameter in different simulations and comparing the simulated microstructures with experimental observations can yield the proper value of the parameter. [41]

3.10. Historical evolution of multi-phase field models

The following paragraphs will describe the different steps towards the development of multi-phase field models in a chronological way, starting from the very first phase field models.

3.10.1. General technique

It is generally accepted that Van der Waals [54] laid the foundations of the phase field technique at the end of the 19th century by modelling a liquid-gas system with a density function that varied continuously over the interface. From general thermodynamic considerations he rationalized that a diffuse interface between stable phases of a material is more natural than the assumption of a sharp interface with a discontinuity in at least one property of the material. [21] In contrast, initial theoretical treatments of interfaces assumed two adjoining phases being homogeneous up to their common interface [55,56] or the existence of a single intermediate layer [57,58]. Another step in the right direction was taken by Rayleigh [59], who noted the inverse proportionality between the interface tension and interface thickness. However, he did not take into account the increase in free energy due to the presence of non-equilibrium material in a diffuse interface and thus was not able to estimate the interfacial thickness. Others [60,61] were able to do the latter, but the calculations were based on the nearest neighbour regular solution model, making it less generally valid.

50 years ago, Ginzburg and Landau [62] proceeded on the ideas of Van der Waals [54] and used a complex valued order parameter and its gradients to model superconductivity. [2] Subsequently, Cahn and Hilliard [40] described diffuse interfaces in non-uniform systems by accounting for gradients in thermodynamic properties and even treating them as independent variables. This originated from the idea that the local free energy should depend both on the local composition and the composition of the immediate environment. The average environment that a certain region ‘feels’ is different from its own chemical composition due to the curvature in the concentration gradient. [16] As a result, the free energy of a small volume of non-uniform solution can be expressed as the sum of two contributions, one being the free energy that this volume would have in a homogeneous solution and the other a ‘gradient energy’ which is a function of the local composition. [40] A more mathematical explanation was also presented by a Taylor expansion limited to the first and second order terms. This expression was reduced to possess only even orders of discretization as the free energy should be invariant to the direction of the gradient. However, it is not clear to which extent his Taylor expansion remains valid. [16]

Cahn and Hilliard [40] also deduced a general equation to determine the specific interfacial free energy of a flat interface between two coexisting phases. The limitations of their treatment are the assumptions that the metastable free energy of the system must be a continuous function of the property concerned and that the ratio of the maximum in this free energy coefficient to the gradient energy coefficient should be small relative to the square of the intermolecular distance. If the latter condition is not fulfilled, there is a steep gradient across the interface and thus not only the second order derivatives should be taken into account in the Taylor series with respect to the gradient.

This method is quite similar to the one of Van der Waals [54], as was discovered shortly after the publication of [40] by Cahn and Hilliard. In a second paper [63], Cahn shows that their thermodynamic treatment of non-uniform systems is equivalent to the self-consistent thermodynamic formalism of Hart [64], which is also based on the assumption that the energy per unit volume depends explicitly on the space derivatives of density. Hart defined all thermodynamic variables rigorously and related them uniquely with measurable variables. 20 years later, Allen and Cahn [35] extended the original Cahn-Hilliard model and described non-coherent transformations with non-conserved variables by the introduction of gradients of long-range order parameters into a diffusion equation. This is in contrast with the Cahn-Hilliard model, originally describing the kinetics of transformation phenomena with conserved field variables. [2] Thus, about a quarter of a century ago, these diffuse interface models were introduced into microstructural modelling. The term 'phase field model' was first introduced in research describing the modelling of solidification of a pure melt [65–67] and nowadays, advanced metallurgical variants are capable of addressing a variety of transformations in metals, ceramics, and polymers. [2]

3.10.2. Alloy solidification

The idea of using a phase field approach to modelling solidification processes was motivated by the desire to predict the complicated dendritic patterns during solidification without explicitly tracking the solid-liquid interfaces. Its success was first demonstrated by Kobayashi [68] (and later by others [28]), who simulated realistic three-dimensional dendrites using a phase field model for isothermal solidification of a single-component melt. [3] They developed a scheme to solve Stefan's problem for the solidification of a pure substance in an undercooled melt by replacing the sharp interface moving boundary problem by a diffuse interface scheme. [21] The model which was originally proposed for simulating dendritic growth in a pure undercooled melt was extended to solidification modelling of alloys by a formal analogy between an isothermal binary alloy phase field model and the non-isothermal phase field model for a pure material. [69,70]

A number of phase field models have been proposed for binary alloy systems and may be divided into three groups depending on the construction of the local free-energy functions. [3] The first type includes the models that are extensions of the models for pure materials by Losert et al. [71] and Löwen et al. [70]. The second is a model by Wheeler, Boettinger, and McFadden (WBM) [72]. The third type is a model by Steinbach et al. [25] and Tiaden et al. [73]:

- The first type of phase field models for solidification are of the type of the model by Losert et al. [71]. This model has two unrealistic assumptions: the liquidus and solidus lines in the phase diagram were assumed to be parallel and the solute diffusivity was constant in the whole space of the system. These assumptions are clearly not generally true. [69]
- The WBM model is derived in a thermodynamically consistent way, as it guarantees spatially local positive entropy production. [72] The basic approach is to construct a generalized free

energy functional that depends on both concentration and phase by superposition of two single-phase free energies and weighting them by the alloy concentration. [21] In the model, any point within the interfacial region is assumed to be a mixture of solid and liquid both with the same composition. Due to this fact that the compositions for all phases are the same, problems arise with the different phase diffusion potentials[8]. [16,51] Moreover, fictitious interfacial-chemical contributions are present which do not allow scaling of the interface width independently of other parameters. [42]

The phase field model of a binary alloy in WBM1 is based on a single gradient energy term in the phase field variable ϕ and constant solute diffusivity. At first, solute trapping[9] was not observed in the limit under consideration: asymptotic analysis of the model in the limit of the sharp interface exposed a decrease in the concentration jump as a function of the velocity, as opposed to what is experimentally observed in the solute trapping effect. Therefore, subsequent work resulted in WBM2 [74]: a phase field model of solute trapping in a binary alloy that included gradient energy terms in both ϕ and c. This model could demonstrate solute trapping, but reconsideration of WBM1 showed that solute trapping can be recovered without the necessity of introducing a solute gradient energy term, but in a different limit than first considered. [29]

- The model by Steinbach et al. [25,73] uses a different definition for the free energy density: the interfacial region is assumed to be a mixture of solid and liquid with different compositions, but constant in their ratio, specified by a partition relation. Even though the derivation of governing equations in the model was not made in a thermodynamically consistent way, there is no limit in the interface thickness. However, the initial model was only thermodynamically correct for a dilute alloy. [69]

3.10.2.1. Thin-interface limit

For quantitative computations, the relationships between the model parameters and the material characteristics should be precisely determined in such a way that the interface dynamics of the PFM correspond to that of the real interface. A simple way to determine the relationships is to set the interface width in the PFM as the real interface width. In this case, however, the computational grid

[8] $\tilde{\mu}_\alpha = \frac{\partial g_\alpha}{\partial c_\alpha}$ is here called phase diffusion potential, to distinguish it from the diffusion potential of the total phase mixture $\tilde{\mu} = \frac{\partial g}{\partial c}$, and from the chemical potential $\mu_\alpha = \frac{\partial G_\alpha}{\partial n_\alpha}$. Where g_α and G_α denote the chemical free energy density and the total chemical free energy of phase α, respectively; n_α denotes the number of moles in the solute component. This difference is illustrated in driving forces for solute diffusion and phase transformation: the gradient of phase diffusion potentials (for component i in phase α) $\nabla\tilde{\mu}_\alpha^i$ determines the driving force for solute diffusion, whereas the difference in chemical potential between the phases ($\mu_\beta^i - \mu_\alpha^i$) is the chemical driving force for phase transformation. [51]

[9] Solute trapping occurs when a phase diffusion potential gradient exists across the diffuse interface. [69] A reduction is observed in the segregation predicted in the liquid phase ahead of an advancing front. The dependency of the jump in concentration on velocity of the interface is called solute trapping. In the limit of high solidification speeds, alloy solidification without redistribution of composition, not maintaining local equilibrium, is expected. [74] Thus, during rapid solidification, solute may be incorporated into the solid phase at a concentration significantly different from that predicted by equilibrium thermodynamics. In phase field models, at low solidification rates, equilibrium behaviour is recovered, and at high solidification rates, non-equilibrium effects naturally emerge, in contrast to the traditional sharp-interface descriptions. [29]

size needs to be smaller than the real interface width of about 1 nm. Mesoscale computations then become almost impossible because of the small grid size. [75,76] This stringent restriction of the interface width was overcome by Karma and Rappel's remarkable findings [7].

They noted that the driving force is not constant if there is a significant concentration gradient on the scale of the interface width, as it depends on the local supersaturation and thereby on the concentration profile within the interface. Thus, Karma and Rappel [7] decoupled the interface width of the model from the physical interface width. They divided the driving force into two separate contributions: a constant part which represents the kinetic driving force acting on the atomistic interface, and a variable part that stems from the diffusion gradient in the bulk material apart from the atomistic interface. [21]

They showed that the dynamics of an interface with a vanishingly small width (classical sharp interface) can be correctly described by a PFM with a thin, but finite, interface width if a new relationship between the phase field mobility and the real interface mobility is adopted. In this thin-interface PFM, the interface width needs to be much smaller than the characteristic length scales of the diffusion field as well as the interface curvature. [75] To obtain this, a phenomenological point of view is used: the phase field variable is no longer used as a physical order parameter or density, but as a smoothed indicator function. The equilibrium quantities and transport coefficients are then interpolated between the phases with smooth functions of the phase field variables. [77] Moreover, the interpolation function, which weighs the bulk energies of the different phases in the system, should satisfy certain conditions: it should be a smooth function equalling the correct values (i.e. -1, 0 or +1) in its minima and has a derivative that equals zero at these minima. Otherwise, the global minima of the energy functional of the system no longer lie at the proposed values of the phase field variables. But these restrictions appear to be significantly less severe than those in previous PFMs, and the thin-interface PFM enables computation of the microstructure evolution on practical scales by ensuring correct behaviour despite the presence of a diffuse interface between phases. [9]

3.10.2.2. Quasi-equilibrium condition

A second important development was implemented by Tiaden et al. [73]. This model is actually an extension of the model of Steinbach et al. [25]. The model of Steinbach et al. [25] did not include solute diffusion, but two years after the original model, Tiaden et al. [73] added solute diffusion to the multi-phase model of Steinbach. The driving force for this solute diffusion was the gradient in composition and the diffusive law of Fick was solved in each phase. They assumed at any point within the interface a mixture of phases with different phase compositions, fixed by a quasi-equilibrium condition. In contrast to local equilibrium, this quasi-equilibrium condition assumes a finite interface mobility. [42] In the model of Tiaden et al. [73], partition coefficients were used to model phases with different solute solubilities.

Kim et al. [69] showed later that the quasi-equilibrium condition is equivalent to the equality of the phase diffusion potentials for locally coexisting phases. [43,69] This is based on the assumption that the diffusional exchange between the phases is fast compared to the phase transformation itself. [42] By assuming that quasi-equilibrium is reached, the phase compositions can adjust instantaneously in an infinitesimally small volume, leaving the phase fields and mixture compositions constant, but changing the diffusion potentials until a partial minimum of the local free energy is attained, i.e. to obtain a common value for the diffusion potential. This is the case if independent variation of the functional with respect to the phase compositions equals zero. This leads to the

constraint that all phase diffusion potentials equal the mixture diffusion potential and thus also each other. Hence the term 'quasi-equilibrium', as the system does not necessarily need to be in equilibrium, even locally. During such phase transformations, diffusion potentials are locally equal, but the chemical potentials are still different from each other. Thus, the driving force for phase transformations remains present. This can be visualized by the parallel tangent construction (representing the equal diffusion potentials) (Figure 3.5 (b)) versus the common tangent construction (representing equal chemical potentials) (Figure 3.5 (a)). [51]

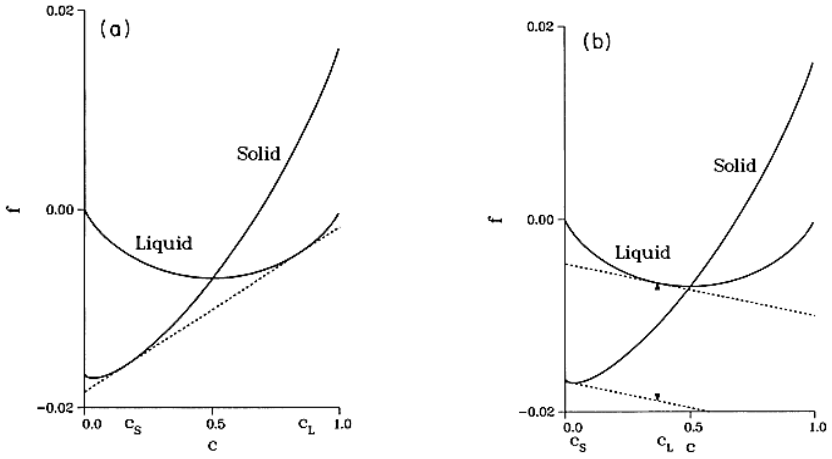

Figure 3.5 Representation of the parallel tangent (a) and common tangent (b) constructions

Kim et al. [69] developed a more general version of this type of phase field model, usually abbreviated as the KKS model, for solidification in binary alloys by natural extension of the phase field model for a pure material. They did this by direct comparison of the variables for pure material solidification and alloy solidification and also derived it in a thermodynamically consistent way. At first, the model appeared to be equivalent with the Wheeler-Boettinger-McFadden (WBM1) model [72]. The WBM model, however, has a different definition of the free energy density for interfacial region and this removes the limit in interface thickness that was present in the WBM model. The interfacial region in the KKS model is defined as a mixture of solid and liquid with compositions different from each other, but with a same phase diffusion potential. [16,69] This is represented in Figure 3.6.

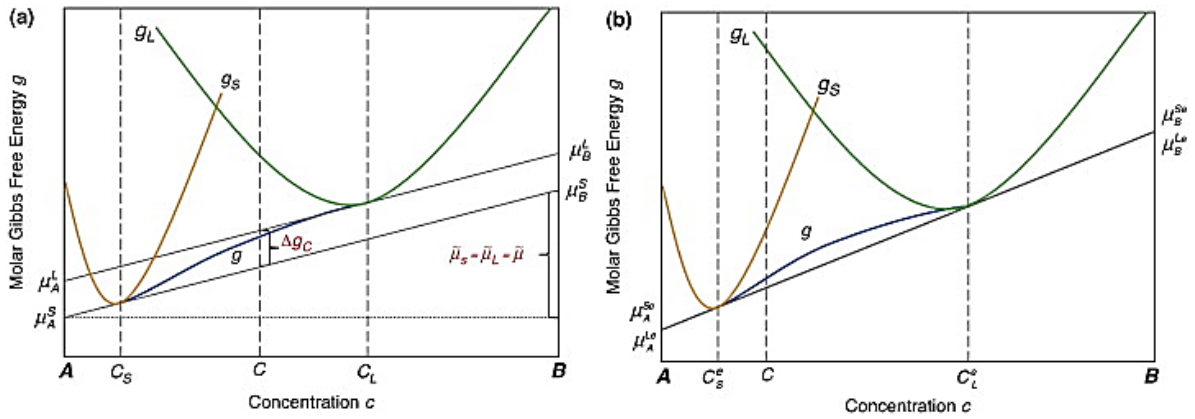

Figure 3.6 Molar Gibbs energy diagram for the phase field model with the condition of equal diffusion potentials: non-equilibrium (a) and equilibrium (b) solidification. Under equilibrium conditions, the interface and bulk contributions are completely decoupled [78]

In the WBM model, on the contrary, the interfacial region was defined as a mixture of solid and liquid with a same composition, but with different phase diffusion potentials, as shown in Figure 3.7. [69]

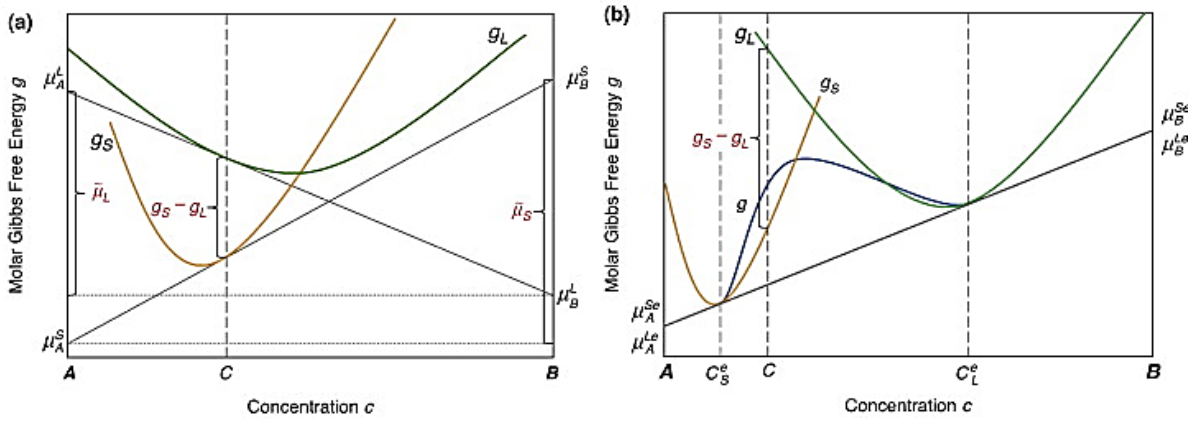

Figure 3.7 Molar Gibbs energy diagram for the phase field model with the condition of equal concentrations $C_S = C_L = C$: non-equilibrium (a) and equilibrium (b) solidification. Under equilibrium conditions (i.e. $\mu^{Se}_A = \mu^{Le}_A$ and $\mu^{Se}_B = \mu^{Le}_B$), $g_S - g_L$ = the driving force from the bulk contribution for phase field propagation = 0 cannot hold and the interface and bulk contributions are not decoupled [78]

Note that the condition of equal phase diffusion potentials in the KKS model does not imply a constant phase diffusion potential throughout the interfacial region. The phase diffusion potential varies across the moving interface depending on the position because the phase diffusion potentials are equal only at the same position. It is constant across the interface only at a thermodynamic equilibrium state. The phase diffusion potential can vary across the moving interface from the phase diffusion potential at the solid side to the phase diffusion potential at the liquid side of the interface, which results in the solute trapping effect, when the interface velocity is high enough. The energy dissipated by the boundary motion is called solute drag. In models, this solute drag is described as a fraction of the entire free-energy change upon solidification which is dissipated at the interface. [29,69]

Both the WBM and the KKS model were reformulated from the entropy or free energy functional or from thermodynamic extremal principles[10] by Wang et al. [78]. Which definition for the interfacial region is more physically reasonable does not matter, because the interfacial region in PFMs cannot be regarded as a physical real entity, but rather as a mathematical entity for technical convenience. [69]

The solid curves in Figure 3.8 show typical free energy curves of solid and liquid as a function of the composition. The free energy density in the interfacial region in the WBM model lies on the red dotted curve and the chemical free energy contribution to the interface energy is graphically represented by the area under the free energy curves and the common tangent (PQ). The extra potential in the WBM model may be negligible compared to $wg(\phi_0)$ either at the sharp interface limit where $w \rightarrow \infty$ or in an alloy with a very small c_L^e-c_S^e where the height of the extra potential itself is very small. With increasing interface thickness or increasing c_L^e-c_S^e, however, the extra potential height becomes significant and cannot be ignored. In the KKS model, on the other hand, the interfacial region at an equilibrium state is defined as a mixture of solid and liquid with constant compositions c_L^e and c_S^e, respectively and the excess energy in the interface region is removed by making the free energy equal to that of a two-phase mixture (i.e. the common tangent). The extra potential in the WBM model does not appear in the KKS model because the free energy is fraction-

[10] These include all the thermodynamic principles for modelling non-equilibrium dissipative systems, e.g. Onsager's least energy dissipation principle, the maximal entropy production principle, etc.

weighted after evaluation of the free energies of the phases in their respective equilibrium compositions, which corresponds to the common tangent line itself. [69]

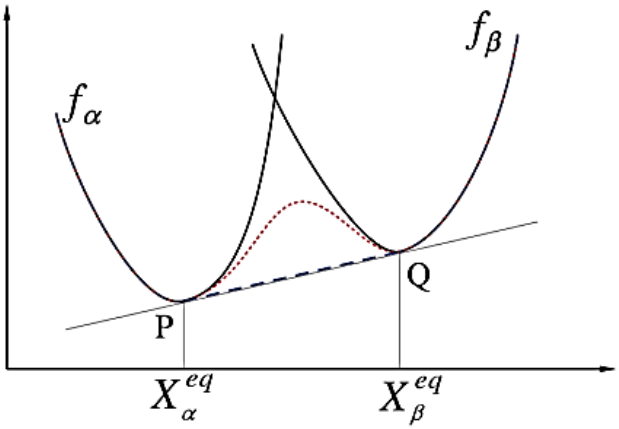

Figure 3.8 Free energy density curves of the individual phases (solid curves), of the WBM model (red dotted curve) and of the KKS model (blue dashed curve) as a function of concentration [69]

The KKS model is reduced to the model of Tiaden et al. [73] for a binary alloy at a dilute solution limit. Afterwards, Eiken (given name Tiaden) et al. [51] deduced the local quasi-equilibrium condition from a variational principle and showed again that it is equivalent to postulating equal diffusion potentials for coexisting phases. In summary, the thin-interface formulation combined with the quasi-equilibrium condition, used in the models of Tiaden et al. [51,73] and Kim et al. [69], dictates, on the one hand, that, at each position, the diffusion potentials are equal in all phases and, on the other hand, that the bulk and interfacial energy are decoupled. [43] Imposing the equal phase diffusion potential condition upon the solid and liquid phases at a point of the system has two advantages over the traditional equal composition condition. The first is the relaxation of the restriction on the interface width in computations. The second is that the profile of the equilibrium phase field gradient becomes symmetric. [75]

If instead of a free energy functional, a grand-potential ($\Omega = F - \mu N$) functional is used to generate the equations of motion, both types of abovementioned models can be obtained by the standard variational procedure. The dynamical variable is then the chemical potential instead of the composition. Here, the quasi-equilibrium condition is not required to be solved, and as the solution of these non-linear equations in each point of the interface are computationally complex, a potentially large gain in computational performance is offered. However, this model, based on a grand-potential functional, was not yet extended to multicomponent systems. [77] This generalization should, however, be straightforward and is roughly sketched in [79].

3.10.2.3. Anti-trapping current term

The first step towards an improved (thin-interface) model was obtained by adopting the condition of equal diffusion potentials and finding a new relationship between the phase field mobility and the real interface mobility with the thin-interface condition. However, this model still suffered from anomalous interface diffusion and/or an anomalous chemical potential jump at the interface which induces an exaggerated solute-trapping effect. [75] This chemical potential jump can be understood by looking to the composition profile around the interfacial region. Consider a one-dimensional solidifying system at instantaneous steady state with an interface velocity *V* in Figure 3.9. Assume

that the interface width is sufficiently smaller than the diffusion boundary layer width in the liquid, that is, the thin-interface condition. [75]

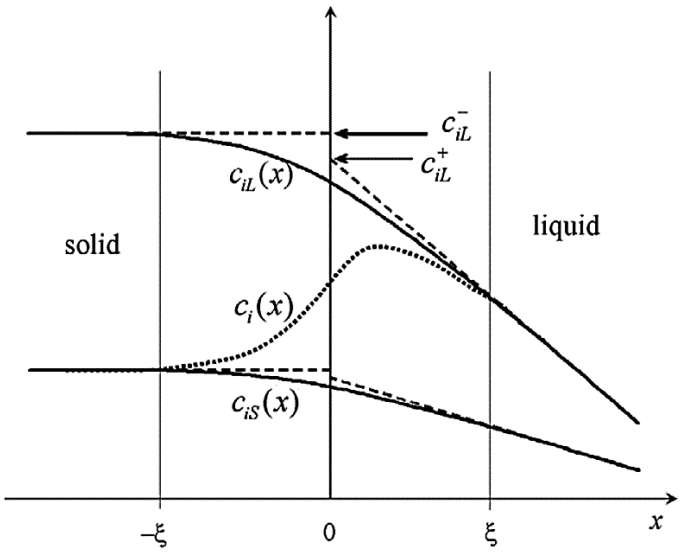

Figure 3.9 Composition profiles across the interface -ξ < x < ξ. The composition profile $c_{iS}(x)$ of i^{th} solute in the solid, $c_{iL}(x)$ in the liquid and the mixture composition $c_i(x)$ are denoted by the lower thick curve, the upper thick curve and the dotted curve, respectively. The origin (x = 0) was defined as the position with ϕ=0.5. The dashed lines are the extrapolations of the linear parts in $c_{iS}(x)$ and $c_{iL}(x)$ into the interfacial region. [75]

There exist two straight parts in the profile of $c_{iL}(x)$. One is at the bulk solid side near the interface and the other at the bulk liquid side. These two straight parts can be extrapolated into the interfacial region, as shown by the dashed lines. Then the dynamics of the diffuse interface with the composition profiles of the thick curves represent effectively that of the classical sharp interface with the composition profile of the dotted line. These two extrapolated lines from the solid and liquid sides intersect the vertical axis at $c_{iL} = c^{-}_{iL}$ and $c_{iL} = c^{+}_{iL}$. For an interface with a finite width, there exists a finite difference between c^{-}_{iL} and c^{+}_{iL}. This yields a corresponding difference in chemical potential, which has been called the chemical potential jump [76,80]. These anomalous interface effects become significant with increasing interface width in the simulation. Even though each of the anomalous interface effects can be effectively suppressed by adopting the relevant interpolation function with a specific symmetry, not all of them can be suppressed simultaneously. [75] Thus, quantitative modelling is not possible. Therefore, the addition of a non-variational anti-trapping current became necessary, to decouple bulk and interface kinetics: all the anomalous interface effects could be suppressed by introducing an anti-trapping current term into the diffusion equation which acts against the solute-trapping current driven by the phase diffusion potential gradient and eliminates simultaneously all the interface effects. This was introduced by Karma [76] for dilute binary alloys with $D_S << D_L$ (i.e. a one-sided model with zero diffusivity in the solid [18]) and worked out by Echebarria et al. [80] and Ramirez et al. [81] for binary dilute alloys with negligible diffusion in the solid, yielding quantitative simulations of alloy solidification. These were later extended to also model alloy solidification in multi-phase [82,83] and multicomponent alloys [75]. These models are, however, introduced in a non-variational way [84].

The anti-trapping current is a compensation of the asymmetric fluxes in the interfacial region if the diffusivity differs a lot in the two phases and equals $j_A^i = A^i \dot{\phi} \vec{n}$. The trapping function A^i will be determined by the condition of a vanishing potential jump. [21,43] The anti-trapping current is non-vanishing only in the diffuse interface region. It produces a solute flux from the solid to the liquid

along the direction normal to the interface that counterbalances the trapping current associated with the jump of phase diffusion potential across the interface. This current makes it possible to eliminate the jump, while leaving enough freedom to choose the other functions in the model to eliminate the modifications to the mass conservation conditions (interface stretching and surface diffusion). [76]

Following Karma's finding, two similar methods were proposed independently. Both methods are based on the fact that all the anomalous interface effects originate from the finite interface width in the diffusion equation, not in the phase field equation. The anomalous interface effects can then be suppressed by decoupling the interface width in the diffusion equation from the width in the phase field equation and taking the limit that the width in the diffusion equation goes towards 0. The other possibility is the anti-trapping PFM, where the solute-trapping phenomenon can be controlled independently of the grid size. Anti-trapping PFMs were first limited to binary dilute alloys, until Kim [75] extended this to non-dilute multi-component alloys. This model was restricted to solidification to a single solid phase. Solidification of useful multicomponent alloys, however, often accompanies two or more solid phases. Recently Folch and Plapp [83] developed an anti-trapping PFM for eutectic solidification where two solid phases form simultaneously from a liquid phase. They used a smooth free-energy functional with a parabolic form for the chemical energy which ensured the absence of any third phases in the interfaces and eliminate all thin-interface corrections to the desired free-boundary dynamics. Their model is, however, restricted to dilute binary alloys. Kim [75] later extended the anti-trapping PFM further to multicomponent systems with arbitrary thermodynamic properties. Recently, several extensions of the anti-trapping current were put forward to generalize the approach to the case of finite diffusivity in the solid [85,86]. The former simulations are done for a planar interface [85] and the latter for free dendritic growth [86], which show that the approach works well.

Another completely variational approach was taken by Brener and Boussinot [84]: they developed a phase field model for isothermal transformations that includes Onsager kinetic cross-coupling between the conserved and non-conserved variables. As the classical variational formulations of the evolution equations is of a diagonal form, i.e. the change of one variable in time only depends on the functional derivative of the free energy with respect to that same variable and not the other variable present in the system description, they introduced kinetic cross coupling into the phase field equations with a non-diagonal formulation. This resulted in a term ($M_C W \dot{\phi} \nabla \phi$) in the diffusive equation with the same shape as the antitrapping current (where $\nabla \phi$ is used as a vector normal to the interface) mentioned above, but now it is obtained in a variationally derived phase field model. Moreover, another term also appears in the equation describing the evolution of the non-conserved variable. This model was limited to a two-component system with only two phases.

3.10.2.4. Finite interface dissipation

It is not clear at what point the assumptions of irreversible thermodynamics, on which the equations describing microstructural evolution are based, would fail. Furthermore, the usual phase field framework is not well suited for the description of strong non-equilibrium effects because the equations for interface motion are often obtained by a Taylor expansion around the equilibrium solution, which is formally valid only for small driving forces. Moreover, little is known about the initial stage when the two materials are far from common equilibrium. This is in contrast with the abovementioned quasi-equilibrium models, which assume equal diffusion potentials from the start of the simulation. [87]

For two materials, with certain initial compositions, in contact, these compositions are, generally, out of equilibrium, i.e. the chemical potentials do not coincide. As soon as a common interface is formed, its composition can change. It is a plausible assumption that the interface composition should lie somewhere between the initial compositions of the two phases. However, it is not possible to determine the interface composition based on thermodynamics, since thermodynamic equilibrium is not present in the system and the problem is actually a kinetic one. To solve this, Steinbach et al. [87] developed a phase field model with finite interface dissipation. In practice, this means that the 'static' quasi-equilibrium condition is replaced by a kinetic equation that drives the concentration fields to the desired equilibrium. Such a kinetic equation is not solved for the global concentration, but for the phase compositions. The point of solving these equations separately avoids the need to employ an extra condition to fix the concentrations for each phase. Instead, the separated concentration evolution equations of each phase can be used for the iteration in time. For slow kinetics or rapidly moving interfaces, a difference between the chemical potentials in the two phases appears naturally. This difference in chemical potentials can be controlled by the rate constant of the kinetic equation, which is called the interface permeability and which can be used to tune the interface dissipation. The model naturally recovers the model with equal diffusion potentials (high permeability / fast exchange), solute trapping and phase transformations out of diffusion control. [87]

Later, Zhang and Steinbach also extended this model to become applicable to multi-component multi-phase alloys. [88] The formulation is proposed in two different models. In model I, the overall mass conservation between the phases of a multiple junction is used, whereas, in model II, the concentrations of each pair of phases have to be conserved during the transformations. Both models demonstrate the decomposition of the non-linear interactions between different phases into pairwise interaction of phases in multiple junctions. Both models converge to the same equilibrium state, while in non-equilibrium states they differ.

3.10.3. Multi-phase field models

Early phase field models for a three-phase change problem, were developed for eutectic systems and consisted of a dual phase field model (for solid and liquid) superposed by a Cahn–Hilliard model for demixing in the solid. Thus, they were restricted to a three-phase transformation. To be applicable to an arbitrary number of different phases or differently-oriented grains of the same phase, multi-phase field models were developed. [21]

First, Steinbach et al. [25] developed a multi-phase field model, where each phase is identified with an individual phase field and the transformation between all pairs of phases is treated with its own characteristics. The free energy functional describing the system is actually an expansion in a series over the pairwise interaction energies between the different phases. Tiaden et al. [73] extended this model to also account for diffusion in multi-phase systems and to describe the evolution of the microstructure during solidification processes in alloy systems. They used this model to compute the peritectic solidification process of steel. The free energy functional of the system is described by equation (3.42).

$$F\left(x_\alpha^i, \phi_k\right) = \int \left[\sum_{\beta=1}^{p} \sum_{\alpha=1}^{\alpha=\beta} \frac{1}{2} \epsilon_{\alpha\beta} \left(\phi_\alpha \vec{\nabla}\phi_\beta - \phi_\beta \vec{\nabla}\phi_\alpha\right)^2 + \frac{1}{a_{\alpha\beta}} \phi_\alpha^2 \phi_\beta^2 - m_{\alpha\beta} \left(\frac{1}{3}\phi_\alpha^3 + \phi_\alpha^2 \phi_\beta - \frac{1}{3}\phi_\beta^3 - \phi_\beta^2 \phi_\alpha\right) \right] dV \quad \textbf{(3.42)}$$

$\epsilon_{\alpha\beta}$ is the gradient energy coefficient and $1/a_{\alpha\beta}$ is proportional to the pairwise energy barrier height. The driving force for the phase transition between the phases α and β is defined by the deviation from the two-phase equilibrium and is described by $m_{\alpha\beta}$. [73] The first term in (3.42) is the kinetic term, obtained from an expansion in a series over powers and considering aspects of symmetry. This term can be interpreted as follows: the gradient of one order parameter $\nabla\phi_\alpha$ measures the interface energy to all the rest of the phases. The contribution of one specific interface type $\phi_\beta \rightarrow \phi_\alpha$, therefore, is weighted by the density of these states. $\nabla\phi_\beta$ has no contribution to the phase transformation $\phi_\beta \rightarrow \phi_\gamma$, if $\phi_\gamma = 0$ in the local volume. i.e. if no phase γ is present. The operator $\phi_\alpha \nabla\phi_\beta - \phi_\beta \nabla\phi_\alpha$ fulfils this requirement to the lowest order ϕ_β and $\nabla\phi_\beta$. The last two terms in (3.42) represent the potential part of the local free energy and are a direct extension of the standard double-well function, this is called a multi-well potential and is characterized by the proportionality to $\phi_\beta^2\phi_\alpha^2$ instead of the proportionality to $\phi_\beta\phi_\alpha$ that would be the case for the multi-obstacle potential. The pair potential contributions ($\phi_\beta\phi_\alpha^2$, $\phi_\beta^2\phi_\alpha$ and $\phi_\beta^2\phi_\alpha^2$) are non-zero only at the interface and define the potential barrier between both phases to prevent spontaneous phase transitions. [25]

As the phase fields should sum up to be one, the phase fields are not independent field variables, yielding non-linearities, which were originally attributed to triple point energies and energies of multiple interactions of higher order. Moreover, the physical assumption was made that these triple point energies and energies of multiple interactions of higher order have negligible influence on the total energy of the system and thus, the corresponding non-linearities were neglected. This approximation, however, was shown [89] to violate the conservation of interfacial stresses at multiple points. Thus, the torque terms should be taken into account as the multiple phase energies will influence the local physics significantly. [90]

Both the models of Steinbach et al. [25] and Tiaden et al. [73] are applicable for binary alloys, but not for systems with more components, which is more common in practice. The model by Eiken et al. [51] is an extension for multicomponent systems of the multi-phase field model and is based on those of Tiaden et al. [73] and Steinbach et al. [25]. Moreover, Eiken et al. [51] reformulated the model in an almost thermodynamically consistent form and derived the governing equations and the local quasi-equilibrium constraint from the free energy functional with variational principles. These systems with more than two coexisting phases are mainly used to simulate grain growth. [3,73]. In a multi-phase field model, p phase fields ϕ_k (comprised in a vector) describe the p coexisting phases. The phase fields represent the local fractions of the different phases and thus should sum up to one at every point in the system. The free energy as a functional of the molar fractions $x_i(r,t)$ and phase fields $\phi_k(r,t)$ can be split into the chemical and the interface free energy density and has the form [25,51]:

$$F\left(x_\alpha^i, \phi_k\right) = \int f^{chem}\left(x_\alpha^i, \phi_k\right) + f^{intf}\left(\phi_k\right) dV$$
$$= \int \left[\sum_{\alpha=1}^{p} \phi_\alpha f_\alpha \left(x_\alpha^i\right) + \sum_{\alpha,\beta=1}^{p} \frac{4\sigma_{\alpha\beta}}{\eta_{\alpha\beta}} \left[-\frac{\eta_{\alpha\beta}^2}{\pi^2} \nabla\phi_\alpha \cdot \nabla\phi_\beta + \phi_\alpha \phi_\beta \right] \right] dV \quad \textbf{(3.43)}$$

where $\sigma_{\alpha\beta}$ is the interface energy between phase α and phase β in a multi-phase junction with p phases or differently oriented grains and $\eta_{\alpha\beta}$ is the interface width. Moreover, a double obstacle potential is used. The chemical part of the free energy density functional is formulated as the sum of the free energy densities of the individual phases f_α weighted by the respective phase fields (i.e. the phase fractions). Note that the free energies of the individual phases depend on individual phase compositions x_α^i, which are constant over an interface in equilibrium, in contrast to the continuous mixture composition variables x_i. The phase compositions are non-conserved, whereas the global compositional variables are conserved. [51]

Moreover, due to the weighing of the free energies of the individual phases with the respective phase fractions, the following relation between the phase diffusion potentials and the (mixture) diffusion potential is found: [51]

$$\tilde{\mu}^i = \sum_{\alpha=1}^{p} \phi_\alpha \sum_{j=1}^{n} \tilde{\mu}_\alpha^j \frac{\partial x_\alpha^j}{\partial x_i} \quad \textbf{(3.44)}$$

Assuming quasi-equilibrium, an independent variation of the functional with respect to the phase compositions should equal zero. This leads to the constraint that all phase diffusion potentials equal the mixture diffusion potential and thus, also each other. [51] A more general approach weights the free energy densities of the individual phases with an interpolation function that should be smooth and should equal 1 where the corresponding phase field equals 1 and should equal 0 where the corresponding phase field equals 0. [25] Afterwards, Carré et al. [91] formulated a general expression for the anti-trapping current in such a multicomponent multi-phase field model with a double obstacle potential, based on the approach proposed by Kim [75]. The anti-trapping correction is needed when the diffusivity in one phase can be considered negligible, whereas, if the diffusivities in both phases are equal, no corrections are required.

A problem of the abovementioned multi-phase field formalism is that the exact dynamics of multiple junctions are not represented correctly: a third phase may appear at the interface between two phases, which affects the interfacial properties and complicates parameter assessment. This finds its origin in the third term of the most right-hand side of (3.43): the diffusive terms are weighted with the phase field variables of the counter phase, to concentrate the thermodynamic driving force to the centre of the interface. These equations cannot be derived rigorously from a free energy formulation and may thus violate the energy balance at triple junctions. [51]

Efforts were made to find formulations that reduce or avoid this unphysical third-phase effect. A multi-obstacle potential can diminish the interference of third phases at two-phase interfaces (‘ghost phases’) as it suppresses the spreading out of multiple junctions into the interface region. In contrast, the double-well potential is cubic in the phase field variable, which energetically favours multiple junctions. For the double-well, the growth of the third phase reduces the potential energy and the dual interface becomes intrinsically unstable. Thus, a strong counter-energy is needed to suppress spreading out of the multiple junctions into the interface region. The use of a double- or multi-obstacle potential also reduces to a certain extent the artificially large interaction between

neighbouring particles. [51] Only solving the equations at the interfaces would also be a possibility, but is sometimes combined by just putting the 'extra' phase field equal to zero when it appears after a certain number of time steps in the simulations, making it a questionable method. Alternatively, higher-order terms $\propto \phi_i\phi_j\phi_k$ can be used with high factors in front of them [92]. But it remains unclear what the influence of the latter is on triple junctions, which are not unphysical in nature. [1]

Moreover, another general problem arose: the interpolation functions for two-phase systems do not extend to multi-phase systems. [21,43] The interpolation functions should have zero slope at the equilibrium values of the non-conserved variables representing the different phases, should allow for a thermodynamically consistent interpolation of the free energies and thus, be suitable for multiple junctions, and cannot violate the sum constraint $\sum \alpha=1,..,N\ h(\phi_\alpha) = 1$. [21,43]

For example $h(\phi) = \phi^3 (10 - 15\phi + 6\phi^2)$ is frequently used as an interpolation function in a solid-liquid system, but does not generalize to multi-phase systems. Generalizing to multi-phase models with $\phi_i = 1$ and $\phi_j = 0,\ \forall j \neq i$ representing phase i and $\sum\phi_i = 1$, would give a bulk free energy of the form $f_b = \sum h_i(\phi_i)\, f$. Which, without extra constraints for $h_i(\phi_i)$, is thermodynamically inconsistent since $\sum h_i(\phi_i) \neq 1$ and this will result in energy generation in multi-junctions. Thus, even though an interpolation function of the form $h_i(\phi_i) = \phi_i$ is often used in multi-phase field models, this shifts the local minima of the total free energy, resulting in difficult-to-control inaccuracies. [43]

Folch and Plapp [83] formulated a free energy functional for systems with three phases with polynomials of the fifth-order in the phase fields as interpolation functions. These interpolation functions allow for a thermodynamic consistent interpolation between the free energies of the three coexisting phases and keep the local minima of the free energy at the intended positions. A generalization to multi-phase systems, however, was unfeasible, as the order of the interpolation polynomial has to increase with the number of phases to maintain satisfying all requirements for a quantitative phase field model. [43] Multi-order parameter representations are also possible, but do not extend to multi-phase models, as they do not require the order parameters to sum up to one, as the phase field variables in a multi-phase field model. Moelans [43] introduced a new type of interpolation function for quantitative phase field modelling for multi-phase systems. The interfacial free energy for polycrystalline structures introduced by Moelans et al. [41,93] was extended to multi-phase systems and a bulk free energy was derived, starting from the thin-interface approach of Tiaden et al. [51,73] and Kim et al. [69], but using a different type of interpolation function between the free energies of the different phases:

$$f_b = \sum_{ip} h_{ip} f_{ip}(x_1^{ip}, \dots, x_k^{ip}, \dots, x_{C-1}^{ip}) \qquad \textbf{(3.45)}$$

The interpolation functions h_{ip} must have a zero slope at the equilibrium values of the non-conserved phase fields or order parameters representing the different phases and $\sum h_{ip}$ must equal 1. Moreover, due to the quasi-equilibrium condition, the phase diffusion potentials of all components should be equal in all coexisting phases:

$$\tilde{\mu}_k = \frac{\partial f_{1p}(x_k)}{\partial x_k^{1p}} = \cdots = \frac{\partial f_{np}(x_k)}{\partial x_k^{np}}, \qquad \forall\ k \qquad \textbf{(3.46)}$$

And the overall composition of a component k should relate to the phase compositions as

$$x_k = \sum_{ip} h_{ip} x_k^{ip} \tag{3.47}$$

An important advantage of this approach compared to other quantitative alloy approaches is that composition-dependent Gibbs energy expressions for multi-component systems optimized according to the CALPHAD approach can be used directly in the phase field bulk energy in equation (3.45). Moelans introduced the following interpolation function for these multi-phase systems: [43]

$$h_{ip} = \phi_{ip} = \frac{\eta_{ip}^2}{\sum_{ip=1p}^{np} \eta_{ip}^2} \tag{3.48}$$

Note the change in notation: η_{ip} now represents the phase field variable and ϕ_{ip} represents the phase fraction. Typically, $\sum_{ip=1p}^{np} \eta_{ip} \neq 1$. In this model, the interfacial free energy functional is represented by:

$$f_s = m f_0(\eta) + \frac{\kappa(\eta)}{2} \sum_{\rho} \sum_{i=1}^{p_\rho} \left(\vec{\nabla} \eta_{\rho i}\right)^2 \tag{3.49}$$

With f_0 a fourth order Landau polynomial of the order parameters:

$$f_0(\eta) = \sum_{\rho} \sum_{i=1}^{p_\rho} \left[\frac{\eta_{\rho i}^4}{4} - \frac{\eta_{\rho i}^2}{2} \right] + \sum_{\rho} \sum_{i=1}^{p_\rho} \left[\sum_{\sigma} \sum_{j=1, \rho i \neq \sigma j}^{p_\sigma} \frac{\gamma_{\rho i, \sigma j}}{2} \eta_{\rho i}^2 \eta_{\sigma j}^2 \right] + \frac{1}{4} \tag{3.50}$$

Which is based on the model of Chen and Yang [11] for normal grain growth in pure single-phase materials. Each term in the first set of summations is a double-well potential with minima located at -1 and +1 for $\eta_{\rho i}$. The cross terms ($\gamma_{\rho i, \sigma j} \eta_{\rho i}^2 \eta_{\sigma j}^2$) were added to make it energetically unfavourable to have two order parameters different from zero at the same position in the system because it gives a positive contribution to the local free-energy density for each extra phase field variable with a value different from 0. By consequence, within the grains only one of the phase field variables differs from 0 and at a grain boundary and multi-junctions, only those phase field variables representing the adjacent grains are different from zero. [41,94]

Both the multi-phase field (MPF) type of models, based on the approach of Steinbach et al. [25,51,73], and the continuum field (CF) models, based on the approach of Chen and Yang [11], are still used in phase field modelling. A major distinction between those two types of phase field models is in the interpretation of the phase fields. In continuum-field models, the field variables are treated as being independent. At the diffuse grain boundaries, the variables change monotonously between values without any constraint. In multi-phase field models, in contrast, the phase fields are interpreted as volume fractions which therefore are subject to the constraint that the sum of the phase fields must be equal to one at each position in the system. Furthermore, the thermodynamic free energy in the continuum field model has multiple degenerate minima, one for each grain orientation. The free energy of the multi-phase field model has a single minimum for all phase fields equal to zero. It is the constraint on the sum of the phase fields that forces one of them to equal 1 within the grains.

Moelans et al. [95] compared both types of models in the context of grain growth and derived relationships to obtain equivalent parameters in both types of models. The advantage of the MPF

model is that most parameters are directly related to physical quantities, whereas it requires the numerical calculation of an integral to relate the model parameters in the CF model to physical quantities. In the MPF model, on the other hand, third-order interaction coefficients in the free energy potential are required to prevent unwanted phase fields from contributing at interfaces. Depending on the system properties, it can be cumbersome to find appropriate values for these coefficients, as they are not related to a physical quantity. From a mathematical point of view, the evolution equations obtained in the two approaches, have different solutions. However, both phase field approaches are suitable to study the statistics and mean field characteristics of grain growth in bulk materials, even if they do not result in identical dynamics for vanishing grains.

3.11. Commercial phase field software

Several commercial software packages exist to perform phase field simulations.

- MICRESS [96] has been developed based on the multi-phase field model of Steinbach et al. [21], and is coupled with the Thermo-Calc software for thermodynamic calculations. [1] The origin of MICRESS is in the simulation of solidification of metallic alloys and the development later has continued towards solid state transformations in alloys.
  - \+ MICRESS is based on a multicomponent multi-phase field model. Thus, no limitations on the amount of components or phases are present.
  - \- Most simulated systems up till now are for steels and almost no systems with oxides were simulated yet, except for the reactive air brazing process.
  - \- In the case of multicomponent alloys, the required thermodynamic data can either be provided in the form of locally linearized phase diagrams, or by direct coupling to thermodynamic data sets via a special TQ interface being developed in collaboration with Thermo-Calc. Unfortunately, the interface only works with 'ges5' files which have to be created by Thermo-Calc Software and the respective databases. None of the existing databases for Thermo-Calc, however, describe the system of interest for this research project.
  - \- Unfortunately, it is not always clear which interpolation functions are used in the multi-phase field model by Steinbach et al. [25] and thus also in the MICRESS software: "The function $h(\phi)$ is a monotonously changing function from $h(0) = 0$ to $h(1) = 1$.". Most often $h(\phi) = \phi$ is used, but this is not thermodynamically consistent as it has non-zero derivatives in the equilibrium values and shifts the local minima of the total free energy and can yield inaccurate simulations in this way. E.g. the interfacial energy is not consistent and sometimes an extra phase k is found at the ij interface, which is sometimes solved by only solving the equations at the interfaces with the use of an adaptive meshing and the phase field variable of the extra phase ϕ_k is put back to zero during every step of the renewal of the meshing [97–99]. Another possibility is the addition of higher-order terms $\propto \phi_i\phi_j\phi_k$ with high factors in front of them to make the appearance of the third phase unfavourable. But it is unclear what the influence of the latter is on triple junctions, which are not unphysical in nature.
  - \- Parallelization (based on OpenMP) is only possible for some of the partial differential equations being solved but not for the entire code.

  - At a certain point within every simulation step, the constraint of equal diffusion potentials together with mass balance equations, forms a set of equations to be solved to obtain the local phase concentrations for a given global composition and set of phase fields. In MICRESS, this is done with an iterative Newton-Raphson scheme. [42] Such iterative solutions do not have the best accuracy.
- COMSOL Multiphysics® [100] is a software-platform based for modelling and simulating physics-based problems.
  + It is possible to define all the governing equations, which are then solved in a finite element framework.
  - It was already used to simulate non-selective oxidation of metals which captures both the oxidation kinetics and stress generation [101]. But this model was limited to binary systems and the implementation of a general multicomponent multi-phase system is not straightforward as every equation has to be inserted separately.
  - Moreover, running COMSOL in parallel (based on MPI) is not very efficient and it is unclear whether it is possible to link the model to thermodynamic databases.

Other software packages that are actually not-commercial, but open source and therefore also very interesting are OpenPhase and MOOSE:

- OpenPhase an open source software project (distributed under the GNU General Public License (GPL) and free of charge) for phase field simulations of complex scientific problems involving microstructure formation in systems undergoing first order phase transformation. It is based on the model by Steinbach et al. [25], has the form of a library and is written in object oriented C++.
  + It has a modular structure which allows easy extensions of the library and simplifies the development of user programs.
  - The project is in the early test stage. Only modules which passed the tests are available to download but the list of available modules will increase in the near future after careful testing. At the moment of the start of this doctoral work, it was not yet possible to simulate multi-component systems and the parallelization (using OpenMP) was also not yet available.
- MOOSE / MARMOT [102]: The Multiphysics Object-Oriented Simulation Environment (MOOSE) is a finite-element, multiphysics framework primarily developed by Idaho National Laboratory since 2008. It has been created to speed up the development of nuclear energy related engineering applications but has since been applied to many areas of science and engineering (material microstructure evolution, chemistry, geomechanics, superconductivity and more). The framework (called MARMOT) consists of advanced numerical tools to facilitate rapid model development.
  + The system of phase field partial differential equations are solved simultaneously together with PDEs describing additional physics, e.g. solid mechanics and heat conduction, using the Jacobian-Free Newton Krylov method.
  + The MARMOT framework is automatically parallel.
  + Mesh adaptivity is integrated.
  - No multicomponent possible yet.
  - No coupling to thermodynamic databases possible yet.

These packages were not used in this doctoral research for two reasons. On one hand, we have free access to the FORTRAN code of the multicomponent model of Heulens, which enables us to adapt this code in the way we want. On the other hand, most of these commercial (and thus not free) packages are not yet able to simulate the subject of this investigation. Moreover, the implementation code is 'hidden' and we cannot adapt it in the way we want and even do not know how certain calculations are performed. Some of the packages are coupled to thermodynamic databases, but require these databases to be of a certain type, to which we, unfortunately, have no access or which are even unable to describe the system of interest.

References

[1] N. Moelans, B. Blanpain, P. Wollants, An introduction to phase-field modeling of microstructure evolution, Calphad. 32 (2008) 268–294. doi:10.1016/j.calphad.2007.11.003.

[2] D. Raabe, Introduction, in: Comput. Mater. Sci., Wiley-VCH Verlag GmbH & Co. KGaA, 1998: pp. 111–118. http://onlinelibrary.wiley.com/doi/10.1002/3527601945.ch8/summary (accessed January 22, 2015).

[3] L.-Q. Chen, Phase-Field Models for Microstructure Evolution, Annu. Rev. Mater. Res. 32 (2002) 113–140. doi:10.1146/annurev.matsci.32.112001.132041.

[4] The Minerals, Metals & Materials Society (TMS), Modeling Across Scales: A Roadmapping Study for Connecting Materials Models and Simulations Across Length and Time Scales, A Study Organized by The Minerals, Metals & Materials Society, Warrendale, PA: TMS, 2015. www.tms.org/multiscalestudy.

[5] M. Stan, Discovery and design of nuclear fuels, Mater. Today. 12 (2009) 20–28. doi:10.1016/S1369-7021(09)70295-0.

[6] J.E. Guyer, D. Wheeler, J.A. Warren, FiPy: Partial Differential Equations with Python, Comput. Sci. Eng. 11 (2009) 6–15. doi:10.1109/MCSE.2009.52.

[7] A. Karma, W.-J. Rappel, Quantitative phase-field modeling of dendritic growth in two and three dimensions, Phys. Rev. E. 57 (1998) 4323–4349. doi:10.1103/PhysRevE.57.4323.

[8] W.J. Boettinger, J.A. Warren, C. Beckermann, A. Karma, Phase-Field Simulation of Solidification, Annu. Rev. Mater. Res. 32 (2002) 163–194. doi:10.1146/annurev.matsci.32.101901.155803.

[9] J. Heulens, Isothermal Crystallization of Metallurgical Slags: Phase Field Simulations Combined with In Situ Experiments (Isotherme kristallisatie van metallurgische slakken: faseveldsimulaties in combinatie met in situ experimenten), PhD thesis, KU Leuven, 2011. https://lirias.kuleuven.be/handle/123456789/318339.

[10] Y.U. Wang, Computer modeling and simulation of solid-state sintering: A phase field approach, Acta Mater. 54 (2006) 953–961. doi:10.1016/j.actamat.2005.10.032.

[11] L.-Q. Chen, W. Yang, Computer simulation of the domain dynamics of a quenched system with a large number of nonconserved order parameters: The grain-growth kinetics, Phys. Rev. B. 50 (1994) 15752–15756. doi:10.1103/PhysRevB.50.15752.

[12] D. Rodney, Y. Le Bouar, Phase field methods and dislocations, Acta Mater. 51 (2003) 17. doi:10.1016/S1359-6454(01)00379-2.

[13] H. Henry, H. Levine, Dynamic instabilities of fracture under biaxial strain using a phase field model, Phys. Rev. Lett. 93 (2004) 105504.

[14] R. Spatschek, E. Brener, A. Karma, Phase field modeling of crack propagation, Philos. Mag. 91 (2011) 75–95. doi:10.1080/14786431003773015.

[15] D.N. Bhate, A. Kumar, A.F. Bower, Diffuse interface model for electromigration and stress voiding, J. Appl. Phys. 87 (2000) 1712–1721. doi:10.1063/1.372082.

[16] R.S. Qin, H.K. Bhadeshia, Phase field method, Mater. Sci. Technol. 26 (2010) 803–811. doi:10.1179/174328409X453190.

[17] L.-Q. Chen, Y. Wang, The continuum field approach to modeling microstructural evolution, JOM. 48 (1996) 13–18. doi:10.1007/BF03223259.

[18] M. Plapp, Remarks on some open problems in phase-field modelling of solidification, Philos. Mag. 91 (2011) 25–44. doi:10.1080/14786435.2010.486757.
[19] J.-O. Andersson, J. Ågren, Models for numerical treatment of multicomponent diffusion in simple phases, J. Appl. Phys. 72 (1992) 1350–1355. doi:10.1063/1.351745.
[20] I. Prigogine, Introduction to thermodynamics of irreversible processes, 1967. http://adsabs.harvard.edu/abs/1967itti.book.....P (accessed April 13, 2015).
[21] I. Steinbach, Phase-field models in materials science, Model. Simul. Mater. Sci. Eng. 17 (2009) 073001. doi:10.1088/0965-0393/17/7/073001.
[22] J. Ågren, Binary and Multicomponent Diffusion, in: Charact. Mater., 2002.
[23] L. Onsager, Theories and Problems of Liquid Diffusion, Ann. N. Y. Acad. Sci. 46 (1945) 241–265. doi:10.1111/j.1749-6632.1945.tb36170.x.
[24] A.M. Meirmanov, The Stefan Problem, Walter de Gruyter, 1992.
[25] I. Steinbach, F. Pezzolla, B. Nestler, M. Seeßelberg, R. Prieler, G.J. Schmitz, J.L.L. Rezende, A phase field concept for multiphase systems, Phys. Nonlinear Phenom. 94 (1996) 135–147. doi:10.1016/0167-2789(95)00298-7.
[26] H. Ravash, 3D phase-field simulations of sintering and coarsening in polycrystalline multi-phase materials, KU Leuven, 2014.
[27] J.A. Warren, R. Kobayashi, A.E. Lobkovsky, W. Craig Carter, Extending phase field models of solidification to polycrystalline materials, Acta Mater. 51 (2003) 6035–6058. doi:10.1016/S1359-6454(03)00388-4.
[28] S.-L. Wang, R.F. Sekerka, A.A. Wheeler, B.T. Murray, S.R. Coriell, R.J. Braun, G.B. McFadden, Thermodynamically-consistent phase-field models for solidification, Phys. Nonlinear Phenom. 69 (1993) 189–200. doi:10.1016/0167-2789(93)90189-8.
[29] N.A. Ahmad, A.A. Wheeler, W.J. Boettinger, G.B. McFadden, Solute trapping and solute drag in a phase-field model of rapid solidification, Phys. Rev. E. 58 (1998) 3436–3450. doi:10.1103/PhysRevE.58.3436.
[30] D. Sun, M. Zhu, S. Pan, D. Raabe, Numerical modeling of dendritic growth in alloy solidification with forced convection, Int. J. Mod. Phys. B. 23 (2009) 1609–1614. doi:10.1142/S0217979209061342.
[31] A. Younsi, A. Cartalade, M. Quintard, Lattice Boltzmann Simulations for Anisotropic Crystal Growth of a Binary Mixture, in: 2014. http://oatao.univ-toulouse.fr/11934/ (accessed July 28, 2015).
[32] S. Chen, G.D. Doolen, Lattice Boltzmann Method for Fluid Flows, Annu. Rev. Fluid Mech. 30 (1998) 329–364. doi:10.1146/annurev.fluid.30.1.329.
[33] P. Lallemand, L.-S. Luo, Theory of the lattice Boltzmann method: Dispersion, dissipation, isotropy, Galilean invariance, and stability, Phys. Rev. E. 61 (2000) 6546–6562. doi:10.1103/PhysRevE.61.6546.
[34] Y.H. Qian, D. D'Humières, P. Lallemand, Lattice BGK Models for Navier-Stokes Equation, EPL Europhys. Lett. 17 (1992) 479. doi:10.1209/0295-5075/17/6/001.
[35] S.M. Allen, J.W. Cahn, A microscopic theory for antiphase boundary motion and its application to antiphase domain coarsening, Acta Metall. 27 (1979) 1085–1095. doi:10.1016/0001-6160(79)90196-2.
[36] E.W. Weisstein, Euler-Lagrange Differential Equation, (n.d.). http://mathworld.wolfram.com/Euler-LagrangeDifferentialEquation.html.
[37] J. Zhu, L.-Q. Chen, J. Shen, V. Tikare, Coarsening kinetics from a variable-mobility Cahn-Hilliard equation: Application of a semi-implicit Fourier spectral method, Phys. Rev. E. 60 (1999) 3564–3572. doi:10.1103/PhysRevE.60.3564.
[38] T.W. Heo, L.-Q. Chen, Phase-Field Modeling of Nucleation in Solid-State Phase Transformations, JOM. 66 (2014) 1520–1528. doi:10.1007/s11837-014-1033-9.
[39] Q. Bronchart, Y. Le Bouar, A. Finel, New Coarse-Grained Derivation of a Phase Field Model for Precipitation, Phys. Rev. Lett. 100 (2008) 015702. doi:10.1103/PhysRevLett.100.015702.

[40] J.W. Cahn, J.E. Hilliard, Free Energy of a Nonuniform System. I. Interfacial Free Energy, J. Chem. Phys. 28 (1958) 258. doi:doi:10.1063/1.1744102.
[41] N. Moelans, B. Blanpain, P. Wollants, Quantitative analysis of grain boundary properties in a generalized phase field model for grain growth in anisotropic systems, Phys. Rev. B. 78 (2008) 024113. doi:10.1103/PhysRevB.78.024113.
[42] B. Böttger, J. Eiken, M. Apel, Multi-ternary extrapolation scheme for efficient coupling of thermodynamic data to a multi-phase-field model, Comput. Mater. Sci. 108, Part B (2015) 283–292. doi:10.1016/j.commatsci.2015.03.003.
[43] N. Moelans, A quantitative and thermodynamically consistent phase-field interpolation function for multi-phase systems, Acta Mater. 59 (2011) 1077–1086. doi:10.1016/j.actamat.2010.10.038.
[44] L.-Q. Chen, J. Shen, Applications of semi-implicit Fourier-spectral method to phase field equations, Comput. Phys. Commun. (1998) 147–158. doi:10.1016/S0010-4655(97)00115-X.
[45] A. Gilat, Numerical Methods for Engineers and Scientists, 3 edition, Wiley, Hoboken, NJ, 2013.
[46] P. Concus, G.H. Golub, Use of Fast Direct Methods for the Efficient Numerical Solution of Nonseparable Elliptic Equations, SIAM J. Numer. Anal. 10 (1973) 1103–1120.
[47] J. Shen, Efficient Spectral-Galerkin Method I. Direct Solvers of Second- and Fourth-Order Equations Using Legendre Polynomials, SIAM J. Sci. Comput. 15 (1994) 1489–1505. doi:10.1137/0915089.
[48] N. Moelans, Computational Thermodynamics in Materials Design, (2014).
[49] J.-O. Andersson, T. Helander, L. Höglund, P. Shi, B. Sundman, Thermo-Calc & DICTRA, computational tools for materials science, Calphad. 26 (2002) 273–312. doi:10.1016/S0364-5916(02)00037-8.
[50] Pandat 8.0 Download (Free trial) - Pandat.exe, Softw. Inf. (n.d.). http://pandat.software.informer.com/8.0/ (accessed February 4, 2015).
[51] J. Eiken, B. Böttger, I. Steinbach, Multiphase-field approach for multicomponent alloys with extrapolation scheme for numerical application, Phys. Rev. E. 73 (2006) 066122. doi:10.1103/PhysRevE.73.066122.
[52] K. Lejaeghere, V. Van Speybroeck, G. Van Oost, S. Cottenier, Error Estimates for Solid-State Density-Functional Theory Predictions: An Overview by Means of the Ground-State Elemental Crystals, Crit. Rev. Solid State Mater. Sci. 39 (2014) 1–24. doi:10.1080/10408436.2013.772503.
[53] Y. Wang, J. Li, Phase field modeling of defects and deformation, Acta Mater. 58 (2010) 1212–1235. doi:10.1016/j.actamat.2009.10.041.
[54] J.D. van der Waals, Thermodynamische theorie der capillariteit in de onderstelling van continue dichtheidsverandering (Dutch; English translation in J. Stat. Phys., 1979, 20:197), Verhand Kon Akad V Wetensch Amst. 1 (1893). doi:10.1007/BF01011514.
[55] T. Young, G. Peacock, J. Leitch, Miscellaneous works of the late Thomas Young .., London, J. Murray, 1855. http://archive.org/details/miscellaneouswo01youngoog (accessed February 5, 2015).
[56] R. Becker, Die Keimbildung bei der Ausscheidung in metallischen Mischkristallen, Ann. Phys. 424 (1938) 128–140. doi:10.1002/andp.19384240115.
[57] E.A. Guggenheim, The number of arrangements on a lattice of molecules each occupying several sites, Trans. Faraday Soc. 41 (1945) 107–115. doi:10.1039/TF9454100107.
[58] R. Defay, I. Prigogine, Surface tension of regular solutions, Trans. Faraday Soc. 46 (1950) 199–204. doi:10.1039/TF9504600199.
[59] Lord Rayleigh, XLIII. On Laplace's theory of capillarity, Philos. Mag. Ser. 5. 16 (1883) 309–315. doi:10.1080/14786448308627434.
[60] T. Murakami, S. Ono, M. Tamura, M. Kurata, On the Theory of Surface Tension of Regular Solution, J. Phys. Soc. Jpn. 6 (1951) 309.
[61] M. Hillert, A Theory of Nucleation of Solid Metallic Solutions, Mass. Inst. Tech, 1956.

[62] V.L. Ginzburg, L.D. Landau, On the Theory of Superconductivity (1950), in: Supercond. Superfluidity, Springer Berlin Heidelberg, 2009: pp. 113–137. http://link.springer.com/chapter/10.1007/978-3-540-68008-6_4 (accessed February 5, 2015).
[63] J.W. Cahn, Free Energy of a Nonuniform System. II. Thermodynamic Basis, J. Chem. Phys. 30 (1959) 1121–1124. doi:10.1063/1.1730145.
[64] E.W. Hart, Thermodynamics of Inhomogeneous Systems, Phys. Rev. 113 (1959) 412–416. doi:10.1103/PhysRev.113.412.
[65] G.J. Fix, Free Boundary Problems: Theory and Applications, (1983) 580.
[66] J.B. Collins, H. Levine, Diffuse interface model of diffusion-limited crystal growth, Phys. Rev. B. 31 (1985) 6119–6122. doi:10.1103/PhysRevB.31.6119.
[67] J.S. Langer, Models of pattern formation in first–order phase transitions, in Directions in Condensed Matter Physics, (1986).
[68] R. Kobayashi, Modeling and numerical simulations of dendritic crystal growth, Phys. Nonlinear Phenom. 63 (1993) 410–423. doi:10.1016/0167-2789(93)90120-P.
[69] S.G. Kim, W.T. Kim, T. Suzuki, Phase-field model for binary alloys, Phys. Rev. E. 60 (1999) 7186–7197. doi:10.1103/PhysRevE.60.7186.
[70] H. Löwen, J. Bechhoefer, L.S. Tuckerman, Crystal growth at long times: Critical behavior at the crossover from diffusion to kinetics-limited regimes, Phys. Rev. A. 45 (1992) 2399–2415. doi:10.1103/PhysRevA.45.2399.
[71] W. Losert, D.A. Stillman, H.Z. Cummins, P. Kopczyński, W.J. Rappel, A. Karma, Selection of doublet cellular patterns in directional solidification through spatially periodic perturbations, Phys. Rev. E - Stat. Phys. Plasmas Fluids Relat. Interdiscip. Top. 58 (1998). http://umaryland.pure.elsevier.com/en/publications/selection-of-doublet-cellular-patterns-in-directional-solidification-through-spatially-periodic-perturbations%281c691b89-00c9-4b13-8051-bd64f442bd46%29.html (accessed March 6, 2015).
[72] A.A. Wheeler, W.J. Boettinger, G.B. McFadden, Phase-field model for isothermal phase transitions in binary alloys, Phys. Rev. A. 45 (1992) 7424–7439. doi:10.1103/PhysRevA.45.7424.
[73] J. Tiaden, B. Nestler, H.J. Diepers, I. Steinbach, The multiphase-field model with an integrated concept for modelling solute diffusion, Phys. D. 115 (1998) 73–86. doi:10.1016/S0167-2789(97)00226-1.
[74] A.A. Wheeler, W.J. Boettinger, G.B. McFadden, Phase-field model of solute trapping during solidification, Phys. Rev. E. 47 (1993) 1893–1909. doi:10.1103/PhysRevE.47.1893.
[75] S.G. Kim, A phase-field model with antitrapping current for multicomponent alloys with arbitrary thermodynamic properties, Acta Mater. 55 (2007) 4391–4399. doi:10.1016/j.actamat.2007.04.004.
[76] A. Karma, Phase-Field Formulation for Quantitative Modeling of Alloy Solidification, Phys. Rev. Lett. 87 (2001) 115701. doi:10.1103/PhysRevLett.87.115701.
[77] M. Plapp, Unified derivation of phase-field models for alloy solidification from a grand-potential functional, Phys. Rev. E. 84 (2011) 031601. doi:10.1103/PhysRevE.84.031601.
[78] H. Wang, X. Zhang, C. Lai, W. Kuang, F. Liu, Thermodynamic principles for phase-field modeling of alloy solidification, Curr. Opin. Chem. Eng. 7 (2015) 6–15. doi:10.1016/j.coche.2014.09.004.
[79] M. Plapp, Phase-Field Models, in: Handb. Cryst. Growth, Elsevier, 2015: pp. 631–668. http://linkinghub.elsevier.com/retrieve/pii/B9780444563699000150 (accessed November 7, 2016).
[80] B. Echebarria, R. Folch, A. Karma, M. Plapp, Quantitative Phase Field Model of Alloy Solidification, Phys. Rev. E. 70 (2004). doi:10.1103/PhysRevE.70.061604.
[81] J.C. Ramirez, C. Beckermann, A. Karma, H.-J. Diepers, Phase-field modeling of binary alloy solidification with coupled heat and solute diffusion, Phys. Rev. E Stat. Nonlin. Soft Matter Phys. 69 (2004) 051607.
[82] R. Folch, M. Plapp, Towards a quantitative phase-field model of two-phase solidification, Phys. Rev. E. 68 (2003) 010602. doi:10.1103/PhysRevE.68.010602.

[83] R. Folch, M. Plapp, Quantitative phase-field modeling of two-phase growth, Phys. Rev. E. 72 (2005) 011602. doi:10.1103/PhysRevE.72.011602.
[84] E.A. Brener, G. Boussinot, Kinetic cross coupling between nonconserved and conserved fields in phase field models, Phys. Rev. E. 86 (2012) 060601. doi:10.1103/PhysRevE.86.060601.
[85] A. Gopinath, R.C. Armstrong, R.A. Brown, Second order sharp-interface and thin-interface asymptotic analyses and error minimization for phase-field descriptions of two-sided dilute binary alloy solidification, J. Cryst. Growth. 291 (2006) 272–289. doi:10.1016/j.jcrysgro.2006.03.001.
[86] M. Ohno, K. Matsuura, Quantitative phase-field modeling for dilute alloy solidification involving diffusion in the solid, Phys. Rev. E. 79 (2009) 031603. doi:10.1103/PhysRevE.79.031603.
[87] I. Steinbach, L. Zhang, M. Plapp, Phase-field model with finite interface dissipation, Acta Mater. 60 (2012) 2689–2701. doi:10.1016/j.actamat.2012.01.035.
[88] L. Zhang, I. Steinbach, Phase-field model with finite interface dissipation: Extension to multi-component multi-phase alloys, Acta Mater. 60 (2012) 2702–2710. doi:10.1016/j.actamat.2012.02.032.
[89] H. Garcke, B. Nestler, B. Stoth, On anisotropic order parameter models for multi-phase systems and their sharp interface limits, Phys. Nonlinear Phenom. 115 (1998) 87–108. doi:10.1016/S0167-2789(97)00227-3.
[90] I. Steinbach, F. Pezzolla, A generalized field method for multiphase transformations using interface fields, Phys. Nonlinear Phenom. 134 (1999) 385–393. doi:10.1016/S0167-2789(99)00129-3.
[91] A. Carré, B. Böttger, M. Apel, Implementation of an antitrapping current for a multicomponent multiphase-field ansatz, J. Cryst. Growth. 380 (2013) 5–13. doi:10.1016/j.jcrysgro.2013.05.032.
[92] B. Nestler, H. Garcke, B. Stinner, Multicomponent alloy solidification: Phase-field modeling and simulations, Phys. Rev. E. 71 (2005) 041609. doi:10.1103/PhysRevE.71.041609.
[93] N. Moelans, B. Blanpain, P. Wollants, Quantitative Phase-Field Approach for Simulating Grain Growth in Anisotropic Systems with Arbitrary Inclination and Misorientation Dependence, Phys. Rev. Lett. 101 (2008) 025502. doi:10.1103/PhysRevLett.101.025502.
[94] N. Moelans, Phase-Field Simulations of Grain Growth in Materials Containing Second-Phase Particles (Faseveldsimulaties van korrelgroei in materialen met tweede-fase-deeltjes), PhD, KU Leuven, 2006. https://lirias.kuleuven.be/handle/1979/309 (accessed October 9, 2013).
[95] N. Moelans, F. Wendler, B. Nestler, Comparative study of two phase-field models for grain growth, Comput. Mater. Sci. 46 (2009) 479–490. doi:10.1016/j.commatsci.2009.03.037.
[96] about MICRESS, n.d. http://web.micress.de/aboutmicress.html (accessed July 27, 2016).
[97] W. Villanueva, K. Grönhagen, G. Amberg, J. Ågren, Multicomponent and multiphase modeling and simulation of reactive wetting, Phys. Rev. E. 77 (2008) 056313. doi:10.1103/PhysRevE.77.056313.
[98] W. Villanueva, W.J. Boettinger, J.A. Warren, G. Amberg, Effect of phase change and solute diffusion on spreading on a dissolving substrate, Acta Mater. 57 (2009) 6022–6036. doi:10.1016/j.actamat.2009.08.033.
[99] W. Villanueva, W.J. Boettinger, G.B. McFadden, J.A. Warren, A diffuse-interface model of reactive wetting with intermetallic formation, Acta Mater. 60 (2012) 3799–3814. doi:10.1016/j.actamat.2012.03.047.
[100] COMSOL Multiphysics® Modeling Software, n.d. https://www.comsol.com/ (accessed July 27, 2016).
[101] M. Asle Zaeem, H. El Kadiri, An elastic phase field model for thermal oxidation of metals: Application to zirconia, Comput. Mater. Sci. 89 (2014) 122–129. doi:10.1016/j.commatsci.2014.03.042.
[102] M.R. Tonks, D. Gaston, P.C. Millett, D. Andrs, P. Talbot, An object-oriented finite element framework for multiphysics phase field simulations, Comput. Mater. Sci. 51 (2012) 20–29. doi:10.1016/j.commatsci.2011.07.028.

B. Binary two-phase model

“entia non sunt multiplicanda praeter necessitate / Entities should not be multiplied beyond necessity”
(Do not postulate the existence of things you have no reason to)

– Ockham’s razor / principle of philosophical parsimony

4. Model description

To get acquainted with the modelling techniques and algorithms, a binary model with limited complexity was implemented in Matlab [1]. The model descriptions in the publications on this model were sometimes concise, thus, this chapter provides the reader with a more in-depth explanation of the model. The chapter starts with an overview of the previous models considering phase field modelling of non-reactive wetting [11], followed by the formulation and numerical implementation of our model. Finally, some extra information is given on phenomena present in the system under consideration.

4.1. Previous models for non-reactive wetting

Wetting of a foreign wall by fluids has been studied extensively. Various methods have been applied to address these problems such as continuum models and atomistic simulations. Despite this inventory, recent studies addressing heterogeneous crystal nucleation rely almost exclusively on the classical spherical cap model, which assumes mathematically sharp interfaces. [2,3]

If the influence of the solid is short-ranged compared to the thickness of the diffuse interface, it can be accounted for by appropriate boundary conditions at the solid surface. Typically, a simple Dirichlet boundary condition is enforced on the solid surface. [4] From this boundary condition, a certain 'standard' contact angle can be derived, but this value has nothing to do with a 'true' contact angle at the solid surface. The latter is not defined in these phase field models, since different iso-levels behave in qualitatively different ways as the solid surface is approached. The only level that hits the solid surface at the right angle is the one with the value of the Dirichlet boundary condition. Another option to introduce fluid-wall interactions is the use of a third phase field with a very high viscosity to represent a solid wall [5].

Regarding heterogeneous nucleation, the phase field method has also been used to describe a system with an arbitrary contact angle. Here the wall-liquid and wall-solid interactions are characterized by the contact angle θ that is determined from the interfacial free energies by Young's equation: $\gamma_{WL} = \gamma_{WS} + \gamma_{SL}\cos(\theta)$, where subscripts W, S, and L refer to the wall, the solid, and the liquid, respectively. Both a single component system [2] and a binary alloy system [3] were already investigated. Numerical approaches to obtain a certain wetting behaviour are designed to either ensure the desired contact angle or fixing the value of the phase field at the wall or the normal component of the phase field gradient [2,3]. The three different models are illustrated in Figure 4.1 and can be summarized as: [2,3]

- Model A is a diffuse interface implementation of the classical spherical cap model with a contact angle that is independent of the driving force. This contact angle is ensured by a specific surface function. This model places the mathematical surface at which the boundary condition acts slightly beyond the boundary layer. Thus, the bulk liquid and solid phases in contact with the wall are connected through an unperturbed solid-liquid interface profile, and the derivation of the interface function for the desired contact angle is straightforward. The total free energy of the system incorporates both a volumetric and a surface contribution.

[11] Which can be found in the following publication: I. Bellemans, N. Moelans, K. Verbeken, Phase field modelling in extractive metallurgy, Critical Reviews in Solid State Materials Sciences. Submitted

- Model B is a non-classical formulation assuming a fixed phase field value at the interface, leading to certain surface (dis)ordering, a strongly supersaturation-dependent contact angle. In this model, only local states present in the solid-liquid interface can be realized at the wall. A shortcoming of this model is its implicit assumption that the wall enforces the formation of a specific layer of the solid-liquid interface. In this case, the free energy of the system only consists of a volumetric contribution.
- Model C is a non-classical approach, which fixes the normal component of the phase field gradient, leading to surface (dis)ordering, a supersaturation-dependent contact angle. This model has a less straightforward physical interpretation, but can prescribe local conditions that are not present at the solid-liquid interface.

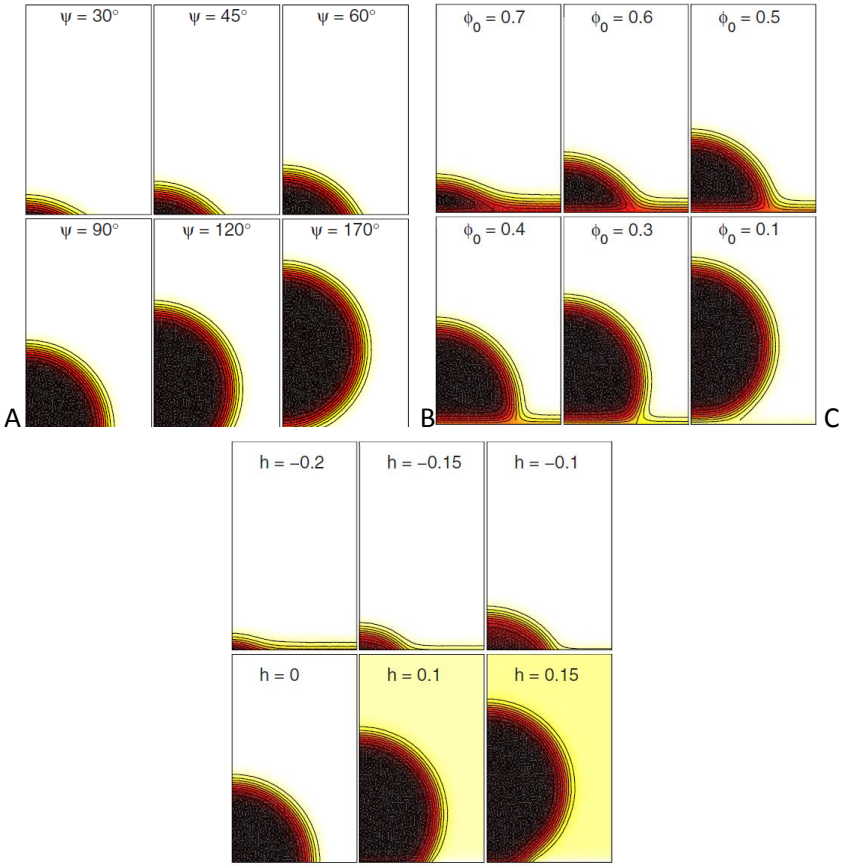

Figure 4.1 Structure of heterogeneous nuclei in model A for various contact angles; in model B for various phase field values at the wall and in model C for various values of the gradient of the phase field variable. There is a symmetry plane on the left edge of every simulation. The contour lines of the phase field variable vary between 0.1 and 1.0 by increments of 0.1. [3]

4.2. Model formulation

A phase field model for solid-liquid binary systems is implemented to simulate the metal droplet formation and growth in slags with non-reacting solid particles. This model captures the important features of the droplet formation and growth, but for which the simulation and computational requirements are reasonable. A hypothetical binary system O-M was considered, where M is a certain metal, and the microstructure is described by the position- and time-dependent field variables: a non-conserved phase field variable ϕ, used to distinguish between solid ($\phi = 1$) and liquid ($\phi = 0$), and a conserved composition field x_M, i.e. the local molar fraction of the metallic element

(e.g. x_M = 0.5 in stoichiometric MO, x_M = 0.333 in stoichiometric MO_2 and x_M is close to 1 for the metallic droplet). The position of the boundaries as a function of time is implicitly given by the field variables, i.e. the variables continuously change from one bulk value to another bulk value over the interface.

Several assumptions were made:

- the concentration of the solute in the solid precipitate is fixed
- the solid particle does not react [12]
- the molar volume V_m is the same in all phases
- the molar volume V_m is composition independent
- the solid particles are present before the metallic droplets form
- convection is not included

Both the evolution of the conserved and the non-conserved variables are governed by the minimization of the total Gibbs energy. The total free energy (J) of the system is formulated as:

$$F = \int \left[f_{S-L,interf}(\phi) + \left(1 - h(\phi)\right) f_{Liquid}(x_M) + h(\phi) f_{Solid}(x_M) + f_{\nabla x_M} \right] dV \quad \textbf{(4.1)}$$

The first term only differs from 0 at the solid-liquid interfaces and is therefore the contribution of the interfacial energy for the solid-liquid interfaces and has the form

$$f_{S-L,interf}(\phi) = W g(\phi) + \frac{\kappa_\phi}{2} (\nabla \phi)^2 \quad \textbf{(4.2)}$$

with W (J/m³) and κ_ϕ (J/m) model parameters. g(ϕ) is a double-well function with minima at 0 and 1: g(ϕ) = $\phi^2(1-\phi)^2$. W is proportional with the depth of the wells. The second term in (4.2) is a gradient free energy term and it is responsible for the diffuse character of the interface between liquid and solid. The Cahn-Hilliard Gibbs free energy of the liquid phase has a homogeneous part f_{Liquid}, described by a fourth order polynomial

$$f_{Liquid}(x_M) = \frac{A_{Sp}}{2} \left(x_M - x_{eq,LO}\right)^2 \left(x_M - x_{eq,LM}\right)^2 \quad \textbf{(4.3)}$$

And a gradient part $f_{\nabla x_M}$ responsible for the diffuse character of the interface between the two different liquid phases and has the form

$$f_{\nabla x_M} = \frac{\kappa_{x_M}}{2} (\nabla x_M)^2 \quad \textbf{(4.4)}$$

Where $x_{eq,LO}$ and $x_{eq,LM}$ are the 2 minima of the free energy curve of the liquid, between which spinodal decomposition takes place, as this free energy describes a miscibility gap between these two equilibrium compositions in the compositional region where $\partial^2 G / \partial x_M^2 < 0$ [7,8]. These two equilibrium compositions of the oxidic liquid (slag) and metallic liquid are indicated with 'LO' and 'LM', respectively. A_{Sp} (J/m³) can be used to adjust the solubilities of the two phases. The uniform supersaturation of the initial oxidic liquid is represented by x_i. The gradient energy contribution for the concentration field is required to stabilize phase separation when the liquid concentration is inside the region of the miscibility gap. [6]

[12] Note that Wang et al. [6] did simulate spinodal decomposition in a liquid that was also solidifying by incorporating a gradient energy contribution for the composition, similarly as in this study. The growth of the solid phase would perturb the concentration field in the liquid.

The bulk contribution of the solid phase as a function of composition, $f_{Solid}(x_M)$, is modelled with a parabolic function:

$$f_{Solid}(x_M) = \frac{A_S}{2}(x_M - x_S)^2 \quad \textbf{(4.5)}$$

Solid phases in oxide systems are often modelled with paraboloid Gibbs energies to provide a continuum model formulation of solids described as stoichiometric compounds in thermodynamic databases [9,10]. x_S and A_S (J/m³) are model parameters that determine the position of the minimum and the curvature of the parabola.

The interpolation function h(ϕ) has the form

$$h(\phi) = \phi^3(10 - 15\phi + 6\phi^2) \quad \textbf{(4.6)}$$

and is frequently used in solid-liquid systems [8,11]. With h(ϕ = 1) = 1 in the solid and h(ϕ = 0) = 0 in the liquid.

Two different gradient terms are present in the total energy expression, corresponding to two types of interfaces: solid - liquid and liquid oxide - liquid metal. These gradient free energy terms are responsible for the diffuse character of the interfaces. Following the approach of Cahn and Hilliard [12], it can be determined that the interfacial energy (J/m²) of the liquid-liquid interface $\gamma_{LO,LM}$ equals:

$$\gamma_{LO,LM} = \frac{1}{6}\sqrt{\kappa_{x_M} A_{Sp}}\left(x_{eq,LM} - x_{eq,LO}\right)^3 \quad \textbf{(4.7)}$$

The width of the diffuse liquid-liquid interface is defined based on the absolute value of the gradient of the composition profile at the middle of the diffuse interface, where the profile is steepest.

$$l_{LO,LM} = \left| \frac{x_{eq,LM} - x_{eq,LO}}{\left.\frac{dx_M}{dn}\right|_{x_M = 0.5(x_{eq,LM} + x_{eq,LO})}} \right| = 4\sqrt{\frac{\kappa_{x_M}}{A_{Sp}}}\left| \frac{1}{x_{eq,LM} - x_{eq,LO}} \right| \quad \textbf{(4.8)}$$

Where *n* is taken along the normal to the interface.

Especially noteworthy about the developed model is the expression for the interfacial energy (J/m²) of the solid-liquid. The interfacial energies (J/m²) of the solid-liquid can refer to either solid-liquid oxide interfaces or solid-liquid metal interfaces, with the respective interfacial energies $\gamma_{S,LO}$ or $\gamma_{S,LM}$. These interfacial energies are not necessarily equal, but are composed in the same way and consist of two contributions:

$$\gamma_{S,LO} \text{ or } \gamma_{S,LM} = \frac{1}{3\sqrt{2}}\sqrt{W\kappa_\phi} + \gamma_{S,Lk}{}^{\nabla x_M} \quad \textbf{(4.9)}$$

with *k* = O or *M*, when the oxide or the metal liquid phase is involved, respectively. The first term in (4.9) originates from the double-well function and the gradient term for ϕ (see equation (4.2)) following the approach of Allen and Cahn [13]. The second term originates from the fact that x_M also varies between the two equilibrium values across the solid-liquid interface. This yields a non-zero gradient term for x_M. Because this contribution cannot be evaluated analytically, the following assumption was made: the composition dependence of the Gibbs energy across the interface is approximated by a spinodal function:

$$f_{approx}(x_M) = \frac{0.5\left(A_{sp} + A_s\right)}{2}(x_M - x_S)^2\left(x_M - x_{eq,k}\right)^2 \quad \textbf{(4.10)}$$

giving,

$$\gamma_{S,Lk}{}^{\nabla x_M} \approx \frac{1}{6}\sqrt{\kappa_{x_M} 0.5\left(A_{sp}+A_s\right)}\left(\left|x_S - x_{eq,Lk}\right|\right)^3 \quad \textbf{(4.11)}$$

This gives a dependence of the second term in the solid-liquid interfacial energy on x_S, the constant composition of the solid particle. This approximation was validated by measurement of the contact angles in several simulations, and the observed values agreed well with the predicted values. The width of the solid-liquid diffuse interface profiles $l_{S,LO}$ and $l_{S,LM}$ (m) is defined based on the absolute value of the steepest gradient of the phase field profile along the interface.

$$l_{S,LO} = l_{S,LO} = \left|\frac{1}{\left.\frac{d\phi}{dn}\right|_{\phi=0.5}}\right| = 2\sqrt{2}\sqrt{\frac{\kappa_\phi}{W}} \quad \textbf{(4.12)}$$

In contrast to the solid-liquid interfacial energies, $l_{S,LO}$ equals $l_{S,LM}$ because the phase field variable ϕ changes the same way over a solid – liquid oxide interface as over a solid – liquid metal.

The interfacial thickness in real materials ranges from a few Ångstrom to a few nanometre. It was pointed out by Fan and Chen [14] that the interface should contain enough grid points to resolve the evolution of the phase field variables at boundaries, so that the velocity of the boundaries is reproduced properly. Thus, there must be at least 5–10 grid points within the interfacial regions to maintain numerical stability and only very small systems are feasible when using a uniform grid spacing. In this model, the interfacial width is considered as a numerical parameter that can be modified for numerical reasons without affecting other system properties, such as interfacial energy, diffusion behaviour or bulk thermodynamic properties ('thin interface' model). [8] It follows from equation (4.8) that multiplication of A_{Sp} and κ_{xM} with a same factor will not affect the liquid – liquid interfacial width. Due to equation (4.7), however, multiplying A_{Sp} and κ_{xM} with a same factor will adjust the liquid - liquid interfacial energy. A similar line of reasoning can be made for the solid-liquid interfaces with the parameters W and κ_ϕ.

Microstructural evolution is driven by the minimization of the total Gibbs energy. The temporal and spatial evolution of the conserved field x_M is governed by the following mass balance equation

$$\frac{\partial x_M}{\partial t} = \nabla \cdot \left[M \nabla\left[\left(1-h(\phi)\right) f'_{Liquid}(x_M) + h(\phi) f'_{Solid}(x_M) - \kappa_{x_M}\nabla^2 x_M\right]\right] \quad \textbf{(4.13)}$$

The coefficient M (m^5/ (J s)) relates to the interdiffusion coefficient D[13], as defined in Fick's law, $J_M = -D\nabla x_M$, of the liquid as

$$D = A_{Sp} M \quad \textbf{(4.14)}$$

For every 100th time step, a random noise term from a normal distribution with mean 0 and standard deviation 0.001, was added to initiate spinodal decomposition. The evolution of the non-conserved phase field variable ϕ is governed by the following equation [13]

$$\frac{\partial \phi}{\partial t} = -L\frac{\delta F}{\delta \phi} = -L\left[W g'(\phi) + h'(\phi)\left(f_{Solid} - f_{Liquid}\right) - \kappa_\phi \nabla^2 \phi\right] \quad \textbf{(4.15)}$$

L is the kinetic coefficient related to the velocity at which atoms can hop over an interface.

The values of the parameters in the evolution equations were linked with physical system properties, such as diffusion coefficients, interfacial energies and initial supersaturation of the slag. However, as

[13] Note that this means that a volume- or number-fixed frame of reference was used.

this study investigates a model system, the values of the properties are chosen as typical orders of magnitudes. Nonetheless, some compromises have been made to obtain higher calculation speed, while retaining numerical stability.

4.3. Numerical implementation

All data processing was performed using a commercial software package (MATLAB 7.12 (R2011a), The MathWorks Inc., Natick, MA, 2013) [1]. The kinetic equations are solved numerically with the semi-implicit Fourier spectral method [15] The benefits of this method are its implicit treatment of the Laplacian, hereby eliminating the need of solving a large system of coupled equations, and a better numerical stability, allowing larger time steps compared to the completely explicit treatment. Limitations of the method are the inherent periodic boundary conditions and the fact that the values of the gradient energy parameters and kinetic parameters have to be constant.
In practice, a Fast Fourier Transform (FFT) algorithm was used in the implementation, as this has an efficiency of the order of $N \log_2 N$ (with N the system size) instead of an order of N^2 which is associated with a normal Discrete FT. This better efficiency is grace to the recursively breaking down of the Fourier Transforms using the periodicity and symmetry characteristic in the sine and cosine functions. This has the wonderful advantage of a very fast transformation.
An alternative solution method was also implemented, for this a finite difference method with a five-point stencil was used. Because at first, the finite difference results were intended to be compared to the results obtained with the semi-implicit Fourier spectral method, periodic boundaries were implemented with the use of sparse matrices. However, no real simulation were performed with this implementation, because numerical stability restrictions for finite difference implementations are far stricter ($\Delta t/(\Delta x)^2 < 1/4$) and thus the time step must be much smaller. In this case the time step should be taken 10^{10} times smaller for numerical stability and thus the simulations with these parameters would not consider the same phenomena as the simulations with the semi-implicit Fourier spectral method.
Typical computation times on an Intel® Core™ i7-3610QM CPU @ 2.30GHz processor with 8Gb RAM ranged from 2h to 4h for a system size of [256 256 1] and a simulation time of 10^6 time steps and from 10h to 13h for a system size of [512 512 1] and a simulation time of 10^6 time steps.

4.4. Post-processing

The results of a simulation are stored in arrays with the same size as the system and the values within these arrays lie between 0 and 1, representing x_M on the one hand and ϕ on the other hand. These arrays are stored at several time-steps throughout the simulations, to be able to investigate the evolution of the composition and phase field. To quantify the results, the total metal fraction, the area of metallic phase attached to a particle and the fraction of metallic phase attached to the particle were determined from the simulated microstructures as a function of time.

The total metal fraction is defined as the ratio between the total area of all droplets divided by the total area of supersaturated liquid:

$$f_{metal} = \frac{A_{metal}}{A_{matrix,t=0}} = \frac{A_{metal}}{A_{system} - A_{particle,t=0}} \quad \textbf{(4.16)}$$

Thus, the area occupied by the particle at time step zero is subtracted from the total system size for the denominator (equation (4.16)). A metal droplet is defined as the connected domain for which $0.71 < x_M - \phi \cdot x_S$ holds. This value of 0.71 was not chosen arbitrarily, but after verification of the model

in the equilibrium system (at $50 \cdot 10^6$ time steps) without a particle for several initial supersaturations. This threshold provided values of metallic fractions which differed minimally (the difference between the actual and predicted fraction was 0.0007 for $x_i = 0.61$, 0.0001 for $x_i = 0.63$ and 0.0007 for $x_i = 0.65$) with the prediction by the lever rule[14], which also accounted for the Gibbs-Thomson effect.

The predicted metal fraction was calculated with the lever rule considering equilibrium values of the phases for which the influence of interfaces on equilibrium (i.e. the interface curvature) was taken into account. This influence of the interface curvature is called the Gibbs-Thomson effect and was evaluated with a molar volume of 10^{-5} m³/mol [17] at 1500 K [18]. The Gibbs–Thomson effect modifies the solubility limits given by equilibrium thermodynamics (phase diagram) [19] because the curved interface raises the free energy of the precipitate phase relative to the free energy of a planar interface with an amount of $\Delta G_\gamma = 2\gamma V_m / r$. Where γ is the interfacial energy between the matrix phase α and the spherical β precipitates, with radius r and molar volume V_m. [17] The influence of this Gibbs-Thomson effect on the solubility limits is illustrated in Figure 4.2.

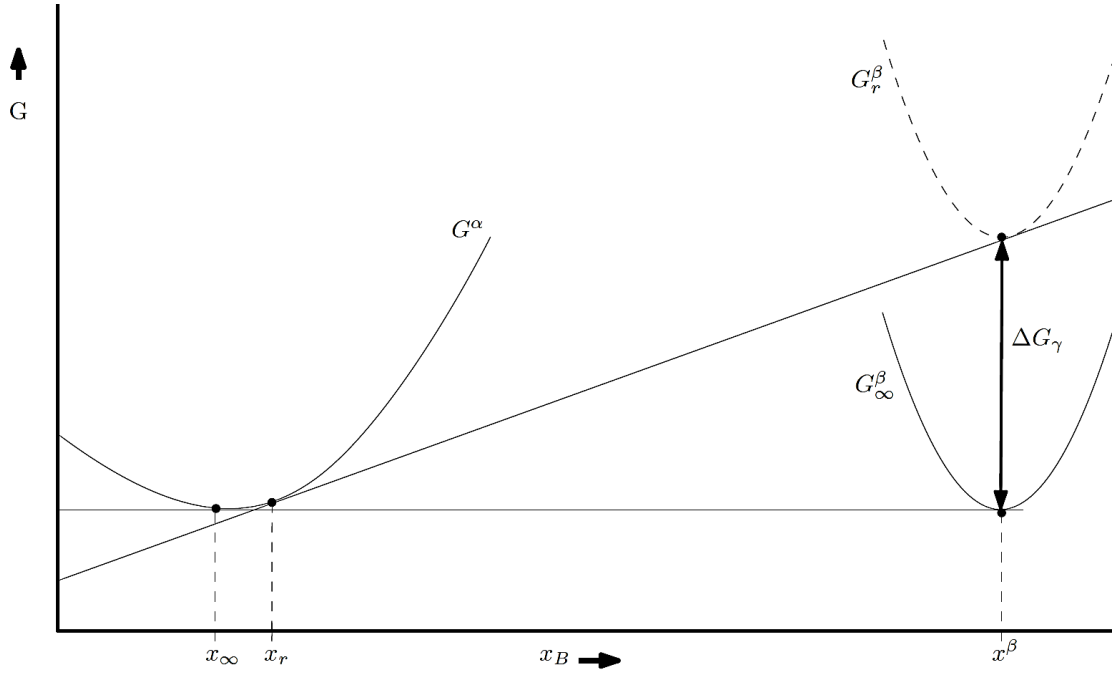

Figure 4.2 The effect of interface curvature on the free energy and thus on the solubility

The corrected solubility limit of B atoms in the α matrix becomes [19]

$$x_r = x_\infty exp\left(\frac{2\gamma V_m}{rRT}\right) \tag{4.17}$$

This correction, however, does not apply to a compound β phase (e.g. A_XB_Y), as does the following equation

$$\frac{2\gamma V_m}{rRT} = (1 - x_p)\ln\left(\frac{1 - x_r}{1 - x_\infty}\right) + x_p \ln\left(\frac{x_r}{x_\infty}\right) \tag{4.18}$$

[14] The relative amounts (as fraction or as percentage) of the phases present at equilibrium can be computed from a phase diagram with the lever rule. First, the tie line is constructed across the two-phase region at the temperature of the alloy, then the overall alloy composition is located on the tie line. The fraction of one phase is computed by taking the length of the tie line from the overall alloy composition to the phase boundary for the other phase, and dividing this by the total tie line length. [16]

Where x_p represents the mole fraction of B in the β phase and equals $y/(x+y)$. This equation simplifies to (4.17) whenever the mole fraction of the B atoms is 1. [19] Note that the Gibbs-Thomson effect with the used parameters (molar volume of 10^{-5} m³/mol [17] at 1500 K [18]) has only a limited influence on the equilibrium composition of the non-curved phase.

To investigate the attachment of the droplets to the solid particle, the droplet (defined as $0.71 < x_M - \phi \cdot x_S$) was enlarged with 2 grid point layers around the droplet and the particle (defined as $0.5 < \phi$) with 3 grid point layers. When these extended domains overlap, the droplets are considered to be 'attached'.

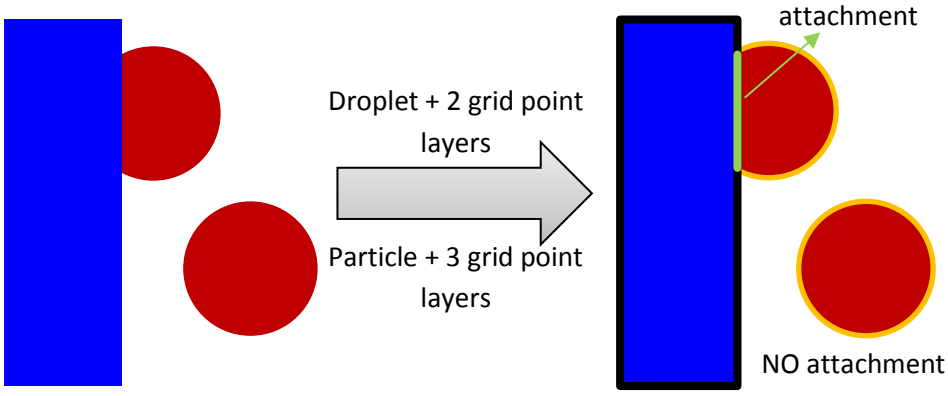

Figure 4.3 Illustration of the way to determine the attachment of a metallic droplet (red) to a solid particle (blue). The black (or orange) edge around the particle (or droplet) represents the 3 (or 2) extra grid point layers. When these extra layers overlap, the droplet is considered as 'attached', which is shown as the green area.

The total area of the attached droplets is determined as the number of grid points located within attached droplets and multiplied by Δx^2. The fraction of attached metal is defined as the ratio of the total area of the attached droplets to the total area of metal droplets in the system (equation (4.19)).

$$f_{attached\ metal} = \frac{A_{attached\ metal}}{A_{metal\ total}} \tag{4.19}$$

To illustrate the results, colour plots were made of $x_M - \phi \cdot x_S$. This is done to make the particle more visible (blue on the right-hand side of Figure 4.4), as just plotting x_S could make it hard in certain situations to distinguish the solid particle from the supersaturated liquid oxide. In these plots, the metal droplets are represented by a red colour and the slag phase by a green colour.

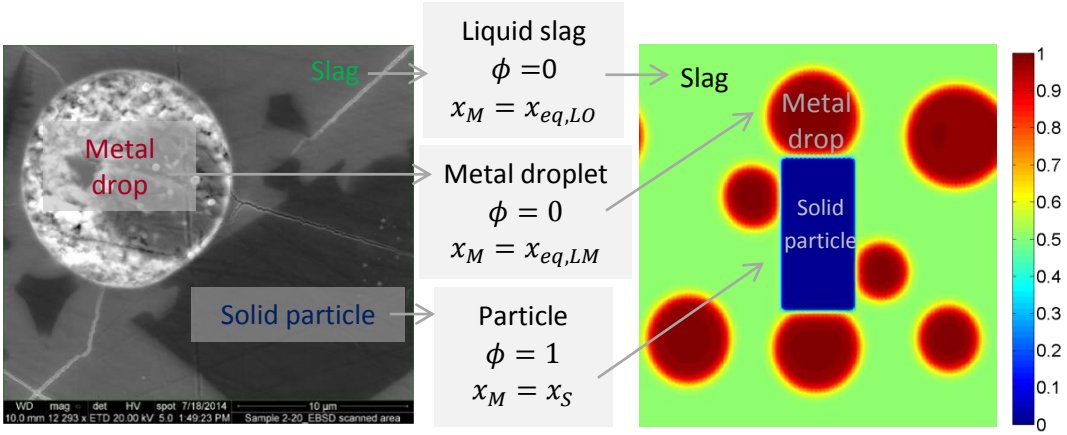

Figure 4.4 Illustration of value of field variables in the simulations (on the right) to correspond to the experimental situation (left)

Moreover, contour plots of $x_M - \phi x_S = 0.71$ were obtained at different times during the simulations, to illustrate the evolution of the microstructure. Contact angles (in °) and contact lengths (in pixels) were measured on contour plots at the final time step with a software program (ImageJ 1.47v, Rasband WS. ImageJ, U.S. National Institutes of Health, Bethesda, Maryland, USA) .

4.5. Accuracy and tolerance

To evaluate the validity of the expressions of the interfacial energies, the Gibbs-Thomson effect was also investigated. Several systems of size [256 256 1] with a solid sphere in a liquid matrix were used for this purpose. The solid sphere had different x_S-values in the different systems and the liquid matrix possessed one of the two equilibrium compositions. The kinetic coefficient was changed into $L = 0.5 \cdot 10^{-8}$ m³/(Js), to obtain a spherical solid particle. The equilibrium composition according to Gibbs-Thomson and the values obtained by the simulations are summarized in Table 4.1.

	x_S	Equilibrium composition (with Gibbs-Thomson effect)	Equilibrium composition (from simulation)	Difference
Solid – Liquid O	0.4	0.4998	0.4956	0.0042
	0.5	0.5002	0.5005	0.0003
	0.6	0.5002	0.5047	0.0046
	0.7	0.5002	0.5081	0.0079
	0.8	0.5002	0.5096	0.0094
	0.9	0.5003	0.5076	0.0073
Solid – Liquid M	x_S	Equilibrium composition (with Gibbs-Thomson effect)	Equilibrium composition (from simulation)	Difference
	0.4	0.9786	0.9772	0.0015
	0.5	0.9791	0.9770	0.0021
	0.6	0.9794	0.9712	0.0082
	0.7	0.9796	0.9705	0.0090
	0.8	0.9796	0.9728	0.0069
	0.9	0.9796	0.9768	0.0028

Table 4.1 The equilibrium composition according to Gibbs-Thomson and the values obtained by the simulations for several x_S-values

The presented model is employed for the study of growth of metal droplets in the presence of a non-reactive solid particle. Several simulations ($x_i = 0.63$; $x_S = 0.50$; 0.60; 0.70; 0.80 in a system with size [256 256 1]) were performed four times to investigate the spread on the results. The average and standard deviation of the results at the last time step can be found in Table 4.2.

	$x_S = 0.50$	$x_S = 0.60$	$x_S = 0.70$	$x_S = 0.80$
Fraction metallic phase in the system	0.264 ± 0.001	0.263 ± 0.0003	0.261 ± 0.0002	0.268 ± 0.0003
Area of metal attached to solid	$5.13\ 10^{-11}$ $\pm\ 6.53\ 10^{-11}$	$1.19\ 10^{-10}$ $\pm\ 1.07\ 10^{-11}$	$7.55\ 10^{-11}$ $\pm\ 6.82\ 10^{-12}$	$2.33\ 10^{-10}$ $\pm\ 3.95\ 10^{-12}$
Fraction of metal attached to solid	0.202 ± 0.257	0.466 ± 0.042	0.298 ± 0.027	0.898 ± 0.014

Table 4.2 Average values and standard deviations of the results at the last time step of 4 simulations for each x_S-value for x_i=0.63

Standard deviations for the fraction metallic phase were generally three orders of magnitude smaller than the average value and those of the area and fraction attached metal are both at least one order of magnitude smaller than the average value. It is clear that the amount of attached metal varies a

lot in the case of x_S =0.50. This is reflected in a standard deviation larger than the average value and is in contrast with the expectation that the metal does not attach itself to the solid for this x_S-value. The latter is indeed the case for 3 out of the 4 simulations. An extension of the simulation time for the simulation with the attached droplets showed that the droplets detach from the particle again and indicates that the droplets were attached to the particle by coincidence. Despite the fact that this result is clearly related to a statistical spread in the obtained results and the arbitrary choice of the simulation time, it was decided to include it with the other obtained simulation results. The particle probably hindered the droplets in their growth and therefore the droplets gave the impression to be attached.

The graphs in the results section display error bars corresponding to the abovementioned standard deviations. This value is only significant when wetting occurs. Thus, if wetting occurs, the maximum value of the standard deviation for every wetting regime was plotted.

Furthermore, at the considered time, the amount of attached metal for x_i = 0.63 and x_S = 0.70 is lower than that for x_i = 0.63 and x_S = 0.60. For x_S = 0.60, the droplets are not attached to the particle from the start, but are attracted towards the particle. However, the amount of attached metal levels off once several droplets are attached to the particle. In contrast, for the case of x_S = 0.70, the droplets grow directly on the sides of the particle and steadily grow, yielding a continuous increase in attached metal. After extension of the simulation time, the correct sequence (more attached metal for x_S = 0.70) was found. These observations indicate some statistical spread in the simulations and demonstrate the arbitrary nature of the simulation time chosen as 10^6.

The interface widths were measured as the length over which the parameter changed from the one equilibrium value to the other using a close-up of the interface. The width of the solid-liquid interface was approximately 8 grid points, which corresponds well with the predicted value. However, the liquid-liquid interface width was approximately 20 grid points, which is much larger than predicted. This could find its origin in the fact that x_M varies between the two equilibrium values across the solid-liquid interface. This variation is taken into account in the solid-liquid interfacial energy expression (equation (4.11)), but not in the expression for the interfacial width.

4.6. Extra information on phenomena playing a role

4.6.1. Spinodal decomposition

Whenever a miscibility gap is present in a phase diagram (denoted by the binodal), such as in Figure 4.5 (a), any homogeneous solution that is cooled into this gap will tend to decompose into A-rich and B-rich regions with a net reduction of the free energy. Two mechanisms are possible to form the two equilibrium phases starting from an initial solution within the miscibility gap: the classical nucleation and growth or spinodal decomposition. The former is, according to Gibbs, large in degree but small in extent and the latter is infinitesimal in degree but large in extent. E.g. for nucleation and growth, large compositional fluctuations are required before phase separation can take place at a limited number of positions. I.e. nucleation and growth require a certain nucleus to achieve the composition corresponding to the equilibrium composition of the precipitated phase. This nucleus should be larger than a certain critical size and thus, this only takes place at a small number of places. Whereas, in spinodal decomposition, a small composition fluctuation spreads over a large volume and the phase is unstable to this fluctuation, thus, there is no barrier (other than a diffusional one) for a continuous transformation to a more stable phase. [7]

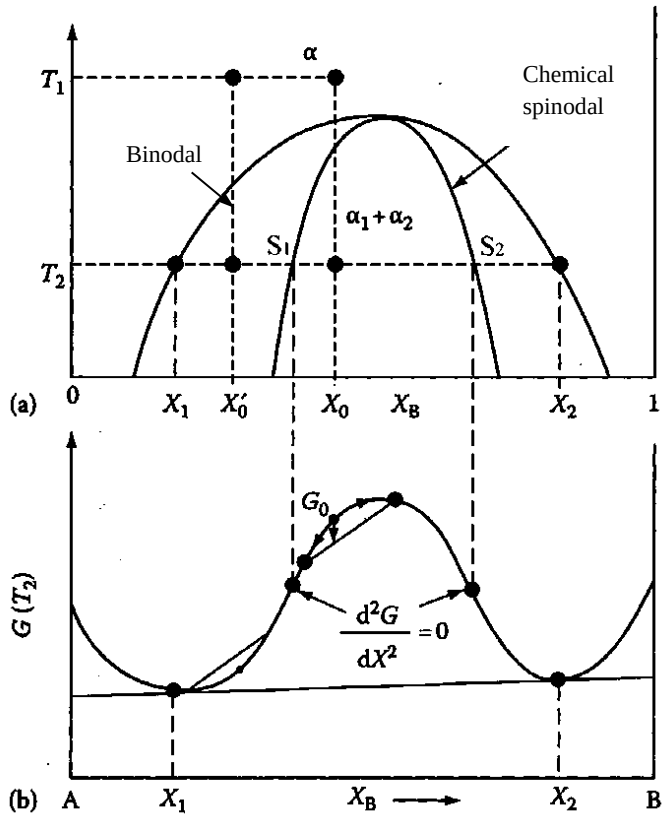

Figure 4.5 (a) A phase diagram with a miscibility gap and the chemical spinodal curve with (b) the corresponding free energy curve as a function of composition at temperature T_2 (adapted from [17])

When spinodal decomposition takes place, the compositional fluctuations are small in amplitude at first but then grow with time to form identifiable precipitates of equilibrium composition, as illustrated in Figure 4.6. In nucleation and growth, on the other hand, a sharp interface instantly appears between the parent and product phases. Moreover, the precipitate reaches the equilibrium composition immediately and this remains the case for all stages of its existence.

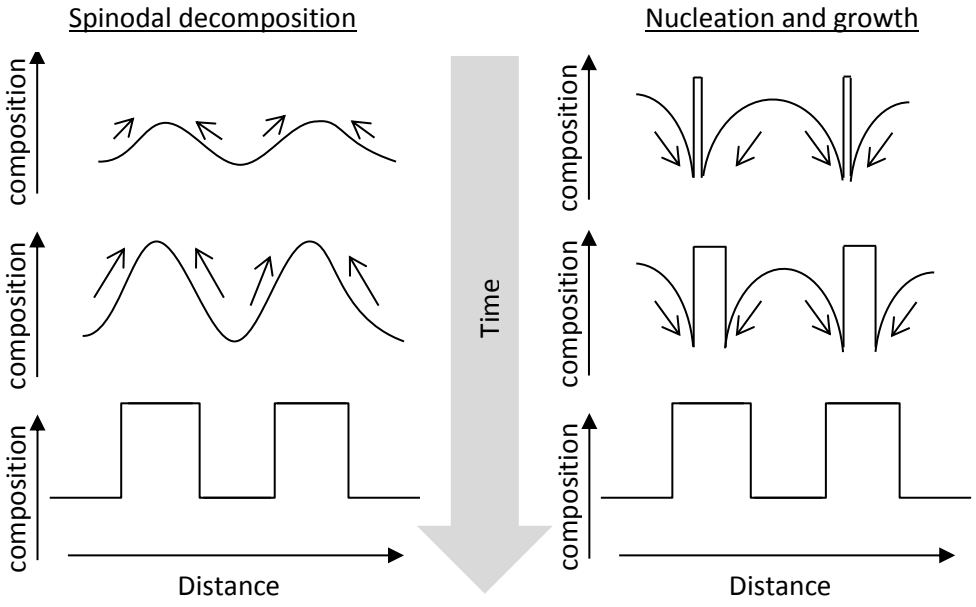

Figure 4.6 Evolution of the phase separation in spinodal decomposition and in nucleation and growth. The black arrows indicate the diffusional direction

Gibbs found that a necessary condition for a phase to be stable to such a fluctuation is that the chemical potential of each component should increase with increasing density of that component. E.g. for a binary system: $\partial^2 G/\partial x_B^2 > 0$. Thus spinodal decomposition can occur when the Gibbs energy has a convex part (where $\partial^2 G(x_B)/\partial x_B^2 < 0$, as shown in Figure 4.5 (b)). [7] Thus spinodal decomposition involves uphill diffusion whereas nucleation and growth occurs with diffusion down the concentration gradient. The rate of spinodal decomposition is controlled by the interdiffusion coefficient, which is negative when $\partial^2 G(x_B)/\partial x_B^2 < 0$.

The equilibrium phase compositions are those corresponding to the free energy minima. Regions of negative curvature ($\partial^2 G(x_B)/\partial x_B^2 <0$) lie within the inflection points of the curve ($\partial^2 G(x_B)/\partial x_B^2 = 0$) which are called the spinodes (marked as S_1 and S_2). For a composition within the spinodal regions, local demixing, caused by an infinitesimal compositional perturbation, results in a lower energy. Phase separation occurs uniformly. This is in contrast with growth from discrete nucleation sites usually observed for phase transitions and demixing at compositions outside the spinodal region, but within the miscibility gap in Figure 4.5. At the beginning of spinodal decomposition, the microstructures are very fine, but in time, the microstructures coarsen through diffusion to reduce the amount of interface. [17]

These two mechanisms are compatible and the mechanism of nucleation approaches the mechanism of spinodal decomposition continuously as the spinodal is approached. There is no nucleation barrier when the solution is unstable to infinitesimal fluctuations, but that does not mean that decomposition will proceed by a spinodal mechanism. Within the unstable part of the phase diagram, sufficiently near the limit of metastability such a mechanism will be slower than a nucleation and growth mechanism whose rate need not vanish at the limit. [7]

Initially, some controversy was present about the absence of surface tension in the theories of spinodal decomposition, but within the spinodal the solution is not unstable to fluctuations which form small droplets, but unstable to long range fluctuations, which are sufficiently large in extent that the surface tension contributions are always smaller than the volume energy contributions. To distinguish both mechanisms experimentally, it is best to bear in mind that spinodal decomposition should possess the following properties: it should occur everywhere within a sample, except that near a structural imperfection the rate or mechanism may be different. [7]

4.6.2. Ostwald ripening

This phenomenon is a direct consequence of the Gibbs-Thomson effect and appears in systems with a second phase with several sizes situated within a matrix. The larger particles or droplets will grow and the smaller ones will disappear in time, as illustrated in Figure 4.7. This takes place due to the fact that the chemical potential of the matrix is influenced by the radius of the second phase droplets or particles. Thus two droplets or particles with different radii will result in a difference in the chemical potential of the matrix phase surrounding these droplets or particles. Moreover, because the Gibbs free energy depends inversely on the radius, the smaller particles have a larger energy and also give rise to an apparent higher solubility. Thus, the smaller particles dissolve into the matrix with a higher solubility and this dissolved solute is then redeposited onto larger particles or droplets, because the solubility in the matrix surrounding these larger particles or droplets is smaller.

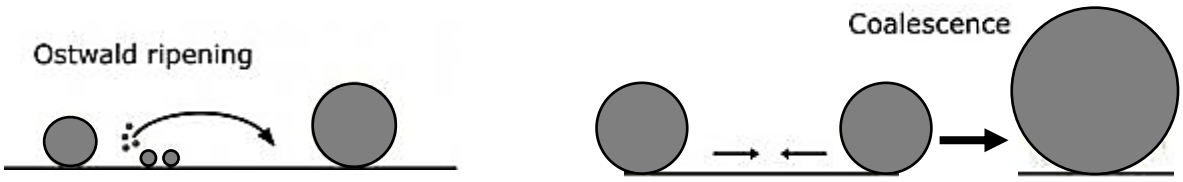

Figure 4.7 Illustration of Ostwald ripening (left) and coalescence (right)

Aside from Ostwald ripening, particles and droplets can also grow due to coalescence (shown on the right hand side of Figure 4.7). Coalescence is the merging of two particles or droplets, which lowers the interface area and thus the energy of the system.

4.6.3. Interfacial energies

4.6.3.1. Interfacial energy vs. stress

Interfacial energy expresses itself in such a way that the surface of a liquid surrounded by a vapour phase behaves like a membrane under tension. The terms surface energy and surface stress are usually used interchangeably. These two values, however, do not always represent the same quantity. Therefore, the thermodynamic and mechanical definitions of both quantities, respectively, are given and some of the most used expressions for these quantities will be given as well. [20,21] The surface energy γ_{ij} in J/m² is the excess energy of molecules at interfaces with respect to the bulk cohesive energy or the energy cost to create more free surface, owing to the disruption of the intermolecular forces of attraction in a condensed phase when a surface is created from the bulk. [22] The surface stress Γ_{ij} in N/m is the mechanical work required to create an additional surface area divided by this area. It is also the force per unit length acting along an interface aiming to shrink the interfacial area. [20,21]

For situations where the liquid is the condensed phase, i.e. liquid-gas or liquid-liquid interfaces without any surfactants, both quantities are equal and are unified into a single name as the surface tension. In a solid, however, the surface energy depends on the strain in the bulk and gives an extra elastic contribution to the surface stress. This is shown in the Shuttleworth equation: [20,21]

$$\Gamma_{ij} = \gamma_{ij} + \frac{\partial \gamma_{ij}}{\partial \varepsilon} \tag{4.20}$$

Where ε is the bulk strain parallel to the interface. Thus, if there is no strain in the bulk, the interface stress and the interface energy are equal. [21]

Note that the Laplace pressure (used to obtain equations (4.17) and (4.18)) on a curved interface is actually proportional to surface stress and not surface free energy. It is the pressure increase upon crossing an interface with a mean curvature κ between two fluids with an interfacial stress Γ:

$$\Delta p_L = 2\kappa\Gamma \tag{4.21}$$

Wetting ability or wettability between a liquid phase in contact with a solid surface is the ability of bonding or adherence between both phases at the point of interfacial contact. The degree of contact between the liquid and the solid surface is determined by the resultant of adhesive and cohesive forces which finds its primary cause in the intermolecular interactions between solid and liquid. In case of strong adherence or wetting, the liquid will spread over the surface of the solid, whereas the liquid drop balls up to avoid as much contact as possible in case of non-wetting. The degree of wetting contact is quantified through the contact angle formed at the S/L interface. The contact angle is

inversely related to the degree of wetting. Thus strong wettability implies a low contact angle (between 0° and 90°), whereas weak or low wettability will result in a contact angle larger than 90° (Figure 4.8). [23]

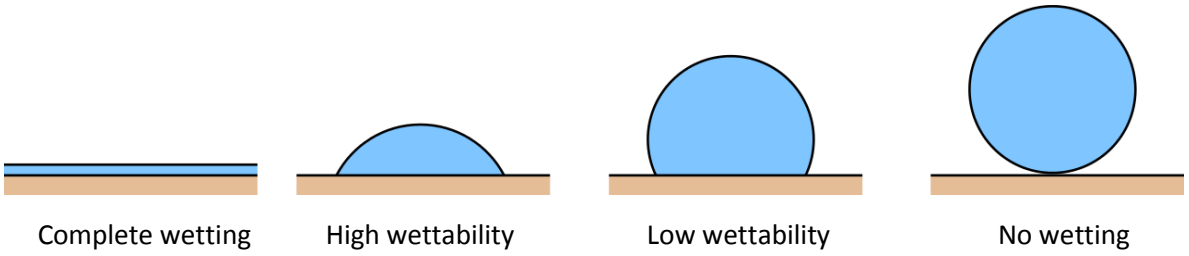

Figure 4.8 Illustration of different wettability regimes

Young's equation defines the equilibrium value of the contact angle for a flat, undeformable, perfectly smooth and chemically homogeneous solid surface in contact with a non-reactive liquid in the presence of a vapour phase. The usual equation was adapted for the system in this dissertation, i.e. a metal droplet (LM) on top of a solid (S) surrounded by a liquid oxide phase (LO):

$$\cos\theta = \frac{\gamma_{SLO} - \gamma_{SLM}}{\gamma_{LOLM}} \tag{4.22}$$

This equation only involves surface energies. The usual accompanying explanation, however, is based on a mechanical equilibrium of forces is shown on the left hand side of Figure 4.9 and is incomplete as there is no vertical or torque balance and thus, no complete mechanical equilibrium. Moreover, it is not clear which force is pulling on what, i.e. the subsystem is not clearly defined. The right hand side of the figure shows a liquid wedge as a subsystem which is in perfect mechanical equilibrium. The solid exerts a purely normal force on the liquid, which near the contact line has a strength $\Gamma sin\theta$. [20] Another possibility is defining a control volume, as shown in Figure 4.10.

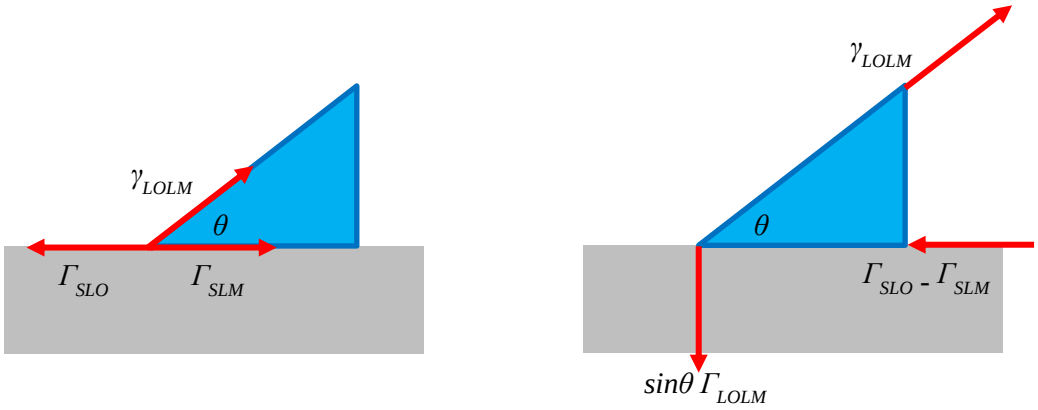

Figure 4.9 illustration of (in)correct use of force balances in a three-phase equilibrium

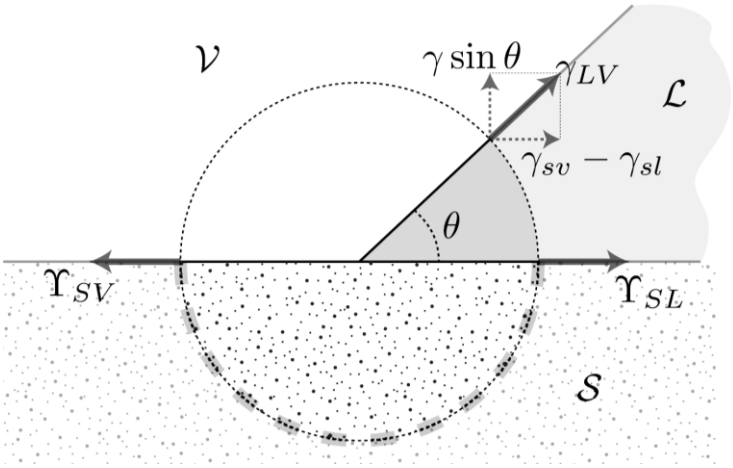

Figure 4.10 Stresses acting on a circular control volume situated around the contact line. Note that for solids generally $\gamma_{sx} \neq \Gamma_{sx}$ and thus there exists an imbalance of the interfacial stresses in both the normal and the tangential directions. This imbalance is counteracted by elastic stresses in the solid, along the thick grey dashed line. [20]

Note that the equilibrium contact angle in equation (4.22) does not involve the surface stresses of the solid, but the surface energies. This is not inconsistent with Figure 4.10 because Young's equation represents an equilibrium (i.e. minimal free energy from a thermodynamic perspective and a force balance from a mechanical perspective) inside the liquid alone and thus requires a different control volume that does not include the solid. As a consequence, the surface stresses in Figure 4.10 do not balance in the direction perpendicular to the solid. [20]

Young's equation illustrates that the contact angle results from the competition between two types of forces: cohesion and adhesion forces. Thus, depending on the relative values of the S/L and L/L interactions, different contact angles can be obtained, as listed in Table 4.3.

S/L interaction / L/L interaction	Weak	Strong
Weak	High wettability ($0° \leq \theta \leq 90°$)	Perfect wetting ($\theta = 0°$)
Strong	Low wettability ($90° \leq \theta \leq 180°$)	High wettability ($0° \leq \theta \leq 90°$)

Table 4.3 Different wettability regimes according to the strength of S/L and L/L interactions [24]

It is obvious that good wetting does not necessarily mean a thermodynamically strong interface, but rather that the interfacial bond is energetically nearly as strong as the cohesion bond of the liquid itself. [24] Thus the values of the interfacial energies relative to one another determine the wettability regime and not the absolute values of the interfacial energies on their own. The equilibrium contact angle is thus a unique characteristic for each particular combination of materials.

4.6.3.2. Non-reactive wetting

Pure metal/oxide interfacial energies are characterized by weak Van der Waals and electronic interactions and thus, the contact angle in these systems are typically larger than 90°. Ceramic/metal interfaces are expected to have higher energies than ceramic/gas or metal interfaces because of chemical and structural incompatibilities at the interface. In non-reactive systems, chemical reactions between the metal M and ceramic $M'O_n$ such as $M + M'O_n = MO_m + M' + 2(n-m)O_2$ do not occur to any significant extent. [25]

However, surface active species such as oxygen, sulphur or other elements of group VI, present at ppm levels in the bulk materials may have profound effects on the surface tension of the metal and its bonding to the ceramic. Because most metals will form oxides even at very low oxygen potentials. Oxygen dissolved in the metal adsorbs at the interfaces with liquid metal, leading to improved wetting with contact angles as low as 70°. At the surface of the liquid metal, the adsorption of oxygen (or other group VI elements) leads to the formation of clusters of stoichiometry M_pO. Aside from the metalloids such as oxygen, alloying additions are also dissolved in the metal. They do not lead to reactions with the ceramic or the metal with the concomitant formation of bulk phases (whether this occurs or not is clearly determined by the chemical potential of the solutes). Solutes that are most effective in decreasing the surface tension of the solvent typically exhibit surface tensions smaller than the solvent and larger atomic radii. Segregation of the alloying element at the liquid metal/ceramic interface will decrease the interfacial tension and, hence, the contact angle. [25]

The roughness of the ceramic increases the apparent contact angle and may lead to the formation of composite surfaces that are not fully penetrated by the metal, because Young's equation assumes a flat substrate. [25] The equation will still be valid locally on a rough or contaminated surface, however. The observed contact angle may depend on whether the liquid is advancing or receding on the surface, this phenomenon is called "contact angle hysteresis". A liquid typically advances on a previously dry surface and recedes on a previously wet surface. Thus, if by a chemical reaction or absorption, the solid substrate has been altered due to previous contact with the liquid, this can produce time-dependent contact angles.

The Young equation can be derived from the minimization of the free energy of the system when considering the displacement of the triple line parallel to the solid interface ((a) in Figure 4.11) and thus the contact angle obtained in this way corresponds to a metastable equilibrium configuration.

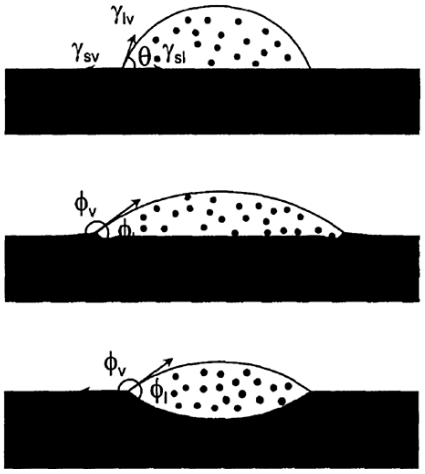

Figure 4.11 The geometry of a liquid drop on an isotropic solid depends on the contact time; (a) initially the solid is rigid allowing the 1D horizontal junction motion to give the metastable contact angle; (b) subsequently a small ridge will form that obeys the 2D junction equilibrium; (c) growth of the perturbation will eventually yield total equilibrium [26]

Whenever the solid deforms, the triple line also moves in other directions. Thus the full description would require three dihedral angles (θ_1 between the LO-LM interface and the S-LM interface; θ_2 between the LO-LM interface and the S-LO interface; θ_3 between the S-LO interface and the S-LM interface) which sum up to 360° and moreover are linked to the interfacial energies by Smith's relationship:

$$\frac{\gamma_{SLO}}{\sin\theta_1} = \frac{\gamma_{SLM}}{\sin\theta_2} = \frac{\gamma_{LOLM}}{\sin\theta_3} \quad \textbf{(4.23)}$$

This equation describes a configuration corresponding to local equilibrium. Saiz et al. [26] investigated the ridging effects when a substrate is not perfectly rigid and inert. The system was investigated at high experimental temperatures and thus, some local diffusion or solution-precipitation will probably be present and a small ridge will develop eventually at the triple junction. To obtain complete equilibrium (Figure 4.11(c)), the ridge propagates. When a ridge is present, distinction should be made between the macroscopically measured contact angle and the microscopic angle determined by equilibrium according to (4.23). A solid can be approximated as rigid and insoluble at low temperatures, because the vertical component of the surface tension can be resisted by very small elastic distortions of the solid.

The system can behave in three different ways: spreading, absorption or a combination of both. In a spreading reaction, a temperature increase causes the contact angle (CA) to decrease but the base diameter (BD) increases. In the absorption regime, the base diameter decreases and in the case of an ideal process, the contact angle remains practically constant. Both spreading and absorption are shown in Figure 4.12.

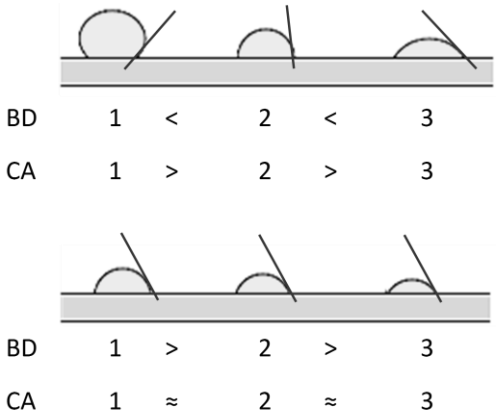

Figure 4.12 Schematic representation of spreading (at the top) and absorption (at the bottom) when the temperature increases from left to right

In conclusion, for a non-reactive and non-wetting pure metal on an oxide, improved wetting can be achieved either by adsorption at the metal/oxide interface of oxygen supplied by a gas with a controlled $_{pO2}$ or by introducing certain specific alloying elements modifying in situ the interface. [24] When the concentrations of one of the solutes, oxygen or metal, exceed the solubility limits, precipitation of new phases may occur in the liquid metal or at the metal/ceramic interface. Controlled precipitation of a selected compound at the metal/ceramic interface or surface modification of the ceramic to produce this phase upon contact with the liquid metal may improve wetting considerably if the liquid metal wets this phase. This is called reactive wetting. [25]

4.6.3.3. Reactive wetting

It is clear that in the case investigated here (alloys on spinel substrates), chemical interactions can be present. Thus, the system under consideration is in such a case dynamic and the time dependency of the contact angle measurement becomes very important. Chemical reactions lie at the base of reactive wetting and even spreading can occur after a certain period of time, because reactive wetting can have a large influence in the control of spreading wetting. [23]

For metal (M) on oxide (A_nO_m) systems at high temperatures, there is always some dissolution of the oxide in the liquid metal, but sometimes it is unclear to what extent this reactivity can affect the wettability. Reactive or not, the systems will initially present the dissolution of the oxide in the metal. The fraction of oxygen in the metal can then be regarded as the reactivity, because a mole fraction of dissolved oxygen larger than the solubility limit of oxygen in M results in the precipitation of M_pO_q oxides. Eustathopoulos and Drevet [24] plotted the contact angles of several metal/oxide systems as a function of this fraction of oxygen in the metal, called X_O, as illustrated in Figure 4.13.

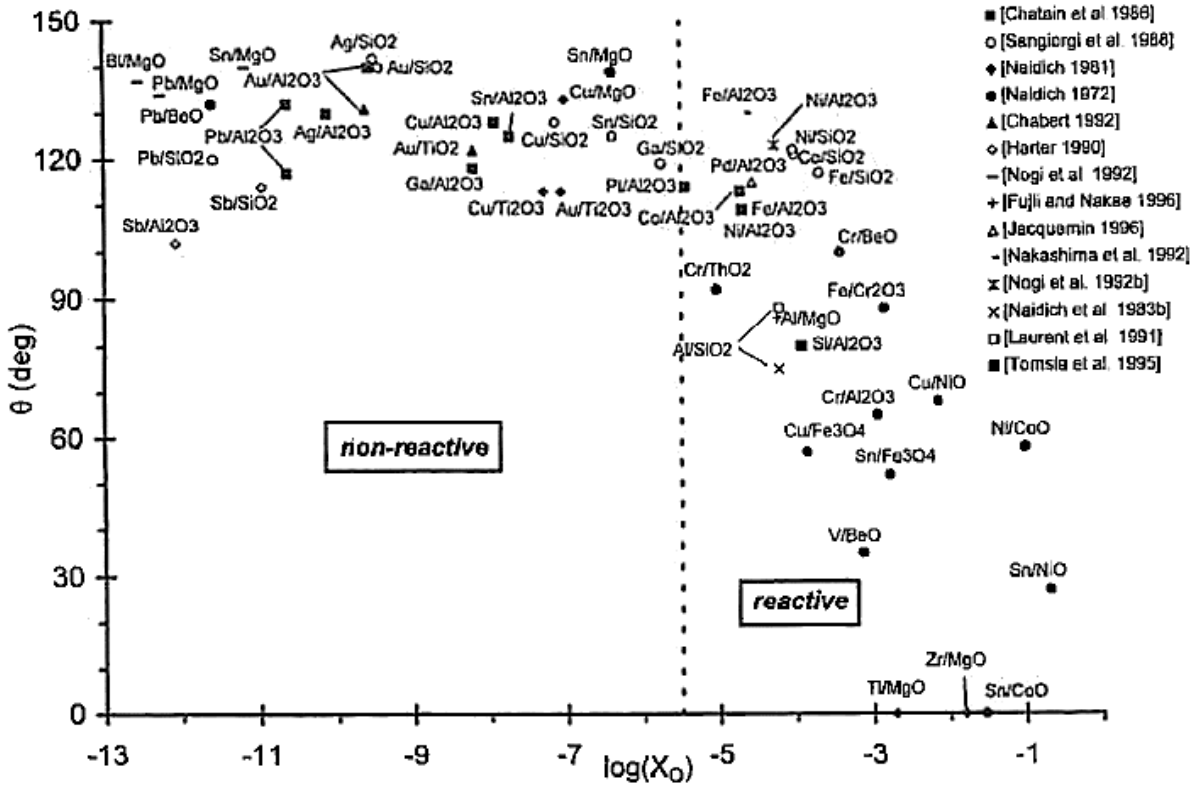

Figure 4.13 Experimental contact angles for pure liquid metal/oxide systems (taken form the references given in the Figure) versus calculated values of the molar fraction of oxygen in the liquid caused by dissolution of the oxide [24]

They then divided the pure metal/oxide systems into three categories. For the molar fraction of oxygen dissolved in the liquid metal coming from the oxide = $X_O < 10^{-6}$, all theta values (except that of Sb/Al_2O_3) lie between 110 and 140° and are considered to be non-reactive regarding wettability. Weak physical metal/oxide interactions are localized at a sharp interface and result in work of adhesion values smaller than the work of cohesion of the metal. The wetting in these systems is also frequently categorized as 'dissolutive wetting', as the solid dissolves into the liquid, which leads to an increase of the base diameter and a decrease of the apparent/ visible contact angle. Within this category, two subcategories can be distinguished with dissolution-insensitive interfacial tensions on the one hand (only a change in the position of the triple line is observed) and dissolution-sensitive interfacial tensions on the other hand (observation of dissolution of a tension-active species able to decrease significantly the interfacial tensions). [24]

The contact angle decreases steeply and tends towards zero as reactivity increases. This reactivity first consists of dissolution reactions, just as for the dissolutive wetting systems, and then of reactions to form new phases at the interface. For $X_O > 10^{-5}$, dissolved oxygen and metal atoms from the oxide can produce significant improvements in wetting by forming 2D adsorption layers (with a typical

thickness of 1nm) at the metal/oxide interface, but that do not react to form a new phase. These adsorption layers can lead to contact angles lower than 90° but usually above 60°. Even lower contact angles can be achieved by metals that react with the oxide forming 3D compounds at the interface which are, at least partially, metallic in their bonding characteristics. This will promote wetting if the 3D compound is more wettable than the initial substrate. [24]

They also concluded that the interfacial metal–oxide bond energy is mainly due to physical interactions, as they found a correlation between the work of adhesion of pure metals on alumina and the liquid metal–vapour surface energy ($W_a \cong 0.4\sigma_{LV}$). Any major deviation of W_a from this value due to physical interactions would result from the development of chemical interactions at an interface of increased thickness, due to a chemical modification of metal and oxide phases in the vicinity of the initial interface. Although these conclusions were drawn from results of metal–alumina couples, there is evidence that they also hold true for other metal–ionocovalent oxide systems. [24]

References

[1] Matlab 7.12.0 (R2011a), The MathWorks Inc., Natick, MA, 2011.

[2] L. Gránásy, T. Pusztai, D. Saylor, J.A. Warren, Phase Field Theory of Heterogeneous Crystal Nucleation, Phys. Rev. Lett. 98 (2007) 035703. doi:10.1103/PhysRevLett.98.035703.

[3] J.A. Warren, T. Pusztai, L. Környei, L. Gránásy, Phase field approach to heterogeneous crystal nucleation in alloys, Phys. Rev. B. 79 (2009) 014204. doi:10.1103/PhysRevB.79.014204.

[4] L.M. Pismen, Y. Pomeau, Disjoining potential and spreading of thin liquid layers in the diffuse-interface model coupled to hydrodynamics, Phys. Rev. E. 62 (2000) 2480–2492. doi:10.1103/PhysRevE.62.2480.

[5] A. Badillo, Quantitative phase-field modeling for wetting phenomena, Phys. Rev. E. 91 (2015) 033005. doi:10.1103/PhysRevE.91.033005.

[6] F. Wang, A. Choudhury, C. Strassacker, B. Nestler, Spinodal decomposition and droplets entrapment in monotectic solidification, J. Chem. Phys. 137 (2012) 034702. doi:10.1063/1.4734485.

[7] J.W. Cahn, On spinodal decomposition, Acta Metall. 9 (1961) 795–801. doi:10.1016/0001-6160(61)90182-1.

[8] N. Moelans, B. Blanpain, P. Wollants, An introduction to phase-field modeling of microstructure evolution, Calphad. 32 (2008) 268–294. doi:10.1016/j.calphad.2007.11.003.

[9] S.Y. Hu, J. Murray, H. Weiland, Z.K. Liu, L.Q. Chen, Thermodynamic description and growth kinetics of stoichiometric precipitates in the phase-field approach, Calphad. 31 (2007) 303–312. doi:10.1016/j.calphad.2006.08.005.

[10] J. Heulens, B. Blanpain, N. Moelans, A phase field model for isothermal crystallization of oxide melts, Acta Mater. 59 (2011) 2156–2165. doi:10.1016/j.actamat.2010.12.016.

[11] S.-L. Wang, R.F. Sekerka, A.A. Wheeler, B.T. Murray, S.R. Coriell, R.J. Braun, G.B. McFadden, Thermodynamically-consistent phase-field models for solidification, Phys. Nonlinear Phenom. 69 (1993) 189–200. doi:10.1016/0167-2789(93)90189-8.

[12] J.W. Cahn, J.E. Hilliard, Free Energy of a Nonuniform System. I. Interfacial Free Energy, J. Chem. Phys. 28 (1958) 258. doi:doi:10.1063/1.1744102.

[13] S.M. Allen, J.W. Cahn, A microscopic theory for antiphase boundary motion and its application to antiphase domain coarsening, Acta Metall. 27 (1979) 1085–1095. doi:10.1016/0001-6160(79)90196-2.

[14] D. Fan, L.-Q. Chen, Computer simulation of grain growth using a continuum field model, Acta Mater. 45 (1997) 611–622. doi:10.1016/S1359-6454(96)00200-5.

[15] L.-Q. Chen, J. Shen, Applications of semi-implicit Fourier-spectral method to phase field equations, Comput. Phys. Commun. (1998) 147–158. doi:10.1016/S0010-4655(97)00115-X.

[16] Wiley: Materials Science and Engineering, 9th Edition SI Version - William D. Callister, David G. Rethwisch, (n.d.). http://eu.wiley.com/WileyCDA/WileyTitle/productCd-1118319222.html?filter=TEXTBOOK (accessed July 31, 2015).
[17] D.A. Porter, K.E. Easterling, Phase transformations in metals and alloys, Van Nostrand Reinhold, 1981.
[18] J.P. Neumann, T. Zhong, Y.A. Chang, The Cu−O (Copper-Oxygen) system, Bull. Alloy Phase Diagr. 5 (1984) 136–140. doi:10.1007/BF02868948.
[19] M. Perez, Gibbs–Thomson effects in phase transformations, Scr. Mater. 52 (2005) 709–712. doi:10.1016/j.scriptamat.2004.12.026.
[20] J.H. Weijs, B. Andreotti, J.H. Snoeijer, Elasto-capillarity at the nanoscale: on the coupling between elasticity and surface energy in soft solids, ArXiv13036779 Cond-Mat. (2013). http://arxiv.org/abs/1303.6779 (accessed January 8, 2015).
[21] P. Müller, A. Saúl, Elastic effects on surface physics, Surf. Sci. Rep. 54 (2004) 157–258. doi:10.1016/j.surfrep.2004.05.001.
[22] P.-S. Yen, R. Datta, Butler–Sugimoto monomolecular bilayer interface model: The effect of oxygen on the surface tension of a liquid metal and its wetting of a ceramic, J. Colloid Interface Sci. 426 (2014) 314–323. doi:10.1016/j.jcis.2014.04.019.
[23] K. Verhiest, S. Mullens, J. Paul, I. De Graeve, N. De Wispelaere, S. Claessens, A. DeBremaecker, K. Verbeken, Experimental study on the contact angle formation of solidified iron–chromium droplets onto yttria ceramic substrates for the yttria/ferrous alloy system with variable chromium content, Ceram. Int. 40 (2014) 2187–2200. doi:10.1016/j.ceramint.2013.07.137.
[24] N. Eustathopoulos, M.G. Nicholas, B. Drevet, Wettability at High Temperatures, Elsevier, 1999.
[25] B.M. Gallois, Wetting in nonreactive liquid metal-oxide systems, JOM. 49 (1997) 48–51. doi:10.1007/BF02914715.
[26] E. Saiz, A.P. Tomsia, R.M. Cannon, Ridging effects on wetting and spreading of liquids on solids, Acta Mater. 46 (1998) 2349–2361. doi:10.1016/S1359-6454(98)80016-5.

5. Simulation set-up

The simulations with the binary two-phase model allowed evaluating several parameters on the attachment of metallic droplets to solid particles as a function of time. The results were published in three journal papers [1–3]. Which paper covered which influence is summarized in Table 5.1.

Publication	Investigated influence	Varied parameter
[1]	The solid-liquid interfacial energies	x_S
[1]	The initial slag composition	x_i
[2]	The particle fraction	System size with same particle size
[2]	The particle perimeter per area	Particle aspect ratio
[2]	The particle shape, size and distribution	Particle configuration at time step 0
[3]	The origin of the interaction	Initialization method

Table 5.1 List of investigated parameters in the publications in the following chapters

5.1. Constant parameters

The values of the parameters in the evolution equations are linked with physical system properties, such as diffusion coefficients and interfacial energies. In this study, a model system is considered. For most parameters, a typical order of magnitude was chosen, but some compromises were needed to limit the computation time, as explained below for each parameter. The model parameters are listed in Table 5.2.

Symbol	Description	Value(s)
N	System size	[256 256 1] grid points
Δx	Grid spacing	$(4/\sqrt{10})\cdot 10^{-7}$ m
Δt	Time steps spacing	10^{-4} s
$x_{eq,LO}$	Oxidic equilibrium composition of free energy curve of spinodal decomposition	0.50
$x_{eq,LM}$	Metallic equilibrium composition of free energy curve of spinodal decomposition	0.98
A_{Sp}	Curvature of free energy curve of spinodal decomposition	$4\cdot 10^8$ J/m³
A_S	Curvature of free energy curve of solid	$20\cdot 10^8$ J/m³
W	Depth of the double well function	$15\cdot 10^6$ J/m³
κ_ϕ	Gradient energy coefficient for the solid-liquid interfaces	$(15/8)\ 10^6$ J/m
L	Kinetic coefficient for the evolution of ϕ	10^{-30} m³/(J s)
$L_{initial}$	Kinetic coefficient for the evolution of ϕ for the first 1000 time steps	10^{-7} m³/(J s)
κ_{x_M}	Gradient energy coefficient for the liquid-liquid interfaces	$6\cdot 10^{-6}$ J/m
M	Mobility coefficient of the metal	10^{-19} m⁵/(J s)

Table 5.2 Values and descriptions of several constant parameters in the model

This work focusses on some of the possible affecting parameters. Therefore, the obtained results are primarily of theoretical importance. One of the differences with industrial practice is found in the fact that the industrial metal fractions are of the order of 5%, whereas in this study fractions ranged from 10 to 31%. Moreover, the interfacial energy is also affected by system parameters such as temperature and chemical composition, which were considered constant in this study.

Figure 5.1 displays the free energy curves of the liquid and solid phases. To avoid compositional changes in the solid phase during the initial stage of the simulation, the free energy curve of the solid was made five times steeper than the curve of the liquid phase.

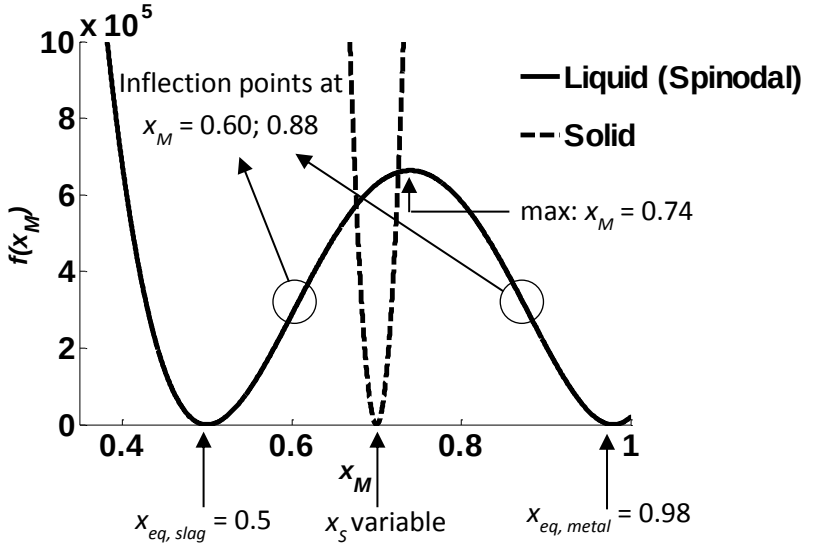

Figure 5.1 Free energy curves of the liquid (spinodal) and solid phases as a function of the mole fraction of metal M (here, for a solid phase with a fixed mole fraction of 0.70)

If the initial saturation of the solution was chosen between the inflection points of the liquid curve (where $\partial^2 G/\partial x_M^2 < 0$) [4], namely: *0.60 < x_i < 0.88*, the metal droplets will form through spinodal decomposition of the supersaturated slag, due to the added noise. Spinodal decomposition provides an easy way to initialize the metal droplet formation. Since it is not known whether the metal droplets in slags form through spinodal decomposition in reality, the physical interpretation of the simulations will be limited to the droplet growth. Moreover, the estimates for $\gamma_{S,LO}$ and $\gamma_{S,LM}$ only apply after decomposition of the liquid. The maximum of the curve lies at $x_M = 0.74$.

M is chosen in such a way that the diffusion coefficient $D = 4 \cdot 10^{-11}$ m²/s. According to literature [5,6], $\gamma_{LO,LM}$ is of the order of 1 N/m. Furthermore, the interfaces should at least contain five grid points for a sufficient resolution of the diffuse transition at interfaces and to reproduce accurately the surface energies [7]. With the values mentioned in Table 5.2, the liquid-liquid interfacial energy and the interfacial widths possess the following values for all simulations: $l_{LO,LM}$ = 8.0687 grid points, $\gamma_{LO,LM}$ = 0.9030 N/m and $l_{S,LO}$ = 7.9057 grid points for the interface between solid and liquid oxide and $l_{S,LM}$ = 7.9057 grid points for the interface between solid and liquid metal. It is assumed that the particle does not transform. Therefore, a very small value of the kinetic coefficient *L* is chosen. The variables have sharp steps at the interfaces in the beginning of a simulation. The particle is assumed to not react in these simulations, requiring a very small value of *L*, but a larger value of *L* is used during the first 1000 time steps, allowing the interface to become diffuse (Table 5.2).

Experimentally observed dimensions [8] of solid particles in slags are of the order of µm. In the simulations, the particle size of a single large rectangular particle is taken as 100 by 50 grid points, corresponding to 12.65 by 6.32 µm. For a system size of 256 by 256 grid points, corresponding to 32.38 by 32.38 µm, the particle volume fraction is thus 0.0763. In reality, large variations are found (from 2-6 wt% [9] to 25 wt% [8]) for the particle volume fraction. The conditions of the slag production are mainly responsible for this variation. These percentages, however, are averages over the complete slag phase and we are explicitly interested in regions with more solid particles. These

regions were therefore considered in more detail in this doctoral work and thus the simulations also deal with larger particle densities than the values averaged over the complete slag phase.

5.2. Variable parameters in this study

The reference system has a system size of [256 256 1] grid points (or [32.38 32.38 0.13] nm), with a slag with initial supersaturation of x_i = 0.63, unless stated otherwise. The reference simulation time is 10^6 time steps. As illustrated previously, x_S can be used as a parameter to adapt the interfacial energy. Thus, for a given $\gamma_{LO,LM}$, the contact angle (as defined by Young's equation: $\gamma_{S,LO} = \gamma_{S,LM} + \gamma_{LO,LM} \cos\theta$) is determined by the x_S-value.

The effects of the solid-liquid interfacial energies and initial slag composition were investigated, as well as the effect of the particle density, particle perimeter and particle shape. The particle characteristics were investigated in two regimes: low wettability (x_S = 0.60; $\gamma_{S,LO}$ = 1.2641; $\gamma_{S,LM}$ = 2.0260; $\gamma_{LO,LM}$ = 0.903; θ = 147.5°) and high wettability (x_S = 0.80; $\gamma_{S,LO}$ = 1.6318; $\gamma_{S,LM}$ = 1.3325 ; $\gamma_{LO,LM}$ = 0.903; θ = 70.6°). Moreover, two initialization methods were compared to acquire information on the origin of the interaction. During the latter comparison, real micrographs of the solid spinel particles were used to define the solid-liquid assignment of the system.

5.2.1. Influence of solid-liquid interfacial energy

Since it is assumed that the solid does not react and its composition is constant, x_S can be used as a parameter to adapt the interfacial energy. The composition of the solid particle remains constant during a single simulation and determines the value of the solid-liquid interfacial energies, as shown by equations (4.9) and (4.11). Thus, for a given $\gamma_{LO,LM}$, this x_S-value will determine the contact angle. The different interfacial energies determine whether or not wetting will occur, as described by Young's equation (5.1)

$$\gamma_{S,LO} = \gamma_{S,LM} + \gamma_{LO,LM} \cos\theta \qquad \textbf{(5.1)}$$

The effect of the x_S-value on the solid-liquid interfacial energies and the contact angle is demonstrated in Table 5.3. Non-wetting is expected for $x_S \leq 0.57$, a low wettability corresponding to 90°≤ θ ≤ 180° for x_S between 0.58 and 0.74, a high wettability corresponding to 0°≤ θ ≤ 90° for x_S between 0.74 and 0.90 and full wetting with a non-existing contact angle for x_S-values higher than 0.9.

x_S	$\gamma_{S,LO}$ (N/m)	$\gamma_{S,LM}$ (N/m)	$\gamma_{LO,LM}$ (N/m)	θ (°)
0.4	1.2641	4.0093	0.903	/
0.5	1.2500	2.8140	0.903	/
0.6	1.2641	2.0260	0.903	147.538
0.7	1.3631	1.5604	0.903	102.621
0.74	1.4455	1.4455	0.903	90.000
0.8	1.6318	1.3325	0.903	70.643
0.9	2.1551	1.2572	0.903	6.092
0.95	2.5387	1.2504	0.903	/

Table 5.3 Variation in x_S, the corresponding variation in the interfacial S-L energies and in the contact angle

5.2.2. Influence of initial supersaturation

Industrial metal fractions in slags after decantation are of the order of 5%. According to the lever rule, the minimal achievable value of the metal fraction in this model system is 0.211. Therefore, the x_i-values were kept minimal, but within the spinodal region. Furthermore, for $x_i > 0.66$, metal strands are formed instead of droplets in the model system. The following three x_i-values were therefore considered: 0.61; 0.63 and 0.65. According to the lever rule, the metal fractions are then 0.229, 0.271 and 0.312, respectively.

5.2.3. Influence of particle fraction

Observed dimensions [8] of solid particles in slags are of the order of µm. The particle size of a single large rectangular particle is [100 50] grid points, corresponding to [12.65 6.32] µm. By changing the system size, two particle densities were considered. In reality, large variations are found: from 2-6 wt% [9] to 25 wt% [8]. For a system size of [256 256 1], the particle volume fraction is 0.0763. The particle volume fraction corresponding to a system size of [512 512 1] is 0.0191.

5.2.4. Influence of particle perimeter per area

Several length/width ratios (summarized in Table 5.4) are used to investigate the influence of the perimeter per area, while the area of the particle remains constant and has a value of 2400 grid points, which corresponds to a particle volume fraction of 0.0366.

Length (grid points)	Width (grid points)	Area (*A*) (grid points ^{2})	Circumference (*P*) (grid points)
50	48	2400	192
60	40	2400	196
80	30	2400	216
160	15	2400	346

Table 5.4 Variation of the length/width ratio of a rectangular particle and the corresponding variation in perimeter while maintaining a constant area

5.2.5. Influence of particle shape, size and distribution

The shape, the orientation and the distance between the solids are also investigated, while maintaining an approximately constant area and thus volume fraction of solids. The different particle characteristics are given in Table 5.5.

Description	Orientation	Area (A) (grid points ^{2})	Circumference (P) (grid points)
1 large rectangle	Vertically	5000	296
4 small rectangles	- Far apart - Close together - 2 horizontal and 2 vertical, far apart - 2 horizontal and 2 vertical, close together	5000	584
1 large triangle	Point upwards	4900	276
4 small triangles	- Far apart - Close together	4900	544
1 large hexagon	2 sides horizontally	5001	208
4 small hexagons	- Far apart - Close together	4972	416
Experimentally relevant particle	Cavity with channel	5000	492

Table 5.5 Description of variations in particle characteristics (size and shape) and the corresponding variations in perimeter and area

5.2.6. Investigation of origin of interaction

The first simulations only considered particles with simplified geometries. These simple morphologies approximate the spinel structure, which was observed for the solid particles to which the droplets attach in experiments. However, it is possible that the particle shape and distribution affect the amount of attached metal. Therefore, in this work the microstructure of the solid particles considered in other simulations was constructed based on actual experimental micrographs of these solid particles. In order to do this, the micrographs in the left hand side of Figure 5.2 were used as input for the 'imread' command in Matlab, turning every pixel of the photograph into a greyscale value. The micrographs are named photo 1 – 4 starting in the upper left corner to the lower right corner.

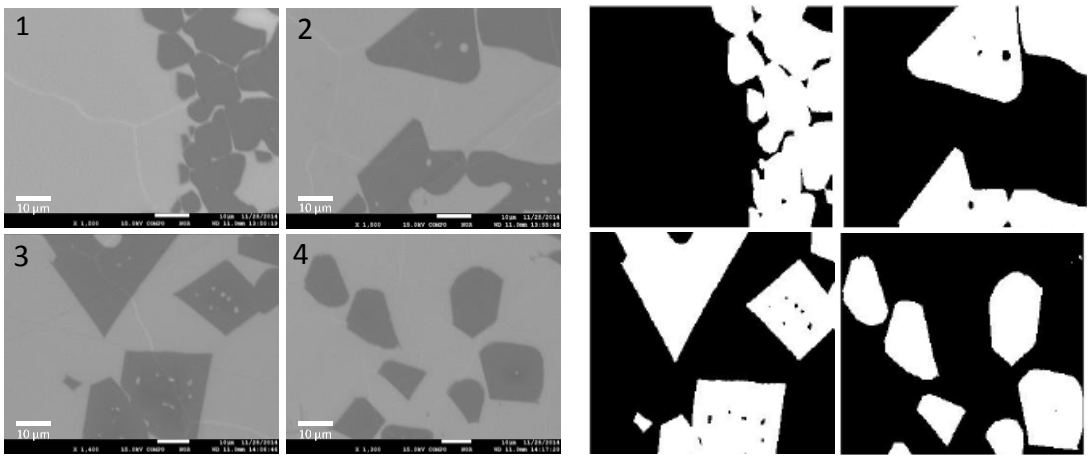

Figure 5.2 Left: SEM micrograph of experimentally obtained microstructure of solid oxide particles in a slag that was quenched to 'freeze' its high temperature condition [10]; Right: Black-and-white pictures that were used as initialization for the solid particles (white: $\phi = 1$) within a liquid phase (black: $\phi = 0$)

The edge with SEM information is then cut off, the pixels with a greyscale value above a certain threshold are treated as solid phase ($\phi = 1$) and the array containing these zeros and ones is then rescaled to the system size N in each dimension. The threshold value to which the greyscale values

are compared is obtained by trial-and-error and can depend on the type of micrographs and the settings used to obtain them. For these SEM micrographs, a threshold value of 140 gave good results. This yielded the black-and-white figures in the right-hand side of Figure 5.2, where white represents the solid ($\phi = 1$) and black the liquid ($\phi = 0$). The corresponding particle fractions (defined by the area of all particles divided by the total system size, which is 65536 grid points for all cases) are tabulated in Table 5.6.

Photo	A = X*Y [grid points]	Particle density
1	19964	0.305
2	23989	0.366
3	26868	0.410
4	18646	0.285

Table 5.6 The calculated particle fractions for every photograph

As stated previously, in reality, large variations are found: from 2-6 wt% [9] to 25 wt% [8] in the particle fraction. These values, however, are averages over the complete slag phase and we are explicitly interested in regions with more solid particles. These regions were therefore considered in more detail in the experimentally obtained micrographs in Figure 5.2 and thus the simulations also deal with larger particle densities than the values averaged over the complete slag phase.

The simulations discussed up till the previous section used spinodal decomposition as a convenient way to introduce the metallic droplets in the system. However, it is not known whether spinodal decomposition is the real mechanism of formation for the metal droplets in slags. The exact mechanism behind the interaction between the solid particles and liquid metal is not known. It is also not understood how and where the metal droplets originate. We compared two methods to initialize the metal droplets in the simulations: by spinodal decomposition of a supersaturated liquid (from now onward called 'spinodal initialization') and by a random positioning of droplets within the liquid phase (from now onward called 'random initialization'). The first would correspond in practice to a case where the droplets are formed by a reaction in which both the droplets and the spinel solids are involved. The latter corresponds to a situation where the droplets and particles are formed separately and independently and are then mixed in the slag. In both methods, the solid particles within the liquid slag are initialised by setting the value of ϕ equal to 1 and x_M equal to x_S within the areas corresponding to the solid particles in the original micrographs. The remaining liquid phase has a value of ϕ equal to 0.

The spinodal initialization provides an easy way to introduce the metals in the system. For decomposition into a liquid metal ($x_M = x_{eq,LM} = 0.98$) and a liquid oxide ($x_M = x_{eq,LO} = 0.50$), the uniform initial saturation of the solution x_i should be chosen between the inflection points of the spinodal liquid curve (where $\frac{\partial^2 G}{\partial x_M^2} < 0$) [4], namely: $0.601 < x_i < 0.879$. To initiate the spinodal decomposition, random noise is added, from a normal distribution with mean 0 and standard deviation 0.001, in every 100th time step. Industrial metal fractions in slags after sedimentation are of the order of 5%. According to the lever rule, the minimal achievable value of the metal fraction in this model system is 0.211. Therefore, the x_i-values were kept minimal, but within the spinodal region. Furthermore, for $x_i > 0.66$, metal strands are formed instead of droplets in the model system. Therefore, an x_i value of 0.605 was chosen for the simulations, which corresponds to a volume fraction of metal of 0.219.

The alternative initialization method with 'random initialization' consists of randomly positioning droplets with a radius chosen from a discrete uniform random distribution between 1 and 10 times

Δx in the system until the proposed volume fraction of metallic droplets is reached or slightly exceeded. Before the droplets are finally positioned within the system, it is checked that no overlap is present with the solid phase or other droplets already present in the system. Whenever this is the case, another position is looked for within the system. If no appropriate position is found after 20 trials, the initialization is aborted and the simulation is started with the droplets positioned in the system until then. The droplets are immediately initialized with their equilibrium composition of 0.98 ($x_{eq,LM}$) and the slag in between the droplets is initialised with a composition of 0.50 ($x_{eq,LO}$). The volume fraction of metal droplets was 0.20, corresponding to x_i-values of 0.596, which is close to the value of x_i used for spinodal decomposition, thus enabling us to compare both methods. The random noise term is not included in the simulations with random initialization.

References

[1] I. Bellemans, N. Moelans, K. Verbeken, Phase field modelling of the attachment of metallic droplets to solid particles in liquid slags: Influence of interfacial energies and slag supersaturation, Comput. Mater. Sci. 108, Part B (2015) 348–357. doi:10.1016/j.commatsci.2015.03.019.

[2] I. Bellemans, E. De Wilde, N. Moelans, K. Verbeken, Phase field modelling of the attachment of metallic droplets to solid particles in liquid slags: Influence of particle characteristics, Acta Mater. 101 (2015) 172–180. doi:10.1016/j.actamat.2015.08.074.

[3] I. Bellemans, E. De Wilde, N. Moelans, K. Verbeken, Phase field simulation study of the attachment of metallic droplets to solid particles in liquid slags based on real slag–spinel micrographs, Comput. Mater. Sci. 118 (2016) 269–278. doi:10.1016/j.commatsci.2016.03.022.

[4] J.W. Cahn, On spinodal decomposition, Acta Metall. 9 (1961) 795–801. doi:10.1016/0001-6160(61)90182-1.

[5] T. Sakai, S.W. Ip, J.M. Toguri, Interfacial phenomena in the liquid copper-calcium ferrite slag system, Metall. Mater. Trans. B. 28 (1997) 401–407. doi:10.1007/s11663-997-0105-4.

[6] H.P. Sun, K. Nakashima, K. Mori, Influence of slag composition on slag-iron interfacial tension, Isij Int. 46 (2006) 407–412. doi:10.2355/isijinternational.46.407.

[7] N. Moelans, A quantitative and thermodynamically consistent phase-field interpolation function for multi-phase systems, Acta Mater. 59 (2011) 1077–1086. doi:10.1016/j.actamat.2010.10.038.

[8] E. De Wilde, I. Bellemans, S. Vervynckt, M. Campforts, K. Vanmeensel, N. Moelans, K. Verbeken, Towards a methodology to study the interaction between Cu droplets and spinel particles in slags, in: Proc. EMC 2013, 2013: pp. 161–174.

[9] S. Mostafaee, M. Andersson, P. Jönsson, Petrographic and thermodynamic study of slags in EAF stainless steelmaking, Ironmak. Steelmak. 37 (2010) 425–436. doi:http://dx.doi.org/10.1179/030192310X12646889256022.

[10] E. De Wilde, I. Bellemans, M. Campforts, A. Khaliq, K. Vanmeensel, D. Seveno, M. Guo, A. Rhamdhani, G. Brooks, B. Blanpain, N. Moelans, K. Verbeken, Wetting behaviour of Cu based alloys on spinel substrates in pyrometallurgical context, Mater. Sci. Technol. 31 (2015) 1925–1933. doi:10.1179/1743284715Y.0000000052.

6. Results and discussion

6.1. General observations

The different stages of spinodal decomposition near a solid particle with $x_S = 0.60$ in a system of size [512 512 1] with an initial supersaturation of $x_i = 0.63$ are illustrated in Figure 6.1. Figure 6.1a-g show $x_M - \phi x_S$ and the figures are scaled to the interval [0 1] in such a way that values lower/higher than the minimum/maximum value are converted to the minimum/maximum, respectively. Thus, the particle, defined as $0.5 < \phi$, appears as a black rectangle. Figure 6.1h shows a set of contour plots of $x_M - \phi x_S = 0.71$ (definition of metal droplets) at different time steps, to illustrate the evolution of the microstructure. The particle is displayed as a black rectangle. The legend corresponding to the different time steps represented in the contour plots is shown on the right of Figure 6.1h and will be the same throughout this study (the last time step is plotted with a bold black line).

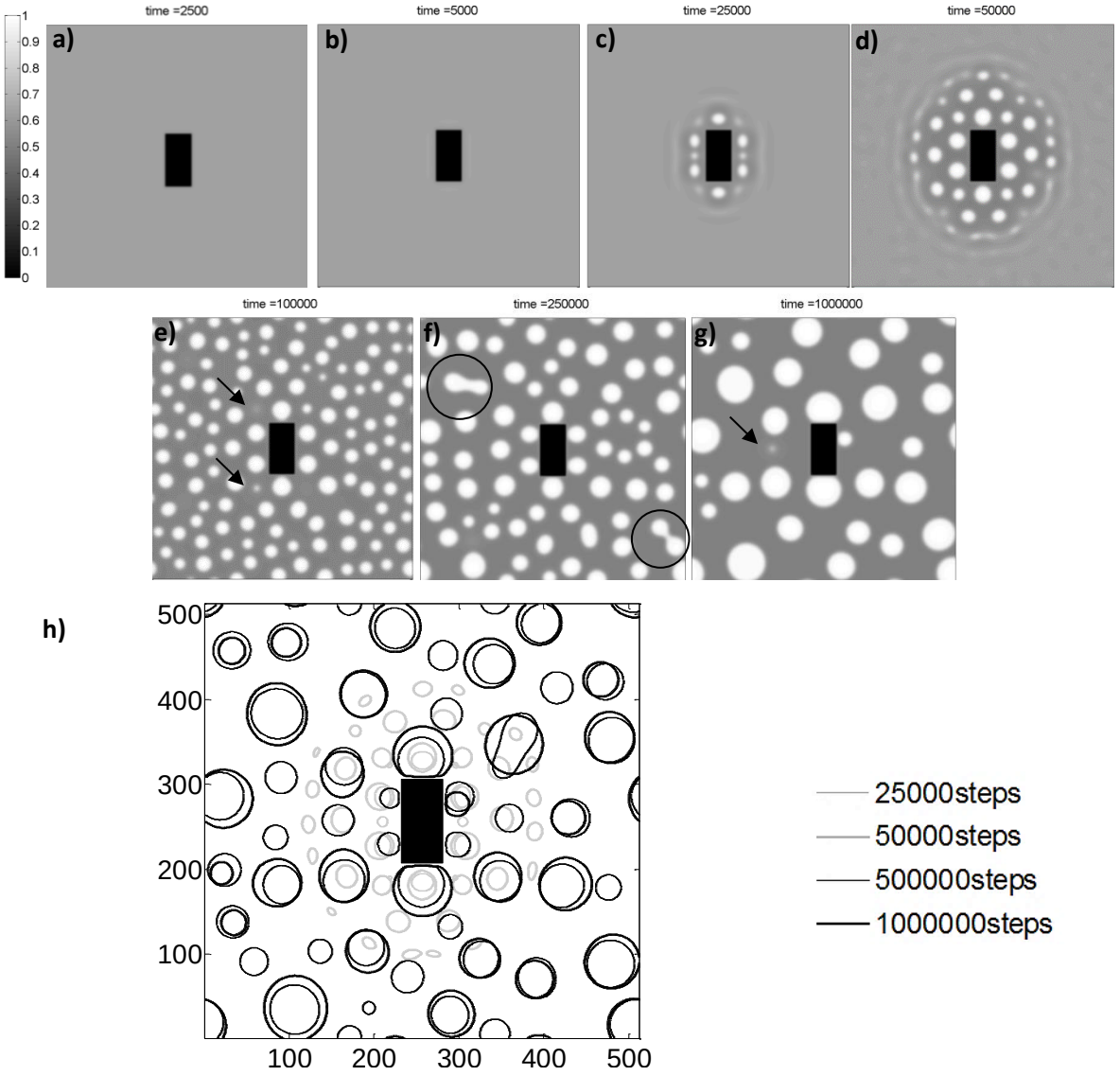

Figure 6.1 Illustration of the different stages in the spinodal decomposition near a solid particle at different time steps with plots of $x_M - \phi x_S$ (a-g) and a summary of this in a series of contour plots of $x_M = 0.71$ at different time steps (h) for the simulation with x_i=0.63 and x_S=0.60 in a system of size [512 512 1] with the corresponding legend on the right (this legend will be the same throughout this paper)

We can distinguish three stages in the simulations. In the first stage, localized spinodal decomposition takes place near the particle, as is clear in Figure 6.1c-d. Secondly, non-localized decomposition takes place in the remaining supersaturated liquid. This is visible in the corners of Figure 6.1d. Finally, Ostwald ripening (the growth of larger droplets at the expense of smaller droplets, as indicated by the black arrows in Figure 6.1e and g) and coalescence (the merge of two droplets, as indicated by the black circles in Figure 6.1 f) occur.

Figure 6.2 and Figure 6.3 illustrate the evolution of the area and fraction of metallic phase attached to the particle and the metal fraction in the system with time. This simulation was performed for $2 \cdot 10^6$ time steps. Similar trends were observed for the other simulations. Generally, the attached droplets were observed at various positions at the particle with several configurations, which also varied in time. As mentioned before, however, in this study we will mainly focus on the coarsening stage and will mostly compare the final values of the fraction of metal in the system found in the simulations after a certain simulation time (at which all considered systems are well within the coarsening regime).

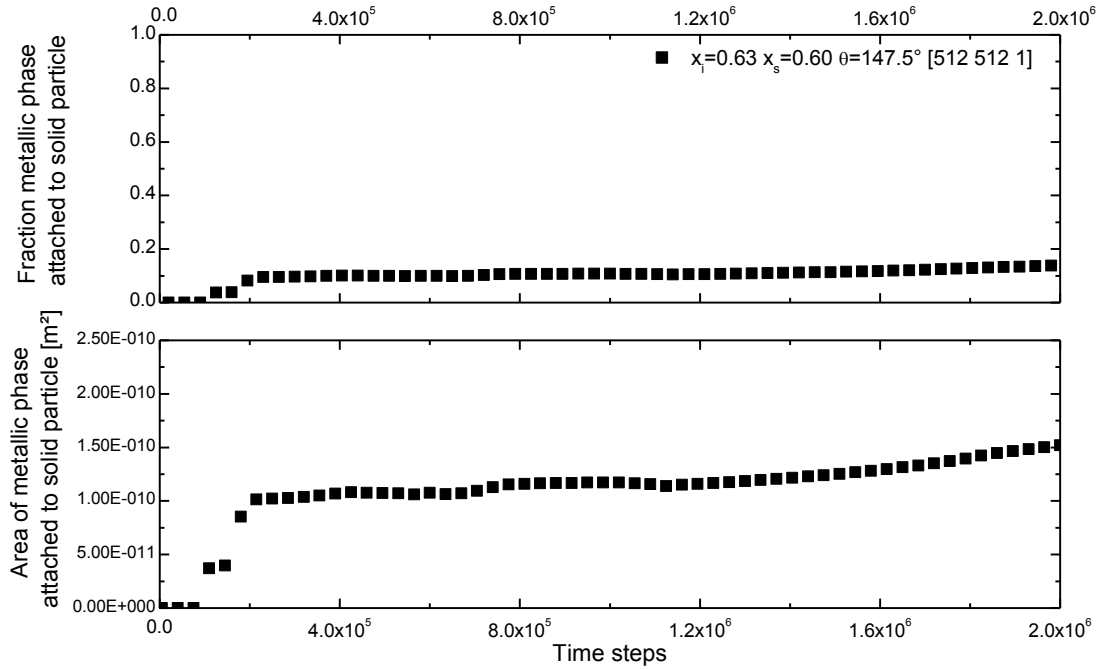

Figure 6.2 The evolution of the attachment of the metallic phase (top: fraction of attached metal; bottom: area of attached metal) to a solid with x_s=0.60 in a system with size [512 512 1] and with x_i=0.63

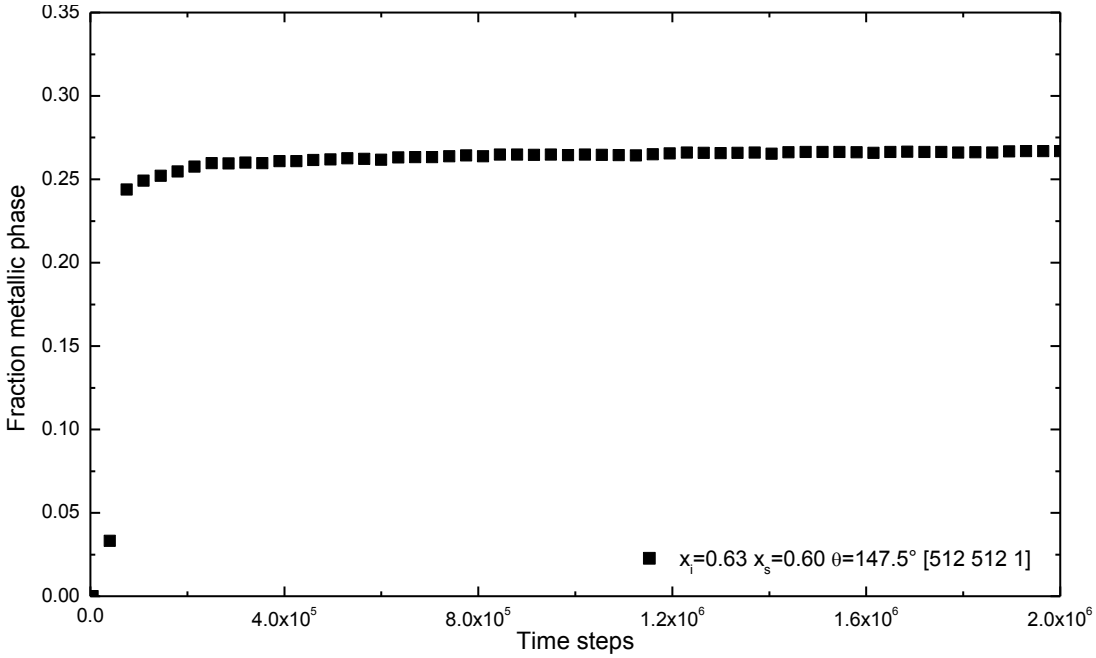

Figure 6.3 The evolution of the metal fraction in the system with size [512 512 1], x_i=0.63 and a solid with x_s=0.60

6.2. Influence of solid-liquid interfacial energies and initial slag composition

The effect of the solid-liquid interfacial energies was investigated by variation of the parameter x_S. The area occupied by the metallic droplets attached to the solid and the fraction of the metallic phase attached to the solid obtained in the simulations at time step 10^6 are shown in Figure 6.4 for initial slag compositions x_i-values of 0.61, 0.63 and 0.65.

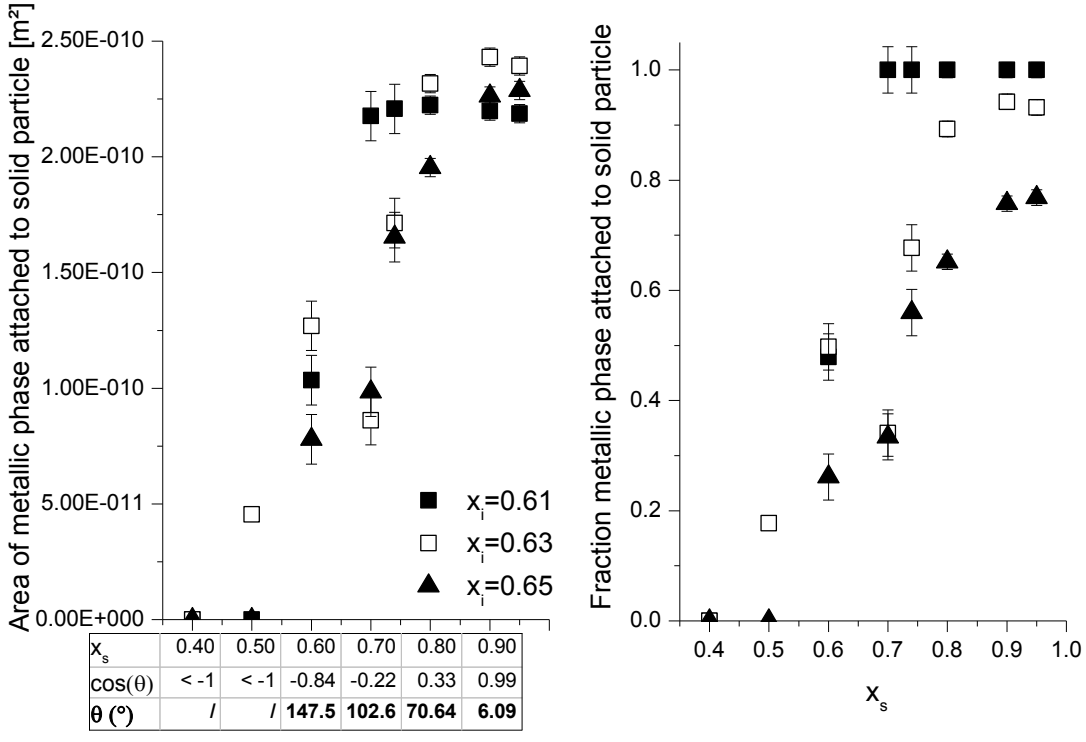

x_s	0.40	0.50	0.60	0.70	0.80	0.90
cos(θ)	< -1	< -1	-0.84	-0.22	0.33	0.99
θ (°)	/	/	**147.5**	**102.6**	**70.64**	**6.09**

Figure 6.4 Influence of x_S (and the corresponding contact angle and its cosine in the table underneath the left x-axis) on the Effect of initialisation method

Generally, a lower contact angle results in an increasing amount of attached metal. The discrepancy between the observed and expected trend for $x_i = 0.63$ ($x_S = 0.60$ and $x_S = 0.70$) was already discussed in section 4.5 and disappears when the simulation time is increased.

The initial supersaturation primarily affects the fraction of metallic phase present in the system. Higher initial supersaturations have more metal in the system and require a longer simulation time to let all the metal attach itself to the particle, causing a smaller fraction of attached metal. Moreover, if x_i increases, full wetting starts to take place at higher x_S-value (lower contact angle). This may seem as contra-intuitive because an increase in x_i results in a larger metal fraction in the system and thus in a larger chance of attachment to the solid particle. However, because more droplets are present in the system, the chance of growth (and thus Ostwald ripening) of a non-attached droplet also increases, unless the driving force for attachment to the particle (reflected in the interfacial energies and contact angle) is large enough, which is only the case for high wettability. Moreover, time may also play a role in the observation of full wetting. Figure 6.5 shows the evolution of the droplets and their attachment by means of contour plots of the droplets at different time steps.

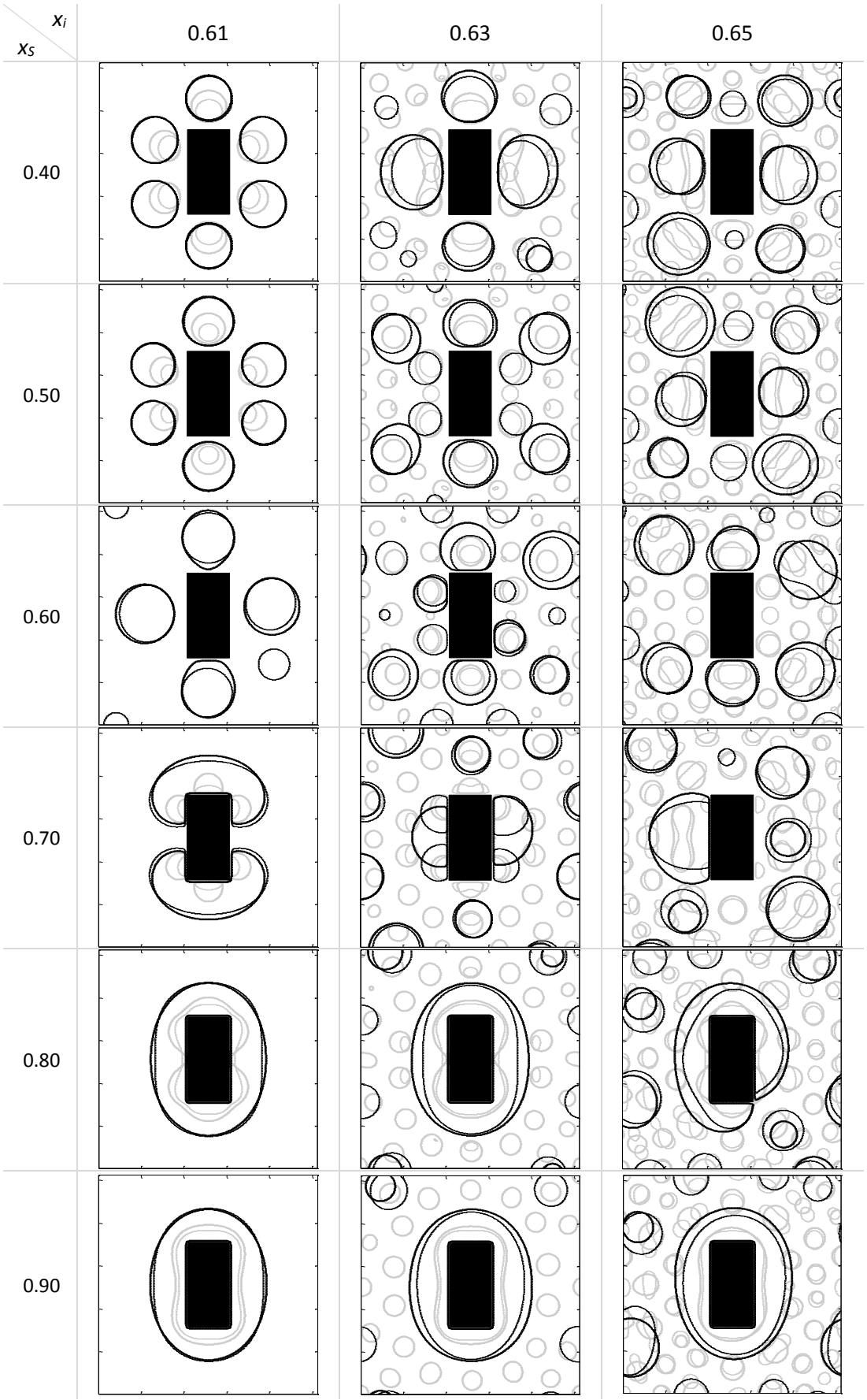

Figure 6.5 Contour plots of x_M=0.71 at different times in the simulations to illustrate the influence of the interfacial energies through the parameter x_S for values from 0.40 to 0.90 and of the initial supersaturation through the parameter xi for values of 0.61, 0.63 and 0.65 on the attachment of the droplets to the particle

In general, two features seem to influence the behaviour of the droplets: Ostwald ripening due to the Gibbs-Thomson effect and an effect due to the interfacial energies between the solid and the different liquids. Four different wetting behaviours are observed.

For non-wetting, non-existing θ or θ = 180° (x_S ≤0.58), Ostwald ripening has the largest influence. In this case, the $\gamma_{S,LO}$ value is much smaller than $\gamma_{S,LM}$. For this reason the liquid oxide is preferentially attached to the solid instead of the metallic liquid phase. Moreover, the absolute value of the difference between the two S/L interfacial energies is larger than 0.903, which is the value of $\gamma_{LO,LM}$. Resulting in a non-existing contact angle, i.e. only liquid oxide is attached to the solid particle. The growth of the droplets seems to be restricted by the presence of the particle: first, the droplets gain a flattened shape and then the centre of the droplets shifts away from the particle to obtain a spherical shape while maintaining the preferential attachment of the liquid oxide instead of the metal. At an initial supersaturation of x_i = 0.63, it seems (Figure 6.5) that the droplets start to stick to the particle and stay there. However, this observation should be treated with care (as discussed in Section 4.5). Note that the standard deviation on the measurements indicated a large uncertainty for x_S = 0.50 simulations.

For low wettability (90° ≤ θ ≤ 180°, x_S = 0.58-0.74), the interfacial energy effect becomes larger and the droplets move towards the solid. Moreover, the absolute value of the difference between $\gamma_{S,LO}$ and $\gamma_{S,LM}$ becomes smaller than 0.903, but $\gamma_{S,LM}$ remains the larger value, which still favours the attachment of liquid oxide to the particle, but to a lesser extent. Thus, the solid particle is covered predominantly with liquid oxide and the metallic droplets cover only a small fraction of the particle's surface. The droplets either first grow next to the particle and eventually deflect to the particle (at x_S = 0.60, as is especially clear for the case of x_i = 0.61) or nucleate immediately on the sides of the solid and either grow directly with metal provided by diffusion (at x_i = 0.61) or dissolve again due to Ostwald ripening of other droplets nucleated elsewhere in the system (x_i = 0.63 or 0.65). The droplets are probably not immediately attached to the particle in the x_S = 0.60 and x_i = 0.61 case, because the slag around the particle reaches a composition just above 0.50, corresponding to $\gamma_{S,LO}$ ≈ 1.255 and $\gamma_{LO,LM}$ ≈ 0.744. This combination of interfacial energies yields, according to Young's equation, a non-existing contact angle. This slag composition continuously changes, which provides a slow movement of the droplet towards the particle. This does not happen at higher initial supersaturations as the amount of metal is higher in such systems.

At high wettability, (0° ≤ θ ≤ 90°, x_S values of 0.74 -0.90), the flat droplets grow immediately on the solid, coalesce there and eventually form a metallic layer surrounding the particle because the $\gamma_{S,LM}$ value becomes smaller than $\gamma_{S,LO}$ and thus the metallic liquid is preferentially attached to the solid. However, the absolute value of the difference between $\gamma_{S,LO}$ and $\gamma_{S,LM}$ remains smaller than 0.903, this results in partial wetting with the majority of the particle's surface being covered by the metal.

In the case of full wetting (x_S > 0.90), the absolute value of the difference between $\gamma_{S,LO}$ and $\gamma_{S,LM}$ is larger than 0.903 and $\gamma_{S,LO}$ is the larger one of the two. In this case, the metal forms as a layer on the solid, as opposed to the previous case, where initially the droplet shape can still be recognized.

The contact angles were measured and are listed in Table 6.1 together with the contact angles expected from Young's equation (5.1). In general, the agreement is good, showing that the approximation made in equations (4.9) and (4.11) is acceptable. The differences between the measured and the predicted angles can be attributed to measurement errors and also depends on the post-processing.

x_S	$\theta_{predicted}$ (°)	$\theta_{xi=0.61}$(°)	$l_{xi=0.61}$ (pixel)	$\theta_{xi=0.63}$ (°)	$l_{xi=0.63}$ (pixel)	$\theta_{xi=0.65}$ (°)	$l_{xi=0.65}$ (pixel)
0.4	/	/	/	/	/	/	/
0.5	/	/	/	164.2±5.2	33.5±7.8	/	/
0.6	147.5	152.8±2.3	64.25±0.0	148.1±9.2	81.5±36.5	155.3±7.2	95.4±13.8
0.7	102.6	103.3±5.7	345.10±3.76	104.3±8.9	192.0±22.6	111.8±2.7	266.0±0.0
0.74	90.0	Full	Full	87.1±2.7	336.0±0.1	85.4±5.7	175.4±69.0
0.8	70.6	Full	Full	Full	Full	70.4±4.1	937.9±0.0
0.9	6.1	Full	Full	Full	Full	Full	Full
0.95	/	Full	Full	Full	Full	Full	Full

Table 6.1 Comparison of the predicted and measured contact angles (°) and contact lengths (pixels) of the metallic droplets attached to the solid particle. The annotation 'Full' depicts full wetting.

Apart from the angles, the contact length in Figure 6.5 was also measured in pixels as an indication of the wetting character. As a reference: the particle had a perimeter of 947 pixels. It should be noted that the droplet in the case of x_i = 0.63 and x_S = 0.50, had only a small contact area/length with the solid particle and probably did not represent a real attachment of the droplet to the particle, as an extension of the simulation time also showed that the droplets detached. Moreover, for x_i = 0.61 and x_S = 0.74 (not shown but the behaviour is between x_S = 0.70 and x_S = 0.80 in Figure 6.5), first six droplets are present with each a contact angle of approximately 90°. These coalesce to two droplets with contact angles of 90° and finally one droplet is formed which encloses the particle, resulting in full wetting. This indicates that the simulation time also has an important influence.

6.3. Influence of particle fraction

By changing the system size, the influence of the particle density is investigated. The results for system sizes of [256 256 1] and [512 512 1] for one x_i,x_S -combination are compared in Figure 6.6. By enlarging the system size, the interaction radius of the particle was also investigated. Moreover, peripheral effects may occur in a too small system.

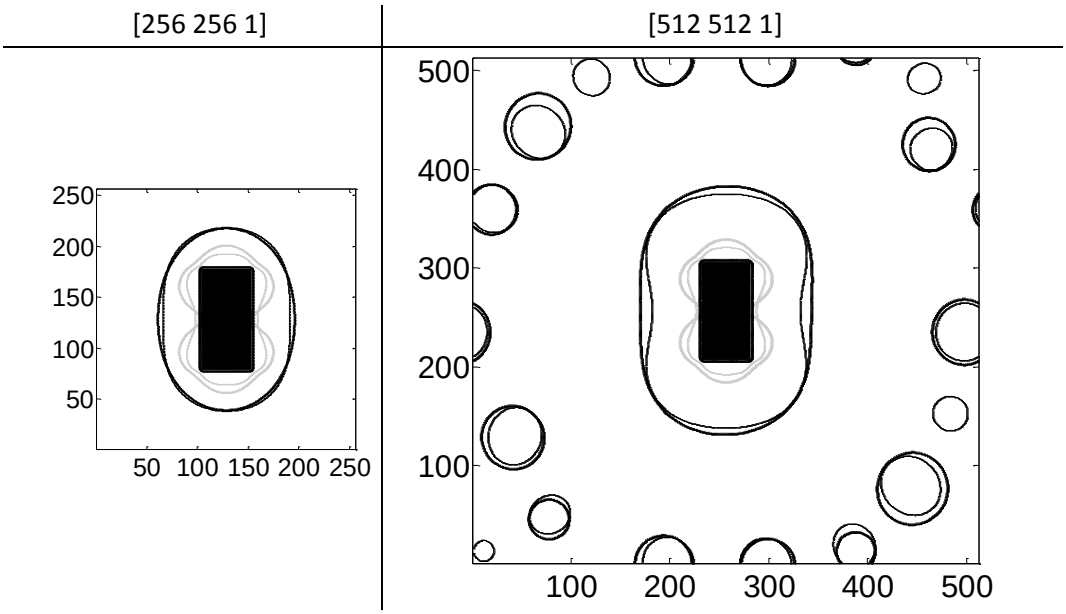

Figure 6.6 Contour plots of x_M=0.71 at different times in the simulations to illustrate the influence of the particle density (by variation of the system size) for x_i=0.61 and x_S=0.80

Generally, the resulting microstructures are qualitatively the same for both system sizes (whether attachment occurs or not and as droplets or a layer). A few minor differences can be present, because a larger system requires the metallic component to diffuse over longer distances. Thus, a longer

simulation time for the larger system yields the same results (attachment of droplets to the particle) as the reference simulation time in the smaller system. The influence of the particle density is illustrated in Figure 6.7.

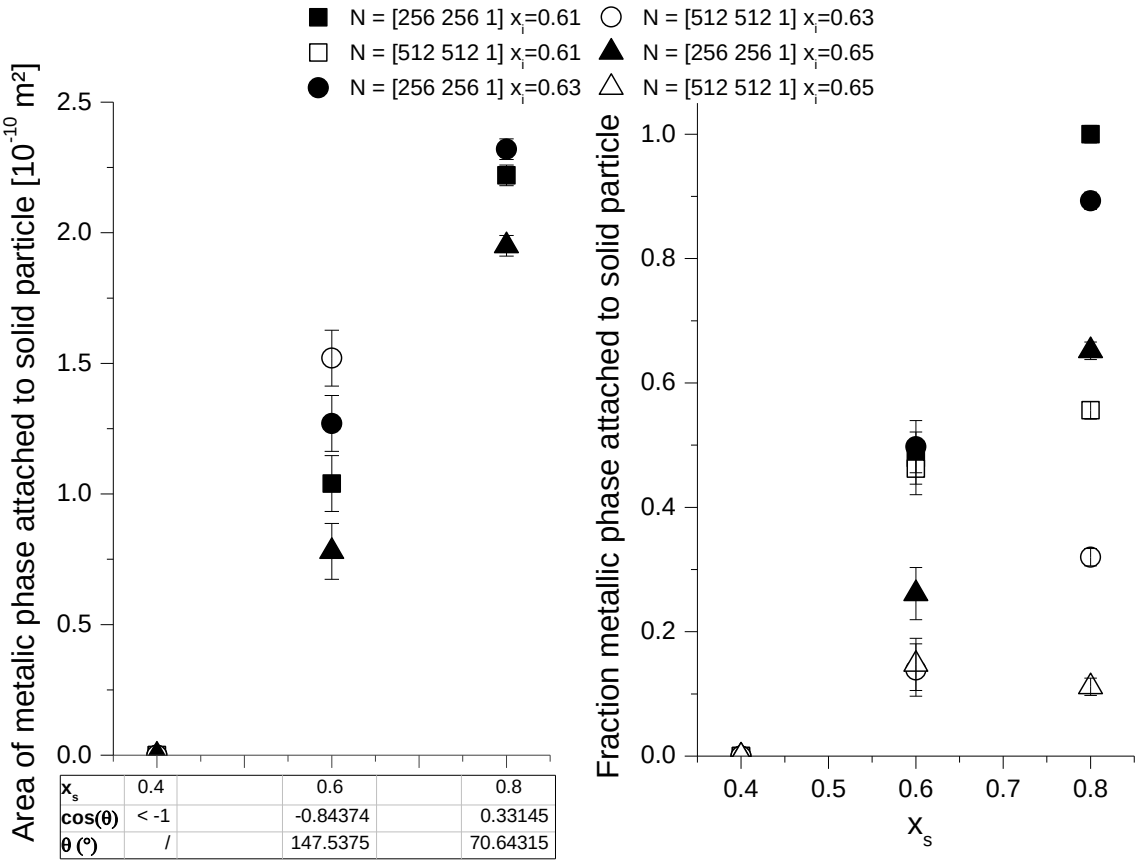

Figure 6.7 Influence of the particle density on the area and the fraction of the metallic phase attached to the solid by changing the system size ([256 256 1] or [512 512 1]) for x_i =0.61; 0.63 and 0.65 and x_S = 0.40 (θ=/); 0.60 (θ=147.5°) and 0.80 (θ=70.6°)

By increasing the system size (and decreasing the particle fraction in the system), more metal is present in the system, resulting in a larger amount of metal attached to the solid for most cases. Due to the larger diffusion distance, however, the fraction attached metal is lower in the larger systems.

6.4. Influence of particle perimeter per area

The influence of the perimeter per area on the attachment of the metal is investigated by changing the aspect ratio of a rectangular particle on the one hand, of which the results are depicted in Figure 6.8, and by changing the particle shape on the other hand, of which the results are shown at the end of this section. All these simulations were performed for an initial supersaturation of x_i = 0.63 and compositions of the solid particle of x_S = 0.60 (θ = 147.5°, corresponding to low wettability) and of x_S = 0.80 (θ = 70.6°, corresponding to high wettability) in a system of size [256 256 1].

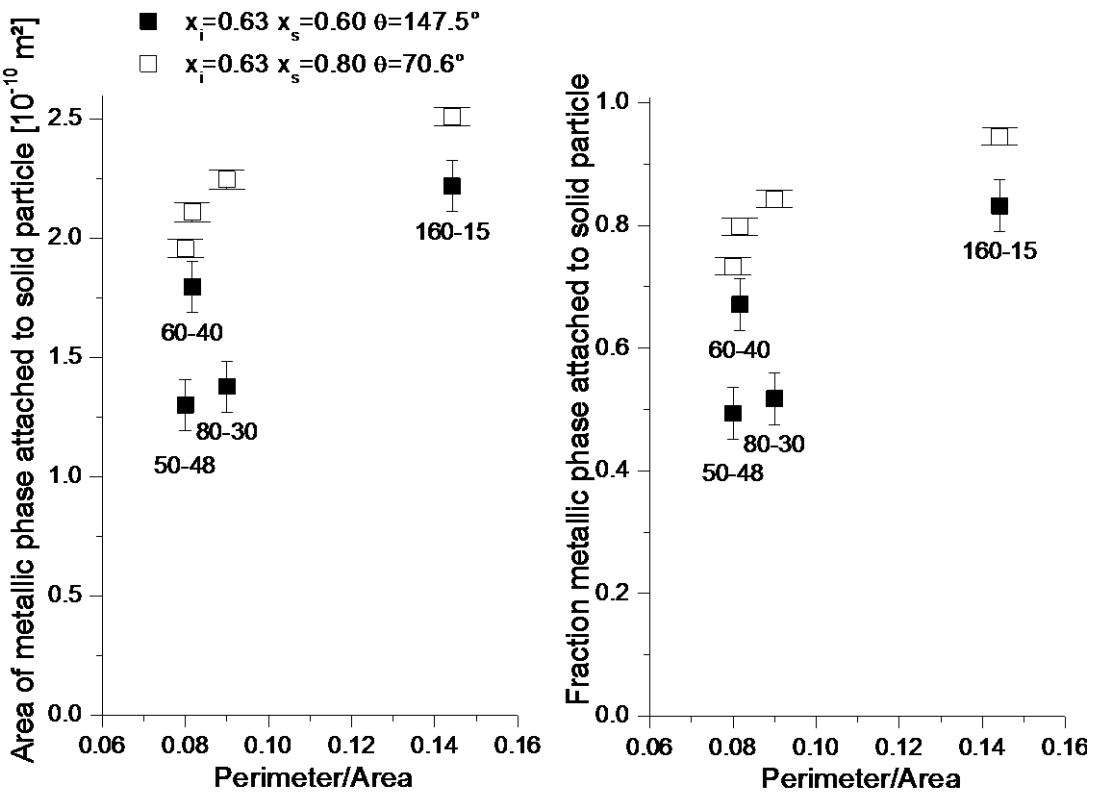

Figure 6.8 Influence of the perimeter/area of a rectangular particle on the area and the fraction of the metallic phase attached to the solid for x_i =0.63 and x_S =0.60 (θ=147.5°) or x_S =0.80 (θ=70.6°); The aspect ratios of the rectangles are mentioned labels of the closed data points; the error bars with the large (small) base correspond to the standard deviation for x_S =0.80 (0.60) or the open (closed) symbols

It is expected that a larger perimeter per area results in a larger amount of attached metal. This sequence is, however, only obtained at high wettability, i.e. the open symbols (x_S = 0.80) show the expected relation, whereas the closed symbols (x_S = 0.60) are scattered. Thus, the perimeter per area influences the amount of attached metal in the case of high wettability. For low wettability, no effect of the perimeter per area was observed, as the particle's surface is expected to be covered by liquid oxide rather than metal, thus the perimeter per area of the particle has no significant influence and the amount of attached metal is predominantly determined by the statistical spread. For high wettability, on the contrary, the particle's surface is covered by the metal droplet and thus the perimeter per area has a large influence on the amount of attached metal. Contour plots of two different aspect ratios for low and high wettability are shown in Figure 6.9.

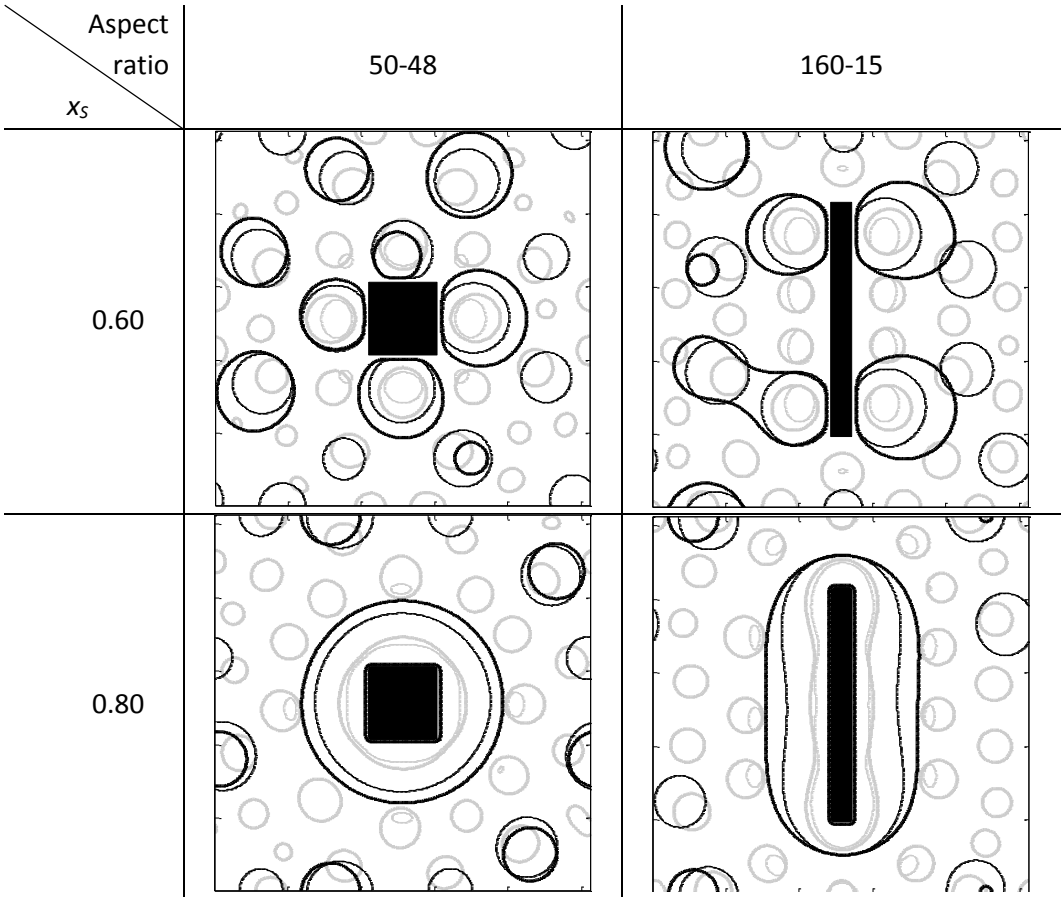

Figure 6.9 Contour plots of x_M=0.71 at different times in the simulations to illustrate the influence of the perimeter per area of the particles (by varying the aspect ratio) on the attachment of the droplets to the particle in low (x_S =0.60) and high (x_S =0.80) wettability regimes

From these contour plots it becomes clear why the higher perimeter per area results in more attached metal in the case of high wettability. A lower perimeter per area corresponds (for rectangles) to an almost equal height and width of the particle. This shape is closer to a sphere than the stretched particles with a high perimeter value. Because the shape is 'less spherical', more metal is required to achieve the energetically preferred spherical shape of a droplet.

The variation of the perimeter per area by changing the shape of the particles is shown in Figure 6.10. Several simulations were carried out for the smaller particles: far versus close and with different orientations relative to each other. To evaluate the influence of the perimeter per area, the average within one perimeter per area value was calculated and plotted for the same shape and wetting behaviour. These average values are labelled as 'Mean'. The legend gives information on the greyscales of the data points and the symbols indicate the shape of the particles used.

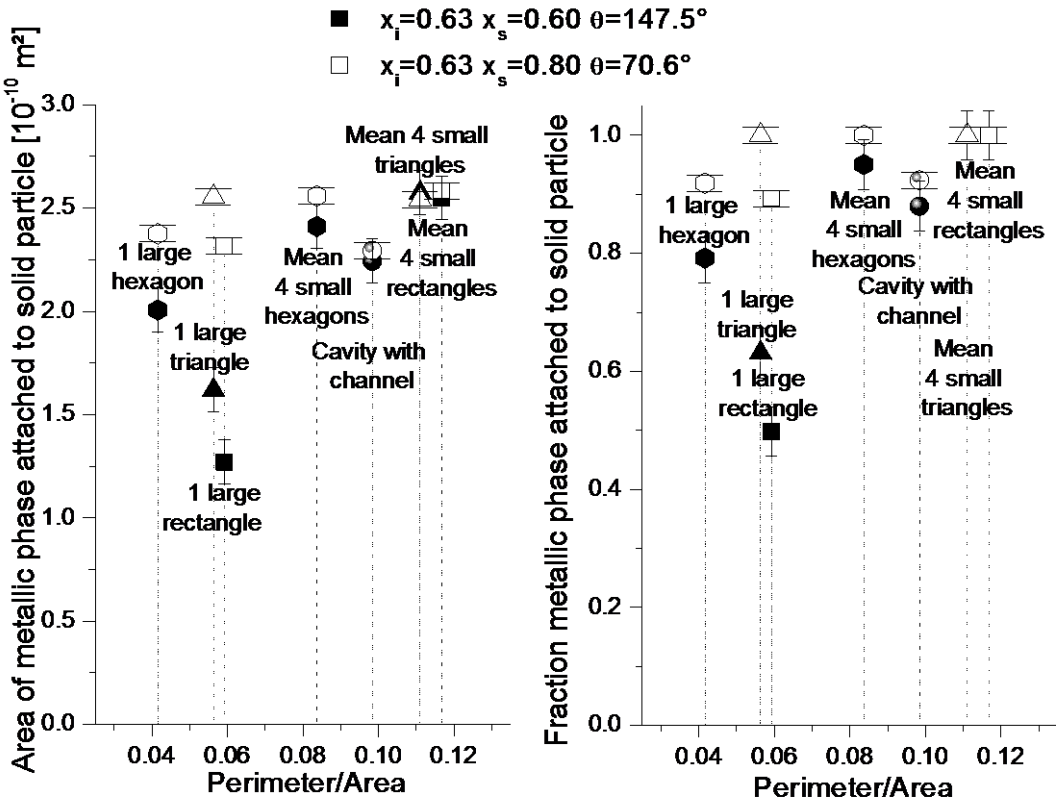

Figure 6.10 Influence of perimeter/area of the particle by variation of its shape on the area and the fraction of the metallic phase attached to a solid with x_S = 0.60 and x_S =0.80. The legend gives information on the greyscales used in the data points, whereas the symbols indicate the shape of the particles used. the error bars with the large (small) base correspond to the standard deviation for x_S =0.80 (0.60) or the open (closed) symbols

In all cases, the difference between low and high wettability is small and again, the sequence found in the graph is not the expected one for low wettability. This time, however, the sequence was also not so obvious for high wettability. This might find its origin in the influence of the particle shape.

6.5. Influence of particle shape, size and distribution

Besides the influence of the shape of the particles on the attachment of the metal, of which the results are shown in Figure 6.10, the influence of the distribution of the particles is also investigated. All simulations were performed for an initial supersaturation of x_i = 0.63 and compositions of the solid particle of x_S = 0.60 (θ = 147.5°, corresponding to low wettability) and of x_S = 0.80 (θ = 70.6°, corresponding to high wettability) in a system of size of [256 256 1].

The influence of the particle shape is not clear from the results in Figure 6.10 as no significant differences for the different shapes were found. Nevertheless, it is very clear that several small particles yield more attached metal than one large particle, as dividing one large particle in 4 small ones conserves the area of the particle but nearly doubles the perimeter.

Figure 6.10 mentions the experimentally relevant case of the cavity with a channel (which connects the outside matrix with the inside of the cavity). This approximates real observations, as indicated in Figure 6.11 by the white circles.

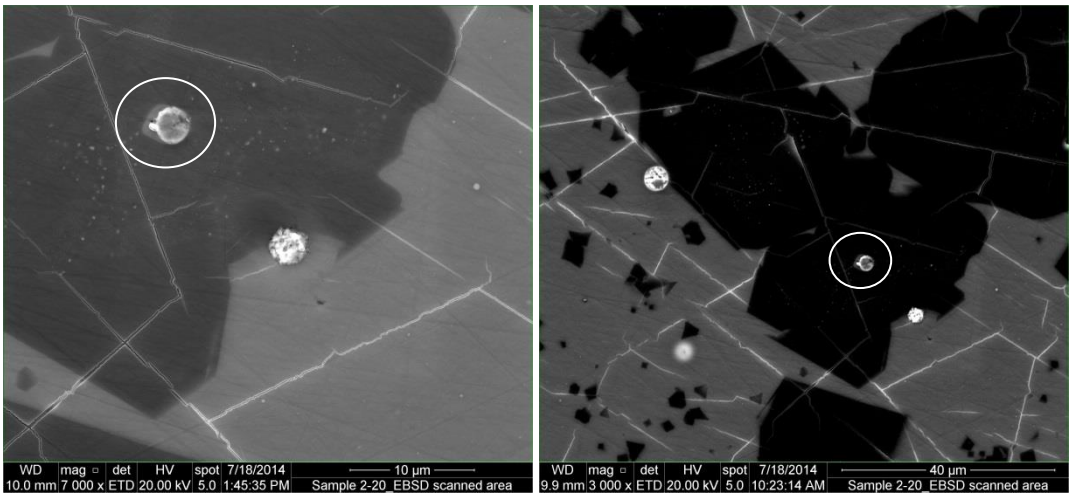

Figure 6.11 Experimentally obtained micrographs of Cu droplets within a cavity inside a solid particle indicated by white circles. These micrographs were obtained with scanning electron microscopy on a quenched sample after smelting down all components in a PbO-FeO-CaO-SiO_2-Cu_2O-ZnO-Al_2O_3 system at 1200°C [1]

The contour plots of the droplets in Figure 6.12 illustrate the results of such a particle with a cavity and a channel.

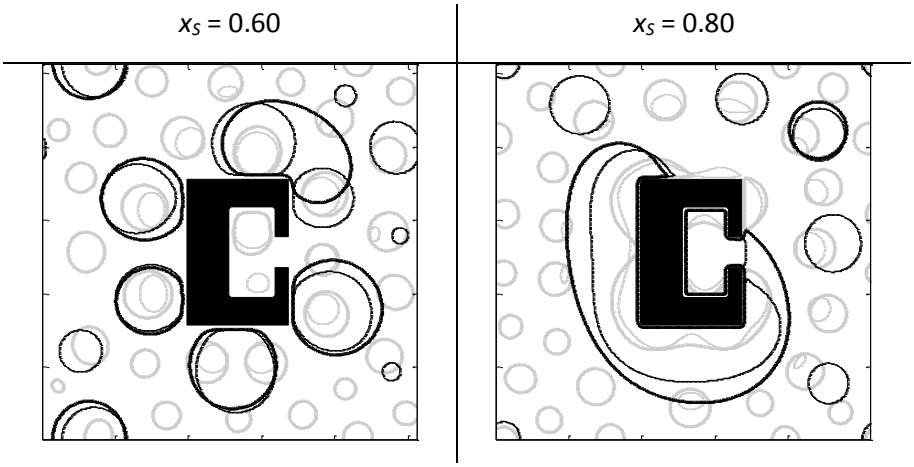

Figure 6.12 Contour plots of x_M=0.71 at different times in the simulations to investigate a cavity and a channel in a particle as an approximation of the experimentally observed particle in Figure 6.11 in low (x_S = 0.60) and high (x_S = 0.80) wettability regimes

In the case of high wettability (x_S = 0.80) the droplet grows in the cavity and the cavity restricts further growth of the droplet. Thus, the cavity limits the amount of attached metal even though it provides the particle with a large perimeter/area ratio. Therefore, the amount of attached metal is relatively low (one of the lowest open symbols) for such a large perimeter/area ratio in the case of high wettability. Therefore, an important conclusion is that not only the perimeter per area, but also the space available for the droplet to grow is important.

In contrast, for low wettability (x_S = 0.60), the amount of attached metal is not one of the lowest. If a droplet is formed inside the cavity, it is either trapped there or it dissolves again and the amount of attached metal is only slightly lower for such a large perimeter/area. A comparison with the experimental micrograph in Figure 6.11 indicates that the corresponding system correlates best with the low wettability case, due to the spherical shape of the droplets.

Figure 6.13 displays the influence of the proximity of the particles and their relative orientations. The legend gives information on the greyscales used in the data points, whereas the symbols indicate the

shape of the particles used. Note that the small rectangles always yield the same total perimeter of 584, but for the sake of visibility, the differently oriented rectangles were plotted at a perimeter/area equal to 0.12.

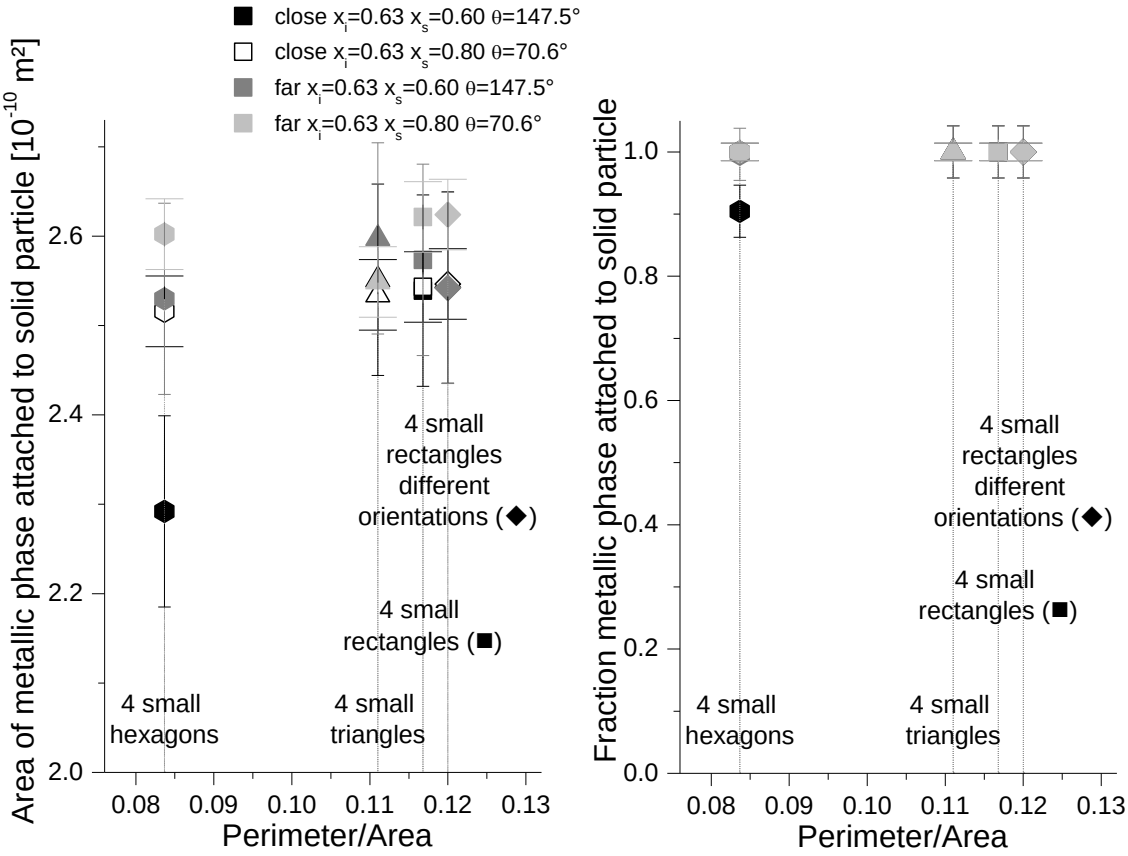

Figure 6.13 Influence of proximity and relative orientations between the different small particles on the area and the fraction of the metallic phase attached to a solid with x_S =0.60 and x_S =0.80. The legend gives information on the greyscales used in the data points, whereas the symbols indicate the shape of the particles used. the error bars with the large (small) base correspond to the standard deviation for x_S =0.80 (0.60) or the open (closed) symbols

The results indicate that the amount of attached metal is mostly larger for particles that are farther apart than for particles close together. This effect is largest for low wettability, but as the perimeter per area increases, the effect decreases. Qualitative contour plots at different time steps in the simulations can be found in Figure 6.14.

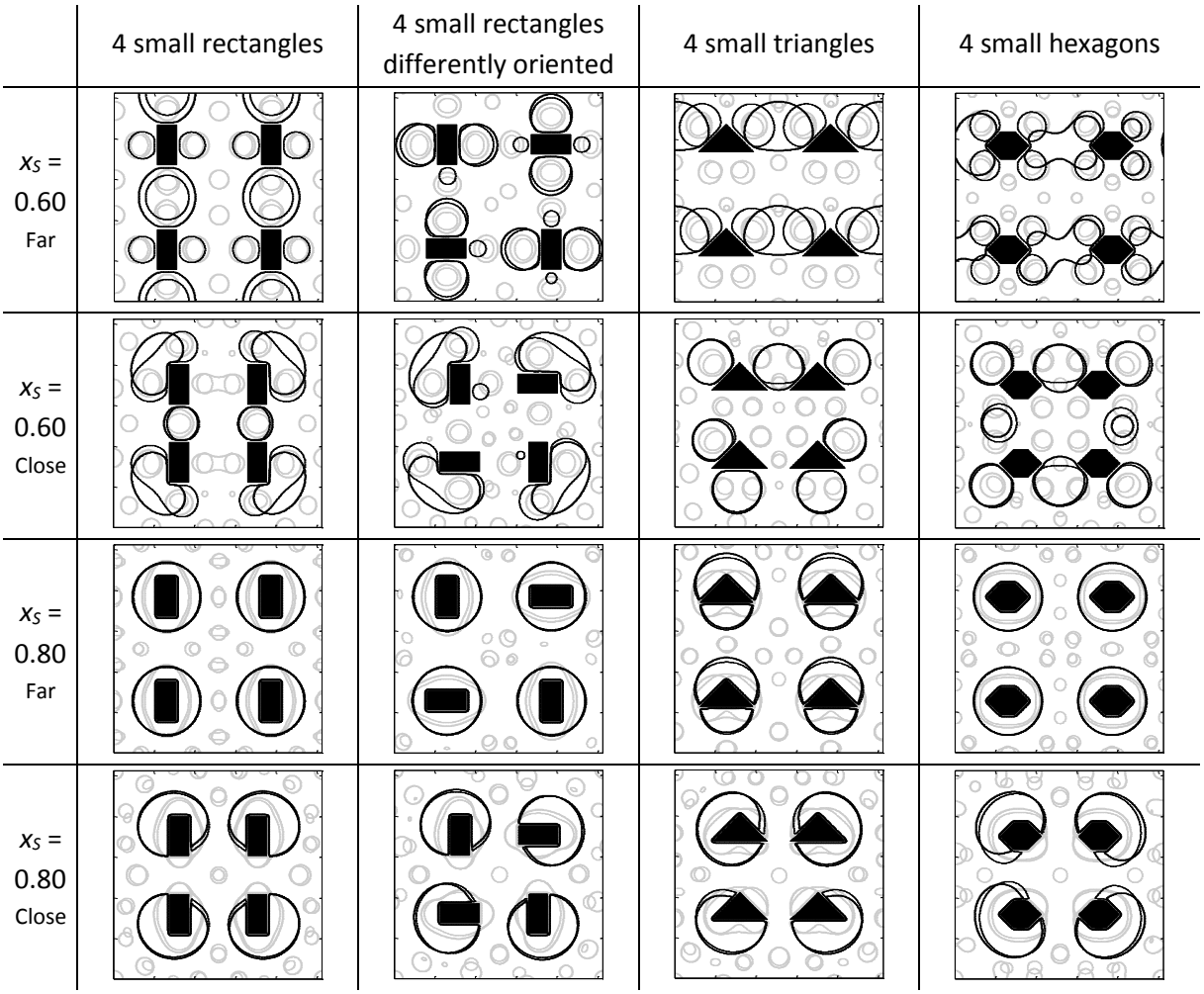

Figure 6.14 Contour plots of x_M=0.71 at different times in the simulations to illustrate the influence of proximity and relative orientation between the different small particles on the attachment of the metallic phase to a solid with x_S =0.60 (the two rows on top) and x_S =0.80 (the two rows at the bottom) at x_i=0.63

When the particles are located close together, the metal is mostly located on the side of the particles not oriented to the other particles. This is very clear in the x_S = 0.80-case, as particles far apart are completely covered by metal, but the particles close together have at least one free edge (always the smallest edge, even when the particles are oriented differently). This change in shape of the metallic droplet does not have a large influence on the final total amount of attached metal (cfr. Figure 6.13).

Experimentally, one metallic droplet is sometimes observed to have several small solid particles attached to it, as shown in Figure 6.15. This is only visible in the simulations of low wettability, indicating again that the experimental system corresponds most to the low wettability case. A possible explanation for this is that the high wettability regime favours complete wetting of the particles and hence pulls all the metal away from in between the particles, not leaving any metal to share with another particle. In the case of low wettability, the metal does not predominantly cover the particle, which leaves room to share a droplet with another particle.

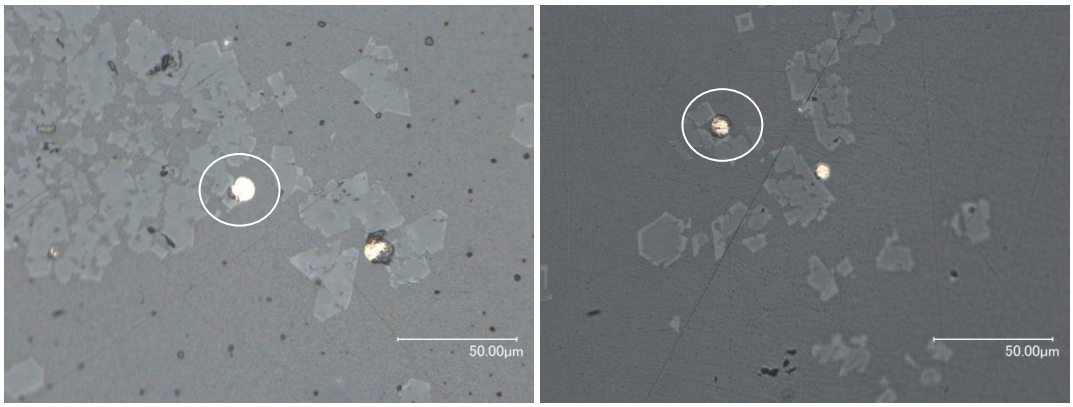

Figure 6.15 Experimentally obtained micrographs of one Cu droplet with several spinel particles attached to it, indicated by white circles. These optical micrographs were obtained from optical microscopy on a quenched sample after smelting down all components in a PbO-FeO-CaO-SiO_2-Cu_2O-ZnO-Al_2O_3 system at 1200°C [1]

At the moment, the model does not include anisotropy in the interfacial energy, thus any effect of the different orientation at the moment can be attributed to a slight change in distance between the particles. Different orientations of the solid particles did not yield a clear influence of the orientation, as could be expected from the absence of anisotropy in the model.

6.6. Investigation of origin of interaction

6.6.1. First investigation of random initialization

For the results discussed up till now, spinodal decomposition was used as a convenient way to introduce the metallic droplets in the system. To verify the effect of droplet initialization on the findings discussed in the previous section, results obtained with an alternative initialisation method, namely by randomly positioning droplets with a radius chosen from a discrete uniform random distribution in the system until the proposed volume fraction of metallic droplets is reached, can be found in Figure 6.16. The actual initial metal fractions are 0.1009±0.0005 for a proposed volume fraction of 0.10 and 0.2010±0.0009 for a proposed volume fraction of 0.20.

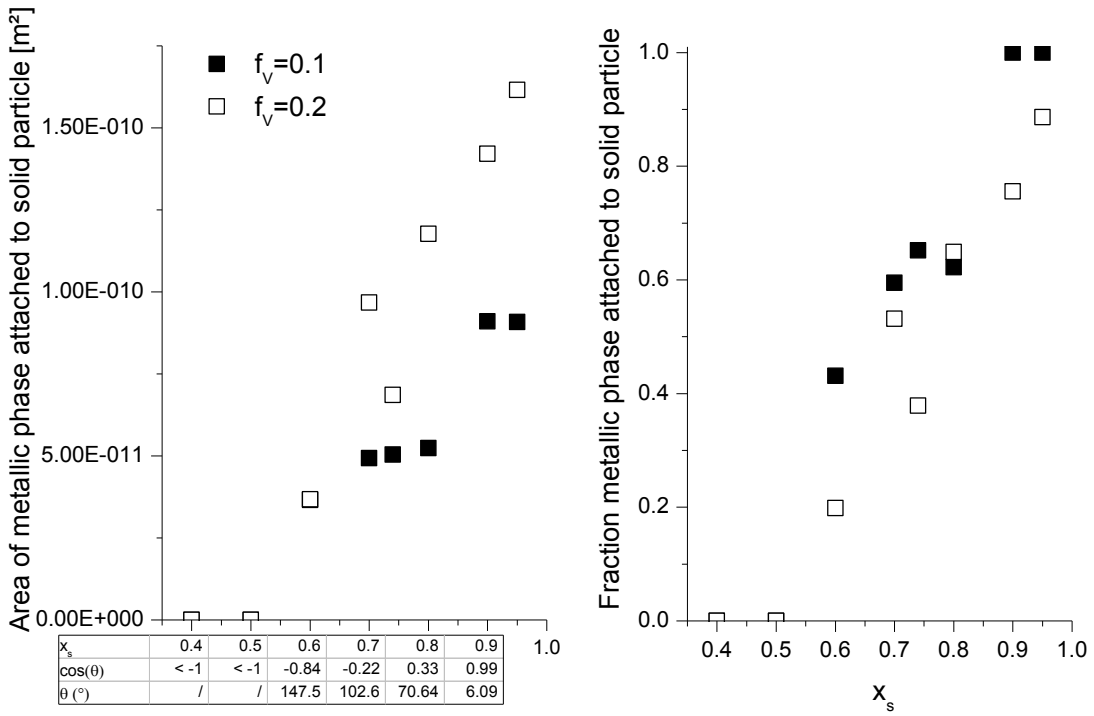

Figure 6.16 Influence of x_s (and the corresponding contact angle and its cosine in the table underneath the left x-axis) on the area and the fraction of the metallic phase attached to the solid at volume fractions of metal of 0.1 and 0.2 for an alternative initialisation method

Generally, the amount of attached metal is smaller in comparison with the simulations using spinodal decomposition, because the volume fractions are chosen to correspond to smaller x_i-values. However, the number of droplets is larger for this initialisation method. Nevertheless, again no favourable positions on the particle were observed for the droplets. Increasing the volume fraction of metal has a similar effect as an increase of x_i, as discussed in section 6.2. Furthermore, a decrease in the predicted contact angle results in increasing amounts of attached metal. In the low wettability regime, the droplet needs to be initialized close enough to the particle and should be large enough to be attached to the solid. If the droplet is not large enough, it will dissolve, even though it was initially attached to the particle. Larger droplets, when positioned nearby the solid, will move towards it. In comparison with the initialisation by spinodal decomposition, the alternative initialisation method yields more, but smaller droplets attached to the solid for low wettability.

In the high wettability regime, the size of the droplet has less influence on the final attachment as even intermediately sized droplets can be attached to the solid or can dissolve in favour of the formation of a metallic layer around the particle.

A disadvantage of the alternative initialisation method is that it is possible that all larger droplets are, by coincidence, concentrated in the border of the system, although the droplets are initialized randomly. The smaller droplets, situated around the particle, will dissolve and no droplets are attached to the particle, even though this is favoured by the interfacial energies. Consequently, a larger number of simulations are required to draw relevant conclusions than when the droplets form through spinodal decomposition, since the droplets are then first formed close to the particle. As we are interested in the interaction between the particles and the droplets, the spinodal decomposition is thus preferred as initialisation method as it allows obtaining the same conclusions in a more efficient way.

6.6.2. Qualitative comparison of the initialization methods

To illustrate the main differences between the two different initialization methods, a simplified morphology was chosen for the solid spinel particle: a rectangular particle of size [50 100 1]. Moreover, the wettability was chosen in between the low and high wettability regime, i.e. a contact angle of 90°, corresponding to an x_S-value of 0.74. The spinodal initialization was carried out for an initial supersaturation of x_i = 0.605 and for the random initialization, a volume fraction of 0.20 was proposed. Colour plots of x_M - ϕx_S of several time steps in the simulation with spinodal initialization are shown in Figure 6.17.

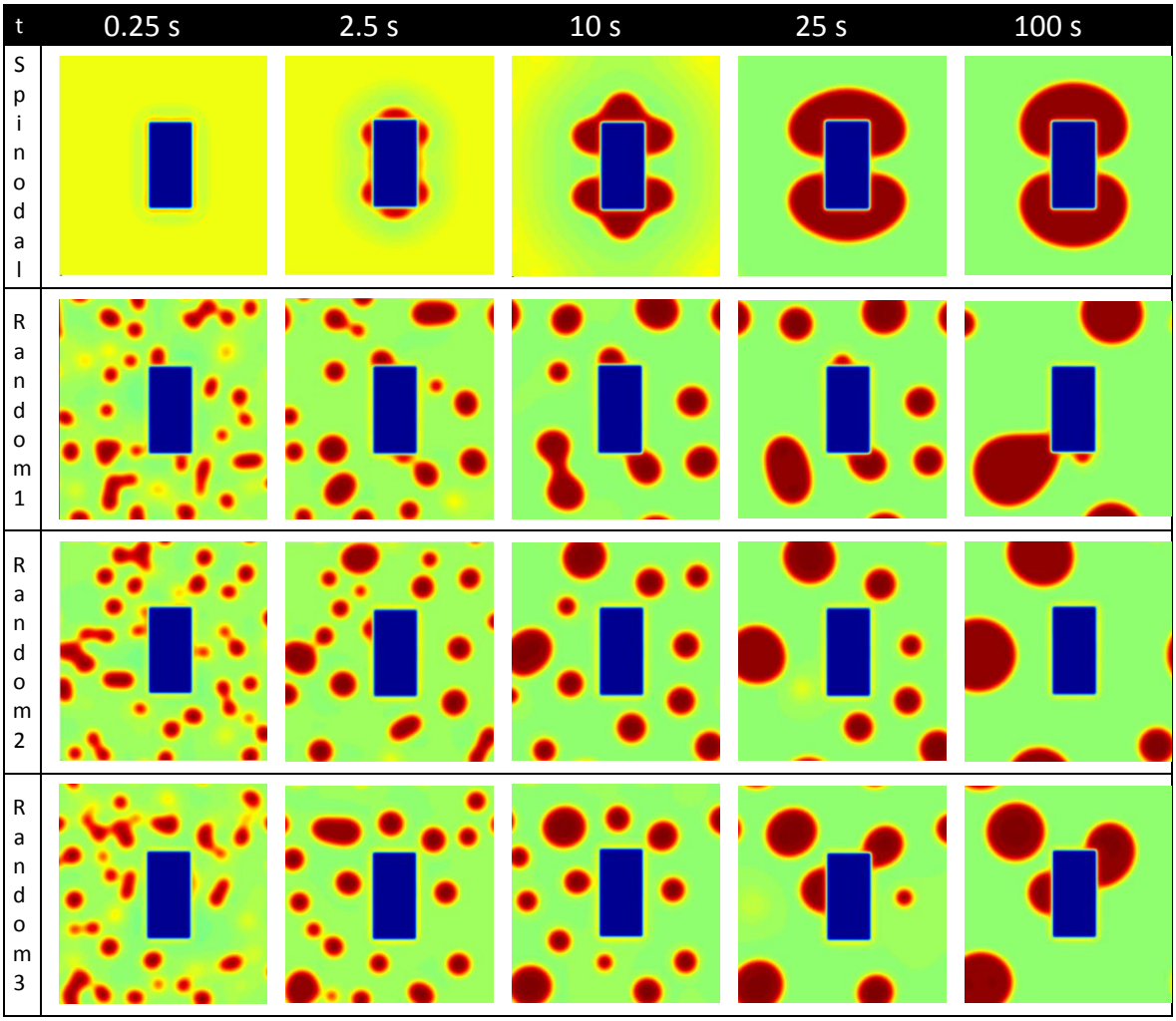

Figure 6.17 Colour plots of x_M - ϕ x_S after several time steps in the simulation in a system of size [256 256 1] and with a solid particle of size [50 100 1] x_S=0.74; First row: spinodal initialization with x_i=0.605; second row: random initialization with f_V=0.20; Third row: second simulation of random initialization with f_V=0.20; Fourth row: third simulation of random initialization with f_V=0.20

As was briefly mentioned in section 6.1, first, 'localized' spinodal decomposition takes place around the solid particle. At low initial supersaturations, all metal is attached to the solid particle and thus the result is the same for several repeated simulations using different seedings for the random noise. For large x_i values, this is no longer the case, but the metal droplets still originate first near the solid particle. Colour plots of x_M - ϕx_S of several time steps in the simulation with the random initialization are shown in the second row of Figure 6.17. It is immediately clear that in the resulting microstructure in a simulation with random initialization the metallic droplets are more scattered over the complete slag phase. The attachment, however, is less obvious: e.g. the third row of Figure 6.17 shows colour

plots of a simulation that initially has a small droplet attached to the particle, but due to Ostwald ripening of larger droplets which are not attached to the solid, the attached droplet disappears and in the end, no metal is attached to the solid, even though this is energetically favourable.

Furthermore, a third possibility exists: first no metal is attached to the solid particle, but then medium-sized droplets get attached to the solid (because this is energetically favourable) and these droplets grow by Ostwald ripening. This is illustrated in the bottom row of Figure 6.17. Thus it is immediately clear that the spread on the results for the random initialization will be far greater than for the spinodal initialization. For the random initialization, the droplets are positioned randomly over the entire system (except for the points where solid particles or other droplets are present). This may result in fewer attached droplets. E.g. it is possible that all larger droplets are concentrated in the border of the system, although the droplets are initialized on random positions. In such a case, the smaller droplets, situated around the particle, will dissolve and no droplets are attached to the particle, even though this might be favoured by the interfacial energies. Why such a situation occurs frequently in the simulations can be explained by considering Figure 6.18. It shows a system with size *[N N 1]* and a hatched particle with size *[Y X 1]*. The edge of the blue area is at an equal distance between the edges of the system and those of the solid particle.

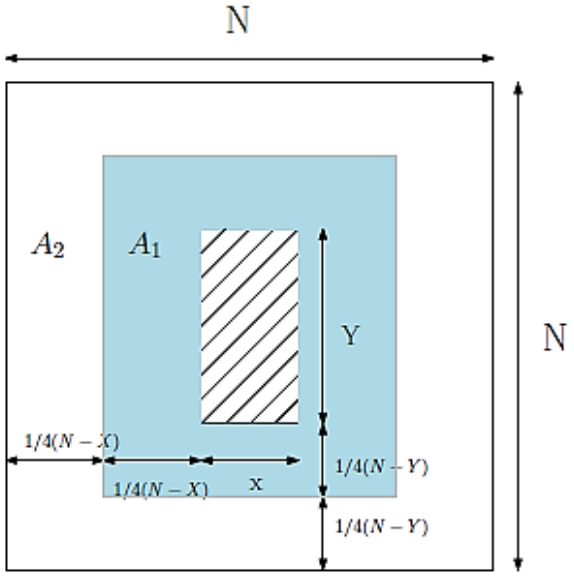

Figure 6.18 Illustration of the areas under consideration in the random initialization

The chance that a droplet is placed within a certain rectangle closer to or further away from the particle is determined by the amount of available positions within these rectangles. The area of the blue rectangle is

$$A_1 = \left(X + \frac{1}{2}(N - X)\right)\left(Y + \frac{1}{2}(N - Y)\right) - XY \qquad \textbf{(6.1)}$$

And the total area available for droplets is $A_{tot} = N^2 - XY$. Thus, the chance that a droplet is placed within the rectangle closer to the particle is

$$\frac{A_1}{A_{tot}} = \frac{1}{4}\frac{N^2 + N(X + Y) - 3XY}{N^2 - XY} \qquad \textbf{(6.2)}$$

For the values in this work (*N*=256, *X*=50 and *Y*=100), this fraction is 0.367 and thus it is more likely that the droplets will be positioned further away from the solid particle. However, when real slag-spinel micrographs are used, the solid particles are usually more evenly distributed throughout the

system and thus the effect of the position of the solid particles on the distribution of the randomly positioned metal droplets will be reduced.

6.6.3. Quantitative comparison of initialization methods

The spread on the results of simulations initialized with the spinodal decomposition method was determined based on three simulations with x_i = 0.605; x_S = 0.74 (the contact angle of the metal droplet on the solid particle is predicted to be θ = 90° and lies in between the low and high wettability regimes) in a system with size [256 256 1] with a rectangular particle of size [50 100 1]. The spread on the results of simulations with random initialization was determined based on five simulations with f_V = 0.20; x_S = 0.74 in a system with size [256 256 1] and a rectangular particle with size [50 100 1]. The values, averages and standard deviations of the results of these simulations can be found in the first two columns in Table 6.2.

	Spinodal decomposition **x_S = 0.74 ; x_i = 0.605**	***Random positioning*** **x_S = 0.74 ; f_V = 0.20**	***Spinodal decomposition*** **x_S = 0.60 ; x_i = 0.63**
Fraction metallic phase in the system	0.21311	0.18723	0.26348
	0.21296	0.18688	0.26378
	0.21306	0.18539	0.26297
	-	0.18939	0.26300
	-	0.18690	-
Average ± stdev	0.213 ± 7.64 10^{-5}	0.187 ± 0.00144	0.263 ± 0.0004
Fraction of metal attached to solid	1	0.57208	0.49749
	1	0	0.40669
	1	0	0.44576
	-	0.34331	0.51316
	-	0.33357	-
Average ± stdev	1 ± 0.0	0.250 ± 0.247	0.466 ± 0.042

Table 6.2 Values, averages and standard deviations in the fraction metallic phase in the system and fraction metal attached to the solid particles, for the results of both initialization methods at the last time step of several simulations

Standard deviations for the fraction metallic phase in the system were generally three orders of magnitude smaller than the average value for random initialization and five orders of magnitude for spinodal initialization. There is a larger spread on the fraction of metal present in the system for the random initialization because the final volume fraction of metal was never exactly equal to 0.20. Metallic droplets are namely placed within the system as long as the actual volume fraction of metal does not exceed the prescribed value. The difference between both values can range from very small to large, as it is for example possible that the actual volume fraction only differs slightly from the prescribed value and that the last added droplet is quite large. Thus, in most cases, the actual volume fraction of metal after initialization (i.e. at the end of time step zero) will be larger than the intended value. However, in one case, the 20 trials for checking the overlap of the new droplet with the solid particles and the already present droplets in the system, did not suffice and the initialization was aborted. Then, the volume fraction of metal droplets was considerably smaller (0.1784) than the intended 0.20. One such exceedance was observed for micrograph 2 for the no wetting case (x_S = 0.50). This single simulation was repeated and the result of the second simulation are presented in

this paper. The average value of the fraction of metal in the system given in Table 6.2 is smaller than the prescribed value, because the metal droplets are initialized with an x_M value of 0.98, but with sharp interfaces within a slag matrix with an x_M value of 0.50. The interfaces will become diffuse after time step zero and thus some of the metal that first belonged to a droplet will dissolve into the slag phase to form the diffuse interfaces. Hence, lowering the fraction of metallic droplets in the system.

For the fraction attached metal, the standard deviation is of the same order of magnitude as the average value for random initialization. For spinodal initialization, the standard deviation appeared to be zero for this case with an x_S value of 0.74 (in between the low and high wettability regime, characterized with a contact angle of 90°), because all the metal present in the system was attached to the solid in all three simulations, i.e. a fraction of one for every simulation, as shown in Table 6.2. Section 4.5, however, showed that in general a certain spread is also present on the fraction of attached metal for the spinodal initialization: simulations for x_i = 0.63; x_S = 0.60 were performed four times in a system with size [256 256 1] and a rectangular particle dimensions [50 100 1]. These results are shown in the last column of Table 6.2. This shows that the standard deviation for the fraction attached metal is at least one order of magnitude smaller than the average value.

Generally, the spinodal initialization method has a smaller spread on the results than the method with random positioning of metal droplets. The smaller spread on the amount of attached metal for the spinodal initialization can be explained by the fact that in the case of spinodal decomposition, the droplets are formed next to the solid particle and thus will be more easily attached to the solid if this is energetically favoured by the interfacial energy values. Moreover, as was explained above, with the random initialization, it is possible that all larger droplets are concentrated in the border of the system, resulting in the dissolution of the smaller droplets, situated around the particle, leaving no metal attached to the particle, even though this might be favoured by the interfacial energies: e.g. simulations 2 and 3 in Table 6.2.

6.6.4. Simulations with realistic spinel microstructures

Two initialization methods were compared to investigate which corresponds best to the real mechanism behind the interaction between the solid particles and liquid metal. The spinodal initialization would correspond in practice to some sort of reaction, whereas the random initialization corresponds more to the situation when the droplets and particles are formed separately and then mixed in the slag. Realistic microstructures based on actual micrographs were used for the solid particles.

The spinodal initialization was carried out for an initial supersaturation of x_i = 0.605, which corresponds to a volume fraction of metal of 0.219. For the random initialization, the actual initial metal fraction is 0.2016 ± 0.0016 for x_S = 0.50 and 0.2015 ± 0.0008 for x_S = 0.58 for a proposed volume fraction of 0.20. Both initialization methods were applied for a non-wetting situation (x_S = 0.50) and an extremely low wetting case (x_S = 0.58 is the limit between the low and no wettability regimes). The results are shown as colour plots at different time steps throughout the simulation in Figure 6.19 and Figure 6.20, respectively.

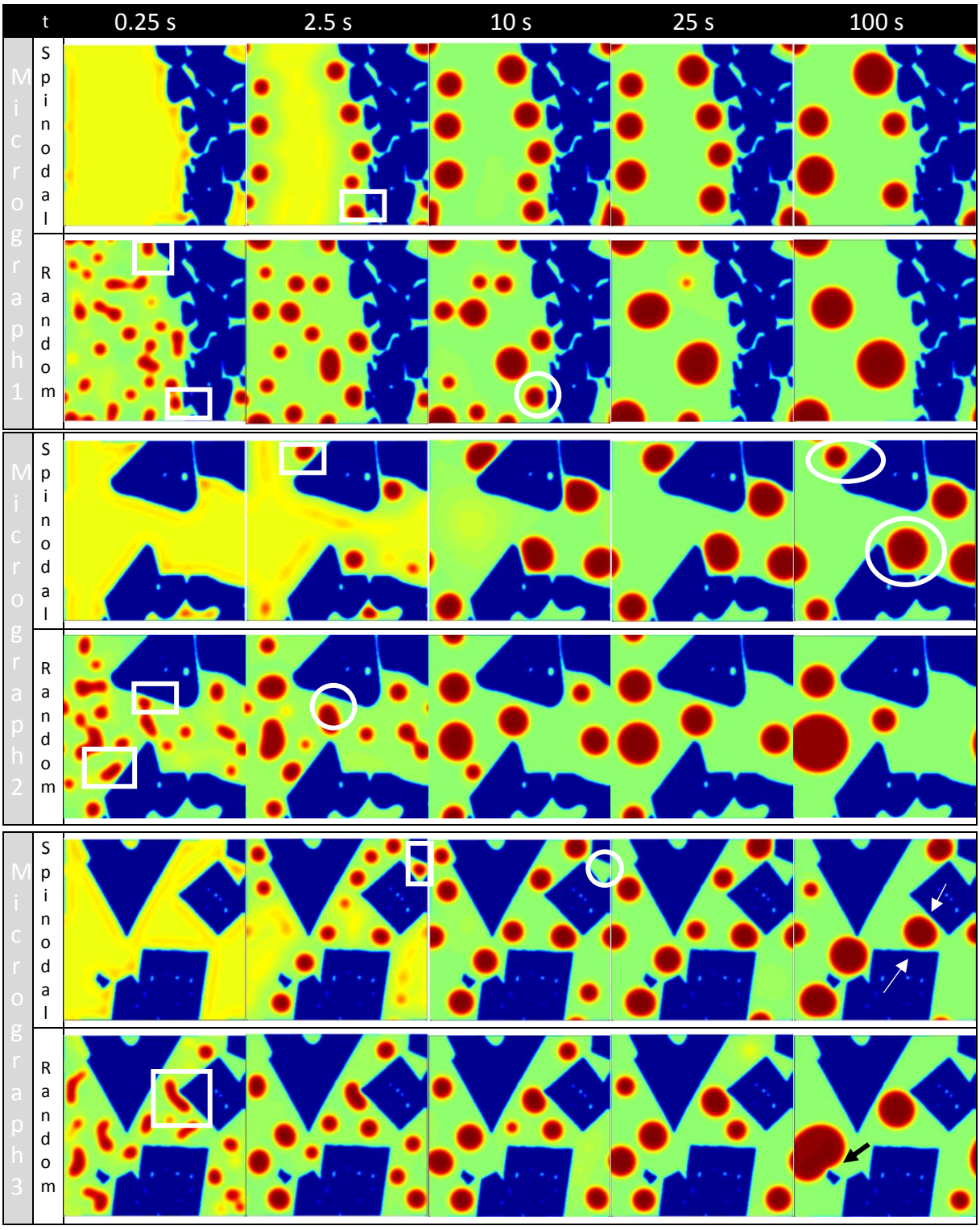
t
0.25 s
2.5 s
10 s
25 s
100 s
Micrograph1
Spinodal
Random
Micrograph2
Spinodal
Random
Micrograph3
Spinodal
Random

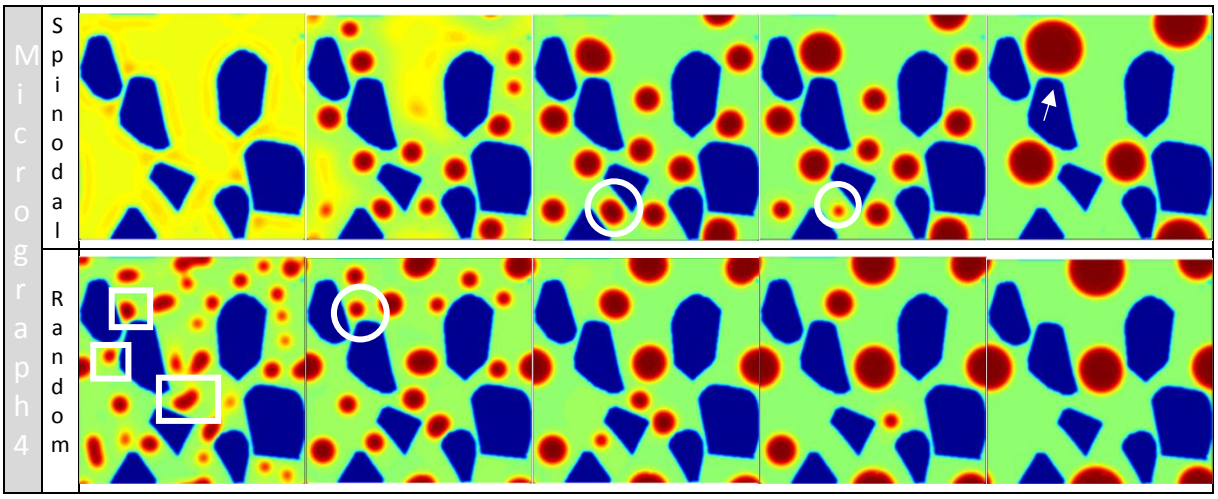

Figure 6.19 Comparison of the spinodal (upper row) and random (lower row) initialization methods in a non-wetting situation (x_S = 0.50)

In the case of spinodal decomposition, some metal is attached to solid particles in the first time steps, as indicated by the rectangles. Then this metal detaches or sometimes dissolves, marked by the circles. Depending on the shape of the particles, or more precisely, the amount of space available around the solid particles, some droplets are attached to solid particles again at intermediate time steps, as pointed to by the white arrows.

In the random initialization, some droplets are immediately attached to the solid particles, designated by the rectangles, but detached or dissolved again after approximately 10 s, indicated by the circles. In one simulation, one droplet was still attached to the solid at the final time step of 100 s. This was, however, a very large droplet attached to a very small solid particle, as illustrated by the black arrow.

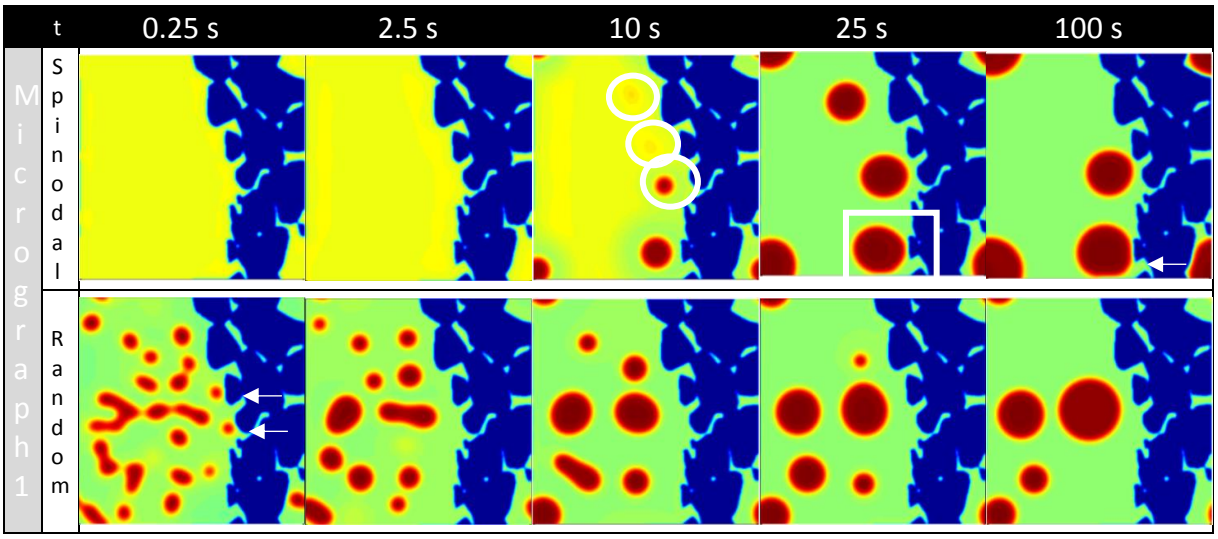

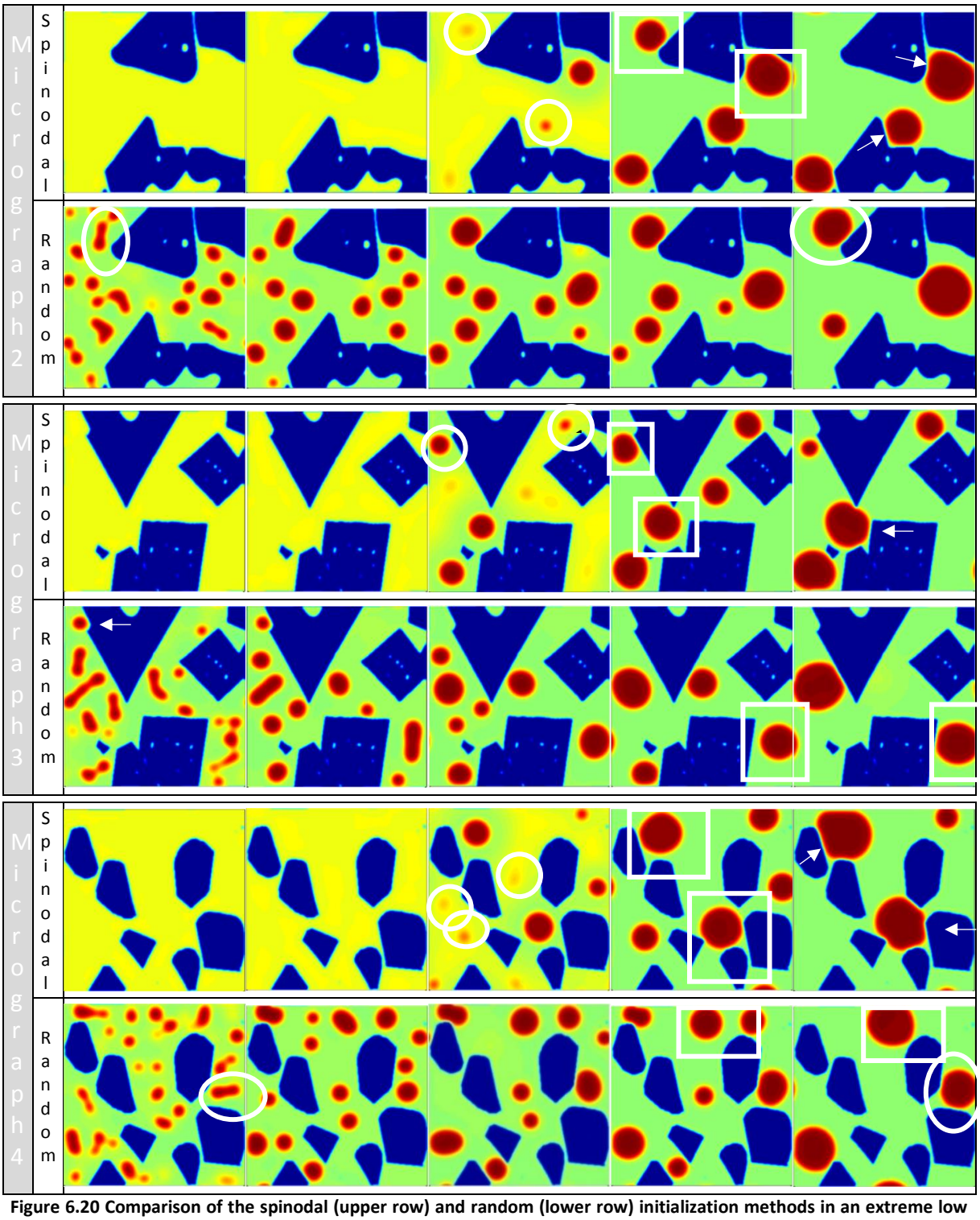

Figure 6.20 Comparison of the spinodal (upper row) and random (lower row) initialization methods in an extreme low wetting situation (x_s = 0.58)

For the spinodal initialization in the extreme low wetting case, the droplets initiate next to the solid particle, indicated by the circles, and grow subsequently to 'touch' the particle, marked by the rectangles. The droplets remain attached to the particles and even adopt their shape to the surrounding particles, as pointed to by the white arrows.

For the random initialization, three possibilities exist: the droplets are attached from the start to the end to the solid particles, indicated by the circles, the droplets are 'drawn' towards the solid particle and stay there until the end of the simulation, marked by the rectangles, or the attached droplets

detach/dissolve immediately and no more droplets are attached afterwards, illustrated by the white arrows. The droplet needs to be initialized close enough to the particle and should be large enough to remain attached to the solid. If the droplet is not large enough, it will dissolve, even though it was initially attached to the particle. Larger droplets, when positioned nearby the solid, will move towards it in the case of low wettability.

Not only does spinodal decomposition provide a convenient way to introduce the metallic droplets in the system, it appears that in both wetting regimes, the spinodal decomposition corresponds best with the experimentally obtained microstructures. Moreover, it was observed experimentally that the attachment of the droplets is a non-equilibrium phenomenon [2]. This indicates that the droplets may originate through reaction with or together with the solid particles, but that afterwards, once the reaction is finished, the droplets detach again. This corresponds with the observations for the simulations with spinodal decomposition in the non-wetting case.

It should be noted, however, that for the random initialization, attachment of droplets is also observed. This is mostly observed for the low wettability case and generally to a lesser extent than for the spinodal initialization. The fraction attached metal as a function of the particle fraction, which is characteristic for each micrograph, at the final 10^{6th} simulation step, which corresponds to 100 s, is shown in Figure 6.21.

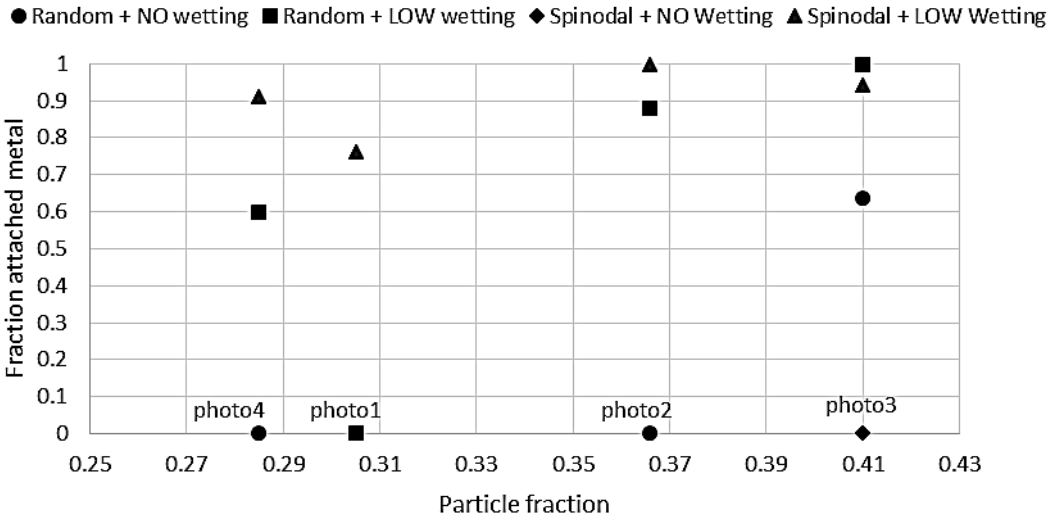

Figure 6.21 The fraction attached metal as a function of the particle fraction at the final simulation step (10^6), which corresponds to 100 s. The particle fraction is characteristic for each micrograph, which is indicated by the label above the x-axis

This shows that when the attachment is energetically favourable in the low wettability regime, both initialization methods yield attached metal droplets. The 'no' wettability case, only provided attached metal droplets for micrograph 3 with the random initialization, as indicated by the black arrow in Figure 6.19. Micrograph number 1 with the random initialization did not yield any attached droplets in both wetting regimes, because the droplets were not initialized close enough to the particles. The random initialization would correspond to mixing separately formed metal droplets and solid particles and it would require in practice intensive mixing to make them collide.

The spinodal initialization yields attached droplets in both the no and the low wettability regime in the initial stages, but the droplets in the low wettability case remain attached to the solids. The droplets in the non-wetting case, however, remain in close proximity of the particles.

References

[1] E. De Wilde, I. Bellemans, M. Campforts, A. Khaliq, K. Vanmeensel, D. Seveno, M. Guo, A. Rhamdhani, G. Brooks, B. Blanpain, N. Moelans, K. Verbeken, Wetting behaviour of Cu based alloys on spinel substrates in pyrometallurgical context, Mater. Sci. Technol. 31 (2015) 1925–1933. doi:10.1179/1743284715Y.0000000052.

[2] E. De Wilde, I. Bellemans, L. Zheng, M. Campforts, M. Guo, B. Blanpain, N. Moelans, K. Verbeken, Origin and sedimentation of Cu-droplets sticking to spinel solids in pyrometallurgical slags, Mater. Sci. Technol. 32 (2016) 1911–1924. doi:10.1080/02670836.2016.1151998.

7. Rigid body motion [15]

In the existing model, it is possible to use two initialization methods for the liquid metal droplets. One of the initialization methods uses spinodal decomposition of a supersaturated slag to introduce the metallic droplets, whereas the other initialization consists of positioning metallic droplets in the slag in a random way. The first initialization corresponds to a practical situation where the droplets are formed by a reaction nearby (and possibly together with) the spinel particles, whereas the latter initialization method corresponds to the situation where the droplets and particles are formed separately and then mixed randomly in the slag. However, one drawback of the model remained the absence of any convection or movement of the particles with respect to the fluids in the system. Therefore, the existing phase field model was extended to consider the motion of one phase with respect to the others.

7.1. Usual phase field modelling of convection or fluid flow

Numerical implementations of phase field models are able to use conventional advection routines because interface profiles can be maintained against distortion. [1] Usually, the phase field models for multi-component fluid flows with interfacial phenomena consist of a Navier-Stokes system coupled with a multi-component Cahn-Hilliard system. For this a concentration-dependent surface tension force is used, as well as a variable density and viscosity and an advection term. [2] The most popular model is the convective Cahn-Hilliard model:

$$\partial_t c + V\nabla c = \nabla\left(M\nabla\frac{\delta F}{\delta c}\right) \tag{7.1}$$

$$\rho_0\frac{DV}{Dt} = -\nabla P - \nabla(\eta(c)\nabla V \otimes \nabla V) + F_{body} + \nabla\tau \tag{7.2}$$

$$\nabla V = 0 \tag{7.3}$$

$$\mu = \frac{\delta F}{\delta c} \tag{7.4}$$

With V the macroscopic velocity field, c the concentration field, M the diffusive mobility, ρ the density (which varies with the phase field variable), P the pressure, η the viscosity (which also varies with the phase field variable), F_{body} the body forces and $\nabla\tau$ the surface tension force (which depends on the concentration field). Moreover, the D/Dt operator is the substantive derivative and equals $Dx/Dt = \partial_t x + V\nabla x$. [2] The capillary force term is complicated to evaluate and can be expressed in a simplified form:

$$\rho_0\frac{DV}{Dt} = -\nabla P + \mu\nabla c + F_{body} + \nabla\tau \tag{7.5}$$

The simultaneous solution of the large number of discrete equations arising form (7.2) and (7.3) is very costly. An efficient approximation can be obtained by decoupling the solution of the momentum equations from the solution of the continuity equation by a projection method, i.e. the pressure and the phase field are stored at the cell centre, whereas the velocities are stored at the cell interfaces. [2] Furthermore, the model ca be extended to consider stresses, heat, etc. [3]

[15] This chapter is based on the following publication: I. Bellemans, N. Moelans, K. Verbeken, Influence of rigid body motion on the wetting and attachment of metallic droplets to solid particles in liquid slags – a phase field study, Minerals & Metallurgical Processing, Submitted.

7.2. Proposed method for rigid body motion in phase field modelling

In this study, the previously described phase field model is extended to include rigid body motion of the solid particles with respect to the liquid. For this, the Navier-Stokes equation for fluid flow will not be solved, but an equation is added to move the phase field profiles in space, resulting in the displacement of the particle with respect to the slag:

$$\frac{\partial \phi}{\partial t} = -\nabla \cdot \left[m_x h(\phi), m_y h(\phi) \right] \tag{7.6}$$

This equation represents the movement of the particle, where m_x and m_y determine the speed with which this happens. The equation is similar to the equations used in the level-set method [4–6] and moves the ϕ-profile, after which the x_M adjusts itself to the new ϕ-profile. This is in contrast with a convection equation for x_M, where the ϕ-value adapts to the new x_M-value in the next time step. But in this study, a very small L-value was assumed (to simulate a non-reacting particle), which makes this second method very slow. Thus, a rigid body motion equation in ϕ was used instead. To apply this rigid body motion equation, very small time steps are needed, for which a sub-cycling implementation was used (i.e. for every phase field time step, 100 rigid body motion time steps passed).

7.3. Numerical implementation

The same parameters as in our previous studies [7–9] were used. To record a movement of the solid particle, very small time steps are required, but to reduce the computational time, this equation is solved using a different time step than the one used to solve the other evolution equations: for every phase field time step, 100 rigid body motion time steps passed. One simulation for system with size [256 256 1] and 10^6 time steps, typically took 6 to 7 days to be completed on an Intel® Core™ i7-3610QM CPU @ 2.30GHz processor with 8Gb RAM ranged from for a system size of.

During the first simulations, it became clear that this implementation indeed resulted in a solid particle shift, in the present case, towards the right-hand side of the system. However, the diffuse particle-liquid interface was not shifted along with the particle. Resulting in microstructures such as the one illustrated in Figure 7.1.

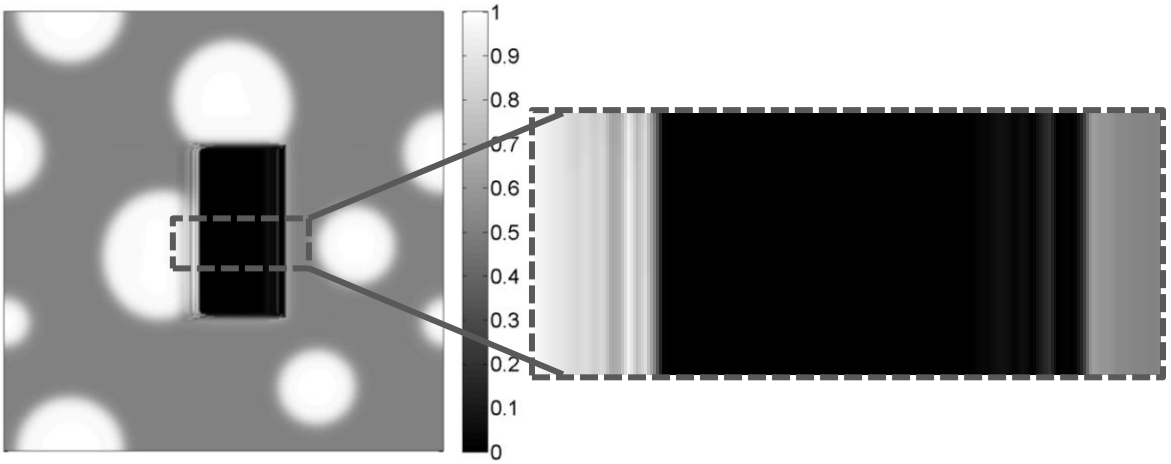

Figure 7.1 Illustration of loss of correct diffuseness for a simulation with spinodal initialization, x_I = 0.63 and x_S = 0.70 (low wetting regime) with a zoomed-in inset

On the right side of the particle, a sharp edge is formed, whereas on the left side of the particle, the diffuse remains of the particle do not move along with the rest of the particle. This is a clear anomaly as opposed to the simulations without rigid body motion. As mentioned previously, during the first 1000 time steps, a larger kinetic coefficient of $L_{initial} = 10^{-7}$ m³/(J s) for the phase field evolution was used, in contrast to $L = 10^{-30}$ m³/(J s) in the rest of the simulation, to allow the boundaries of the particle to become diffuse. To obtain a correct diffuse interface profile at all particle interfaces, L was taken equal to L_{inital} every 100th time step over the whole simulation. This results in the microstructural image as shown in Figure 7.2.

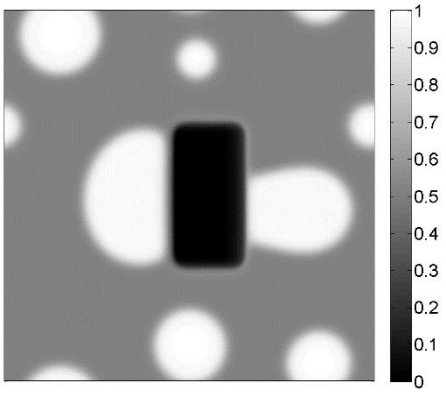

Figure 7.2 Microstructure when $L_{initial}$ is also used every 100th time step to obtain correct diffuseness of the interfaces for a simulation with spinodal initialization, $x_i = 0.63$ and $x_s = 0.70$ (low wetting regime)

The diffuseness at the edges is better, i.e. the right edge is no longer sharp and on the left edge, the diffuse remains of the particle from previous time steps are no longer present. It is, however, clear that the corners of the rectangular particle become more blunted by this action. The change in area for the simulation in which L is taken equal to $L_{initial}$ every 100th time step is 1.51 % (= 100 * (5000 - A_{final}) / 5000), whereas the change in area is 0.12 % if $L_{initial}$ is only used in the first 1000 time steps. As an area reduction of 1% probably has negligible influence on the results, the implementation of the abovementioned use of $L_{initial}$ in every 100th time step was chosen. However, after every simulation, special care was taken to investigate the change in area of the solid particle to assure that it did not shrink too much. A large change in particle area would make it impossible to compare the simulations with rigid body motion to simulations without rigid body motion

To reconstruct the diffuse solid-liquid interfaces during the rigid body motion of the particles, the very small L–value is replaced by the larger $L_{initial}$–value in every 100th time step. The influence of this was investigated for the simulations with the spinodal initialization and x_i = 0.605; 0.63 and 0.65, respectively, and for all the x_S-values. The change in area of the solid particle (over the whole simulation) is calculated by summing ϕ over all grid points and multiplying with $(\Delta x)^2$ and is expressed as the relative error (= 100 * | $A_{\text{with extra Linitial}} - A_{\text{without}}$ | / A_{without}) in Table 7.1. The error is mostly of the order of 1% and thus relatively low.

x_s	x_i=0.605	x_i=0.63	x_i=0.65
0.5	1.20	1.28	1.40
0.6	0.41	1.26	1.28
0.7	1.95	1.40	1.39
0.74	2.10	1.66	1.43
0.8	2.11	2.02	1.80
0.9	1.52	1.52	1.51

Table 7.1 Relative error [%] of the change in area of the solid particle for the different x_i,x_S-combinations

7.4. Results and discussion

7.4.1. Influence of rigid body motion on the microstructure

The influence of the rigid body motion with a speed of 1 Δx per 10 s ($1.26 \cdot 10^{-8}$ m/s) on the finally obtained microstructures is illustrated in Figure 7.3 and Figure 7.4 for the spinodal and the random initialization, respectively (x_S = 0.74 is not shown but the behaviour is between x_S = 0.70 and x_S = 0.80).

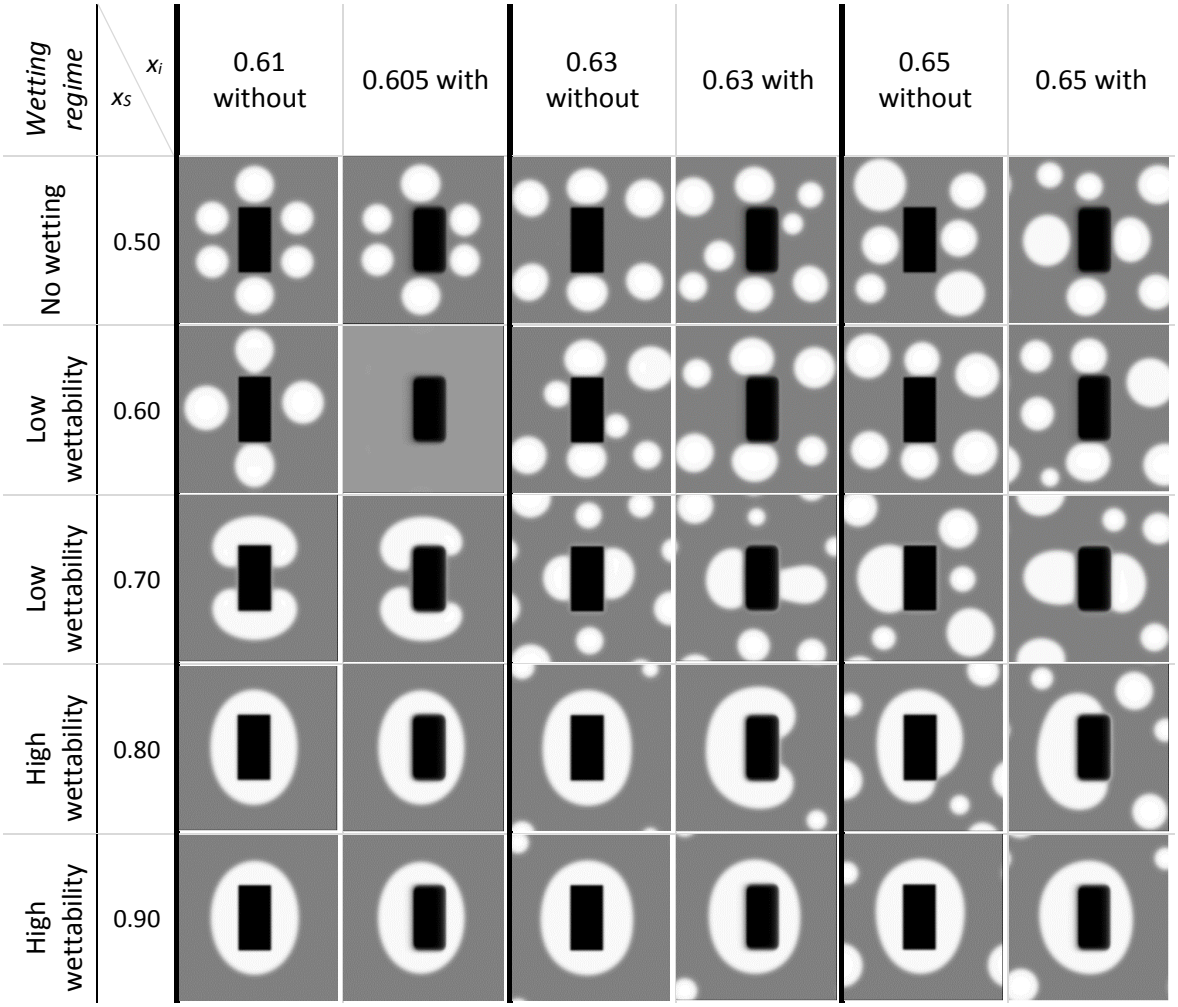

Figure 7.3 the influence of x_i and x_S (wetting regime) on the resulting microstructures for spinodal initialization

It should be noted that for x_i = 0.605 and x_S = 0.60, no spinodal decomposition took place, because the system can be considered as almost 'stable', as both compositions are very close to one another. The combination in this study yields an even more stable situation than for x_S = 0.60 and x_i = 0.61 in section 6.2, where it also took quite some time before spinodal decomposition took place.

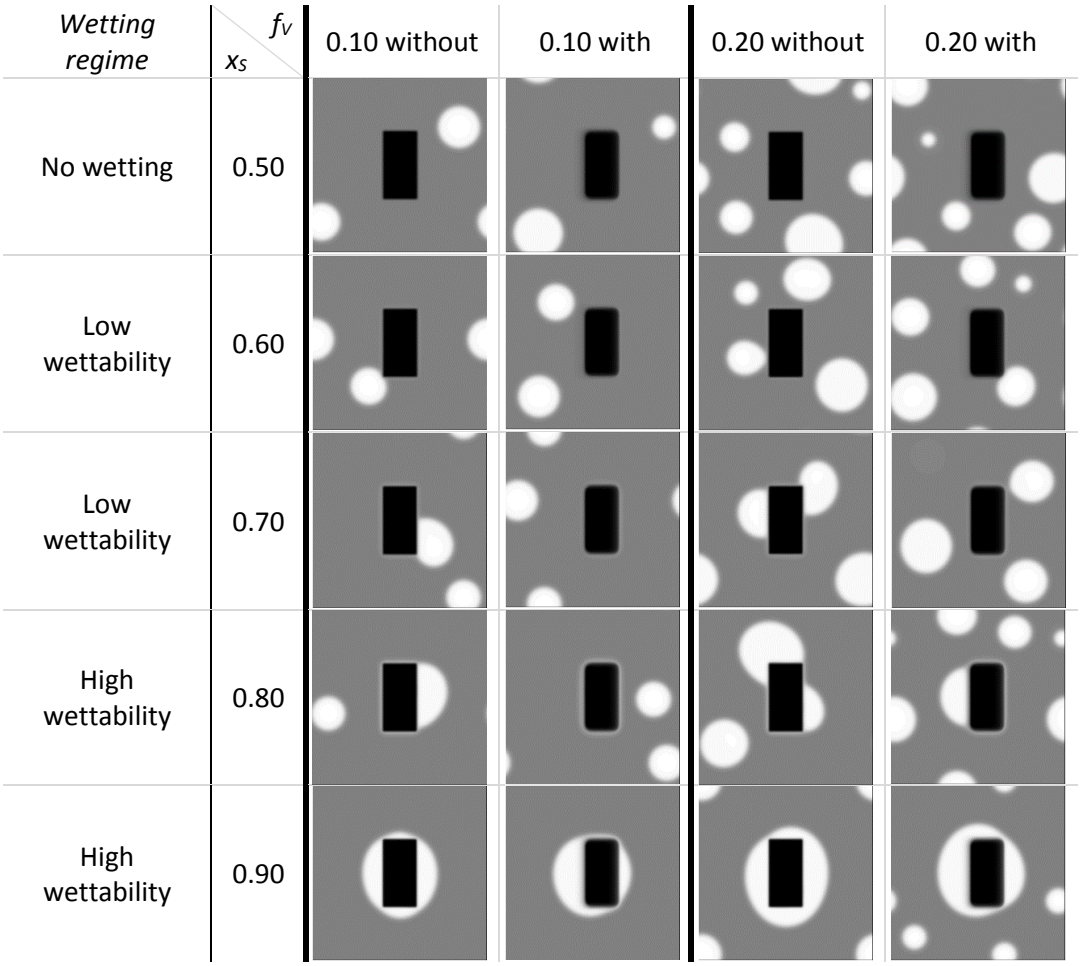

Figure 7.4 the influence of x_i and x_S on the resulting microstructures for random initialization

In the no wetting regime, the influence of the rigid body motion seems to be twofold. As the solid particle moves, it can either have metal droplets already attached to it, due to interfacial energies, but can lose this when the droplet is attached to the side of the particle in the opposite way of the rigid body motion (i.e. here the left side of the solid particle), for example in the x_i = 0.65; x_S = 0.50-case. However, it is also possible that a particle initially did not have metal attached to it, but 'meets' a droplet on its way, which also happens in the x_i = 0.65; x_S = 0.50-case.

From the low wettability regime onwards, the influence of the interfacial energies come into play and this results in the movement of the droplets towards the solid particle, as illustrated by the left side of the particle in the f_V = 0.20; x_S = 0.60-case without rigid body motion. If the rigid body motion is then added, a solid particle without metal attached to it, moves towards a metal droplet, which in turn will also be slightly attracted to the solid particle due to the interfacial energies. If a solid particle has a metal droplet attached to it, no detachment from the particle was observed when the particle was moving away from the attached droplet, even though the attachment is not very strong.

At the higher wetting regimes, the influence of the interfacial energies becomes more important, i.e. attachment of metal to the solid particle is extremely favourable from an energetic point of view. This results in the droplet remaining attached to the solid particle.

7.4.2. Influence of rigid body motion on the amount of attached metal

The influence of the rigid body motion on the area of attached metal is shown in the graphs in Figure 7.5. The simulation results (denoted 'with') are compared to the results from section 6.2, in which rigid body motion was not present (denoted 'without').

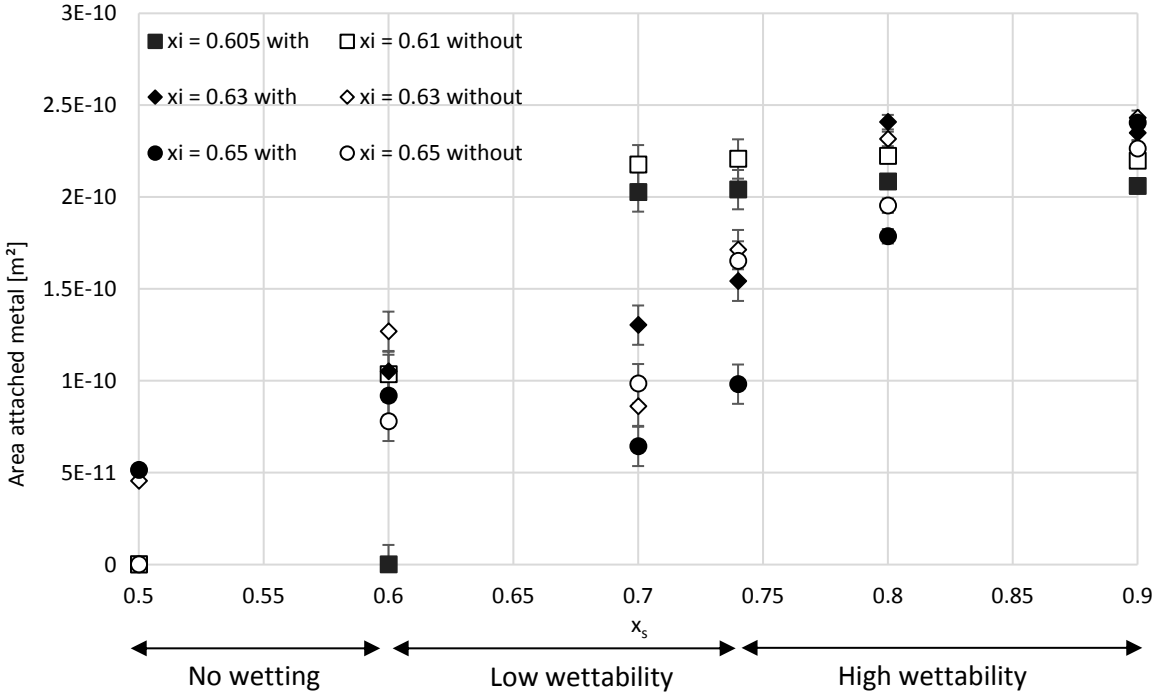

Figure 7.5 area attached metal for several x_i,x_s-combinations to investigate the influence of rigid body motion (assigned as 'with')

For x_i = 0.605, more metal is attached to the solid particle when no rigid body motion is present in the system, except for x_S = 0.60. However, this finds its origin in the fact that in this study we investigated x_i = 0.605 instead of 0.61 as in the previous study (this x_i = 0.605 in turn was chosen to be able to compare to the other initialisation method with f_V = 0.20). Because x_i = 0.605 was investigated, less metal was present in the system and this also influences the amount of attached metal. This is also visible in the fact that the fraction of attached metal does not change when rigid body motion is applied to the system. Moreover, for x_i = 0.605 and x_S = 0.60, no spinodal decomposition took place, as observed previously.

For x_i = 0.63, no conclusive effect of the presence of rigid body motion of the solid particle on the amount of attached metal can be observed. For x_i = 0.65, except for the non and the full wetting case, the simulations with rigid body motion have less attached metal to the solid particle. However, on average, there is no effect on the amount of metal attached to the solid particle. The same comparison between presence and absence of rigid body motion was made for the random initialization, as shown in Figure 7.6.

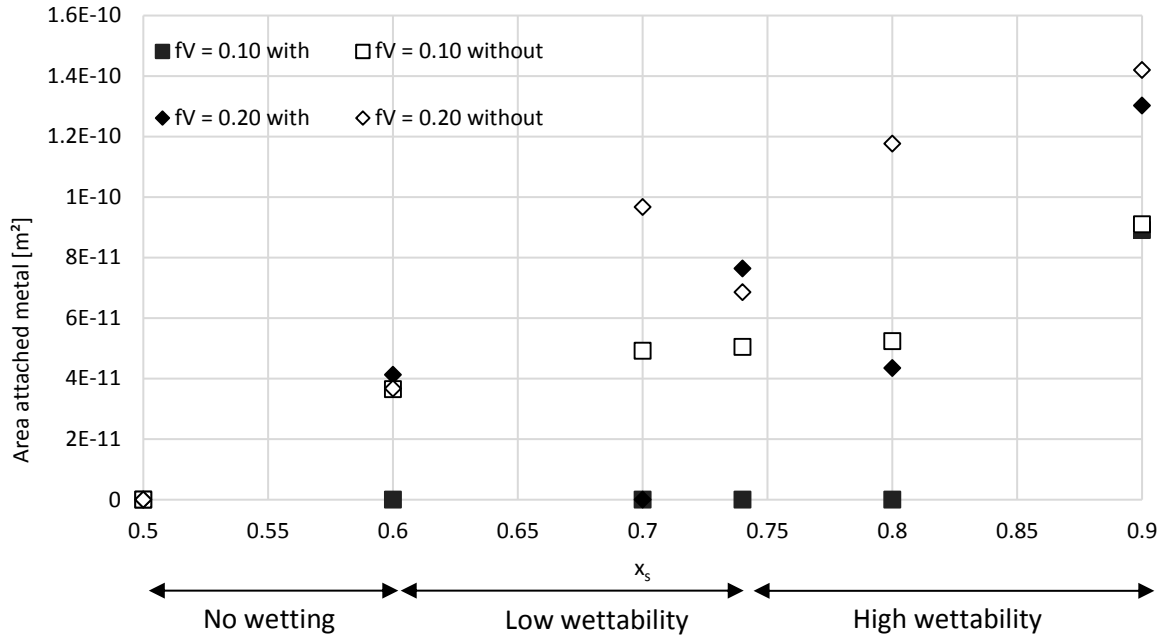

Figure 7.6 area attached metal in several f_V,x_S-combinations to investigate the influence of rigid body motion (assigned as 'with')

In most cases, the amount of attached metal seems larger for the cases without rigid body motion.

7.4.3. Influence of rigid body motion on the contact angle

Another quantitative measure of the influence of the rigid body motion on the microstructure can be found in the apparent contact angle. A comparison of the mean contact angles for situations with and without rigid body motion are tabulated in Table 7.2 and Table 7.3, for the spinodal and random initializations, respectively.

x_S	$\theta_{predicted}$ (°)	$\theta_{xi=0.61}$(°) without	$\theta_{xi=0.61}$(°) with	$\theta_{xi=0.63}$ (°) without	$\theta_{xi=0.63}$ (°) With	$\theta_{xi=0.65}$ (°) without	$\theta_{xi=0.65}$ (°) with
0.5	/	/	/	164.2±5.2	/	/	150.2±3.9
0.6	147.5	152.8±2.3	/	148.1±9.2	158.1±10.7	155.3±7.2	143.3±7.8
0.7	102.6	103.3±5.7	105.5±16.3	104.3±8.9	123.8±16.2	111.8±2.7	115.0±9.4
0.74	90.0	Full	73.5±2.8	87.1±2.7	114.1±27.3	85.4±5.7	112.1±18.3
0.8	70.6	Full	Full	Full	55.1±4.5	70.4±4.1	81.8±5.9
0.9	6.1	Full	Full	Full	Full	Full	Full

Table 7.2 Comparison of the predicted and measured contact angles (°) of the metallic droplets attached to the solid particle for the spinodal initialization

x_S	$\theta_{predicted}$ (°)	$\theta_{fV=0.1}$(°) without	$\theta_{fV=0.1}$(°) with	$\theta_{fV=0.2}$(°) Without	$\theta_{fV=0.2}$(°) with
0.5	/	/	/	/	/
0.6	147.5	146.9±7.6	/	128.9±2.7	160.2±2.3
0.7	102.6	111.4±38.5	/	96.1±10.4	/
0.74	90.0	102.2±7.6	/	79.5±38.5	98.6±13.4
0.8	70.6	73.4±15.8	/	71.2±13.2	77.4±11.0
0.9	6.1	Full	Full	Full	Full

Table 7.3 Comparison of the predicted and measured contact angles (°) of the metallic droplets attached to the solid particle for the random initialization

For x_i = 0.605 and x_i = 0.63, the full wetting regime is encountered at larger x_S-values (corresponding to higher wetting regimes) when rigid body motion is present. Moreover, in most of the cases, the apparent contact angle is larger when rigid body motion is present. Except for the x_i = 0.65; x_S = 0.50-case, which was an illustration that the rigid body motion can increase the attachment of the metal to the solid particle in the no and low wetting cases. On the other hand, a larger apparent contact angle corresponds to a lower wettability. The reason for this can be that the particle 'pushes' its way through the liquid metal. It should be noted that this effect is very clear, even though the speed of movement of the solid particle is rather low. Ogino et al. [10] and Muhmood et al. [11] also observed that during intense mass transfer between two phases, a low apparent interfacial tension is the result.

The fact that rigid body motion makes it appear that a lower wetting regime is present than expected based on the contact angles predicted by Young's equation sheds a new light on the previous comparison of experimental observations in a PbO-FeO-CaO-SiO_2-Cu_2O-ZnO-Al_2O_3 system [12] to our simulations in chapter 6. It could imply that the actual wetting regime is not a low-almost-no wetting regime, but, depending on the velocity with which the particles move in the liquid, it could as well correspond to a higher (but still low) wetting regime.

It would be expected that the influence of the rigid body motion on the apparent contact angle disappears again once the rigid body motion is stopped. This was also checked with simulations without rigid body motion starting from the final situation (x_M and ϕ-values) of a simulation with rigid body motion. These simulations ran for 10^7 time steps and the measured apparent contact angles are tabulated in Table 7.4.

x_S	$\theta_{predicted}$ (°)	$\theta_{xi=0.63}$ (°) without	$\theta_{xi=0.63}$ (°) With	*Equilibration after with*
0.5	/	164.2±5.2	/	/
0.6	147.5	148.1±9.2	158.1±10.7	144.4±12.8
0.7	102.6	104.3±8.9	123.8±16.2	108.0±4.4
0.74	90.0	87.1±2.7	114.1±27.3	100.3±13.0
0.8	70.6	full wetting	55.1±4.5	41.4±19.7
0.9	6.1	full wetting	full wetting	Full wetting

Table 7.4 Comparison of the predicted and measured contact angles (°) of the metallic droplets attached to the solid particle for the spinodal initialization with x_i = 0.63 without and with rigid body motion and for a simulation without rigid body motion, starting from the final simulation step of a rigid body motion simulation

It is observed that these 'equilibration' simulations result in contact angles that return towards the values corresponding to the motionless simulations, as expected. Only the x_S = 0.80-case did not return to the full wetting situation where the solid is surrounded by a metallic droplet, as illustrated in Figure 7.7.

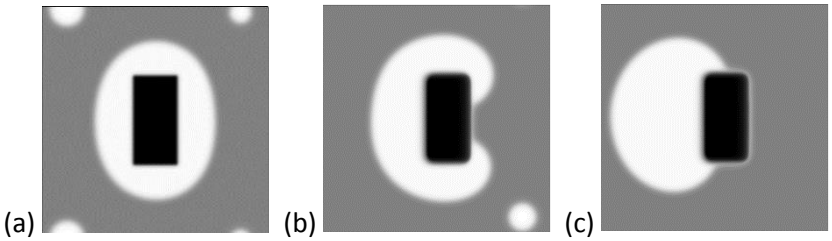

Figure 7.7 The comparison of the apparent contact angle between three different cases: (a) without movement of the solid particle; (b) with the rigid body motion of the solid particle; (c) an 'equilibration' simulation without movement of the solid particle (starting from the final result in (b)).

7.4.4. Influence of the speed of rigid body motion

The speed of the rigid body motion of the solid particles, *m*, was varied: the solid particle moved with either 5 *Δx* per 10 s ($6.32 \cdot 10^{-8}$ m/s) or 10 *Δx* per 10 s ($1.26 \cdot 10^{-7}$ m/s). These results will be compared with the results of our previous study at a speed of 1 *Δx* per 10 s ($1.26 \cdot 10^{-8}$ m/s). As a reference, the characteristic diffusion distance is $\sqrt{Dt}$ and can be considered as a measure for the distance the metal can diffuse during the simulation. In this case, i.e. for 100 s, this distance equals $6.32 \cdot 10^{-5}$ m, which results in an average speed of $6.32 \cdot 10^{-7}$ m/s. The influence of the rigid body motion on the finally obtained microstructures is illustrated in Figure 7.3.

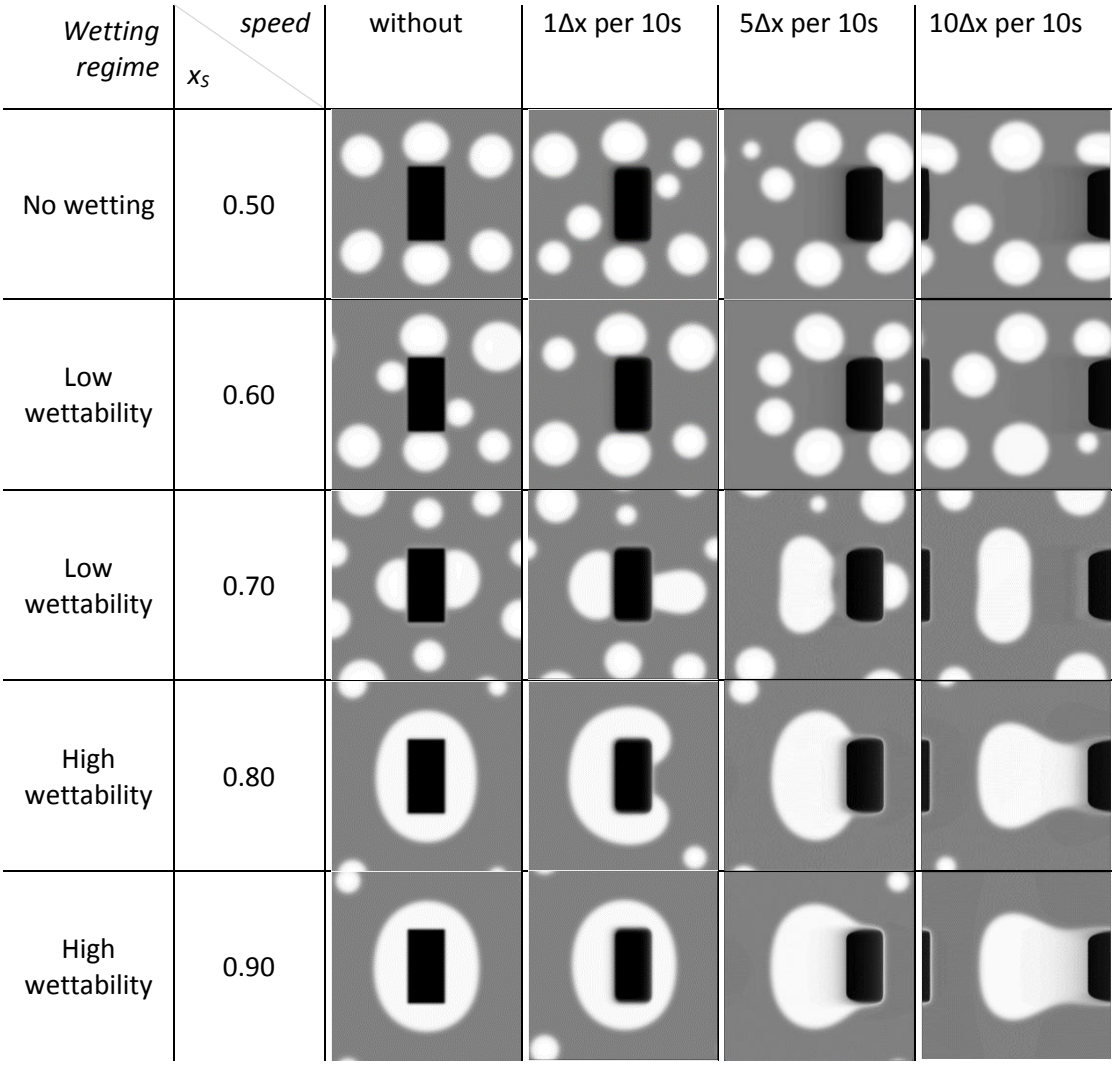

Figure 7.8 the influence of the speed of motion of the solid particle and x_S on the resulting microstructures for spinodal initialization (x_i = 0.63)

The fact that the shape of the solid particles is changed, i.e. the angles and corners are softened, finds it origin in taking the kinetic coefficient for the phase field evolution larger every 100th time step, which in turn is needed to move the diffuse interface along with the bulk solid particle when rigid body motion takes place. In the non-wetting regime, it is clear that the attachment of the metal to the solid particle depends on coincidence, i.e. whether or not a metal droplet is present on the path in which the solid particle moves. Thus, there is no influence of the solid particle speed. For the low, and high wetting regimes, however, the influence of the interfacial energies becomes larger, which means that the metal will try to remain attached to the solid particle, by moving along with it.

However, if the solid moves too fast, for example in the 10Δx per 10s case, the metal liquid cannot keep up with the solid and the attachment disappears. Finally, in the full wetting case (x_s = 0.90), the interfacial energy attraction of the metal towards the solid is so high that the liquid follows the solid even at very high velocities.

The influence of the speed of rigid body motion on the area of attached metal is shown in the graphs in Figure 7.6 for the different x_S-values, and thus for different wetting regimes.

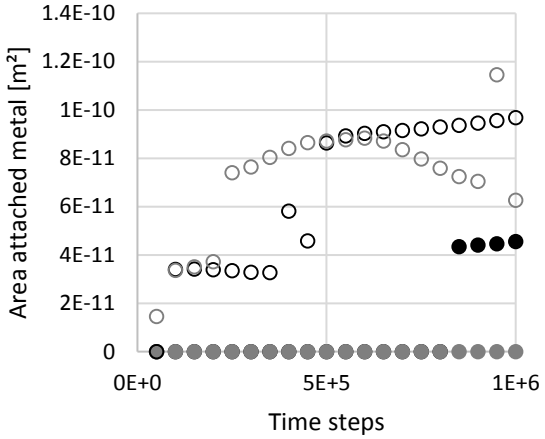

(a) x_S = 0.50 (non-wetting)

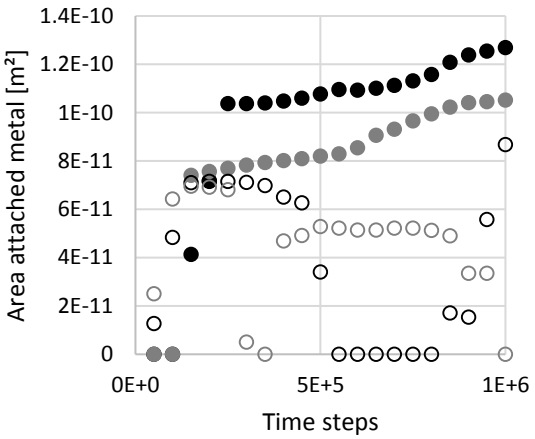

(b) x_S = 0.60 (low wetting)

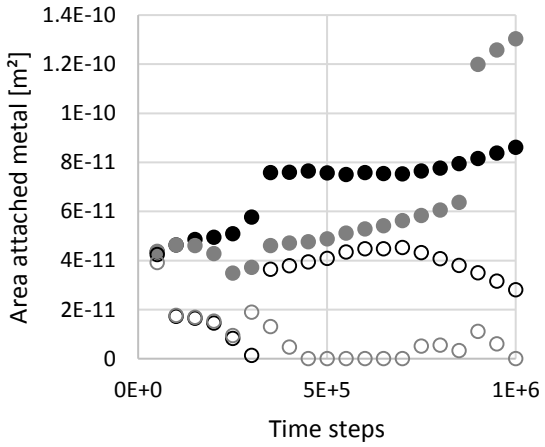

(c) x_S = 0.70 (low wetting)

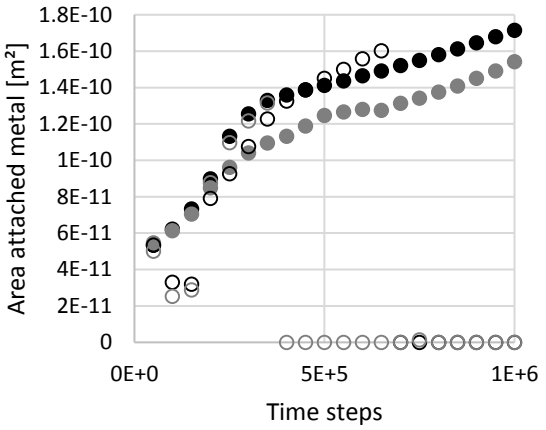

(d) x_S = 0.74 (contact angle of 90°)

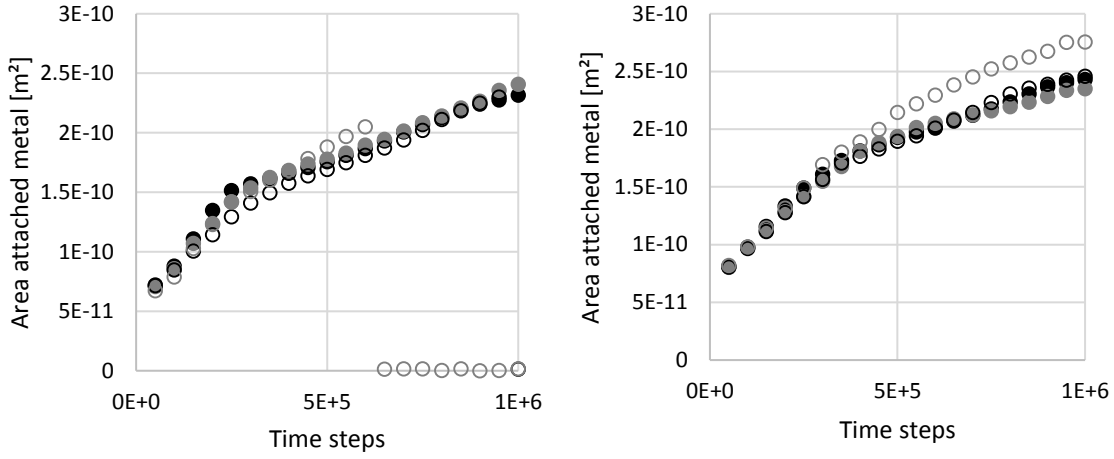

(e) x_S = 0.80 (high wetting) (f) x_S = 0.90 (high wetting)

Figure 7.9 area attached metal for several values of the speed of motion of the solid particles for different x_S-values (or wetting regimes). Full black symbols represent the simulations without rigid body motion; grey full symbols represent the simulation with a solid particle velocity of 1 *Δx*/10 s; the open black symbols represent the simulation with a solid particle velocity of 5 *Δx*/10 s and the open grey symbols represent the simulation with a solid particle velocity of 10 *Δx*/10 s

It is clear that at a low speed of the solid particle, it does not influence the amount of attached metal significantly, as was already observed in section 7.4.2. However, when the solid particle moves faster, a clearer influence becomes visible, depending on the wetting regime.

For the non-wetting case (x_S = 0.50), there is no clear influence of the movement of the solid particle, it results in either a 'pick up' of droplets, hereby increasing the amount of attached metal, or it can lose an already attached metal droplet.

For the low wettability cases (x_S = 0.60 and 0.70), the amount of attached metal decreases as the speed of motion of the solid particle increases. At x_S = 0.74, with an expected contact angle of 90°, the velocities of x5 and x10 clearly show the disappearance of attached metal to the solid particle. Also note that this detachment happens faster at a velocity of x10.

For the high wetting regime (x_S = 0.80), the interfacial energies favour the attachment of the metal to the solid more, which is also seen in the fact that the detachments for both the x5 and x10 velocity take place at a later time step than for x_S = 0.74.

Finally, at a value of x_S = 0.9, which corresponds to very high wetting, the attachment of the metal to the solid is energetically so favourable that the metal remains attached during the whole simulation, even during the very fast movement of the solid particle.

7.4.5. Realistic microstructures for solid particles

The influence of rigid body motion with a relatively low speed of 1 *Δx* per 10 s ($1.26 \cdot 10^{-8}$ m/s) was investigated while comparing two initialization methods, moreover, realistic microstructures, based on actual micrographs, were used for the solid particles. The spinodal initialization was carried out for an initial supersaturation of x_i = 0.605, which corresponds to a volume fraction of metal of 0.219. For the random initialization, the actual initial metal fractions are: 0.202 ± 0.001; 0.202 ± 0.001; 0.205 ± 0.002 and 0.201 ± 0.001, respectively for micrographs 1 until 4, for a proposed volume fraction of 0.20. Both initialization methods were applied for a non-wetting situation (x_S = 0.50), an extremely low wetting case (x_S = 0.58 is the limit between the low and no wettability regimes) and a low wetting

case (x_S = 0.60). The results are shown as greyscale plots at the final time step in Figure 7.10, Figure 7.12 and Figure 7.14. For the x_S = 0.50 and x_S = 0.58 cases, the resulting microstructures are compared to the microstructures without the presence of rigid body motion, from our previous work [9]. For the x_S = 0.60 case, extra simulations without rigid body motion were conducted for comparison.

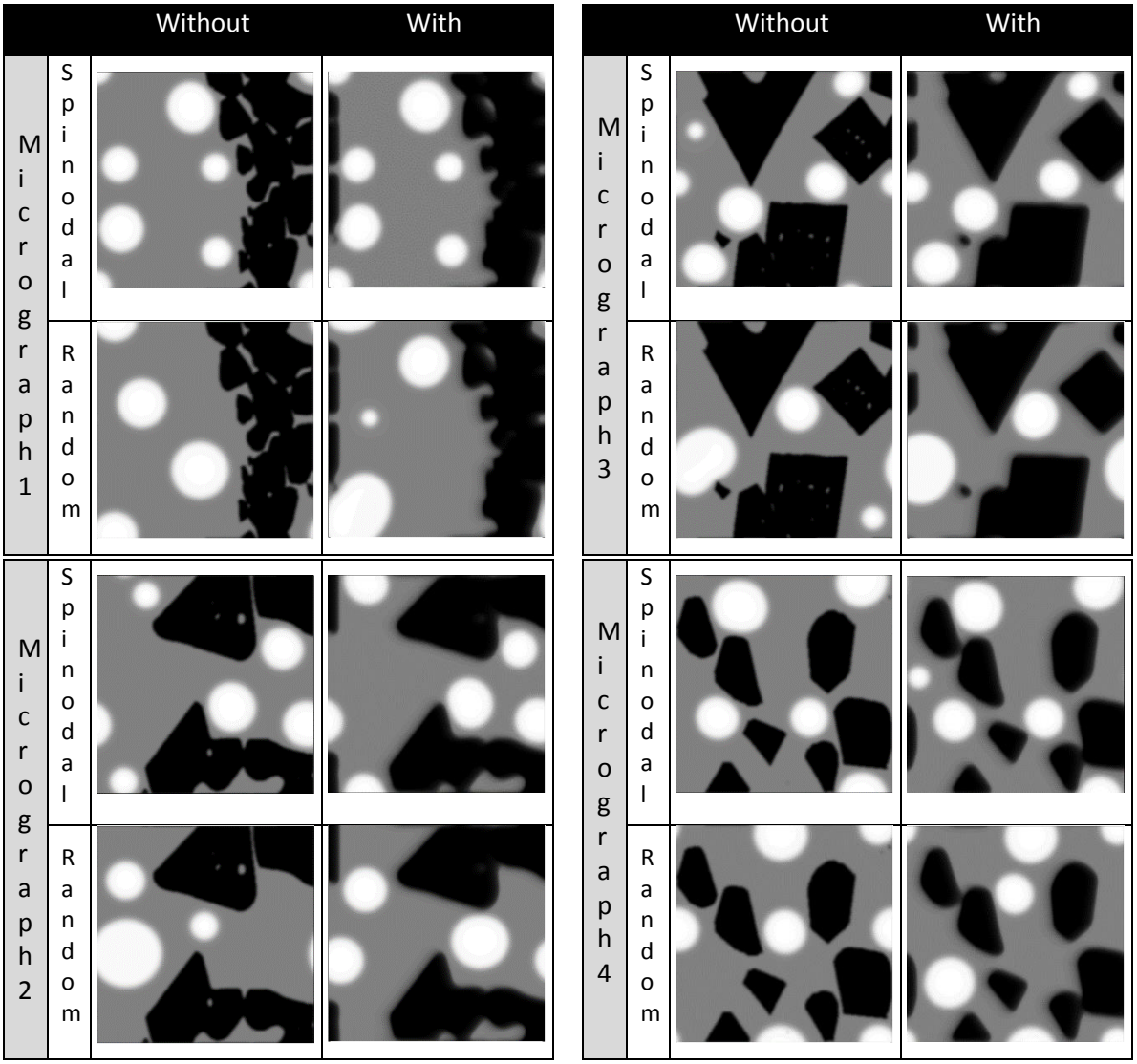

Figure 7.10 Comparison of the spinodal (upper row) and random (lower row) initialization methods in a non-wetting situation (x_S = 0.50)

In the no-wetting regime, the rigid body motion can be responsible for both attachment and detachment of solid particles, as was already observed in section 7.4.1. The area and fraction attached metal as a function of the particle fraction, which is characteristic for each micrograph, at the final $10^{6\,th}$ simulation step, which corresponds to 100 s, are shown in Figure 7.11.

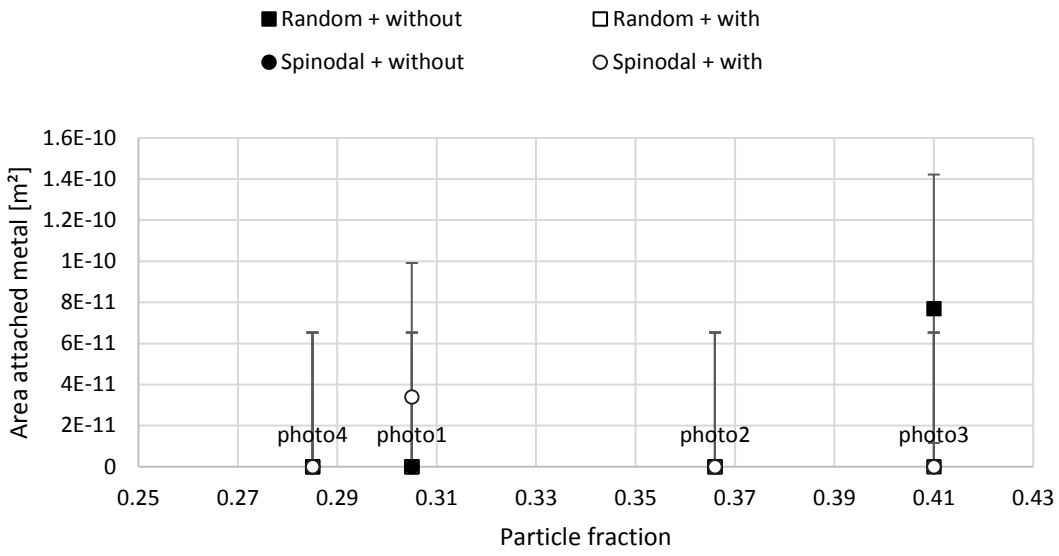

Figure 7.11 The area and fraction attached metal as a function of the particle fraction at the final simulation step (10^6), which corresponds to 100 s for the non-wetting case ($x_S = 0.50$). The particle fraction is characteristic for each micrograph, which is indicated by the label above the x-axis

In the non-wetting case, most of the metal remains unattached. Rigid body motion can both increase the amount of attached metal, such as for the spinodal initialization for micrograph 1, or decrease it, such as for the random initialization for micrograph 3. However, it should be noted that this seems to be somewhat arbitrary and that an increase is also possible for the random initialization and a decrease for the spinodal initialization.

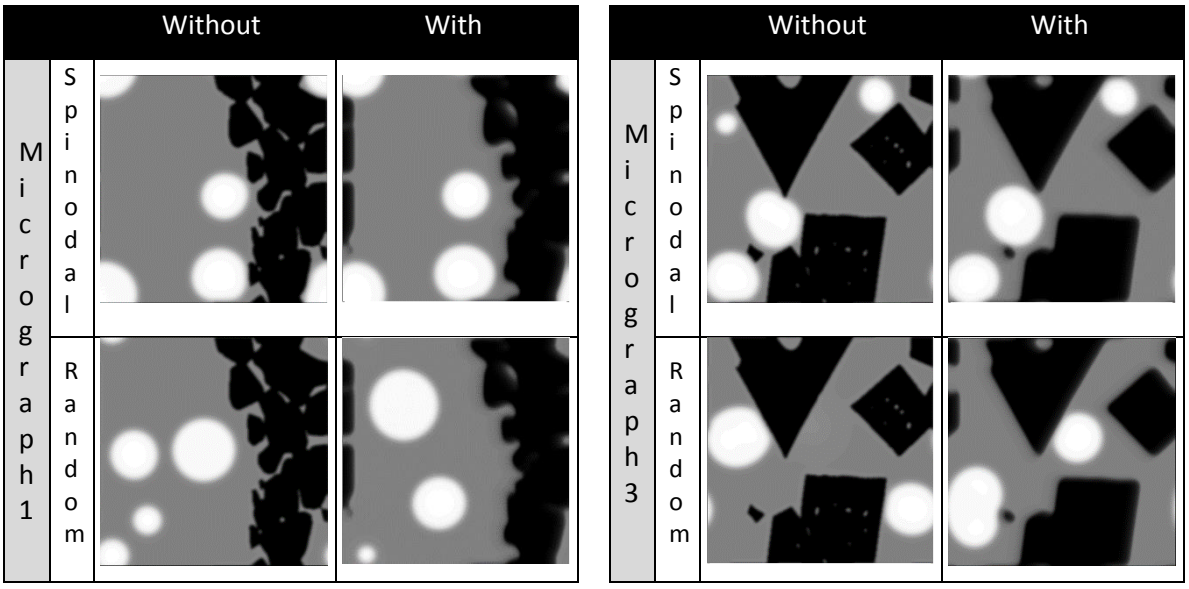

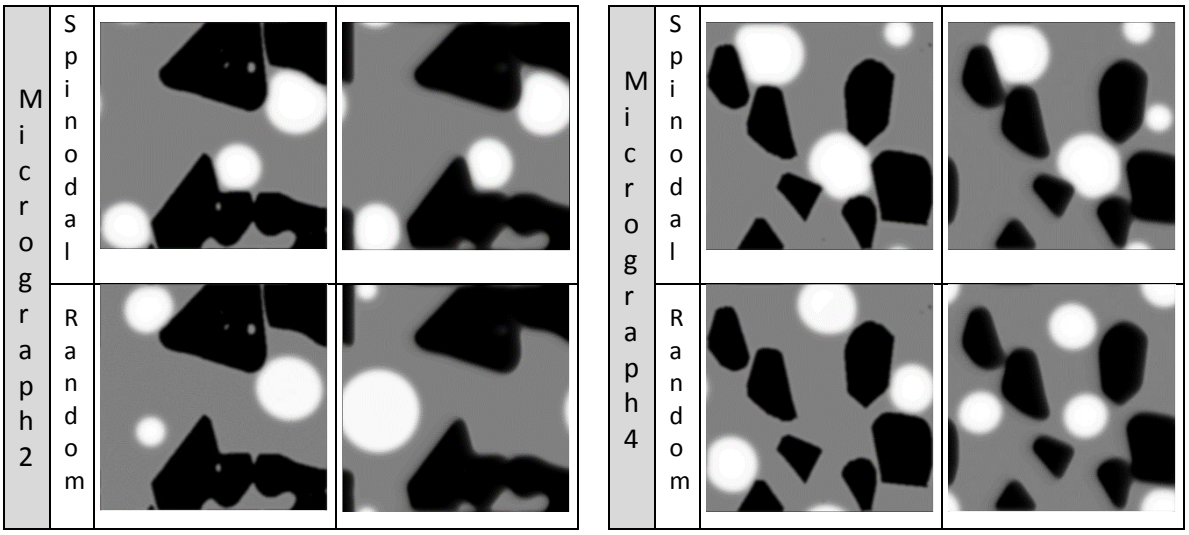

Figure 7.12 Comparison of the spinodal (upper row) and random (lower row) initialization methods in an extreme low wetting situation (x_s = 0.58)

In between the no and low wetting case (x_S = 0.58), the rigid body motion can also cause both detachment and attachment of the metal droplets to the solid particles. But the movement of the solid seems to mainly decrease the amount of attached metal, as also illustrated quantitatively in Figure 7.13.

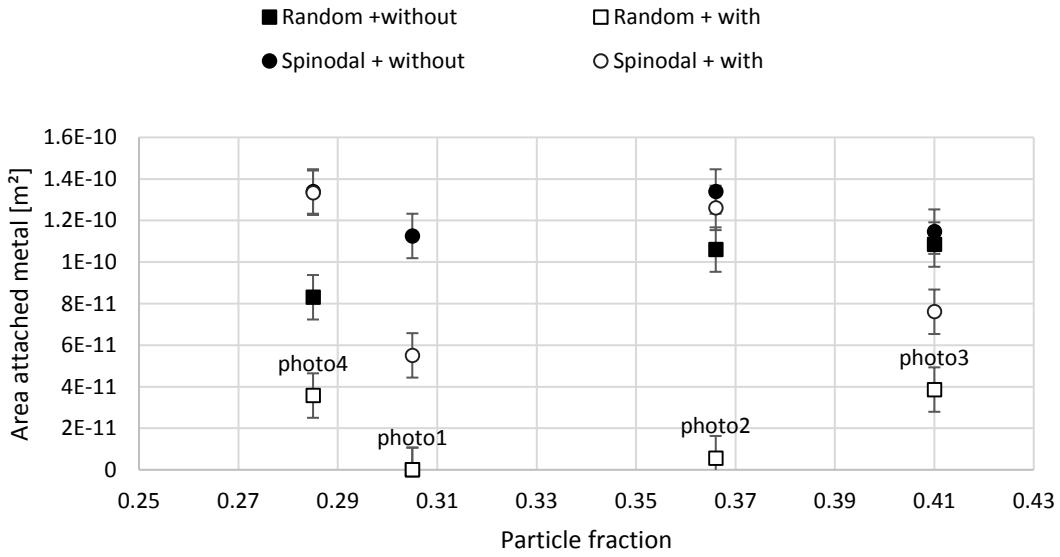

Figure 7.13 The area and fraction attached metal as a function of the particle fraction at the final simulation step (10^6), which corresponds to 100 s for the limiting case (x_S = 0.58). The particle fraction is characteristic for each micrograph, which is indicated by the label above the corresponding white rectangle

As observed in section 7.4.2, in the low wettability case, the amount of attached metal is lower when rigid body motion is present in the system. Whether this is also the case for the low wetting case (x_S = 0.60) is investigated qualitatively in Figure 7.14 and quantitatively in Figure 7.15.

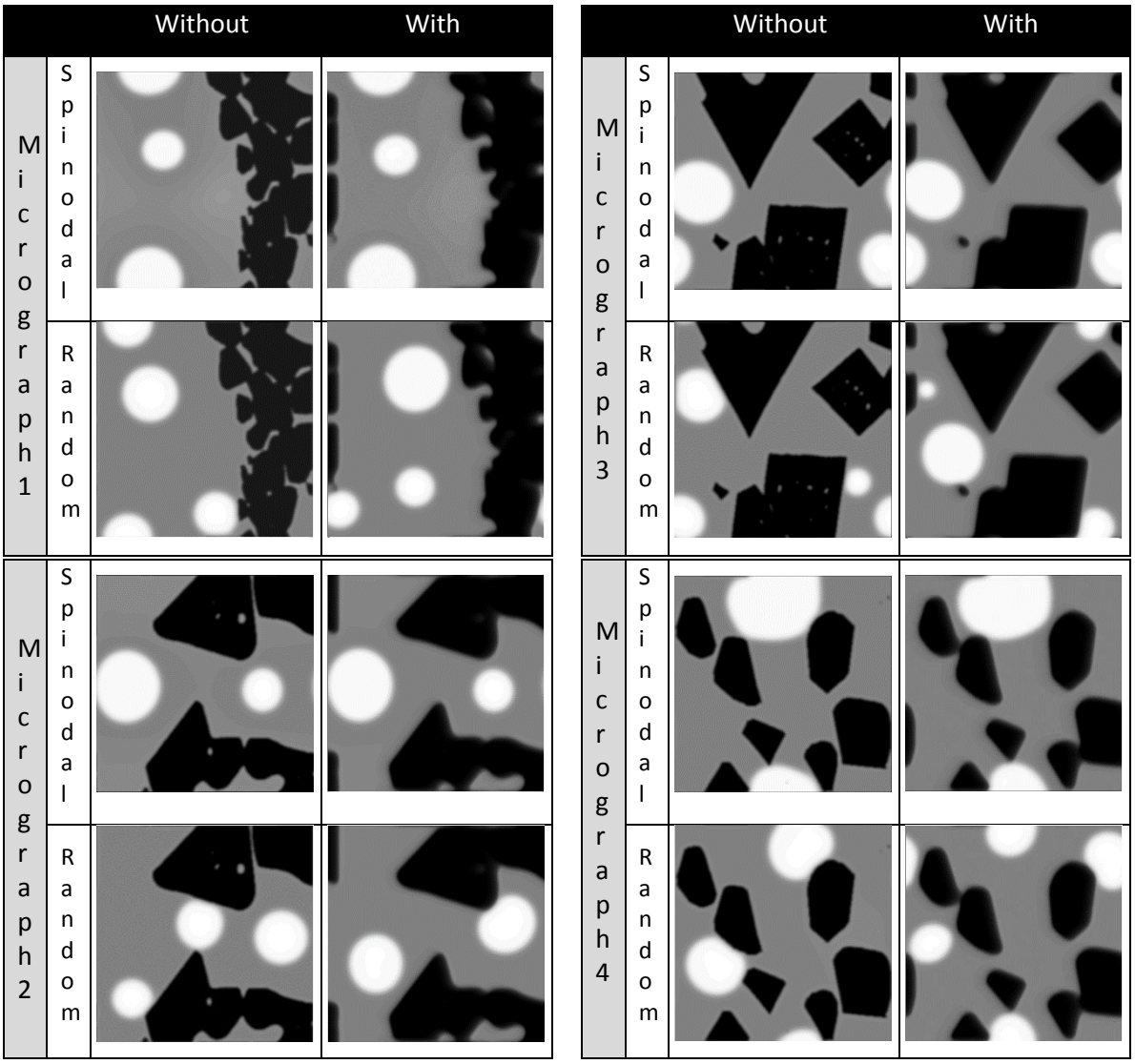

Figure 7.14 Comparison of the spinodal (upper row) and random (lower row) initialization methods in an extremely low wetting situation (x_s = 0.60)

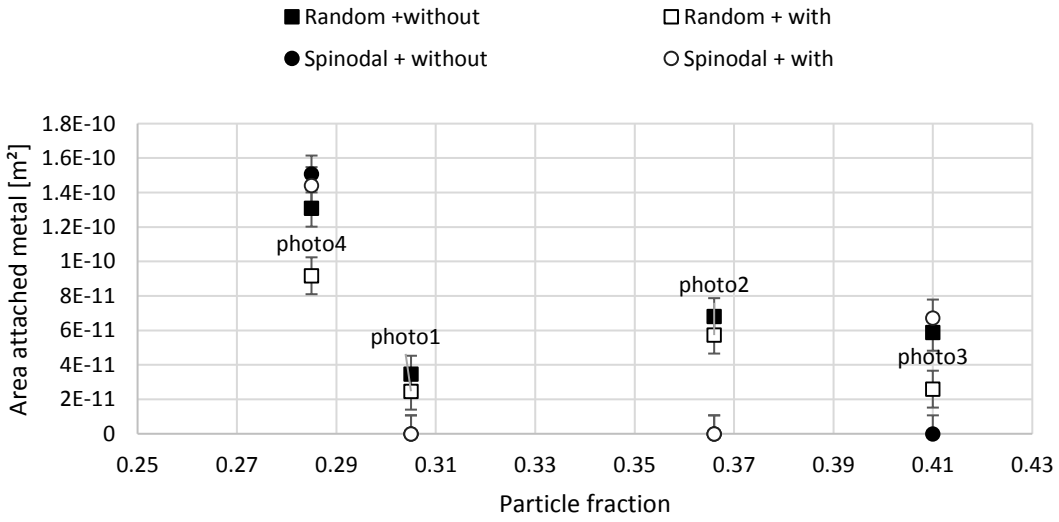

Figure 7.15 The area and fraction attached metal as a function of the particle fraction at the final simulation step (10^6), which corresponds to 100 s for the limiting case (x_S = 0.60). The particle fraction is characteristic for each micrograph, which is indicated by the label above the corresponding white rectangle

Again, the rigid body motion seems to decrease the amount of attached metal, except for micrograph 3 with the spinodal initialization. The differences between the 'with' and 'without' simulations are lower as compared to the x_S = 0.58 case. This can be due to the fact that the interfacial energy situation in the x_S = 0.60 case favours the attachment of metal a little more than the x_S = 0.58 case, resulting in less detachment of the metal from the solid.

These results show that the conclusions from our previous work for a single solid particle are still valid for multi-particle systems. The resulting simulations can also be compared to experimental observations in the FeO- SiO_2-Cu_2O- Al_2O_3 system [13], such as in Figure 7.16, made in the Fe-Al-Si-Cu system which was first oxidized to dissolve all the metallic copper in the slag and subsequently reduced to provoke the formation of metallic copper, either as a free droplet or attached to a spinel solid particle [13].

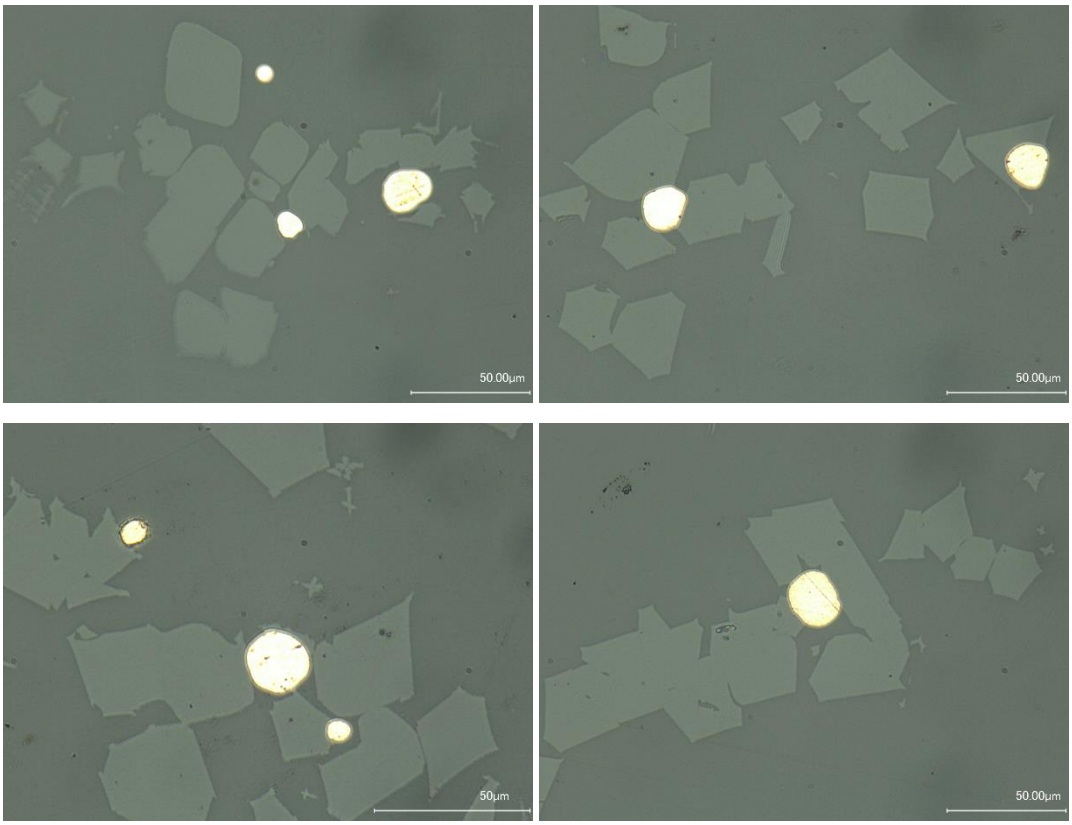

Figure 7.16 Experimental micrograph of Cu droplets attached to solid particles in the FeO- SiO_2-Cu_2O- Al_2O_3 system [13]

The rigid body motion seems to decrease the amount of attached metal for the non-wetting and low wetting cases, which is in accordance with the first results obtained in this chapter. In all wettability regimes, the attached metal droplets have a less spherical shape when rigid body motion is present in the system. This can also be observed in the experiments (Figure 7.16). It can also be clearly observed than one metal droplet is surrounded by more than one solid particle in most cases. In the simulations, this behaviour is best observed for micrograph 4. Clearly, the non-wetting regime (x_S = 0.50) does not correspond well to the experimental observations, whereas a good correspondence is observed with the simulations in the low wetting regimes.

References

[1] D. Jacqmin, Calculation of Two-Phase Navier–Stokes Flows Using Phase-Field Modeling, J. Comput. Phys. 155 (1999) 96–127. doi:10.1006/jcph.1999.6332.

[2] J. Kim, Phase-Field Models for Multi-Component Fluid Flows, Commun. Comput. Phys. 12 (2012) 613–661. doi:10.4208/cicp.301110.040811a.

[3] D.M. Anderson, G.B. Mcfadden, A.A. Wheeler, Diffuse-Interface Methods in Fluid Mechanics, ResearchGate. 30 (1997). doi:10.1146/annurev.fluid.30.1.139.

[4] S. Osher, R.P. Fedkiw, Level Set Methods: An Overview and Some Recent Results, J. Comput. Phys. 169 (2001) 463–502. doi:10.1006/jcph.2000.6636.

[5] J.A. Sethian, P. Smereka, Level Set Methods for Fluid Interfaces, Annu. Rev. Fluid Mech. 35 (2003) 341–372. doi:10.1146/annurev.fluid.35.101101.161105.

[6] S. Osher, J.A. Sethian, Fronts propagating with curvature-dependent speed: algorithms based on Hamilton-Jacobi formulations, J. Comput. Phys. 79 (1988) 12–49.

[7] I. Bellemans, N. Moelans, K. Verbeken, Phase field modelling of the attachment of metallic droplets to solid particles in liquid slags: Influence of interfacial energies and slag supersaturation, Comput. Mater. Sci. 108, Part B (2015) 348–357. doi:10.1016/j.commatsci.2015.03.019.

[8] I. Bellemans, E. De Wilde, N. Moelans, K. Verbeken, Phase field modelling of the attachment of metallic droplets to solid particles in liquid slags: Influence of particle characteristics, Acta Mater. 101 (2015) 172–180. doi:10.1016/j.actamat.2015.08.074.

[9] I. Bellemans, E. De Wilde, N. Moelans, K. Verbeken, Phase field simulation study of the attachment of metallic droplets to solid particles in liquid slags based on real slag–spinel micrographs, Comput. Mater. Sci. 118 (2016) 269–278. doi:10.1016/j.commatsci.2016.03.022.

[10] K. Ogino, S. Hara, T. Miwa, S. Kimoto, The Effect of Oxygen Content in Molten Iron on the Interfacial Tension between Molten Iron and Slag, Trans. Iron Steel Inst. Jpn. 24 (1984) 522–531. doi:10.2355/isijinternational1966.24.522.

[11] L. Muhmood, N.N. Viswanathan, S. Seetharaman, Some Investigations into the Dynamic Mass Transfer at the Slag–Metal Interface Using Sulfur: Concept of Interfacial Velocity, Metall. Mater. Trans. B. 42 (2011) 460–470. doi:10.1007/s11663-011-9482-9.

[12] E. De Wilde, I. Bellemans, L. Zheng, M. Campforts, M. Guo, B. Blanpain, N. Moelans, K. Verbeken, Origin and sedimentation of Cu-droplets sticking to spinel solids in pyrometallurgical slags, Mater. Sci. Technol. 32 (2016) 1911–1924. doi:10.1080/02670836.2016.1151998.

[13] I. Bellemans, V. Cnockaert, N. Moelans, K. Verbeken, Metal droplet entrainment by solid particles in slags: an experimental approach, (n.d.) In preparation.

8. Conclusions

In this part of the doctoral work, several influences on the attachment of liquid metal droplets to solid particles in liquid slags with a binary phase field model were studied. The following parameters were addressed:

- the initial supersaturation of the liquid
- the interfacial energies
- the particle morphology (particle fraction, perimeter, shape and distribution)
- initialization method
- movement of the solid particle
- the speed of movement of the solid particle

In practice, when a fraction of the metallic phase is attached to the solid particles, this fraction cannot settle and the yield of the phase separation will decrease, which in turn means an important loss of valuable metals.

In the simulations with the spinodal initialization, three stages were observed: first 'localized' spinodal decomposition takes place near the particle, then, the non-localized decomposition occurs in the remaining supersaturated liquid. Finally, Ostwald ripening and coalescence take place. Depending on the interfacial energies, four regimes were observed: no wettability of the metal on the particle, low wettability, high wettability and full wetting. A higher initial supersaturation generally resulted in a higher metal fraction in the system. The effect of the initial supersaturation on the fraction of attached metal was, however, not fully conclusive and also varied with time. The simulations show that the attached droplets do not have preferred positions, as various places with several configurations and variations in time were encountered.

As the fraction of solid particles in the system decreases, a lower fraction of the metal is attached to the solids. In the case of low wettability, the amount of attached metal does not increase with an increasing perimeter per area, even though the number of available positions for the metal increases. For high wettability, the expected increase in attached metal for an increasing perimeter per area is observed. The shape of the particles was also varied. Unfortunately, no clear trends were discovered regarding the shape of the particles. Nevertheless, it became clear that several small particles yield more attached metal than one large particle. The distance between the particles slightly influences the amount of metal attached, as the metallic droplets do orient themselves away from the other solid particles when these are too close to one another. Moreover, some of the simulations with particles with cavities confirmed that not only the perimeter per area, but also the available space for the droplet to grow is an important factor.

The model was also extended to consider realistic microstructures based on actual micrographs of the solid particles. The origin of the attachment was investigated by comparing two initialization methods for the metal droplets: by spinodal decomposition of a supersaturated liquid, corresponding in practice to a reactive origin of the droplets, and a method with random positioning of the droplets, corresponding to the separate formation of particles and droplets. Based on previous research, both methods were considered for two wettability regimes: no and low wettability. From a simulation point of view, the random initialization allows for more flexibility in the metal fraction of the system as there are no restrictions on the metal volume fraction f_v, as opposed to the spinodal decomposition, where the initial supersaturation x_i should be selected in between the inflection

points of the free energy curve representing the spinodal decomposition. The random initialization, however, has a much larger spread on the results than the spinodal initialization. As a consequence, a larger number of simulations are required to draw relevant conclusions for the random initialization than when the droplets form through spinodal decomposition of a supersaturated slag, since the droplets are then first formed close to the particle. In the non-wetting case, the spinodal initialization gave microstructures with the best correspondence with the experiments, but in the low wettability case, the simulation results of both initialization methods correspond well with the experimental system. This confirms that the droplet-particle interaction can have multiple origins: either reactive or non-reactive

Afterwards, it was investigated how rigid body motion of the solid particle influences liquid metal droplet attachment to that solid particle in liquid slags with a phase field model. Regarding the amount of attached metal, no actual trends could be observed. At no wettability, the microstructures show that the rigid body motion could either 'pick up' droplets, hereby increasing the amount of attached metal, or it can lose an already attached metal droplet. The low wettability case is similar, but the loss of an already attached droplet was not observed. However, this might no longer be the case if the solid particle moves faster. At higher wetting regimes and full wetting, the influence of the rigid body motion seems to be smaller, as the attachment is more determined by the interfacial energies and the metallic phase 'follows' the solid particle when it moves. Again, this might no longer be the case if the solid particle moves faster. However, on average, there is no effect on the amount of metal attached to the solid particle.

A major observation, on the other hand, is the fact that the apparent contact angle of the metal is larger when rigid body motion is present, which corresponds to a lower apparent wettability. This effect was very clear, even at the small rate with which the solid particle moved in this study. This fact could indicate that a previous classification of the experimental PbO-FeO-CaO-SiO_2-Cu_2O-ZnO-Al_2O_3 system as a system with very low wettability has to be revised.

The study on the influence of the speed of the rigid body motion showed that there is a trade-off between the speed of the movement of the liquid metal on the one hand, which depends on the attraction of the metal towards the solid particle by interfacial energies and the speed of the movement of the solid particle, which we varied. For slow solid motion, the interfacial energies have the upper hand, but for larger velocities, the metal cannot necessarily keep up with the movement of the solid. Thus, the amount of metal will decrease in case of faster movement. However, this is only the case for the low and high wettability regimes. For the non-wetting case, metal droplets coincidentally present on the path of the solid particle will get attached, but the solid particle movement can similarly decrease the amount of the attached metal by moving away from the metal droplet. On the other hand, for the very high (almost full) wetting case, the interfacial energy attraction of the metal to the solid is so large that even the largest velocity did not decrease the amount of attached metal.

For the real-micrograph-based simulations, the simulation in the absence or presence of rigid body motion for the spinodal initialization corresponds better to the experimentally observed micrographs than the one with the random initialization. Moreover, the trends for the different wetting regimes observed for a single solid particle were observed to still be valid for multi-particle systems.

In this work, the interaction between the solid particles and metallic droplets resulted from the interfacial energies between the solid, the liquid oxide and the liquid metal. It should also be

mentioned that chemical reactions between the solid and the two liquid phases can take place and might affect the interaction, as shown by Villanueva et al. [1].

The better correspondence to the spinodal initialization shows that the droplet-particle interaction could result from a reactive origin, as was also confirmed experimentally by De Wilde et al. [2–7] in a synthetic slag system. These experiments show the growth of solid spinel particles on the edge of already existing metallic droplets or their formation together with new droplets. They also proposed a mechanism for this observation: the spinel solids and copper droplets form together due to a simultaneous reduction of copper oxides into metallic copper and the oxidation of slag oxides into more stable spinel structures. Additionally, the spinel solids can also form on an already present Cu droplet in an analogous way. Moreover, experimentally, the actual 'attachment' of the droplets seems to be a non-equilibrium phenomenon, which is in correspondence with the results for the spinodal initialization, as in that case the droplets are first attached to the solid as they are formed simultaneously and are afterwards also detached/dissolved. Explicit implementation of a model of the formation of the solid particles within a liquid slag on the side of or together with a metal droplet in a multicomponent multiphase system will allow us to simulate and study the reactive origin for the attachment in more detail. Therefore, future investigations will include additional parameters and phenomena such as the redox reactions occurring in the system under evaluation.

References

[1] W. Villanueva, W.J. Boettinger, G.B. McFadden, J.A. Warren, A diffuse-interface model of reactive wetting with intermetallic formation, Acta Mater. 60 (2012) 3799–3814. doi:10.1016/j.actamat.2012.03.047.

[2] E. De Wilde, I. Bellemans, M. Campforts, A. Khaliq, K. Vanmeensel, D. Seveno, M. Guo, A. Rhamdhani, G. Brooks, B. Blanpain, N. Moelans, K. Verbeken, Wetting behaviour of Cu based alloys on spinel substrates in pyrometallurgical context, Mater. Sci. Technol. 31 (2015) 1925–1933. doi:10.1179/1743284715Y.0000000052.

[3] E. De Wilde, I. Bellemans, L. Zheng, M. Campforts, M. Guo, B. Blanpain, N. Moelans, K. Verbeken, Origin and sedimentation of Cu-droplets sticking to spinel solids in pyrometallurgical slags, Mater. Sci. Technol. 32 (2016) 1911–1924. doi:10.1080/02670836.2016.1151998.

[4] E. De Wilde, I. Bellemans, M. Campforts, M. Guo, B. Blanpain, N. Moelans, K. Verbeken, Investigation of High-Temperature Slag/Copper/Spinel Interactions, Metall. Mater. Trans. B. 47 (2016) 3421–3434. doi:10.1007/s11663-016-0805-8.

[5] I. Bellemans, E. De Wilde, L. Claeys, T. De Seranno, M. Campforts, B. Blanpain, N. Moelans, K. Verbeken, Investigation of reactive origin for attachment of Cu-droplets to solid particles, Metall. Mater. Trans. B. (2017).

[6] E. De Wilde, I. Bellemans, M. Campforts, M. Guo, B. Blanpain, N. Moelans, K. Verbeken, Sessile drop evaluation of high temperature copper/spinel and slag/spinel interactions, Trans. Nonferrous Met. Soc. China. 26 (2016) 2770–2783. doi:10.1016/S1003-6326(16)64344-3.

[7] E. De Wilde, I. Bellemans, M. Campforts, M. Guo, K. Vanmeensel, B. Blanpain, N. Moelans, K. Verbeken, Study of the Effect of Spinel Composition on Metallic Copper Losses in Slags, J. Sustain. Metall. 3 (2017) 416–427. doi:10.1007/s40831-016-0106-0.

C. Experiments

“It doesn't matter how beautiful your theory is, it doesn't matter how smart you are. If it doesn't agree with experiment, it's wrong.”

- Richard P. Feynman

9. Sessile drop experiment [16]

In De Wilde's previous work [1], the interaction between $MgAl_2O_4$, a copper droplet and a synthetic PbO-based slag was studied using an adapted sessile drop experiment to focus on the simultaneous copper-spinel-slag interaction. During the experiment, the copper droplet moved towards the slag droplet and a certain emulsification took place between the slag and copper droplet, after which the copper droplet positioned itself on top of the slag droplet. An extensive microstructural study was performed afterwards to study the spinel-copper-slag interactions. Within the slag droplet, small entrained copper droplets were observed to be attached to spinel particles. A reactive origin was proposed: the spinel solids and copper droplets form together due to a simultaneous reduction of copper oxides into metallic copper and the oxidation of slag oxides into more stable spinel structures. As spinel solids are characterized by very fast formation rates, new spinel solids can form directly next to the metallic copper droplets, leading to copper droplets, which are attached to spinel solids. However, the presence of the small metal droplets within the large slag droplet could also find its origin in the emulsification step.

The aim of this work was to investigate this hypothesis. Therefore, additional experiments with the adapted sessile drop set-up were performed. Moreover, several Cu-Ag alloys were used as Ag fulfilled the role of a tracer element. Ag is very noble and very unlikely to undergo oxidation, thus it will remain in the metallic phase. If the small metal droplets within the large slag droplet do not contain the tracer element, this confirms the fully reactive origin hypothesis. Whereas, if the tracer element is observed within the small metal droplets in the large slag droplet, these small metal droplets originated fully or partially from the emulsification step. Moreover, as a combined origin would result in lower Ag-contents in the smaller droplets than in the large metal droplet, several Ag-contents in the alloys were investigated to investigate this possibility.

9.1. Experimental procedure

9.1.1. Production of the slag system

The same industrially relevant synthetic slag system (PbO-CaO-SiO_2-Cu_2O-Al_2O_3-FeO-ZnO) as previously used [1] was employed. It was produced by melting oxides of appropriate quantities, corresponding to a slag composition in the spinel primary phase field. The targeted slag composition is shown in Table 9.1.

	ZnO	PbO	SiO_2	Al_2O_3	Cu	CaO	FeO
wt%	6.5	39.3	13.8	7.3	3.9	9.8	19.4

Table 9.1 Selected targeted synthetic slag composition based on thermodynamic calculations with FactSage (FactPS and FTOxid databases; Input: 100 g of this composition; Selection of all possible pure compound species and all solution species; Conditions: 1473K (1200°C), 1 atm total pressure and fixed partial pressure of O_2 of 10^{-7}; resulting in three phases at equilibrium: liquid metallic copper phase, liquid slag phase and solid spinel phase)

FeO was added as a combination of metallic iron and hematite and CaO was added as limestone. 400 g of the targeted composition was weighed, mixed and transferred in an Al_2O_3 crucible (270 ml). The Al_2O_3 crucible, surrounded by a protective SiC crucible, was heated in an inductive furnace

[16] Based on the following publication: I. Bellemans, E. De Wilde, B. Blanpain, N. Moelans, K. Verbeken, Investigation of origin of attached Cu-Ag-droplets to solid particles during high temperature slag/copper/spinel interactions, Metallurgical and Materials Transactions B. Submitted

(Indutherm, MU3000) up to a temperature of 1073K (800°C), under a protective N_2 atmosphere. At 1073K (800°C), the N_2 atmosphere was replaced by a CO/air mixture with volume ratio of 1 to 2.44, corresponding to an oxygen partial pressure (p_{o2}) of 10^{-7}atm, with a total flow rate of 60 l/h. This atmosphere was kept constant during the remainder of the experiment. The slag was heated to 1473K (1200°C) and this temperature was kept for 30 min to melt all components. Subsequently, N_2 (60 l/h) was bubbled through the slag for homogenization purposes. Afterwards, the induction furnace was kept at 1473K (1200°C) for 150 min. The high-temperature state of the slag was obtained using a cold sampling bar, which was directly quenched in water and subsequently dried in a dry chamber at 423K (150°C).

A representative sample of the quenched slag was investigated microscopically previously [1]. Three phases were observed: slag (SL), spinel (SP) and copper droplets (Cu-dr). Some of the present copper droplets display a sticking behaviour to spinel particles. The spinel often had a border richer in Fe with respect to the core, which was generally richer in Al. Similarly, the Cu-droplets often had a Pb-rich border. The various phases present in the system are illustrated in Figure 9.1. WDS analysis was also performed on the various phases. The resulting compositions are summarized in Table 9.2.

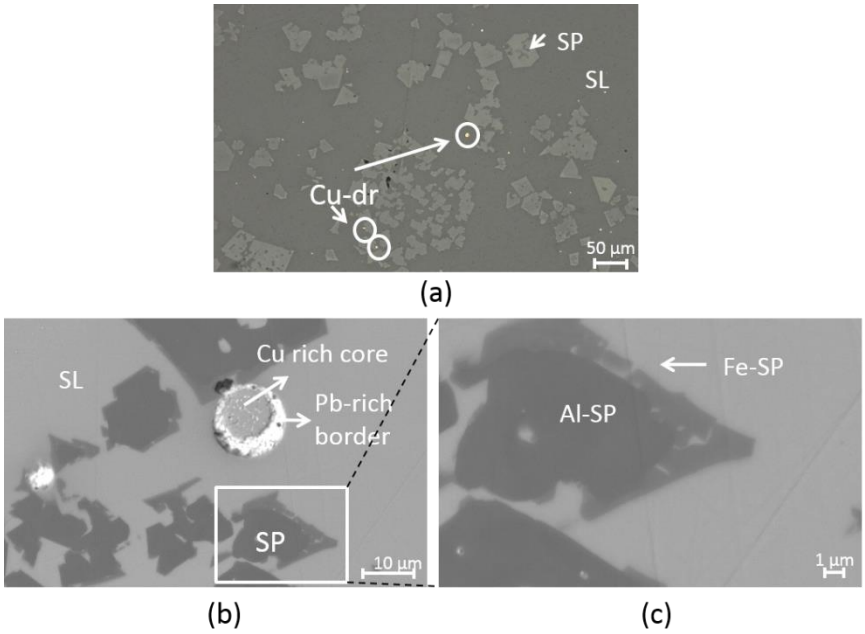

Figure 9.1 Representative LOM (a) and BSE (b,c) images of quenched slag system obtained after 150 min equilibration at 1523K (1250°C). (SP = spinel, SL = slag, Cu-dr = Cu-alloy droplets, Al-SP = Al-rich spinel phase, Fe-SP = Fe-rich spinel phase) [1]

wt%	Al_2O_3	'FeO'	'Cu_2O'	CaO	ZnO	PbO	SiO_2
Slag	7.1	16.1	1.3	8.7	5.5	36.4	25.7
Al-rich spinel	36.9	39.7	0	0	22.5	0.1	0.2
Fe-rich spinel	17.7	63.6	0.1	0	14.3	0.3	0.4
Cu core	0.7	0	1.5	95.0	0	0.5	1.2
Pb-rich border	3.4	0	1.4	1.9	0.12	0.9	92.3

Table 9.2 Overview WDS analysis of the slag, Fe-rich spinel phase, Al-rich spinel phase and Cu-rich core and the Pb-rich border of the present Cu-Pb alloy droplets. [1]

The composition of the slag itself was different compared to the targeted composition in Table 9.1. For Cu, this difference can be explained by the formation of alloy droplets within the slag phase. Moreover, Pb will dissolve mostly in the alloy phase rather than in the slag phase, in accordance with

the findings of Takeda et al. [2], resulting in a lower PbO content of the slag (see Table 9.2). Takeda et al. [2] also showed that Zn dissolves more in the slag phase, but the amount of ZnO in Table 9.2 is lower than the start composition given in Table 9.1, as it is one of the major spinel-forming components. The spinel solids consist of the three spinel forming components in the slag (i.e., 'FeO', ZnO and Al_2O_3). Some of the spinel particles consist of two phases, namely an Fe-rich spinel phase at the border (Fe-SP) and an Al-rich spinel phase in the core (Al-SP) of the particle. Other spinel particles consist completely of the Fe-rich spinel phase. Under the present experimental conditions, Cu-Pb droplets with a phase separation between a Cu-rich core and a Pb rich border are formed. The phase separation is a direct consequence of the low Pb solubility in Cu at lower temperatures, and therefore this phase separation is expected not to be present at the high temperature during the experiment.

9.1.2. Spinel preparation

Spinel ($MgAl_2O_4$) substrates were produced in a similar way as in the previous work [1], using a spark plasma sintering set-up (type HP D25/1, FCT system Rauenstein, Germany, equipped with a 250 kN uniaxial press)). The $MgAl_2O_4$ powder (Sigma Aldrich, spinel nano powder, < 50 nm particle size) was sintered at a temperature of 1573K (1300°C) under a load of 60 MPa. Subsequently, the sintered spinel plates were annealed at 1273K (1000°C) for 3 h and were in a final step polished to a mirror finish using 9 µm, 3 µm and 1 µm diamond pastes. The spinel phase was confirmed by XRD analysis (Siemens diffractometer D5000), while some additional small corundum peaks were present in the XRD spectrum as well. The roughness parameter R_A of the $MgAl_2O_4$ substrates has an average value of 0.19 ± 0.08 µm (Talysurf profilometer).

9.1.3. Alloy production

The Cu-Ag-alloys were produced with an inductive micro-granulation furnace (Indutherm, GU500), allowing the production of granules with proper dimensions for the contact angle measurements. Four different Cu-Ag alloys were produced, containing respectively 5wt% Ag, 12.5wt% Ag, 20wt% Ag and 30 wt% Ag. Appropriate amounts of the metals were weighed and melted under a protective Ar-atmosphere in graphite crucibles. Once molten, the high frequency magnetic field ensured mixing of the alloying elements during 15 min. Subsequently, the alloy was granulated into small granules.

9.1.4. Sessile drop experiments

9.1.4.1. Set-up

The interaction between $MgAl_2O_4$ and copper or slag was studied using an infrared heating furnace, included in the confocal scanning laser microscopy set-up (Lasertec 1LM21- SVF17SP, CSLM). The infrared heating furnace allows fast heating and cooling with a 1.5 kW halogen lamp placed in the lower focal point of a small Au-coated gastight ellipsoidal chamber that reflects the light to the other focal point where the observed sample is positioned. A programmable PID controls the temperature, read from a type B (Pt-6%Rh / Pt-30%Rh) thermocouple, which is part of the sample holder. An extra window is placed on the side of the heating chamber, allowing to monitor the wetting of the droplet on the substrate, which is recorded with a camera (Ganz ZC-F10C3), placed on the same height. An oxygen gas analyser in the gas outlet monitors p_{O2} variations in the heating chamber (Cambridge Sensotec LTD, Rapidox 2100).

9.1.4.2. Performed experiment

The simultaneous interaction of copper and slag with a $MgAl_2O_4$ substrate was evaluated under a protective Ar atmosphere. Before the start of the experiment, the $MgAl_2O_4$ substrate was cleaned ultrasonically in acetone and the copper was etched using a $1H_2O$: 1HCl solution, to remove the outer copper oxide layer. The $MgAl_2O_4$ substrate was placed on the sample holder and levelled carefully. Subsequently, both copper and slag were placed on the substrate. The heating chamber was closed and flushed three times with Ar. First, the temperature was raised to 573K (300°C), with a heating rate of 50K/min. After 1 min at 573K (300°C), the temperature was increased further to 1173K (900°C), with a heating rate of 200K /min. After 1 min at 1173K (900°C), the chamber was further heated to 1523K (1250°C), which was maintained for 8 min. Finally, the sample was cooled down with a cooling rate of 500K/min. The complete process, starting from the melting of the droplet until the final cooling, was monitored and an example of the measured temperature in the sample holder is shown in Figure 9.2.

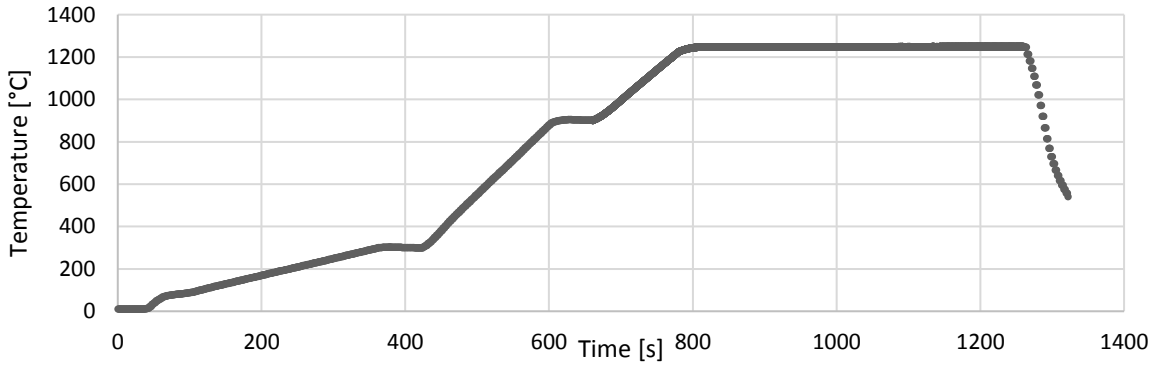

Figure 9.2 Temperature as a function of time during one of the experiments

Special care was taken to assure that the masses of the slag and copper alloy were very similar. The average weights of slag and copper alloys during the experiments were 0.0269 ± 0.0041 g and 0.0265 ± 0.0048 g, respectively. The experiment was repeated multiple times to ensure the reproducibility of the observations and to investigate whether the wt%Ag in the Cu-Ag alloys has a certain influence. The monitored p_{O2} value during the experiments was of the order of $1.5\ 10^{-5}$ ± 1% atm**.**

The obtained sessile drop samples were analysed using light optical microscopy (LOM, Keyence VHX-S90BE) and electron probe microanalysis, using the secondary electron (SE) microscopy mode (SEM-SE, FEI Quanta 450 with field emission gun). For the latter, the sample was coated with a conductive carbon layer. The composition of the different phases was analysed using energy dispersive spectroscopy (SEM-EDX, FEI Quanta 450 with field emission gun).

9.2. Results and discussion

9.2.1. Melting, wetting and interaction behaviour of copper alloy and slag on $MgAl_2O_4$

A typical example of the melting and wetting behaviour of slag and copper on a spinel substrate is presented in Figure 9.3 using the captured video images obtained during the experiment. The moment at which the slag starts to melt is considered as the start of the experiment and is chosen as zero-point for the time-scale of the experiment ($t_{melt\ slag} = t_{start} = 0$ s). It should be noted that the first three images of Figure 9.3 were slightly adapted in contrast and brightness to make the slag and

copper droplet more visible. These phases were not clearly visible at these temperatures (1273K (1000°C)), because the extra side-window of the heating chamber used for the sideways observation, was obscured. This was done because the sample emits too much light at the higher temperatures (1523K (1250°C)), which would make the interaction at higher temperatures not observable. Thus, even though the sample is already radiating light at 1273K (1000°C), this was not enough to cancel out the effect of the obscured side window.

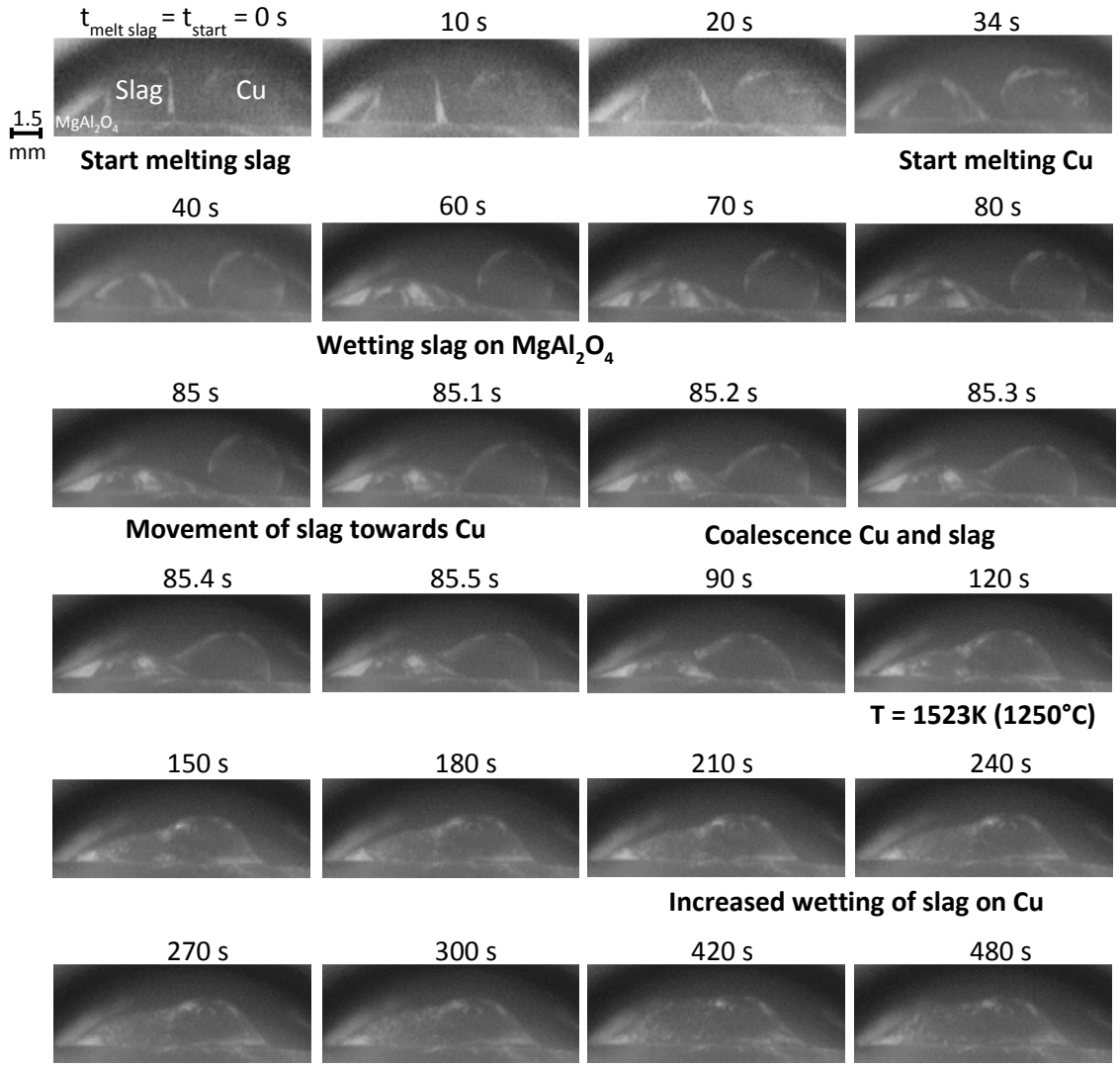

Figure 9.3 Captured images during the high-temperature CSLM experiment with Cu-20wt%Ag. Above each image, the time in seconds is shown, where the melting point of the slag is taken as the zero-point for the timescale ($t_{melt\ slag} = t_{start} = t_0$). Different stages were defined within the melting and heating process: melting of the slag; melting of the copper; wetting of slag on the substrate, movement of the slag towards the Cu; coalescence of Cu and slag and increased wetting of slag on top of the Cu.

Different stages during the experiment can be distinguished, as indicated on Figure 9.3. First, the slag droplet melts, followed by the melting of the copper alloy. Usually, as the viscosity of molten metals is very low, the time needed for millimetric size droplets to reach capillary equilibrium in non-reactive systems is less than 10^{-1} s, whereas the spreading times in reactive metal/ceramic systems, usually lay in the range of 10^{1}-10^{4} s and these systems are typically controlled by the interfacial reaction itself. [3] Once the slag is completely molten, a good wetting with the spinel substrate is observed. The apparent contact angle is 25.9 ± 1.7°. The copper alloy, on the other hand, is almost spherical

with an apparent contact angle of 118.5 ± 1.4°, indicating a very low wettability of the alloy on the spinel. This wetting behaviour is in good correspondence with previous observations by De Wilde et al. [4]. The wetting behaviour of the slag with respect to the spinel appears to be much higher than that of the alloy. The slag gradually spreads on the spinel substrate and eventually reaches the copper droplet, which continuously keeps it spherical shape.

After 85 s, the slag touches the copper droplet. Once this takes place, the coalescence of the slag and copper happens very rapidly, i.e. the copper droplet gets on top of the slag in about half a second. After the coalescence, the liquid copper stays on top of the slag and this image gives the impression that the copper droplet is not in contact with the $MgAl_2O_4$ substrate. Based on the densities of copper and slag, the opposite behaviour would be expected. It should be noted that due to the very low masses of slag and copper used in the sessile drop experiment, the gravity effect on the droplets is limited and it can be assumed that the interfacial energies between the spinel substrate and both liquids will be the dominant factor in our experiment [5].

After the coalescence, during the interaction time of 8 min at 1523K (1250°C), the slag starts to wet the copper droplet, which lies on top of the slag. This is particularly visible when considering the height of the left side of the slag with respect to the height of the copper droplet on top of the slag. First, the copper droplet is clearly situated in a higher position, but in the end of the experiment, the slag on the left side, reached the same height.

Because the coalescence happens so fast, the small metal droplets attached to spinel particles that were observed in the slag phase in similar experiments previously [1] might result from this fast 'sweeping' of the slag in between the copper alloy droplet and the spinel substrate. This is why, in this study, copper-silver alloy droplets were used. If the mechanically entrained copper alloy droplets have the same composition as the large alloy droplet, the origin of the attachment of the small copper droplets to the solid spinel particles, lies in the fast mixing of the two phases during the coalescence. However, when the mechanically entrained copper alloy droplets have a different composition than the large alloy droplet, this would be a strong indication that the entrainment of the copper droplets has a reactive origin, as was proposed in previous work [1,6]. If the small metal droplets within the large slag droplet do not contain the tracer element Ag at all, the origin can be stated as fully reactive. If the concentration of the tracer element is less than the large alloy droplet, a combined origin would be responsible for the mechanically entrained small droplets.

The adapted sessile drop experiment allowed the simultaneous study of the interactions between both liquid slag and liquid copper with a solid spinel $MgAl_2O_4$ substrate. Consequently, the relevant interactions that determine the phenomenon of sticking copper droplets in slags will be examined in the next section. The microstructures and compositions of different regions within the high temperature CSLM samples are examined for the different Ag alloys.

9.2.2. Microstructural analysis

9.2.2.1. General overview

The LOM images of the cross-section of the $MgAl_2O_4$-slag-Cu(30wt%)Ag sample are shown in Figure 9.4. Central in this figure, a global overview is shown, surrounded by more detailed micrographs of several regions in the cross-section. Similar results were obtained for the other Cu-Ag alloys.

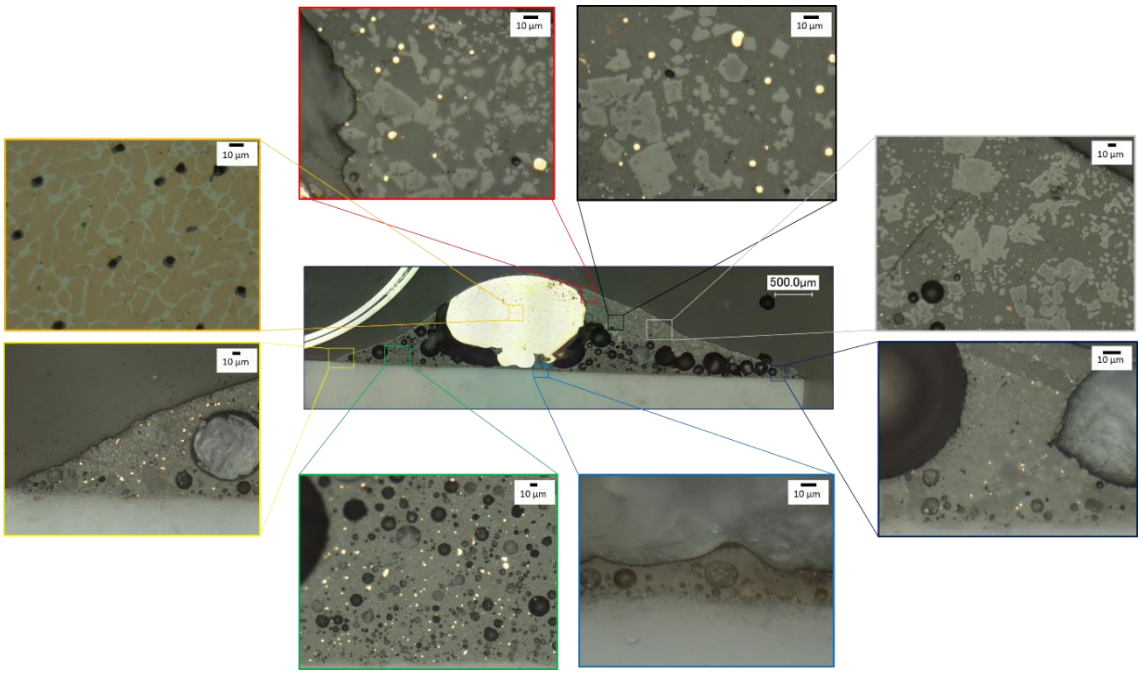

Figure 9.4 LOM of the cross-section of the $MgAl_2O_4$-slag-Cu(30wt%)Ag sessile drop sample. (central) General overview of slag droplet and copper droplet on the substrate. (surrounding) Detailed overview of the microstructure of the slag droplet within the copper or slag droplet

The general overview image (central in Figure 9.4) confirms that there is no direct contact between the $MgAl_2O_4$ substrate and the large copper droplet. The large Cu-Ag droplet has undergone a certain phase separation during the cooling down, as the Cu-Ag phase diagram predicts one completely liquid Cu-Ag phase at high temperatures, but a phase separation between a Cu-rich and a Ag-rich phase at temperatures below the eutectic temperature of 1052K (779°C).

The slag situated close to the big copper alloy droplet contains several small metal droplets attached to spinel particles within the slag. Further away from the large copper alloy droplet, smaller non-attached metal droplets are also present alongside finely dispersed spinel solids. In the outer regions of the slag phase, less or almost no metallic droplets are observed. Underneath the big copper alloy droplet, a very thin interaction layer can be observed. However, it is immediately clear that this slag layer is much thinner (on the order of 10µm) than in the previous work [1] (on the order of 100 µm). The different zones were also investigated with SEM-EDX and are discussed into more detail in the following sections.

9.2.2.2. Big alloy drop

The phase separation within the big droplet can be observed by both the SE images and the elemental maps in Figure 9.5. The Cu-Ag alloy clearly separates into a copper-rich and a silver-rich phase. The average measured composition of the complete droplets and the compositions of the separate phases for the 20 and 30 wt% Ag alloys are shown in Table 9.3. Only the amounts of Cu and Ag are presented here, because the other elements were detected in amounts lower than the error of the measurement.

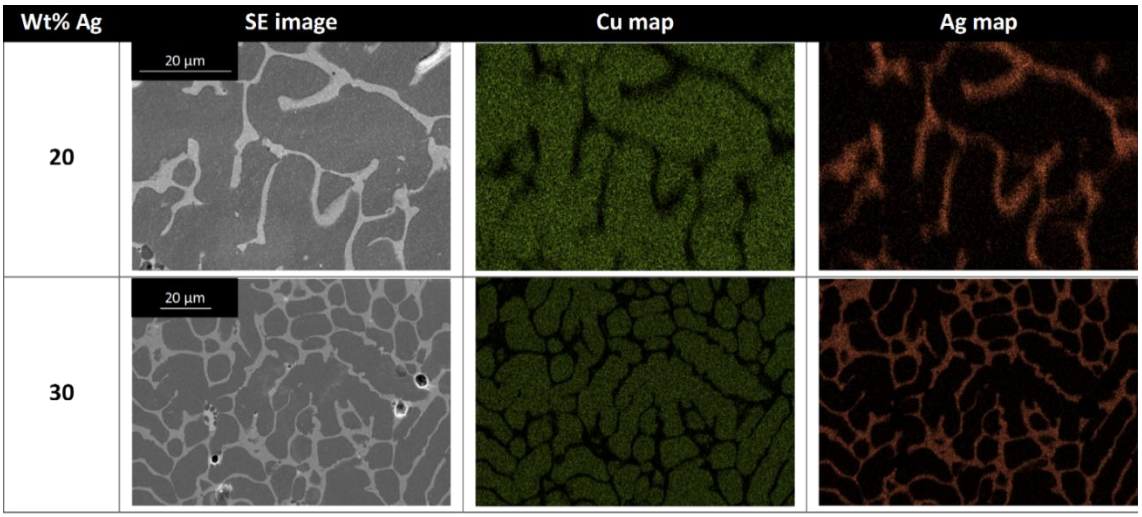

Figure 9.5 SE images and Cu and Ag EDX-maps illustrating the phase separation within the big Cu-Ag droplet

Proposed wt% Ag	Measured average composition	Composition of Ag-rich phase	Composition of Cu-rich phase
20	17.2 wt% Ag	/	94.7 wt% Cu – 5.3 wt% Ag
30	22.2 wt% Ag	18.4 wt% Cu – 81.6 wt% Ag	94.4 wt% Cu – 5.6 wt% Ag

Table 9.3 Average measured composition of the complete droplets and the compositions of the separate phases for the 20 and 30 wt% Ag alloys

The Ag-rich phase in the 20wt%Ag alloy could not be measured accurately due to the limits of spatial resolution of the EDX. However, it is clear that such an Ag-rich phase is present, as the SE images clearly indicate this and the average composition has more Ag than the Cu-rich phase.

The Cu-Ag phase diagram, calculated with the Factsage thermodynamic software [7], predicts a homogeneous liquid Cu-Ag phase at 1523K (1250°C). Upon cooling a phase separation occurs which shows characteristics of spinodal decomposition instead of a nucleation and growth mechanism [8]. Therefore, the temperature at which the alloy droplet solidified and simultaneously decomposed spinodally can be approximated by a Factsage calculation which fits the observed phase compositions to the theoretical ones. The compositions of the two measured phases correspond to the equilibrium situation at a temperature of 1003K (730°C) and 1051K (778°C), respectively, where the latter temperature is the eutectic temperature (the temperature at which the last liquid phase disappears under equilibrium cooling).

9.2.2.3. Slag at the side of big alloy drop

An overview of the microstructures at the side of the large metal droplet for the different Cu-Ag alloys is given in Figure 9.6. For the 5, 12.5 and 30 wt%Ag alloys, the microstructures are similar and contain metal droplets attached to solid spinel particles in the slag phase. This is not the case for the 20wt%Ag alloy, where small darker solids are also present. An elemental map of an attached droplet for the 5wt%Ag sample is shown in Figure 9.7.

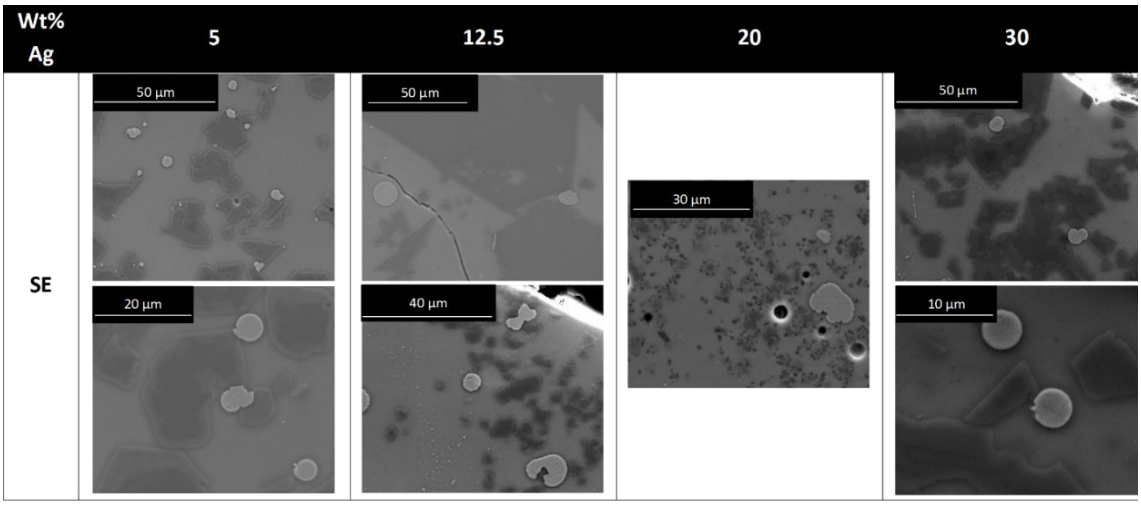

Figure 9.6 SE images of the microstructures at the side of the big copper alloy droplet for the different Cu-Ag alloys.

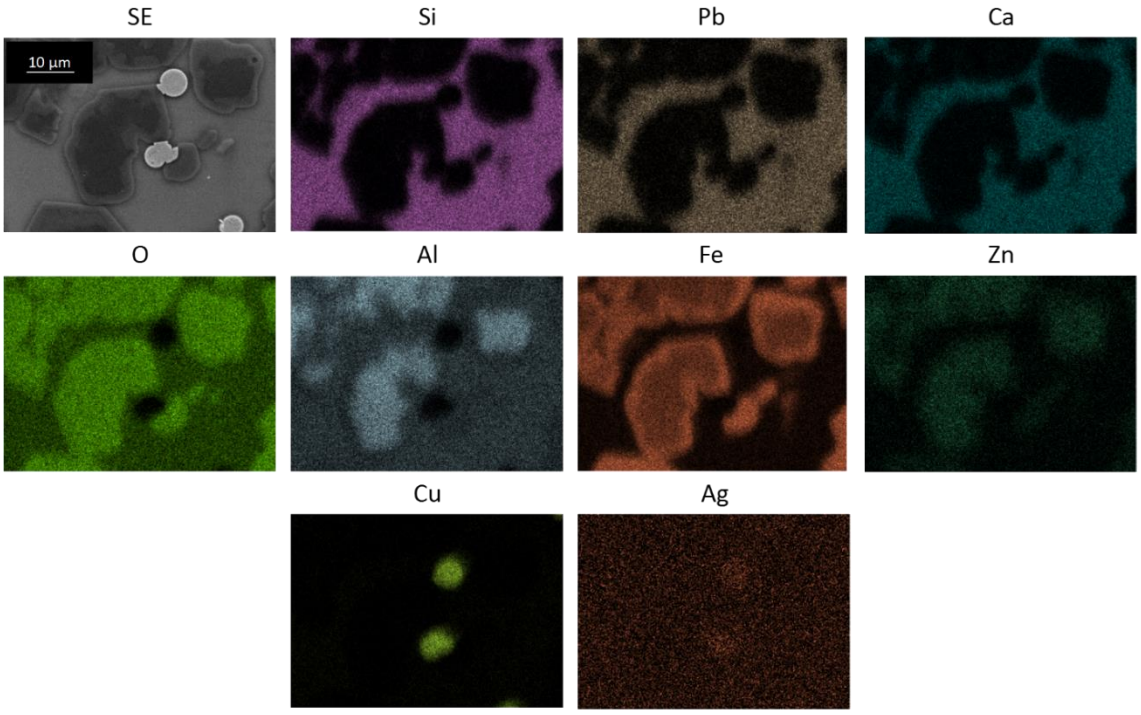

Figure 9.7 Elemental map of the microstructure next to the large Cu-5wt%Ag droplet.

It is clear from this map that the spinel forming elements are O, Al, Fe and Zn. Si, Pb and Ca only appear inside the slag phase while the metal droplets consist of Cu and Ag. The latter is more clear for the 30 wt% Ag alloy, as shown in Figure 9.8. In Figure 9.7, it is also shown that the spinel particle has a core which contains Fe, Al and Zn, but the border of the particle, clearly contains a higher concentration of Fe. Quantitatively, this is also reflected in the compositions obtained by EDX measurements, as summarized in Table 9.4.

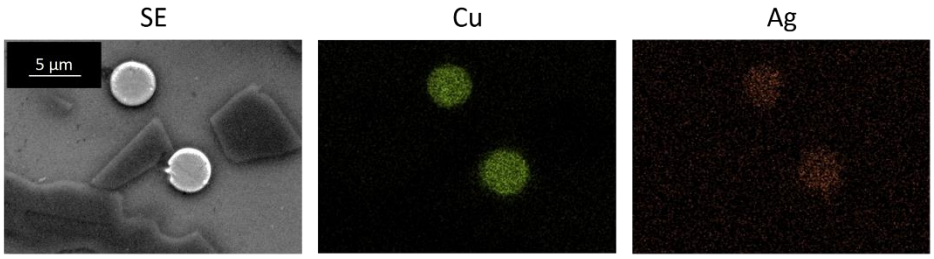

Figure 9.8 Elemental map of the attached metal droplets next to the large Cu-30wt%Ag droplet.

Sample	Phase	Wt% Si	Wt% Pb	Wt% Ca	Wt% Mg	Wt% O	Wt% Al	Wt% Fe	Wt% Zn	Wt% Cu	Wt% Ag
5	Slag	17.0	14.6	7.2	-	31.7	6.5	19.4	4.4	2.5	-
	Inner spinel	-	-	-	-	30.9	12.8	42.0	12.7	-	-
	Outer spinel	9.7	10.6	5.6	-	26.5	5.6	18.2	3.8	19.2	-
	Attached Cu	-	-	-	-	5.3	1.9	4.1	1.1	79.3	-
	Non-attached Cu	-	-	-	-	-	-	2.0	-	94.2	1.0
12.5	Slag	14.9	23.4	8.5	-	30.2	6.3	7.1	1.9	6.9	-
	Inner spinel	-	-	-	-	28.2	5.2	50.2	14.7	-	-
	Outer spinel	1.1	1.4	-	1.1	30.4	7.7	46.2	10.0	1.5	-
	Attached Cu	-	-	-	-	-	-	2.6	-	90.6	3.0
	Non-attached Cu	-	-	-	-	-	-	-	-	94.5	2.6
	Other solids	2.6	3.3	1.4	-	11.2	2.6	11.2	2.8	61.3	2.8
20	Slag	15.9	23.6	9.0	-	29.9	6.8	5.0	1.4	7.3	-
	Outer spinel	1.4	1.6	1.0	2.8	31.6	15.1	32.8	12.2	1.4	-
	Attached Cu	2.1	3.5	1.5	-	1.5	1.1	1.5	-	84.3	3.2
	Other solids	16.0	13.1	12.5	1.7	34.9	7.2	11.1	1.1	2.3	-
30	Slag	15.8	24.7	8.7	-	30.3	6.0	6.5	2.4	5.0	-
	Inner spinel	-	-	-	-	30.7	10.8	44.1	11.8	-	-
	Outer spinel	2.1	2.3	-	-	30.6	11.3	39.4	11.5	1.2	-
	Attached Cu	-	-	-	-	-	-	2.8	-	88.6	6.0

Table 9.4 Average measured compositions for the various phases in the microstructure at the side of the large alloy for the different Cu-Ag alloys. Compositions below 1wt% were assigned with '-'.

These measurements show that Pb, Si and Ca are mainly present in the slag. Mg, which could only come from diffusion from the substrate, is nearly always measured in concentrations below the detection limit. The spinel particles mainly consist of O, Al, Fe and Zn while the outer rim of the spinel clearly contains less Al and Zn. However, the amount of Fe also seems lower, as opposed to what is expected from the elemental map in Figure 9.7. Moreover, the amounts of the slag forming elements are also higher. This is probably due to the interaction volume (typically of the order of µm) inherent to SEM-EDX measurements and the fact that the spinel border is very thin and thus has slag underneath it, which will be measured by the EDX as well.

The metal droplets within the slag phase, either attached or non-attached, clearly contain Ag. They contain, however, less Ag than the proposed and actually measured (cfr. Table 9.3) Ag content of the alloy. The Ag content in the slag or the spinel phases is mostly below the detection limit as Ag mainly resides in the metal phase. The amount of Ag in the attached Cu droplets increases with the increasing Ag content in the Cu-Ag alloy. The attached metal droplets have a higher fraction of other elements (mainly Fe) than the non-attached metal droplets which could be related to interactions with the spinel particles. However, another possible explanation of the very high Fe-content is

secondary X-ray fluorescence [17]. This secondary fluorescence of X-ray spectra of small Cu-particles in Fe-containing slags was already investigated and modelled with Monte Carlo simulations [9].

The behaviour of the slag and the copper alloy droplet on the $MgAl_2O_4$ substrate during the high temperature CSLM experiment (Figure 9.3), indicate that the copper-$MgAl_2O_4$ interaction is not stable in the presence of a slag phase. This seems to be in contradiction with the presence of the small entrained sticking copper droplets in the slag droplet, and with the observations of the attached droplets in slags in the previous work of De Wilde et al. [6]. In [1], it was already demonstrated that an attached copper droplet is more stable than a non-attached droplet from a thermodynamic point of view, assuming that the surface of the droplet does not change after the attachment, when the following condition is valid [6]: $\gamma_{SL\text{-}Cu} + \gamma_{SP\text{-}SL} \geq \gamma_{SP\text{-}Cu}$. With $\gamma_{SL\text{-}Cu}$ the slag-copper interfacial energy, $\gamma_{SP\text{-}SL}$ the spinel-slag interfacial energy and $\gamma_{SP\text{-}Cu}$ the spinel-copper interfacial energy.

Unfortunately, at present, only limited data is available on $\gamma_{SL\text{-}Cu}$ for calcium ferrite slags [10], and, to our knowledge, no data is available for $\gamma_{SP\text{-}Cu}$ or $\gamma_{SP\text{-}SL}$. However, it was already shown that the spinel composition influences the wetting behaviour of copper alloys [11]: the contact angle of copper on $ZnFe_2O_4$ substrates (88°) was lower than on $MgAl_2O_4$ substrates (123°). The composition of the small spinel particles within the slag in our experiment are more related to the $ZnFe_2O_4$ substrate, thus the attachment of small alloy droplets within the slag is thermodynamically feasible and not in contradiction with the non-wetting behaviour of the large copper-alloy droplet on the $MgAl_2O_4$ substrate.

On the other hand, the origin of sticking droplets was proposed to be found in a chemical reaction, as elaborated in [1,6]. It is suggested that dissolved Cu can precipitate by reduction of the copper oxide, while the iron oxides in the slag next to the copper droplet are oxidized to form spinel solids, according to the following overall reaction [1,6]:

$$(Cu_2O, CuO)_{slag} + (FeO)_{slag} + (ZnO)_{slag} + (Al_2O_3)_{slag} \rightarrow (Zn^{2+}, Fe^{2+}, Cu^{2+})(Al^{3+}, Fe^{3+})_2O_4 + \text{Cu-alloy droplet}$$

However, the fact that silver is present in a lower concentration in the attached copper droplets compared to the master alloys in this study indicates that the origin of the attachment is not purely dispersive. Moreover, it is almost impossible that the Ag would dissolve in such large amounts into the slag, as illustrated by the SEM-EDX measurements in Table 9.4. This is confirmed by the observations of Takeda et al. [2]. They showed that Ag dissolves slightly into the slag with a distribution coefficient (= % in slag / % in Cu-Ag alloy) of the order 10^{-4} to 10^{-2} atm for partial pressures of oxygen going from 10^{-11} to 1 atm. Note that even if it were possible for more Ag to dissolve into the slag, this would also not result in precipitation of the Ag, as the equilibrium allows for more Ag to be dissolved, unless the slag drop on the spinel substrate possesses variations in composition or p_{O2}.

However, as Ag-diffusion cannot be excluded, a purely reactive origin is possible, as is a combination of dispersion and reaction. In the latter case, it is suggested that during the coalescence of the copper alloy and slag droplets on the substrate during the high-temperature CSLM experiment, some Cu-Ag

[17] After a characteristic X-ray is emitted, it can be absorbed again by an atom in the sample. Then, the absorbing atom is excited, but subsequently relaxes, emitting its own characteristic X-rays. This is called *secondary fluorescence*. Because X-rays (primary or secondary) can travel relatively large distances through the sample, it is possible that the secondary emission process may occur at a location remote from that of primary emission, further degrading the spatial resolution of the X-ray signal.

alloy is introduced into the slag phase as small dispersed alloy droplets. However, some Cu and Ag also dissolve into the slag under the high temperature and low oxygen partial pressure conditions. The small alloy droplets introduced in the slag during the coalescence, can be considered as heterogeneous nucleation sites, where dissolved Cu and Ag can precipitate by reduction of the copper and silver oxides, while the iron oxides in the slag next to the copper droplet are oxidized to form spinel solids, according to the overall reaction (cfr. Supra) as suggested by De Wilde et al. [1,6].

A higher amount of Cu was observed in the outer spinel (Table 9.4), which confirms the above mechanism. Moreover, a higher concentration of Fe was also observed in the outer part of the spinel (Figure 9.7), which endorses the mechanism suggested further. Furthermore, it was already observed by Scheunis et al. [12,13] that spinel solids can form and grow very fast within the slag, which would be essential for the reactive origin of the attachment.

9.2.2.4. Alloy droplet – slag interface

The interface between the large copper alloy droplet and the slag phase, could only be visualized for the 20 wt%Ag alloy (Figure 9.9), as all the other samples had no clearly visible interface due to a large number of pores concentrated at this interface.

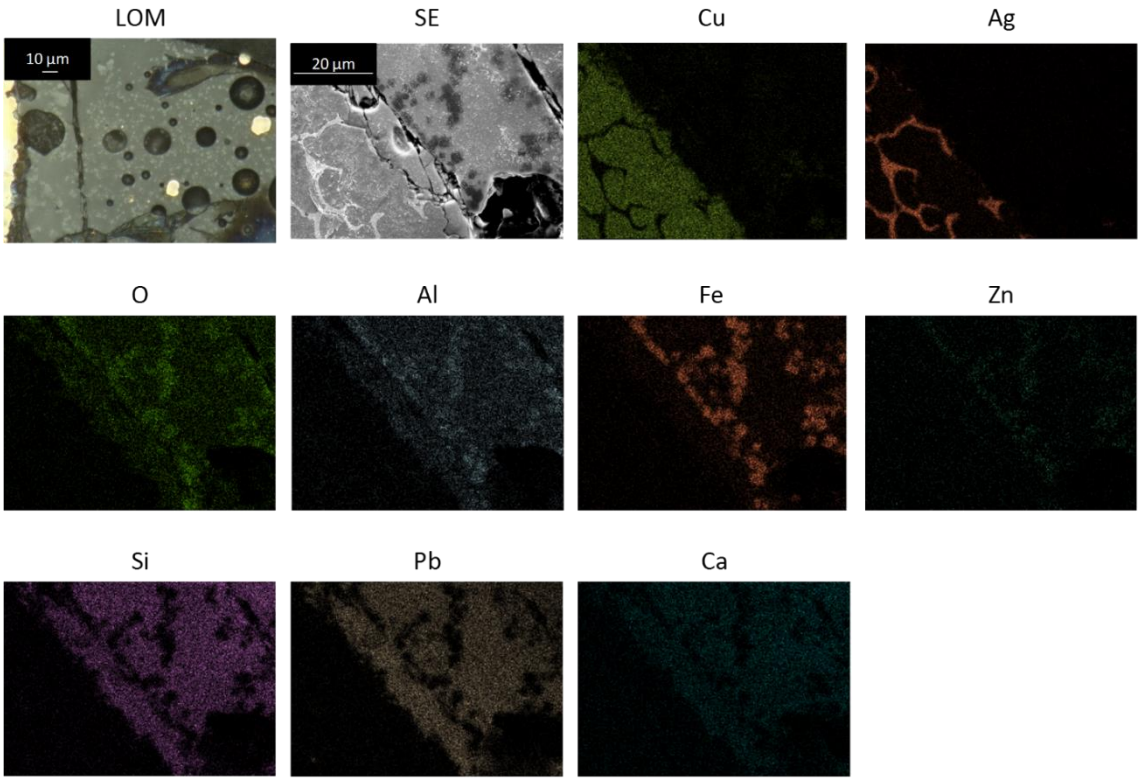

Figure 9.9 Optical micrograph, SE image and elemental map of the interface between the large alloy droplet (20 wt% Ag) and the slag phase. The scale bar in the in the SE image and elemental maps are the same.

The large copper alloy droplet is situated in the lower left corner of the SE image as can also be seen on the elemental Cu and Ag EDX maps. When moving towards the slag phase over the interface, no intermediate phase, such as a copper-oxide phase, was observed. Directly next to the alloy droplet, a slag layer with Si, Pb, Al and O is found. This slag layer is flanked by a set of spinel solids (consisting of O, Al, Fe and Zn).

De Wilde et al. [1] observed the presence of an intermediate copper oxide layer between the large copper drop and slag phase. They presented two possible explanations for this: a quenching effect or a reaction between the copper and slag. The quenching effect was considered unlikely as the remainder of the microstructure of the sample did not contain any other quench effects. The slag phase in our work also contains a higher amount of Cu with respect to the amount initially present in the slag phase, also indicating the dissolution of the copper alloy drop in the slag. It is possible that the presence of Ag in the copper alloy retarded or stopped the formation of the copper oxide layer at the interface between the two phases. De Wilde et al. [14] also found different behaviour between oxygen and Cu-Ag alloys compared to pure copper in sessile drop experiments. As stated by Lee et al.[15] and Fima et al. [16], this could be attributed to the accumulation of Ag at the surface, which is then responsible for the different behaviour with oxygen either in the atmosphere in the sessile drop experiments, or in the slag in this study.

9.2.2.5. Slag further away from the big alloy droplet

Further away from the big alloy droplet and in the lower slag phase (closer to the substrate), some attached copper droplets are also observed as can be seen in Figure 9.10. However, they are present to a smaller extent in these areas. Moreover, more darker solids are present, as already observed in the slag directly next to the alloy drop for the 20 wt% Ag case. An elemental map illustrating the distribution of the elements over the different phases in the slag phase further away from the big alloy drop is shown in Figure 9.11.

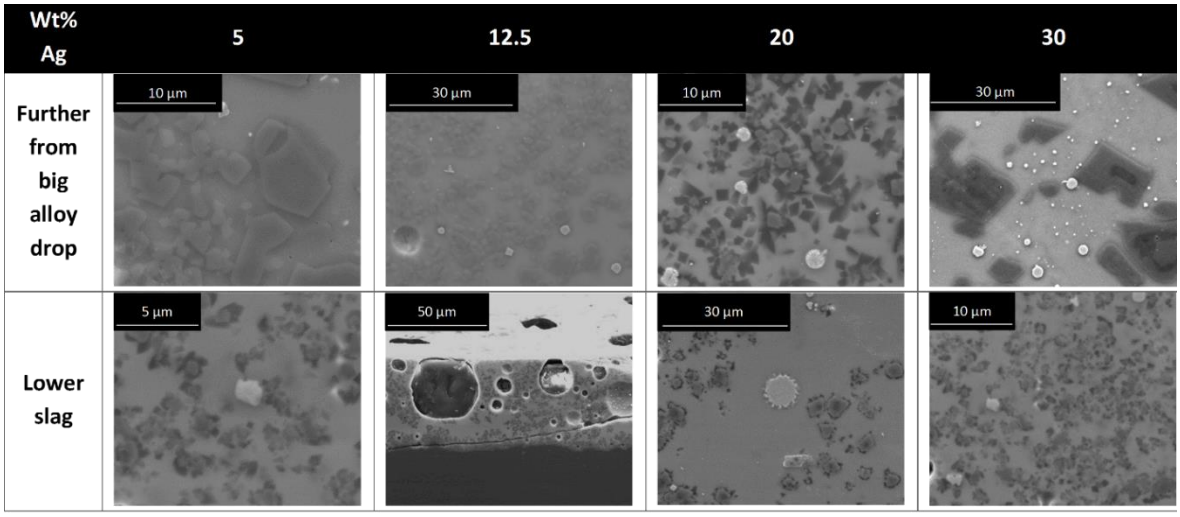

Figure 9.10 SE images of the microstructures further away from the big copper alloy droplet and in the lower slag phase for the different Cu-Ag alloys

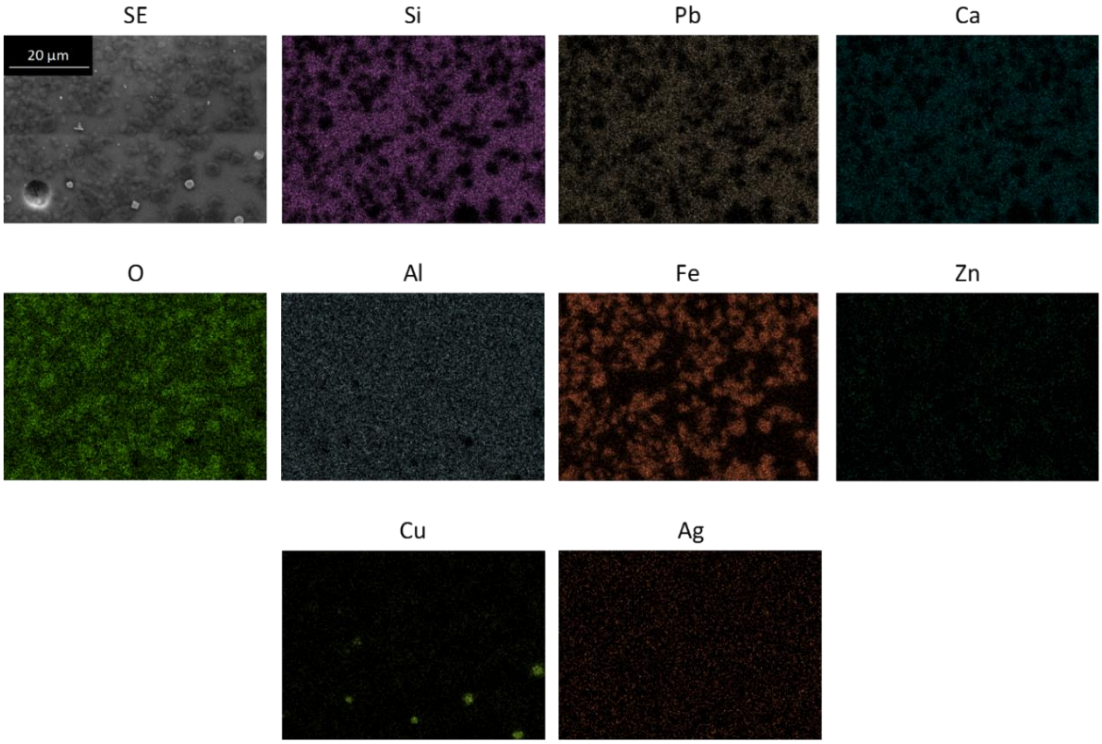

Figure 9.11 Elemental map of the microstructure slag further away from the big alloy drop with 12.5 wt%Ag. The scale bar in the in the SE image and elemental maps are the same.

The amount of attached metal droplets is lower and the spinel particles seem smaller. The compositions of the different constituents in the microstructures further away from the big alloy drop were measured with EDX and the results are shown in Table 9.5.

Sample	Phase	Wt% Si	Wt% Pb	Wt% Ca	Wt% Mg	Wt% O	Wt% Al	Wt% Fe	Wt% Zn	Wt% Cu	Wt% Ag
5	Slag	13.4	14.3	7.2	1.0	30.6	7.9	18.4	4.3	2.7	-
	Inner spinel	1.2	1.1	-	1.2	30.3	7.4	49.0	8.2	-	-
20	Outer spinel	6.9	3.1	5.3	4.1	35.6	15.6	21.8	6.8	-	-
	Attached Cu	5.2	4.4	2.2	-	4.7	3.4	2.0	-	76.1	-
	Non-attached Cu	-	-	-	-	-	-	1.2	-	95.8	-
	Solids	16.3	8.7	14.1	1.9	35.1	8.3	11.2	-	3.6	-
30	Inner spinel	-	-	-	-	30.6	13.4	39.4	14.9	-	-
	Attached Cu	1.3	2.5	1.1	-	1.3	-	3.7	1.0	84.5	3.1
	Non-attached Cu	-	-	-	-	-	-	2.2	-	91.1	3.2

Table 9.5 Average measured compositions of the various phases in the microstructure further away from the large alloy drop for the different Cu-Ag alloys. Compositions below 1wt% were assigned with '-'.

The compositions of all phases are very similar to the ones listed in Table 9.4. The spinel particles are again mainly constituted of O, Al, Fe and Zn and the same observations can be made regarding the inner and outer spinel parts. The attached metal droplets clearly contain less Cu as more of the other elements (not Cu or Ag) are present within the droplets. Due to the very small dimensions of these solids, it is not straightforward to quantify the amounts of Fe and Al precisely and to determine the chemical formula. Based on the composition, it could be suggested that the small darker solids are hedenbergite ($CaFeSi_2O_6$) or esseneite ($CaFeAlSiO_6$), which is in accordance with the findings of De Wilde et al. [1]. The compositions of the different constituents in the microstructure in the lower slag

were measured with EDX and are very similar to the compositions corresponding to the slag phase further away from the large alloy droplet.

9.2.2.6. Slag – spinel substrate interface

The large copper alloy drop did not have direct contact with the spinel substrate, but the slag did and a certain interaction between the slag and the spinel substrate could be observed, as shown in Figure 9.12.

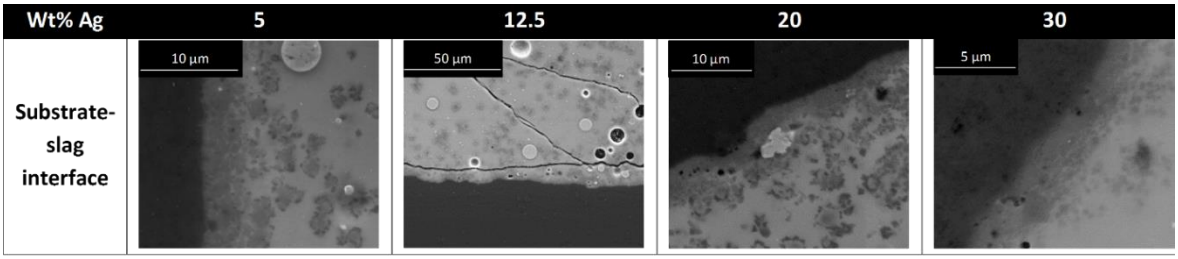

Figure 9.12 SE images of the microstructures at the interface between the slag phase and the $MgAl_2O_4$ substrate for the different Cu-Ag alloys

An intermediate layer is formed between the slag and the $MgAl_2O_4$ substrate. The SE image of the 12.5 wt% Ag sample does not give a clear intermediate layer, but it is present, as confirmed by the elemental map in Figure 9.13.

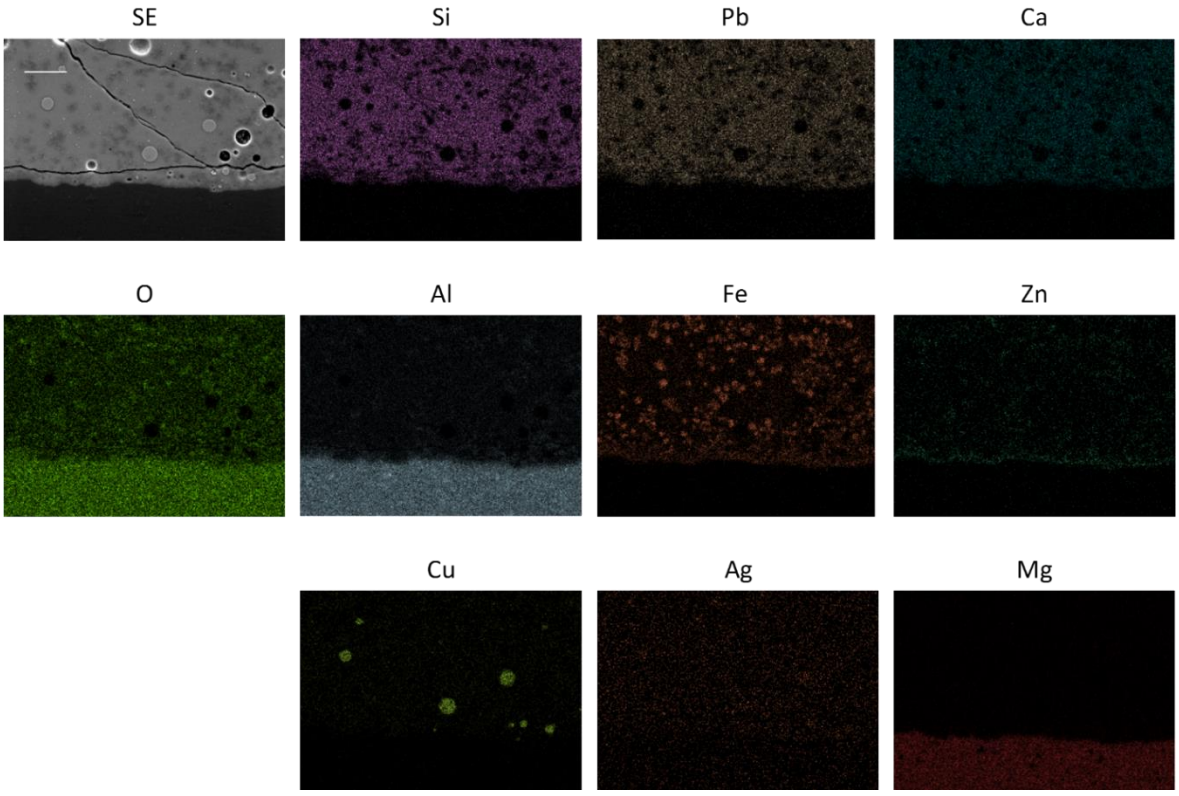

Figure 9.13 Elemental map of the microstructure of the slag-substrate interface for the 12.5 wt% Ag sample. The scale bar in the in the SE image and elemental maps are the same.

The Zn and Fe map in particular illustrate the presence of the intermediate layer. This is even clearer in a sample with a larger intermediate layer, such as the 5 wt%Ag sample in Figure 9.14. Moreover, the EDX measurements of the slag, intermediate layer and the substrate for all the samples are shown in Table 9.6.

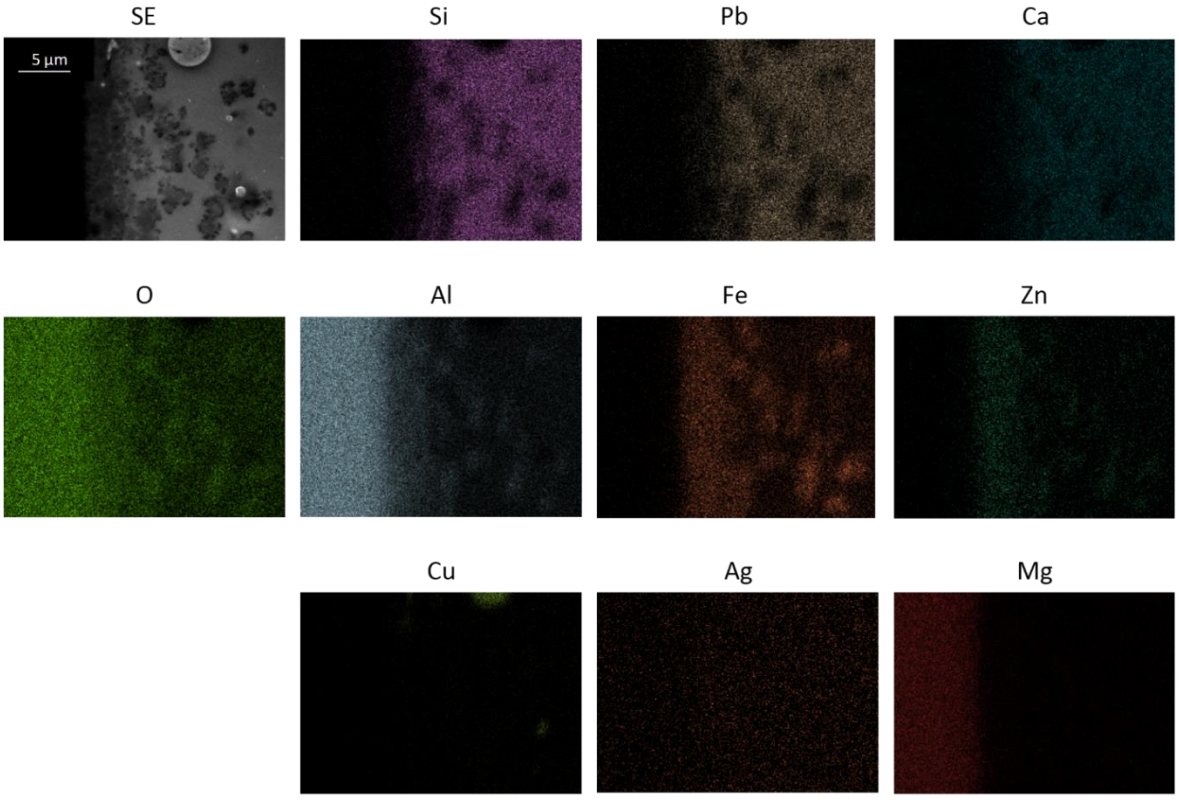

Figure 9.14 Elemental map of the microstructure of the slag-substrate interface for the 5 wt% Ag sample. The scale bar in the in the SE image and elemental maps are the same.

Sample	Phase	Wt % Si	Wt % Pb	Wt % Ca	Wt % Mg	Wt % O	Wt % Al	Wt % Fe	Wt % Zn	Wt % Cu	Wt % Ag
5	Substrate	-	-	-	13.9	43.3	41.9	-	-	-	-
	Intermediate layer	2.0	2.5	-	3.5	35.1	24.4	15.0	16.0	-	-
	Attached Cu in slag	-	-	-	-	1.9	-	1.0	-	93.6	-
12.5	Substrate	-	-	-	14.0	43.0	42.3	-	-	-	-
	Intermediate layer	4.0	5.2	1.9	4.3	36.1	22.5	12.4	11.9	1.7	-
	Slag	15.0	24.6	8.3	0.7	30.8	6.4	5.3	1.3	7.4	-
	Attached Cu in slag	-	-	-	-	-	-	-	-	93.1	2.4
	Non-attached Cu in slag	-	-	-	-	-	-	1.2	-	94.0	1.6
20	Substrate	-	-	-	15.1	41.3	42.7	-	-	-	-
	Intermediate layer	-	-	-	11.1	36.2	34.3	7.6	7.9	1.0	-
	Slag	15.6	20.6	10.0	1.2	31.8	7.4	7.0	1.4	4.7	-
	Spinel in slag	14.5	19.4	9.0	-	32.1	7.3	10.2	1.6	4.6	-
	Solids in slag	12.5	11.7	9.6	1.9	35.1	9.9	12.6	3.8	2.8	-
30	Substrate	-	-	-	14.2	42.3	42.5	-	-	-	-
	Intermediate layer	2.5	3.3	1.3	8.2	37.8	28.4	10.5	7.5	-	-
	Slag	15.8	22.8	8.7	1.6	32.6	9.4	5.8	-	-	-

Table 9.6 Average measured compositions of the various phases in the microstructure at the interface between the slag and the $MgAl_2O_4$ substrate for the different Cu-Ag alloys. Compositions below 1wt% were assigned with '-'.

The substrate consists of Mg, Al and O and virtually no other elements. It should be noted, however, that the points measured in the substrate were situated at a specific distance from the intermediate layer, where no diffusion processes are expected to alter the substrate composition. The

intermediate layer is a spinel solid solution of Mg, O, Al, Fe and Zn, but with a different composition than the spinel solids in the slag phase. The large difference with the spinel solids in the slag phase, is the presence of the Mg. Some non-spinel forming elements (such as Si and Pb) are also measured to a small amount. The slag phase near the intermediate slag layer contains more Mg than in the other regions of the samples. This Mg can only originate from a diffusion process from the $MgAl_2O_4$ substrates, which indicates its dissolution. Additionally, the amount of Al in the slag is a little bit higher next to the interaction layer with respect to the other regions in the samples, which also confirms that the $MgAl_2O_4$ dissolves into the slag. De Wilde et al. [1] observed gradients in composition seen on the elemental maps, which could result from the diffusion of Fe and Zn from the slag and intermediate layer into the spinel substrate. However, this is not visible in our results and it should be noted that De Wilde et al. [1] also indicated that the gradients in composition seen on the elemental maps could also be due to an interference with the interaction layer.

Both the captured images during the high temperature CSLM experiment (Figure 9.3) and the microstructural overview of the samples (Figure 9.4) demonstrate that the big copper alloy droplet is not in contact with the spinel substrate after coalescence with the slag. This agrees with the results of standard sessile drop experiments in literature: copper generally displays a non-wetting behaviour on spinel substrates, whereas slags display good wetting on spinel substrates. This good wetting of the slag on the $MgAl_2O_4$ substrate was also observed previously by Abdeyazan et al. [17], Tran et al. [18] and Donald et al. [19]. Moreover, an interaction layer consisting of (Mg, Zn, Fe)(Al, Fe)$_2O_4$, is formed. This is in accordance with the results of De Wilde et al. [1,4], i.e. that the $MgAl_2O_4$ substrate dissolves into the slag. Due to this dissolution, the concentration in spinel-forming elements becomes very high, inducing the formation of the spinel intermediate layer. They proposed the following reaction taking place at the studied $MgAl_2O_4$-slag interface:

$$MgAl_2O_{4\ solid} + (Fe_2O_3, FeO, ZnO\ Al_2O_3)_{slag}$$
$$\rightarrow (Mg^{2+}, Zn^{2+}, Fe^{2+})(Al^{3+}, Fe^{3+})_2O_{4\ interaction\ layer} + (MgO)_{slag} + (Al_2O_3)_{slag}$$

Furthermore, this overall reaction was confirmed previously by thermodynamic calculations using FactSage [4].

9.3. Conclusions

In this study, the attachment of copper droplets to spinel particles in slags, retaining the sedimentation of the droplets, is studied. Adapted sessile drop experiments were performed, in which both copper alloys and slag were placed on a spinel substrate. Several copper-silver alloys, a synthetic PbO-CaO-SiO_2-Cu_2O-Al_2O_3-FeO-ZnO slag and a $MgAl_2O_4$ substrate were used to represent the copper alloy droplets, slag and spinel solids, respectively. The silver was added to the copper alloy as a trace element to get more insights into the origin of the attachment.

The slag displayed a very good wetting behaviour on the $MgAl_2O_4$ substrate, whereas the copper alloy drop did not wet the spinel substrate. During the high temperature CSLM experiment, the slag moved towards the alloy drop and coalescence occurred, after which the slag positioned itself between the substrate and the alloy drop. Thus, no direct interaction between the copper and the $MgAl_2O_4$ substrate was possible.

The microstructures within the different samples were studied and the compositions of the different phases present were determined. A (Mg, Zn, Fe)(Al, Fe)$_2O_4$ interaction layer was formed at the slag-

$MgAl_2O_4$ interface. At the slag-copper droplet interface, no interaction layer was observed, but copper dissolution into the slag was noted.

Small entrained copper droplets sticking to spinel solids were present within the slag droplet. A mechanism is proposed to explain the presence of those sticking droplets: either purely reactive or a combination of dispersion and reaction. In the latter case, it is suggested that during the coalescence phase in the high temperature CSLM experiment, some small Cu-Ag droplets are dispersed within the large slag drop. These Cu-Ag droplets then act as nucleation sites for a simultaneous reduction of copper and silver oxides into metallic copper and the oxidation of slag oxides into more stable spinel structures. In this way, the spinel solids grow at the side of the Cu-Ag droplets, which in turn are enriched with Cu and grow. This leads to copper droplets attached to spinel solids within the slag phase.

References

[1] E. De Wilde, I. Bellemans, M. Campforts, M. Guo, B. Blanpain, N. Moelans, K. Verbeken, Investigation of High-Temperature Slag/Copper/Spinel Interactions, Metall. Mater. Trans. B. 47 (2016) 3421–3434. doi:10.1007/s11663-016-0805-8.

[2] Y. Takeda, S. Ishiwata, A. Yazawa, Distribution Equilibria of Minor Elements between Liquid Copper and Calcium Ferrite Slag, Trans. Jpn. Inst. Met. 24 (1983) 518–528. doi:10.2320/matertrans1960.24.518.

[3] N. Eustathopoulos, Dynamics of wetting in reactive metal/ ceramic systems, Acta Mater. 46 (1998) 2319–2327. doi:10.1016/S1359-6454(98)80013-X.

[4] E. De Wilde, I. Bellemans, M. Campforts, M. Guo, B. Blanpain, N. Moelans, K. Verbeken, Sessile drop evaluation of high temperature copper/spinel and slag/spinel interactions, Trans. Nonferrous Met. Soc. China. 26 (2016) 2770–2783. doi:10.1016/S1003-6326(16)64344-3.

[5] N. Eustathopoulos, M.G. Nicholas, B. Drevet, Wettability at High Temperatures, Elsevier, 1999.

[6] E. De Wilde, I. Bellemans, L. Zheng, M. Campforts, M. Guo, B. Blanpain, N. Moelans, K. Verbeken, Origin and sedimentation of Cu-droplets sticking to spinel solids in pyrometallurgical slags, Mater. Sci. Technol. 32 (2016) 1911–1924. doi:10.1080/02670836.2016.1151998.

[7] C.W. Bale, P. Chartrand, S.A. Degterov, G. Eriksson, K. Hack, R. Ben Mahfoud, J. Melançon, A.D. Pelton, S. Petersen, FactSage thermochemical software and databases, Calphad. 26 (2002) 189–228. doi:10.1016/S0364-5916(02)00035-4.

[8] J.W. Cahn, On spinodal decomposition, Acta Metall. 9 (1961) 795–801. doi:10.1016/0001-6160(61)90182-1.

[9] X. Llovet, E. Valovirta, E. Heikinheimo, Monte Carlo Simulation of Secondary Fluorescence in Small Particles and at Phase Boundaries, Microchim. Acta. 132 (2000) 205–212. doi:10.1007/s006040050013.

[10] T. Sakai, S.W. Ip, J.M. Toguri, Interfacial phenomena in the liquid copper-calcium ferrite slag system, Metall. Mater. Trans. B. 28 (1997) 401–407. doi:10.1007/s11663-997-0105-4.

[11] E. De Wilde, I. Bellemans, M. Campforts, M. Guo, K. Vanmeensel, B. Blanpain, N. Moelans, K. Verbeken, Study of the Effect of Spinel Composition on Metallic Copper Losses in Slags, J. Sustain. Metall. 3 (2017) 416–427. doi:10.1007/s40831-016-0106-0.

[12] L. Scheunis, M. Campforts, P.T. Jones, B. Blanpain, A. Malfliet, The influence of slag compositional changes on the chemical degradation of magnesia-chromite refractories exposed to PbO-based non-ferrous slag saturated in spinel, J. Eur. Ceram. Soc. 35 (2015) 347–355. doi:10.1016/j.jeurceramsoc.2014.08.017.

[13] S.A. Nightingale, B.J. Monaghan, Kinetics of Spinel Formation and Growth during Dissolution of MgO in CaO-Al2O3-SiO2 Slag, Metall. Mater. Trans. B. 39 (2008) 643–648. doi:10.1007/s11663-008-9186-y.

[14] E. De Wilde, I. Bellemans, M. Campforts, A. Khaliq, K. Vanmeensel, D. Seveno, M. Guo, A. Rhamdhani, G. Brooks, B. Blanpain, N. Moelans, K. Verbeken, Wetting behaviour of Cu based alloys on spinel substrates in pyrometallurgical context, Mater. Sci. Technol. 31 (2015) 1925–1933. doi:10.1179/1743284715Y.0000000052.

[15] J. Lee, T. Tanaka, Y. Asano, S. Hara, Oxygen adsorption behavior on the surface of liquid Cu-Ag alloys, Mater. Trans. 45 (2004) 2719–2722. doi:10.2320/matertrans.45.2719.

[16] P. Fima, N. Sobczak, Thermophysical Properties of Ag and Ag–Cu Liquid Alloys at 1098K to 1573K, Int. J. Thermophys. 31 (2010) 1165–1174. doi:10.1007/s10765-010-0798-5.

[17] H. Abdeyazdan, N. Dogan, M. Rhamdhani, M. Chapman, B. Monaghan, Dynamic wetting of CaO-Al2O3-SiO2-MgO liquid oxide on MgAl2O4 spinel, Metall. Mater. Trans. B - Process Metall. Mater. Process. Sci. 46 (2014) 208–219. doi:10.1007/s11663-014-0207-8.

[18] T. Tran, D. Xie, Y.B. Cheng, Effects Of Slag Chemistry And Temperature On Wetting And Penetration Of Refractories By Slags, in: The South African Institute of Mining and Metallurgy, 2004. http://www.onemine.org/document/abstract.cfm?docid=47131&title=Effects-Of-Slag-Chemistry-And-Temperature-On-Wetting-And-Penetration-Of-Refractories-By-Slags (accessed August 12, 2016).

[19] J.R. Donald, J.M. Toguri, C. Doyle, Surface interactions between fayalite slags and synthetic spinels and solid solutions, Metall. Mater. Trans. B-Process Metall. Mater. Process. Sci. 29 (1998) 317–323. doi:10.1007/s11663-998-0108-9.

10. Smelting experiment [18]

De Wilde et al. [1,2] developed a methodology for smelting experiments to observe the attachment of metal droplets to solid spinel particles in synthetic slags. These synthetic slags contained over 7 components to be industrially relevant. However, one of the limitations of modelling is the 'curse of dimensionality' [3], i.e. the more components in the system, the more computational time is required to simulate this system. The dependence is even exponential. Thus, from a modelling point of view, smelting experiments with as few as possible elements are interesting. Of course, the number of elements required should exceed a certain value to be able to capture the attachment of the metal droplet to the spinel particle in a liquid slag phase. The following paragraphs describe the requirements for such a system, the changes in methodology which were required [4], as systems with fewer elements typically encounter certain problems and finally an oxidation-reduction experiment in the Fe-Si-Al-O system with Cu-Ag droplets is described.

10.1. Introduction

First, the slag-copper system was calculated using the FactSage 6.4 thermodynamic software package to obtain a suitable elemental composition, together with the temperature and the equilibrium partial pressure of oxygen for which attached copper alloy droplets can possibly occur. The temperature and the equilibrium partial pressure of oxygen together determine the degree of oxidation of the system which is very important for controlling parameters like chemical losses, fractions of micro-solids and slag viscosities.

10.1.1. Temperature and p_{O2}

The temperature can be easily controlled by providing feedback from a temperature sensor, placed in the liquid slag-copper system, to the power control of the furnace. The equilibrium partial pressure of oxygen is expressed in the same units as pressure and represents the pressure of oxygen gas that needs to be applied above the liquid slag-alloy system in order to prevent the net exchange of oxygen between the gas and the system. From basic thermodynamics, it can be understood that when a slag is brought into contact with a gas mixture containing a higher partial pressure of oxygen than the equilibrium oxygen partial pressure of the slag, oxygen transfer from the gas to the slag will occur.

The best way to obtain a gas with a known partial pressure of oxygen is to create a mixture of carbon monoxide (CO) and carbon dioxide (CO_2). When this gas mixture is exposed to the high temperatures of the furnace, a certain oxygen fraction is produced by the Boudouard reaction. The thermodynamics of these type of CO/CO_2 mixtures is very well known and the oxygen partial pressure at equilibrium, depending on the temperature, can be calculated accurately. Thus, at equilibrium, the oxygen partial pressure is given by $p_{O2} = K_p * (p_{CO2}/p_{CO})^2$. Where K_p is the equilibrium constant of the Boudouard reaction. This reaction constant depends strongly on the temperature and thermodynamic properties of the reactants and products. The value of K_p can be calculated with software such as FactSage.

[18] Based on some of the work in the master's thesis of V. Cnockaert titled "Investigation of the attachment of metallic droplets to solid particles in liquid slags", during academic year 2015-2016 at Ghent University.

10.1.2. System selection

The system that needs to be considered should have a high enough volume fraction of metal alloy, should contain slag-forming elements and spinel-forming elements and should have a sufficiently low viscosity. The first element that is required is copper (Cu), as we want to study the attachment of liquid copper to spinel micro-crystals in the liquid slag. For spinel particles to be formed, iron (Fe) is a very useful element, as it can occur in both the +3 and the +2 oxidation states, which are required to form the spinel crystal structure. Thus, it can even form a spinel particles by itself in the form of magnetite (Fe_3O_4). Moreover, iron oxide is the main compound for many copper smelting and converting slags. The third element is aluminium (Al), as the crucible containing the high-temperature system is made of alumina (Al_2O_3) and the interaction between the slag and the alumina crucible, temperature sensors and gas injection pipes should be kept as low as possible. Significant dissolution of the crucible and equipment can be prevented by using a slag that is close to alumina saturation. Moreover, aluminium can form spinel solids together with iron. The elements iron, copper and aluminium, together with oxygen, are able to create a system that contains the required three phases in equilibrium. However, such slags typically will possess high melting temperatures, thus the slag is fluxed, similarly as in industry. For this, silicon (Si) was added and is expected to stay in the slag as it is not a spinel-forming element.

For the volume of the copper alloy, a rough estimate can be made by using the approximation that the copper alloy phase only contains copper. The copper content of the system was chosen to be approximately 25wt% of the entire system. In this way, the alloy represents about $1/8^{th}$ of the entire liquid bath, by volume. This amount should be sufficient to create a fine suspension of copper droplets in the liquid slag during stirring by bubbling.

To be able to investigate the interaction between the different phases, all phases are required to be present in the system. This can be visualized in a phase diagram, such as in Figure 10.1, wherein the important regions are the ones where alloy and slag (1) and alloy, slag and spinel (2) phases are in equilibrium with each other. The region containing alloy, slag and spinel (2) is the most interesting for this study.

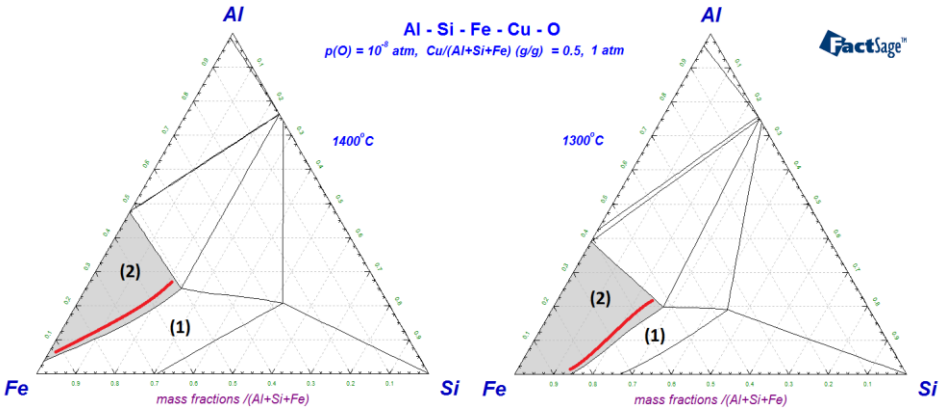

Figure 10.1 Phase diagram for a system containing iron, aluminium, silicon and copper at a partial pressure of oxygen of 10^{-8} atm. The coloured region (2) in the diagram shows where alloy, slag and spinel are in equilibrium within the system. Region (1) corresponds to the compositions where alloy and slag are in equilibrium with each other. The thick line in region (2) indicates the compositions where the liquid slag contains about 10 wt% of solid spinel particles. [4]

A small fraction of silver metal was also added to the system. This silver metal acts as a tracer element for the alloy phase. By measuring the silver content of alloy droplets in the slag phase, the origin of

the alloy droplets in the slag phase can be investigated, i.e. whether the droplet precipitated from the supersaturated slag or if the droplet was just ripped from the bulk liquid alloy phase at the bottom of the crucible. In the former case, no silver in the droplet is expected. In the latter case, the droplet originates from the alloy which contains silver and thus the occurrence of silver in the alloy droplets is expected.

10.1.3. Viscosity

Note that it is not sufficient to consider any composition within the alloy, slag and spinel (2) region, but that the viscosity of the slag itself and the combination of the spinel solids within this slag should remain low enough to have a workable slag. A low viscosity slag is preferred in industry because it makes stirring and good mixing of the liquid phase possible, is easy to pour and decreases decantation times.

The mass fraction of spinel particles in the slag depends on the exact position of the state of the system within this region. This fraction of spinel particles can be estimated with the lever rule within the three-phase region (2). Because the spinel micro-solids have almost the same density as the slag, the mass fraction can be approximated as the volume fraction of micro-solids in the slag phase. These small spinel crystals float around in the liquid slag phase and create a slurry. The viscosity of the slurry strongly increases with increasing volume fraction of micro-solids as described by an Einstein-Roscoe type equation ($\eta = \eta_0(1 - af)^{-n}$). Here, η and η_0 are the viscosity of the slurry and the viscosity of the liquid slag in the absence of micro-solids, respectively, and f is the volume fraction of solid particles. The constants a and n depend on the general shape and size of the micro-particles: for a slag-spinel system, these constants have been determined to be 4.4 and 2.5 for a and n, respectively [5]. This means that a slurry with a solid particle volume fraction of 16% can have a viscosity that is 20 times larger than the slag itself. A weight fraction of maximum 10% should give a good balance between the required presence of spinel particles, needed for the attachment of copper droplets, and the increasing viscosity of the system. A volume fraction of 10% spinel particles would quadruple the viscosity of the slag.

The viscosity of the slag on its own represents the minimal viscosity of the slurry. The Viscosity module of the software package FactSage can be used to estimate the viscosity of the liquid slag. Although this is a very useful tool, it does not take the presence of copper oxides into account because data for these kind of slags is not available. It is assumed that the contribution of copper oxide to the viscosity of the slag is negligible at low copper concentrations in the slag phase.

Figure 10.2 (right) shows a part of the ternary phase diagram for the system at the previously mentioned conditions. The section of interest (2) is coloured and the compositions that could be used during high-temperature experiments are indicated with the thick red line AB. For these compositions, the system exists of a liquid copper and slag phase, together with a small fraction of spinel micro-solids. For these compositions, the slag viscosity can be seen in Figure 10.2 (left). The composition in this plot changes according to line AB in the phase diagram at the right side of the figure. It can be seen that the slag viscosity is at its lowest when the slag mainly exists of iron oxide (A). The viscosity increases when more alumina or silica is present in the slag (B). When even more of the iron oxide gets replaced by other compounds, the spinel particles get unstable or other solid phases become stable.

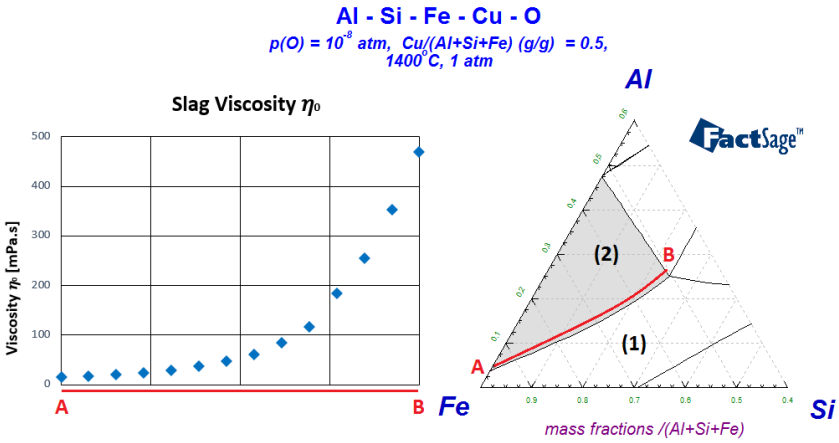

Figure 10.2 Viscosities of liquid slags that can exist in equilibrium with solid spinel particles in the Fe-Al-Si-Cu system at a temperature of 1400 °C and a partial pressure of oxygen of 10^{-8} atm for compositions ranging from A to B as calculated by FactSage 6.4. [4]

10.1.4. Avoiding quench effects

Preliminary experiments have shown that slags with high amounts of iron oxides show quenching effects, such as the needles in parts (a) and (b) of Figure 10.3. This is in contrast with a slag containing lesser iron oxides (parts (c) and (d) of Figure 10.3), where no such needles are observed. From SEM and EDX analyses, it could be concluded that the fine crystals that are present in the quenched slag exist mainly of ferrous oxide (FeO).

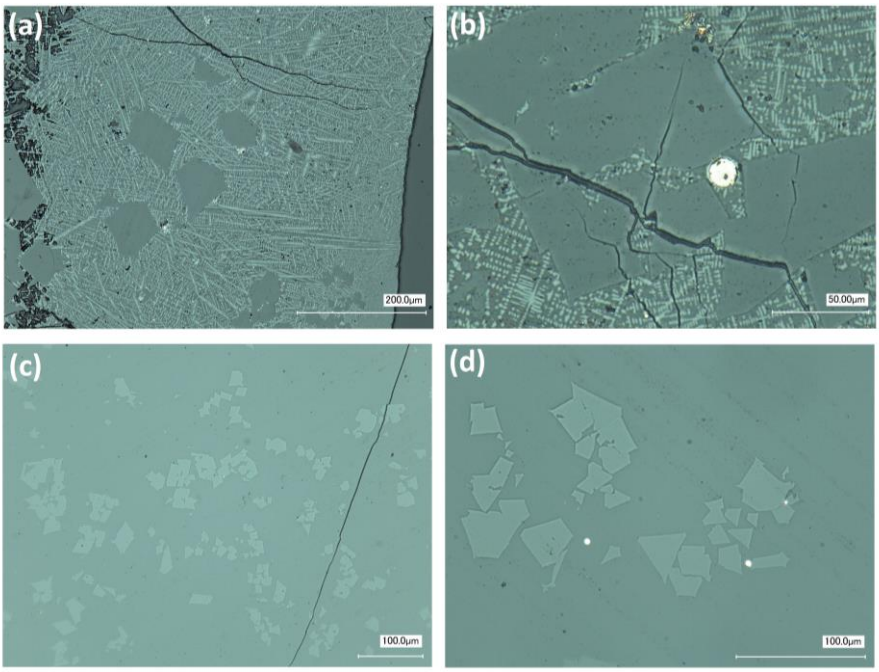

Figure 10.3 Optical microscope images of the quenched samples, collected during the high-temperature experiment. Images (a) and (b) correspond to a composition high in iron oxides, images (c) and (d) correspond to a composition lower in iron oxides. [4]

The reason for the presence of this quench effect is that the Fe-monoxide has a very simple crystal structure and thus can be easily formed within the slag. This is illustrated by Factsage calculations at various temperatures in Figure 10.4. During the cooling of a composition rich in iron oxides, the metal monoxide gets stable from a temperature of about 1240 °C. Performing the same calculation for a

composition with less iron oxides, for which no quench effects were observed, shows that the stability of this monoxide phase does not occur. Instead, it is replaced by the stability of a different, more complex clinopyroxene, phase which becomes thermodynamically stable below approximately 1175 °C. Clinopyroxene is a group name for all pyroxene minerals with a monoclinic crystal structure. Pyroxenes are chain silicate minerals with the general formula $AB(Si,Al)_2O_6$. This much more intricate structure works as a kinetic barrier for the phase to actually form during quenching.

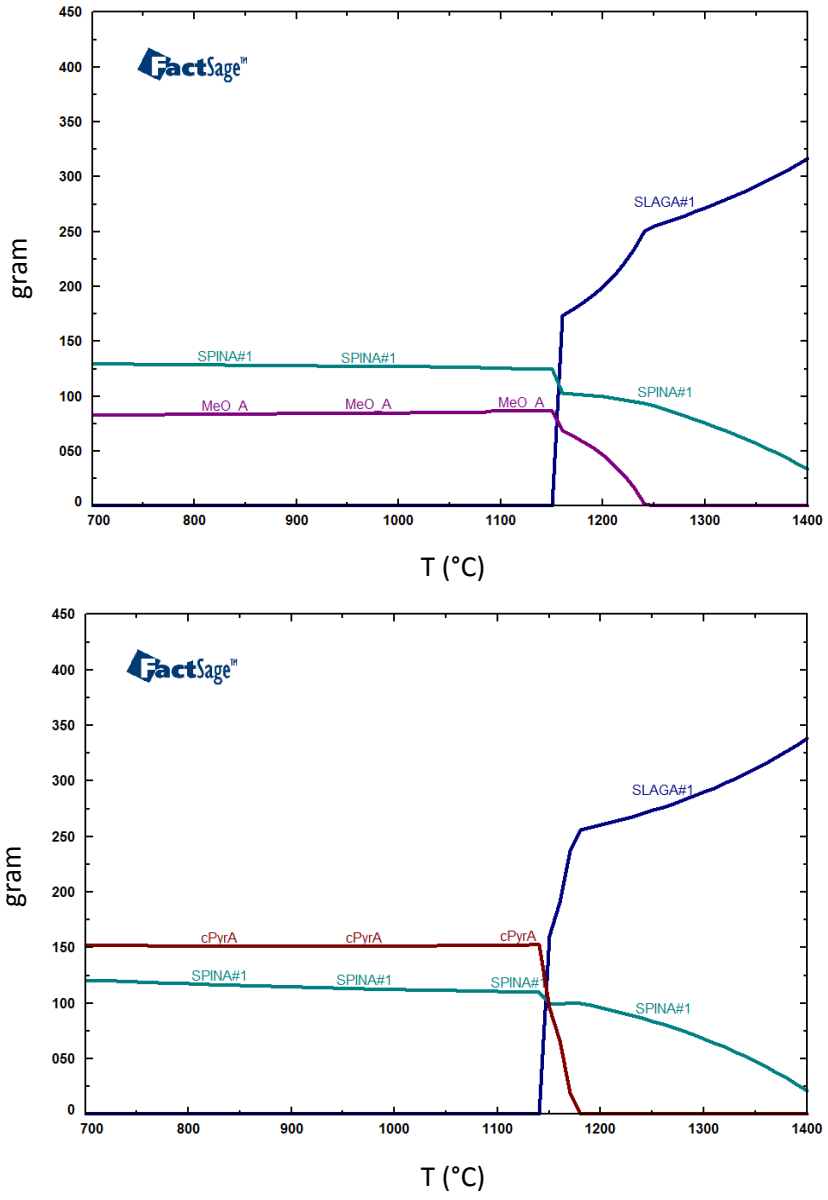

Figure 10.4 Thermodynamic stable phases of the Fe-Al-Si-Cu system with on top a composition rich in iron oxides and on the bottom a composition with less iron oxides at different temperatures. [4]

When the calculations are repeated for more slag compositions along the boundary between region (1) and (2), the transition from ferrous oxide stability during cooling and pyroxene stability lays around a Fe/(Al+Si+Fe) -ratio of 0.75 under the specified conditions. This means that we can assume that the slag from a system with a Fe/(Al+Si+Fe)-ratio of more than 0.75 will develop quench effects during cooling while a system with a Fe/(Al+Si+Fe)-ratio of less than 0.75 will be able to be quenched without distortion due to unintentional crystal growth. It should be noted, however, that it is likely that the reality is more complex and that the occurrence of quench effects depends on more than

just the thermodynamically stability of unwanted phases during quenching. Nevertheless, this method of calculating the stable phases during cooling can be a good guideline for in which cases quench effects in solidified slag can be expected or not.

Figure 10.4 also shows that the equilibrium fraction of spinel particles increases during cooling. This means that the existing spinel particles will have the tendency to grow during quenching, if sufficient rearrangement of atoms due to diffusion can occur. Diffusion is also necessary for the growth of the ferrous oxide crystal structures, starting from nuclei in the solidified slag. For liquids, this diffusion coefficient D related to the viscosity η as given by the Stokes–Einstein equation: $D = k_B T/ (6\pi\eta r)$. In this equation k_B is the Boltzmann constant and r is the radius of the diffusing atom. This equation shows that the diffusion coefficient is inversely proportional to the viscosity of the liquid phase. This means that by choosing a mixture with a low slag viscosity we also choose for a slag with a higher diffusion coefficient which might increase the occurrence of quench effects and unwanted phase growth during quenching. Thus, for the choice of the system, a slag with low viscosity is required for practical reasons but this results in a high diffusion coefficient. Therefore, there will always be the need to find a compromise between low viscosity and high diffusivity.

10.2. Experimental method

10.2.1. Experimental set-up

The smelting experiments were executed in an Indutherm induction melting furnace. A schematic representation of the different parts of the furnace are shown in Figure 10.5. The walls of the furnace (1) are made of insulating material, wherein the water-cooled copper electromagnetic coil (2) is embedded. A silicon carbide crucible (3) is placed inside the furnace, for conductivity and safety purposes. Three smaller alumina crucibles (4) of 400 ml are placed inside the large silicon carbide crucible. Heating of these small non-coupled crucibles occurs due to conduction, convection and radiation from the inductively heated silicon carbide crucible. The small crucibles contain slag and alloy (5), for which the temperature is measured with thermocouples inside alumina tubes (6). Moreover, gas is injected in the liquid phases through extra alumina tubes (6). The measured temperature is used as feedback for the furnace control. Small covers made of refractory stone with some holes for the thermocouple and bubbling pipes were positioned on top of the small alumina crucibles.

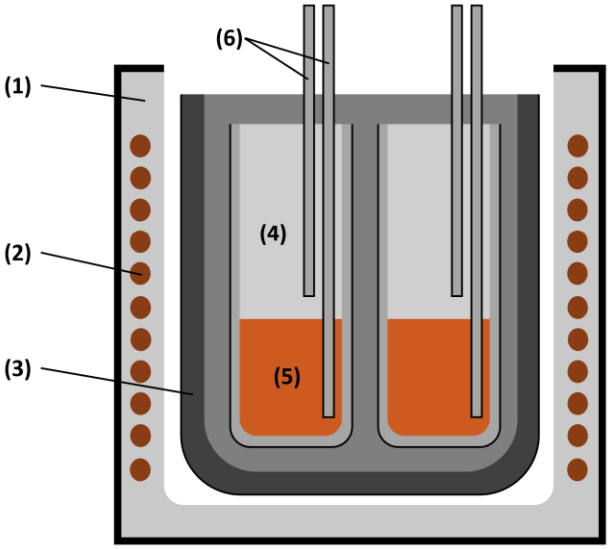

Figure 10.5 A schematic of the experimental set-up for performing high-temperature experiments in an Indutherm inductive melting furnace. Here, the insulating outside (1), water-cooled copper electromagnetic coil (2), silicon carbide crucible (3), alumina crucibles (4), slag and alloy (5) and extra equipment (6) are shown. [4]

10.2.2. Input compounds

The systems were prepared by melting oxides of appropriate quantities. The targeted system composition, based on thermodynamic FactSage calculations, is shown in Table 10.1. The total mass of the system in a 400 ml crucible was chosen as approximately 600g, to have a liquid volume of less than about half of the total crucibles volume, to avoid too much splashing or foaming. FeO was added as a combination of metallic iron and hematite, while CaO was added as limestone, which decomposes in quicklime and carbon dioxide at high temperatures.

Cu [wt%]	Ag [wt%]	Al_2O_3 [wt%]	Fe [wt%]	Fe_2O_3 [wt%]	SiO_2 [wt%]
24.6	1.4	18.6	9.4	26.9	19.1

Table 10.1 Targeted composition in wt% for the input compounds

10.2.3. Partial melting

The preliminary experiments also showed that certain mixtures, which were predicted to be liquid at high temperatures and a reductive atmosphere, stayed in a very thick pastry like state. This was due to the high-melting temperatures of the pure compounds. Iron oxide is the only slag compound that will melt below a working temperature of 1400°C and thus the higher melting compounds need to dissolve in the already liquid iron oxide, which requires a long time. Moreover, it should be noted that the furnace control is not exactly accurate: the uncertainty on temperature can be approximately 10 °C and the control of the partial pressure of oxygen, using a CO/CO_2 gas mixture, is even more challenging. These uncertainties can be taken into account to a certain extent in the thermodynamic calculations, as shown in Figure 10.6. The variations of the boundaries between the different regions in the phase diagram at 1450°C and a p_{O2} of 10^{-8} atm (red lines) are denoted with dotted lines (temperature ± 15°C and/or $\log(p_{O2})$ ± 0.5 atm). The composition aimed for during this experiment, lies close to the boundary between region (1) and (2), to obtain liquid alloy and liquid slag, but with a reasonable amount of solid spinel particles, to avoid too high viscosities.

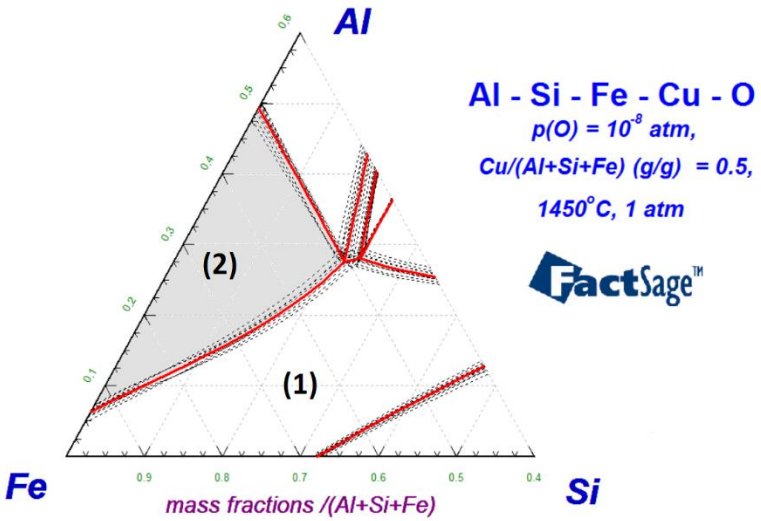

Figure 10.6 Ternary phase diagram for the Fe-Al-Si-Cu system at a temperature of 1450 °C and a partial oxygen pressure of 10^{-8} atm. This diagram (solid) is overlaid with the phase diagrams of the system under small variations of the applied conditions (dotted). These variations are ±15°C for the temperature and ±0.5 for log(p_{O2}). [4]

To prevent problems involving the ease of melting and related to the viscosity, a method of partial melting was used, as illustrated in Figure 10.6. [4] During partial melting, the system is melted in a multiple-step process. The targeted mixture of compounds (composition B) that needs to be melted is split into two parts. A low-temperature melting part (composition A), close to the eutectic, and a high-temperature melting part (composition C) containing the remaining compounds. First, the low-temperature melting part is mixed and brought to the operating temperature. This low-temperature melting mixture is designed to be fully molten from approximately 100 °C below the temperature at which the experiment will be performed. When this mixture is fully molten, the remaining compound mixture (denoted as 'additive') is added stepwise. This will give rise to the melting point of the system until the liquidus temperature of the slag becomes equal to the operating temperature. Adding more of the additive will result in the formation of spinel particles and thus, also in an increase in viscosity of the slag-spinel slurry. With the step-wise addition, the addition of this high-temperature melting mixture can be stopped before the viscosity of the liquid becomes too high. This multiple-step process is visualized in Figure 10.7 for the Fe-Al-Si-Cu system at a temperature of 1400 °C and a partial pressure of oxygen of 10^{-8} atm. With this method, an uncertainty on the exact position of the boundary between region (1) and region (2) is allowed, as long as this boundary lies between point A and point B. The viscosity increases and the addition of composition C can be stopped in time. In this way, the volume fraction of solid spinel in the liquid slag will never be too high to be able to perform an experiment. The used masses for this partial melting procedures are listed in Table 10.2.

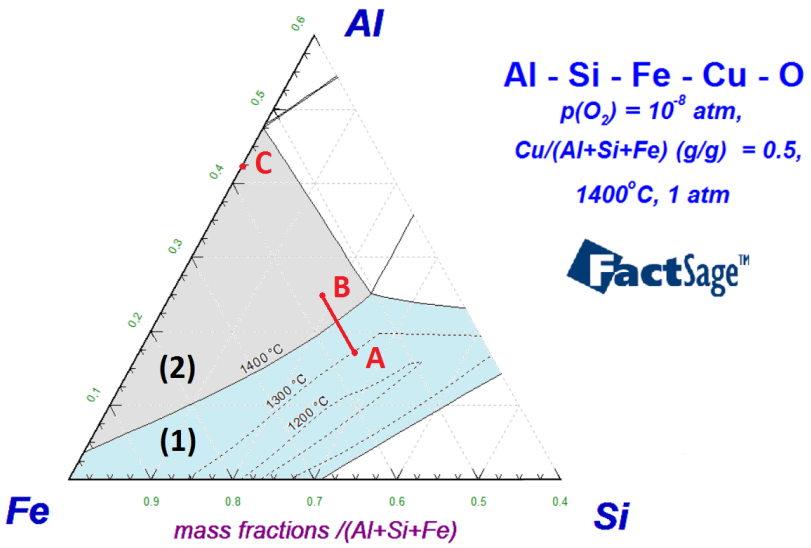

Figure 10.7 Ternary phase diagram for the Fe-Al-Si-Cu system at a temperature of 1400 °C and a partial oxygen pressure of 10^{-8} atm. In the liquid region (1), the isotherms of the liquidus surface are shown. [4]

	Cu	Ag	Al_2O_3	Fe	Fe_2O_3	SiO_2	Total
A START [g]	150.00	8.40	75.81	47.20	134.97	116.12	532.50
C ADDITIVE [g]	0	0	37.55	9.94	28.41	0	75.90
B TOTAL [g]	150.00	8.40	113.36	57.14	163.38	116.12	608.40
B TOTAL [wt%]	24.65	1.38	18.63	9.39	26.85	19.09	/

Table 10.2 Amounts of the different compounds corresponding to the compositions of the low-melting temperature mixture (composition A), the additive (composition C) and the targeted composition (composition B)

10.2.4. Oxidation – reduction

The control over the oxygen content and equilibrium of the system is important because one of the suggested mechanisms [6,7] is the formation of a copper droplet and spinel by the simultaneous precipitation of copper and formation of spinel solid in an over-oxidized slag. To replicate this phenomenon, the oxygen equilibrium partial pressure in the system will be varied throughout the experiment. For the copper to be precipitated, copper should first be dissolved in the slag by oxidizing the system, followed by reducing the system to lower the solubility of copper in the slag in turn.

Thus, the Fe-Al-Si-Cu system will be first oxidized and subsequently reduced by bubbling a CO/CO_2 gas mixture in the liquid system. The system was first oxidised with pure CO_2 for a period of 70 minutes, followed by a reducing step of 60 minutes using a CO/CO_2 gas mixture with a CO/CO_2 volume ratio of 2. The total gas flow of the used gas is in both cases 60 l/h. This will result in a supersaturated copper solution from which copper droplets can easily precipitate under the right conditions. The corresponding change in equilibrium partial pressure of oxygen was predicted by FactSage and is shown in Figure 10.8.

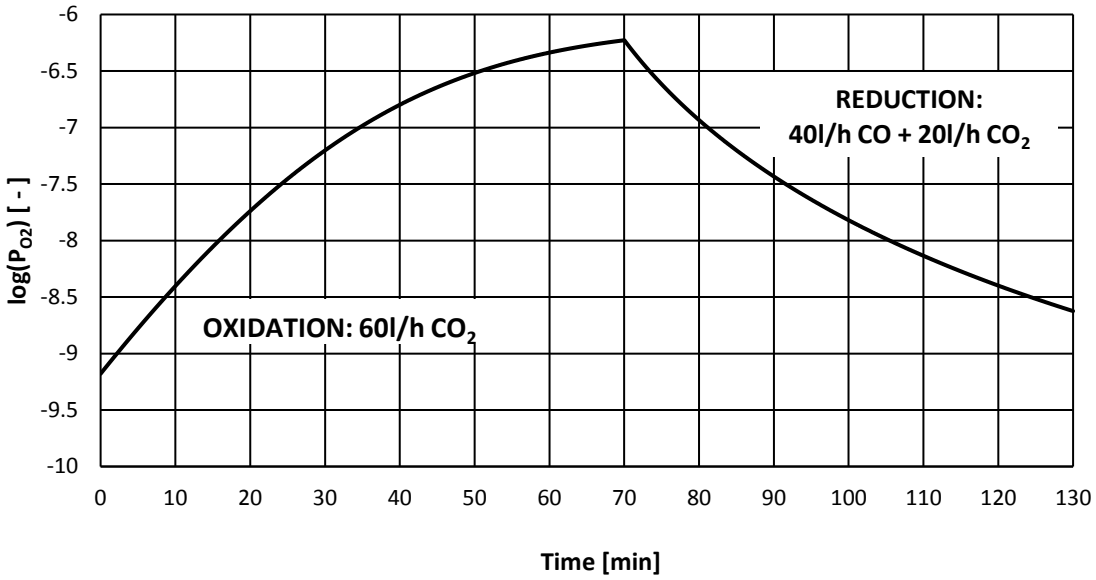

Figure 10.8 The calculated change in equilibrium oxygen partial pressure for the Fe-Al-Si-Cu system during the course of the high-temperature experiment at 1400°C. During this experiment, the melt is sequentially bubbled with a pure CO_2 gas for 70 min and with a CO/CO_2 gas mixture with a volume ratio of 2. The gas flow is in both cases 60 l/h. [4]

The system starts with a partial pressure of oxygen of approximately $10^{-9.35}$ atm. During the oxidation step, the partial pressure of oxygen rises to a maximum of approximately $10^{-6.25}$ atm after 70 minutes of oxidation. The rate of oxidation slows down at higher partial pressures of oxygen. When the reducing step starts, the partial pressure of oxygen drops again. For this prediction, equilibrium was assumed between the escaping gas mixture and the system. Thus, the exchange between the gas and the liquid system is at its maximum and the presented change in equilibrium oxygen partial pressure is the maximum change rate for the oxygen partial pressure. It is expected that the real oxygen content varies less quickly due to non-equilibrium effects. The change in phase fractions with the equilibrium partial pressure of oxygen can also be predicted by FactSage, as shown in Figure 10.9.

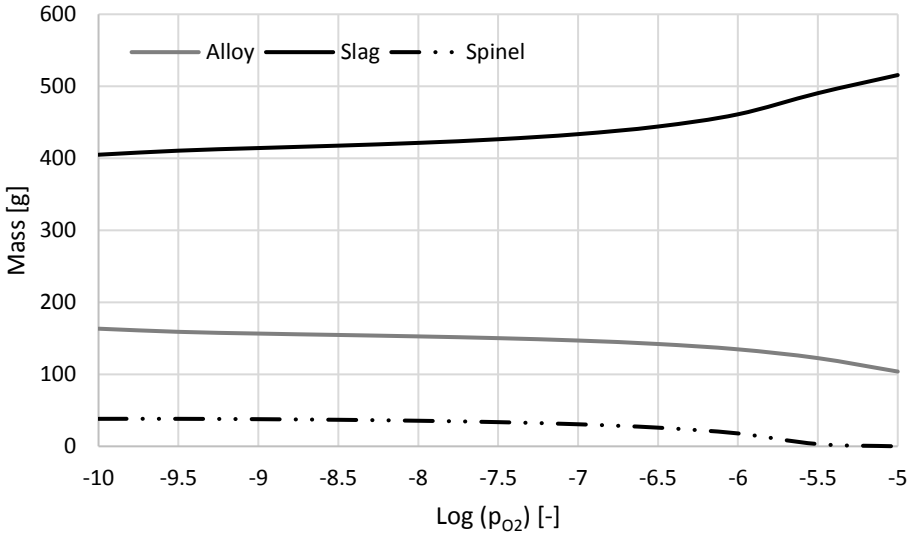

Figure 10.9 Mass of the phases present at equilibrium in the system at 1400°C as a function of the equilibrium partial pressure of oxygen.

Moreover, the elemental composition variation of the different phases can also be predicted by FactSage, as illustrated in Figure 10.10. The element oxygen was omitted from these calculations and the compositions were recalculated.

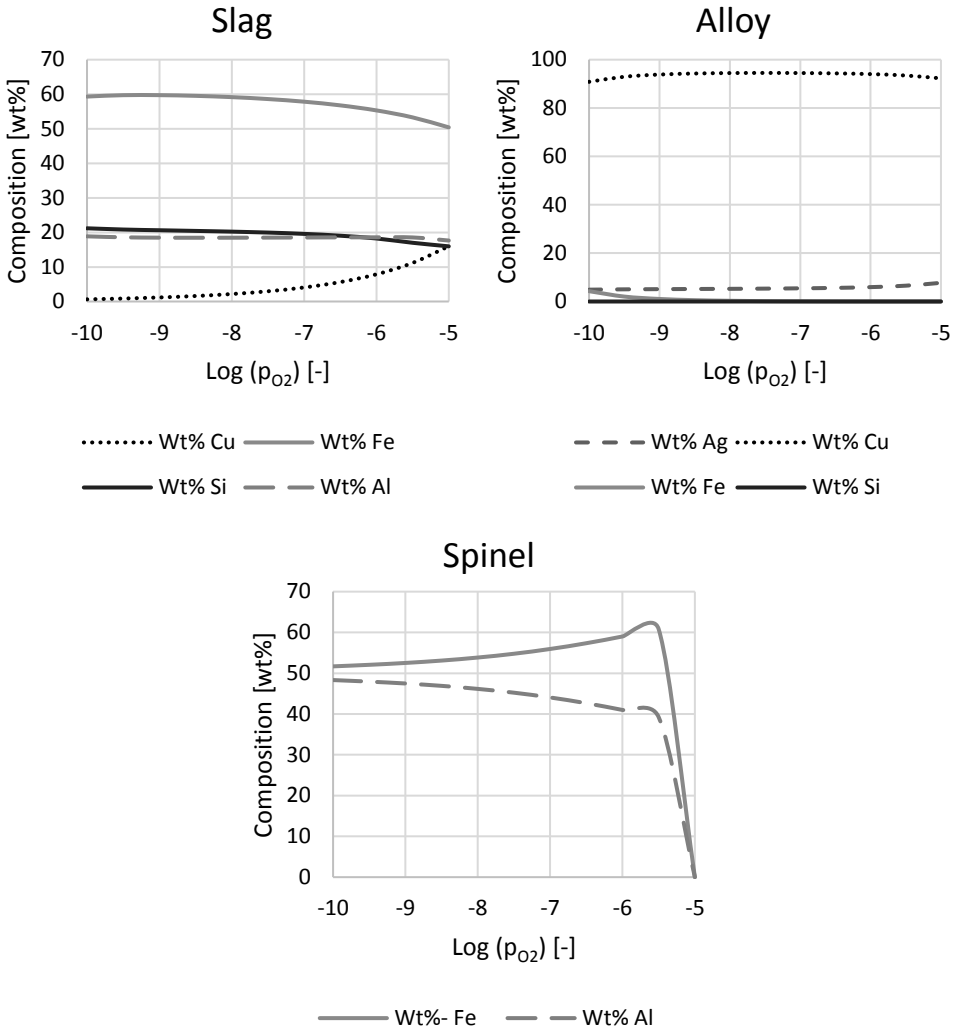

Figure 10.10 Prediction of the composition of the slag, spinel and alloy phases according to FactSage.

10.2.5. Smelting experiment

The previously calculated amounts of pure substances for the low-smelting temperature composition are mixed and put in the small alumina crucibles. The mixture is then heated and melted by the furnace. During heating and melting, a protective atmosphere is placed above the mixture's surface to protect it from oxidation by contact with air. This is done by blowing a constant stream of pure nitrogen over the surface. When the temperature of the slag-copper system reaches 800°C, the nitrogen stream is replaced by a gas mixture of carbon monoxide and carbon dioxide: 40 l/h CO and 20 l/h CO_2. Once the bath is liquid, the additive was added in small steps and in the meantime, the gas mixture was blown through the slag to ensure faster mixing. The mixture was then left to rest for 10 min, during which no gas was blown through the slag. The slag was sampled by dipping a steel rod in the slag and quenching it in water, as illustrated in Figure 10.11. The first dip sample of the slag also corresponds to the start of the time reference (t = 0 min).

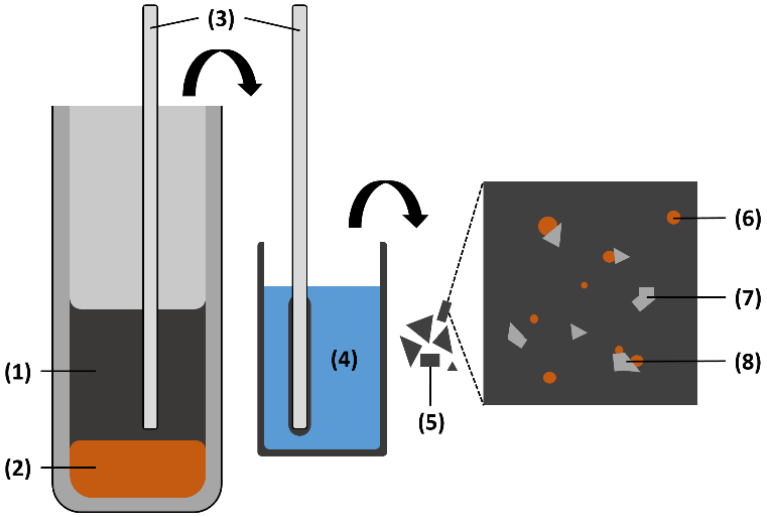

Figure 10.11 Schematic overview of the sample collection by dipping with a steel rod and quenching in water. (1) slag phase; (2) metal alloy; (3) dipping steel bar which is then quenched in water; (4) cold water; (5) quenched slag particles; (6) entrained metal droplets in the slag microstructure; (7) solid spinel particles in the slag microstructure; (8) attached metal droplets to solid spinel particles in the slag microstructure. [4]

After the first dipping sample at t = 0 min, the oxidative part of the cycle was started: the bubbling pipe is lowered into the slag phase and the gas mixture is switched to 60 l/h pure CO_2. Above the bath, a 60 l/h N_2 atmosphere was used. At 10, 40 and 70 min dip samples were taken. The 70 min sample was taken after switching of the pure CO_2 gas stream and letting the system decant for 5 min. After this dip sample, the reductive part of the cycle was started by blowing a gas mixture of 40 l/h CO and 20 l/h CO_2 through the slag and keeping a 60 l/h N_2 atmosphere above the bath. Dip samples were taken at 5, 10, 25 and 50 min after the start of the reductive part of the cycle. The last dip sample was taken after a 5 min decantation time after switching of the gas stream blowing through the slag. The different names for these samples are shown in Table 10.3.

	Oxidation				Reduction			
Sample nr.	1	2	3	4	5	6	7	8
Time	00'00"	10'03"	39'36"	70'00"	5'12"	9'53"	24'43"	55'06"

Table 10.3 Overview of the different times at which the dip samples were taken and the corresponding sample number.

10.2.6. Sample preparation

Because the steel bar used for sampling is below the melting temperature of the slag, a layer of solid slag material is quickly formed around the steel bar. The bar is dipped in the slag for about a second before it is transferred to a bucket of water to quench the hot slag. Because of the quick cooling of the slag, the internal structure is frozen in the state that it existed at elevated temperatures. The solidified slag is recovered in small parts from the quenching. These slag granules were dried in a drying chamber at 150 °C.

The obtained slag sample was embedded, ground and polished using 9 and 3 µm diamond pastes. The sample was analysed using light optical microscopy (Keyence VHX-S90BE) and scanning electron microscopy (SEM; FEG SEM JSM-7600F, JEOL). The latter was used in combination with energy dispersive X-ray spectroscopy (EDAX, EDX) to measure the phase compositions.

10.3. Results and discussion

10.3.1. Microstructural evolution during oxidation

Representative LOM images for the four samples during the oxidation part of the experiment are shown in Figure 10.12. Only a small amount of droplets is present and those present are small with a diameter of approximately 5 µm at most. The amount of droplets in the slag increases during the course of the oxidation part of the experiment. Some droplets were found to be unattached to solid spinel particles, whereas the majority of the droplets was attached to spinel particles. Some BSE-SEM images are shown in Figure 10.13 and they also confirm these observations.

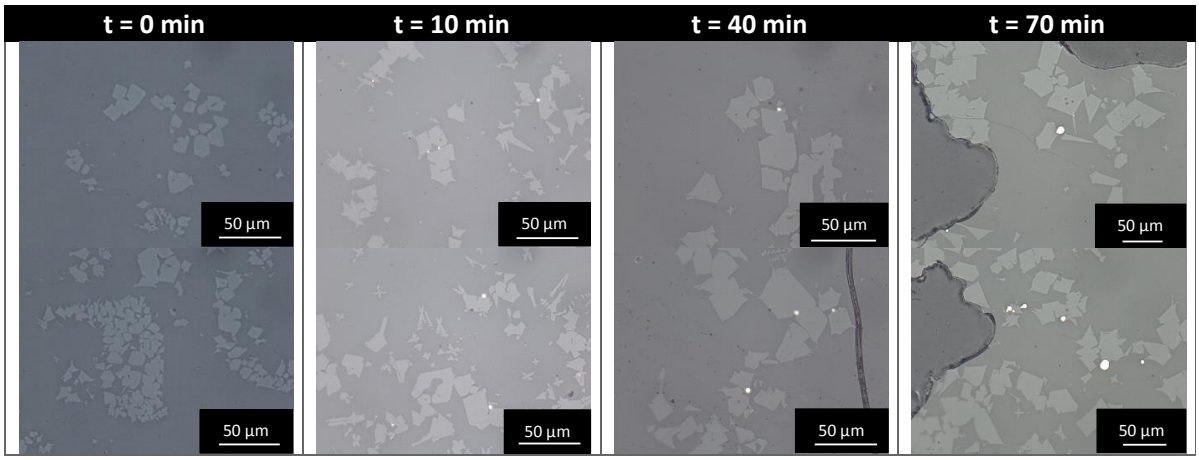

Figure 10.12 Optical images taken from the samples that were taken during the high-temperature oxidation part of the experiment.

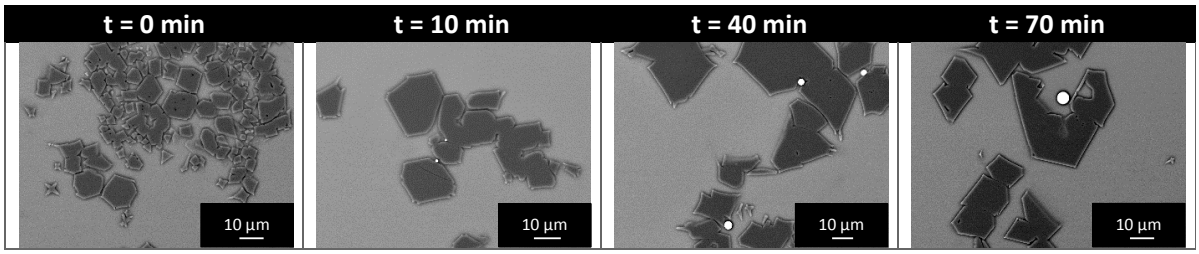

Figure 10.13 BSE SEM images taken from the samples that were taken during the high-temperature oxidation part of the experiment.

The amount and size of droplets increases, which is in contrast with the prediction by FactSage in Figure 10.9. However, as the system was left to rest before the start of the oxidative part of the experiment, once the oxidation started by blowing pure CO_2 through the slag, the liquid slag was disturbed, which in turn disturbed the underlying alloy layer, thus introducing small metal droplets into the slag phase.

10.3.1. Microstructural evolution during reduction

Representative LOM images for the four samples during the reduction part of the experiment are shown in Figure 10.14. It can be seen that the amount and size of copper droplets in the slag increases during this part of the experiment and the diameter of the alloy droplets clearly increases. Moreover, the alloy droplets are mostly attached to solid spinel particles, but some unattached droplets can also be noted. The attached solid spinel particles also seem to increase in size. However, the total

fraction of spinel solids seems to remain similar. Some BSE-SEM images are shown in Figure 10.15 and they also confirm these observations.

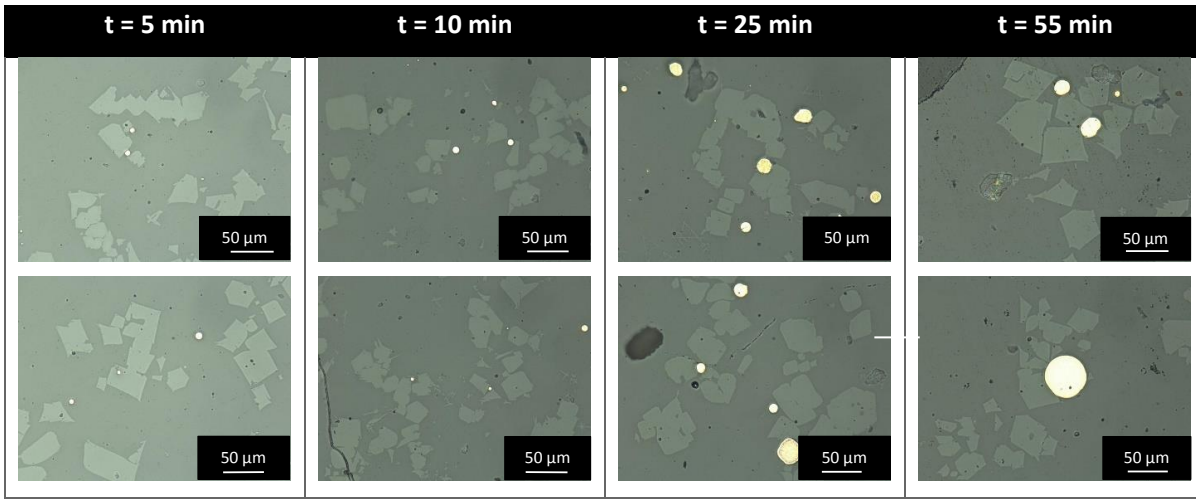

Figure 10.14 Optical images taken from the samples that were taken during the high-temperature reduction part of the experiment.

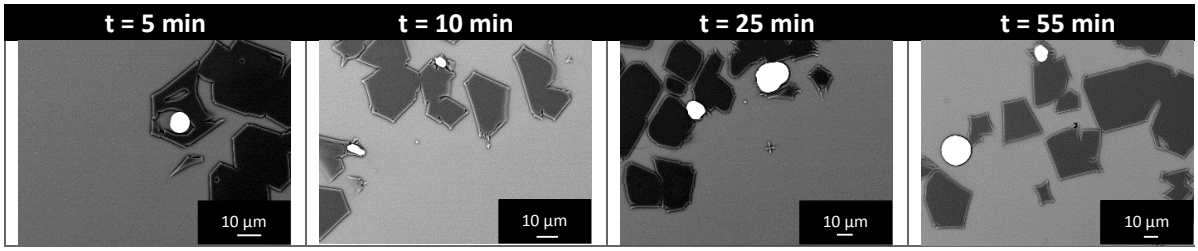

Figure 10.15 BSE SEM images taken from the samples that were taken during the high-temperature reduction part of the experiment

The fact that the spinel particles get bulkier suggests that they grow during the reduction phase of the experiment, similarly as the alloy droplets. This can be due to two reasons or a combination of both. Firstly, the equilibrium fraction of the liquid alloy phase and solid spinel particles in the system are higher at lower equilibrium partial pressures of oxygen, as shown in the FactSage prediction in Figure 10.9. Secondly, as most of the alloy droplets are attached to the solid spinel particles, it is possible that the reductive gas stream causes the reduction of copper dissolved in the slag, which is counteracted by the oxidation of certain iron oxides, which in turn can react with other slag components to form solid spinel particles. The latter reactive origin was suggested by De Wilde et al. [7–9] and was also confirmed by Bellemans et al. [10].

10.3.2. Compositional variation during experiment

The SEM-EDX results for the compositions of the different samples taken during the experiment are listed in Table 10.4. The measurement of oxygen was excluded in these measurements as EDX does not yield reliable results for oxygen or other light elements.

Sample	Phase	Fe	Si	Al	Cu	Ag
1	Slag	54.9 ± 0.4	24.5 ± 0.3	20.0 ± 0.7	0.6 ± 0.0	-
	Spinel	51.5 ± 0.2	0.2 ± 0.1	48.2 ± 0.2	0.1 ± 0.0	-
2	Slag	56.6 ± 0.1	23.5 ± 0.1	19.2 ± 0.1	0.8 ± 0.1	-
	Spinel	51.6 ± 0.2	0.3 ± 0.0	47.9 ± 0.1	0.1 ± 0.0	-
3	Slag	56.3 ± 0.1	23.0 ± 0.1	18.8 ± 0.1	1.9 ± 0.0	-
	Spinel	52.2 ± 0.2	0.3 ± 0.0	47.3 ± 0.2	0.1 ± 0.0	-
	Alloy	6.5 ± 0.6	0.8 ± 0.7	1.1 ± 0.9	89.8 ± 2.5	1.4 ± 0.4
4	Slag	55.7 ± 0.4	24.1 ± 0.9	16.6 ± 1.2	3.5 ± 0.2	-
	Spinel	54.6 ± 0.0	0.4 ± 0.0	44.7 ± 0.1	0.3 ± 0.1	-
	Alloy	7.3 ± 2.4	1.6 ± 1.7	1.5 ± 1.1	87.7 ± 5.4	1.9 ± 0.2
5	Slag	55.4 ± 0.4	23.1 ± 0.2	17.9 ± 0.4	3.6 ± 0.3	-
	Spinel	54.7 ± 0.2	0.3 ± 0.1	44.7 ± 0.2	0.3 ± 0.0	-
	Alloy	5.2 ± 0.5	0.3 ± 0.1	1.3 ± 0.6	90.6 ± 0.8	2.6 ± 1.4
6	Slag	55.9 ± 0.5	24.2 ± 1.6	16.8 ± 1.6	3.1 ± 0.6	-
	Spinel	54.7 ± 0.2	0.4 ± 0.1	44.7 ± 0.3	0.2 ± 0.1	-
	Alloy	6.5 ± 2.4	0.6 ± 0.3	2.5 ± 1.0	88.3 ± 3.5	2.2 ± 0.7
7	Slag	56.2 ± 0.1	21.3 ± 0.0	19.6 ± 0.3	2.9 ± 0.2	-
	Spinel	54.1 ± 0.2	0.4 ± 0.1	45.3 ± 0.1	0.3 ± 0.1	-
	Alloy	3.8 ± 0.5	0.3 ± 0.1	1.4 ± 0.9	91.5 ± 1.0	3.0 ± 0.2
8	Slag	56.3 ± 0.3	23.7 ± 0.4	18.1 ± 0.4	1.9 ± 0.2	-
	Spinel	52.6 ± 0.1	0.3 ± 0.1	46.9 ± 0.2	0.2 ± 0.1	-
	Alloy	3.8 ± 0.8	0.3 ± 0.0	1.2 ± 0.6	92.9 ± 0.6	1.8 ± 0.5

Table 10.4 Measured compositions of the different phases in the eight quenched slag samples. The measurement of oxygen was excluded in these measurements.

The copper content of the slag increases during the oxidative part and decreases during the reduction, which is expected by the FactSage prediction in Figure 10.10. The iron content of the slag remains approximately constant. According to the FactSage prediction, the Fe content should decrease slightly, as some of the iron is used to form spinel solids. The silicon content remains approximately constant, but a slight decrease was predicted. Aluminium in the slag phase decreases during the oxidative part and increases again during the reductive part, where it is predicted to remain constant. Thus, it looks as if the amounts of iron and aluminium were switched. In reality, more Al is incorporated in the spinel than predicted by FactSage. This can be quantified by looking at the predicted Fe/Al ratio for the spinel at a p_{O2} of 10^{-6} atm, which equals 60/40 = 1.5. The ratio for the observed composition on the other hand is 55/45 = 1.22. It is possible that an interaction with the alumina crucible is responsible for this. Heating up the slag in an alumina crucible will dissolve part of it, resulting in a higher amount of alumina in the slag, which results in a higher driving force to incorporate this dissolved alumina in the spinel solids. After melting of the slag, once the oxidation starts, the spinel solids within the slag can no longer be formed and some of the alumina will precipitate against the crucible wall. Once the reduction part of the experiment starts, spinel solids will form again, reducing the alumina content of the slag.

The spinel solids contain an increasing amount of Fe during the oxidative part, whereas this amount remains approximately constant during the reductive part of the cycle. The aluminium content in the spinel decreased during the oxidation and increased during the reduction. This is also shown in the

FactSage prediction in Figure 10.10. However, the iron content during the reduction was expected to decrease, which was not observed. This suggests a higher Fe content than thermodynamically predicted, which could point towards a reactive formation of the spinel solids. This change in composition and the presence of an Fe-rich border of the solid spinel particles was also observed by De Wilde et al. [7,10,11].

It is clear that all metal droplets, when they are observed (i.e. starting from sample 3), contain Ag. Moreover, no Ag was observed to be dissolved in the slag or spinel phases. The amount of Ag in the alloy droplets is much lower than the initially targeted amount: 8.4 g Ag / 150 g Cu = 0.056. E.g., the maximally measured value of that ratio is 3 wt% Ag / 91.5 wt% Cu = 0.033. The amount of iron in the alloy increases as the oxidation takes place and decreases again during the reduction. The latter is in contrast with the prediction by FactSage in Figure 10.10. Moreover, the amount of Fe in the alloy is very high compared to the prediction. This could be explained by secondary X-ray fluorescence, which was already modelled with Monte Carlo simulations for systems with small Cu-particles in Fe-containing slags [12]. The behaviour of the other elements, on the other hand, is in accordance with this prediction.

The origin of sticking droplets was proposed to be found in a chemical reaction, as elaborated in [7,9]. It is suggested that dissolved Cu can precipitate by reduction of the copper oxide, while the iron oxides in the slag next to the copper droplet are oxidized to form spinel solids, according to the following overall reaction [7,9]:

$$(Cu_2O, CuO)_{slag} + (FeO)_{slag} + (Al_2O_3)_{slag} \rightarrow (Fe^{2+}, Cu^{2+})(Al^{3+}, Fe^{3+})_2O_4 + \text{Cu-alloy droplet}$$

However, the fact that silver is present in a lower concentration in the attached copper droplets compared to the master alloys in this study indicates that the origin of the attachment is not purely dispersive. Moreover, it is almost impossible that the Ag would dissolve in such large amounts into the slag, as illustrated by the SEM-EDX measurements in Table 10.4. This is confirmed by the observations of Takeda et al. [13]. They showed that Ag dissolves slightly into the slag with a distribution coefficient (= % in slag / % in Cu-Ag alloy) of the order 10^{-4} to 10^{-2} atm for partial pressures of oxygen going from 10^{-11} to 1 atm.

However, as Ag-diffusion cannot be excluded, a purely reactive origin is possible, as is a combination of dispersion and reaction. In the latter case, it is suggested that during the first oxidative blow of the experiment, some Cu-Ag alloy is introduced into the slag phase as small dispersed alloy droplets. Moreover, the Cu dissolved into the slag and during the reductive blow, this copper precipitates again. The small alloy droplets introduced in the slag, can be considered as heterogeneous nucleation sites, where dissolved Cu can precipitate by reduction of the copper oxide, while the iron oxides in the slag next to the copper droplet are oxidized to form spinel solids, according to the overall reaction as suggested by De Wilde et al. [7,9] (cfr. supra).

Furthermore, an elemental analysis was performed to check if any quench effects or phase growth during quenching did occur. The equilibrium fraction of the spinel phase namely increases when the temperature decreases, i.e. during cooling, in the FactSage prediction in Figure 10.9. If the spinel solids would grow during quenching, a local segregation of silicon is expected, because that element does not occur in the spinel solids and would thus be pushed out of the growing particle. This segregation of silicon around the spinel particles in the quenched slag is indeed observed in multiple locations, which is illustrated in Figure 10.16.

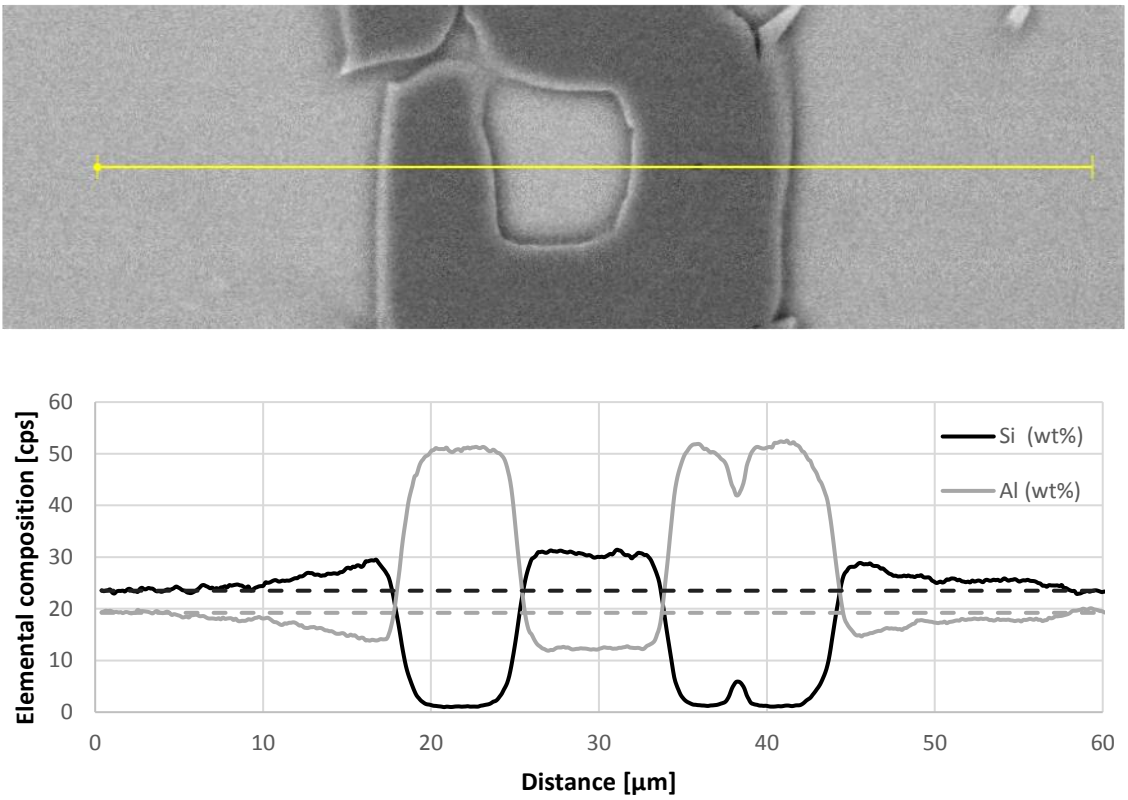

Figure 10.16 Variation in aluminium and silicon weight fraction along a line as measured. Oxygen was excluded from the measurements.

The spinel solid indeed grew during quenching, as the aluminium was depleted and the silicon was enriched at the edge of the spinel particle. The dotted lines in the graph show the composition of aluminium and silicon that are measured in the bulk quenched slag of the sample, far away from any spinel particles or copper droplets. The segregation effect is even more clear in the contained pocket of slag inside the spinel particle.

From the quenched slag samples, the actual partial pressure of oxygen present in the system can also be estimated by fitting the measured compositions of the experiment to the predictions of FactSage. As it was seen in the previous paragraphs, the slag around the spinel particles may suffer a change in composition due to segregation and particle growth. Thus, the measurement of the composition of the slag phase to fit to the prediction by FactSage is not an ideal choice. Therefore, the measured compositions of the spinel particles were fitted to the calculations of FactSage. As the main elements of the spinel particles, the iron over aluminium weight ratio was used to fit the equilibrium partial pressure of oxygen.

Before this fitting, the measured weight fractions were corrected with the expected composition of the spinel particles in the initial system, before oxidation or reduction was started, predicted by FactSage. This is done because although the precision, i.e. the attainment of the correct composition with a low statistical variability, of the EDS measurement is generally quite good (± 0.2 wt%), the accuracy, the appearance of systematic errors, of the technique is low (± 2 wt%). By using the initially expected spinel concentration as a benchmark, the weight fractions obtained during the further course of the experiment can be corrected. Then, the Fe/Al weight ratio is fitted to the values

obtained by FactSage calculated to obtain the actual equilibrium pressures of oxygen present during the experiment. The results are summarized in Figure 10.17.

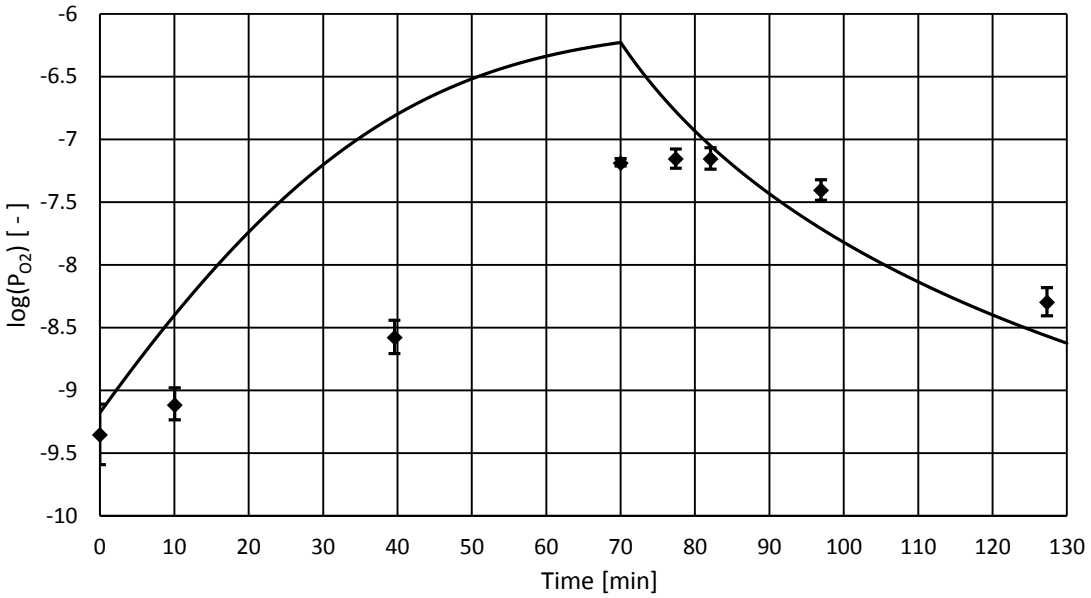

Figure 10.17 Full line: predicted change in equilibrium oxygen pressure of a Fe-Al-Si-Cu system during the oxidation/reduction high-temperature experiment. The data points (squares for the oxidation and triangles for the reduction part) were gathered by fitting the composition of the samples to thermodynamic predictions using FactSage.

The general expected trend in change of equilibrium oxygen pressure was followed during the experiment. The expected equilibrium oxygen pressure of $10^{-6.25}$ atm after 70 minutes of CO_2 injection at the rate of 60 l/h is not reached. Instead, a maximum oxygen partial pressure of approximately $10^{-7.16}$ atm is found. This lower oxygen pressure can be expected as the calculated curve corresponds with the maximum rate of oxygen exchange and the real oxygen transfer will always be lower due to non-equilibrium effects. A possible mechanism here is that during reactive gas injection, only the liquid boundary in direct contact with the gas takes up the oxygen from the gas. This layer is oxidized to a large extent and is characterized by a larger equilibrium partial pressure of oxygen than the surrounding liquid system. This oxidised layer is then transported to the bulk of the system where it oxidizes surrounding slag and spinel particles while the layer itself is reduced, this is similar as the observations made by [14,15]. This is a way in which the equilibrium oxygen pressure is equilibrated over the whole system due to convection. This would mean that the liquid system would contain a complex structure of regions with high and regions with low oxygen partial pressure.

10.4. Conclusions

In this study, the attachment of copper droplets to spinel particles in slags, retaining the sedimentation of the droplets, is studied. A high-temperature smelting experiment was executed for this. The methodology was adapted from previous studies [1,2] to be able to perform these experiments with as few components as possible. The latter is meant for a comparison to modelling results, for which more components in the system result in more computational time required.

Certain problems were encountered during the adaptation of the experimental methodology, but these were solved by considering thermodynamic modelling and the use of the ‘partial melting’

method. During partial melting, the system is melted in a multiple-step process. The targeted mixture of compounds that needs to be melted is split into two parts. A low-temperature melting part, close to eutectic, and a high-temperature melting part. First, the low-temperature melting part of the compounds is mixed and brought to the operating temperature until it is fully molten. Then, the 'additive' is added stepwise, resulting in the formation of spinel particles and thus, also in an increase in viscosity of the slag-spinel slurry. With the step-wise addition, the addition of this high-temperature melting mixture can be stopped before the viscosity of the liquid becomes too high.

The control over the oxygen content and equilibrium of the system is important because one of the suggested mechanisms [6,7] is the formation of a copper droplet and spinel by the simultaneous precipitation of copper and formation of spinel solid in an over-oxidized slag. Therefore, an oxidation-reduction experiment in the Fe-Si-Al-O system with Cu-Ag droplets was executed. For the copper to be precipitated, copper should first be dissolved in the slag by oxidizing the system, followed by reducing the system to lower the solubility of copper in the slag in turn.

The amount and size of copper droplets and spinel particles increase during the complete experiment. This is in accordance with the expectations from the suggested mechanism during the reductive part, but during the oxidation part, this is not expected. Because the system was left to rest before the start of the oxidative part of the experiment, it is possible that the disturbance of the underlying alloy layer by the blowing of the gas through the slag phase, introduces small metal droplets into the slag phase.

During oxidation, iron oxide has a tendency to shift towards Fe_2O_3 and the metallic copper is oxidized. During the reductive part of the experiment, a lack of oxygen becomes apparent and because copper is more noble than iron, Cu_2O acts as oxygen donor for the oxidation of iron oxide, thereby precipitating metallic copper: $2FeO + Cu_2O <-> 2Cu^0 + Fe_2O_3$. The resulting increase of Fe_2O_3 leads to the formation of magnetite spinel particles by reaction with FeO. The former is also similar to the reactions observed by Durinck et al. [16] for iron oxides and chromium oxides. However, in this case, iron is the more noble element.

The silver was added to the copper alloy as a trace element to get more insights on the origin of the attachment. The fact that this silver is present in the attached copper droplets in a smaller concentration than the master alloy in this study indicates that the origin of the attachment is not purely dispersive and either a purely reactive or a dispersion-reaction combination is possible. In the latter, small Cu-Ag droplets were introduced in the slag during the first oxidative blow. During the reductive blow, these droplets then act as nucleation sites for a simultaneous reduction of copper oxides into metallic copper and the oxidation of slag oxides into more stable spinel structures. In this way, the spinel solids grow at the side of the Cu-Ag droplets, which in turn are enriched with Cu and grow. This leads to copper droplets attached to spinel solids within the slag phase.

References

[1] E. De Wilde, Methodology Development and Experimental Determination of the Origin of Sticking Copper Droplets in Pyrometallurgical Slags, PhD thesis, Ghent University, 2015.

[2] E. De Wilde, I. Bellemans, S. Vervynckt, M. Campforts, K. Vanmeensel, N. Moelans, K. Verbeken, Towards a methodology to study the interaction between Cu droplets and spinel particles in slags, in: Proc. EMC 2013, 2013: pp. 161–174.

[3] N. Vervliet, O. Debals, L. Sorber, L. De Lathauwer, Breaking the curse of dimensionality using decompositions of incomplete tensors : Tensor-based scientific computing in big data analysis, IEEE Signal Process. Mag. 31 (2014) 71–79.
[4] V. Cnockaert, Investigation of the attachment of metallic droplets to solid particles in liquid slags, Master thesis, Ghent University, 2016.
[5] S. Wright, L. Zhang, S. Sun, S. Jahanshahi, Viscosities of calcium ferrite slags and calcium alumino-silicate slags containing spinel particles, J. Non-Cryst. Solids. 282 (2001) 15–23. doi:10.1016/S0022-3093(01)00324-6.
[6] E. De Wilde, I. Bellemans, M. Campforts, A. Khaliq, K. Vanmeensel, D. Seveno, M. Guo, A. Rhamdhani, G. Brooks, B. Blanpain, N. Moelans, K. Verbeken, Wetting behaviour of Cu based alloys on spinel substrates in pyrometallurgical context, Mater. Sci. Technol. 31 (2015) 1925–1933. doi:10.1179/1743284715Y.0000000052.
[7] E. De Wilde, I. Bellemans, L. Zheng, M. Campforts, M. Guo, B. Blanpain, N. Moelans, K. Verbeken, Origin and sedimentation of Cu-droplets sticking to spinel solids in pyrometallurgical slags, Mater. Sci. Technol. 32 (2016) 1911–1924. doi:10.1080/02670836.2016.1151998.
[8] E. De Wilde, I. Bellemans, M. Campforts, M. Guo, B. Blanpain, N. Moelans, K. Verbeken, Sessile drop evaluation of high temperature copper/spinel and slag/spinel interactions, Trans. Nonferrous Met. Soc. China. 26 (2016) 2770–2783. doi:10.1016/S1003-6326(16)64344-3.
[9] E. De Wilde, I. Bellemans, M. Campforts, M. Guo, B. Blanpain, N. Moelans, K. Verbeken, Investigation of High-Temperature Slag/Copper/Spinel Interactions, Metall. Mater. Trans. B. 47 (2016) 3421–3434. doi:10.1007/s11663-016-0805-8.
[10] I. Bellemans, E. De Wilde, L. Claeys, T. De Seranno, M. Campforts, B. Blanpain, N. Moelans, K. Verbeken, Investigation of reactive origin for attachment of Cu-droplets to solid particles, Metall. Mater. Trans. B. (2017).
[11] E. De Wilde, I. Bellemans, M. Campforts, M. Guo, K. Vanmeensel, B. Blanpain, N. Moelans, K. Verbeken, Study of the Effect of Spinel Composition on Metallic Copper Losses in Slags, J. Sustain. Metall. 3 (2017) 416–427. doi:10.1007/s40831-016-0106-0.
[12] X. Llovet, E. Valovirta, E. Heikinheimo, Monte Carlo Simulation of Secondary Fluorescence in Small Particles and at Phase Boundaries, Microchim. Acta. 132 (2000) 205–212. doi:10.1007/s006040050013.
[13] Y. Takeda, S. Ishiwata, A. Yazawa, Distribution Equilibria of Minor Elements between Liquid Copper and Calcium Ferrite Slag, Trans. Jpn. Inst. Met. 24 (1983) 518–528. doi:10.2320/matertrans1960.24.518.
[14] M.A. Rhamdhani, G.A. Brooks, K.S. Coley, Kinetics of metal/slag reactions during spontaneous emulsification, Metall. Mater. Trans. B-Process Metall. Mater. Process. Sci. 36 (2005) 219–227. doi:10.1007/s11663-005-0023-2.
[15] M.A. Rhamdhani, K.S. Coley, G.A. Brooks, Role of oxygen in interfacial phenomena during high temperature reactions, in: G. Irons, S. Sun (Eds.), Hamilton, Ontario, Canada, 2004: pp. 203–217.
[16] D. Durinck, P.T. Jones, B. Blanpain, P. Wollants, Air-Cooling of Metallurgical Slags Containing Multivalent Oxides, J. Am. Ceram. Soc. 91 (2008) 3342–3348. doi:10.1111/j.1551-2916.2008.02597.x.

11. Conclusions

Previous work by De Wilde et al. [1,2] suggested that sticking droplets can originate from a chemical reaction. A reaction scheme was proposed, where, on the one hand, the spinel solids and copper droplets form together due to a simultaneous reduction of copper oxides into metallic copper and, on the other hand, slag oxides oxidize into more stable spinel structures. Additionally, the spinel solids can also form by heterogeneous nucleation on an already present Cu droplet in an analogous way.

This hypothesis was based on the observations made during a sessile drop experiment of both Cu and slag on top of a $MgAl_2O_4$ substrate [2]. An extensive microstructural study afterwards showed the presence of small entrained copper droplets attached to spinel particles, leading to the reactive origin hypothesis. However, during the experiment, the copper droplet moved towards the slag droplet and a certain emulsification took place between the slag and copper droplet, after which the copper droplet positioned itself on top of the slag droplet. This emulsification step could in fact also be responsible for the presence of the small metal droplets attached to spinel particles within the large slag droplet.

To investigate the hypothesis, adapted sessile drop experiments were performed, in which both copper alloys and slag were placed on a spinel substrate. Several copper-silver alloys, a synthetic PbO-CaO-SiO_2-Cu_2O-Al_2O_3-FeO-ZnO slag and a $MgAl_2O_4$ substrate were used to represent the copper alloy droplets, slag and spinel solids, respectively. The silver was added to the copper alloy as a trace element to get more insights into the origin of the attachment.

The microstructures within the different samples were studied and the compositions of the different phases present were determined. Small entrained copper droplets sticking to spinel solids were present within the large slag droplet and contained Ag. It is suggested that during the coalescence phase in the high temperature CSLM experiment, some small Cu-Ag droplets are dispersed within the large slag drop. These Cu-Ag droplets then act as heterogeneous nucleation sites for a simultaneous reduction of copper oxides into metallic copper and the oxidation of slag oxides into more stable spinel structures. In this way, the spinel solids grow at the side of the Cu-Ag droplets, which in turn are enriched with Cu and grow. This leads to copper droplets attached to spinel solids within the slag phase.

Moreover, a high-temperature smelting experiment was executed. The methodology was adapted from previous studies [3,4] to be able to perform these experiments with as few components as possible. The latter is meant for a comparison to modelling results, for which more components in the system result in more computational time required. An oxidation-reduction experiment in the Fe-Si-Al-O system with Cu-Ag droplets was executed. For the copper to be precipitated, copper should first be dissolved in the slag by oxidizing the system, followed by reducing the system to lower the solubility of copper in the slag in turn.

The amount and size of copper droplets and spinel particles increase during the complete experiment. This is in accordance with the expectations from the suggested mechanism during the reductive part, but during the oxidation part, this is not expected. Because the system was left to settle before the start of the oxidative part of the experiment, it is possible that the disturbance of the underlying alloy layer by the blowing of the gas through the slag phase, introduces small metal droplets into the slag phase.

During oxidation, iron oxide has a tendency to shift towards Fe_2O_3 and the metallic copper is oxidized. During the reductive part of the experiment, a lack of oxygen becomes apparent and because copper is more noble than iron, Cu_2O acts as oxygen donor for the oxidation of iron oxide, thereby precipitating metallic copper: $2FeO + Cu_2O <-> 2Cu^0 + Fe_2O_3$. The resulting increase of Fe_2O_3 leads to the formation of magnetite spinel particles by reaction with FeO.

The fact that the silver, added as a trace element, is present in the attached copper droplets in a smaller concentration than in the master alloy in both studies indicates that the origin of the attachment is not purely dispersive. Therefore, the attached metal droplets can be formed either due to a purely reactive formation (simultaneous reduction of copper and silver oxides to metallic phase and the oxidation of slag oxides to spinel) or a combination of dispersion and reaction. In the latter case, small Cu-Ag droplets are introduced in the slag during the emulsification step or during the first oxidative blow. afterwards, these droplets act as nucleation sites for a simultaneous reduction of copper oxides into metallic copper and the oxidation of slag oxides into more stable spinel structures. In this way, the spinel solids grow at the side of the Cu-Ag droplets, which in turn are enriched with Cu and grow. This leads to copper droplets attached to spinel solids within the slag phase.

References

[1] E. De Wilde, I. Bellemans, L. Zheng, M. Campforts, M. Guo, B. Blanpain, N. Moelans, K. Verbeken, Origin and sedimentation of Cu-droplets sticking to spinel solids in pyrometallurgical slags, Mater. Sci. Technol. 32 (2016) 1911–1924. doi:10.1080/02670836.2016.1151998.

[2] E. De Wilde, I. Bellemans, M. Campforts, M. Guo, B. Blanpain, N. Moelans, K. Verbeken, Investigation of High-Temperature Slag/Copper/Spinel Interactions, Metall. Mater. Trans. B. 47 (2016) 3421–3434. doi:10.1007/s11663-016-0805-8.

[3] E. De Wilde, Methodology Development and Experimental Determination of the Origin of Sticking Copper Droplets in Pyrometallurgical Slags, PhD thesis, Ghent University, 2015.

[4] E. De Wilde, I. Bellemans, S. Vervynckt, M. Campforts, K. Vanmeensel, N. Moelans, K. Verbeken, Towards a methodology to study the interaction between Cu droplets and spinel particles in slags, in: Proc. EMC 2013, 2013: pp. 161–174.

D. Multi-component phase field model

“Software is like entropy. It is difficult to grasp, weighs nothing, and obeys the second law of thermodynamics; i.e. it always increases.”

- Norman Ralph Augustine

12. Phase field modelling in slag systems [19]

The previous binary model discussed in part B was focussed on the growth and wetting behaviour of the metal droplets. The experimental study of the attachment of metal droplets to spinel particles in slags showed that the origin of this attachment lies in a redox reaction within the slag. However, the phase field model in part B of this work considered a binary model in which the solid particles and metallic droplets interact through differences in interfacial energies between the various phases. Moreover, the solid particle was assumed to not react, whereas it was shown in the experiments that the solid spinel particles grow on a small metallic droplet-nucleus, while this metal droplet also grows and remains attached to the solid. Therefore, a better phase field approximation would first of all consider a thermodynamically-sound multi-component multi-phase field model for the growth of the solid phase in a liquid slag. For this, we will use the implementation and model of Heulens [1]. This chapter gives some details on general aspects of slags and then on the possibilities of this model, and the next chapter goes into more detail in the implementation of that model.

12.1. Slag structure

A slag phase is a mixture of metal oxides and silicate melts typically consist of a network of charged complex silicate, aluminate and phosphate ions, introducing a certain ordering in the phase. An illustration of this network can be found in Figure 12.1. The slags consist of the silicate tetrahedral SiO_4^{4-} or larger charged complexes, such as $Si_2O_7^{6-}$ and the different metal cations are distributed throughout to maintain electroneutrality. A silicate slag may also be considered as a nearly close-packed arrangement of larger oxygen anions with smaller metal cations that occupy the interstices and interact with each other. The properties of a silicate slag can be related to the internal slag structure through the concentrations of three different types of oxygen: 'bridging O' (O^0 – connected to two silicon atoms), 'non-bridging O' (O^- - connected to only one silicon) and 'free O' (O^{2-} - associated with no silicon cations). [2,3] The anionic matrix contains silicate chains that have a polymeric nature. Moreover, O^{2-} can be responsible for the charge transfer resulting in acid-base type reactions. The length of the silicate chains depends on the degree of polymerization of the melt. The latter can be expressed by the ratio of NBO/T, where NBO stands for non-bridging oxygen atoms and T for tetrahedrally bound silicon. The value of NBO/T ranges from 0 to 4, corresponding to a fully polymerized silicate melt and a non-polymerized melt, only containing SiO_4^{4-} tetrahedrons, respectively. The degree of polymerization is a strong function of composition as there can be either network breaking ions, such as Ca^{2+} or Fe^{2+}, or network forming ions, such as Si^{4+} or Fe^{3+}. [4]

[19] This chapter is based on the following publication: I. Bellemans, E. De Wilde, N. Moelans, K. Verbeken, Metal losses in pyrometallurgical operations - a review, Advances in Colloid and Interface Science. Submitted

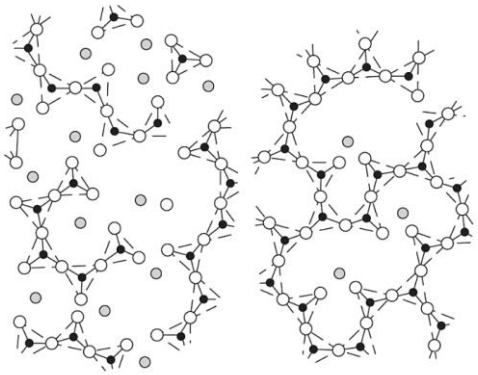

Figure 12.1 Schematic representation of the silicate network with the dissolution of metal oxides in silicate melts. Si-ions are represented as black circled, O-ions as white circles and other cations as grey circles. [3]

It is clear that the phase has a structural complexity that cannot be described by ideal or regular solutions. To describe the Gibbs energy of a slag phase, the modified quasi-chemical model was introduced by Pelton et al. [5–8] and describes the Gibbs energy as a function of the pair fractions, amongst others. The description is quite intricate for more than two components and thus it becomes appropriate to establish a coupling with a thermodynamic database (which essentially calculates Gibbs energies using the modified quasi-chemical model).

The local oxidation state of iron, i.e. the ratio of ferrous (Fe^{2+}) to ferric (Fe^{3+}) cations, in a silicate melt is very important to slag practice in pyrometallurgy as it determines the physical, chemical and structural properties of silicate melts. If the slag is in equilibrium with an atmosphere, the Fe^{2+}/Fe^{3+} or FeO/Fe_2O_3 ratio depends on the activity of oxygen in the atmosphere, the temperature and composition of the silicate melt. When a silicate melt, which contains Fe, is not in thermodynamic equilibrium with the surrounding atmosphere, a redox reaction will take place within the melt. The diffusion of oxygen to or from the atmosphere is typically assumed to be the rate-determining step for these redox processes in slags. [1] The super-fast diffusion of oxygen in liquid iron oxide slags has been considered to be the result of the semi-conductive nature of the slag and of the multitude of mobile charge carriers. [9] However, when alkali cations are present, their diffusion influences the redox behaviour a lot. [1]

12.2. Modelling oxide systems

As became clear above, a slag phase typically has a structural complexity that cannot be described by ideal or regular solutions and thus the modified quasi-chemical model is used to describe the Gibbs free energy of the phase. This model description is complex for multicomponent systems and thus it becomes appropriate to establish a coupling with a thermodynamic database.

This was done by Heulens [1] to model the isothermal crystallization of oxide melts, based on the model of Moelans et al. [10–12]. The model of Heulens et al. [1] considers different phases but not different orientations, and is thus a more simplified version of the model of Moelans et al. [10–12], but it was also extended in another aspect. He implemented a multicomponent, multiphase system, and coupled the model with a thermodynamic database for oxides (FTOxid from Factsage / Chemapp) to obtain the bulk thermodynamic properties of the liquid slag as a function of composition. The stoichiometric solid phases were modelled with a paraboloid Gibbs energy with specific constraints to ensure correct phase equilibria and minimal solubility in the stoichiometric phase and the interfacial mobility and interfacial energy were modelled with anisotropy, as both faceted and

dendritic crystallization can take place in oxide systems. The model was able to describe both crystallization and dissolution of the stoichiometric phase. The influence of the surface energy on the crystallization of wollastonite ($CaSiO_3$) is illustrated in Figure 12.2.

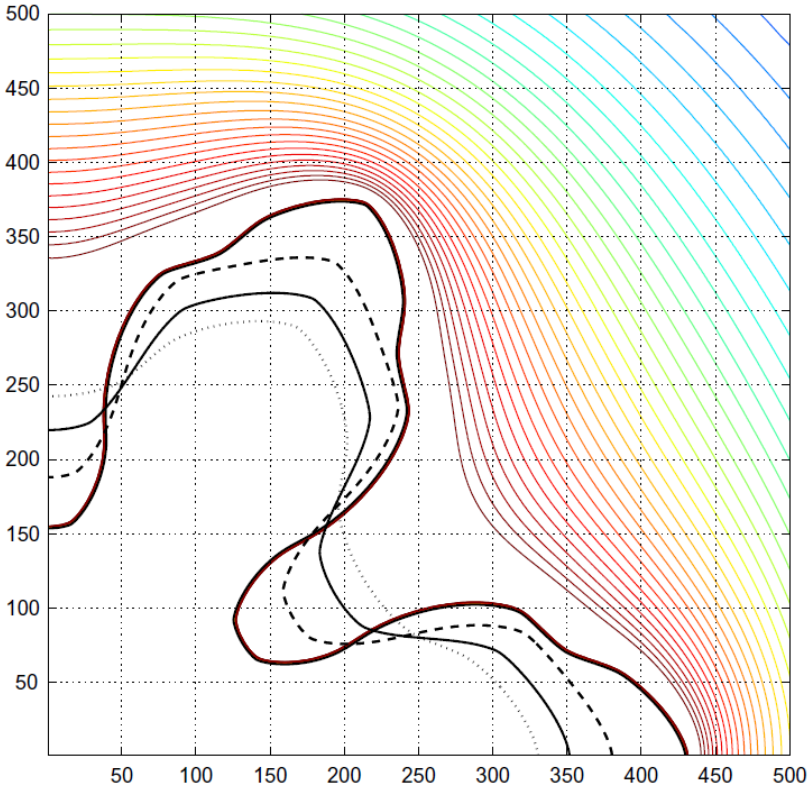

Figure 12.2 Simulation results of 2-D crystallization of wollastonite in a $CaO–Al_2O_3–SiO_2$ melt with four different surface energies, 0.3 (outer solid), 0.4 (dashed), 0.5 (solid) and 0.6 J/m² (dotted), and six-fold symmetry as observed in experiments. As the interfacial energy increases, the tip radius increases while the dendrite tip velocity decreases. For the simulation with r = 0.3, the diffusion field of Al_2O_3 is plotted as well. The system size is 12.5 x 12.5 µm, and the total simulation time for all four cases was 0.2226 s. Only the left lower quarter of the simulation domain is plotted to increase the readability. [1]

They also treated the redox dependent behaviour of multivalent cations when an oxygen-containing atmosphere is present above an iron-containing melt [13]. If such an iron-bearing silicate melt is not in thermodynamic equilibrium with its oxygen-containing atmosphere, the melt is subjected to a redox reaction. In this model, the diffusion is assumed to be much slower than the redox reaction kinetics, and the redox ratio of FeO/Fe_2O_3 is thus locally in equilibrium with the oxygen activity in the melt. He simulated the crystallization of Fe_3O_4 in FeO_x-SiO_2 melts under oxidizing conditions. The oxidizing conditions were present on the upper boundary of the system with a condition to ensure conservation of Fe while the FeO/Fe_2O_3 ratio is in equilibrium with the oxygen fugacity of the atmosphere. Two-dimensional simulations were performed with different nucleation densities of Fe_3O_4 and varying oxygen fugacity in the atmosphere. They concluded that, for the considered nucleation densities, the crystallization of the melt has a larger effect on the oxidation state than the oxygen fugacity of the atmosphere. This is illustrated in Figure 12.3.

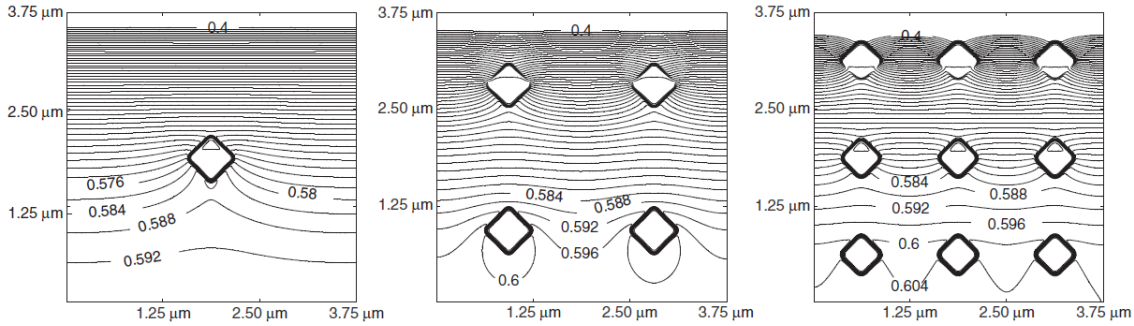

Figure 12.3 Contour plots of the mole fraction of FeO, showing the effect of the number of nucleation sites. From left to right, the number of crystal nuclei is 1, 4 and 9 and corresponds to a nucleation density of 7.1×10^{6} cm–2, 2.8×10^{7} cm^{-2} and 6.4×10^{7} cm^{-2}, respectively. All three contour plots are scaled between x_{FeO}=0.40 and x_{FeO}=0.62 with a step of 0.004. The oxygen fugacity of the atmosphere was $f_{O2}=1.5\times10^{-3}$ while the melt has initially an equilibrium oxygen activity of $a_{O2}=2.4\times10^{-5}$. [13]

Liu et al. [14] also used this model to simulate the isothermal crystallization of wollastonite in the $CaO\text{-}Al_2O_3\text{-}SiO_2$ system. The effects of composition and temperature on the crystallization behaviour were studied. The simulations show that for the considered cases, the wollastonite morphology is mainly determined by anisotropy in the interface energy and hardly affected by anisotropy in the interface kinetics. Some simulated shapes of isothermally crystallized wollastonite at different undercooling temperatures are compared with the experimental observations in Figure 12.4.

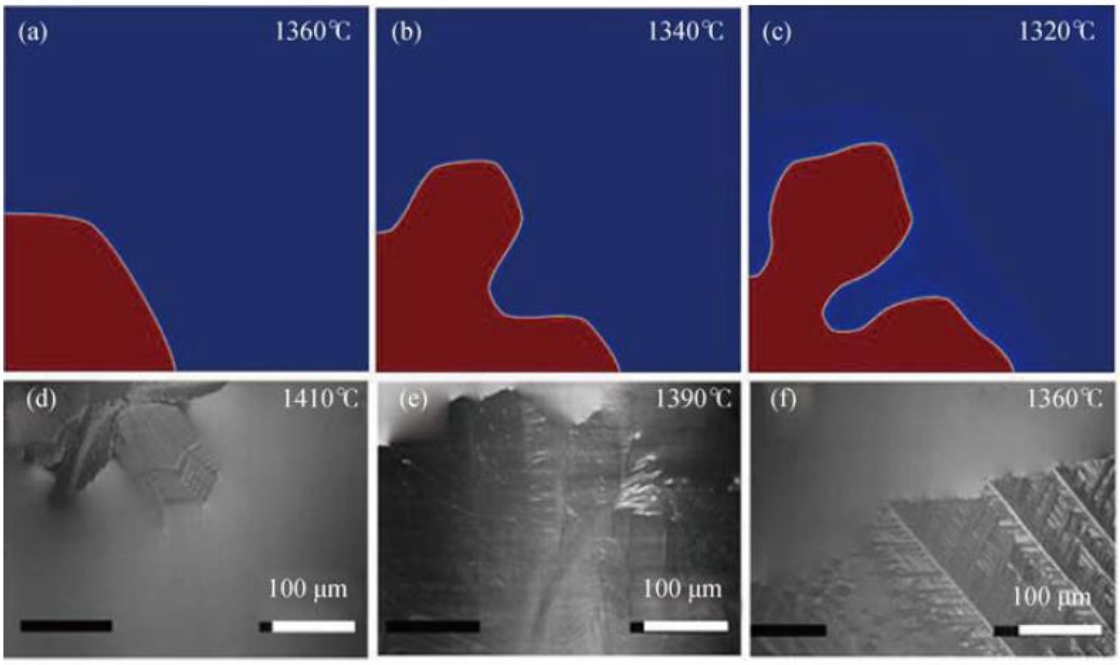

Figure 12.4 Simulated and experimental morphologies of wollastonite for different undercooling temperatures for slag A (initial composition 42wt%CaO - 48wt%SiO_2 - 10wt%Al_2O_3): (a) Δ=65°C; (b) Δ=8°C; (c) Δ=105°C after a simulation time of 1 s and (d) Δ=15°C; (e) Δ=35°C; (f) Δ=65°C observed in the experiments.

In agreement with the observations from in-situ experiments [15,16], the simulations show a transition from planar (a) to dendritic (b-c) growth with decreasing temperature and the dendritic structure becomes finer (c) when the temperature is decreased further. Even though the experiments and simulations correspond well qualitatively, the temperature at which the transition occurs deviates from the experimentally observed transition temperature. Possible reasons for these deviations between experiments and simulations are found in the intrinsic errors in the

experimentally determined temperatures. The transition from a flat to dendritic growth with decreasing temperature can be primarily explained by an instability of the planar interface due to the larger driving force for crystallization at higher undercoolings.

Later, Liu et al. [17] also used this model to investigate the dissolution of Al_2O_3 in a CaO-Al_2O_3-SiO_2 slag. The simulation results fit well to the analytical solution for dissolution in a one dimensional system and the dissolution rate of a circular Al_2O_3 particle. The simulations also agree well with experimental data [18]. Furthermore, the simulation results demonstrate that (1) the dissolution rate of Al_2O_3 increases with temperature, (2) the dissolution rate increases with increasing CaO content and with decreasing Al_2O_3 content for a fixed CaO/SiO_2 ratio.

12.3. Conclusion

Although it is clear that the phase field method has been successfully applied to numerous applications, it is still a challenge to apply the phase field method to multi-component systems and for realistic conditions. So far, only few simulations were performed in real ternary systems, even less for oxide systems. This part of the doctoral work will therefore focus on the study of the growth of the spinel phase in a realistic quaternary slag system.

References

[1] J. Heulens, B. Blanpain, N. Moelans, A phase field model for isothermal crystallization of oxide melts, Acta Mater. 59 (2011) 2156–2165. doi:10.1016/j.actamat.2010.12.016.

[2] Z. Sun, M. Suzuki, P. Hayes, E. Jak, Quasi-chemical viscosity model for copper-containing multi-component liquid slags, in: Santiago (Chili), 2013: pp. 95–107.

[3] E.T. Turkdogan, R.J. Fruehan, Fundamentals of iron and steelmaking, Mak. Shap. Treat. Steel Steelmak. Refin. Vol. 11th Ed RJ Fruehan Ed AISE Steel Found. Pittsburgh. (1998) 125–126.

[4] J. Heulens, Isothermal Crystallization of Metallurgical Slags: Phase Field Simulations Combined with In Situ Experiments (Isotherme kristallisatie van metallurgische slakken: faseveldsimulaties in combinatie met in situ experimenten), PhD thesis, KU Leuven, 2011. https://lirias.kuleuven.be/handle/123456789/318339.

[5] A.D. Pelton, S.A. Degterov, G. Eriksson, C. Robelin, Y. Dessureault, The modified quasichemical model I—Binary solutions, Metall. Mater. Trans. B. 31 (2000) 651–659. doi:10.1007/s11663-000-0103-2.

[6] A.D. Pelton, P. Chartrand, The modified quasi-chemical model: Part II. Multicomponent solutions, Metall. Mater. Trans. A. 32 (2001) 1355–1360. doi:10.1007/s11661-001-0226-3.

[7] P. Chartrand, A.D. Pelton, The modified quasi-chemical model: Part III. Two sublattices, Metall. Mater. Trans. A. 32 (2001) 1397–1407. doi:10.1007/s11661-001-0229-0.

[8] A.D. Pelton, P. Chartrand, G. Eriksson, The modified quasi-chemical model: Part IV. Two-sublattice quadruplet approximation, Metall. Mater. Trans. A. 32 (2001) 1409–1416. doi:10.1007/s11661-001-0230-7.

[9] Y. Sayadyaghoubi, S. Sun, S. Jahanshahi, Determination of the chemical diffusion of oxygen in liquid iron oxide at 1615 °c, Metall. Mater. Trans. B. 26 (1995) 795–802. doi:10.1007/BF02651726.

[10] N. Moelans, A quantitative and thermodynamically consistent phase-field interpolation function for multi-phase systems, Acta Mater. 59 (2011) 1077–1086. doi:10.1016/j.actamat.2010.10.038.

[11] N. Moelans, B. Blanpain, P. Wollants, Quantitative analysis of grain boundary properties in a generalized phase field model for grain growth in anisotropic systems, Phys. Rev. B. 78 (2008) 024113. doi:10.1103/PhysRevB.78.024113.

[12] N. Moelans, B. Blanpain, P. Wollants, Quantitative Phase-Field Approach for Simulating Grain Growth in Anisotropic Systems with Arbitrary Inclination and Misorientation Dependence, Phys. Rev. Lett. 101 (2008) 025502. doi:10.1103/PhysRevLett.101.025502.

[13] J. Heulens, B. Blanpain, N. Moelans, Phase field modeling of the crystallization of FeOx–SiO2 melts in contact with an oxygen-containing atmosphere, Chem. Geol. 290 (2011) 156–162. doi:10.1016/j.chemgeo.2011.09.005.

[14] J.-J. Liu, J. Heulens, M.-X. Guo, N. Moelans, Isothermal Crystal Growth Behavior of CaSiO3 in Ternary Oxide Melts, J. Inorg. Mater. 31 (2016) 547. doi:10.15541/jim20150516.

[15] J.-J. Liu, G. Chen, P.-C. Yan, B. Planpain, N. Moelans, M. Guo, In-situ observation of isothermal CaSiO3 crystallization in CaO–Al2O3–SiO2 melts: A study of the effects of temperature and composition, J. Cryst. Growth. 402 (2014) 1–8. doi:10.1016/j.jcrysgro.2014.05.002.

[16] J. Heulens, B. Blanpain, N. Moelans, Analysis of the isothermal crystallization of CaSiO3 in a CaO–Al2O3–SiO2 melt through in situ observations, J. Eur. Ceram. Soc. 31 (2011) 1873–1879. doi:10.1016/j.jeurceramsoc.2011.03.038.

[17] J. Liu, J. Zou, M. Guo, N. Moelans, Phase field simulation study of the dissolution behavior of Al2O3 into CaO–Al2O3–SiO2 slags, Comput. Mater. Sci. 119 (2016) 9–18. doi:10.1016/j.commatsci.2016.03.034.

[18] J. Liu, F. Verhaeghe, M. Guo, B. Blanpain, P. Wollants, In Situ Observation of the Dissolution of Spherical Alumina Particles in CaO–Al2O3–SiO2 Melts, J. Am. Ceram. Soc. 90 (2007) 3818–3824. doi:10.1111/j.1551-2916.2007.02062.x.

13. The multi-component model

This part of the doctoral work focusses on studying the growth of the spinel solid within a realistic slag system. The model for this purpose will use the already existing model of Heulens et al. [1–3] for the isothermal crystallization of oxide melts as starting point. This model, in turn, is based on the multi-component multi-phase field model developed by Moelans et al. [4,5]. However, different from these previous models, we did not consider different grains or crystallographic orientations in the phases. Some details of the model of Heulens will be briefly described in this chapter and it will be discussed how the code was adapted to eliminate some of the remaining limitations.

13.1. Model and implementation by Heulens et al. [1–3]

13.1.1. Free energy functional

The model by Heulens et al. [1–3] was constructed from a phase field model for multi-phase systems, based on the grain growth model of Moelans et al. [4] and the multi-component approach of Eiken et al. [6], and describes the isothermal crystallization of oxide melts. The total free energy of a heterogeneous isothermal system with *p* phases and *c* components is formulated as a functional of the non-conserved phase field variables η_i and the conserved concentration fields x_k (i.e. the mole fractions of the different components). The free energy functional decreases monotonously during microstructural evolution towards thermodynamic equilibrium and consists of interfacial and bulk Gibbs free energies, but no elastic or magnetic contributions were considered:

$$F = \int f(\eta_i, \vec{\nabla}\eta_i, x_k)\, dV = \int [f_{in}(\eta_i, \vec{\nabla}\eta_i) + f_b(\eta_i, x_k)]\, dV \quad \textbf{(13.1)}$$

In this model, the interfacial free energy density is represented by:

$$f_{in} = m f_0(\eta_i) + \frac{\kappa}{2}\sum_{i=1}^{p}\left(\vec{\nabla}\eta_i\right)^2 \quad \textbf{(13.2)}$$

With f_0 a fourth order Landau polynomial of the order parameters, representing a homogeneous free energy of the double-well type:

$$f_0(\eta_i) = \sum_{i=1}^{p}\left[\frac{\eta_i^4}{4} - \frac{\eta_i^2}{2}\right] + \gamma\sum_{i=1}^{p}\sum_{j>i}^{p}\eta_i^2\eta_j^2 + \frac{1}{4} \quad \textbf{(13.3)}$$

Each term in the first set of summations is a double-well potential with minima located at -1 and +1 for η_i. The cross term ($\eta_i^2\eta_j^2$) was added to make it energetically unfavourable to have two order parameters different from zero at the same position in the system because it gives a positive contribution to the local free-energy density for each extra phase field variable with a value different from 0. By consequence, within the grains only one of the phase field variables differs from 0 and at a grain boundary and multi-junctions, only those phase field variables representing the adjacent grains are different from zero. [4,7] The parameter γ is taken constant and equal to 1.5 because the phase field profiles are symmetrical and cross each other at 0.5 in the interface in this case, as investigated previously by Moelans et al. [4]. With this constant value, κ_{ij} and m_{ij} define the physical properties of an interface between phases *i* and *j*, such as the interfacial energy σ_{ij} and the diffuse interface width l_{ij}. [4,8] The local values of the model parameters ($\kappa(r)$, $m(r)$ and $L(r)$ with r

representing the space) are defined as a weighted sum of the interfacial parameters κ_{ij}, m_{ij} and L_{ij} [3–5]:

$$\kappa(r) = \frac{\sum_{i=1}^{p}\sum_{j>i}^{p}\kappa_{ij}\eta_i(r)^2\eta_j(r)^2}{\sum_{i=1}^{p}\sum_{j>i}^{p}\eta_i(r)^2\eta_j(r)^2}$$
$$m(r) = \frac{\sum_{i=1}^{p}\sum_{j>i}^{p}m_{ij}\eta_i(r)^2\eta_j(r)^2}{\sum_{i=1}^{p}\sum_{j>i}^{p}\eta_i(r)^2\eta_j(r)^2} \quad \textbf{(13.4)}$$
$$L(r) = \frac{\sum_{i=1}^{p}\sum_{j>i}^{p}L_{ij}\eta_i(r)^2\eta_j(r)^2}{\sum_{i=1}^{p}\sum_{j>i}^{p}\eta_i(r)^2\eta_j(r)^2}$$

The interfacial energy σ_{ij} of the phase boundary between the phases *i* and *j* can be calculated analytically for symmetrical phase field profiles (if γ=1.5) [3–5]:

$$\sigma_{ij} = \frac{\sqrt{2}}{3}\sqrt{m_{ij}\kappa_{ij}} \quad \textbf{(13.5)}$$

Moreover, the interfacial width can be calculated as [3–5]:

$$l_{ij} = \sqrt{\frac{8\kappa_{ij}}{m_{ij}}} \quad \textbf{(13.6)}$$

In thin-interface models, it is recommended to take l_{ij} equal for all interfaces in the system to maintain a similar accuracy. The bulk energy density part of the total free energy of the system is derived from the Gibbs energies of all phases as a function of temperature and composition, $G_m(x_k,T)$, but divided by the molar volume to get the energy density per phase (f_i).

$$f_b = \sum_i h_i f_i(x_1^i, \dots, x_k^i, \dots, x_{C-1}^i) \quad \textbf{(13.7)}$$

The following interpolation function was used:

$$h_i = \phi_i = \frac{\eta_i^2}{\sum_i \eta_i^2} \quad \textbf{(13.8)}$$

Where η_i represents the phase field variable and ϕ_i represents the local phase fraction. Note that the local phase fractions sum up to one, but there is no restriction on the phase field variables η_i.

As proposed by Kim et al. [9], every phase has its own set of composition variable x_k^i, called the phase compositions. These differ from the local composition x_k but are unambiguously defined at each point by the requirement of equal phase diffusion potentials for all components in all coexisting phases, due to the thin-interface approach, and a mass balance equation (at constant molar volume) for each component to relate the overall composition of a component *k* to the phase compositions:

$$\tilde{\mu}_k = \frac{\partial f_1(x_k)}{\partial x_k^1} = \dots = \frac{\partial f_p(x_k)}{\partial x_k^p}, \qquad \forall\, k \quad \textbf{(13.9)}$$

$$x_k = \sum_i h_i x_k^i \quad \textbf{(13.10)}$$

The diffusion potential of component *k* in phase *i* is defined as the difference between the chemical potential of that component and the chemical potential of a reference component (say component 0):

$$\tilde{\mu}_k = \tilde{\mu}_k^i = \mu_k^i - \mu_0^i, \qquad k = 1 \dots c-1 \tag{13.11}$$

Actually, the difference between the chemical potentials of a certain component and the chemical potential of the reference component in the same phase, i.e. the diffusion potential, equals the derivative of the molar Gibbs free energy of that phase to the mole fraction. However, for constant molar volumes, an assumption usually made in phase field models, these relations are equivalent for Gibbs energies and chemical potentials per volume.

13.1.2. Phase field equations

The evolution of each phase field variable is assumed to be linear with its driving force, according to the linear non-equilibrium thermodynamics theory of Onsager: if the free energy is not minimal with respect to a local variation of the non-conserved variable, a direct change will take place in the value of that variable. Every change in the phase field variables should decrease the total energy *F* of the system. The evolution equation of η_i, is thus written as a time-dependent Ginzburg-Landau equation for non-conserved variables:

$$\frac{\partial \eta_i}{\partial t} = -L\left(m\frac{\partial f_0}{\partial \eta_i} + \frac{\partial f_b}{\partial \eta_i} - \nabla_x\left(\frac{\partial f}{\partial \nabla_x \eta_i}\right) - \nabla_y\left(\frac{\partial f}{\partial \nabla_y \eta_i}\right)\right) \tag{13.12}$$

Where the ∇_x and ∇_y operators are equivalent to the one-dimensional partial derivatives *∂/∂x* and *∂/∂y*. The expansion of these terms depends on whether or not anisotropy is taken into account. For the isotropic derivation, both terms can be replaced by a single term of $-\kappa\nabla^2\eta_i$. The anisotropic case is derived in the following section. The other terms in (13.12) have the following expressions:

$$\frac{\partial f_0}{\partial \eta_i} = {\eta_i}^3 - \eta_i + 2\gamma\eta_i\left(\sum_{j\neq i}^{p} {\eta_j}^2\right) \tag{13.13}$$

$$\frac{\partial f_b}{\partial \eta_i} = \sum_{j=1}^{p}\frac{\partial \phi_j}{\partial \eta_i}\left(f_j - \sum_{k=1}^{C-1}\tilde{\mu}_k x_k^j\right) \tag{13.14}$$

$$\frac{\partial \phi_j}{\partial \eta_i} = \frac{-2\eta_i{\eta_j}^2 + 2\delta_{ij}\eta_i\left(\sum_{r=1}^{p}{\eta_r}^2\right)}{\left(\sum_{r=1}^{p}{\eta_r}^2\right)^2} \tag{13.15}$$

Where δ_{ij} represents the Kronecker delta, being 1 if *i=j* and 0 if not. Because of the cross products, ghost fields (i.e. other phase fields than those representing the neighbouring phases but contributing at the phase boundaries) always result in an increase of the local free energy and are accordingly unstable. Therefore, expressions for the grain boundary properties derived for two-grain structures remain valid for individual grain boundaries in polycrystalline structures, except for very small grains. [5]

$\partial m/\partial \eta_i$ and $\partial \kappa/\partial \eta_i$ are not taken into account, because they give rise to extra phase field variables at an interface between two phases. The dependence of κ on the phase field variable was determined [4] to be merely present to locate and characterize the grain boundaries and must be omitted in the derivation of the driving force. Thus, the expressions above are not obtained in a fully variational manner. The effect of the omitted derivatives is, however, significant for multi-junctions, which are not expected in the case of isothermal crystallization.

13.1.3. Anisotropy

The morphology of a growing crystal depends on the properties of the solid-liquid interface, i.e. the anisotropy of the interfacial energy and mobility. The degree of anisotropy will have a significant effect on the growth morphology and equilibrium shape of particles [10], as illustrated by the evolution of flat interfaces according to the Wulff construction [11]. Two types of interfaces can be distinguished, atomically smooth and atomically rough. Both types of interfaces differ in their response to the thermodynamic driving force present in a supersaturated melt. An atomically smooth interface is present during reaction-controlled crystal growth and results in faceted crystal growth, while an atomically rough interface is present during diffusion-controlled growth and induces non-faceted growth, such as dendrites. This thermodynamic description uses the Jackson factor (a measure of smoothness of the interface) and indicates the tendency for the formation of atomically smooth or rough interfaces, but is based on a simplified two-layer model. Another approach is investigating the kinetics of the roughening: at low velocities and low driving forces, atomically smooth interfaces are expected, whereas high velocities and high driving forces yield atomically rough interfaces. [3] Both dendritic and faceted growth morphologies are frequently observed in multi-component oxides: many minerals exhibit a faceted shape in a melt at low supersaturation, whereas high supersaturation mostly yield dendrites. [1]

For two-dimensional systems, the normal to the interface $\vec{n} = (n_1, n_2)$, which is in fact the normal to contours of constant value of a phase field variable η_i, is given by

$$(n_1, n_2) = \frac{1}{\sqrt{\left(\frac{\partial \eta_i}{\partial x}\right)^2 + \left(\frac{\partial \eta_i}{\partial y}\right)^2}} \left(\frac{\partial \eta_i}{\partial x}, \frac{\partial \eta_i}{\partial y}\right) \tag{13.16}$$

and the angle θ between the normal to the interface between phases *i* and *j* and the *x*-axis is

$$\tan(\theta_{ij} - \theta_0) = \frac{\left|\nabla \eta_i - \nabla \eta_j\right|_y}{\left|\nabla \eta_i - \nabla \eta_j\right|_x} \tag{13.17}$$

With θ_0 the initial orientation of the interface. In all simulations, this was set as zero, as Heulens already demonstrated the rotation-invariance of the model [12].

In the case of dendrite growth, the morphology is determined by a weak anisotropy in the interface energy. [1] Several approaches are possible to introduce interfacial energy anisotropy in phase field models. [10] One of the simplest ways to include anisotropy in realistic simulations, is giving $\sqrt{\kappa}$ the same orientation dependence as the interfacial energy, because generally the interfacial energy is proportional to $\sqrt{\kappa}$. [13] Another possibility is to add higher order gradient energy terms, but most often the first method is used. [14] For weak anisotropy, the following formulation is commonly applied for two-dimensional systems [8,15]:

$$\sqrt{\kappa} = \bar{\kappa}(1 + \upsilon \cos(k\theta)) \tag{13.18}$$

With υ (<1/15) a measure of the amplitude of anisotropy, usually a few percent, and *k* the order of anisotropy, e.g. four- or six-fold. The amplitude as a parameter which is difficult to measure and must satisfy the following inequality in such a way that the stiffness of the interface is always positive:

$$\upsilon < \frac{1}{k^2 - 1} \tag{13.19}$$

If the energy gradient coefficient κ depends on the orientation of the interface, the interfacial thickness varies along the interface. These variations may result in artefacts, such as enhanced particle coalescence along high-energy interfaces or numerical pinning along low-energy orientations. Therefore, a better approach would be to make both the energy gradient coefficient and the height of the double-well potential orientation dependent in such a way that the orientation dependence of the interfacial energy is reproduced, while the interfacial thickness is constant along the interface. [13] Thus the same orientation dependent function used for κ is used for *m*:

$$\kappa_{ij} = \bar{\kappa}_{ij}\lambda_{ij}(\theta_{ij}) \tag{13.20}$$

$$m_{ij} = \bar{m}_{ij}\lambda_{ij}(\theta_{ij}) \tag{13.21}$$

With λ_{ij} the expression between brackets in the right-hand side of equation (13.18).

For faceted crystal growth in oxide systems, the orientation dependence is characterized by strong anisotropy in the interface kinetics and thus the phase field mobility L_{ij} is incorporated to have cusps at slow growth directions that define the growth geometry of the crystal. An example of orientation dependence resulting in strong anisotropy:

$$\lambda_{ij}(\theta_{ij}) = 1 + v\left(\left|\sin\theta_{ij}\right| + \left|\cos\theta_{ij}\right|\right) \tag{13.22}$$

describes square particles and

$$\lambda_{ij}(\theta_{ij}) = \frac{1}{1+v}\left(1 + v\left|\cos\theta_{ij}\right|\right) \tag{13.23}$$

results in plate-like particles. v defines the amplitude of the anisotropy. In this model, facetted growth with sharp cusps at the facet plane orientations is described by the following orientation-function for the kinetic coefficient *L*:

$$\lambda_{ij}(\theta_{ij}) = 1 - \beta_{ij} + 2\beta_{ij}\, tanh\left(\frac{r_{ij}}{\left|tan(a_{ij}\theta_{ij})\right|}\right) \tag{13.24}$$

With β_{ij} a measure for the depth of the cusps (i.e. the difference in mobility between the fast and slow crystal planes), *r* the sharpness of the cusps (influencing the corner formation at the edges of two crystal planes) and $2a_{ij}$ the mode of symmetry of the anisotropy (mostly a value of 4 or 6 for minerals such as spinel or corundum).

When anisotropy is taken into account in the surface energy and thus also in the gradient free energy coefficient, the term $-\nabla\left(\frac{\partial f}{\partial \nabla\eta_i}\right)$ in the variational derivative in equation (13.12) becomes:

$$\begin{aligned}\frac{\partial f}{\partial \nabla_x \eta_i} = f_0\left(\frac{-\nabla_y\eta_i}{(\nabla\eta_i)^2}\right)\left(\sum_{j\neq i}^{p}\Omega_{ij}\bar{m}_{ij}\frac{d\lambda_{ij}}{d\theta_{ij}}\right) \\ + \frac{1}{2}\left(\frac{-\nabla_y\eta_i}{(\nabla\eta_i)^2}\right)\left(\sum_{j\neq i}^{p}\Omega_{ij}\bar{\kappa}_{ij}\frac{d\lambda_{ij}}{d\theta_{ij}}\right)\left(\sum_{r=1}^{p}(\nabla\eta_r)^2\right) + \kappa\nabla_x\eta_i\end{aligned} \tag{13.25}$$

With

$$\Omega_{ij} = \frac{{\eta_i}^2{\eta_j}^2}{\sum_{r=1}^{p}\sum_{s>r}^{p}{\eta_r}^2{\eta_s}^2} \tag{13.26}$$

And an analogous expression for $\partial f/\partial\nabla_y\eta_i$.

13.1.4. Diffusion equations

Each C-1 independent component evolves in time according to a diffusion equation, derived from a time-dependent Ginzburg-Landau equation for conserved variables:

$$\frac{\partial x_k}{\partial t} = \nabla \cdot \left[\sum_{i=1}^{p} \phi_i \left(\sum_{l=1}^{C-1} M_{kl}^{i} \nabla \tilde{\mu}_l^i \right) \right] \quad \textbf{(13.27)}$$

Where the gradients in the diffusion potential are the driving forces for multi-component diffusion because cross-terms are included. This mobility M^{i}_{kl} actually represents the Onsager coefficients L''_{ki}, as defined in equation (3.13), that can be linked to the interdiffusion coefficient:

$$D_{kj}^{n} = \sum_{i=1}^{n} L''_{ki} \frac{\partial [\mu_i - \mu_n]}{\partial c_j} \quad \textbf{(13.28)}$$

13.1.5. Coupling to thermodynamic database

There is a constant drive to perform more complex simulations which would allow for quantitative kinetic predictions of microstructural evolution in multicomponent industrial materials. Such simulations require the input of thermodynamic data. However, the thermodynamic and kinetic descriptions used in phase field simulations are often simple and idealized as the use of a proper CALPHAD database would drastically increase simulation time. [16]

In this model, in equation (13.7), the bulk chemical energy density is calculated as a weighed sum of the Gibbs free energies of the different phases, f_i. Previously, phase field models incorporated thermodynamic properties of phases by either evaluating analytical Gibbs energy functions in the model equations or by calling thermodynamic software libraries, such as thermo-calc through TQ-interfaces. Heulens [3] linked his phase field model with commercial thermodynamic databases for oxides by extracting the necessary data from the database once, before the start of the phase field simulation, and storing it in an array, which is loaded at the start of the phase field simulation. This technique was developed because the Gibbs energy expressions of slag phases are not freely available and, moreover, the phase field simulation is run on a parallel computer cluster, which makes coupling to commercial thermodynamic software at run time quite cumbersome and unpractical. Furthermore, in this way, the developed phase field model is not reliant on a specific type of thermodynamic software or database with this method. [3]

The Gibbs energies of the different phases are approximated by a second-order Taylor approximation $\widehat{f_l}$ around $\widehat{\boldsymbol{x}^l} = \left(\widehat{x_1^l}, \dots, \widehat{x_k^l}, \dots, \widehat{x_{C-1}^l}\right)$.

$$\widehat{f_l} = \sum_{k=1}^{C-1} \left(\frac{A_{kk}^i}{2} \left(x_k^i - \widehat{x_k^l}\right)^2 \right) + \sum_{k=1}^{C-1} \left(\sum_{l>k}^{C-1} \left(A_{kl}^i \left(x_k^i - \widehat{x_k^l}\right)\left(x_l^i - \widehat{x_l^l}\right) \right) \right) + \sum_{k=1}^{C-1} \left(B_k^i \left(x_k^i - \widehat{x_k^l}\right) \right) + C^i \quad \textbf{(13.29)}$$

The parameters ***A***, ***B*** and ***C*** are retrieved at every concentration $\widehat{\boldsymbol{x}^l}$ from a thermodynamic database. The FToxid database was used to retrieve the thermodynamic data. The composition domain was first discretized on a square grid with a grid spacing of 0.005 and then ***A***, ***B*** and ***C*** are calculated at

every grid point as $\frac{\partial \tilde{\mu}_k^i}{\partial x_l^i}$, $\tilde{\mu}_k^i$ and $\frac{G_m^i}{V_m}$ [8], respectively with Chemapp [17]. $\frac{\partial \tilde{\mu}_k^i}{\partial x_l^i}$, however, does not correspond to a function incorporated in Chemapp. Thus, a centred finite difference is implemented to determine these derivatives:

$$\frac{\partial \tilde{\mu}_k^i}{\partial x_l^i} = \frac{\tilde{\mu}_k^i\left(x_l^i + \delta x\right) - \tilde{\mu}_k^i\left(x_l^i - \delta x\right)}{2\delta x} \tag{13.30}$$

With δx=10^{-6}. All these thermodynamic data are saved in several .txt files, which in turn will be read as input for the phase field program itself.

The coupling to the thermodynamic database for oxides present in FactSage (FToxid) happens through the Chemapp-interface. Chemapp uses the same concept of a thermochemical system as FactSage: a thermochemical system consists of a number of chemical components and a number of phases. Some of the phases may have a composition expressed as amounts of a number of phase constituents, and others can have an invariant composition. Phases are divided into three groups in Chemapp: the gaseous phase, condensed mixtures and condensed stoichiometric phases. The latter consist of a single phase constituent only. Phases and phase constituents always have thermodynamic properties. Phase constituents have compositions expressed as amounts of a number of components. [17] The slag phase is typically described by the oxides in the database.

First, an equilibrium calculation incorporating all relevant phases is required for different 'pure' situations, i.e. a system containing only one mole of a certain oxide in the slag phase. These reference states are required to obtain absolute values for the chemical potential, because Chemapp actually only gives the RT ln (activity) part when asked for the chemical potential. These chemical potentials are calculated for phase constituents in Chemapp with a reference to the standard state of the pure phase at the chosen temperature. However, these standard states differ for different phases or temperatures. However, in the final phase field simulations, the 'absolute' chemical potentials, i.e. referred to the same standard state, are required to be able to simulate phase transitions. Thus, the actual chemical potential value can be obtained by calculating $\mu_{absolute} = G°_{reference} + \mu_{from\ Chemapp}$. Thus, we need to add the obtained chemical potential value from Chemapp to the previously obtained $G°_{reference}$-value. In this way, the standard state for the chemical potentials is changed from the pure phase at the considered temperature to the standard state for the calculations of *G*, which is the most stable phase at 298.15K, because $G°_{reference}$ is actually the ΔG-value for changing the reference temperature from the temperature of the calculation to 298.15K.

13.1.6. Stoichiometric precipitates

Intermetallic precipitates in which there is no solubility or the solubility is extremely small are known as 'line compounds'. The free energy of a line compound, by definition, is represented by a single Gibbs free energy value at a given temperature. Modelling the growth of stoichiometric line compounds via the phase field approach poses serious numerical challenges since it is not compatible with a continuum model and the derivative of the free energy does not exist, hence no diffusion would be possible through that phase. One possible approach is to approximate the free energy of a line compound by a steep parabolic function of composition, as was done by Hu et al. [14]. They examined the effect of different approximations of chemical free energies on predicted precipitate growth kinetics with phase field modelling. They demonstrated that the parabolic function provides a good description for the chemical free energy of a stoichiometric compound while the growth

kinetics are sensitive to the approximation of chemical free energy for the solution phase. As the second derivative of the free energy of the matrix phase decreases, the overall driving force or effective diffusivity decreases, in turn reducing the driving force. The fact that the chemical contribution is formulated as a function of the phase composition x_k^i and not the mixture composition x_k turns out to be essential for phases which are stoichiometric or have a restricted solubility range for certain elements. [18]

The stoichiometric phases were treated by Heulens et al. [1–3] in such a way to ensure that a correct Gibbs free energy value is found at the stoichiometric composition. Moreover, all components have the same chemical diffusion potential as the solution phases, to ensure the validity of equation (13.9) from the start of the simulation onwards. Furthermore, the curvature of the parabolic Gibbs free energy should be high enough (at least 10 times that of the liquid) to minimize the deviation from the expected equilibrium compositions in the coexisting solution phases and to minimize the solubility in the stoichiometric phase. Note that a too high value for the curvature will yield an ill-conditioned set of equations, which becomes unsolvable. To avoid changes in the steady-state growth and solute trapping effects, the mobilities of the different components are chosen to have values of the same order of magnitude as in the liquid and the off-diagonal elements in this mobility matrix are zero. The expression of Gibbs free energy of the stoichiometric compound as a function of the complete composition domain is described as:

$$F = \frac{A}{2}x_1^2 + \frac{B}{2}x_2^2 + Cx_1 + Dx_2 + E \tag{13.31}$$

With x_1 and x_2 the mole fractions of the components within the stoichiometric phase and $x^S{}_1$ and $x^S{}_2$ corresponding to the stoichiometric composition. A, B, C, D and E are constant for all phase concentrations. To get a solution for the above equation, we need a set of 5 equations:

$$\begin{aligned} \frac{\partial F}{\partial x_1} &= Ax_1^S + C = \tilde{\mu}_1^{liquid} \\ \frac{\partial F}{\partial x_2} &= Bx_2^S + D = \tilde{\mu}_2^{liquid} \\ F &= \frac{G}{V_m} \\ A &\geq 10\frac{\partial \tilde{\mu}_1^{liquid}}{\partial x_1} \\ B &\geq 10\frac{\partial \tilde{\mu}_2^{liquid}}{\partial x_2} \end{aligned} \tag{13.32}$$

Here, the Gibbs free energy of 0.5 moles of the stoichiometric phase is used. This is because in the phase field model, a mole fraction of 0.5 of each component will react to form the stoichiometric phase. Moreover, the chemical diffusion potential of the liquid is evaluated at a liquid composition in equilibrium with the stoichiometric phase. However, the liquid interface composition is not known before the simulation. However, Heulens et al. [1] already investigated the influence of this initial equilibrium, used to construct the paraboloid, and found that this does not affect the steady state growth of the stoichiometric phase if the paraboloid is taken at least 10 times steeper than the Gibbs energies of the solution phases. The solution of the set of equations in (13.32) is:

$$A = 10\frac{\partial \tilde{\mu}_1^{liquid}}{\partial x_1}$$
$$B = 10\frac{\partial \tilde{\mu}_2^{liquid}}{\partial x_2}$$
$$C = \tilde{\mu}_1^{liquid} - Ax_1^S \qquad \textbf{(13.33)}$$
$$D = \tilde{\mu}_2^{liquid} - Bx_2^S$$
$$E = \frac{G_m}{V_m} - \frac{A}{2}\left(x_1^S\right)^2 - \frac{B}{2}\left(x_2^S\right)^2 - Cx_1^S - Dx_2^S$$

In some cases, e.g. wollastonite in the CaO-Al_2O_3-SiO_2 system, the stoichiometric phases have a composition on the edge of the composition domain. This would make it impossible to determine all parameters in the paraboloid expression and thus the paraboloid is moved slightly inwards and constructed with a slightly different composition. [1] Because a phase field model incorporates the full diffusion matrix correctly for all phases and ensure chemical equilibrium at the interface, if the interface mobility is chosen appropriately, it will automatically select the correct tie-line and interface velocity.

One should note that within the model of Heulens et al. [1], the concentration fields are coupled by the condition that at every point in space and at every time step, the diffusion potentials should be the same for all coexisting phases. Moreover, the initial compositions are chosen in such a way that the diffusion potentials in the initial system are equal from the start. This is, however, not generally true: when two materials with different initial compositions are brought into contact, the diffusion potentials do not coincide. E.g. the model by Steinbach et al. [19] takes into account finite interface dissipation and enables starting from a system with different diffusion potentials. The model is based on that of Tiaden et al. [20], but the equal diffusion-potential-condition between the concentration fields is replaced by a kinetic equation that drives the concentration fields to the desired equilibrium and actually describes the transfer of components from one side of the interface to the other. The associated rate constant influences the interface dissipation. This model by Steinbach et al. [19] was limited to binary systems with only two phases, but it was extended by Zhang and Steinbach [21] to multi-component multi-phase systems.

13.1.7. Parallelization of the implementation

Although the present research has a clear focus on materials science and engineering, a well-developed expertise in the numerical and code implementation is required when dealing with the computational technique of phase field modelling. Thus, the implementation of the code and the parallelization of the HPC cluster are described in this section.

The code was compiled using the Intel C/C++/Fortran compilers, present in the HPC environment (intel-2016b). Parallelization of the code was executed on the HPC cluster of UGent (STEVIN Supercomputer Infrastructure at Ghent University). The program was run in parallel on the cluster, i.e. the system is divided into several subsystems and the code is executed for each of these subsystems on one processor of the cluster. Each processor executes the same compiled source code containing the actual phase field program. As the different subsystems are not independent from one another, communication between the different subsystems is required. This was done by using the Message Passing Interface (MPI) formalism.

The MPI formalism creates a 'world of processors' which all have their own boundaries (either another processor/subsystem or the global system border). This is illustrated in Figure 13.1 for the subdivision of the global system into four subsystems and thus dividing the 'work' over four processors.

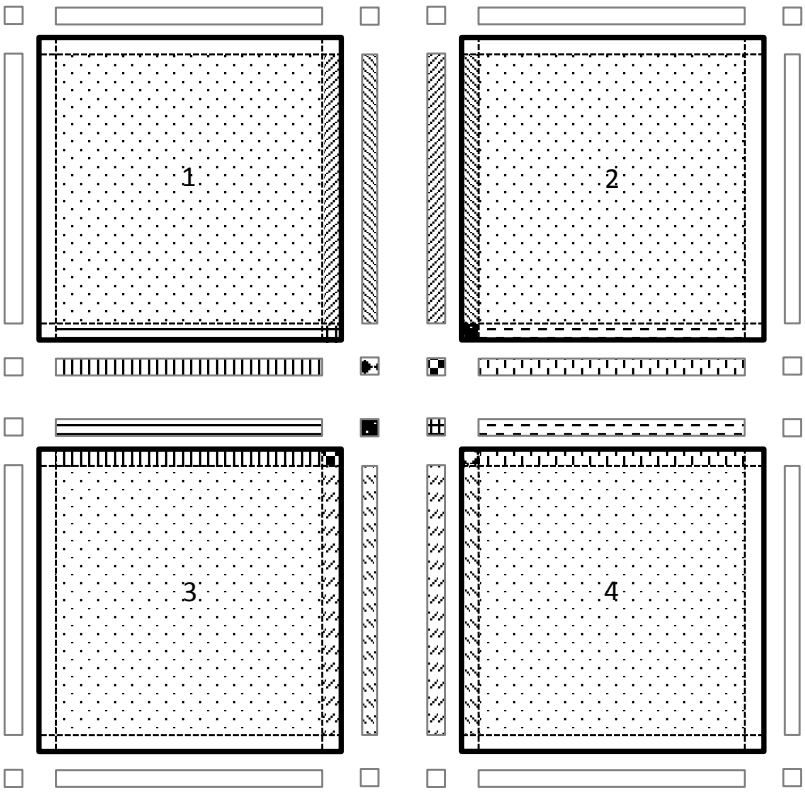

Figure 13.1 Schematic representation of communication between processors in parallel simulations. The simulation domain per processor is indicated by the bold black line and within these domains, two parts are distinguished: the bulk part (dotted square) and the border (separated from the bulk by dashed lines). The bulk part can be solved without communication during a parallel simulation, whereas the border part requires information from neighbouring processors (which one is indicated by the use of the same texture fill in the rectangles representing the ghost nodes of the processor under consideration and the border of the neighbouring processor). [3]

The solution of the phase field equations in the bulk of the subsystems does not require communication with the other processors during a parallel simulation, whereas the border part requires information from neighbouring subsystems. The ghost nodes of the subsystem under consideration should equal the border of the neighbouring subsystem and vice versa. This requires communication between the different processors by routines provided by the MPI library. This also results in the fact that the processor under consideration can only start solving the evolution equations in the border, when it received the required information in the ghost nodes of the neighbouring processor.

The scaling behaviour of a parallel implementation is investigated by performing parallel simulations of the same computational problem with a different amount of processors. The total computing time decreases for an increasing number of processors *N*. However, this increase stagnates, as the addition of a large amount of processors greatly increases the amount of time required for the communication between the different processors and will, from a certain number on, outweight the benefit of more computing power received by the larger amount of processors. The speed-up of a parallelization is the computing time required by one processor divided by the computing time

required by *N* processors. The efficiency of a parallelization is the speed-up divided by the number of processors *N*. These were calculated by Heulens and can be found in Figure 13.2[3].

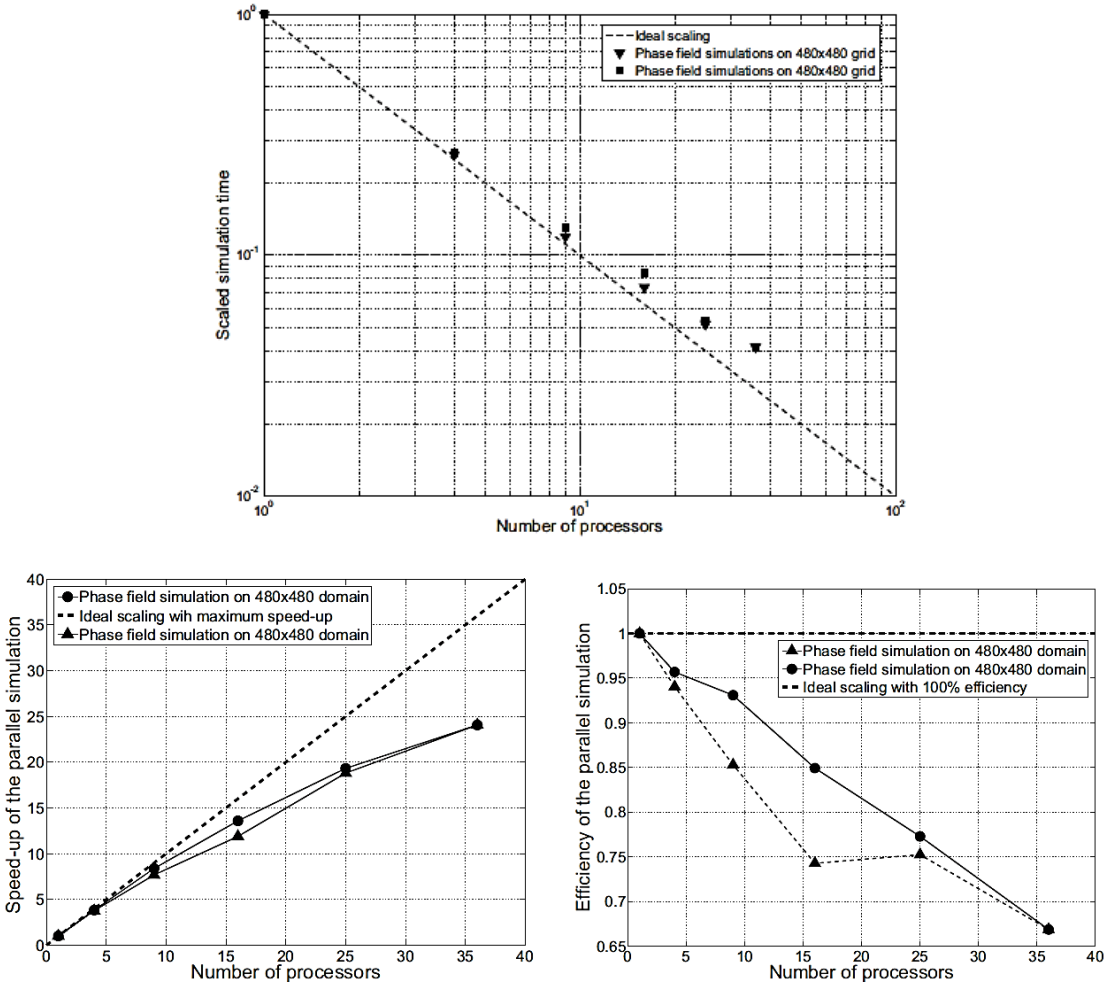

Figure 13.2 The scalability, the speed-up and the efficiency of the parallel implementation of the model, as investigated by Heulens [3]

The HPC cluster of UGent (STEVIN Supercomputer Infrastructure at Ghent University) uses CPUs (central processing units) to parallelize simulations. Another possibility, however, is the use of GPUs (graphical processing units). [22] Although GPU was originally developed as a visualization processing unit, since GPU offers high computing ability and high memory bandwidth and GPU is quite low priced comparing to the cluster computer with many CPUs, GPU is utilized as an accelerator for scientific simulations. [23] Some basics of parallel computing are similar to MPI, but the main differences with GPUs are the different layers of memory available (with different size and inversely scaling access time). [22] In one GPU, several streaming multiprocessors (SMPs) are present and one SMP contains several scalar processors (SP). A large global memory is present, and in each SMP, a shared memory can be found. A GPU cannot directly access the global memory of other GPUs, thus, host CPUs are used as bridges for data exchange. For phase field models, it would be possible to store all data for the phase fields and the concentrations in the global memory and all SP can access the data in the global memory. On the other hand, only SPs in the same SMP can access the data in the shared memory. Although the available amount of the shared memory is much lower than that of the global memory, the data transfer rate of the shared memory is higher than that of the global memory. Therefore, to reduce long latency for accessing the global memory, it is important to make effective

use of the shared memory. Thus, it is advisable to retrieve only necessary data to calculate the governing equations by the threads from the global memory and copy it to the shared memory. [23]

Two main bottlenecks exist with GPU computing:

- the total size of the calculation on one GPU (a few GBs)
- memory transfer, which is now the main source of time spent during the calculation (not the calculation/mathematics itself, but the memory transfer/copies between the CPU host and the GPU device)

GPUs can accelerate calculations immensely (up to approximately 150 times with basic implementations), but only for large enough calculations. Combining 4000 GPUs and 16000 CPUs in a supercomputer even made it possible to simulate multiple dendrites in the typical scales of microstructural patterns in a 5000^3 mesh. [22]

13.1.8. Implementation

The numerical implementation of this model was done in Fortran 90. The system is divided into a two-dimensional grid with equal distances between grid points in both the x- and y-axis. The evolution equations for both the conserved and non-conserved field variables are solved with spatial central finite differences and temporal forward finite differences. To be able to account for different boundary conditions for the system, ghost nodes were introduced next to the outer rim of the system grid points, as illustrated by the outer rows and columns of empty circles in Figure 13.3. The ghost nodes were implemented because of the complexity of the variational derivative in the phase field equations, especially in anisotropic systems. [3]

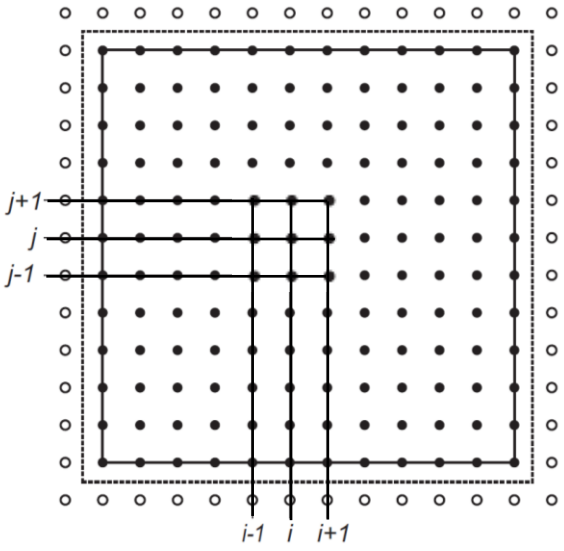

Figure 13.3 Illustration of the spatial numerical grid with the use of ghost nodes. The simulation domain consists of the black-filled grid points. This domain is extended with extra rows and columns of ghost nodes, indicated by empty circles. The dashed line indicates the physical boundary of the system, which lies between the outer grid points (solid black rectangle) and the ghost nodes. [3]

The program starts by reading the input:

- the number of phases, the number of components, the grid spacing, the time step, the number of processors used, the number of time steps, the number of outputs and whether

a previous simulation is loaded to start from or which type of initial microstructure should be used (pre-defined types),
- the .txt files containing the thermodynamic data,
- the constants in the phase field equations: $m_{0,ij}$, κ_{ij}, L_{ij}, M_{ki} and anisotropy data,
- the initial and equilibrium compositions of the different phases.

Afterwards, the system is initialized:

- the initial microstructure is set for the phase fields
  (the solid phases are initialized by the insertion of a number of seeds of the solid phase, to provide nucleation positions),
- the global concentration of one component is set according to (13.10) to a weighted sum of the product of the phase field variables and the initial concentration of that component in that phase,
- the ghost nodes at the boundary of the complete system are given values according to the type of boundary (adiabatic, a certain p_{O2}),
- the phase concentrations are set to the equilibrium values.

Then, a loop is started for the requested number of time steps and in every time step the following steps occur:

- Start up the communication between the different processors by filling the information packages to be sent with the values in the outer grid points from the previous time step and preparing the packages to be received from the correct neighbouring processor.
- Solving the bulk
  - Computation of the phase fractions ϕ_i from its definition and the computation of the phase compositions x_k^p from the mass balance equation (13.10) and the quasi-equilibrium condition (13.9).

    The derivative of the second-order Taylor expansion (13.29) to the phase composition is taken and then the quasi-equilibrium condition is used to obtain a part of the system of linear equations. The coefficients in the left hand side of the equations are the ***A***-values for all combinations of 2 components in all phases. On the right hand side, a combination of ***A*** and ***B*** values and the $\widehat{x_k^p}$ values are used. Where ***A*** and ***B*** are calculated at the local phase composition using a bilinear interpolation[20] and the $\widehat{x_k^p}$ values are actually the x_k^p values from the previous time step. This is in accordance with the condition for Taylor expansions that the point around which the expansion is taken, lies close enough to the point in which the actual value will be calculated. The other part of equations in the system of linear equations has on the left hand side the phase fractions ϕ_i and on the right hand side the global mole fractions (13.10) of the *C-1* independent components. The system of equations is solved for the new phase compositions x_k^p. The latter happens with the use of LU-decomposition with partial pivoting of the matrix representing the

[20] The bilinear approximation is an extension of the linear interpolation and is used to interpolate functions of two variables on a regular 2D grid. The key idea is to first interpolate linearly in one direction and then again in the other direction. Thus each step is linear in the sampled values and position, but the bilinear interpolation as a whole is not linear, but rather quadratic in sample location. [24]

coefficients in the system of equations and the vector representing the right hand side of the equations (Crout's method). The LU-decomposition is based on a Fortran 90 numerical recipe [25].

- Computation of the local $\kappa(r)$, $m(r)$ and $L(r)$ values according to equations (13.4) First the interface angle is determined based on equation (13.17) and the gradients herein are calculated with a higher accuracy nine-point stencil to treat anisotropic interfaces:

$$\begin{aligned}\nabla_x \eta_{r_{i,j}} &= \frac{1}{8}\left(\frac{\eta_{r_{i+1,j-1}} - \eta_{r_{i-1,j-1}}}{2\Delta x}\right) + \frac{6}{8}\left(\frac{\eta_{r_{i+1,j}} - \eta_{r_{i-1,j}}}{2\Delta x}\right) \\ &\quad + \frac{1}{8}\left(\frac{\eta_{r_{i+1,j+1}} - \eta_{r_{i-1,j+1}}}{2\Delta x}\right) \\ \nabla_y \eta_{r_{i,j}} &= \frac{1}{8}\left(\frac{\eta_{r_{i-1,j+1}} - \eta_{r_{i-1,j-1}}}{2\Delta y}\right) + \frac{6}{8}\left(\frac{\eta_{r_{i,j+1}} - \eta_{r_{i,j-1}}}{2\Delta y}\right) \\ &\quad + \frac{1}{8}\left(\frac{\eta_{r_{i+1,j+1}} - \eta_{r_{i+1,j-1}}}{2\Delta y}\right)\end{aligned} \quad \textbf{(13.34)}$$

  This nine-point stencil is required to reduce the effect of the grid anisotropy and provide a stable solution for the orientation-dependence. The factors were chosen to approximate a numerical isotropic discrete Laplacian. Then the normal dendritic anisotropy (13.18) and the facetted anisotropy (13.22) are calculated for κ_{ij} and m_{ij} with the obtained interface angle and weighed with a function χ to enable the user to indicate what the characteristics (dendritic or faceted) are of the different interfaces between the different possible combinations of phases. Finally, the global κ and m are calculated according to (13.4). Similarly, the orientation dependence can be implemented for the phase field mobility with a weighed sum between the isotropic mobility and facetted growth (interface controlled growth) according to (13.24).
- Computation of f_i and $\tilde{\mu}_k^i$ at the local phase concentrations using a bilinear interpolation between the values of ***C*** and ***B***, respectively, which were tabulated and read as input from .txt files. Thus, the second order approximation of the Gibbs free energy is not used for this, it is only used to solve the system of equations (13.9) and (13.10).
- Computation of the phase field and concentration gradients:
  - Diffusion equation

    The temporal differential is discretized with a forward finite difference, i.e. the mole fraction at time step *n+1* is calculated with the values of the previous time step *n*. The gradient can also be split up into its two components, yielding:

$$(x_k)_{i,j}^{n+1} = (x_k)_{i,j}^{n} + \Delta t\left(\nabla \cdot \left[\sum_{i=1}^{p} \phi_i \left(\sum_{l=1}^{C-1} M_{kl}^i \left(\nabla_x \tilde{\mu}_l^i + \nabla_y \tilde{\mu}_l^i\right)\right)\right]\right)^n \quad \textbf{(13.35)}$$

    These gradients are discretized as:

$$(x_k)_{i,j}^{n+1} = (x_k)_{i,j}^{n} + \Delta t\left(\frac{\xi_{x,i,j}^n - \xi_{x,i-1,j}^n}{\Delta x} + \frac{\xi_{y,i,j}^n - \xi_{y,i,j-1}^n}{\Delta y}\right) \quad \textbf{(13.36)}$$

    With

$$\xi^n_{x,i,j} = \left[\sum_{i=1}^{p} \frac{(\phi_i)^n_{i+1,j} + (\phi_i)^n_{i,j}}{2} \left(\sum_{l=1}^{C-1} M^i_{kl} \frac{\left(\tilde{\mu}^i_l\right)^n_{i+1,j} - \left(\tilde{\mu}^i_l\right)^n_{i,j}}{\Delta x} \right)\right]$$
$$\xi^n_{y,i,j} = \left[\sum_{i=1}^{p} \frac{(\phi_i)^n_{i,j+1} + (\phi_i)^n_{i,j}}{2} \left(\sum_{l=1}^{C-1} M^i_{kl} \frac{\left(\tilde{\mu}^i_l\right)^n_{i,j+1} - \left(\tilde{\mu}^i_l\right)^n_{i,j}}{\Delta y} \right)\right] \quad \textbf{(13.37)}$$

- Phase field equation

The gradients in the phase field equations were computed in a more elaborate way to take the anisotropy correctly into account. The temporal differential is discretized with a forward finite difference, i.e. the phase field at time step *n+1* is calculated with the values of the previous time step *n*, yielding:

$$(\eta_r)^{n+1}_{i,j} = (\eta_r)^n_{i,j} + \Delta t \left[-L \left(m \frac{\partial f_0}{\partial \eta_r} + \frac{\partial f_b}{\partial \eta_r} - \frac{\xi^n_{x,i,j} - \xi^n_{x,i-1,j}}{\Delta x} - \frac{\xi^n_{y,i,j} - \xi^n_{y,i,j-1}}{\Delta y} \right) \right]^n \quad \textbf{(13.38)}$$

The first two terms in the large brackets are determined by equations (13.13) and (13.14) and are evaluated at time step *n*. The last terms in the large brackets are the gradient parts of the phase field equation and are numerically solved according to equation (13.25), together with equations (13.13)-(13.15). Moreover, ξ in equation (13.38) is defined as

$$\begin{aligned}
&\xi^n_{x,i,j} \\
&= \left[\left(\frac{f_{0\,i,j} + f_{0\,i+1,j}}{2} \right) \left(\sum_{s \neq r}^{p} \Omega_{rs} \bar{m}_{rs} \frac{d\lambda_{rs}}{d\theta_{rs}} \left(\frac{-(\nabla_y \eta_r - \nabla_y \eta_s)}{(\nabla_x \eta_r - \nabla_x \eta_s)^2 + \left(\nabla_y \eta_r - \nabla_y \eta_s\right)^2} \right) \right) \right. \\
&+ \frac{1}{2} \left(\sum_{s \neq r}^{p} \Omega_{rs} \bar{\kappa}_{rs} \frac{d\lambda_{rs}}{d\theta_{rs}} \left(\frac{-(\nabla_y \eta_r - \nabla_y \eta_s)}{(\nabla_x \eta_r - \nabla_x \eta_s)^2 + \left(\nabla_y \eta_r - \nabla_y \eta_s\right)^2} \right) \right) \left(\sum_{t=1}^{p} (\nabla_x \eta_t)^2 \right. \\
&\left. \left. + \left(\nabla_y \eta_t\right)^2 \right) + \left(\frac{\kappa_{i,j} + \kappa_{i+1,j}}{2} \right) \nabla_x \eta_r \right]
\end{aligned} \quad \textbf{(13.39)}$$

With $\nabla_x \eta_r = \frac{1}{8}\left(\frac{(\eta_r)^n_{i+1,j+1} - (\eta_r)^n_{i,j+1}}{\Delta x}\right) + \frac{6}{8}\left(\frac{(\eta_r)^n_{i+1,j} - (\eta_r)^n_{i,j}}{\Delta x}\right) + \frac{1}{8}\left(\frac{(\eta_r)^n_{i+1,j-1} - (\eta_r)^n_{i,j-1}}{\Delta x}\right)$

and $\nabla_y \eta_r = \left(\frac{(\eta_r)^n_{i,j+1} + (\eta_r)^n_{i+1,j+1} - (\eta_r)^n_{i,j-1} - (\eta_r)^n_{i+1,j-1}}{4\Delta y}\right)$

and θ_{rs} determined with these gradients.

An analogous expression for $\xi^n_{y,i,j}$ was used (the only difference is that the numerators in the first two terms contain $+(\nabla_x \eta_r - \nabla_x \eta_s)$ instead of $-(\nabla_y \eta_r - \nabla_y \eta_s)$.

- Step evolution in the phase field equations according to equation (13.36).
- Step evolution in the diffusion equations according to equation (13.38).
- The phase field equations are only solved in proximity of interfaces to increase the numerical efficiency, while the diffusion equations are solved everywhere.

- Updating the values of the conserved and non-conserved variables on the ghost nodes according to the boundary conditions. This is only done for the sides of the subsystem, which have no neighbouring subsystems.
    - No-flux boundary conditions: demonstrated here for all boundaries on one processor. In reality, several processors are present and not all boundaries of the subsystem will be subject to such a boundary condition.

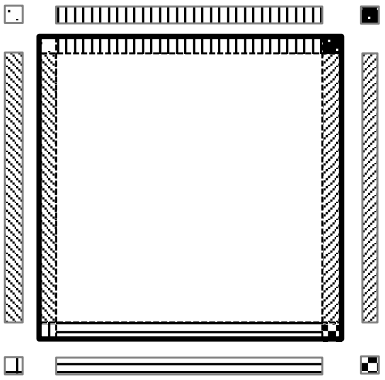

The values in ghost nodes are put equal to the values in the outer rows and columns, i.e. the border.

- Corresponding to an atmosphere with a certain p_{O2}:
  this was implemented by Heulens [2] for an FeO_x-SiO_2 melt, where the FeO/Fe_2O_3 ratio can be linked to the local oxygen potential in the melt. If the melt is in contact with an oxygen-containing atmosphere, the melt will be oxidized or reduced, depending on whether the oxygen fugacity in the atmosphere is higher or lower than its activity in the melt. At this boundary, representing the contact with an oxygen-containing atmosphere, there is only an exchange possible for oxygen, but not for the other elements. For this, the atmosphere is assumed to be an ideal gas (thus the activity of a gaseous component equals its partial pressure and its fugacity) and diffusion is assumed to be much slower than the redox reaction, which are present in the melt when it is not in thermodynamic equilibrium with the oxygen-containing atmosphere. Moreover, the melt is assumed to be in local equilibrium with the gaseous atmosphere at the interface with the atmosphere. From these assumptions, the FeO/Fe_2O_3 ratio can be used as a direct measure for the oxygen activity within the atmosphere. Note, however, that this is not generally the case. Thus, the FeO/Fe_2O_3 ratio can be varied, but the amount of Fe should remain constant.
  Assuming the physical system boundary lies between the ghost nodes ($i = 0$) and the border ($i = 1$) and linearly interpolating the mole fractions of FeO and Fe_2O_3 between the corresponding two indices, together with the conservation of mass for Fe, yields the following set of equations at the boundary:

$$\left(\frac{x_{FeO}^{i=1} - x_{FeO}^{i=0}}{\Delta z}\right)\left(\frac{\Delta z}{2}\right) + x_{FeO}^{i=0} = \omega\left[\left(\frac{x_{Fe2O3}^{i=1} - x_{Fe2O3}^{i=0}}{\Delta z}\right)\left(\frac{\Delta z}{2}\right) + x_{Fe2O3}^{i=0}\right] \qquad \textbf{(13.40)}$$

$$x_{FeO}^{i=0} + 2x_{Fe2O3}^{i=0} = x_{FeO}^{i=1} + 2x_{Fe2O3}^{i=1}$$

With ω the FeO/Fe_2O_3 ratio to be determined with the help of Factsage. This set of equations is solved for $x_{FeO}^{i=0}$ and $x_{Fe2O3}^{i=0}$ to define the values of the global compositions in the ghost nodes for this boundary.
For the non-conserved phase field variables, the no-flux boundary is still used.

- Before the border can be solved, all packages should be received from the correct neighbour or the system boundaries should be updated, thus we need to await receipt of all information from other processors before continuing. The values of the ghost nodes of the processor under consideration are then inserted from the values in the boundaries of the neighbouring processors.
- Solve the border:
  - computation of the phase fractions ϕ_i and the computation of the phase compositions x_k^p,
  - computation of the local $\kappa(r)$, $m(r)$ and $L(r)$ values,
  - calculate the diffusion and phase field gradients ,
  - step evolution in the diffusion and phase field equations.
- Send the information from the border to other processors that require this as ghost nodes before a new time step can be taken in the simulation loop.

13.2. Limitations of previous implementation

Heulens implemented this model during his PhD [3]. During the investigation of the code, a few points were encountered where the implementation is limited to three components in practice:

- Solving the set of equations (the mass balance equation (13.10) and the quasi-equilibrium condition (13.9)) to determine the phase compositions x_k^p was hard-coded.
- The Gibbs free energy, the chemical diffusion potential and the derivative of the chemical diffusion potential to the phase compositions are extracted from the thermodynamic database and saved to .txt files before the actual simulation starts for the complete compositional domain. This domain can be represented by a compositional triangle, i.e. two dimensions for two independent composition variables as the sum of the mole fractions always equals one. This extraction was implemented in a system-specific way and limits the number of components to 3, because more than three components would require more than two dimensions to describe the compositional domain. Moreover, the size of the variable space scales with the power of the number of components. [16] The compositional domain can still be scanned completely in a similar way, but saving the thermodynamic data for each composition to .txt files will need a different implementation.
- The thermodynamic data extracted from the database are then read as input during an actual simulation. To obtain the correct values of the thermodynamic data corresponding to a certain composition, which does not necessarily lie on the investigated composition grid during the coupling with the thermodynamic database, the thermodynamic values lying on the grid are interpolated bi-linearly. The latter also limits the implemented code to two independent components.
- The stoichiometric phases are described as paraboloid functions of two compositional variables. When more components are present, the expression should be extended.

13.3. Adaptations of previous implementation code

As the implemented code of Heulens was limited to three component systems and this study requires systems with at least four components, some changes were made to the implementation of Heulens [3] to make it generally applicable to multi-component multi-phase systems. In the following paragraphs, the various steps taken to generalize the code are described into more detail. For every change made, a simulation in the FeO-Fe_2O_3-SiO_2 system was repeated with the new implementation but the original input-parameters, to ensure that the same results were obtained and to investigate the influence of the changes made on the computational time.

13.3.1. Solve mass balance and quasi-equilibrium in a more general way

The first step in the solution is the computation of the phase compositions x_k^p from the mass balance equation (13.10) and the quasi-equilibrium condition (13.9). In the as-received code, this part was hard-coded for three components. This part was generalized to *N* components by a clear investigation of how the set of equations was constructed. The set of equations was translated into the following matrix representation:

$$\begin{bmatrix} \left[\frac{\partial\tilde{\mu}_1}{\partial x_1}\right] & \left[\frac{\partial\tilde{\mu}_1}{\partial x_2}\right] & \dots & \left[\frac{\partial\tilde{\mu}_1}{\partial x_{N-1}}\right] \\ \left[\frac{\partial\tilde{\mu}_2}{\partial x_1}\right] & \left[\frac{\partial\tilde{\mu}_2}{\partial x_2}\right] & \dots & \left[\frac{\partial\tilde{\mu}_2}{\partial x_{N-1}}\right] \\ \vdots & \vdots & \ddots & \vdots \\ \left[\frac{\partial\tilde{\mu}_{N-1}}{\partial x_1}\right] & \left[\frac{\partial\tilde{\mu}_{N-1}}{\partial x_2}\right] & \dots & \left[\frac{\partial\tilde{\mu}_{N-1}}{\partial x_{N-1}}\right] \\ \left[\vec{\phi}\right]_1 & \left[\vec{\phi}\right]_2 & \dots & \left[\vec{\phi}\right]_{N-1} \end{bmatrix} \begin{bmatrix} \overrightarrow{x_1} \\ \overrightarrow{x_2} \\ \vdots \\ \overrightarrow{x_{N-1}} \end{bmatrix} = \begin{bmatrix} \vec{R} \\ \vec{x} \end{bmatrix} \quad \textbf{(13.41)}$$

Where the following notations for the submatrices and vectors are used:

$$\left[\frac{\partial\tilde{\mu}_k}{\partial x_l}\right] = \begin{bmatrix} \frac{\partial\tilde{\mu}_k^1}{\partial x_l^1} & -\frac{\partial\tilde{\mu}_k^2}{\partial x_l^2} & 0 & \dots & 0 & 0 & 0 \\ 0 & \frac{\partial\tilde{\mu}_k^2}{\partial x_l^2} & -\frac{\partial\tilde{\mu}_k^3}{\partial x_l^3} & \dots & 0 & 0 & 0 \\ \vdots & \vdots & \vdots & \ddots & \vdots & \vdots & \vdots \\ 0 & 0 & 0 & \dots & \frac{\partial\tilde{\mu}_k^{p-2}}{\partial x_l^{p-2}} & -\frac{\partial\tilde{\mu}_k^{p-1}}{\partial x_l^{p-1}} & 0 \\ 0 & 0 & 0 & \dots & 0 & \frac{\partial\tilde{\mu}_k^{p-1}}{\partial x_l^{p-1}} & -\frac{\partial\tilde{\mu}_k^{p}}{\partial x_l^{p}} \end{bmatrix} \quad \textbf{(13.42)}$$

With *p-1* rows and *p* columns. Also, $\vec{\phi}$ collects all phase fractions in one row:

$$\left[\vec{\phi}\right]_i = \begin{bmatrix} 0 & 0 & \dots & 0 \\ \vdots & \vdots & \ddots & \vdots \\ \phi_1 & \phi_2 & \dots & \phi_p \\ \vdots & \vdots & \ddots & \vdots \\ 0 & 0 & \dots & 0 \end{bmatrix} \quad \textbf{(13.43)}$$

With *N-1* rows and *p* columns and only non-zero elements on the *i*th row of this submatrix. $\overrightarrow{x_j}$ has *p* rows and represents the vector of all phase compositions of one component *j*:

$$\vec{x_j} = \begin{bmatrix} {x_j}^1 \\ {x_j}^2 \\ \vdots \\ {x_j}^p \end{bmatrix} \tag{13.44}$$

$\vec{R}$ has *(p-1)(N-1)* rows and represents the right hand side of the Taylor expansion for the quasi-equilibrium condition. The element on the *(p-1)(k-1)+ip* th row equals:

$$\sum_{l=1}^{N-1} \left(\frac{\partial \tilde{\mu}_k^{ip}}{\partial x_l^{ip}} \widehat{x_l^{ip}} - \frac{\partial \tilde{\mu}_k^{ip+1}}{\partial x_l^{ip+1}} \widehat{x_l^{ip+1}} \right) - \tilde{\mu}_k^{ip} + \tilde{\mu}_k^{ip+1} \tag{13.45}$$

Also $\vec{x}$ has *N-1* rows and represents the global compositions of all components, which satisfy the mass balance

$$\vec{x} = \begin{bmatrix} x_1 \\ x_2 \\ \vdots \\ x_{N-1} \end{bmatrix} \tag{13.46}$$

The coefficients on the left-hand side of (13.41) are the ***A***-values for all combinations of two components in all phases. On the right-hand side, a combination of ***A*** and ***B*** values and the $\widehat{x_k^p}$ values, which are the x_k^p values from the previous time step, are used. This is in accordance with the condition for Taylor expansions that the point around which the expansion is taken, lies close enough to the point in which the actual value will be calculated. The other part of equations in the system of linear equations has on the left-hand side the phase fractions ϕ_i and on the right-hand side the global mole fractions (13.10) of the *N-1* independent components. The system of equations is solved for the new phase compositions x_k^p. The latter happens with the use of a LU-decomposition with partial pivoting of the matrix representing the coefficients in the system of equations and the vector representing the right-hand side of the equations (Crout's method). This was implemented in the following subroutine

```
subroutine convert_composition(ix,iy) ! ix, iy is the position within the system
   integer :: ix, iy, ip, k, l
   real(8) :: r
   real(8), dimension(1:np*(nc-1)) :: sol, RT
   real(8), dimension(1:np*(nc-1),1:np*(nc-1)) :: coeff
   integer, dimension(1:np*(nc-1)) :: IPIV
   coeff = 0.d0
   RT = 0.d0
   ! Equilib for all components
      do k=1,nc-1
         do ip=1,np-1
            do l=1,nc-1
               coeff((np-1)*(k-1)+ip,(l-1)*np+ip) = dmudx(k,l,ip,ix,iy)
               coeff((np-1)*(k-1)+ip,(l-1)*np+ip+1) = -dmudx(k,l,ip+1,ix,iy)
               RT((np-1)*(k-1)+ip) = RT((np-1)*(k-1)+ip) + dmudx(k,l,ip,ix,iy)*
                      xp(l,ip,ix,iy) - dmudx(k,l,ip+1,ix,iy)*xp(l,ip+1,ix,iy)
            end do
            RT((np-1)*(k-1)+ip) = RT((np-1)*(k-1)+ip)- mu(k,ip,ix,iy)+
mu(k,ip+1,ix,iy)
         end do
      end do
      ! Mass balance for all components
      do k = (nc-1)*(np-1)+1,(nc-1)*np
         do ip=1,np
            coeff(k,np*(k-(nc-1)*(np-1)-1)+ip) = phi(ip,ix,iy)
```

```
      end do
      RT(k) = x(k-(nc-1)*(np-1),ix,iy,old)
    end do
    sol = RT(:)
    ! solve set of equations
    call ludcmp(coeff,np*(nc-1),np*(nc-1),IPIV,r)
    call lubksb(coeff,np*(nc-1),np*(nc-1),IPIV,sol)
    ! put solutions in correct variables
    do k=1,nc-1
      xp(k,1:np,ix,iy) = sol((k-1)*np+1:k*np)
    end do
  end subroutine convert_composition
```

13.3.2. Multilinear interpolation

Any $\frac{\partial \tilde{\mu}_k^i}{\partial x_l^i}$, $\tilde{\mu}_k^i$ and $\frac{G_m^i}{V_m}$ values in the program were calculated previously by a bilinear interpolation between the values that were extracted from the thermodynamic database. The reason for this type of interpolation and how to extend it to an arbitrary number of components is linked to the shape of the composition domain as a function of the number of components. This is illustrated with the phase diagrams in Figure 13.4.

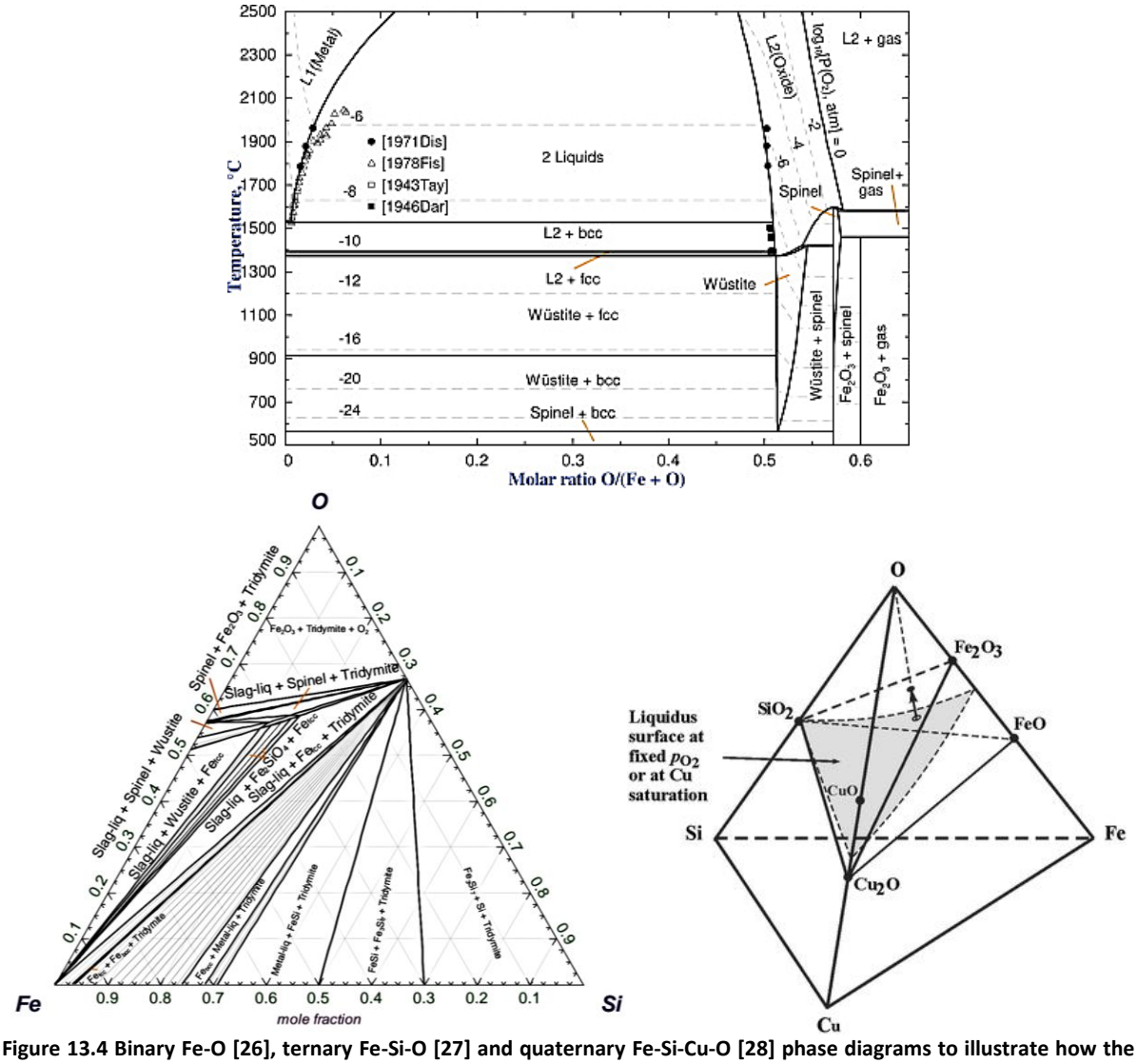

Figure 13.4 Binary Fe-O [26], ternary Fe-Si-O [27] and quaternary Fe-Si-Cu-O [28] phase diagrams to illustrate how the number of components influences the compositional domain

The binary (Fe-O) system has only one independent mole fraction of a certain component. The mole fraction of the other component is determined by this value because they need to sum up to one. Thus, the composition can be described by a single line, i.e. the x-axis in the binary phase diagram in Figure 13.4. The ternary system has two independent mole fractions to describe the composition of the system. Again, all mole fractions sum up to one and here the compositional domain can be described by a triangle. For a quaternary system, three independent mole fractions can be chosen to describe a certain composition and the compositional domain can be represented by a tetrahedron.

These compositional domains should be 'scanned' on a certain grid, with grid points $5 \cdot 10^{-3}$ apart from each other, to obtain the thermodynamic data in the coupling to the thermodynamic database. To obtain the correct values during the simulations, the values on the grid points are interpolated in a way depending on the dimensions of the grid. To interpolate in the binary case, a normal linear interpolation is required, as illustrated in the left part of Figure 13.5. The blue dots represent the grid points and the red dot is the point where the interpolated value is required.

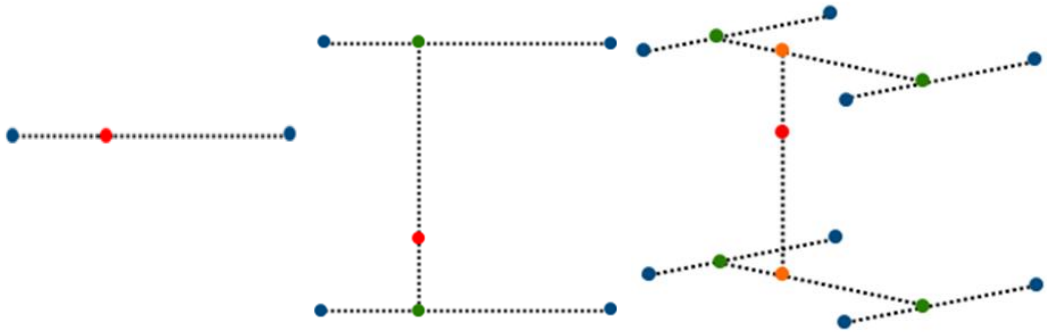

Figure 13.5 Illustration of linear, bilinear and trilinear interpolation. The blue points represent the grid dots; the red dot represents the point where the value should be calculated by the interpolation and the other colours are intermediate interpolation points.

In a ternary system (middle part of Figure 13.5), the grid becomes two-dimensional and a bilinear interpolation is required to obtain a value in the red dot. Thus, first the grid values are interpolated linearly in one direction. This gives the green dots, which in turn are interpolated linearly in the other direction perpendicular on the first direction to obtain the value in the red dot. Analogously, a quaternary system (right part of Figure 13.5) is described by a three-dimensional grid and thus the grid values (blue dots) are first linearly interpolated in one direction, these values (green dots) are then again interpolated in another direction perpendicular on the first direction and finally, these values (orange dots) are interpolated linearly in a direction perpendicular to the other two directions to yield the final requested interpolation function (represented by the red dot).

As can be concluded from the previous paragraph, a multilinear interpolation is required to be able to model systems with an arbitrary number of components. Moreover, at the moment, the bilinear interpolation is hard-coded. Therefore, the implement a recursive linear interpolation method was opted to make the model applicable to an arbitrary number of components. For this, the following function was introduced:

```
      function linear_interpolation (xg,x1,deltax,y1,y2)
            real(8) :: linear_interpolation,xg,x1,deltax,y1,y2
      ! Returns linearly interpolated y-value at x between 2 points:
(x1,y1) and (x1+deltax,y2)
            linear_interpolation = y1 + (y2-y1)*(xg-x1)/deltax
```

```
end function linear_interpolation
```

This linear interpolation function should be applied $2^{N-1}-1$ times starting from 2^{N-1} grid points (blue dots in Figure 13.5, surrounding the red point where the interpolated value is requested). These surrounding points are determined according to:

```
do k = 1,nc-1
      indx(k)=floor(xp(k,ip,ix,iy)/thermo_dx+0.5d0)+1
enddo
```

The required values in these grid point are stored in the first column of a 'help' variable (a matrix with 2^{N-1} rows and N columns) in a particular way to simplify the application of the recursive linear interpolation. The surrounding point values are stored in the first column in such a way that the first index will change every other row, the second index every two rows, the third every four rows, etc. This is illustrated for a system with four components, i.e. three independent composition variables, in equation (13.47).

$$help|_{first\ column} = \begin{bmatrix} f(indx(1), & indx(2), & indx(3)) \\ f(indx(1)+1, & indx(2), & indx(3)) \\ f(indx(1), & indx(2)+1, & indx(3)) \\ f(indx(1)+1, & indx(2)+1, & indx(3)) \\ f(indx(1), & indx(2), & indx(3)+1) \\ f(indx(1)+1, & indx(2), & indx(3)+1) \\ f(indx(1), & indx(2)+1, & indx(3)+1) \\ f(indx(1)+1, & indx(2)+1, & indx(3)+1) \end{bmatrix} \quad (13.47)$$

The index of this function can be divided into:

$$index\ of\ help|_{first\ column} = \begin{bmatrix} indx(1), indx(2), indx(3) \\ indx(1), indx(2), indx(3) \\ indx(1), indx(2), indx(3) \\ indx(1), indx(2), indx(3) \\ indx(1), indx(2), indx(3) \\ indx(1), indx(2), indx(3) \\ indx(1), indx(2), indx(3) \\ indx(1), indx(2), indx(3) \end{bmatrix} + \begin{bmatrix} 0,0,0 \\ 1,0,0 \\ 0,1,0 \\ 1,1,0 \\ 0,0,1 \\ 1,0,1 \\ 0,1,1 \\ 1,1,1 \end{bmatrix} = newindex \quad (13.48)$$

Where the latter part is the inverse binary representation of the row number of that element. As this is the inverse, this method will also be useful for any number of components, i.e. an extension to more indices than the three in the example above, as extra indices will appear naturally in such a case. The inverse binary representation of an integer is calculated as follows:

```
function integer2binaryandinverse(il) result(bin)
! Returns binary value of integer il but going from left to right (1
2 4 8 are the values of the columns from left to right)
      integer,intent(in) :: il
      integer, dimension(32) :: bin
      integer kl,jl
      bin=0
      jl=il
      do kl=1,size(bin)
            bin(kl)=mod(jl,2)
            jl=jl/2
      enddo
end function
```

The remaining columns of the help variable are then obtained by linear interpolation according to the following scheme:

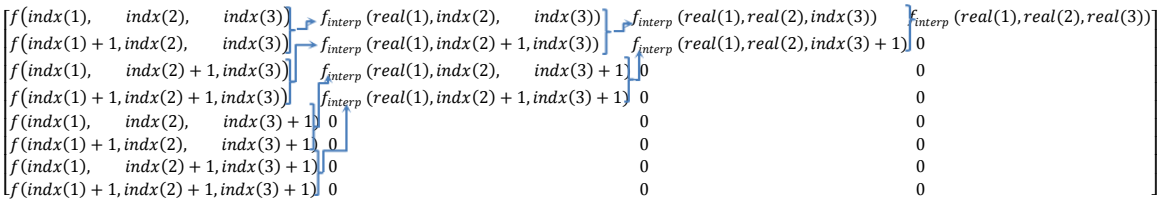

Moreover, a more practical limitation became apparent during the implementation of this scheme: the number of indices in Fortran is limited to 7 and the use of an allocatable array (with a size that is not known at the beginning of the compilation of the code) as an index of another array is not possible. If this were possible, the *newindex* would be used as an index in the arrays containing the thermodynamic data obtained by scanning the grid of the composition domain. However, a possible solution is proposed for this: hashing[21] all the indices into a single index that describes the composition of interest. Here, the following function was chosen:

$$z = \sum_{k=1}^{N-1} indx(k) \cdot (thermo\_n)^{k-1} \tag{13.49}$$

Where *thermo_n* is the number of subdivisions in the grid that is used to scan the composition domain during coupling to the thermodynamic database. The maximum value of z is $(thermo\_n)^N/(thermo\_n-1)$, this value determines the size of the arrays containing the thermodynamic data. Any number could be chosen instead of this *thermo_n* as long as it ensures that the hashing function couples one combination of compositions to a single number z and vice versa, that this z represents a single composition. To obtain the composition from z the following procedure should be followed:

$$\begin{gathered} indx(1) = mod(z, thermo\_n) \\ indx(2) = mod\left(\frac{z - indx(1)}{thermo\_n}, thermo\_n\right) \\ indx(3) = mod\left(\frac{z - indx(1) - indx(2) \cdot thermo\_n}{thermo\_n^2}, thermo\_n\right) \\ \text{Etc.} \end{gathered} \tag{13.50}$$

With this hashing function, the indices of blue dots in Figure 13.5 or the grid points surrounding the point where the interpolated value is requested are no longer used as separate indices to the arrays containing the thermodynamic data, but are collected in a single index array, which is then converted to a single number. Thus, the final implementation of the recursive linear interpolation or multilinear interpolation is:

```
! first load the points in the help variable that are situated around the
requested point
      do punt = 1, 2**(nc-1)
            bin=integer2binaryandinverse(punt-1)
            z=0
            do k = 1 , nc-1
                  newindex (k) = indx(k)+bin(k)
```

[21]A hash function is any function that can be used to map data of arbitrary size to data of fixed size.

```
                  z=z+newindex(k)*thermo_n**(k-1)
            enddo
            hulp(punt,1)=GIBBS(thermo_p(ip),z)
      enddo
      ! now use recursive linear interpolation
      do kol = 2,nc
            do rij = 1 , 2**(nc-kol)
                  hulp (rij, kol) = linear_interpolation(xp(kol-
1,ip,ix,iy),(thermo_dx)*(indx(kol-1)-1), (thermo_dx), hulp(rij*2-1,kol-1),
hulp(rij*2,kol-1))
            enddo
      enddo
      f = hulp (1, nc)
```

References

[1] J. Heulens, B. Blanpain, N. Moelans, A phase field model for isothermal crystallization of oxide melts, Acta Mater. 59 (2011) 2156–2165. doi:10.1016/j.actamat.2010.12.016.

[2] J. Heulens, B. Blanpain, N. Moelans, Phase field modeling of the crystallization of FeOx–SiO2 melts in contact with an oxygen-containing atmosphere, Chem. Geol. 290 (2011) 156–162. doi:10.1016/j.chemgeo.2011.09.005.

[3] J. Heulens, Isothermal Crystallization of Metallurgical Slags: Phase Field Simulations Combined with In Situ Experiments (Isotherme kristallisatie van metallurgische slakken: faseveldsimulaties in combinatie met in situ experimenten), PhD thesis, KU Leuven, 2011. https://lirias.kuleuven.be/handle/123456789/318339.

[4] N. Moelans, B. Blanpain, P. Wollants, Quantitative analysis of grain boundary properties in a generalized phase field model for grain growth in anisotropic systems, Phys. Rev. B. 78 (2008) 024113. doi:10.1103/PhysRevB.78.024113.

[5] N. Moelans, B. Blanpain, P. Wollants, Quantitative Phase-Field Approach for Simulating Grain Growth in Anisotropic Systems with Arbitrary Inclination and Misorientation Dependence, Phys. Rev. Lett. 101 (2008) 025502. doi:10.1103/PhysRevLett.101.025502.

[6] J. Eiken, B. Böttger, I. Steinbach, Multiphase-field approach for multicomponent alloys with extrapolation scheme for numerical application, Phys. Rev. E. 73 (2006) 066122. doi:10.1103/PhysRevE.73.066122.

[7] N. Moelans, Phase-Field Simulations of Grain Growth in Materials Containing Second-Phase Particles (Faseveldsimulaties van korrelgroei in materialen met tweede-fase-deeltjes), PhD, KU Leuven, 2006. https://lirias.kuleuven.be/handle/1979/309 (accessed October 9, 2013).

[8] H. Ravash, 3D phase-field simulations of sintering and coarsening in polycrystalline multi-phase materials, KU Leuven, 2014.

[9] S.G. Kim, W.T. Kim, T. Suzuki, Phase-field model for binary alloys, Phys. Rev. E. 60 (1999) 7186–7197. doi:10.1103/PhysRevE.60.7186.

[10] L.-Q. Chen, Phase-Field Models for Microstructure Evolution, Annu. Rev. Mater. Res. 32 (2002) 113–140. doi:10.1146/annurev.matsci.32.112001.132041.

[11] W.C. Johnson, C.L. White, P.E. Marth, P.K. Ruf, S.M. Tuominen, K.D. Wade, K.C. Russell, H.I. Aaronson, Influence of crystallography on aspects of solid-solid nucleation theory, Metall. Trans. A. 6 (1975) 911–919. doi:10.1007/BF02672315.

[12] J. Heulens, N. Moelans, On the rotation invariance of multi-order parameter models for grain growth, Scr. Mater. 62 (2010) 827–830. doi:10.1016/j.scriptamat.2010.02.009.
[13] N. Moelans, B. Blanpain, P. Wollants, An introduction to phase-field modeling of microstructure evolution, Calphad. 32 (2008) 268–294. doi:10.1016/j.calphad.2007.11.003.
[14] S.Y. Hu, J. Murray, H. Weiland, Z.K. Liu, L.Q. Chen, Thermodynamic description and growth kinetics of stoichiometric precipitates in the phase-field approach, Calphad. 31 (2007) 303–312. doi:10.1016/j.calphad.2006.08.005.
[15] McFadden, Wheeler, Braun, Coriell, Sekerka, Phase-field models for anisotropic interfaces, Phys. Rev. E Stat. Phys. Plasmas Fluids Relat. Interdiscip. Top. 48 (1993) 2016–2024.
[16] H. Larsson, L. Höglund, A scheme for more efficient usage of CALPHAD data in simulations, Calphad. 50 (2015) 1–5. doi:10.1016/j.calphad.2015.04.007.
[17] S. Petersen, K. Hack, The thermochemistry library ChemApp and its applications, Int. J. Mater. Res. 98 (2007) 935–945. doi:10.3139/146.101551.
[18] B. Böttger, J. Eiken, M. Apel, Multi-ternary extrapolation scheme for efficient coupling of thermodynamic data to a multi-phase-field model, Comput. Mater. Sci. 108, Part B (2015) 283–292. doi:10.1016/j.commatsci.2015.03.003.
[19] I. Steinbach, L. Zhang, M. Plapp, Phase-field model with finite interface dissipation, Acta Mater. 60 (2012) 2689–2701. doi:10.1016/j.actamat.2012.01.035.
[20] J. Tiaden, B. Nestler, H.J. Diepers, I. Steinbach, The multiphase-field model with an integrated concept for modelling solute diffusion, Phys. D. 115 (1998) 73–86. doi:10.1016/S0167-2789(97)00226-1.
[21] L. Zhang, I. Steinbach, Phase-field model with finite interface dissipation: Extension to multi-component multi-phase alloys, Acta Mater. 60 (2012) 2702–2710. doi:10.1016/j.actamat.2012.02.032.
[22] T. Shimokawabe, T. Aoki, T. Takaki, A. Yamanaka, A. Nukada, T. Endo, N. Maruyama, S. Matsuoka, Peta-scale phase-field simulation for dendritic solidification on the TSUBAME 2.0 supercomputer, in: High Perform. Comput. Netw. Storage Anal. SC 2011 Int. Conf. For, 2011: pp. 1–11.
[23] A. Yamanaka, T. Aoki, S. Ogawa, T. Takaki, GPU-accelerated phase-field simulation of dendritic solidification in a binary alloy, J. Cryst. Growth. 318 (2011) 40–45. doi:10.1016/j.jcrysgro.2010.10.096.
[24] Bilinear interpolation, Wikipedia Free Encycl. (2015). https://en.wikipedia.org/w/index.php?title=Bilinear_interpolation&oldid=687816846 (accessed November 19, 2015).
[25] Numerical Recipes in Fortran 90: Volume 2, Volume 2 of Fortran Numerical Recipes: The Art of Parallel Scientific Computing, 2 edition, Cambridge University Press, Cambridge England ; New York, 1996.
[26] T. Hidayat, D. Shishin, E. Jak, S.A. Decterov, Thermodynamic reevaluation of the Fe–O system, Calphad. 48 (2015) 131–144. doi:10.1016/j.calphad.2014.12.005.
[27] T. Hidayat, Equilibrium studies of complex silicate-based slag in the copper production, (2013). http://espace.library.uq.edu.au/view/UQ:307468 (accessed December 7, 2015).
[28] T. Hidayat, H.M. Henao, P.C. Hayes, E. Jak, Phase Equilibria Studies of the Cu-Fe-O-Si System in Equilibrium with Air and with Metallic Copper, Metall. Mater. Trans. B. 43 (2012) 1034–1045. doi:10.1007/s11663-012-9683-x.

14. Model parameters

After the development of the appropriate phase field model, obtaining results with a desired accuracy requires an accurate selection of model parameters. In principle, a proper selection of input parameters requires information of real physical and chemical properties of the selected material system. In many cases, however, obtaining this information is not at all straightforward. [1]

For example, measuring interfacial free energy of a material by direct experimental techniques is accompanied with inherent difficulties. [2] However, the presence of measurable quantities which are sensitive to the interfacial free energy has made the development of indirect measurement techniques possible. [1] There exist a number of indirect techniques, developed for metal systems [3] and transparent organic materials:

- The nucleation method: the maximum undercooling required for the onset of nucleation is measured. This maximum undercooling, however, is often not achieved due to the presence of preferred nucleation sites in the system.
- The grain boundary groove method: this builds upon the equilibrium conditions at the triple line between solid grains and a liquid.

However, efforts to evaluate the σ_{SL} for oxide materials are very scarce. Tanaka et al. [4] evaluated σ_{SL} of pure fosterite (Mg_2SiO_4) by comparing levitating droplet experiments with classical nucleation theory, according to the method developed by Shao and Spaepen [5]. Another possibility, rather than trying to obtain the interfacial energy experimentally is modelling. Prediction of interfacial energies from first principles is currently not generally possible; however, there have been a number of attempts to develop models for the calculation of interfacial energies in steel slag systems. [6] One approach is to use the approach of Girifalco and Good where the values of surface tension of the initial phases are used to calculate the interfacial energy of the combined phases [7]:

$$\sigma_{SL} = \sigma_S + \sigma_L + 2\Phi(\sigma_S \cdot \sigma_L)^2 \qquad \textbf{(14.1)}$$

Here Φ is an interaction coefficient, which is a measure of the interaction between two condensed phases and has a value of 0.5 for slags free of FeO [8]. To use this equation, knowledge on the surface energies of the solid and liquid are required. Solids should display higher surface energies than liquids, but their atoms are relatively immobile. Consequently, stresses in the surface may exist in addition to the surface tension of the solid [9]. The surface energy of a solid is typically measured by the (compensated) zero-creep method [10,11] (thin wires of the solid material are stressed by various weights and decrease or increase in length accordingly; the stress is determined at which no change in shape takes place and it represents a measure for the surface tension) or pressing together two spheres of the solid [9] (measurement of elastic modulus of the sub-micrometer powder assemblies, knowing the particle diameter, elastic modulus and volume fraction; this method can be adapted to measuring the conductivity for electrically conductive solids as the diameter and conductivity are related and thus a relation can be found between the conductivity and surface energy [12]).

Also, Tanaka et al. [4] propose a new method of evaluating both interfacial energy σ_{SL} and the activation energy of diffusion E_a by analysing a crystallization experiment with the use of gas jet levitation method. They also applied this method to the experiment of crystallization of a melt sphere of fosterite (Mg_2SiO_4). The resulting interfacial energy is 0.613 ± 0.03 N/m. Moreover, Heulens et al. [2] investigated the growth of wollastonite ($CaSiO_3$) in a slag with molar composition 42 CaO – 10 Al_2O_3 – 48 SiO_2 at 1320°C with a combined numerical-experimental approach: they compared two-

dimensional phase field simulations of dendritic crystallization to in-situ high temperature experiments in a confocal laser microscope. The resulting interfacial energy was found to be σ_{SL} = 0.65 ± 0.13 J/m².

In this work, the diffuse interface between the liquid slag and the solid spinel is chosen within the thin-interface limit and equals $l_{12} = 10^{-7}$ m. The interface contains eight grid points, yielding a system discretization with $\Delta x = 0.125 \cdot 10^{-7}$ m. The size of the time discretisation is restricted by stability of diffusion equations and equals $\Delta t = 2.0 \cdot 10^{-7}$ s. To obtain the interface width, the following model parameters were used: $\kappa_{12} = 0.225 \cdot 10^{-7}$ J/m³ and $m_{12} = 1.8 \cdot 10^{7}$ J/m, according to the following equation

$$l_{ij} = \sqrt{\frac{8\kappa_{ij}}{m_{ij}}} \tag{14.2}$$

Moreover, the next equation gives the relation between the model parameters and the interface energy.

$$\sigma_{ij} = \frac{\sqrt{2}}{3}\sqrt{m_{ij}\kappa_{ij}} \tag{14.3}$$

This yields an interface energy of σ_{12} = 0.3 J/m². The molar volume was calculated from literature previously [2,13]: $V_m = 23.6 \cdot 10^{-6}$ m³/mol.

The mobilities are calculated based on the diffusion coefficients and the thermodynamic factors. The most elaborated mobility databases nowadays are part of the DICTRA software package and include data for iron, nickel, aluminium, titanium and silicon based alloys, but no kinetic database has been developed yet for oxide systems. [14] Therefore, we used the previously [13] determined mobilities for FeO and Fe_2O_3, estimated from literature for a Fe_2O_3-CaO-SiO_2 melt at 1400°C [15], where CaO is replaced by FeO. To find a diffusion coefficient for Cu_2O in the slag, the Stokes-Einstein equation was used as an estimation. The ionic radii of the different cations can be used as an inverse measure for the diffusion coefficient[16]: Cu^{+} has 0.077 nm as ionic radius, Fe^{2+} 0.070 nm and Fe^{3+} 0.060 nm. Despite the fact that the Fe^{3+} ion has a lower ionic radius, it has a lower diffusion coefficient than the Fe^{2+} [17], because a larger valence number will yield slower diffusion. Thus, the following values were used for the mobilities in the slag: $M_{Cu2O\text{-}Cu2O} = 0.02 \cdot 10^{-19}$ m⁵/ (J s); $M_{FeO\text{-}FeO} = 0.1 \cdot 10^{-19}$ m⁵/ (J s) and $M_{Fe2O3\text{-}Fe2O3} = 0.05 \cdot 10^{-19}$ m⁵/ (J s).

For the mobilities in the solid, the same order of magnitude as in the liquid was used to avoid solute trapping effects and the off-diagonal elements of the mobility matrix were set to zero. In this respect, it should be noted that Liu et al. [18] observed that the mobility matrix of the solid does not affect the growth of that solid, because there is no diffusion in the solid as the solid crystallizes with its equilibrium composition. The kinetic coefficient L_{12} was chosen to ensure diffusion-controlled growth, as obtained by the following equation

$$L_{crit} = \frac{4m_{ij}}{3\kappa_{ij}\zeta} \tag{14.4}$$

Where

$$\zeta = \sum_{k=1}^{C-1}\left(x_{slag,eq,k} - x_{stoich,eq,k}\right)\sum_{m=1}^{C-1} m_{km}\left(x_{slag,eq,m} - x_{stoich,eq,m}\right) \tag{14.5}$$

With m_{km} the elements of the diffusion mobilities matrix (which contains the averages of the two mobility matrices). L_{crit} in this case is $4.1779 \cdot 10^{-5}$. If $L_{12} = L_{crit}$, the growth is diffusion-controlled; If $L_{12} < L_{crit}$, the eta-profiles will move slower than the composition profiles and if $L_{12} > L_{crit}$, the composition profiles will be slower than the eta-profiles. However, anisotropy is also present in the kinetic coefficient according to the following equation:

$$L_{ij} = \overline{L_{ij}}\left(1 - \beta_{ij} + 2\beta_{ij}\, tanh\left(\frac{r_{ij}}{\left|tan\left(a_{ij}\theta_{ij}\right)\right|}\right)\right) \qquad \textbf{(14.6)}$$

With β_{ij} a measure for the depth of the cusps (i.e. the difference in mobility between the fast and slow crystal planes), r the sharpness of the cusps (influencing the corner formation at the edges of two crystal planes) and $2a_{ij}$ the mode of symmetry of the anisotropy (mostly a value of four for spinel minerals). Moreover, $\overline{L_{ij}}$ should be calculated in such a way that the value of L_{12} for the fast moving/facetted interfaces equals L_{crit}. In this case, $\overline{L_{ij}}$ should be $2.7853 \cdot 10^{-5}$. Moreover, a_{ij} = 2 to yield a 4-fold crystal growth symmetry and β_{ij} = 0.5 to give a high enough difference between the fast growing (facetted) interfaces and the slow interfaces (as illustrated for two different β-values in Figure 14.1).

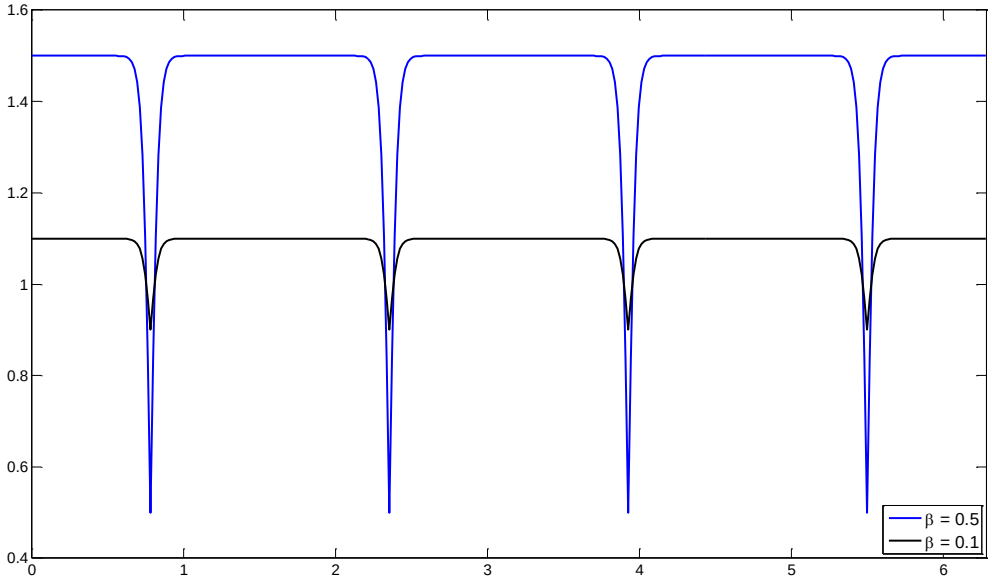

Figure 14.1 Plot of anisotropy function for two *β*-values when r=10 and a=2

The simulations are executed for a 100 x 100 domain (= 1.25 x 1.25 µm²) for 10^6 time steps (= 0.2s). The solid was initialised at its equilibrium composition (0.005 Cu_2O – 0.495 FeO – 0.495 Fe_2O_3 – 0.005 SiO_2) and the slag started as a supersaturated oxide mixture (0.1 Cu_2O – 0.4 FeO – 0.4 Fe_2O_3 – 0.1 SiO_2). According to Factsage such a supersaturated slag should decompose into solid spinel and a slag with the equilibrium composition of 0.15127 Cu_2O – 0.35397 FeO – 0.34349 Fe_2O_3 – 0.15127 SiO_2. The description of the stoichiometric phase ensured that the diffusion potential is the same as for the equilibrium composition of the slag. The thermodynamic data of the slag were extracted from the database with Chemapp with a discretization of 0.005 in the compositional domain. A smaller discretization resulted in encountering memory limits during the phase field simulation when the thermodynamic data is loaded in a first stage of the calculation.

References

[1] H. Ravash, 3D phase-field simulations of sintering and coarsening in polycrystalline multi-phase materials, KU Leuven, 2014.

[2] J. Heulens, Isothermal Crystallization of Metallurgical Slags: Phase Field Simulations Combined with In Situ Experiments (Isotherme kristallisatie van metallurgische slakken: faseveldsimulaties in combinatie met in situ experimenten), PhD thesis, KU Leuven, 2011. https://lirias.kuleuven.be/handle/123456789/318339.

[3] M. Gündüz, J.D. Hunt, The measurement of solid-liquid surface energies in the Al-Cu, Al-Si and Pb-Sn systems, Acta Metall. 33 (1985) 1651–1672. doi:10.1016/0001-6160(85)90161-0.

[4] K.K. Tanaka, T. Yamamoto, K. Nagashima, K. Tsukamoto, A new method of evaluation of melt/crystal interfacial energy and activation energy of diffusion, J. Cryst. Growth. 310 (2008) 1281–1286. doi:10.1016/j.jcrysgro.2007.06.038.

[5] Y. Shao, F. Spaepen, Undercooling of bulk liquid silicon in an oxide flux, J. Appl. Phys. 79 (1996) 2981–2985. doi:10.1063/1.361222.

[6] Y. Chung, A.W. Cramb, Dynamic and equilibrium interfacial phenomena in liquid steel-slag systems, Metall. Mater. Trans. B. 31 (2000) 957–971. doi:10.1007/s11663-000-0072-5.

[7] J. Bulou, J.M. Raynal, J. Vial, An interfacial tension treatment with an improved good—Girifalco equation using solubility parameters, J. Colloid Interface Sci. 98 (1984) 168–174. doi:10.1016/0021-9797(84)90491-0.

[8] K.C. Mills, L. Yuan, R.T. Jones, Estimating the physical properties of slags, J. South. Afr. Inst. Min. Metall. 111 (2011) 649–658.

[9] K. Kendall, N. McN.Alford, J.D. Birchall, A new method for measuring the surface energy of solids, Nature. 325 (1987) 794–796. doi:10.1038/325794a0.

[10] T.H. Heumann, J. Johannisson, Determination of the surface tension, grain boundary energy, the viscosity and the diffusion coefficient of solid lead from creep characteristics in the vicinity of the melting point, Acta Metall. 20 (1972) 617–625. doi:10.1016/0001-6160(72)90017-X.

[11] V.K. Kumikov, The measurement of the surface tension of some pure metals in the solid state, Mater. Sci. Eng. 60 (1983) L23–L24. doi:10.1016/0025-5416(83)90016-2.

[12] K. Kendall, Solid surface energy measured electrically, J. Phys. Appl. Phys. 23 (1990) 1329. doi:10.1088/0022-3727/23/10/012.

[13] J. Heulens, B. Blanpain, N. Moelans, Phase field modeling of the crystallization of FeOx–SiO2 melts in contact with an oxygen-containing atmosphere, Chem. Geol. 290 (2011) 156–162. doi:10.1016/j.chemgeo.2011.09.005.

[14] A. Borgenstam, L. Höglund, J. Ågren, A. Engström, DICTRA, a tool for simulation of diffusional transformations in alloys, J. Phase Equilibria. 21 (2000) 269–280. doi:10.1361/105497100770340057.

[15] Y. Ukyo, K.S. Goto, The interdiffusivity matrix of Fe2O3-CaO-SiO2 melt at 1693 to 1773 K, Metall. Trans. B. 12 (1981) 449–454. doi:10.1007/BF02654313.

[16] M.D. Dolan, R.F. Johnston, Multicomponent diffusion in molten slags, Metall. Mater. Trans. B. 35 (2004) 675–684. doi:10.1007/s11663-004-0008-6.

[17] M. Roskosz, C.M. Alexander, K. Sio, J. Wang, H.C. Watson, N. Dauphas, B.O. Mysen, Redox-dependent, diffusion-driven fractionation of Fe isotopes in silicate melts and its structural controls, in: Geochim. Cosmochim. Acta, PERGAMON-ELSEVIER SCIENCE LTD THE BOULEVARD, LANGFORD LANE, KIDLINGTON, OXFORD OX5 1GB, ENGLAND, 2010: pp. A882–A882. http://scholar.google.com/scholar?cluster=7307569211670342570&hl=en&oi=scholarr (accessed February 23, 2017).

[18] J.-J. Liu, J. Heulens, M.-X. Guo, N. Moelans, Isothermal Crystal Growth Behavior of CaSiO3 in Ternary Oxide Melts, J. Inorg. Mater. 31 (2016) 547. doi:10.15541/jim20150516.

15. Results and discussion

A first simulation with the parameters from the previous chapter, started from a 'one-dimensional' initialization: the left side of the system was set as solid spinel and the right side as supersaturated slag. The facetted growth was not yet considered for the solid phase. The resulting profiles are illustrated in Figure 15.1.

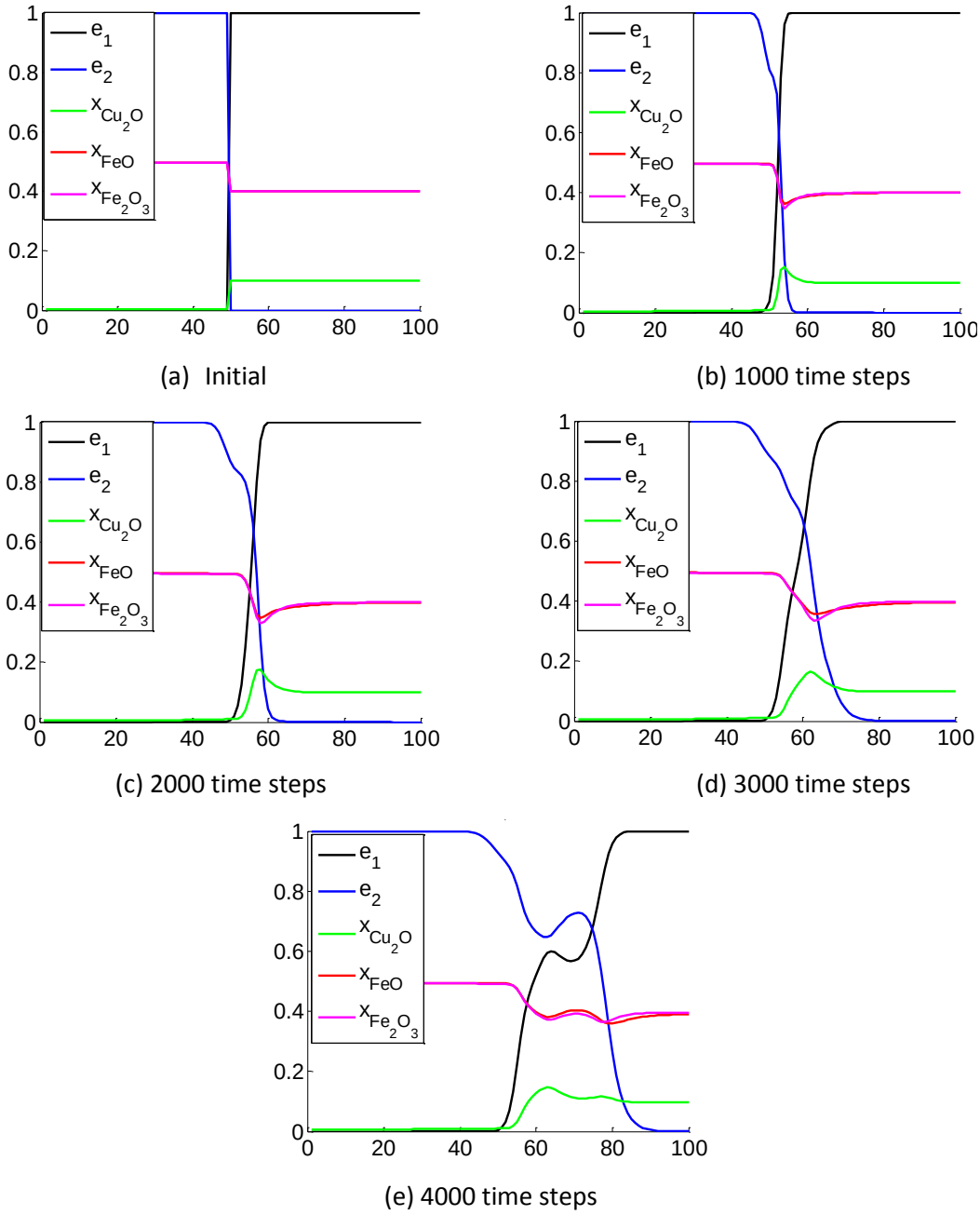

Figure 15.1 Resulting profiles for phase field variables (e_1 represents the slag and e_2 the solid spinel) and molar fractions of different components in a one-dimensional simulation

After 1000 time steps, a sort of bending of the normally symmetric phase field profile can be observed. This bending grows as the simulation progresses. After 4000 time steps, it already looks as if an extra minimum is present in the overall energy of the system. This is an illustration of the limits of the 'thin-interface' implementation of the model.

Normally, the model will yield correct results for realistic interfacial widths (on the order of a couple of Ångstrom or 1 nm). In the thin-interface implementation, the interfacial width can be varied over a certain range without influencing the behaviour of the model. However, this range also has its limits and if the artificial width of the interface is chosen too high, the homogeneous part of the interfacial free energy density is reduced strongly, due to which the bulk free energy density has a larger contribution in the free energy density of the system.

To circumvent this limitation, the parameters as discussed in the previous chapter were chosen to be kept, but the thermodynamic bulk data of both the slag and the solid spinel were divided by a certain constant value, here 100, to diminish the effect of the bulk energies, since the bulk energies of the different phases have a larger relative contribution in the system's energy when a larger interfacial width is used. This is because the latter (a larger l_{12}) corresponds to a smaller m-value and thus the homogeneous part of the interface energy (f_0) contributes less to the system's energy.

The factor 100 was chosen as it is an optimal value to both remove the limit of the thin-interface implementation and also keep the Gibbs-Thomson effect of a different order of magnitude than the other energies of the system. The Gibbs-Thomson effect depends on the temperature (1400°C) and the interfacial energy (0.3 J/m²). The molar volume used in the simulations was $23.6 \cdot 10^{-6}$ m³/mol. For a nucleus with a radius of 3Δx, the change in Gibbs energy due to this curvature is 377.6 J/mol. Thus, the composition of the matrix phase, in this case the slag, will be changed by multiplying with a factor of 1.0257519, which would correspond to a change in composition of 2%, which is reasonable. As a reference, the Gibbs energy of the slag and solid are typically of the order of 10^{10} J/m³or 10^5 J/mol. However, these values are divided by 100, resulting in the lowest Gibbs energies on the order of 10^3 J/mol, which is one order of magnitude difference with the Gibbs-Thomson effect.

When we start from nuclei with a radius of 12 grid points, the change in Gibbs energy is only 94.4 J/mol. The corresponding factor for the change in composition of the slag is 1.00681. Thus, a change of only 0.6% is introduced in that case. The Gibbs-Thomson effect is here clearly of a different order of magnitude than the Gibbs energies of the solid and slag.

A 1-dimensional simulation was also executed for the case where the thermodynamic bulk energies are divided by 100 and the results are illustrated in Figure 15.2. It is clear that the phase field profiles remain symmetric while the solid grows, as needed for an accurate description of the interface behaviour.

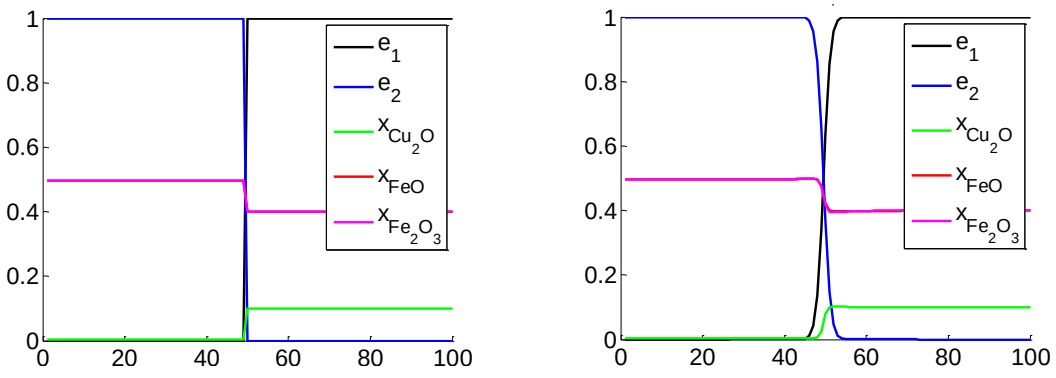

(a) Initial (b) 1000 time steps

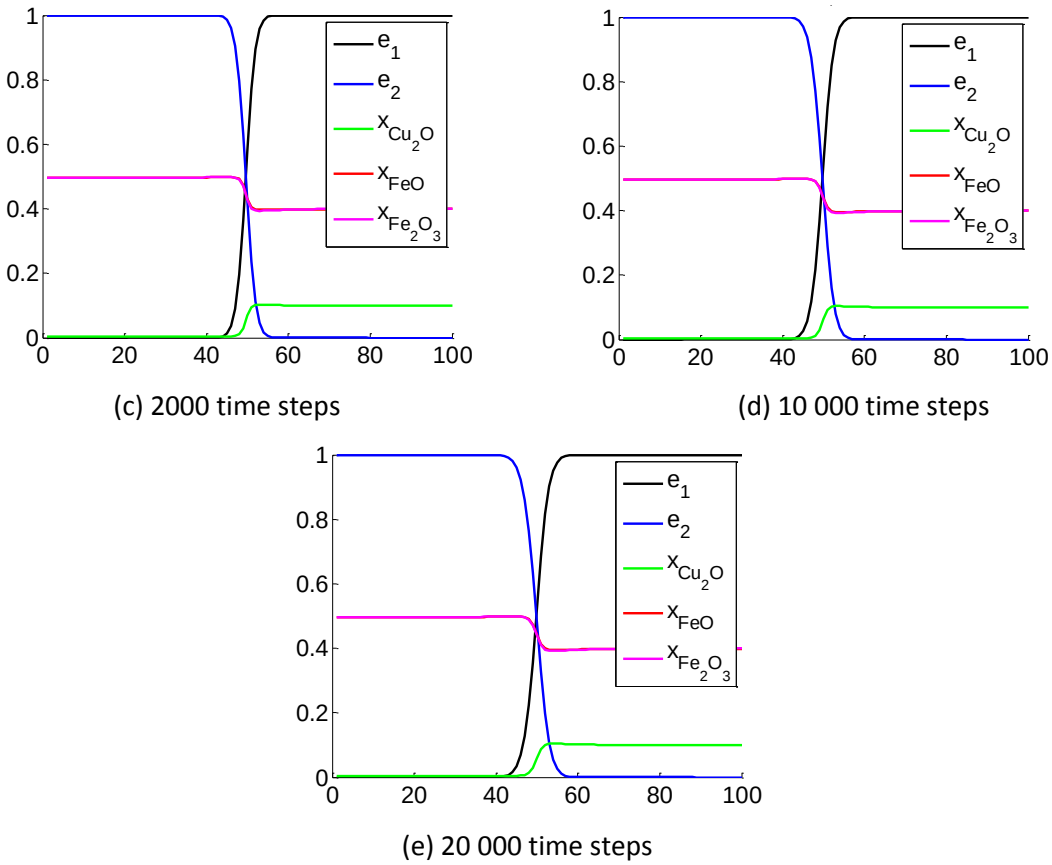

(c) 2000 time steps

(d) 10 000 time steps

(e) 20 000 time steps

Figure 15.2 Resulting profiles for phase field variables (e_1 represents the slag and e_2 the solid spinel) and molar fractions of different components in a one-dimensional simulation with the bulk free energies of the slag and spinel divided by a factor 100

15.1. Facetted growth of spinel in quaternary oxide system

For the two-dimensional simulations, the system is initialized with one quadrant of a circle with a radius of 12 grid points in the lower left corner. This configuration with the nucleus in the lower left corner of the system is representative for a 200x200 system due to symmetry. A first simulation was performed assuming isotropic interfacial energy, using the standard value $L_{12} = 4.1779 \cdot 10^{-5}$, so that no facets are expected to form. The contours of the 0.5-level of the solid for every 100 000th time step are shown in Figure 15.3.

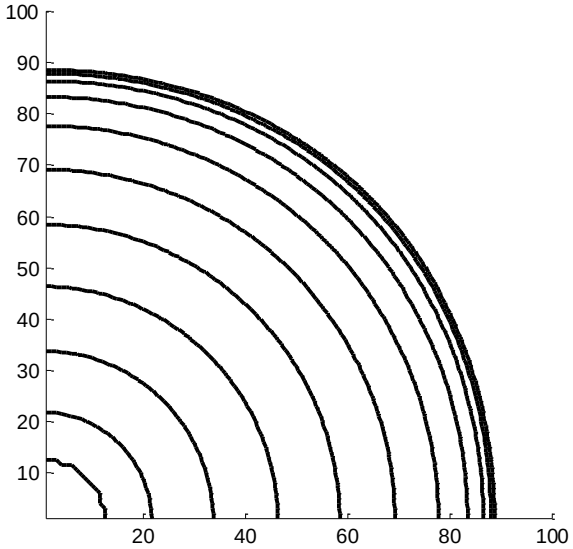

Figure 15.3 Contours of the 0.5-level of the solid for every 100 000th time step in a 2D-simulation with isotropic growth kinetics for the solid phase.

The last couple of contours are clearly located closer together than the first contour lines. The corresponding concentration profiles of Cu_2O, FeO and Fe_2O_3 at a height of 10 grid points are shown in Figure 15.4.

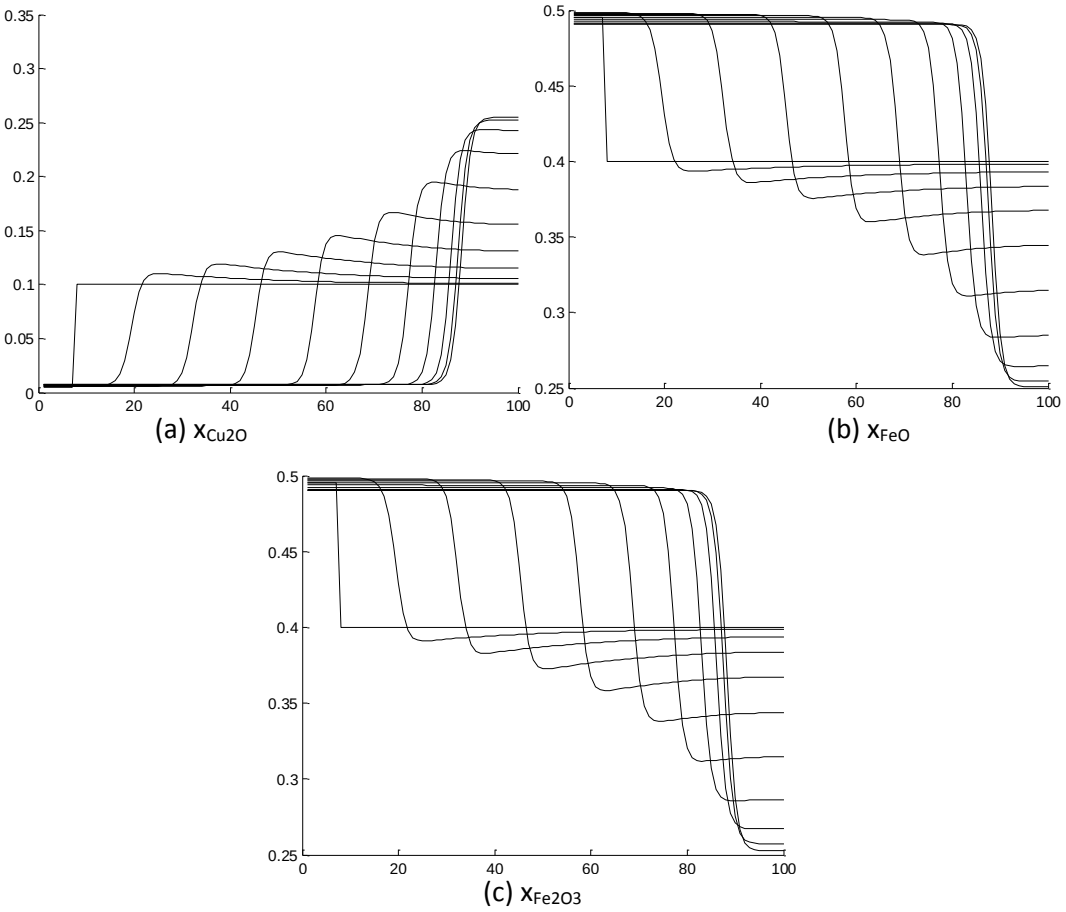

Figure 15.4 Concentration profiles for every 100 000th time step in a 2D-simulation with isotropic growth kinetics for the solid phase.

As the spinel solid grows, the slag is enriched in Cu_2O: the concentration goes from 0.1 to >0.25. The FeO and Fe_2O_3 profiles are very similar, except for a slightly faster diffusion in the slag of FeO. In the

concentration profiles, it also becomes apparent that the last couple of lines lay closer to each other than the first. A reason for this slower movement of the interface after a while is probably the fact that the slag gets saturated with Cu_2O and depleted in the iron oxides.

For the facetted growth of the solid spinel phase, several r-values in equation (14.6), determining the sharpness of the cusps in the interfacial energy, were used. The corresponding plots are shown in Figure 15.5. A larger r will yield only a limited range of angles at which the growth is slower, due to a lower L_{12}-value. A smaller r-value, on the other hand, has a larger range of angles at which the growth is slower. Thus, a larger r-value clearly would result in 'rounder' corners of the spinel particle, but faster general growth.

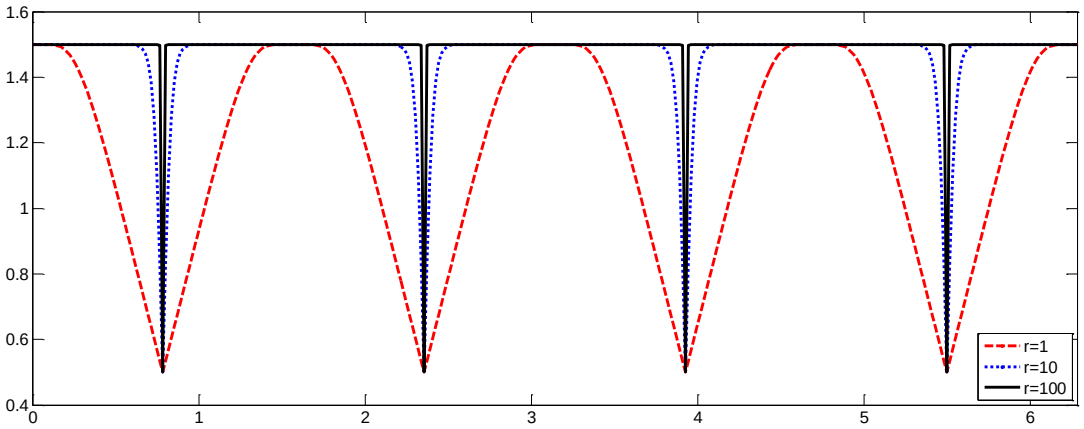

Figure 15.5 Plot of anisotropy function for three r -values with β_{ij} =0.5 and α_{ij}=2 in equation (14.6)

With r=1, it is expected from the plot in Figure 15.5 that the corners of the spinel solids are not too round. The results of this simulation as contour plots and concentration profiles are shown in Figure 15.6 and Figure 15.7, respectively.

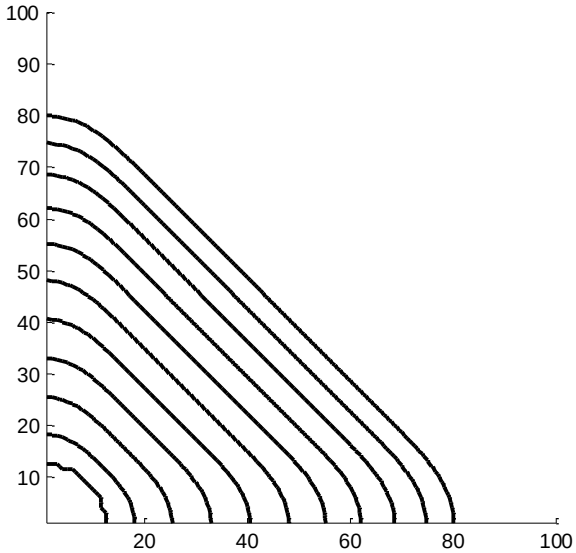

Figure 15.6 Contours of the 0.5-level of the solid for every 100 000th time step in a 2D-simulation assuming strong anisotropy in the solid-liquid interface kinetics with r=1, resulting in facetted growth of the solid phase.

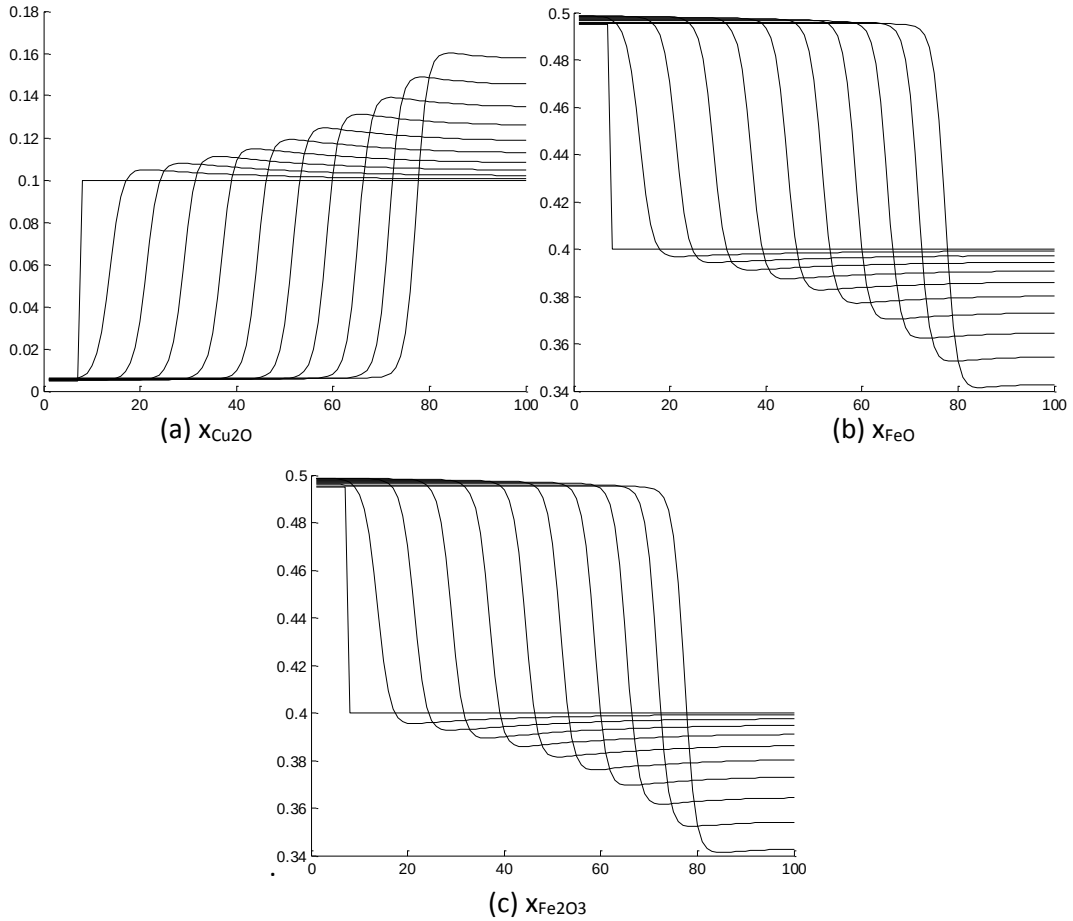

Figure 15.7 Concentration profiles for every 100 000th time step in a 2D-simulation assuming strong anisotropy in the solid-liquid interface kinetics with r=1, resulting in facetted growth of the solid phase.

It is clear from the contour plot that the growth of the spinel solid was slower than without the facetted growth. Because the anisotropy is added to the kinetic coefficient L_{12}, the fastest moving interfaces have an angle of 0 or 90° with the x-axis. The slowest moving interfaces are located at an angle of 45°. But even the fastest moving interface positions, corresponding to the x- and y-direction, are slower than the non-facetted interface movement. It seems as if the slower moving interfaces at 45° restrict the fast movement of the well-oriented interfaces. As the growth is slowed down, the Cu_2O, FeO and Fe_2O_3 concentrations in the slag do not change as much as in the isotropic simulation. Moreover, the last couple of contour lines are not 'piled up' as in the isotropic case, indicating that some solid spinel could still grow from the remaining slag.

The contour plots of the solid and the concentration profiles for the case when r=10 are shown in Figure 15.8 and Figure 15.9.

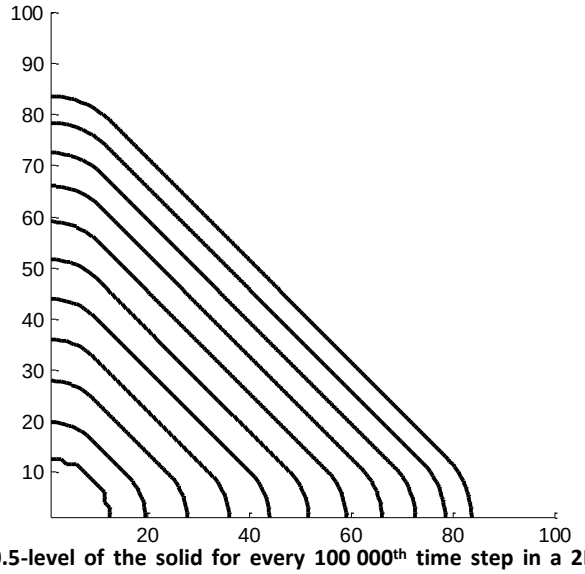

Figure 15.8 Contours of the 0.5-level of the solid for every 100 000th time step in a 2D-simulation assuming strong anisotropy in the solid-liquid interface kinetics with r=10, resulting in facetted growth of the solid phase.

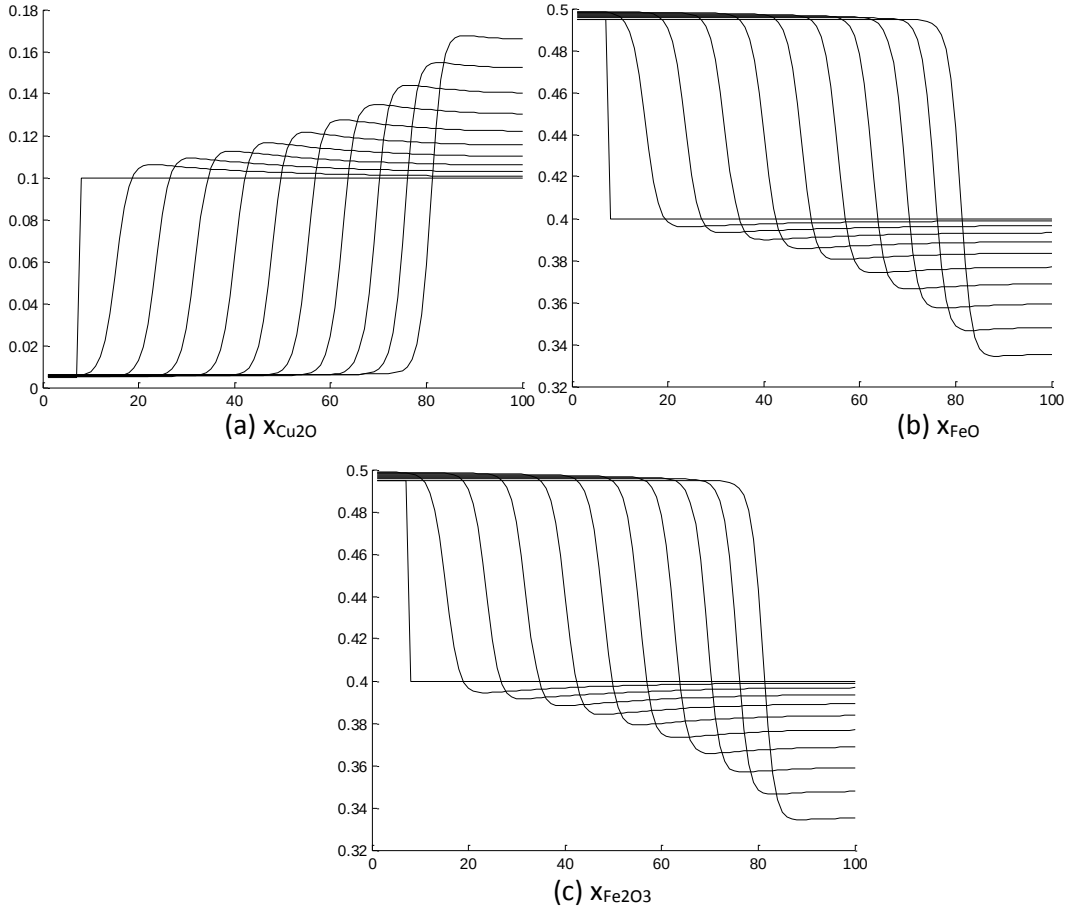

Figure 15.9 Concentration profiles for every 100 000th time step in a 2D-simulation assuming strong anisotropy in the solid-liquid interface kinetics with r=10, resulting in facetted growth of the solid phase.

For a larger r-value, i.e. a sharper cusp in the anisotropy plot, the growth is less limited than for the r=1-case. This is because the kinetic coefficient is limited for only a very small range of angles around 45°, resulting in slower growth in that direction. This is also clearly visible in the concentration profiles. The profiles are also not piled-up, indicating that a longer simulation time would still result

in growth of the solid phase. The contour plots of the solid and the concentration profiles for the case when r=100 are shown in Figure 15.10 and Figure 15.11.

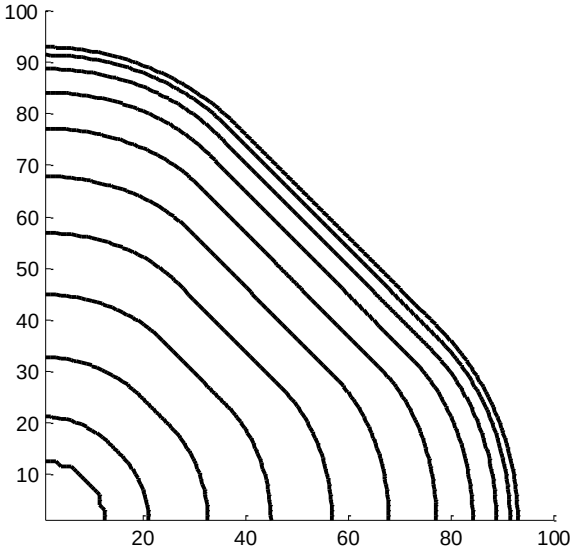

Figure 15.10 Contours of the 0.5-level of the solid for every 100 000th time step in a 2D-simulation assuming strong anisotropy in the solid-liquid interface kinetics with r=100, resulting in facetted growth of the solid phase.

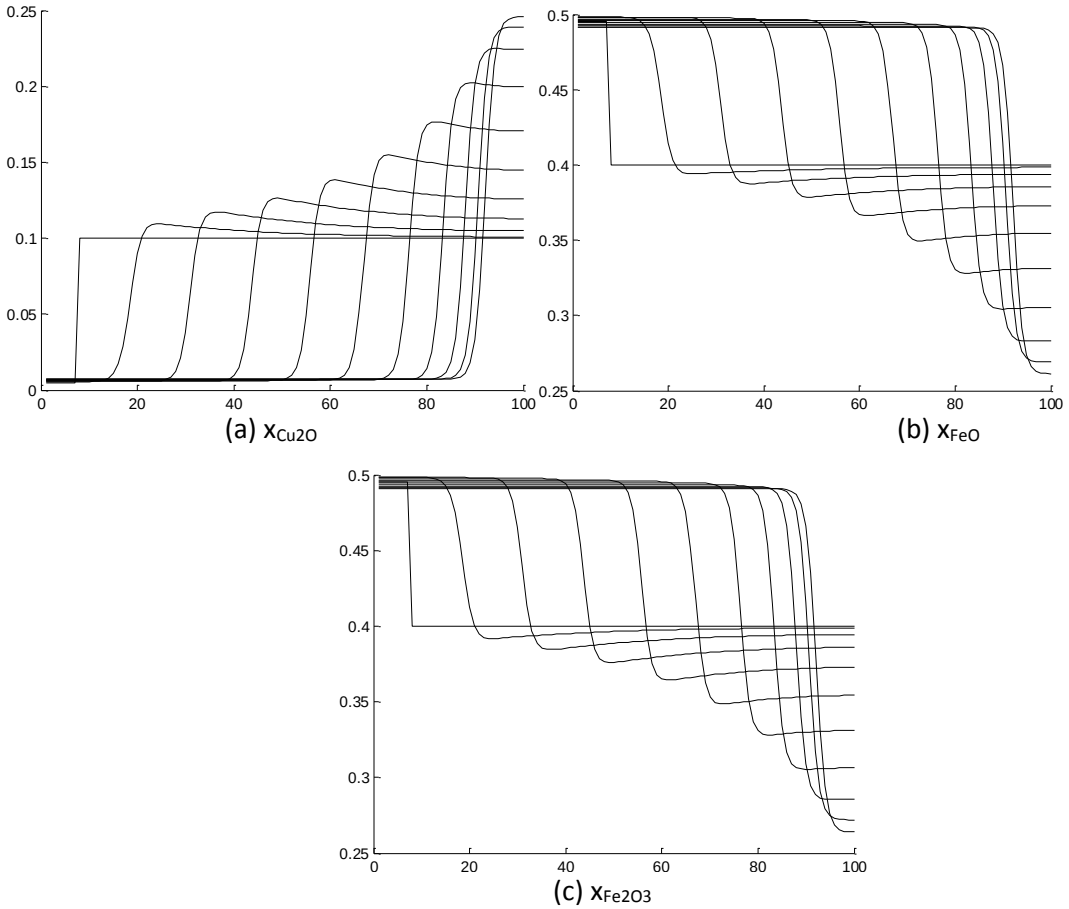

Figure 15.11 Concentration profiles for every 100 000th time step in a 2D-simulation assuming strong anisotropy in the solid-liquid interface kinetics with r=100, resulting in facetted growth of the solid phase.

For an even larger r-value, the growth seems to be even faster as compared to the isotropic growth in the fast-growing directions of 0 and 90°. This is visible in the contour plots where the distance

between the 0.5-contour lines of different time steps increases as the r-value increases. The concentration profiles show that the saturation of Cu_2O and depletion of FeO and Fe_2O_3 is not yet as high as in the isotropic case, although it gets close. The contour plots start to pile-up at the end of the simulation. This is also visible in the concentration profiles.

The way the spinel grows is determined by the anisotropy in the kinetic coefficient L_{12}, but the final form of the solid is determined by the interfacial energy. In these simulations, the growth of the solid particles was mainly investigated and thus, no anisotropy was used for the interfacial energy (through the parameters m and κ). The r-value which was varied in these simulations, influences the range of angles for which the kinetic coefficient will be at its maximum value of L_{crit}. A larger r will yield only a limited range of angles at which the growth is not favoured, due to a lower L_{12}-value. Thus, a larger r-value clearly results in 'rounder' corners of the spinel solid, but faster growth, which was clearly observed in the simulations. In experiments, both the sharp and round corners can be observed as illustrated in Figure 15.12.

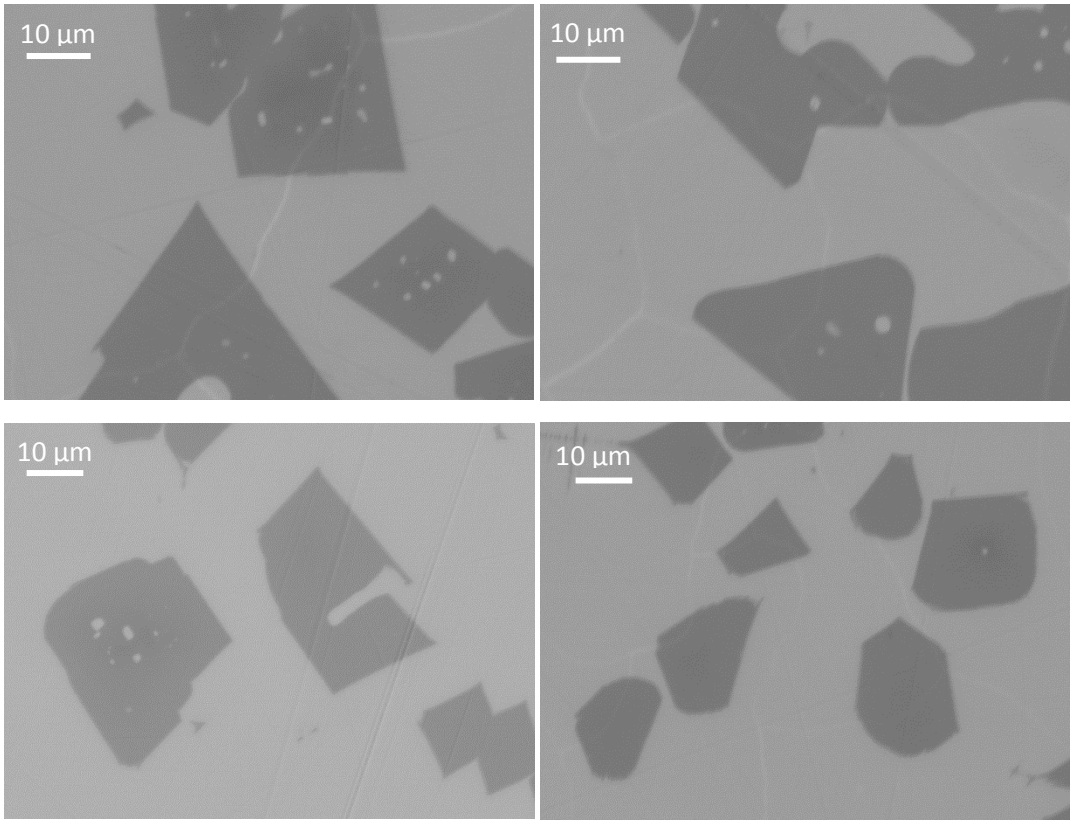

Figure 15.12 SEM micrographs of an experimentally obtained microstructure of solid oxide particles in a slag that was quenched to 'freeze' its high temperature condition [1]

The rounded corners also appear in the experimental system, but the sharp corners in the experiments are much sharper than for the simulations with the lowest r-value. Thus, it might be interesting to also conduct a simulation with a strong anisotropy in the interface energy (via appropriate m and κ values).

15.2. Influence of p_{O2} on facetted growth of spinel in quaternary oxide systems with an open boundary

It is generally accepted that the chemical activity of oxygen, i.e. the oxygen fugacity, may control the oxidation state of iron in liquid oxide mixtures and thus can influence the phase equilibria, rheology and density [2,3]. At the upper boundary of the system, a certain p_{O2} is fixed, which can be implemented by imposing a certain x_{FeO} over x_{Fe2O3} ratio. This ratio is determined by the p_{O2} and can be obtained as a function of p_{O2} using Factsage. The result is plotted in Figure 15.13.

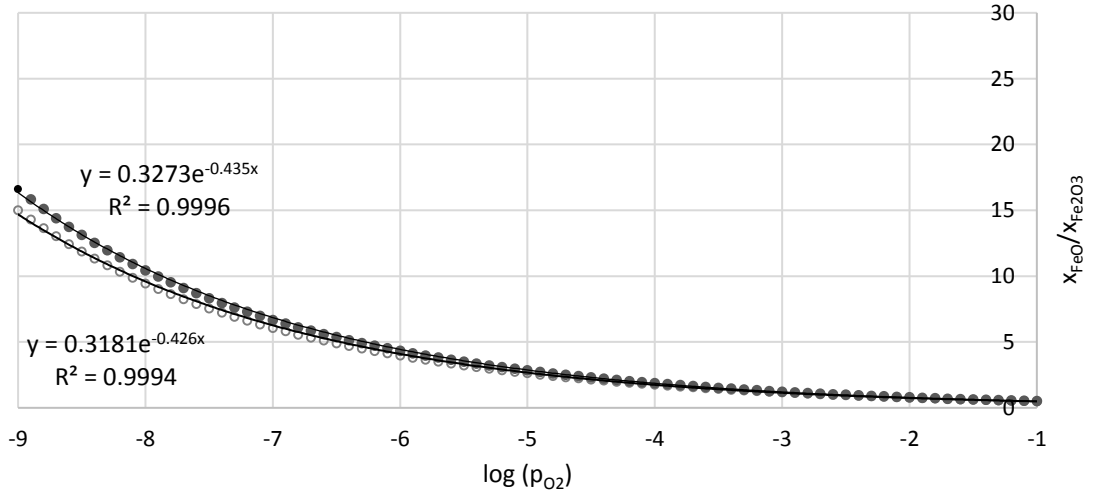

Figure 15.13 x_{FeO} over x_{Fe2O3} ratio in the slag in equilibrium with a certain p_{O2} as calculated by Factsage and fitted with an exponential trend line. The closed data points represent the equilibrium calculation for the equilibrium slag composition and the open data points for the initial slag composition.

The equilibrium composition of the slag (0.15127 Cu_2O – 0.35397 FeO – 0.34349 Fe_2O_3 – 0.15127 SiO_2) has a 'natural' p_{O2} of $2.5185 \cdot 10^{-3}$ atm or $10^{-2.60}$ atm, i.e. this is the partial pressure of oxygen in the gas phase that would not result in any oxidation or reduction of the slag phase. Several simulations with various p_{O2}-values at the upper boundary of the system were executed. Facetted growth of the spinel solid through anisotropy in the kinetic coefficient was used with an r-value of 10. p_{O2} values of $2 \cdot 10^{-3}$ atm, $2.5185 \cdot 10^{-3}$ atm (the natural p_{O2} of the slag); $5 \cdot 10^{-3}$ atm; 10^{-2} atm; 10^{-1} atm were simulated. The resulting contour plots for these different boundaries, can be found in Figure 15.14.

P_{O2} [atm]	Contourplot	P_{O2}	Contourplot
$2 \cdot 10^{-3}$	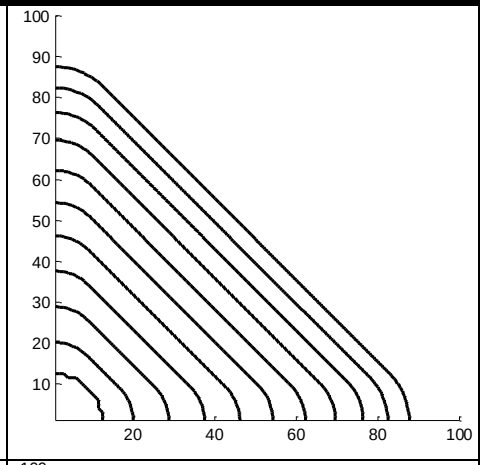	10^{-2}	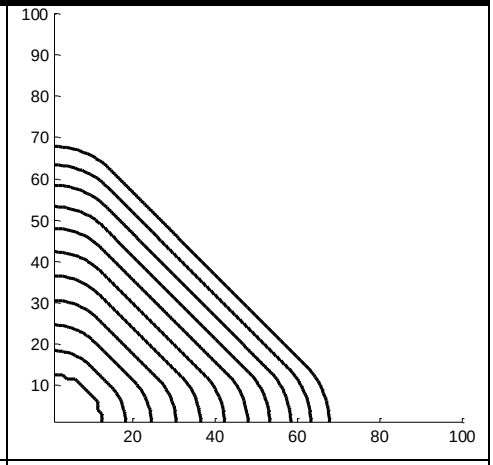
$2.5185 \cdot 10^{-3}$	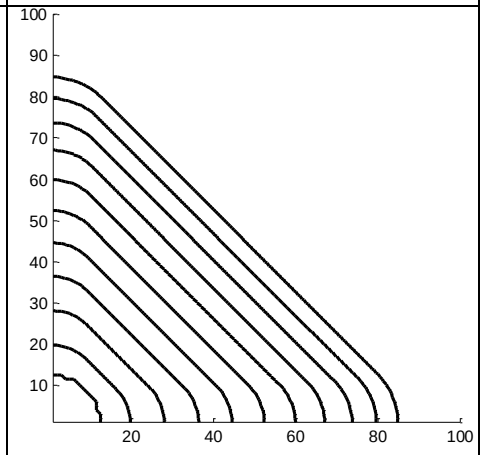	10^{-1}	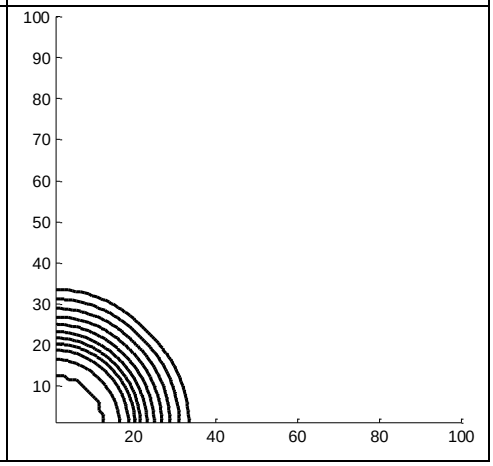
$5 \cdot 10^{-3}$	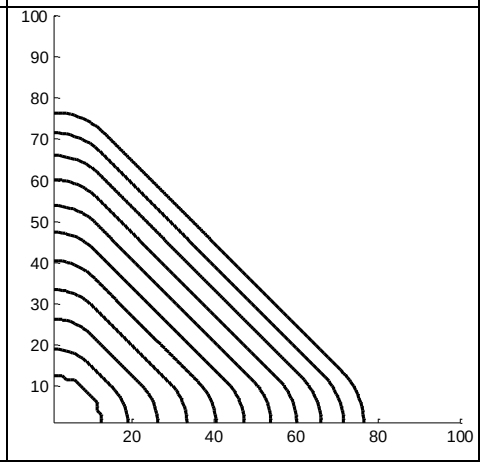		

Figure 15.14 Contour plots of the 0.5-level of the solid for every 100 000th time step in a 2D-simulation assuming strong anisotropy in the solid-liquid interface kinetics with r=10, resulting in facetted growth of the solid phase, for several p_{O2}-values at the upper boundary.

A decreasing p_{O2} clearly yields faster growth. This is in accordance with the lower driving force as predicted by Factsage, as illustrated by the amounts of spinel and slag as a function of the p_{O2} in Figure 15.15.

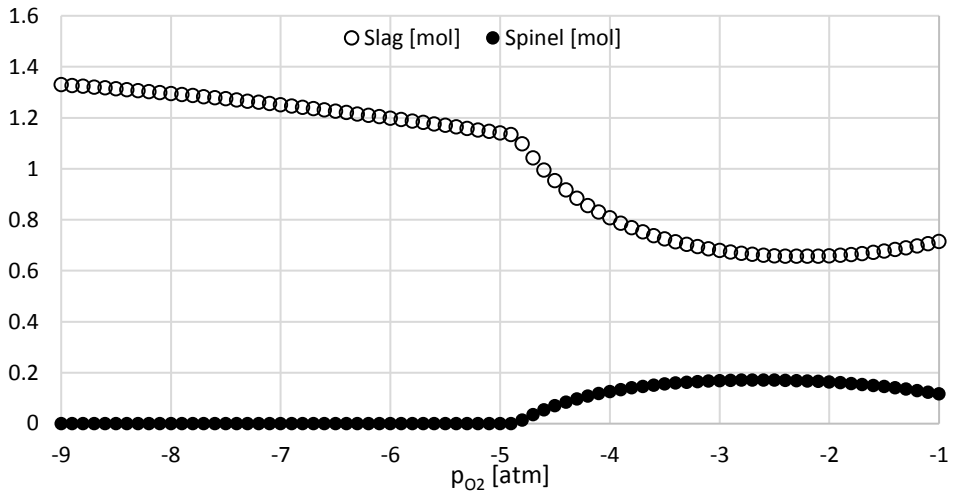

Figure 15.15 Results of equilibrium calculation with Factsage for influence of p_{O2} on the amount of slag and spinel starting from the initial composition of the slag.

As the partial pressure of oxygen increases, the concentration of FeO and Cu_2O at the bottom of the system decreases, whereas the concentration of Fe_2O_3 increases, as is expected by the imposed boundary condition on the upper boundary. Previous results of Heulens [4] also showed that the crystallization of a ternary melt (with two possible oxidation states for Fe) has a larger effect on the oxidation state than the oxygen fugacity of the atmosphere. Furthermore, the growth velocities of the spinel crystals increase with decreasing oxygen fugacity. However, their results were for simulation times of 10^5 time steps. In this study, we conducted 10 times longer simulations, indicating very clearly the influence of the oxygen atmosphere on the growth of the spinel solid and possible inhibition of this growth by the p_{O2}-value.

References

[1] E. De Wilde, I. Bellemans, M. Campforts, A. Khaliq, K. Vanmeensel, D. Seveno, M. Guo, A. Rhamdhani, G. Brooks, B. Blanpain, N. Moelans, K. Verbeken, Wetting behaviour of Cu based alloys on spinel substrates in pyrometallurgical context, Mater. Sci. Technol. 31 (2015) 1925–1933. doi:10.1179/1743284715Y.0000000052.

[2] R. Hill, P. Roeder, The Crystallization of Spinel from Basaltic Liquid as a Function of Oxygen Fugacity, J. Geol. 82 (1974) 709–729.

[3] D. Durinck, P.T. Jones, B. Blanpain, P. Wollants, Air-Cooling of Metallurgical Slags Containing Multivalent Oxides, J. Am. Ceram. Soc. 91 (2008) 3342–3348. doi:10.1111/j.1551-2916.2008.02597.x.

[4] J. Heulens, B. Blanpain, N. Moelans, A phase field model for isothermal crystallization of oxide melts, Acta Mater. 59 (2011) 2156–2165. doi:10.1016/j.actamat.2010.12.016.

16. Conclusions and ideas for model improvements

16.1. Conclusions

To our knowledge, this is the first time that a realistic quaternary oxide system was modelled. We investigated the facetted growth and how the depth of the cusps in the anisotropy of the kinetic coefficient, influences the facetted growth of the spinel and the concentration levels within the remaining slag.

Comparison to experimentally observed microstructures for solid spinel particles, however, showed that only anisotropy for the kinetic coefficient probably does not suffice to obtain completely similar microstructures of the solid particles. Moreover, the upper boundary was set to be in contact with an atmosphere with a certain p_{O2}. This illustrated that an oxidative p_{O2}-value can inhibit the growth of the solid spinel particle.

However, it should be noted that the model at the moment still has some limitations. For example, the oxidation state of Cu-oxides in the FTOxid database of Factsage is assumed to be Cu^{+I}, thus the oxide assumed to form is Cu_2O. Figure 16.1 shows the distribution ratio (amount of the element in the slag / amount in the alloy) of Cu as a function of the partial pressure of oxygen. From the slope of this curve, Takeda et al. [1] state that copper dissolves in the slag in the mono-valent oxide form, i.e. $CuO_{0.5}$ or Cu_2O. However, "in the higher oxygen potential region, possible existence of the divalent form of copper, CuO, may also be suggested from the variation of the slope". This variation of the slope seems to take place at oxygen partial pressures higher than 10^{-4} atm.

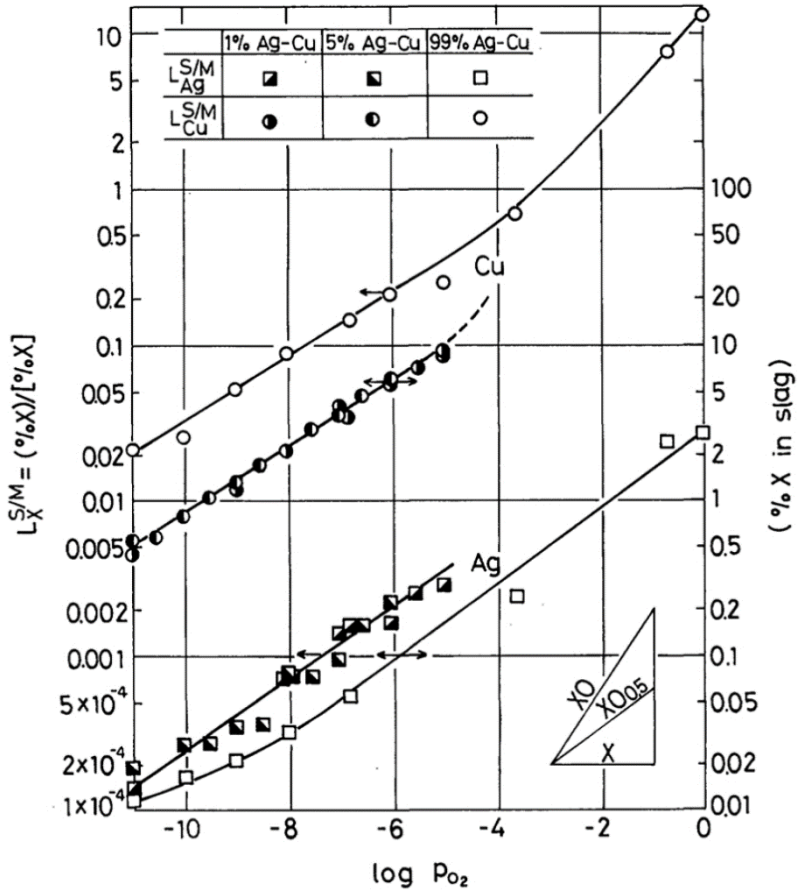

Figure 16.1 Distribution ratios of copper and silver plotted against oxygen potential at 1523 K. [1]

As the natural partial pressure of oxygen for the equilibrium slag is approximately $10^{-2.6}$ atm and the investigated p_{O2}-values lay in this range where oxidized copper would be present as CuO, this system would actually require the thermodynamic description of CuO as well. This equilibrium between CuO and Cu_2O is also a redox reaction in this system. However, at this moment, the oxidic database in Factsage does not acknowledge the existence of CuO, as only the component Cu_2O is contained within the FTOxid database. However, it should also be noted that the transition in slope in Figure 16.1 is not extremely pronounced and thus it would first need to be investigated whether this other oxidation state of Cu-oxides is observed in slags.

Moreover, the Stokes-Einstein equation was used to make an estimate for the mobility of Cu_2O. It is possible that this assumption oversimplifies the complex structure of the slag. In molten slags, the solvent molecules (silicate chains) vary in size with changing composition and the solute ions ($Mn^{2+/3+}$, $Fe^{2+/3+}$, Ca^{2+}) are of a similar or smaller size than the solvent molecules. Furthermore, the charged nature of the solute and solvent molecules reduces the random nature of the diffusion and makes the diffusion dependent on the possible interactions or the network-forming abilities. [2] This can be illustrated with the case of silicium: it has a lower ionic radius, which results in a larger interaction with the oxygen atoms and thus a slower diffusion.

Furthermore, for the composition investigated here, rather high p_{O2}-values were investigated, as compared to the experiments (in the range of 10^{-7}-$10^{-9.5}$ atm). Based on the composition, certain p_{O2}-values can be simulated, but this amount is limited due to numerical stability constraints. However, for other compositions, more reducing p_{O2}-values can probably be reached.

16.2. Future adaptations of the model

At the moment, the model considers mobility values for the solid and liquid only on the diagonal terms in the mobility matrix and the mobilities are chosen of the same order of magnitude in the two phases to avoid artificially high trapping of the phase fields. In reality, however, the mobility values of the different components in the solid will be of a different order of magnitude than the values within the liquid slag. Thus, an anti-trapping current, such as proposed by Karma and Rappel [3], must be implemented.

Ultimately, the multicomponent model would need to be extended to also consider the metallic liquid, to be able to investigate the attachment of metallic droplets to solid spinel particles in liquid slags. The properties of metals (assessed by most phase field models) and oxides (assessed by the model of Heulens) are quite different, but should be combined to finally investigate the interaction of metal droplets and solid particles in a real system. Therefore, the main focus of the future work is adding or adjusting specific features, to enable the investigation of both metals and oxides in one system. We refer to Appendix 1 for more details on how redox reactions were previously implemented in phase field models. The following paragraphs sum up which steps should be undertaken to extend the current model.

16.2.1. Addition of liquid metallic phase to the system

The models mentioned in Appendix 1 describe idealized systems and are only coupled to thermodynamic databases in a limited manner, as they assume ideal solutions or diluted solutions to describe the Gibbs free energies of the different phases. Therefore, possible future work would consist of extending the model by Heulens to also consider metals. The previous electrochemical

models consider the level of the charge separation, electrical fields and electrons, which would also influence the silicate-chains within the slag. Moreover, in the systems being considered here, high temperatures are present and then, the rapid charge redistribution assumption is valid. Because of this mass transfer limitation, the double layer for charge would not be required in the model. Thus, as electrons would not be considered within the model, the rheological behaviour of the metal droplets within the slags can be investigated without consideration of electrochemistry.

A first part of the extension of the model would be to consider the metallic droplet as an extra phase. This is in contrast with our binary model described in this doctoral work, where the metal was 'one part' of the liquid phase and where the two liquids were distinguished from each other by a difference in oxygen concentration and this resulted in gradient terms in the concentration field in the expressions for the interfacial energies. For the binary system, this could be approximated, but this is no longer the case for a multicomponent system. Therefore, the metallic droplet needs to be regarded as an extra phase.

In literature, the composition of the slag phase is mostly expressed in weight percentage of metal oxides. The use of oxides as components in a phase field model for oxide systems was chosen most suitable by Heulens [4], because oxides are often chosen as the independent components in the thermodynamic models for oxide systems (e.g. the Modified Quasi-chemical model), experimental diffusion data are frequently reported in the oxides and it allows distinguishing between different valences (e.g. FeO and Fe_2O_3). This description has one main disadvantage. It explicitly defines the oxygen content of the slag phase, which is directly related to the equilibrium partial pressure of oxygen. This means that the oxygen content of a slag cannot be changed without also changing the equilibrium partial pressure of oxygen and vice versa. Because we also want to describe a metallic phase, which contains almost no oxygen, instead of an oxide-description of the system, a set of elemental compositional variables would be needed e.g. a Cu droplet cannot be described by a set of mole fractions of oxidic components.

16.2.1.1. Elements instead of oxide compounds

By changing the system components from oxides to elements for silicate melts without multivalent cations, there is an extra degree of freedom in Gibbs' phase rule, which is removed by taking the activity of oxygen unity everywhere in the system. For silicate melts containing multivalent cations, such as FeO-Fe_2O_3-SiO_2, the oxygen activity depends on the local redox state of the melt. Furthermore, the number of components is the same in element or oxide form. [5] Thus, in a FeO-Fe_2O_3-Cu_2O-SiO_2 slag, four oxidic variables describe the composition or four elemental variables, i.e. Fe-Cu-Si-O, and these are linked to the oxidic variables through stoichiometry as follows:

$$\begin{aligned} x_{SiO2} &= \frac{n_{Si}}{2n_{Fe} - n_O + 3n_{Si} + n_{Cu}} \\ x_{Cu2O} &= \frac{n_{Cu}/2}{2n_{Fe} - n_O + 3n_{Si} + n_{Cu}} \\ x_{Fe2O3} &= \frac{n_O - 2n_{Si} - n_{Cu}/2 - n_{Fe}}{2n_{Fe} - n_O + 3n_{Si} + n_{Cu}} \\ x_{FeO} &= \frac{3n_{Fe} - 2n_O + 4n_{Si} + n_{Cu}}{2n_{Fe} - n_O + 3n_{Si} + n_{Cu}} \end{aligned} \quad \textbf{(16.1)}$$

Moreover, in most experimental observation techniques, for example EPMA measurements, only the 'FeO' amount can be measured, even though both Fe^{2+} and Fe^{3+} can be present. Furthermore, the goal of the future work would be to develop a model capable of describing microstructures resulting from redox reactions. This inherently involves the elements or ions instead of the oxidic components. Changing the compositional variables from oxide components to elements, requires the thermodynamic data of the elements, as well as diffusion mobilities of the elements.

16.2.1.1.1. Thermodynamic data of elements

Here we present a method to obtain the thermodynamic data of the elements from a database that is originally described as a function of compositions of the oxide components. In Chemapp, a component is a system-wide entity and in Chemapp, these are usually the elements. At complete equilibrium the chemical potentials of the respective system components (here the elements) are the same in the entire system and thus in all phases (which are in equilibrium with each other). [6] The latter sentence is the basis for the calculation of the chemical potentials of the elements in a certain phase, even though that phase might be described by the oxidic compositions in the database, i.e. it is not possible to obtain the chemical potential of an element in a slag phase which is described as a function of the oxidic components in a straightforward way and a small detour is required to obtain the required elemental chemical potential of the slag phase. For this, we need to ensure that the pure phases of the elements are present in the database.

Moreover, the chemical potential is equal for every component in all phases, both entered and dormant[22]. This is essential for the Chemapp-implementation as only the slag phase is considered to be entered, because slags can have supersaturated compositions during the simulations. Hence, by only entering the slag phase in Chemapp, the thermodynamic data for such a supersaturated slag can be calculated. However, the pure elemental phases should also be present in the database-file as these pure elemental phases are required to obtain the chemical potentials of the elements. These pure elemental liquids and solids should not be stable at equilibrium but are only required in the file to serve for the purpose of giving a proper reference state for the elements for which the chemical potentials are to be calculated.

First, an equilibrium calculation incorporating all relevant phases is required for different 'pure' situations, i.e. a system containing only 1 mole of a certain element with all the phases 'entered'. The next step is calculating the Gibbs free energy of the reference phase (this should not necessarily be the stable state if the element at the temperature under consideration, any pure elemental phase will do), this is called $G°_{element}$. This is calculated for all elements separately. Then all phases are put as 'dormant', except the phase for which the thermodynamic data should be collected (here the slag phase). The composition at which these thermodynamic values should be calculated are entered and then the chemical potential values of the elements are obtained by extracting the chemical potentials of the corresponding pure elemental phases (here the same pure elemental phases should

[22] In Chemapp (and Factsage), phases can be inserted into the system with a 'dormant' status. In such a case, only the activity of the components in that phase are calculated but that phase will not be taken into account in the mass balance. The chemical potential value of a component in a dormant phase is exactly the same as that of the same component in the same phase when that phase is entered, i.e. Chemapp calculates the activity of the dormant phase in equilibrium with the entered phases without letting the dormant phase form. Thus, the composition of the selected/entered phase will not change by selection of a number of dormant phases.

consistently be used as the one used to obtain the $G°_{element}$-values). However, these chemical potentials are calculated for phase constituents in Chemapp with a reference to the standard state of the pure phase at the chosen temperature, i.e. Chemapp returns the RT ln (a_i) term of the chemical potential without the $\mu_i°$ and thus it considers different standard states for different phases or temperatures. However, in the final phase field simulations, the 'absolute' chemical potentials, i.e. referred to the same standard state, are required to be able to simulate phase transitions. Thus, we need to add the obtained chemical potential value from Chemapp to the previously obtained $G°_{element}$-value, which is essentially the $\mu_i°$ value. In this way, the standard state for the chemical potentials is changed from the pure phase at the considered temperature to the standard state for the calculations of G, which is the most stable phase at 298.15K, because $G°_{element}$ is actually the ΔG-value for changing the reference temperature from the temperature of the calculation to 298.15K. Thus, $\mu_{element} = G°_{element} + \mu_{from\ Chemapp}$ will automatically yield the same standard state each time. From the $\mu_{element}$-values, the chemical diffusion potentials are obtained for all where Si is chosen to be the independent variable. The derivatives of the diffusion potentials to the mole fractions of the elements are determined according to the previously mentioned method.

It should be noted that oxygen is a special case, as there is no pure solid or liquid of this element possible. Thus, the chemical potentials should be calculated for O (or O_2) in the gas phase and then the $G°_{element}$ should be added to the $\mu_{from\ Chemapp}$-value. However, the $G°_{element}$-value should be calculated for a gas phase consisting of only O (or O_2) and thus the other O-components in the gas phase should be 'repressed', because the $G°_{element}$-value describes the ΔG-value for changing the reference temperature from the temperature of the calculation to 298.15K for a gas phase with only O (or O_2). Moreover, the chemical potential is defined as the change in the Gibbs free energy when 1 mole of a certain component (O or O_2) is added to the system under the form of the reference state. The reference states of O and O_2 are the same (O_2) and 1 mole O_2 = 2 mole O, this means a change in Gibbs free energy of twice the amount and that $\mu(O_2) = 2\mu(O)$, where the $\mu = G°_{element} + \mu_{from\ Chemapp}$ and was confirmed by Chemapp calculations. Here, the main interest lies in the value of O, as an elemental composition approach was chosen, as described previously.

16.2.1.1.2. Diffusion data

It is known that the diffusivity of an element through liquid metal is approximately an order of magnitude larger than diffusivity of the same element through liquid slag, thus diffusion through the slag phase is a rate-limiting step in the overall process. However, only a limited amount of diffusion mobilities for the metal cations in slags is available in literature. For example, the data found in [7] illustrates the limited amount of diffusivities of ions in slags at 1600°C in Figure 16.2.

Ion	D_i^*, cm^2/s
Si^{4+}, O^{2-}	$4 \times 10^{-7} - 1 \times 10^{-6}$
Al^{3+}	$\approx 1 \times 10^{-6}$
Ca^{2+}, Mg^{2+}, Fe^{2+}	$6 \times 10^{-6} - 1 \times 10^{-5}$
S^{2-}	$\approx 4 \times 10^{-6}$

Figure 16.2 Ionic diffusivities for a couple of ions in slags at 1600°C [7]

However, Dolan and Johnston [2] established an empirical model based on the correlation between optical basicity and diffusivity to determine the diffusion of metal cations in multicomponent slag systems. In their work, the multicomponent diffusion coefficients, D_{ij} are defined as

$$J_v^i = -\sum_{i=1}^{N} D_{ij}^v \frac{dC_j}{dx} \quad \textbf{(16.2)}$$

The term *J* is the flux of species *i*, *N* is the number of diffusing species, D_{ij} is the diffusion coefficient of species *i* induced by the concentration gradient in species *j*. *v* represents the solvent, here composed of Al_2O_3 and the free oxygen ions. The model takes into account properties of the bulk slag and the network forming ability of the diffusing species. The relative rate of diffusion of metal cations is proportional to the optical basicity coefficient of that species, while the rate of diffusion of all species increases exponentially with the calculated optical basicity of the bulk slag.

$$D_{ij}^v = (9.3\times10^{-10})\left(\frac{{\Lambda_j}^2}{\Lambda_i}\right)e^{12.5\Lambda} \quad \textbf{(16.3)}$$

Λ_i represents the optical basicity of component *i*, whereas Λ is the weighted average of the optical basicity [8]:

$$\Lambda = \frac{\sum x_i\, n_i \Lambda_i}{\sum x_i\, n_i} \quad \textbf{(16.4)}$$

Where x_i represents the mole fraction of the oxide component corresponding to the metal cation and n_i is the number of oxygen atoms in the corresponding oxide. The condition on the equation for the diffusion coefficient is that *j* = Si, or *j* = *i*. Equation (16.3) can calculate a multicomponent diffusion coefficient in a silicate system and gives the diffusivity at 1500 °C in $cm^2\ s^{-1}$ of D_{ii} or D_{iSi}, with a standard deviation of 15 percent.

It was determined previously that the main factors influencing the ionic diffusion in silicate slags are the bulk slag medium (characterized in the model by the optical basicity of the slag), the interaction between oxygen and metal ions (indicated by the optical basicity coefficient of the diffusing species) and the temperature of the system (which can influence the diffusion coefficient through an Arrhenius dependency). Other minor factors, such as concentration dependence, do not significantly alter diffusivity compared with those points listed previously, and can be ignored. [2]

The phase field model actually requires values for the mobility, which can be obtained from the diffusion matrix and the second derivative of the Gibbs energy. Care should be taken that the dependent variable (previously SiO_2) is the same for the *D* values and the second derivative of the free energy.

16.2.1.1.3. Stoichiometry of slag components

Since the electroneutrality has to be maintained, diffusion of a cation is accompanied by diffusion of the oxygen ion. This actually also takes into account the stoichiometry of the different oxidic slag components.

By only switching from an oxidic to an elementary description of the system's composition, without taking into account the electroneutrality or stoichiometry of the slag components, the implementation was found to give an error very quickly. To incorporate the stoichiometry of the slag components, lambda- or Lagrange-multipliers [9] could be included in the diffusion equation.

16.2.1.2. Extra liquid metal phase

At the moment, the derivatives $\partial m/\partial \eta_i$ and $\partial \kappa/\partial \eta_l$ are omitted in the basic model of Moelans [10] and Heulens et al. [4]. This has significant consequences for multi-junctions. These multi-junctions were not expected in the case of isothermal crystallization, as only two phases are present in that case. For more than two phases, problems might appear: angles that strongly deviate from values of 120° (i.e. angles of almost 180° or 90°) can encounter this effect and will thus not appear correctly in the simulations. In this case it would be more advisable to take the κ and m parameters as constant over the interfaces (thus without dependence on the phase field variables) and insert all anisotropy through the γ parameter. Unfortunately, in that case, the interface width is no longer constant for all interfaces.

16.2.2. More components

The original coupling to the thermodynamic database scanned the complete domain and as known, an increase in the number of components will increase the number of dimensions in the compositional domain. The scanning of a multi-dimensional compositional domain as such is easy to implement, but the output of the coupling to the thermodynamic database was saved in .txt files, which are inherently two-dimensional. Moreover, the discretization interval for the compositional domain was restricted to 0.005 due to memory limits. This larger discretization distance could influence the results. Thus, it became clear that the scanning of the complete compositional domain would become impractical for larger numbers of components.

16.2.2.1. Polyadic decomposition of incomplete tensors

Here, a possible solution for this 'curse of dimensionality'[11] is proposed, namely: randomly sampling the composition domain, followed by a canonical polyadic decomposition of these incomplete tensors. [12] This method was already used to describe the temperature-dependent Gibbs energy of a Sn-Cu-Ag liquid over the complete composition domain [13]. The global approximation error was 0.0010179 and the maximal relative point-wise error 0.012714. Note that a tensorial decomposition is only possible for more than three independent variables, thus a system with at least four components/elements is required.

A tensor is a multi-dimensional array, just as a matrix being a two-dimensional array and a vector being a one-dimensional array. The order of a tensor d equals the number of dimensions in the tensor, in this case equal to the number of independent composition variables, i.e. $N-1$. The number of elements in a tensor increases exponentially with the number of dimensions. [11] The size of a tensor contains the lengths of the tensor for every dimension, e.g. $I_1, I_2, \ldots, I_d$. The rank of a tensor is the rank of the decomposition, i.e. the tensor is approximated by an infinite sum of simple rank-1-tensors[23] and this sum is aborted at a certain point. The rank R is the smallest integer number of rank-1 tensors required to model the data. [14] A (canonical) polyadic decomposition or R-term representation is a decomposition in R rank-1 tensors, which are in turn the outer product of d vectors. This can be written as: [11]

[23] A rank-1 tensor is a tensor for which all elements can be obtained by a tensorial or outer product between d vectors. [14]

$$\mathcal{T} = \sum_{r=1}^{R} \bar{a}_r^{(1)} \otimes \bar{a}_r^{(2)} \otimes \cdots \otimes \bar{a}_r^{(d)} \quad \textbf{(16.5)}$$

The final result of the decomposition is an assembly of *d* 'factor' matrices ($A^{(1)}$, $A^{(2)}$, …, $A^{(d)}$) with *R* columns and I_1, I_2, …, I_d rows. The columns contain the vectors that will yield the rank-1 tensor through an outer product, i.e. the $\bar{a}_r$ vectors. The polyadic decomposition is called a canonical polyadic decomposition when the rank *R* is the minimum number of rank-1 terms needed for (16.5) to be exact. As the number of elements in a tensor increases exponentially with the number of dimensions and the number of free parameters in a decomposition increases linearly with the number of dimensions, such a decomposition can alleviate or remove the 'curse of dimensionality' otherwise inherently present in the use of tensors. [11] In cases where the rank *R* cannot be derived from the problem definition, finding this *R* is the difficult part of composing the decomposition.

Unfortunately, most decomposition algorithms require full tensors, making their use impractical for large data sets. The knowledge that the data is structured and can be represented by a small number of parameters can be exploited by sampling the tensor in only a few elements. Vervliet et al. [11] proposed algorithms for decompositions of such incomplete tensors, as illustrated in Figure 16.3.

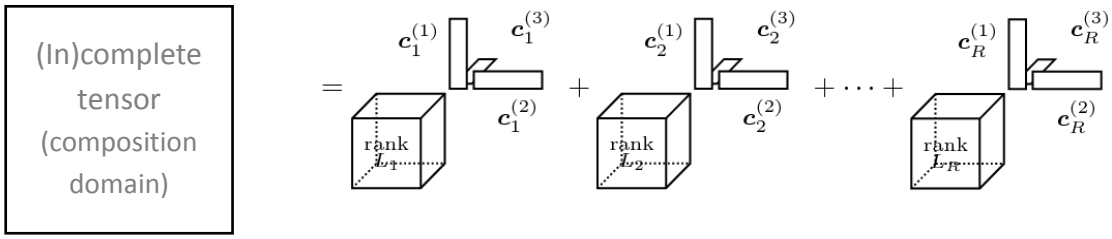

Figure 16.3 Schematic representation of polyadic decomposition of an incomplete tensor

They developed algorithms to compute the decomposition using only a few mode-n vectors of the incomplete tensors. Then they let compressed sensing type methods work on these tensors with only a few known elements. These compressed sensing methods reconstruct signals using only a few measurements taken by a linear projection of the original dataset.

The use of a sampling grid, however, yields a possible problem when the tensor is described as a function of the elemental composition domain. E.g. to obtain the thermodynamic data for the slag phase, the composition that was entered in Chemapp should correspond to a composition where the slag is 'stable' (it can be supersaturated in a certain component), an elemental composition with almost no oxygen will for example not yield a stable slag phase, as this is supposed to be composed of several metal oxides, and thus no thermodynamic data can be obtained for this phase at this composition. Thus, the use of the mode-n vectors to construct the incomplete tensors for the polyadic decomposition seems infeasible.

Therefore, the following artifice was implemented: the tensor is described as a function of the oxidic compositional domain for the slag (not for the metallic phase), but the thermodynamic data are obtained for the elements (e.g. the Gibbs energy, the chemical diffusion potential of the elements and the derivative of the latter to the elemental mole fraction). For this, first the composition is entered in Chemapp as mole fractions of the oxidic components. Then the mole fractions of the

elements corresponding to this composition are calculated and then the thermodynamic data are calculated. The conversion to the mole fractions of the elements is required to be able to determine the derivative of the chemical diffusion potentials of the elements to the mole fractions of the elements. In the phase field model, the elemental mole fractions will still be used and when thermodynamic data of the slag are required, the mole fractions of the oxidic components should be calculated according to (16.1). Then these mole fractions should be converted to the indices in the tensors, with the use of a linear map.

For phases described by a Braggs-William expression for the Gibbs free energy in the thermodynamic database, the configurational entropy is described by a summation of logarithmic terms ($RT(\sum_i x_i \log x_i)$). In practice, the polyadic decomposition of a tensor containing values where these logaritmic terms have been subtracted from, will be much easier and more accurate. These logarithmic terms, namely, go to infinity when the mole fractions go to infinity. These logarithmic terms are aftwerwards added again in the phase field model. Analogously for the chemical potential, the $RT(\log(x_i) - \log(x_{Si}))$ terms would be subtracted. Slags, however, are not described by a Braggs-William expression, but by the modified quasi-chemical model. This model does not contain these 'simple' logarithmic terms, but, as the actual expression is too complex to try to obtain the logaritmic terms, normal logarithmic terms were subtracted from the data, as explained above.

For the quaternary system we discussed in this chapter, the polyadic decomposition was made, based on the sampling of the complete dataset. The resulting tensorial decomposition of the Gibbs energy gave results that were accurate until the first digit after the comma (note that the Gibbs energy is of the order of magnitude of 10^{10} J/m³). This good fit is illustrated in Figure 16.4.

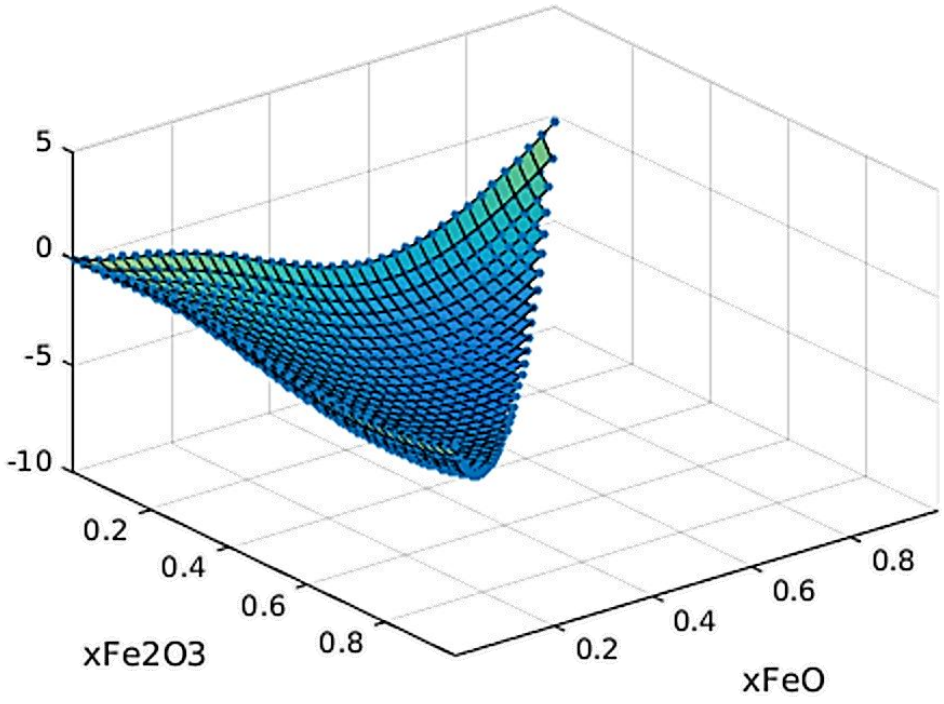

Figure 16.4 The Gibbs energy model obtained by polyadic decomposition (surface) and the original Gibbs energy data (blue dots) after normalization, i.e. subtraction of the plane specified by the Gibbs energies of the pure oxides.

In principle, an incomplete tensor would suffice, as long as the entries within that tensor lie on a random grid, which is not too big, as this determined the number of variables. The number of points

N for a certain variable (only varying one dimension of the tensor, while keeping the others constant) determines the accuracy for that variable according to approximately 1/*vN*.

16.2.2.2. Thermochemistry accelerator

As an alternative coupling to the thermodynamic database, Zietsman developed an efficient storage of slag thermochemical properties for use in multiphysics models [15] which can also be very interesting to model systems with more than four components. In this study, ChemApp was used to perform equilibrium calculations on six binary systems, four ternary systems and one quaternary system. The components that were used included Al_2O_3, CaO, MgO, and SiO_2. A standard set of calculations was done at 1% intervals from 0% to 100% along all composition axes, and at 50K intervals from 1300K to 2300K along the temperature axis. The results are presented in Figure 16.5.

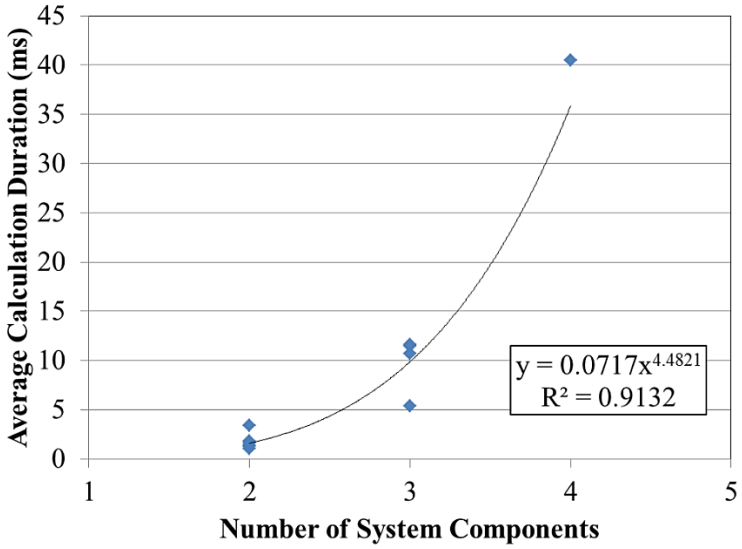

Figure 16.5 Duration of ChemApp equilibrium calculations on an Intel i7 3840QM 2.8 GHz CPU [15]

It is clear that calculation duration increases exponentially with the number of system components. This increase is one reason why it is infeasible to integrate thermochemical calculations of realistic systems directly into a multiphysics model. [15] He developed a software component that makes fast thermochemical calculations available for use in multiphysics models, based on geometrical considerations. The geometric approach (in Python) was able to perform the calculations between 15 and 20 times faster than ChemApp. It is expected that this acceleration will increase by 10 to 1000 times when the algorithms are translated to Fortran. This will provide acceleration between 150 and 20 000 times compared to ChemApp.

Some more general future work is listed in chapter 17.

References

[1] Y. Takeda, S. Ishiwata, A. Yazawa, Distribution Equilibria of Minor Elements between Liquid Copper and Calcium Ferrite Slag, Trans. Jpn. Inst. Met. 24 (1983) 518–528. doi:10.2320/matertrans1960.24.518.

[2] M.D. Dolan, R.F. Johnston, Multicomponent diffusion in molten slags, Metall. Mater. Trans. B. 35 (2004) 675–684. doi:10.1007/s11663-004-0008-6.

[3] A. Karma, W.-J. Rappel, Quantitative phase-field modeling of dendritic growth in two and three dimensions, Phys. Rev. E. 57 (1998) 4323–4349. doi:10.1103/PhysRevE.57.4323.

[4] J. Heulens, B. Blanpain, N. Moelans, A phase field model for isothermal crystallization of oxide melts, Acta Mater. 59 (2011) 2156–2165. doi:10.1016/j.actamat.2010.12.016.
[5] J. Heulens, Isothermal Crystallization of Metallurgical Slags: Phase Field Simulations Combined with In Situ Experiments (Isotherme kristallisatie van metallurgische slakken: faseveldsimulaties in combinatie met in situ experimenten), PhD thesis, KU Leuven, 2011. https://lirias.kuleuven.be/handle/123456789/318339.
[6] S. Petersen, K. Hack, The thermochemistry library ChemApp and its applications, Int. J. Mater. Res. 98 (2007) 935–945. doi:10.3139/146.101551.
[7] E.T. Turkdogan, R.J. Fruehan, Fundamentals of iron and steelmaking, Mak. Shap. Treat. Steel Steelmak. Refin. Vol. 11th Ed RJ Fruehan Ed AISE Steel Found. Pittsburgh. (1998) 125–126.
[8] K.C. Mills, L. Yuan, R.T. Jones, Estimating the physical properties of slags, J. South. Afr. Inst. Min. Metall. 111 (2011) 649–658.
[9] E.W. Weisstein, Lagrange Multiplier, (n.d.). http://mathworld.wolfram.com/LagrangeMultiplier.html (accessed February 28, 2017).
[10] N. Moelans, A quantitative and thermodynamically consistent phase-field interpolation function for multi-phase systems, Acta Mater. 59 (2011) 1077–1086. doi:10.1016/j.actamat.2010.10.038.
[11] N. Vervliet, O. Debals, L. Sorber, L. De Lathauwer, Breaking the curse of dimensionality using decompositions of incomplete tensors : Tensor-based scientific computing in big data analysis, IEEE Signal Process. Mag. 31 (2014) 71–79.
[12] N. Vervliet, L.D. Lathauwer, A Randomized Block Sampling Approach to Canonical Polyadic Decomposition of Large-Scale Tensors, IEEE J. Sel. Top. Signal Process. 10 (2016) 284–295. doi:10.1109/JSTSP.2015.2503260.
[13] N. Vervliet, Sn-Cu-Ag dataset - Liquid test sample, (2014).
[14] B. Weitz, Exploring Tensor Rank, (2011).
[15] J.H. Zietsman, Efficient Storage and Recall of Slag Thermochemical Properties for Use in Multiphysics Models, in: Adv. Molten Slags Fluxes Salts Proc. 10th Int. Conf. Molten Slags Fluxes Salts 2016, Springer, Cham, 2016: pp. 635–644. doi:10.1007/978-3-319-48769-4_68.

E. Conclusion

“In theory, there is no difference between practice and theory. In practice, there is.”

- Yogi Berra (Yankees player)

17. General conclusion and future work

During pyrometallurgical production processes, metal losses in slags, under the form of attached metal droplets to solid particles, are a major issue and limit the overall process efficiency. As these losses have both an economic and possibly ecologic impact, a fundamental understanding of this interaction is required. The goal of this work was to develop a fundamental understanding of the system in which the attachment of metal droplets to solid particles in liquid slags is observed. For this, a combined experimental – phase field modelling approach was used. This chapter summarizes the main results of the different parts of this work.

17.1. Binary model for droplet behaviour

In a first stage, a binary model was used to investigate the growth and wetting behaviour of metal droplets to a non-reactive solid particle. In practice, when a fraction of the metallic phase is attached to the solid particles, this fraction cannot settle and the yield of the phase separation will decrease, which in turn means an important loss of valuable metals in several industries. Several influencing factors were studied: the initial supersaturation of the liquid, the interfacial energies, the particle morphology (particle fraction, perimeter, shape and distribution), initialization method, movement of the solid particle and the speed of movement of the solid particle.

It was observed during the spinodal decomposition of the supersaturated liquid, that first 'localized' spinodal decomposition took place near the solid particle, then, the non-localized decomposition occurred in the remaining supersaturated liquid. Finally, Ostwald ripening and coalescence took place. The simulations showed that the attached droplets did not have preferred positions, as various places with several configurations and variations in time were encountered.

Varying the interfacial energies, resulted in various wetting regimes. Four categories could be made: no wettability of the metal on the particle, low wettability, high wettability and full wetting. This subdivision gave the opportunity to classify experimental observations of attached metal droplets. A higher initial supersaturation generally resulted in a higher metal fraction in the system. The effect of the initial supersaturation on the fraction of attached metal was, however, not fully conclusive and also varied with time.

As the fraction of solid particles in the system decreased, a lower fraction of metal was attached to the solids. In the case of low wettability, the amount of attached metal did not increase with an increasing perimeter per area of the solid particle. For high wettability, on the contrary, an increase in attached metal for an increasing perimeter per area was observed.

The shape of the particles was also varied. No clear trends were discovered regarding the shape of the particles. Nevertheless, it became clear that several small particles yielded more attached metal than one large particle. The distance between the particles slightly influenced the amount of metal attached, as the metallic droplets do orient themselves away from the other solid particles when these are too close to one another. Moreover, some of the simulations with particles with cavities confirmed that not only the perimeter per area, but also the available space for the droplet to grow was an important factor.

The model was also extended to consider realistic microstructures based on actual micrographs of the solid particles. The origin of the attachment was investigated by comparing two initialization methods for the metal droplets: by spinodal decomposition of a supersaturated liquid, corresponding

in practice to a reactive origin of the droplets, and a method with random positioning of the droplets, corresponding to the separate formation of particles and droplets. Based on previous research, both methods were considered for two wettability regimes: no and low wettability. From a simulation point of view, the random initialization allows for more flexibility in the metal fraction of the system as there are no restrictions on the metal volume fraction f_v, as opposed to the spinodal decomposition, where the initial supersaturation x_i should be selected in between the inflection points of the free energy curve representing the spinodal. The random initialization, however, has a much larger spread on the results than the spinodal initialization. Consequently, a larger number of simulations are required to draw relevant conclusions for the random initialization than when the droplets form through spinodal decomposition of a supersaturated slag, since the droplets are then first formed close to the particle. In the non-wetting case, the spinodal initialization gave microstructures with the best correspondence with the experiments, but in the low wettability case, the simulation results of both initialization methods correspond well with the experimental system.

Afterwards, it was investigated how rigid body motion of the solid particle influences liquid metal droplet attachment to that solid particle in liquid slags with a phase field model. With respect to the amount of attached metal, no actual trends could be observed. At no wettability, the microstructures show that the rigid body motion could either 'pick up' droplets, hereby increasing the amount of attached metal, or it can lose an already attached metal droplet. The low wettability case is similar, but the loss of an already attached droplet was not observed. However, this might no longer be the case if the solid particle moves faster. At higher wetting regimes and full wetting, the influence of the rigid body motion seems to be smaller, as the attachment is more determined by the interfacial energies and the metallic phase 'follows' the solid particle when it moves. Again, this might no longer be the case if the solid particle moves faster. However, on average there is no effect on the amount of metal attached to the solid particle.

A major observation, on the other hand, is the fact that the apparent contact angle of the metal is larger when rigid body motion is present, which corresponds to a lower apparent wettability. This effect was very clear, even at the small rate at which the solid particle moved in this study. This fact could indicate that a previous classification of the experimental PbO-FeO-CaO-SiO_2-Cu_2O-ZnO-Al_2O_3 system as a system with very low wettability has to be revised.

The study on the influence of the speed of the rigid body motion showed that there is a trade-off between the speed of the movement of the liquid metal on the one hand, which depends on the attraction of the metal towards the solid particle by interfacial energies and the speed of the movement of the solid particle, which we varied. For slow solid motion, the interfacial energies have the upper hand, but for larger velocities, the metal cannot necessarily keep up with the movement of the solid. Thus, the amount of metal will decrease for faster movement. However, this is only the case for the low and high wettability regimes. For the non-wetting case, metal droplets coincidentally present on the path of the solid particle will get attached, but the solid particle movement can similarly decrease the amount of the attached metal by moving away from the metal droplet. On the other hand, for the very high (almost full) wetting case, the interfacial energy attraction of the metal to the solid is so large that even the largest velocity did not decrease the amount of attached metal.

For the real-micrograph-base simulations, the simulations in the absence or presence of rigid body motion for the spinodal initialization correspond better to the experimentally observed micrographs than the one with the random initialization. Moreover, the trends for the different wetting regimes

observed for a single solid particle from our previous work [1] were still valid for multi-particle systems.

The better correspondence to the spinodal initialization shows that the droplet-particle interaction could result from a reactive origin, as was also confirmed by experimental findings of De Wilde et al. [2–7] in a synthetic slag system. These show the growth of solid spinel particles on the edge of already existing metallic droplets or their formation together with new droplets. They also proposed a mechanism for this observation: the spinel solids and copper droplets form together due to a simultaneous reduction of copper oxides into metallic copper and the oxidation of slag oxides into more stable spinel structures. Additionally, the spinel solids can also form on an already present Cu droplet in an analogous way. Moreover, experimentally, the actual 'attachment' of the droplets seems to be a non-equilibrium phenomenon, which is in correspondence with the results for the spinodal initialization, as in that case the droplets are first attached to the solid as they are formed simultaneously and are afterwards also detached/dissolved. Explicit implementation of a model of the formation of the solid particles within a liquid slag on the side of or together with a metal droplet in a multicomponent multiphase system will allow to simulate and study the reactive origin for the attachment in more detail

17.2. Experiments

Previous work by De Wilde et al. [3,4] suggested that sticking droplets can originate from a chemical reaction. A reaction scheme was proposed, where, on the one hand, the spinel solids and copper droplets form together due to a simultaneous reduction of copper oxides into metallic copper and, on the other hand, slag oxides oxidize into more stable spinel structures. Additionally, the spinel solids can also form by heterogeneous nucleation on an already present Cu droplet in an analogous way.

This hypothesis was based on the observations made during a sessile drop experiment of both Cu and slag on top of a $MgAl_2O_4$ substrate [4]. An extensive microstructural study afterwards showed the presence of small entrained copper droplets attached to spinel particles, leading to the reactive origin hypothesis. However, during the experiment, the copper droplet moved towards the slag droplet and a certain emulsification took place between the slag and copper droplet, after which the copper droplet positioned itself on top of the slag droplet. This emulsification step could in fact also be responsible for the presence of the small metal droplets attached to spinel particles within the large slag droplet.

To investigate the hypothesis, adapted sessile drop experiments were performed, in which both copper alloys and slag were placed on a spinel substrate. Several copper-silver alloys, a synthetic PbO-CaO-SiO_2-Cu_2O-Al_2O_3-FeO-ZnO slag and a $MgAl_2O_4$ substrate were used to represent the copper alloy droplets, slag and spinel solids, respectively. The silver was added to the copper alloy as a trace element to get more insights into the origin of the attachment.

The microstructures within the different samples were studied and the compositions of the different phases present were determined. Small entrained copper droplets sticking to spinel solids were present within the large slag droplet. It is suggested that these droplets form either during a reaction alone or a combination of dispersion and reaction. In the latter case, during the coalescence phase in the high temperature CSLM experiment, some small Cu-Ag droplets are dispersed within the large slag drop. These Cu-Ag droplets then act as nucleation sites for a simultaneous reduction of copper

oxides into metallic copper and the oxidation of slag oxides into more stable spinel structures. In this way, the spinel solids grow at the side of the Cu-Ag droplets, which in turn are enriched with Cu and grow. This leads to copper droplets attached to spinel solids within the slag phase.

Moreover, a high-temperature smelting experiment was executed. The methodology was adapted from previous studies [8,9] to be able to perform these experiments with as few components as possible. The latter is meant for a comparison to modelling results, for which more components in the system result in more computational time required. An oxidation-reduction experiment in the Fe-Si-Al-O system with Cu-Ag droplets was executed. For the copper to be precipitated, copper should first be dissolved in the slag by oxidizing the system, followed by reducing the system to lower the solubility of copper in the slag in turn.

The amount and size of copper droplets increase during the complete experiment. Moreover, the composition of the spinel particles changes during the reductive part. This is in accordance with the expectations from the suggested mechanism during the reductive part, but during the oxidation part, this is not expected. Because the system was left to rest before the start of the oxidative part of the experiment, it is possible that the disturbance of the underlying alloy layer by the blowing of the gas through the slag phase, introduces small metal droplets into the slag phase.

During oxidation, iron oxide has a tendency to shift towards Fe_2O_3 and the metallic copper is oxidized. During the reductive part of the experiment, a lack of oxygen becomes apparent and because copper is more noble than iron, Cu_2O acts as oxygen donor for the oxidation of iron oxide, thereby precipitating metallic copper: $2FeO + Cu_2O <-> 2Cu^0 + Fe_2O_3$. The resulting increase of Fe_2O_3 leads to the formation of magnetite spinel particles by reaction with FeO.

In both experiments, silver was added to the copper alloy as a trace element to get more insights into the origin of the attachment. The fact that this silver is present in the attached copper droplets in a smaller concentration than in the master alloy in both studies indicates that the origin of the attachment is not purely dispersive. Therefore, the attached metal droplets can be formed either due to a purely reactive formation (simultaneous reduction of copper and silver oxides to metallic phase and the oxidation of slag oxides to spinel) or a combination of dispersion and reaction. In the latter case, small Cu-Ag droplets are introduced in the slag during the emulsification step or during the first oxidative blow. Afterwards, these droplets act as nucleation sites for a simultaneous reduction of copper oxides into metallic copper and the oxidation of slag oxides into more stable spinel structures. In this way, the spinel solids grow at the side of the Cu-Ag droplets, which in turn are enriched with Cu and grow. This leads to copper droplets attached to spinel solids within the slag phase.

17.3. Multicomponent model for solid spinel growth

This is the first time that a realistic quaternary oxide system was modelled. The model is an extension of the model of Heulens [10]. The facetted growth was investigated and it was examined how the depth of the cusps in the anisotropy of the kinetic coefficient influences the facetted growth of the spinel and the concentration levels within the remaining slag.

Comparison to experimentally observed microstructures for solid spinel particles, however, showed that only anisotropy for the kinetic coefficient probably does not suffice to obtain completely similar microstructures of the solid particles. Moreover, the upper boundary was set to be in contact with

an atmosphere with a certain p_{O2}. This illustrated that an oxidative p_{O2}-value can inhibit the growth of the solid spinel particle.

17.4. Future work

Throughout this work, some possibilities for future work were already indicated. The following paragraphs give a brief overview of some possible research opportunities for the future.

17.4.1. Modelling

Once the multicomponent model works for elements as system compounds instead of the oxide compounds, the behaviour of a metal droplet within a real metallurgical slag can be examined. The growth kinetics and morphologies can be predicted by the model. Moreover, the interaction between the metal droplets and solid particles can be investigated. The different origins can be investigated: whether the solid grows on a droplet or the other way around or both phases are present and get attached to one another.

For more realistic simulations, the incorporation of the reaction kinetics of the different phases could be a next possible step. At the moment, the simulations assume diffusion-controlled growth, which is not always the case in reality. Experimental investigation of slag reduction to form a metallic phase has been performed previously [11–17], as was the formation and growth of spinel crystals [18–23]. However, this research only considers the 'global' reaction kinetics, which yields empirical correlations between the overall reaction rate and the reaction conditions. A more systematic investigation, i.e. based on the underlying chemistry in terms elementary reaction steps and taking into account possible diffusional limitations would provide better insights in the reaction kinetics.

Other improvements mainly consider obtaining more and reliable input data of slags, as this data is very scarce at the moment. This can be done by experimental work, but usually experimental determination is very intricate, e.g. for diffusional data and interfacial and surface energies

To resolve this issue, coupling to ab-initio models or free volume based models can be used for the diffusional data. Calculation of surface tension might also be possible using Chemapp [24] according to the Butler equation, i.e. assuming that a system is composed of two distinct phases: bulk (b) and surface (s). The surface is assumed to be a mono-atomic layer and the two phases are assumed to be in equilibrium. This method was already used for binary alloys [24], but could be extended to multicomponent mixtures [25].

As shown by our binary model results, the movement of the solid particle can influence the wetting behaviour of the metal on the solid particle. In a next step, the model can either be linked to Navier-Stokes equations to include convection. Alternatively, the profile of the phase field variables can be shifted in very small steps, as was illustrated in this work.

17.4.2. Experimental

The experiments in this work showed that the redox reaction involving Fe laid at the base of the attachment of the metal droplets to the solid particles within the slag. Extra experiments without multivalent cations, but under the same circumstances could confirm the hypothesis of the reactive origin. Moreover, using other multivalent slag components, e.g. MnO/Mn_2O_3, CrO/Cr_2O_3, TiO_2/Ti_2O_3, can be used in another experiment as well.

Furthermore, it would be interesting to further explore the possibilities of the confocal scanning laser microscope. This set-up allows for the in-situ addition of for example a metal drop in a liquid slag. Clearly, these experiments are very intricate. With respect to the sessile drop experiments, additional experiments can be performed, during which the compositions of the spinel, slag and copper droplets are systematically varied, in combination with a variation of the oxygen partial pressure or other known surface-active elements such as sulphur.

In addition, it would also be helpful to explore the effect of stirring and bubbling on the attachment of spinel solids in slags. Therefore, an experiment needs to be designed which allows to detect or quantify the influence of the stirring rate and conditions on the formation of attached droplets.

References

[1] I. Bellemans, N. Moelans, K. Verbeken, Influence of rigid body motion on the wetting and attachment of metallic droplets to solid particles in liquid slags – a phase field study, Miner. Metall. Process. (Submitted).

[2] E. De Wilde, I. Bellemans, M. Campforts, A. Khaliq, K. Vanmeensel, D. Seveno, M. Guo, A. Rhamdhani, G. Brooks, B. Blanpain, N. Moelans, K. Verbeken, Wetting behaviour of Cu based alloys on spinel substrates in pyrometallurgical context, Mater. Sci. Technol. 31 (2015) 1925–1933. doi:10.1179/1743284715Y.0000000052.

[3] E. De Wilde, I. Bellemans, L. Zheng, M. Campforts, M. Guo, B. Blanpain, N. Moelans, K. Verbeken, Origin and sedimentation of Cu-droplets sticking to spinel solids in pyrometallurgical slags, Mater. Sci. Technol. 32 (2016) 1911–1924. doi:10.1080/02670836.2016.1151998.

[4] E. De Wilde, I. Bellemans, M. Campforts, M. Guo, B. Blanpain, N. Moelans, K. Verbeken, Investigation of High-Temperature Slag/Copper/Spinel Interactions, Metall. Mater. Trans. B. 47 (2016) 3421–3434. doi:10.1007/s11663-016-0805-8.

[5] I. Bellemans, E. De Wilde, L. Claeys, T. De Seranno, M. Campforts, B. Blanpain, N. Moelans, K. Verbeken, Investigation of reactive origin for attachment of Cu-droplets to solid particles, Metall. Mater. Trans. B. (2017).

[6] E. De Wilde, I. Bellemans, M. Campforts, M. Guo, B. Blanpain, N. Moelans, K. Verbeken, Sessile drop evaluation of high temperature copper/spinel and slag/spinel interactions, Trans. Nonferrous Met. Soc. China. 26 (2016) 2770–2783. doi:10.1016/S1003-6326(16)64344-3.

[7] E. De Wilde, I. Bellemans, M. Campforts, M. Guo, K. Vanmeensel, B. Blanpain, N. Moelans, K. Verbeken, Study of the Effect of Spinel Composition on Metallic Copper Losses in Slags, J. Sustain. Metall. 3 (2017) 416–427. doi:10.1007/s40831-016-0106-0.

[8] E. De Wilde, Methodology Development and Experimental Determination of the Origin of Sticking Copper Droplets in Pyrometallurgical Slags, PhD thesis, Ghent University, 2015.

[9] E. De Wilde, I. Bellemans, S. Vervynckt, M. Campforts, K. Vanmeensel, N. Moelans, K. Verbeken, Towards a methodology to study the interaction between Cu droplets and spinel particles in slags, in: Proc. EMC 2013, 2013: pp. 161–174.

[10] J. Heulens, B. Blanpain, N. Moelans, Phase field modeling of the crystallization of FeOx–SiO2 melts in contact with an oxygen-containing atmosphere, Chem. Geol. 290 (2011) 156–162. doi:10.1016/j.chemgeo.2011.09.005.

[11] P.C. Hayes, Stability Criteria for Product Microstructures Formed on Gaseous Reduction of Solid Metal Oxides, Metall. Mater. Trans. B. 41 (2010) 19–34. doi:10.1007/s11663-009-9301-8.

[12] S.P. Matthew, P.C. Hayes, Microstructural changes occurring during the gaseous reduction of magnetite, Metall. Trans. B. 21 (1990) 153–172. doi:10.1007/BF02658127.

[13] S.P. Matthew, T.R. Cho, P.C. Hayes, Mechanisms of porous iron growth on wustite and magnetite during gaseous reduction, Metall. Trans. B. 21 (1990) 733–741. doi:10.1007/BF02654252.

[14] D.H.S. John, S.P. Matthew, P.C. Hayes, The breakdown of dense iron layers on wustite in CO/CO2 and H2/H2O systems, Metall. Trans. B. 15 (1984) 701–708. doi:10.1007/BF02657292.
[15] P.C. Hayes, A Review of the Mechanisms of Decomposition of Solids and Their Relevance to Extractive Metallurgical Processes, Miner. Process. Extr. Metall. Rev. 8 (1992) 73–94. doi:10.1080/08827509208952679.
[16] T. Hidayat, M.A. Rhamdhani, E. Jak, P.C. Hayes, Investigation of Nickel Product Structures Developed during the Gaseous Reduction of Solid Nickel Oxide, Metall. Mater. Trans. B. 40 (2009) 462–473. doi:10.1007/s11663-009-9247-x.
[17] T. Hidayat, M.A. Rhamdhani, E. Jak, P.C. Hayes, On the Relationships between the Kinetics and Mechanisms of Gaseous Hydrogen Reduction of Solid Nickel Oxide, Metall. Mater. Trans. B. 40 (2009) 474–489. doi:10.1007/s11663-009-9239-x.
[18] S.A. Nightingale, B.J. Monaghan, Kinetics of Spinel Formation and Growth during Dissolution of MgO in CaO-Al2O3-SiO2 Slag, Metall. Mater. Trans. B. 39 (2008) 643–648. doi:10.1007/s11663-008-9186-y.
[19] L. Scheunis, M. Campforts, P.T. Jones, B. Blanpain, A. Malfliet, The influence of slag compositional changes on the chemical degradation of magnesia-chromite refractories exposed to PbO-based non-ferrous slag saturated in spinel, J. Eur. Ceram. Soc. 35 (2015) 347–355. doi:10.1016/j.jeurceramsoc.2014.08.017.
[20] K. Nagata, R. Nishiwaki, Y. Nakamura, T. Maruyama, Kinetic mechanisms of the formations of MgCr2O4 and FeCr2O4 spinels from their metal oxides, Solid State Ion. 49 (1991) 161–166. doi:10.1016/0167-2738(91)90081-L.
[21] C. Greskovich, V.S. Stubican, Interdiffusion studies in the system MgO-Cr2O3, J. Phys. Chem. Solids. 30 (1969) 909–917. doi:10.1016/0022-3697(69)90288-1.
[22] A. Semykina, J. Nakano, S. Sridhar, V. Shatokha, S. Seetharaman, Confocal Microscopic Studies on Evolution of Crystals During Oxidation of the FeO-CaO-SiO2-MnO Slags, Metall. Mater. Trans. B. 41 (2010) 940–945. doi:10.1007/s11663-010-9392-2.
[23] A. Semykina, J. Nakano, S. Sridhar, V. Shatokha, S. Seetharaman, Confocal Scanning Laser Microscopy Studies of Crystal Growth During Oxidation of a Liquid FeO-CaO-SiO2 Slag, Metall. Mater. Trans. B. 42 (2011) 471–476. doi:10.1007/s11663-011-9505-6.
[24] T. Tanaka, K. Hack, S. Hara, Calculation of surface tension of liquid Bi□Sn alloy using thermochemical application library ChemApp, Calphad. 24 (2000) 465–474. doi:10.1016/S0364-5916(00)85001-4.
[25] S.-K. Kim, W. Wang, Y.-B. Kang, Modeling surface tension of multicomponent liquid steel using Modified Quasichemical Model and Constrained Gibbs Energy Minimization, Met. Mater. Int. 21 (2015) 765–774. doi:10.1007/s12540-015-4619-z.

F. Appendix

“How to quote an appendix?”

- Kim Verbeken

18. Phase field modelling of redox reactions: previous work [24]

Redox reactions occur quite frequently in pyrometallurgy, even though most of the times, an electrode is not explicitly present in the system. The reaction of iron oxide dissolved in liquid slag with solid carbon or carbon from a metal bath is used in iron making processes. Modern electric arc furnaces employ the same reaction to induce slag foaming, thereby increasing efficiency of the furnace. [1,2] With a different purpose, iron oxide is reduced by injected carbon in the 'slag cleaning' stage of copper making processes. This reduces the present magnetite in the slag and thus lowers the slag viscosity, moreover, physical entrainment of copper matte in the slag is reduced. [3] Few existing phase field models include the aforementioned redox reactions, which can take place at the interface between an electrolyte and a cathode or the interface between a metal and an oxide. The phase field formulation of the electrochemical process is not straightforward because a model of the electric field has not been established for this method. Thus, a few phase field models considering electrochemical reactions are presented in literature. Moreover, they are usually not coupled to realistic systems. The different systems concerning redox reactions that were already described with phase field models, are summarized in the following paragraphs.

18.1. Redox reactions on double-layer scale

Guyer et al. [4,5] developed a diffuse interface model for such a system. With a set of simple assumptions, the model captures the charge separation associated with the equilibrium double layer at the electrochemical interface for both electrodeposition and electrodissolution. The presence of charged species leads to rich interactions between concentration, electrostatic potential and phase stability. Poisson's equation (18.1) was solved for the electrostatic potentials arising from the charge density of the components.

$$\nabla \cdot [\varepsilon(\xi)\nabla\phi] + \rho = 0 \qquad \textbf{(18.1)}$$

With ε(ξ) the dielectric constant, which is a function of the phase field ξ, ϕ the potential and ρ the charge density. However, it is complicated to solve Poisson's equation for the electrostatic potential from the component itself since it is numerically challenging to solve this equation coupled with a time-dependent partial differential equation, resulting in a small time scale and meshing in space, as illustrated by the resulting interface profile during electrodeposition in Figure 18.1. Thus, it has only been solved in one dimension. The interface between the phases is a very localized change of the phase variable and is described well by the model. The need to resolve the charge distribution in close proximity of the interface, however, requires discretization of the electrochemical double layer and thus also limits the size of the domain and the time span that could be modelled. This model indicates that the phase field model is suitable to model redox reactions but it considers an idealized system with only two phases (namely an electrode-electrolyte system). This is a nice model for investigating the scale of the interfacial double layer, but it is computationally too intensive to study the morphological changes resulting from redox reactions.

[24] This chapter is based on the following publication: I. Bellemans, E. De Wilde, N. Moelans, K. Verbeken, Metal losses in pyrometallurgical operations - a review, Advances in Colloid and Interface Science. Submitted

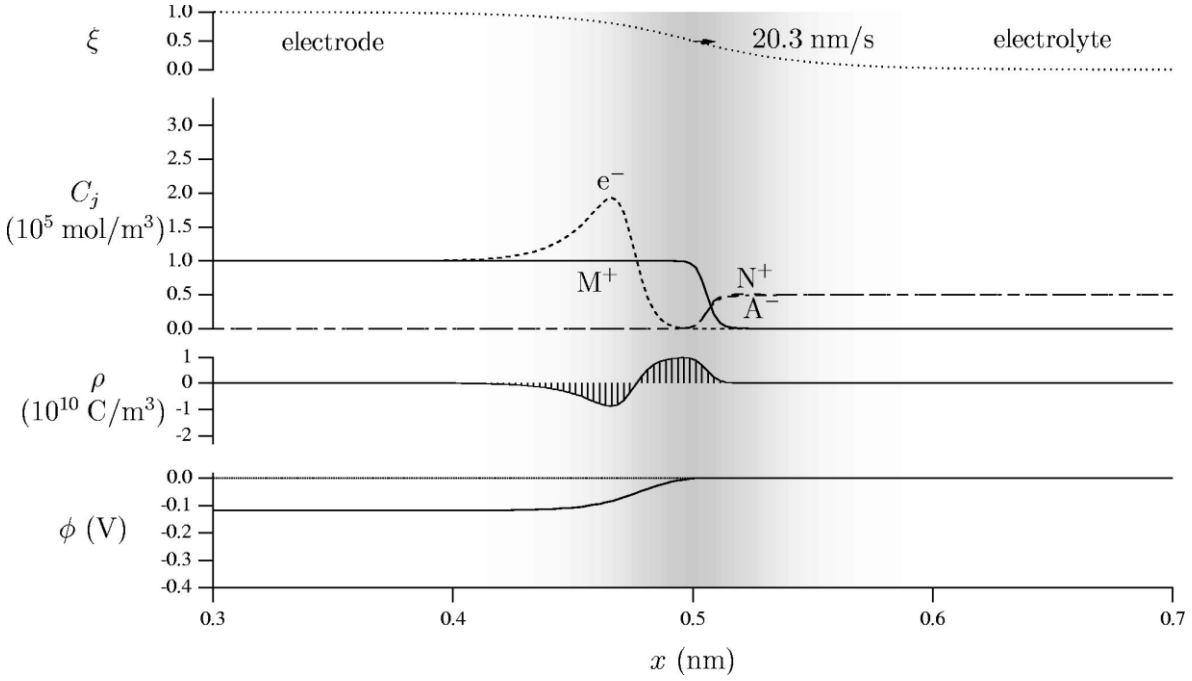

Figure 18.1 Interface profiles for steady state electrodeposition with i=-10² A/m². The concentration profiles for N^+ and A^- are almost coincident on this scale. g(ξ) is mapped onto the background in gray to indicate the location of the phase field interface. [5]

18.2. Redox reactions on larger scale

Before Guyer et al. [4,5] developed their model, Dussault and Powell [6] described a diffuse interface model for a two component liquid/liquid, isothermal system undergoing transport limited electrochemical reactions, by assuming charge neutrality everywhere. First, very general forms of the governing equations were derived after which different scales were derived, which in turn were used to simplify the governing equations. E.g. the conservation of charge equation involved only voltage with a spatial derivative after the simplification, without the originally present concentration or velocity. The electrical potential is only mentioned in the molar flux in a migration term, but the expression for the total free energy of the system itself does not contain the electrical potential. Thus their approach neglects the effects of charge at the interfacial double layer, resulting in the modelling of larger domains and time spans than Guyer et al. [4,5] but without the examination of the physics of the electrocapillary interface. In one of their simulations to resemble the Electric-Field-Enhanced Smelting and Refining (EFESR) process, an isolated Fe droplet was added to the slag layer (FeO). As shown in Figure 18.2, under an electric field, an isolated Fe droplet migrates through the slag. Comparing the result to the zero-voltage result, the drop and the interfaces migrate towards the anode. Also, due to the relatively high voltage gradients near the droplet, a streamer is formed on the cathode.

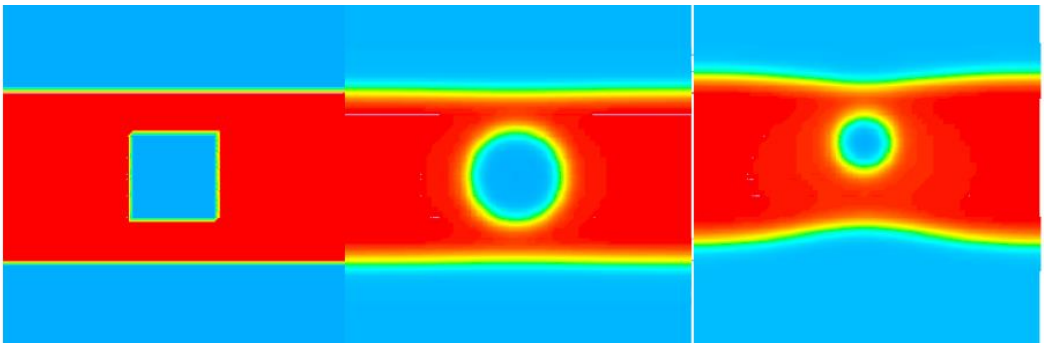

Figure 18.2 Phase field model of droplet migration in the Fe-FeO system, setting the voltage to one at the upper boundary and zero at the lower boundary, with insulating conditions on the sides, makes the bottom Fe layer the cathode and the top the anode. Left: initial condition; Middle: zero-field result; Right: field concentration leading to drop migration. Colour represents oxide ion concentration, with the centre slag layer at its maximum and the outer metal layers at zero. [6]

Assadi [7] used a phase field model to investigate the electro-deoxidation of a solid oxide in a molten salt. I.e. the direct electrochemical reduction of solid oxides in molten salts, during which the oxygen is removed from the solid oxide. The model takes into account oxygen diffusion, electric current, concentration dependence of electrical conductivity and interfacial electrochemical reactions in simple model systems. This model used the continuity of current density as the governing equation for electrical potential, except at the cathode-electrolyte interface. Its diffuse interface was between the metal and oxide in the cathode, and it assumed a sharp interface between the cathode and molten salt, with ohmic resistance at that sharp interface. The use of the sharp interface prevents its use to describe plating from the electrolyte, so this model is limited in application to electro-deoxidation; the assumption of ohmic resistance at the interface also limits it to small overpotentials [8]. The resulting simulations illustrate general features, such as a changing electric-potential drop at the cathode interface. The first results for a one-dimensional system show a transition from diffusion-controlled kinetics to kinetics controlled by electric conduction with decreasing oxide/metal conductivity ratio. For the two-dimensional system, nevertheless, the overall kinetics of electro-deoxidation is predominantly controlled by the diffusion of oxygen in cathode.

Another phase field model, developed by Pongsaksawad et al. [8], improved the formulation of Dussault and Powell [6] by taking the electrostatic contribution in the free energy term into account, similar as presented by Guyer et al. [4,5]. The binary model describes the electrochemical interface dynamics and studies the changes in cathode shape and topology. In this model, the interfacial double layer is negligible. Transport-limited electrolysis and rapid charge redistribution are assumed. Under this first condition, the mass-transfer resistance is much greater than the charge-transfer resistance. This means that cations recombine with electrons as soon as the ions reach the cathode interface. This transport-limited condition is valid at high temperatures (e.g. in metal smelting processes). Low-temperature processes, in contrast, are limited by charge transfer, which causes cations to accumulate in front of the cathode, resulting in a voltage drop across the interface, which is not captured by this model.

The model of Pongsaksawad et al. [8] describes all-solid and all-liquid binary and ternary systems, though mixed solid-liquid systems (e.g. solid electrode and liquid electrolyte) are not yet covered by this model. The motivating applications are the electric-field-enhanced smelting and refining process (EFESR) in which iron is reduced from liquid slag containing iron oxide, and magnesiothermic reduction of titanium dichloride. An illustration of the former is shown in Figure 18.3.

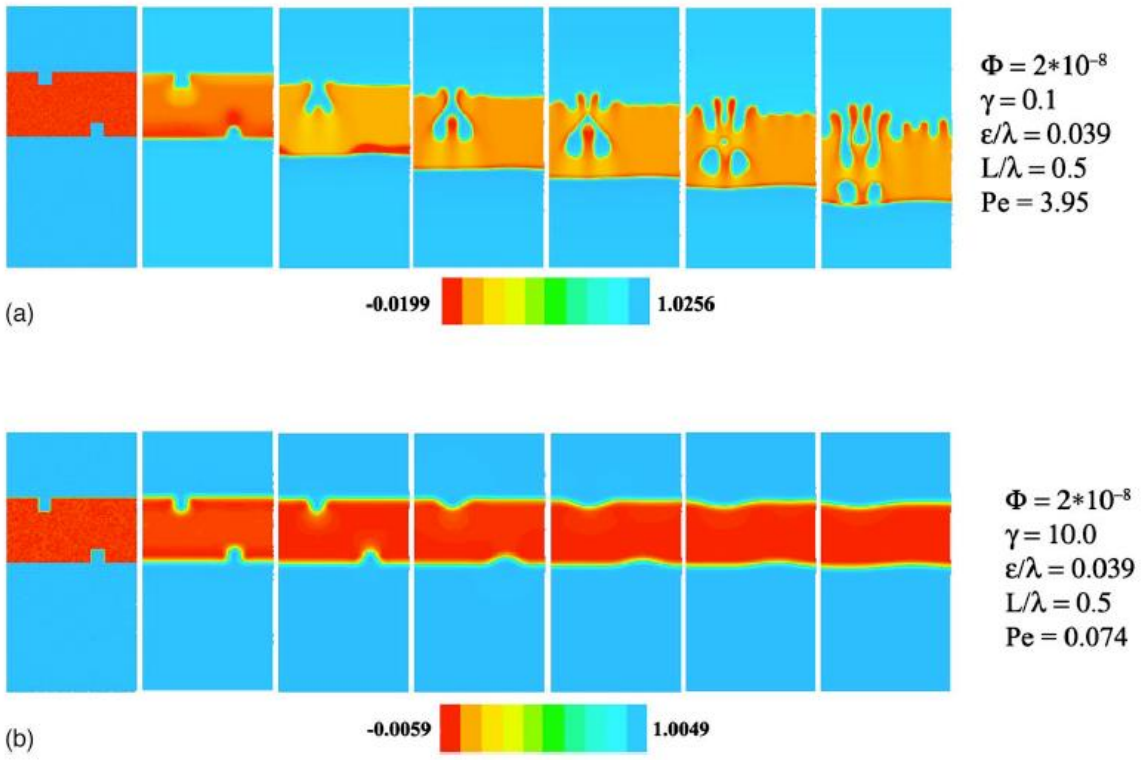

Figure 18.3 Interface dynamics without convection: (a) cathode shape evolution under high electric field on a 150 300 grid (the perturbed cathode interface is unstable) and (b) cathode shape evolution under high surface tension on an 80 160 grid (the perturbed cathode interface is stable). The left contour represents the initial condition with a three-layer structure, metal/electrolyte/metal. The cathode interface evolves with time as shown in the figures on the right. The scales on the bottom of each figure indicate the average maximum and minimum compositions throughout each simulation domain. [8]

Here a simplified three-layer structure of the binary system (Fe–FeO–Fe) is used as an initial condition. The voltage at the upper boundary is set to 0 (cathode) and that at the lower layer is set to 1 (anode). The interface instability due to change in electrical potential and surface energy is investigated first for the solid Fe–FeO system. One small box perturbation is introduced to each electrode interface. The perturbation on the anode disappears because it is preferentially oxidized and dissolved due to the concentration of the electric field there. At a low surface energy shown in Figure 18.3a, large electrical potential results in the formation of dendrites at the cathode, which may short-circuit the system or break into droplets, as observed in experiments. At a larger surface energy shown in Figure 18.3b, the perturbation on the cathode is flattened. They also investigated the influence of viscosity on the electrode stability after perturbations and even performed 3D simulations.

18.3. Electronically mediated reaction

The binary model of Pongsaksawad et al. [8] was extended to a ternary system. This model can capture electronically mediated reactions (EMR), such as metallothermic reduction. They simulated for example the reaction (without any voltage applied on the system) between titanium dichloride and magnesium to produce titanium and magnesium chloride. One- and two-dimensional ternary simulations show qualitatively correct interface motion and electrical potential behaviour. However, this model assumes regular solutions with miscibility gaps, thus, the free energy includes logarithmic

functions, such that values of zero and unity of phase variables are not allowed. Moreover, a chemical driving force for the redox reaction is introduced in the homogeneous free energy expression. However, the argumentation behind the definition of this term is not clear, the use of this term is only applicable for the abovementioned system and the system is still idealized, i.e. it considers regular solutions. Further modification of this model is necessary to include multiphase systems, as at the moment it describes only all-liquid or all-solid systems. Figure 18.4 illustrates the results for a simulation where Mg and Ti are in contact, which allows the electrons from the Mg/$MgCl_2$ interface to be conducted through this metal phase to the $TiCl_2$/Ti interface. The voltage is high where the positive charge is produced at the $TiCl_2$/Ti interface and low where the electrons are produced at the Mg/$MgCl_2$ interface.

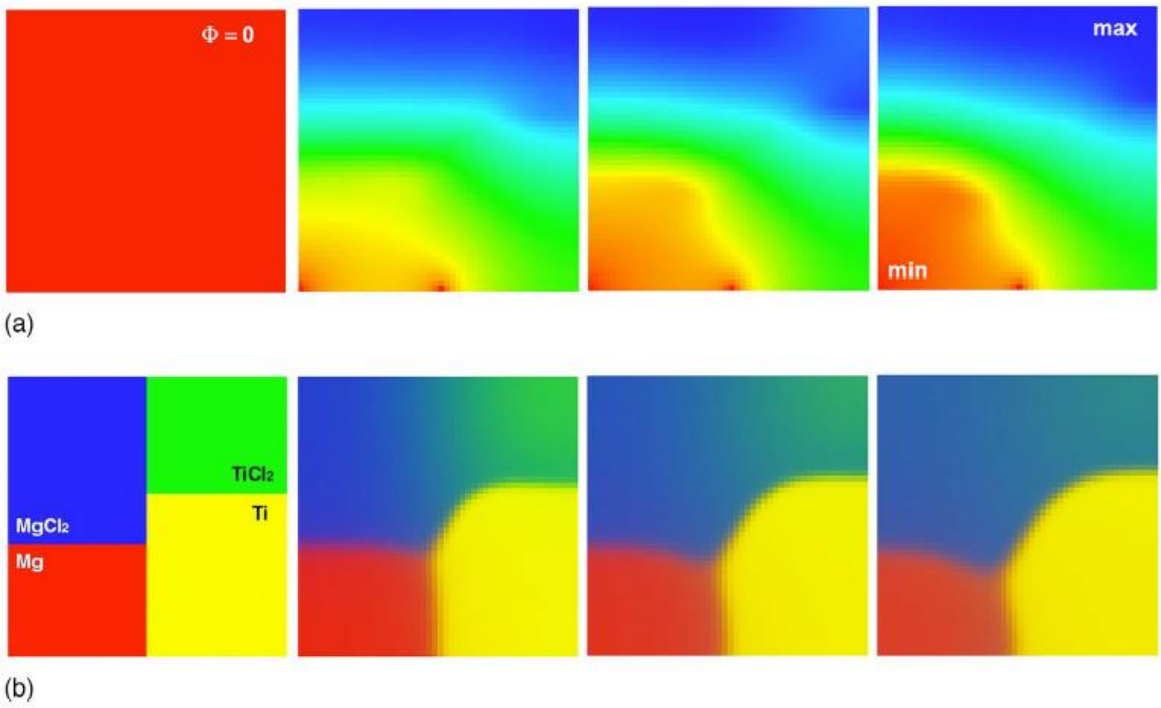

Figure 18.4 Closed-circuit simulation with Ti and Mg phases in contact. In the electrical potential contour plot, red indicates low and blue indicates high value of electrical potential, as labelled by min and max on the figure. The Mg, $MgCl_2$, $TiCl_2$, and Ti phases are coloured red, blue, green, and yellow, respectively, as also shown by labels. Ti formation is by chemical reduction at the Ti–Mg–chlorides triple point and by EMR between the Ti–TiCl2 and Mg–MgCl2 interfaces. The resolution is 50x50. (a) Electrical potential field. (b) Phase field. [8]

This observation clearly illustrates that this is an electronically mediated reaction (EMR), because even though a high-temperature electrochemical reaction is a mass-transport limited process. Nonetheless, the electron transport between metals also has a significant effect on the product morphology as explained by Okabe and Waseda [9]. This simulation illustrates that titanium can be formed even when the reactants ($TiCl_2$ and Mg) are not in physical contact as long as there is an electron conducting medium to transfer electrons (the metal phases) [8]. A further demonstration of the EMR through the product Ti phase is illustrated by Figure 18.5, where Mg and $TiCl_2$ are set up to be in direct contact. The Ti phase then forms at this interface and in contact with the Mg, after which it serves as an electronically conducting path for the EMR.

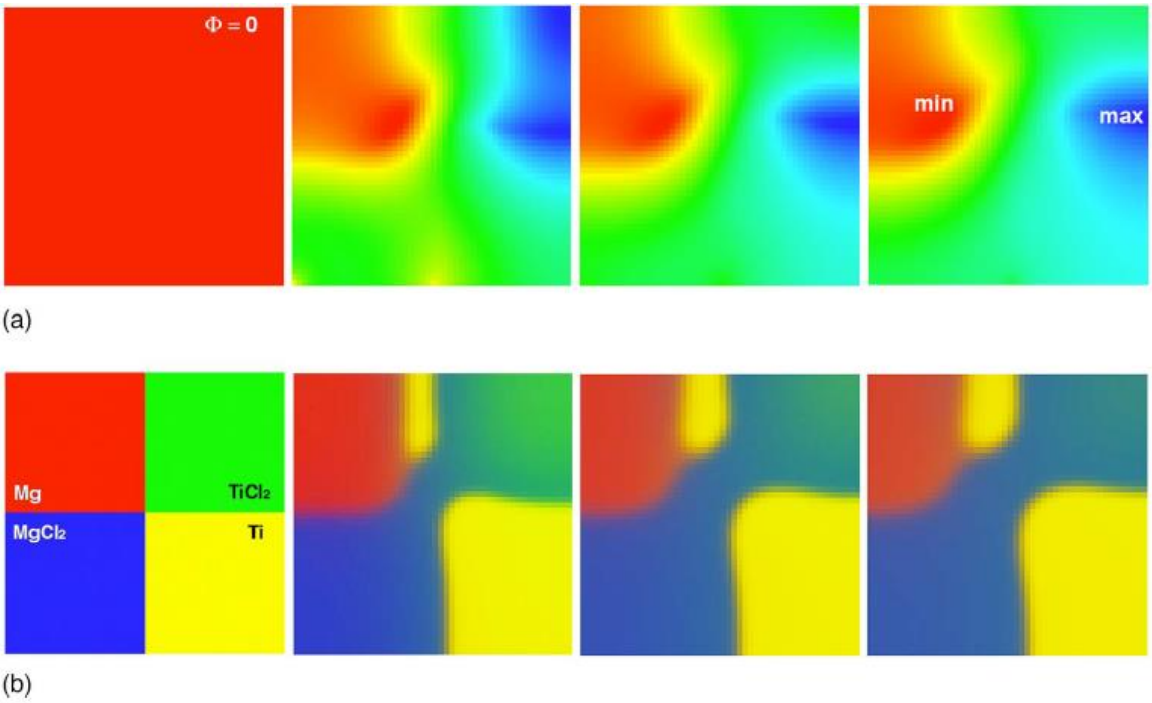

Figure 18.5 2D model with $Mg/TiCl_2$ in contact. Titanium is first formed by a chemical reaction at the $Mg/TiCl_2$ interface. More titanium plating then proceeds by EMR as indicated by the change in voltage across that titanium phase. The resolution is 50 50. (a) Voltage field. (b) Phase field. [8]

Another test run was also done on a simple configuration of a three-layer structure (top: $TiCl_2$ – middle: Ti and $MgCl_2$ – bottom: Mg). First, titanium formation occurs by EMR due to movement of electrons from Mg-$MgCl_2$ interface through titanium to Ti-$TiCl_2$ interface. Later, diffusion of $TiCl_2$ reaches the magnesium layer and titanium nuclei form on the magnesium/electrolyte layer. These nuclei continue to grow. Finally, the small particles coarsen. These simulations suggest that magnesiothermic reduction is delayed when the direct contact between the reactants is blocked. However, since $TiCl_2$ can diffuse into the blocking layer, titanium particles still form spontaneously. All of these observations can be used to understand the basic phenomena that occur in this system and to help design the experimental study. [10]

18.4. Deposition on electrode

Shibuta et al. [11] provide a model similar to the model of Pongsaksawad et al. [8], but use an order parameter field with thin-interface limit parameters, which describe the motion of the interface quantitatively. The model is based on the description by Kim et al. [12] and can capture both deposition and dissolution processes during electrochemical processes. However, a dilute-solution approximation and an ideal-solution approximation are adopted to define the free-energy densities of the electrode and the electrolyte phase, respectively. Using this model, an electrodeposition process of copper deposits from copper-sulphate solution was studied. The dependence of the growth velocity of the electrode on the applied voltage was examined in a one-dimensional system. Then, the growth process of dendritic deposits of Cu was calculated in a two-dimensional (2-D) system. The dependence of morphology on the applied voltage and the electrolyte concentration was examined and is shown in Figure 18.6. Thin and dense branches were observed at a low applied voltage. The shape of the branches became more complicated as the composition ratio was lowered.

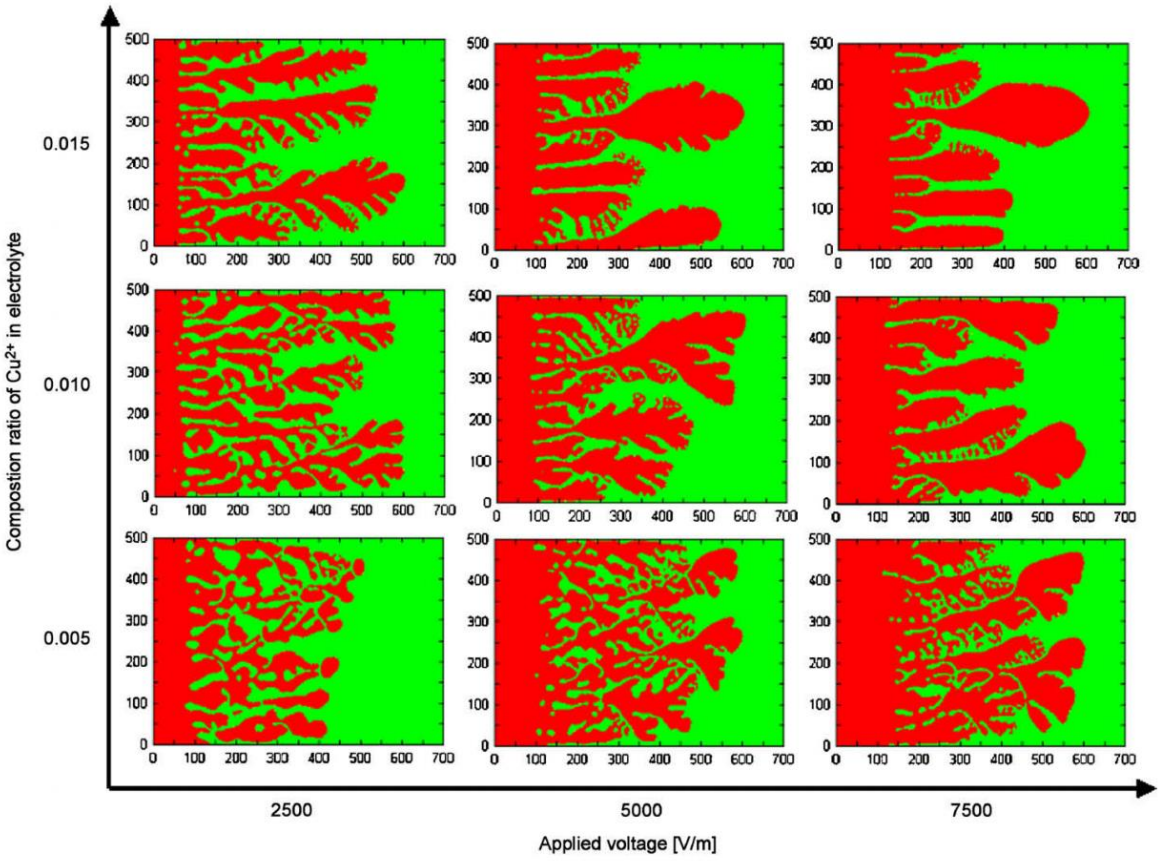

Figure 18.6 A morphological diagram of the electrodeposits as functions of the applied voltage (2500, 5000 and 7500 V/m) and composition ratio of Cu^{2+} in electrolyte (0.015, 0.01 and 0.005). The snapshots taken when the most protruding branch reached 60.0 mm were compared (except for the condition of C_0 = 0.005, 2500 V/m due to the computational limit) [11]

In the previous model [11], the electrical current was considered in terms of the electric potential gradient in the equation of charge conservation. In that equation, the chemical potential gradient was neglected assuming electromigration to be the dominant factor determining the electrical current. The remaining problem in the phase field model of the electrochemical process is how to treat the electrode reaction across the interface since the concept of a redox reaction at the interface was ignored in the previous model.

18.5. Non-linearity

Okajima et al. [13] extended the previous model by taking Butler-Volmer kinetics at the electrode/electrolyte interface into account. This was done by introducing a certain asymmetry, which is characteristic for redox reactions, to the diffusivity, with an exponential factor of the asymmetry coefficient. Using this model, the kinetics and morphology of the electrode/electrolyte interface during an electrode reaction have been investigated. The numerical results satisfied the Nernst relationship and confirmed the relation between the growth velocity of the interface and the overpotential. The tip radius is, in turn, proportional to the inverse of the square root of the growth velocity, which agrees with the dendrite growth theory for solidification. Even though the model includes several assumptions (ideal solution and ideal diluted solutions for the electrolyte and electrode, respectively), it shows that phase field simulations can be helpful to clarify complicated electrochemical reactions.

In a similar way, Ma et al. [14] used an Arrhenius relationship in the expression for the coefficient of the Cahn-Hilliard equation, which describes the evolution of the oxidation state of the material. However, in both models, the diffusional mobility might have an exponential dependence on the overpotential, but the rate of electroplating is still linearly proportional to the thermodynamic driving force. Later, Liang et al. [15] developed a more intricate nonlinear phase field model for electrode-electrolyte interface evolution driven by the overpotential. They wanted to describe the temporal and spatial evolution of the phase field variable by the difference of two exponentials of the driving force, motivated by classical rate theory of chemical reaction kinetics. However, a simplified form of the non-linear equation was required and thus the interface migration velocity was assumed to be linearly proportional to the interfacial energy reduction, but nonlinearly with respect to the overpotential.

18.6. Reactive wetting

Reactive wetting also involves redox reactions, albeit without the presence of an electrode. Villanueva et al. [16–18] developed a phase field model for this purpose. Reactive wetting involves a chemical change and/or diffusion of chemical species. There are two cases: a concentration change of the spreading liquid and the substrate or the formation of a new phase or phases between the liquid and the substrate. The first case was modelled by Villanueva et al. [16,17]. Their model describes a ternary system of substitutional elements with three phases in a system with fluid motion, by introducing convective concentration and coupling to Navier-Stokes equations with surface tension forces. The solid substrate is modelled hydrodynamically with a very high viscosity. For simplicity, an ideal solution was assumed to describe the molar Gibbs free energy and the thermodynamic data were retrieved from simple and idealized phase diagrams. Two stages occurred in the wetting process: a convection-dominated stage where rapid spreading occurs and a diffusion-dominated stage where depression of the substrate-liquid interface and elevation of the contact line region were observed.

The first binary model of Villanueva et al. [16,17] considers droplets that do not exhibit inertial effects due to the small drop size, which is limited by the requirement of having a narrow interface (≈1 nm). Wheeler et al. [19], in contrast, sacrificed the realistic interface width in an attempt to model a system that exhibits inertial effects. Due to the drop size restrictions, the extent of spreading during the inertial stage is limited and the characteristic inertial effects are suppressed by viscous forces. They investigated a three-phase binary alloy in a parameter regime where the inertial effects were initially dominant and the transition from inertial to viscous or diffusive spreading is also characterized well. At late times, after inertial effects have ceased, the local interface equilibration mechanism is controlling the spreading.

The first binary model of Villanueva et al. [16,17] was expanded to a ternary system with four phases to model reactive wetting with intermetallic formation [18], also incorporating fluid flow, phase change and solute diffusion. Numerical simulations were performed using a mesh-adaptive finite element method, revealing the complex behaviour of the reactive wetting process, an illustration is shown in Figure 18.7. Dynamic results showed that the intermetallic can either precede or follow the spreading liquid droplet, depending on the time and the choice of interface energy and kinetic coefficients.

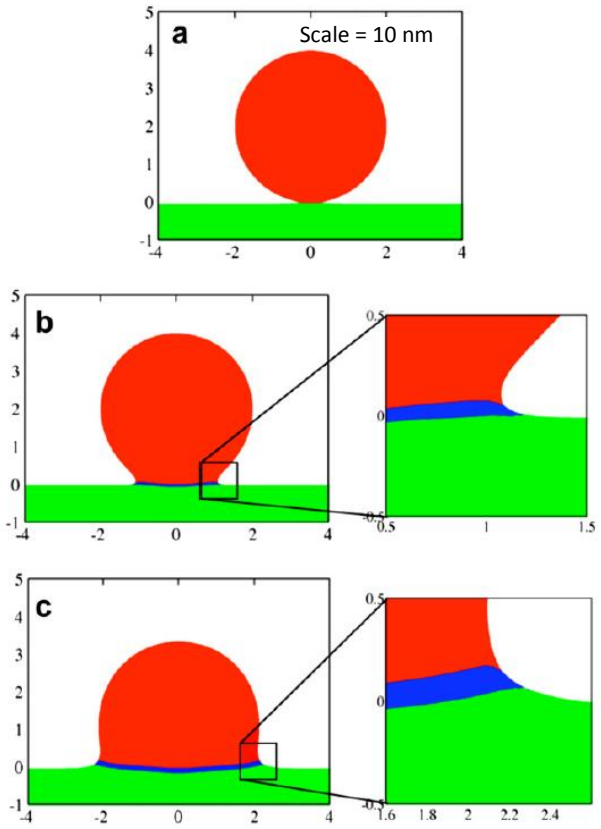

Figure 18.7 Simulation result of the maximum phase field plot at t/t_c = 0, 1, 200 with the base set of parameters [18]

However, the model still used equilibrium states derived from a classical phase diagram, while assuming an ideal solution model for the Gibbs free energy of the liquid, solid and vapour and a regular solution model for the Gibbs free energy of the intermetallic phase. Moreover, only small system sizes can be simulated with this model.

Later, Wang and Nestler [20] investigated the formation of an Al_2Au intermetallic phase at the interface between an Al-liquid droplet on top of an Au solid substrate with 3D simulations. They also present a new concept that lateral spreading of the intermetallic phase is due to wetting, which differs from the idea of grain boundary diffusion.

By placing an Al-liquid droplet on an Au-solid substrate, the amount of Au in the liquid tends to approach the equilibrium mole fraction. This is achieved by diffusion of Au into the Al-liquid. Thereafter, Al and Au combines with a ratio of 2, forming the intermetallic phase Al_2Au. Due to the surface energy relation: $\gamma_{SL} > \gamma_{SI} + \gamma_{LI}$, the triple point of solid–liquid–intermetallic phase is not stable, resulting in the growth of the intermetallic phase in the horizontal direction. This relation was also proposed by Villanueva et al. [18] for the intermetallic Sn–0.7Cu on a Cu substrate. During the spreading of the intermetallic phase, the Au atoms constantly diffuse into the Al-liquid, which provides the source for the later growth of the intermetallic phase in the vertical direction. When the two triple points SIV and LIV are established, i.e. when the solid-liquid interface is completely covered by the intermetallic phase, the spreading of the intermetallic phase in the horizontal direction stops. The intermetallic phase then grows in the vertical direction, increasing its thickness. At this stage, the liquid is no longer in contact with the solid. Since the diffusivity of Au in liquid Al is greater than the one in solid Au, the intermetallic phase grows into the liquid droplet. This is also illustrated in Figure 18.8.

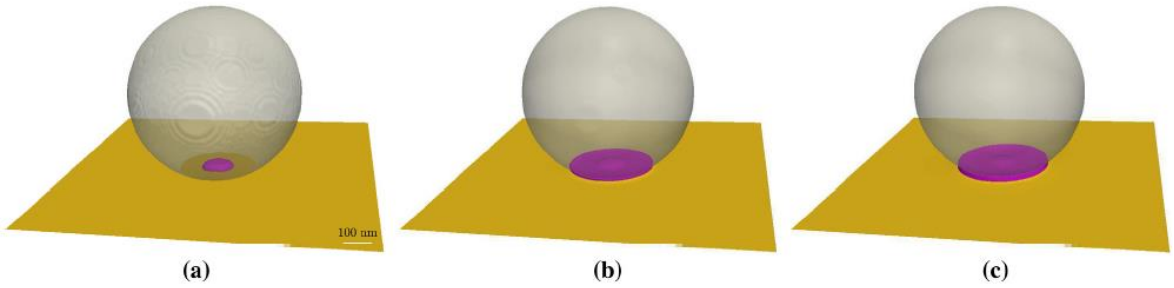

Figure 18.8 Time evolution of the intermetallic phase Al_2Au from a phase field simulation: (a) earlier stage of the intermetallic phase Al_2Au inside the Al-droplet, (b) spreading of the intermetallic phase in the horizontal direction, (c) growth of the intermetallic phase in the vertical direction. [20]

18.7. Incorporation of chemical reaction kinetics

Based on the work of Sekerka and Bi [21], Gathright et al. [22] presented a phase field model for an electrochemical system with chemically active species. They explicitly incorporate a term including the rate of the chemical reaction(s) under consideration. One big disadvantage for such a model is the fact that knowledge is required about which reactions take place in the system and care must be taken that none are forgotten, to be able to model a realistic system. The latter is easy for a binary system, but becomes less self-evident for multicomponent systems. Later, Hong et al. [23] used a similar model to investigate the ionic/electronic transport across the cathode/electrolyte interface in solid oxide fuel cells.

Bazant [24] developed a phase field theory of electrochemical kinetics by combining charge-transfer theory with concepts from statistical physics and non-equilibrium thermodynamics. It resulted in a single equation that generalizes the Cahn-Hilliard and Allen-Cahn equations for reaction-diffusion phenomena and it is called Cahn-Hiliard reaction (CHR) model. For charged species, the theory generalizes the Poisson-Nernst-Planck equations of ion transport, the Butler-Volmer equation of electrochemical kinetics and the Marcus theory of charge transfer for concentrated electrolytes and ionic solids. This equation was used by Cogswell and Bazant [25] to study the physics of nucleation in solid single-crystal nanoparticles, more explicitly: the model is used to simulate phase separation in realistic nanoparticle geometries for Li_xFePO_4, which is used as a cathode material in Li-ion batteries. They showed that the nucleation in single-crystal nanoparticles is size-dependent, due to surface adsorption which leads to coherency strain. Thus, the nucleation barrier decreases with the area-to-volume ratio. The model was extended to three phases and was used to simulate lithium intercalation in a porous iron phosphate cathode and was also used to investigate the changing phase transformations between the three stable phases in a porous graphite anode by Ferguson and Bazant [26]. For the latter, Figure 18.9 illustrates a comparison between experimental observations and the simulation results. For both processes, the phases present were assumed to be regular solutions.

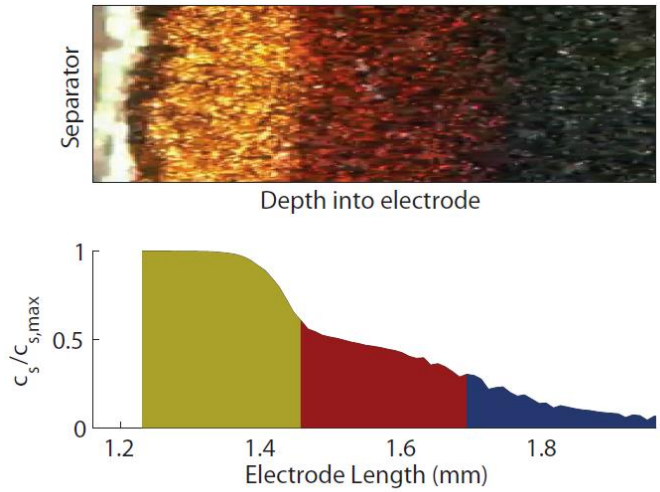

Figure 18.9 Graphite MPET simulations vs. experiment. Experimental image (above) and simulated colour profile (below) at the same moment in time, capturing the blue/red and red/gold interface positions and noise. [26]

Heo et al. [27] also used the CHR model to simulate diffusional phase microstructural evolution at solid surfaces. Depending on the strength of the interaction between the solute and the interface, two different surface spinodal decomposition modes were predicted: the surface mode of coherent spinodal decomposition and the surface-directed spinodal decomposition mode. In the former, no explicit interaction between the solute atoms and the surface can be observed, whereas in the latter, the interaction induces surface segregation of the solute that acts as the dominant perturbation of the surface composition, over the natural thermal fluctuations, resulting in surface-initiated spinodal decomposition. The latter phenomenon was also observed by Bellemans et al. [28] and was denoted 'localized spinodal decomposition'.

18.8. Metal oxidation and possible stress generation

Asle Zaeem and El Kadiri [29] elaborated a multi-phase field model for non-selective oxidation of metals incorporating both the oxidation kinetics and stress generation by coupling the phase field evolution equations to the mechanical equilibrium equations with the use of COMSOL [30]. The model predicts the oxygen composition depth and stress profile in the oxide layer and the metal-oxide interface and proved its usefulness by prediction of the observed evolution of oxide thickness and growth stresses for the oxidation of Zircaloy-4 at 900°C. They concluded that the oxidation generates stresses, which in turn slows downs the oxidation kinetics.

Apel et al. [31] and Berger et al. [32] used the MICRESS [33] software to simulate the microstructure evolution in Ag-Cu brazing fillers for conditions close to reactive air brazing (a method commonly used to join metals to ceramics). The simulations were then used to calculate the volume expansion due to phase transformations (and the resulting eigenstrains) and DSC curves, allowing comparison to experimental observations. However, due to the lack of thermodynamic databases for the brazing filler material in combination with data for the substrate materials, any reactions between brazing filler and base materials were neglected in the simulations. One of the obtained simulation results for an Ag-Cu brazing filler is shown in Figure 18.10.

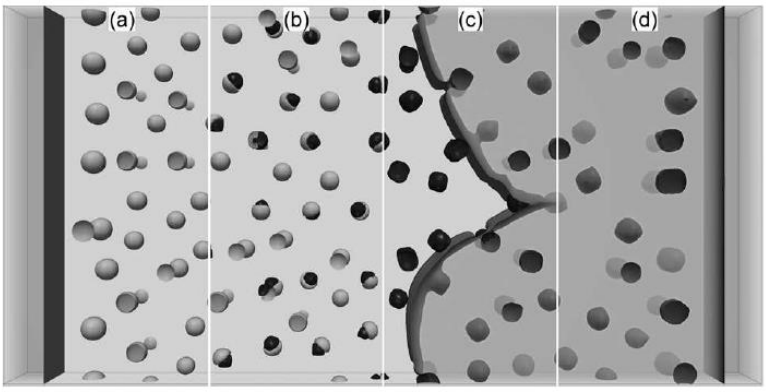

Figure 18.10 Simulated microstructure evolution during RAB, left to right: (a) 1238 K, demixed L2 (a Cu-rich liquid phase) drops in L1 (transparent, an Ag-rich liquid phase), (b) 1223 K, L2 → CuO reaction, (c) 1183 K, L1 → fcc reaction, (d) 1168 K, solidified fcc-Ag with embedded oxide particles (CuO). Microstructure evolution in a brazing joint, Ag8at%Cu. The simulation clearly indicates the general phase formation sequence according to the phase diagram: L1+L2 → L1 + CuO → CuO + fcc-Ag [32]

Similarly, Ta et al. [34] used MICRESS [33] to investigate the effect of a temperature gradient on the microstructure evolution in various Ni-Al-Cr bond coat/substrate systems. As a complete database of the system was present in this case, the phase field model was coupled to a CAPLHAD database.

References

[1] M. Ozawa, S. Kitagawa, S. Nakayama, Y. Takesono, Reduction of FeO in Molten Slags by Solid Carbon in the Electric Arc Furnace Operation, Trans. Iron Steel Inst. Jpn. 26 (1986) 621–628. doi:10.2355/isijinternational1966.26.621.

[2] R.D. Morales, A.N. Conejo, H.H. Rodriguez, Process dynamics of electric arc furnace during direct reduced iron melting, Metall. Mater. Trans. B. 33 (n.d.) 187–199. doi:10.1007/s11663-002-0004-7.

[3] M. Barati, K.S. Coley, Kinetics of CO-CO2 reaction with CaO-SiO2-FeOx melts, Metall. Mater. Trans. B. 36 (2005) 169–178. doi:10.1007/s11663-005-0017-0.

[4] J.E. Guyer, W.J. Boettinger, J.A. Warren, G.B. McFadden, Phase field modeling of electrochemistry. I. Equilibrium., Phys. Rev. E Stat. Nonlin. Soft Matter Phys. 69 (2004) 021603. doi:10.1103/PhysRevE.69.021603.

[5] J.E. Guyer, W.J. Boettinger, J.A. Warren, G.B. McFadden, Phase field modeling of electrochemistry. II. Kinetics, Phys. Rev. E Stat. Nonlin. Soft Matter Phys. 69 (2004) 021604.

[6] D. Dussault, A.C. Powell, Phase Field Modeling of Electrolysis in a Slag or Molten Salt, in: Proc Mills Symp, The Institute of Materials, London, 2002: pp. 359–371.

[7] H. Assadi, Phase-field modelling of electro-deoxidation in molten salt, Model. Simul. Mater. Sci. Eng. 14 (2006) 963. doi:10.1088/0965-0393/14/6/006.

[8] W. Pongsaksawad, A.C. Powell, D. Dussault, Phase-Field Modeling of Transport-Limited Electrolysis in Solid and Liquid States, J. Electrochem. Soc. 154 (2007) F122–F133. doi:10.1149/1.2721763.

[9] T.H. Okabe, Y. Waseda, Producing titanium through an electronically mediated reaction, JOM. 49 (1997) 28–32. doi:10.1007/BF02914710.

[10] W. Pongsaksawad, Numerical modeling of interface dynamics and transport phenomena in transport-limited electrolysis processes, Thesis, Massachusetts Institute of Technology, 2006. http://dspace.mit.edu/handle/1721.1/36209 (accessed July 25, 2016).

[11] Y. Shibuta, Y. Okajima, T. Suzuki, Phase-field modeling for electrodeposition process, Sci. Technol. Adv. Mater. 8 (2007) 511–518. doi:10.1016/j.stam.2007.08.001.

[12] S.G. Kim, W.T. Kim, T. Suzuki, Phase-field model for binary alloys, Phys. Rev. E. 60 (1999) 7186–7197. doi:10.1103/PhysRevE.60.7186.

[13] Y. Okajima, Y. Shibuta, T. Suzuki, A phase-field model for electrode reactions with Butler–Volmer kinetics, Comput. Mater. Sci. 50 (2010) 118–124. doi:10.1016/j.commatsci.2010.07.015.
[14] Y. Ma, X. Yao, W. Hao, L. Chen, D. Fang, Oxidation mechanism of ZrB2/SiC ceramics based on phase-field model, Compos. Sci. Technol. 72 (2012) 1196–1202. doi:10.1016/j.compscitech.2012.04.003.
[15] L. Liang, Y. Qi, F. Xue, S. Bhattacharya, S.J. Harris, L.-Q. Chen, Nonlinear phase-field model for electrode-electrolyte interface evolution, Phys. Rev. E. 86 (2012) 051609. doi:10.1103/PhysRevE.86.051609.
[16] W. Villanueva, K. Grönhagen, G. Amberg, J. Ågren, Multicomponent and multiphase modeling and simulation of reactive wetting, Phys. Rev. E. 77 (2008) 056313. doi:10.1103/PhysRevE.77.056313.
[17] W. Villanueva, W.J. Boettinger, J.A. Warren, G. Amberg, Effect of phase change and solute diffusion on spreading on a dissolving substrate, Acta Mater. 57 (2009) 6022–6036. doi:10.1016/j.actamat.2009.08.033.
[18] W. Villanueva, W.J. Boettinger, G.B. McFadden, J.A. Warren, A diffuse-interface model of reactive wetting with intermetallic formation, Acta Mater. 60 (2012) 3799–3814. doi:10.1016/j.actamat.2012.03.047.
[19] D. Wheeler, J.A. Warren, W.J. Boettinger, Modeling the early stages of reactive wetting, Phys. Rev. E. 82 (2010) 051601. doi:10.1103/PhysRevE.82.051601.
[20] F. Wang, B. Nestler, A phase-field study on the formation of the intermetallic Al2Au phase in the Al–Au system, Acta Mater. 95 (2015) 65–73. doi:10.1016/j.actamat.2015.05.002.
[21] R.F. Sekerka, Z. Bi, Phase field model of multicomponent alloy slidification with hydrodynamics, in: Interfaces 21st Century New Res. Dir. Fluid Mech. Mater. Sci., PUBLISHED BY IMPERIAL COLLEGE PRESS AND DISTRIBUTED BY WORLD SCIENTIFIC PUBLISHING CO., 2002: pp. 147–166. http://www.worldscientific.com/doi/abs/10.1142/9781860949609_0011 (accessed July 26, 2016).
[22] W. Gathright, M. Jensen, D. Lewis, Phase field model of chemical reactions with an example of a solid electrolyte gas sensor, Electrochem. Commun. 13 (2011) 520–523. doi:10.1016/j.elecom.2011.02.038.
[23] L. Hong, J.-M. Hu, K. Gerdes, L.-Q. Chen, Oxygen vacancy diffusion across cathode/electrolyte interface in solid oxide fuel cells: An electrochemical phase-field model, J. Power Sources. 287 (2015) 396–400. doi:10.1016/j.jpowsour.2015.04.090.
[24] M.Z. Bazant, Theory of Chemical Kinetics and Charge Transfer based on Nonequilibrium Thermodynamics, Acc. Chem. Res. 46 (2013) 1144–1160. doi:10.1021/ar300145c.
[25] D.A. Cogswell, M.Z. Bazant, Theory of Coherent Nucleation in Phase-Separating Nanoparticles, Nano Lett. 13 (2013) 3036–3041. doi:10.1021/nl400497t.
[26] T.R. Ferguson, M.Z. Bazant, Phase Transformation Dynamics in Porous Battery Electrodes, ArXiv14017072 Cond-Mat Physicsphysics. (2014). http://arxiv.org/abs/1401.7072 (accessed November 27, 2014).
[27] T.W. Heo, L.-Q. Chen, B.C. Wood, Phase-field modeling of diffusional phase behaviors of solid surfaces: A case study of phase-separating LiXFePO4 electrode particles, Comput. Mater. Sci. 108, Part B (2015) 323–332. doi:10.1016/j.commatsci.2015.03.020.
[28] I. Bellemans, N. Moelans, K. Verbeken, Phase field modelling of the attachment of metallic droplets to solid particles in liquid slags: Influence of interfacial energies and slag supersaturation, Comput. Mater. Sci. 108, Part B (2015) 348–357. doi:10.1016/j.commatsci.2015.03.019.
[29] M. Asle Zaeem, H. El Kadiri, An elastic phase field model for thermal oxidation of metals: Application to zirconia, Comput. Mater. Sci. 89 (2014) 122–129. doi:10.1016/j.commatsci.2014.03.042.
[30] COMSOL Multiphysics® Modeling Software, n.d. https://www.comsol.com/ (accessed July 27, 2016).

[31] M. Apel, G. Laschet, B. Böttger, R. Berger, Phase Field Modeling of Microstructure Formation, DSC Curves, and Thermal Expansion for Ag-Cu Brazing Fillers Under Reactive Air Brazing Conditions, Adv. Eng. Mater. 16 (2014) 1468–1474. doi:10.1002/adem.201400101.
[32] R. Berger, M. Apel, B. Böttger, Phase Field Modeling Applied to Reactive Air Brazing: Investigating Reaction Kinetics with Focus on Oxygen Exchange, Adv. Eng. Mater. 16 (2014) 1475–1481. doi:10.1002/adem.201400103.
[33] about MICRESS, n.d. http://web.micress.de/aboutmicress.html (accessed July 27, 2016).
[34] N. Ta, L. Zhang, Y. Tang, W. Chen, Y. Du, Effect of temperature gradient on microstructure evolution in Ni–Al–Cr bond coat/substrate systems: A phase-field study, Surf. Coat. Technol. (n.d.). doi:10.1016/j.surfcoat.2014.10.061.

List of publications

Publications in internationally peer-reviewed journals

[1] I. Bellemans, N. Moelans, K. Verbeken, Phase field modelling of the attachment of metallic droplets to solid particles in liquid slags: Influence of interfacial energies and slag supersaturation, Comput. Mater. Sci. 108, Part B (2015) 348–357. doi:10.1016/j.commatsci.2015.03.019.

[2] I. Bellemans, E. De Wilde, N. Moelans, K. Verbeken, Phase field modelling of the attachment of metallic droplets to solid particles in liquid slags: Influence of particle characteristics, Acta Mater. 101 (2015) 172–180. doi:10.1016/j.actamat.2015.08.074.

[3] I. Bellemans, E. De Wilde, N. Moelans, K. Verbeken, Phase field simulation study of the attachment of metallic droplets to solid particles in liquid slags based on real slag–spinel micrographs, Comput. Mater. Sci. 118 (2016) 269–278. doi:10.1016/j.commatsci.2016.03.022.

[4] I. Bellemans, E. De Wilde, L. Claeys, T. De Seranno, M. Campforts, B. Blanpain, N. Moelans, K. Verbeken, Investigation of reactive origin for attachment of Cu-droplets to solid particles, Metall. Mater. Trans. B. (Submitted).

[5] I. Bellemans, E. De Wilde, B. Blanpain, N. Moelans, K. Verbeken, Investigation of origin of attached Cu-Ag-droplets to solid particles during high temperature slag/copper/spinel interactions, Metall. Mater. Trans. B. (Submitted).

[6] I. Bellemans, E. De Wilde, N. Moelans, K. Verbeken, Metal losses in pyrometallurgical operations - a review, Adv. Colloid Interface Sci. (Submitted).

[7] I. Bellemans, N. Moelans, K. Verbeken, Phase field modelling in extractive metallurgy, Crit. Rev. Solid State Mater. Sci. (Submitted).

[8] I. Bellemans, N. Moelans, K. Verbeken, Influence of rigid body motion on the wetting and attachment of metallic droplets to solid particles in liquid slags – a phase field study, Min. and Metall. Process. (Submitted).

[9] E. De Wilde, I. Bellemans, M. Campforts, A. Khaliq, K. Vanmeensel, D. Seveno, M. Guo, A. Rhamdhani, G. Brooks, B. Blanpain, N. Moelans, K. Verbeken, Wetting behaviour of Cu based alloys on spinel substrates in pyrometallurgical context, Mater. Sci. Technol. 31 (2015) 1925–1933. doi:10.1179/1743284715Y.0000000052.

[10] E. De Wilde, I. Bellemans, L. Zheng, M. Campforts, M. Guo, B. Blanpain, N. Moelans, K. Verbeken, Origin and sedimentation of Cu-droplets sticking to spinel solids in pyrometallurgical slags, Mater. Sci. Technol. 32 (2016) 1911–1924. doi:10.1080/02670836.2016.1151998.

[11] E. De Wilde, I. Bellemans, M. Campforts, M. Guo, B. Blanpain, N. Moelans, K. Verbeken, Sessile drop evaluation of high temperature copper/spinel and slag/spinel interactions, Trans. Nonferrous Met. Soc. China. 26 (2016) 2770–2783. doi:10.1016/S1003-6326(16)64344-3.

[12] E. De Wilde, I. Bellemans, M. Campforts, M. Guo, B. Blanpain, N. Moelans, K. Verbeken, Investigation of High-Temperature Slag/Copper/Spinel Interactions, Metall. Mater. Trans. B. 47 (2016) 3421–3434. doi:10.1007/s11663-016-0805-8.

[13] E. De Wilde, I. Bellemans, M. Campforts, M. Guo, K. Vanmeensel, B. Blanpain, N. Moelans, K. Verbeken, Study of the effect of spinel composition on metallic copper losses in slags, J. Sustain. Metall. 3 (2017) 416-427. doi:10.1007/s40831-016-0106-0.

Publications in proceedings of international conferences

[14] E. De Wilde, I. Bellemans, S. Vervynckt, M. Campforts, K. Vanmeensel, N. Moelans, K. Verbeken, Towards a methodology to study the interaction between Cu droplets and spinel particles in slags, in: Proc. EMC 2013, 2013: pp. 161–174.

[15] I. Bellemans, N. Moelans, K. Verbeken, Modeling the mechanical entrainment of metal droplets by solid particles in liquid slags, in: Proc. EMC 2015, Düsseldorf, Germany, 2015: pp. 941-958.

[16] E. De Wilde, I. Bellemans, M. Campforts, M. Guo, K. Vanmeensel, B. Blanpain, N. Moelans, K. Verbeken, Wetting behaviour of spinel with copper to understand metalic copper losses to slags, in: Proc. EMC 2015, Düsseldorf, Germany, 2015: pp 3-18.

[17] E. De Wilde, I. Bellemans, M. Campforts, K. Verbeken, B. Blanpain, Study of mechanically entrained copper droplet losses in slags due to interaction with spinel solids, in: High Temp. Process. Symp. 2016, 2016: pp. 57–58.

[18] I. Bellemans, V. Cnockaert, E. De Wilde, N. Moelans, K. Verbeken, Metal droplet entrainment by solid particles in slags: a combined phase field model and experimental approach, in: Proc. 5th International Slag valorisation symposium 2017; 2017: pp 181-184.

[19] I. Bellemans, V. Cnockaert, E. De Wilde, N. Moelans, K. Verbeken, Metal droplet entrainment by solid particles in slags: a phase field - experimental approach, in: Proc. EMC 2017.

[20] V. Cnockaert, I. Bellemans, E. De Wilde, B. Blanpain, K. Verbeken, Towards an Experimental Set-up for Measuring the Foaming Stability of Liquid Slags, in: Proc. EMC 2017.

Presentations on international conferences

1. E. De Wilde, **I. Bellemans**, S. Vervynckt, M; Campforts, K. Vanmeensel, N. Moelans, K. Verbeken, Towards a methodology to study the interaction between Cu droplets and spinel particles in slags. European Metallurgical Conference (EMC 2013), Weimar, Germany. (Oral presentation)

2. **I. Bellemans**, N. Moelans, K. Verbeken, The influence of interfacial energy and particle morphology on the attachment of metallic droplets on a solid particle in liquid slag. Third International Symposium on Phase field Method 2014 (PFM 2014), State College, Pennsylvania, USA. (Poster presentation)

3. **I. Bellemans**, N. Moelans, K. Verbeken, Modelling the mechanical entrainment of metal droplets by solid particles in liquid slags. European Metallurgical Conference (EMC 2015), Düsseldorf, Germany. (Oral presentation)

4. E. De Wilde, **I. Bellemans**, M. Campforts, M. Guo, K. Vanmeensel, B. Blanpain, N. Moelans, K. Verbeken, Wetting behaviour of spinel with copper to understand metallic copper losses to slags. European Metallurgical Conference (EMC 2015), Düsseldorf, Germany. (Oral presentation)

5. **I. Bellemans**, N. Vervliet, L. De Lathauwer, N. Moelans, K. Verbeken, Multi-component multi-phase field model combined with tensorial decomposition. VSC User day 2015, Antwerpen, Belgium. (Poster presentation)

6. **I. Bellemans**, E. De Wilde, N. Moelans, K. Verbeken, Wettability of metal droplets on solid particles in liquid slags. MicroMAST 2016 Conference on Multiscale Applications of Surface Tension, Brussels Belgium. (Oral presentation)

7. **I. Bellemans**, E. De Wilde, N. Moelans, K. Verbeken, Metal droplet entrainment by solid particles in slags: a combined phase field – experimental approach. 8th International Conference on Multiscale Materials Modeling (MMM2016), Dijon, France. (Oral presentation)